A Numerical Investigation of Time Integration Schemes Applied to the Dynamic Solution of Mooring Lines

by

David O. Thomas

A Thesis submitted for the degree of
Doctor of Philosophy

Department of Marine Technology

The University of Newcastle upon Tyne
1993

Abstract

This thesis investigates the use of numerical methods to solve the static and dynamic behaviour of a single mooring line, some part of which may be lying on the seabed. For static analysis both the analytic catenary equations and a 3D numerical formulation are presented. Comparisons of results generated by the two approaches show generally good agreement. The numerical static model is used as the initial equilibrium position for the dynamic solution procedure. The equations of motion are developed in accordance with published theory, but whereas published theory have some aspects neglected, here all possible effects are included in the development of the theory and specific effects are only neglected when this can be justified.

The Central Difference, Houbolt, Wilson-θ and Newmark time integration schemes are then used to solve the 2D equations of motion. An important aspect of any numerical scheme is the accuracy and stability of the results generated by its use. Here the numerical stability and accuracy of the different time integration schemes used are discussed. Whereas these characteristics can be examined analytically when the equations being solved are linear, the aspects of the solution obtained from nonlinear formulations are generally unique in each case and must be examined numerically. It is therefore important that these aspects be explicitly examined to gain confidence regarding the general application of the solvers presented. The different schemes are therefore used in an extensive numerical study of the resulting predictions to determine the efficacy of these schemes when applied to the solution of nonlinear mooring dynamics.

A 3D formulation of the equations of motion is developed and solved with the Houbolt scheme. This more generally applicable solver is used to generate results of relevance to the design of mooring lines. In particular effort is directed towards the calculation of the dynamic tension amplification factors. These generated solutions can then be used to comment upon the safety factors used and required within the rules of the classification societies.

An alternative method of solution which uses the eigensolutions of a matrix form of the equations of motion is also presented. This method is common in small displacement finite element dynamics. However, the large displacement requirement imposed for mooring line dynamics requires some important new aspects in the solution procedure to be considered. These include the updating of the modal matrix and the use of different time steps with the uncoupled equations. Considerations such as these do not appear to have been fully appreciated in the literature associated with mooring line dynamics as solved by modal methods.

A section detailing the influence of 'ground effects' is also presented. These include the effects of suction and friction upon the grounded portion of the line and the discretisation problems caused by the lifting and grounding of the node masses.

This thesis presents for the first time a detailed comparison of the predictions of mooring line dynamics using different time integration schemes. The comparisons indicate which scheme is to be preferred, highlight the numerical problems which can be expected to affect the quality of the solution, and how best to avoid the noted numerical problems.

CONTENTS

LIST OF TABLES

Acknowledgements

I would like to thank my supervisor Professor G. E. Hearn whose undergraduate lectures inspired me to undertake a research program and who gave advice and forbearance during my research.

Drs S. M. Lau and S. Y. Liou provided the greatest encouragement and advice during the early stages of my work. Kadir Sarioz and Paul Goodwin lent immeasurably, both professionally and personally, during the last two years. All are thanked for these kindnesses.

Dr. Eko Panunggal is thanked for allowing ideas to be freely bounced off and Dr. Brian Murray without whom much of the computing would have taken considerably longer.

Financial support during the course of this study has been provided by the Science and Engineering Research Council, for which I am grateful.

Nomenclature

A	Element cross sectional area
$A_{j-\frac{1}{2}}^{n+1}$	Derivative of the segment error function
$A_{ax'}, A_{az'}$	Apparent water particle accelerations in the x' and z' axes
$\underline{A}$	Modal matrix
A_b	Effective bearing area per unit length of the line
A_c	Effective surface area of mooring line element
$\underline{A_i}$	Column modal matrix of displacements for the i^{th} mode
A_e	Vector of excitation amplitudes
$A_{x,y,z}$	Cartesian components of excitation amplitudes
A_m	Amplitude of the m^{th} harmonic of the error term
A_s	Effective sliding area per unit length of the line
$B_{j-\frac{1}{2}}^{n+1}$	Derivative of the segment error function
$\underline{B}$	Normalised modal matrix
$\underline{B_i}$	The i^{th} column of the modal matrix after normalising with the mass matrix
C_1, C_2	Coefficients used in the definition of the mass modifiers
C_a, C_r	Apparent and relative wave celerity
$Cd_{(cw,ssb)}$	Drag coefficients of clump weight and subsurface buoy
C_l	Convergence line
C_{lerr}	Angular error on the convergence line C_l
C_q	Coefficients of the expansion of $\mathcal{L}$
$C_{j-\frac{1}{2}}^{n+1}$	Derivative of the segment error function
C_L	Transverse wave speed in line
C_T	Longitudinal wave speed in line
$\underline{C_i}$	Coefficients of the Taylor series expansion of $\mathcal{L}$
$\underline{C_j}$	Vector defining current components at node j
Cd_n, Cd_t	Normal and tangential drag coefficients
$\underline{D}$	Drag matrix

$D_{j+\frac{1}{2}}$	Original diameter of element $j+\frac{1}{2}$
$\tilde{D}_{j+\frac{1}{2}}$	Diameter of line element $j+\frac{1}{2}$ when loaded
E	Young's modulus
F_n, F_t	Local normal and tangential fluid drag forces
$F_{p,q,r}$	Fluid forces along local element axes
$F_{x,y,z}(s)$	Fluid drag components at a point a distance s from the origin
$\underline{F_j}$	Fluid drag matrix for node j
$F_{(x,y,z)j}$	Fluid force components along global (x, y, z) axes
$F_{x(j+\frac{1}{2})}$	Global fluid loading along the x axis for element $j+\frac{1}{2}$
$\bar{F}$	A general vector force
$\underline{G_j}$	General dynamic vector force at node j
$\underline{G}$	Amplification matrix
H	Wave height
H_j	Weighting factor for Gauss-Legendre Quadrature
I	Coefficient of mooring chain material grades
$\underline{K}$	Stiffness matrix
$\underline{K}_{j+\frac{1}{2}}$	Fluid drag matrix for element $j+\frac{1}{2}$
K	Soil bearing capacity factor
$\underline{L}$	The load amplification matrix
L	The total length of the mooring line
$\mathcal{L}$	The local truncation error of numerical scheme
M_j	The actual mass acting at node j
M_j^*	The additional mass of any line attachments acting at node j
$M_{j+\frac{1}{2}}$	Mass of element $j+\frac{1}{2}$
$\bar{M}$	A general vector moment
M_j	Actual mass lumped at node j
$\underline{M}$	Mass matrix
$\underline{M_j}$	Total vector mass acting at node j
$\underline{N_j}$	Fluid drag and gravity force matrix
N_s	Number of time steps over which the nodal mass modifier is phased in
O	Origin of mooring line - at anchor point
$\hat{O}_j, \hat{P}_j, \hat{Q}_j$	Coefficients of the equations of motion in the global z direction
P	Period
P_m	Minimum period
$P_{p,q,r}$	Local fluid added masses
$P_{x,y,z}$	Global fluid added masses

$\underline{P_j}$	The added mass vector for node j
$\underline{P_j^*}$	The added mass vector for any line attachements acting at node j
$\underline{Q}(t)$	Time dependent external forces applied at each node
R	Spectral radius
R_{perr}	Percentage error on radial position, R_p
R_{ssb}	Radius of SSB
R_{cw}	Radius of clump weight
$\underline{S}$	Column matrix of sine terms
$\hat{R}_j, \hat{S}_j, \hat{T}_j$	Coefficients of the equations of motion for the x direction
MM_1	Mass modifier for the first suspended node
MM_2	Mass modifier for the second suspended node
R_p	Radial position
S_u	Undrained soil shear strength
T	Simulation time
$\bar{T}$	Vector effective tension
T_a, T_r	Apparent and relative wave periods
T_b, T_l	Periods associated with mode b and the limiting mode of accurate integration
$\bar{T}_m$	Overall effective tension mean of time history
$\bar{T}_p, \bar{T}_t$	Effective tension means of peaks and troughs in the solution induced by a sinusoidal excitation
$T_{j+\frac{1}{2}}$	Effective tension in element $j+\frac{1}{2}$
$T_{x,y,z}(s)$	Effective Tension components at the point s along the line
U, V	Resolved current velocities along x' and y' respectively
$\underline{U}, \underline{\dot{U}}, \underline{\ddot{U}}$	General displacement, velocity and acceleration vectors
$\underline{U}_j^n, \underline{\dot{U}}_j^n, \underline{\ddot{U}}_j^n$	General displacement, velocity and acceleration vectors at node j and time step n
$\underline{\tilde{U}}_j^n, \underline{\tilde{\dot{U}}}_j^n, \underline{\tilde{\ddot{U}}}_j^n$	General tentative displacement, velocity and acceleration vectors at node j and time step n
$\underline{U}_n, \underline{\dot{U}}_n, \underline{\ddot{U}}_n$	General displacement, velocity and acceleration vectors written in normal coordinates
$\underline{\ddot{U}}_j^{wc}$	Vector of combined wave and current velocities
$\hat{U}_j, \hat{V}_j, \hat{W}_j$	Coefficients of the equations of motion for the y direction
$V_{ax'}, V_{rx'}$	Apparent and relative wave particle velocities in the direction of wave propagation
$V_{az'}, V_{rz'}$	Apparent and relative wave particle velocites along the z' axis
$V^*_{j(x,y,z)}$	Equivalent volume of line attachement at node j

W_j	Gravity force lumped at node j
W_s	Submerged weight per metre of line on sea bed
$\underline{W}(s)$	External load vector on line element
$\underline{W}_j^v$	Vector defining wave particle velocities at node j
a, b	Proportional coefficients of mass and stiffness matrices
a_j	Abscissa of Gauss-Legendre Quadrature
a_n, a_t	Normal and tangential added mass coefficients
d	Water depth
$e_{j+\frac{1}{2}}$	Global added mass coefficient matrix
f	Soil Coulomb friction force
$f_r(t)$	Point excitation at element r in the displacement vector
f_n, f_t	Normal and tangential soil drag force per unit length
g	Gravitational acceleration
h	Total number of elements
i	Iteration index for static numerical procedure
$\underline{i}, \underline{j}, \underline{k}$	Unit vectors along global cartesian axes
j	General node numbering
k	Wave number
l	Unstretched length of line element
l_g	Unstretched length of grounded line
l'_g	Stretched length of grounded line
$\tilde{l}$	Stretched length of line element
l_m	Minimum size of all mesh elements
l_w	Wavelength of monochromatic wave
$m_{j+\frac{1}{2}}$	The mass per metre of element $j+\frac{1}{2}$
$\underline{m}_j$	The added mass acting at node j
n	Number of time steps to current position in time
$\dot{n}$	Single local velocity component
p_i	Frequency of oscillation for the i^{th} mode
p, q, r	Local cartesian axes
$\dot{p}, \dot{q}, \dot{r}$	Local velocity components
$\ddot{p}, \ddot{q}, \ddot{r}$	Local acceleration components
$\bar{r}$	Position vector to lower end of elemental length
$\bar{r}^n$	Load vector at time n
$\bar{r}_w$	Position vector to centre of external loading
s	Distance from origin to any point measured along the mooring line
t	Time

t_g	Time of nodal grounding
t_o	Initial time
u_n, u_t	Resolved local normal and tangential fluid velocities
$w(s)$	Net weight per metre of the line material at point s
w_j	Net weight of the mass lumped at node j
$\bar{w}(s)$	Resultant vector of $\underline{W}(s)$
x_{gi}	Coordinate of intersection of parabola with seabed
x_{td}	Mooring line touchdown point relative to O
x, y, z	Global cartesian axes
$\dot{x}, \dot{y}, \dot{z}$	Global velocity components
$\ddot{x}, \ddot{y}, \ddot{z}$	Global acceleration components
x_p, y_p, z_p	Boundary condition for line top point
$\dot{x}^r, \dot{y}^r, \dot{z}^r$	Global relative velocity components
$\ddot{x}^r, \ddot{y}^r, \ddot{z}^r$	Global relative acceleration components
x', y', z'	Local axes relative to wave heading
z_c	Calculated mooring line endpoint height above seabed
z_{err}	Percentage error in the depth
z_g	Grounding height for nodes
ΔB	Change in nodal mass modifier to be applied at each of the N_s steps
ΔM	Additional mass to account for the first and last nodes
$\Delta \bar{T}$	Change in vector tension in one element length
Δt_{cr}	Critical time step for CD scheme
Δl	Parabola defined proportion of the element length
$\Delta \bar{r}$	Change in position over elemental length
Δs	Length of line element
Δt	Time step size
$\Phi()$	Wave velocity potential
Ω	Segment error function
$[\Omega]$	Transformation matrix between local and global axes
α	Soil sliding friction factor
α_j	Coefficient for the Linear Multistep method
β	Parameter for Newmark scheme
β_j	Coefficient for the Linear Multistep method
β_m	Frequency of the m^{th} error harmonic
β_0	Angle between line and seabed for partial catenaries
γ_g	Grounding angle

$\gamma_{j+\frac{1}{2}}$	The angle which element $j+\frac{1}{2}$ makes with the global xy plane
δ	Parameter for Newmark scheme
δ_{ij}	Kronecker delta
ϵ	Percentage line extension
$\varepsilon_{j+\frac{1}{2}}$	The angle which element $j+\frac{1}{2}$ makes with the global xz plane
$\underline{\varepsilon}_j^n$	Error term introduced at time n and point j
ξ_e	Vector of excitation phases
ξ_i	Modal damping parameter
$\varepsilon_{x,y,z}$	Cartesian components of the excitation phases
η	Soil surface friction coefficient
η_n	Normal soil surface friction coefficient
ζ	Growth factor
η	Convergence parameter
θ'	Heading of wave system w.r.t the global x axis
θ	Wilson scheme parameter
λ_w	Wave length
λ	Roots of the stability polynomial
μ_j	Net weight of any line attachments at node j
ν	Poisson's ratio
ξ	Modal damping parameter
ρ_m	Material density
ρ	Sea water density
ρ_{cw}	Density of clump weight material
ρ_{ssb}	Density of subsurface buoy material
τ	Time interval between $n\Delta t$ and $(n+\theta)\Delta t$
σ	Stress in line element
ϕ	Resolution angle of u_n
ϕ_i	Phase of the i^{th} mode
ω_a, ω_r	Apparent and relative wave frequencies
$\underline{\omega_e}$	Vector of excitation frequencies

Abbreviations

2D	Two dimensional
3D	Three dimensional
AD	Amplitude Decay
BS	Breaking Strength
CD	Central Difference
CPU	Central Processing Unit
CPU_1	CPU time for code outside of iterations
CPU_2	CPU time for the iterative part of the code
DE	Differential Equation
FD	Finite Difference
FDE	Finite Difference Equation
FE	Finite Element
GRE	Global Rounding Error
GTE	Global Truncation Error
HF	High Frequency
H.O.T.	Higher Order Terms
LF	Low Frequency
LM	Lumped Mass
LMM	Linear Multistep Method
LTE	Local Truncation Error
N	The exact solution of the FDE
NAG	Numerical Algorithms Group
ODE	Ordinary Differential Equation
P	The exact solution of the PDE
PDE	Partial Differential Equation
PE	Period Elongation
RH	Routh-Hurwitz
SF	Safety Factor
SSB	Sub Surface Buoy
TS	Taylor Series

VN	von Neumann
Δ	The numerical solution of the FDE

CHAPTER 1

Introduction

This thesis is essentially concerned with the development of a robust dynamic analysis of a mooring line. In particular comparative studies are undertaken using four of the most commonly implemented time integration schemes to provide solutions to the dynamic mooring line equations. This study was motivated by the ultimate objective of trying to couple the full three dimensional (3D) time domain dynamic motion analysis of an arbitrary floating structure subject to a random seaway with a full 3D dynamic mooring line analysis. To date the full coupling of these two distinct dynamic analyses has not yet been attempted, although several different efforts have been made in this direction (see below). This is despite the increasing trend of thought that mooring line effects may significantly contribute towards the large low frequency motions of the floater.

In first order water wave theory, developed for the analysis of ship motions, the orbits of the wave particles are closed. Since there is no net movement of the water particles there is no net transfer of momentum. This results in a linear model where there should be no need for mooring lines since the predicted ship or floater oscillations in the horizontal plane are about a mean position which remains constant. However, in reality, if the floater were not moored it would drift off station due to the mean second order forces which the structure experiences. These damping effects were demonstrated in a famous set of experiments by Wichers(1979). These were later confirmed in Wichers(1982) by a comparison between further experimentation and theoretically predicted values. This effect is known by several names, e.g. low frequency damping, second order effects and wave drift damping and acts so as to cause the floater to drift a long way off station - hence the need for mooring lines to act as 'restoring springs' to keep the floater on station.

When considering the time domain solution of moored floaters several attempts have been made to include the effects of the mooring lines. These attempts have, to date, always involved some simplification of either the floater model or the mooring line model. In all cases, bar one, the mooring lines are included in a static sense as a modification to the hydrostatic restoration terms. Hairston(1979) uses a simplified three degree of freedom (3 d.o.f.) model to represent the horizontal motions of

the floater and includes the mooring line effects as static forces derived from the catenary equations. Experimental and empirical values were used to provide values of the first order hydrodynamic added mass and fluid damping which means that the model was not able to analyse the more important second order effects. Seidl *et al.*(1987) carried out a full time domain simulation for the floater motions, but with the mooring line being included as a 'look up' table of previously prepared force-displacement characteristics as derived from the catenary equations. This same approach was later adopted by Hearn *et al.*(1988) when investigating the effects of low frequency damping upon the excursions of moored structures, as well as by Ramzan and Mitchell(1985). Wichers and Huijsmans(1990) have determined, both experimentally and computationally, the effect of low frequency surge on mooring line damping using the mooring dynamics model presented by Boom *et al.*(1987). In this case the high frequency effects caused by the first order wave forces were included by calculating the dynamic amplification factors (DTA) from analytical results. Ansari and Khan(1986) present a model which is also based on a 'look up' table of previously prepared mooring line characteristics, but these were dynamic, not static, tensions calculated from a 2D time domain model. However, this model did not allow for the elasticity of the mooring line and the floater motions were formulated as an uncoupled 3 d.o.f. model representing in-plane motions only. Nakajima(1986) presents a coupled simulation where the mooring line dynamics are calculated in 3D and are directly included in the step by step integration of the equations of motion for the floater. The surge, heave and pitch equations for the floater are uncoupled and some indication of how they are solved is given. Chen and Chou(1986) present a strip theory method for the calculation of hydrodynamic quantities which are then used in a full 6 degree of freedom time domain model for the floater. A quasi-static method is then used to calculate the mooring line forces at the vessels equilibrium position. During the simulation the mooring line forces are calculated using the actual position and orientation of the floater. With no indication to the contrary it is assumed that the quasi-static method is used to derive the mooring line forces during the simulation.

This review demonstrates that the integration of the full floater and line analyses has not yet been achieved despite the increasing acceptance that the inclusion of dynamic mooring line effects may have a significant influence upon the motions of a moored floating vessel. See, for example, Ramzan and Robinson(1986), Tein *et al.*(1987) and Huse(1986).

Since the coupling of floater and mooring line dynamics is the ultimate aim, it was decided to undertake a study of the various numerical schemes available for the prediction of the dynamics of mooring lines. In particular, to study the attributes of the time integration schemes being used to integrate the equations of motion. This is necessary because it would be a requirement of the fully coupled analysis that the solution of the mooring line dynamics be robust, and provide sufficient accuracy, so that it would not cause the collapse of the coupled solution process, or, introduce unacceptable errors in the solution.

If a mooring line is regarded as a particular example of the suspended string class of problems, then within the literature it will be seen that there are literally hundreds of solutions. These dating back to 1781 when Euler solved the problem of the pendulum motion of an undamped suspended string hanging vertically in water (see McLachlan(1961)). Since 1781 many analytic solutions have been developed for different problems of differing complexity. However despite all the effort expended in this field, it has not been possible to produce a closed form solution for the full nonlinear 3D mooring line problem. This is because any simplifications to the model which are introduced to produce an analytic solution, tend to remove the more important features of the model (particularly certain nonlinearities). Consequently the available analytic solutions tend to belong to a narrow class of problems. To fully account for the dynamics of mooring lines the nonlinear equations are required to be solved. Hence this thesis is limited to the numerical solution of the equations of motion, and in particular two variants of the same solution process are considered, namely:

1. Direct time integration, and

2. Modal analysis techniques.

To the author's knowledge, the earliest numerical method available for the solution of mooring dynamics problems was by Walton and Polachek(1960), and this paper can be regarded as having founded this class of solution, for this type of problem. In the method proposed by Walton and Polachek, the line is discretised into straight line, massless segments (or elements) with all the line mass and the internal and external forces assumed to act at the nodes connecting the elements. Their 2D model was deficient in respect of cable elasticity, the grounding and lifting of nodes from the seabed, the friction and suction effects of the seabed on the line and the effects of ocean waves. This was probably because they were, at the time, assumed to be negligible. The equations of motion were solved using

the Central Difference (CD) time integration scheme, and the paper included a stability analysis of the resulting explicit Finite Difference (FD) equations. This demonstrated the expected conditional nature of the stability of the explicit CD method through the derivation of the largest time step which could be used to ensure stability. This analysis was later extended in 1963 (see Polachek *et al.*(1963)) to include the effects of elasticity, but unfortunately both papers only provide the briefest indications of the results to be expected from such a procedure.

Following the paper of Walton and Polachek(1960), the attention of other investigators turned to other suspended string problems, for example towing problems and the motion of free falling anchor systems. Consequently it appears that the next reported reference to direct integration being applied to the solution of mooring line dynamics is by Nakajima *et al.*(1982). Here line elasticity is included in the model and a solution method is proposed to cope with the shock loadings introduced into the solution by the lifting and grounding of a node to and from the seabed. However seabed suction and ocean waves were still neglected and the model developed remains 2D only. This paper used the unconditionally stable Houbolt scheme to perform the required time integration. This procedure allows the use of a larger integration time step than is possible with the CD scheme, and subsequently the CD method does not appear to be used again in the reported literature concerned with mooring line analysis.

Ractliffe(1984) presents a time domain model where the aim was to reduce the CPU time and the computer storage associated with the solution process. No indication of which time integration scheme is used is given, although in earlier work (see Ghosh(1980,1981)) most of the common time integration schemes are mentioned as having been considered.

Boom(1985) develops a 2D model in which mooring line elasticity is included and seabed contact is accounted for through the use of a spring-damper model. The primary aim of this paper was to provide a much needed validation study where the results derived from the theory are compared with experimental results. In a subsequent paper (Boom *et al.*(1987)) the model is extended to include simple wave effects as well as the bending moments and shear forces developed by the mooring line. Consequently the model could be applied to riser configurations. In both cases the equations of motion are integrated using the Houbolt scheme, but the numerical effectiveness of this scheme is not investigated.

The paper of Nakajima(1986), which makes an attempt to couple the floater and mooring line dynamics, solves the 3D equations of motion for the line using the Newmark integration scheme. No reason is given for the change of integration scheme from the Houbolt method used in the previous paper, and no study is reported of the numerical properties of the Newmark scheme.

Of all the previous work none, bar that of Ghosh(1981), make any attempt to investigate the numerical properties of the different time integration schemes available. In fact researchers have not even indicated the influence of varying the size of the time step on the solution for any one particular scheme. Even the report of Ghosh(1981) presents no comparisons of the solutions obtained with different schemes. As a result it was deemed necessary that a study be carried out to investigate the relative merits of the schemes most commonly applied in the analysis of mooring line dynamics.

The preceding cited papers represent the principal references concerned with studying the direct time integration schemes applied to the solution of the equations of motion of a mooring line. An alternative finite element (FE) technique has been developed for this type of application; the details of the FE method will not be discussed here, but some useful references are now given:

In Jennings(1962) a numerical procedure is used to determine the static displacement and tension distribution of a cable slung between two supports. Trial values for the horizontal (H) and vertical (V) tensions at one end are required so that from the equilibrium conditions at each node, a position for the cable free end may be determined. In general this position for the free end will not coincide with the required support point position, therefore an iterative process must be applied to the values of H and V. Through the introduction of the concept of link flexibility, the change in the endpoint position for a given change in the values of H and V may be determined. This is then used to give much better estimates of the new trial values for H and V hence reducing the number of iterations needed to converge.

In O'Brien(1967) a numerical procedure is used to obtain a 3D static solution for an arbitrary cable structure. Trial estimates for the resolved tension components in the first element are required to start the solution procedure. The 'misclosure' between the derived cable endpoint position and the required endpoint position generally means that new trial estimates of the tension components in element 1 are needed. To this end a correction procedure based on that of

Jennings(1962) has been adopted to generate estimates of the tension components which will improve the convergence time. Through the analysis of a number of problems some insight has been gained of how the size of the initial errors in the estimates of the tension components can be expected to affect the rate of convergence of the procedure.

The paper of Skop and O'Hara(1972) presents a development of their earlier work (see Skop and O'Hara(1970)) on the method of imaginary reactions to what they have called the extended method. Here, cable array systems can be considered by the introduction of 'cuts' in the array and an imposition of imaginary reactions at these points. Under the action of these imaginary reactions the structure then becomes statically determinant. Initial estimates are made for all the imaginary reactions which have been introduced into the cable array. From this the equilibrium configuration can be calculated. The error function can then be determined with respect to the geometric constraints on the original array. A correction force is then introduced to the initial estimates of the imaginary forces. A new error function can then be calculated; this procedure is then repeated until the error function is less than some predetermined error margin. This method is stated to be globally convergent. i.e. convergence is achieved for any set of initially guessed internal reactions, the proof of which is given in their earlier paper, see Skop and O'Hara(1970).

In Webster(1975) the true finite element method as proposed by Oden(1972) and Zienkiewicz(1971) is used to develop a full 3D description of the problem of underwater cables. A valuable summary of the literature is given before the theory is developed. The mass and the stiffness matrices are fully developed for the case of linear elements with linear material properties. Although this is not the only choice of element type available, this element is selected because.."it is the least complicated and the most readily implemented." Once the equations of motion have been formulated the time integration is carried out through the use of the Newmark scheme where a modified form of Newton-Raphson iteration is used at each time step to obtain convergence. It is indicated that the optimum choice of the γ and β parameteres used in the Newmark scheme for use in this context is the subject of further studies. Three example problems are presented; the static configuration of a sphere towed by a cable, a single degree of freedom dynamic response problem and the results for an anchor drop.

The paper of Peyrot(1980) formulates the mooring line problem as a nonlinear finite element model similar to that proposed by Webster(1975). The principal

difference arises in the derivation of a curved cable element which can be considerably longer than the linear elements often used by investigators of this problem. It is pointed out that the determination of the correct equilibrium position necessary to start the dynamic simulation can be difficult with the use of linear elements, although once established the dynamic solution does not suffer from this. The linear acceleration method is used for the time integration. Iterations during each time step make use of the nodal imbalance vector and the displacements at each iteration. Several diverse examples are given to illustrate the versatility of this method.

The paper of Leonard(1979) outlines the main approaches available for the numerical analysis of steady state three dimensional ocean cable systems. In these methods the nonlinear behaviour of the cable is usually treated either by loading which is incrementally applied or by assuming a trial solution which is corrected according to some resultant error; the latter approach is used in this paper. The error function usually selected for such problems is the difference between the nodal displacements at each iterative step. A new estimate of the solution is either calculated by trial and error or by using the error function to scale the new estimate. In this paper a Newton-Raphson method of gradient scaling is derived for a general situation and these results are then used to analyse the steady state solution of circularly towed cable buoy system.

In addition to the FE formulation being solved by direct time integration schemes, the method of modal analysis is often used. This technique can also be adapted to solve the equations of motion which are not formulated through the use of FE. The main benefit of this technique is that it allows the equations being solved to be uncoupled and to be expressed in terms of a coordinate system which leave the coefficients of the acceleration, velocity and displacement terms as elementary functions of the initial matrices. The 'uncoupled' equations can then be integrated more efficiently than was originally possible. Dominguez and Smith(1972) formulate the equations of motion for each lumped mass in the line discretisation and then assemble the mass, damping and stiffness terms into appropriate matrices. These equations are then uncoupled and integrated using a convolution integral. Johansson(1978) has also formulated a matrix description of the equations of motion, as previously described, but it is not clear what method of solution was adopted. Wilhelmy and Fjeld(1981) calculated the eigensolutions for a matrix system representing the static configuration and then appear to use the

eigensolutions to uncouple the equations of motion where the Newmark scheme is subsequently used for the time integration.

The thesis is divided into 10 chapters where Chapters 2 to 5 recount the theoretical development and Chapters 6 to 8 demonstrate and discuss applications of the computer implementations of the theory. Chapter 2 is concerned only with the static problem, for which the theory associated with the analytical and numerical formulations is presented. It starts with the analytical formulation of the catenary equations and in particular a general expression is developed which describes the 2D displacement of the line under arbitrary loading. When the loading is specified as being constant along the line length, then the catenary equations are derived and developed for both the partial and complete cases, i.e. for nongrounded and grounded mooring lines. The 3D numerical formulation is then given with a description of the discretisation and the lumping procedure, as well as the calculation of the fluid forces. A solution scheme is also presented. In contrast to the remaining theory chapters, this chapter also includes results generated from the computer implementation of the two alternate analyses. In particular, a comparative study is carried out between the analytical and numerical models. For the numerical model a sensitivity study indicating how the number of elements used in the discretisation may be expected to affect the solution is reported.

Chapter 3 represents the main section of work. Here the formulation of the equations of motion are presented together with the solution procedure using the four cited time integration schemes. The derivation of the equations of motion is a relatively straightforward task, but now includes the modification of the acceleration and velocity terms due to the presence of ocean waves and an ocean current. There is also a method of coping with the grounding and lifting of the nodes from the seabed. In the section concerned with the solution procedure a brief statement of the four time integration schemes is given together with the necessary rearrangements of the equations of motion necessary to facilitate the solution process. This process is essentially the same for all four schemes, and therefore details are only explicitly indicated for the Houbolt scheme. The slight differences which arise when the other schemes are used are highlighted. The chapter concludes with a short section detailing the selection of initial conditions and the starting procedures required for each scheme.

Chapter 4 presents the modal method based solution of the equations of motion formulated in Chapter 3. The 2D equations of motion are cast into a matrix form. The natural vibration modes of the solution are then derived from the free

undamped equations. These eigensolutions are then used to extend the solution technique to the case of arbitrarily excited systems. The case of most relevance, that of damped arbitrarily excited systems, is then examined and the procedure required to uncouple the equations of motion indicated together with their reformation in the 'modal form' prior to their solution using any of the available time integration schemes. The chapter concludes with a discussion of the nonlinearities inherent in the formulation, and how the nonlinearities might affect the modal method based solution. Preliminary results which indicate the change in natural frequencies as the mooring line becomes more taut are included.

Chapter 5 is concerned with the derivation, the numerical stability and the accuracy of the four integration schemes. The schemes are briefly restated together with their main characteristics, and the original pertinent references are cited. To fulfil the aims of the chapter a section describing the jargon associated with the numerical analysis of FD schemes (of which the time integration schemes considered here are a subset) is presented. In particular the different types of errors associated with the implementation of the numerical schemes are explained. Then each of the FD schemes are derived; the CD and Houbolt schemes are derived from considerations of the theory of linear multistep methods as applied to first and second order problems, whereas the Newmark and Wilson-θ schemes are derived by making different assumptions regarding the linear variation of the acceleration over each time interval. A more detailed section describing the stability of the numerical schemes is then presented. This includes the stability analysis developed in Walton and Polachek(1960), the method of amplification matrices and the Routh-Hurwitz conditions. The next section presents considerations of the numerical accuracy in terms of the period elongation and amplitude decay and indicates the consequence of these for the results obtained. The last section details the calculation of two time step sizes, namely one which integrates all the modes present in the solution accurately and one which corresponds to the limiting time step size which can be employed with the CD scheme.

Chapter 6 presents the main results of the numerical comparison of the four time integration schemes used. The results are primarily concerned with the numerical properties in the solution of mooring dynamics. Although in Chapter 3 the 3D equations of motion were developed it is their 2D equivalents which are then solved with each of the four time integration schemes. Validation of the different numerical models is carried out by presenting some results for the limiting cases,

that is results corresponding to the cases of no endpoint excitation and when excitation has decayed out. A major section of work is presented where the results obtained from the four schemes are compared for different situations. Points of interest include : The maximum time step which can be used, the influence of time step size and the number of elements, CPU times obtained, starting procedures and the influence of the segment error function. Finally a short conclusion is given for this chapter which summarises the main results.

Chapter 7 uses the recommendations of Chapter 6 with regard to which scheme should be used to solve the 3D equations of motion. A short validation of the 3D model is carried out, as well as a brief parametric investigation. The main section of the chapter is concerned with the definition and the calculation of the dynamic tension amplification (DTA) factors for the cases where the fairleader excitation is coincident with the surge, sway, heave and tangential (to the line at the fairleader) directions. This then allows an assessment of the relative importance of the 'in plane' and 'out of plane' directions upon the dynamic tension history.

Chapter 8 is entirely concerned with an examination of the influence of seabed interactions. These are the friction and suction effects which the seabed soil causes on the mooring line, and the important question of nodal lifting and grounding. The theory in the former is developed and implemented for both the normal and tangential directions, and in each case for the line lying on or submerged in the seabed soil. Results are then presented which show the influence of the various frictional coefficients upon the tension time histories. The nodal lifting and grounding theory is referred to in Chapter 3 and the details are given in Appendix F. Here the potentially adverse effects are illustrated. The tension time histories during the grounding of one node in different circumstances are isolated and plotted together to illustrate the detail of the changes during grounding.

Chapter 9 brings the thesis to a conclusion. Here the main areas of work which have been undertaken are summarised and the main conclusions for each chapter are brought together. Then overall conclusions are derived regarding the impact and relevance of the reported research and recommendations are made regarding the further development of the theoretical model.

Note that throughout the thesis reference to 'tension' is taken to be the effective tension in the line - see Sparks(1983).

CHAPTER 2

The Static Mooring Line Problem

2.1 Introduction

With a mooring line coming under the more general heading of 'suspended strings', even a brief examination of the literature reveals a plethora of solutions and different approaches to the problem. The solution methods may be broken down into two main categories - analytic and numerical methods, with each containing many variants. Most variety occurs in the analytic category where many different simplifying assumptions are made, either to yield a tractable solution or to make the method applicable to a certain class of problems. In the numerical category there is less variety since the basic approach is the same, but certain aspects of the solution may be different. In this chapter the derivation of the so-called catenary equations is presented as an example of the analytic category. This specific form was selected because of its common use in the estimation of mooring line forces but also because the limitations of use are not often pointed out as they will be here. A rigorous development of the two dimensional (2D) form of the catenary equations is given in Dominguez and Filmer(1971) with the use of vector notation. The derivation of the catenary equations is also given in Berteaux(1976) who derives the general elemental forces present and then simplifies them. A detailed description of the forces affecting an element of a mooring line is given by Goodman and Breslin(1976) together with a derivation of the catenary equations are given from first principles. Oppenhiem and Wilson(1982) present an analytic method for determining the static geometry of a line composed of different materials and with line attachments present. Hairston(1979) uses a modified form of the catenary equations in a paper on the dynamics of moored vessels. The catenary form of the equilibrium equations can, in principle, be derived in three dimensions (3D) and although this is indicated in Section 2.2, only an explicit derivation of the 2D form is given. This is done under the simplifying assumption that the out-of-plane effects, such as ocean currents and friction from any grounded portion of the line, can be neglected. The 3D formulation presented here includes general fluid loading, but the derivation of the catenary equations assume that the line is short and heavy, and, as a consequence, the gravity forces are taken to be much greater than the fluid forces so that the latter can effectively be ignored, see

Berteaux(1976). This also has the consequence that the elastic stretch of the line is ignored in the catenary equations, meaning that they are to be regarded as 'stiff' mooring lines.

The numerical method developed in this chapter is a variation of that presented by Nakajima(1986a) where the continuous distributions of mass, geometry and forces are replaced with a 'lumped' model with the mass and forces concentrated at nodes which are connected by straight line, massless springs. Thus the differential equations governing the continuous case are reduced to an equivalent set of algebraic equations which are to be solved at the nodes. The force balance which forms the algebraic equations at each of the nodes is explained in detail along with an indication of how all the forces on the line are to be included. This explanation also includes the numerical integration of the fluid loading and the definition of the mass distribution.

With the catenary equations being an example of the analytic solution category, it will be seen from the ensuing theory that the numerical formulation has two main advantages over the analytic formulation, namely (i) line attachments (e.g. subsea buoys and clump weights) are readily included, and (ii) arbitrary fluid loading from a known 3D current profile can be included in a straight forward manner. The drawbacks to this method are, (i) a slightly more complicated formulation and solution procedure, and (ii) that it requires a longer solution time compared to the time required for the catenary equations. The results in this chapter are divided into two sections; firstly a comparison of the analytic and numerical solutions is undertaken which shows how the geometries, maximum line tensions and tension distributions compare. The second results section details some important features of the numerical model only; in particular the influence of varying the number of elements and the major line parameters are examined.

2.2 Analytical Formulation

Consider Figure 2.1 which shows a line segment which has an external loading of $\underline{W}(s)$ and a resultant of $\bar{w}(s)$ for that segment. The length of the line segment is Δs and $w(s)$ is the net weight per metre of the line material at the point s, where s is measured positively from the origin (anchor point) along the line. In order for the segment to be in equilibrium, there must be no net external force or moment acting on it, that is

$$\sum \bar{F} = 0 \tag{2.1}$$

$$\sum \bar{M} = 0. \tag{2.2}$$

Vector addition of all the forces indicated in Figure 2.1, yields

$$\sum \bar{F} = -\bar{T} + (\bar{T} + \Delta\bar{T}) + \bar{w}(s)\Delta s = 0,$$

and hence

$$\frac{\Delta\bar{T}}{\Delta s} + \bar{w}(s) = 0.$$

In the limit as $\Delta s \to 0$, the last equation reduces to

$$\frac{d\bar{T}}{ds} + \bar{w}(s) = 0. \tag{2.3}$$

Taking moments about the arbitrary point O leads to

$$\sum \bar{M} = (\bar{r} \wedge -\bar{T}) + (\bar{r} + \Delta\bar{r}) \wedge (\bar{T} + \Delta\bar{T}) + (\bar{r}_w \wedge \bar{w}\Delta s) = 0$$

which reduces to

$$\bar{r} \wedge \frac{\Delta\bar{T}}{\Delta s} + \bar{T} \wedge \frac{\Delta\bar{r}}{\Delta s} + \Delta\bar{T} \wedge \frac{\Delta\bar{r}}{\Delta s} + \bar{r}_w \wedge \bar{w}(s) = 0.$$

In the limit as $\Delta s \to 0$, then $\Delta\bar{T} \to 0$ and $\bar{r}_w \to \bar{r}$, therefore the last equation yields

$$\bar{r} \wedge \left[\frac{d\bar{T}}{ds} + \bar{w}(s)\right] + \bar{T} \wedge \frac{d\bar{r}}{ds} = 0.$$

Together with the result in Equation (2.3), this reduces to

$$\bar{T} \wedge \frac{d\bar{r}}{ds} = 0. \tag{2.4}$$

Equations (2.3) and (2.4) represent the sum of forces and moments for the equilibrium condition of the line segment in Figure 2.1. Next consider, in a little more detail, the sum of forces given by Equation (2.3). The two external forces acting on the mooring line are the fluid drag and the self weight of the line, thus $\bar{w}(s)$ can be written as

$$\bar{w}(s) = F_x(s)\underline{i} + F_y(s)\underline{j} + [F_z(s) - w(s)]\underline{k}, \tag{2.5}$$

where $F_x(s)$, $F_y(s)$ and $F_z(s)$ are the fluid loadings in the component directions at a position s along the line. The tension, $\bar{T}$, can also be expressed in component form with respect to the global Cartesian axes as

$$\bar{T} = T_x\underline{i} + T_y\underline{j} + T_z\underline{k}. \tag{2.6}$$

By substituting Equations (2.5) and (2.6) into Equation (2.3), and separating into component parts, the following results are obtained

$$\begin{aligned} \frac{dT_x}{ds} &= -F_x(s) \\ \frac{dT_y}{ds} &= -F_y(s) \\ \frac{dT_z}{ds} &= w(s) - F_z(s). \end{aligned} \tag{2.7}$$

The component tensions at any point s along the line can be obtained by integrating the relevant expression in Equation (2.7) from zero to the point of interest. This shows that the horizontal components of tension are dependent only upon the fluid loading in the component directions. As expected the vertical tension is proportional to both the self weight of the line and the fluid loading in the vertical direction. For zero fluid loading it is required that

$$\bar{w}(s) = -w(s)\underline{k}, \tag{2.8}$$

and thus the horizontal components of the tension in Equation (2.7) will equal zero. This indicates that there is no change in these components along the length of the line with zero fluid loading. The vertical component of tension is given by

$$\frac{dT_z}{ds} = w(s). \tag{2.9}$$

To find the vertical component of tension this expression is integrated with respect to s, the length along the line, to yield

$$T_z(s) = \int_0^s w(s)ds + T_z(0) \tag{2.10}$$

This shows that the vertical component of the tension is directly proportional to the external loading, which in this case is only the self weight of the line.

Now consider the sum of moments as given in Equation (2.4). The position vector $\bar{r}$ can be written in component parts as

$$\bar{r} = x\underline{i} + y\underline{j} + z\underline{k}. \tag{2.11}$$

Substitution of Equations (2.11) and (2.6) into Equation (2.4) yields

$$(T_x\underline{i} + T_y\underline{j} + T_z\underline{k}) \wedge \frac{d}{ds}(x\underline{i} + y\underline{j} + z\underline{k}) = 0 \tag{2.12}$$

which can be conveniently expressed in matrix determinant form as

$$\begin{vmatrix} \underline{i} & \underline{j} & \underline{k} \\ \frac{dx}{ds} & \frac{dy}{ds} & \frac{dz}{ds} \\ T_x & T_y & T_z \end{vmatrix} = \underline{0}. \tag{2.13}$$

Equation (2.13) along with Equation (2.7) completely define the three dimensional equilibrium conditions for a line segment subject to its own net self weight and external fluid loading. By solving this system of equations, the geometry and tension distribution along the mooring line can be obtained. The derivation of the more usual two dimensional equations now proceeds by ignoring the y component in the calculation of the 'determinant' of Equation (2.13). This will be given explicitly, but first an indication of the solution in 3D is given. The expansion of Equation (2.13) yields

$$\underline{i}\left(T_z\frac{dy}{ds} - T_y\frac{dz}{ds}\right) - \underline{j}\left(T_z\frac{dx}{ds} - T_x\frac{dz}{ds}\right) + \underline{k}\left(T_y\frac{dx}{ds} - T_x\frac{dy}{ds}\right) = \underline{0}, \tag{2.14}$$

which can be written as the single scalar relationship

$$(T_y - T_z)dx + (T_z - T_x)dy + (T_x - T_y)dz = 0, \tag{2.15}$$

upon summing the three implicit relationships of Equation (2.14). Dividing Equation (2.15) successively by dx, dy and dz produces an implicit set of equations for $\frac{dy}{dx}$, $\frac{dz}{dy}$ and $\frac{dx}{dz}$ which must be solved iteratively, so that

$$\begin{aligned}
\frac{dy}{dx} &= \frac{(T_y - T_x)}{(T_z - T_x)}\frac{dz}{dx} + \frac{(T_z - T_y)}{(T_z - T_x)} = f(T_x, T_y, T_z), \text{say}, \\
\frac{dz}{dy} &= \frac{(T_z - T_y)}{(T_x - T_y)}\frac{dx}{dy} + \frac{(T_x - T_z)}{(T_x - T_y)} = f_1(T_x, T_y, T_z), \text{say}, \quad \text{and} \\
\frac{dx}{dz} &= \frac{(T_y - T_z)}{(T_x - T_z)}\frac{dz}{dy} + \frac{(T_y - T_z)}{(T_y - T_x)} = f_2(T_x, T_y, T_z), \text{say}.
\end{aligned} \tag{2.16}$$

From differential geometry

$$dx^2 + dy^2 + dz^2 = ds^2 \tag{2.17}$$

which becomes

$$\begin{aligned}
\frac{ds}{dx} &= \left[\left(\frac{dy}{dx}\right)^2 + \left(\frac{dz}{dx}\right)^2 + 1\right]^{\frac{1}{2}} = \frac{1}{f_3(T_x, T_y, T_z)}, \text{say,} \\
\frac{ds}{dy} &= \left[\left(\frac{dx}{dy}\right)^2 + \left(\frac{dz}{dy}\right)^2 + 1\right]^{\frac{1}{2}} = \frac{1}{f_4(T_x, T_y, T_z)}, \text{say,} \\
\frac{ds}{dz} &= \left[\left(\frac{dx}{dz}\right)^2 + \left(\frac{dy}{dz}\right)^2 + 1\right]^{\frac{1}{2}} = \frac{1}{f_5(T_x, T_y, T_z)}, \text{say.}
\end{aligned} \tag{2.18}$$

Therefore by substituting Equation (2.16) into Equation (2.18), the geometry of the line can be obtained from

$$\begin{aligned}
x &= \int_0^s f_3(T_x, T_y, T_z)ds, \\
y &= \int_0^s f_4(T_x, T_y, T_z)ds, \text{and} \\
z &= \int_0^s f_5(T_x, T_y, T_z)ds,
\end{aligned} \tag{2.19}$$

since $s = 0$ at the origin. The solution of Equation (2.19) allows the 3D description of the geometry of the line and hence also of the tension distribution, but depends upon being able to evaluate the quantities in Equation (2.16). The derivation of the 2D equations follows a similar procedure. Setting all the $\underline{j}$ components in Equation (2.13) to zero results in the following expansion of the determinant

$$T_z\left(\frac{dx}{ds}\right) = T_x\left(\frac{dz}{ds}\right)$$

and hence

$$T_z = T_x\frac{dz}{dx}. \tag{2.20}$$

Now substitute Equation (2.10) into Equation (2.20) to yield

$$\frac{dz}{dx} = \frac{1}{T_x}\int_0^s w(s)ds + \frac{T_z(0)}{T_x}. \tag{2.21}$$

Equation (2.21) gives the relationship for the slope of the catenary at any point and shows that it is, as expected, a function of the vertical ($\int_0^s w(s)ds$) and horizontal (T_x) forces at that point. From differential geometry

$$dx^2 + dz^2 = ds^2 \tag{2.22}$$

hence

$$\frac{dz}{dx} = \sqrt{\left(\frac{ds}{dx}\right)^2 - 1}. \tag{2.23}$$

By equating Equations (2.21) and (2.23) and rearranging, it can be shown that

$$x(s) = \int_0^s \frac{ds}{\sqrt{1 + \left[\int_0^s w(s)T_x^{-1}ds + T_z(0)T_x^{-1}\right]^2}}. \tag{2.24}$$

Equation (2.24) now gives the general equation for the displacement of the line in two dimensions under a prescribed vertical loading as defined by $w(s)$. In order to calculate $x(s)$ explicitly Equation (2.24) needs to be integrated. Alternative equivalent descriptions of the mooring line are the Cartesian description (x, z) derived from Equation (2.21) and the (x, s) description derived from Equation (2.24). To determine either, the load $w(s)$ must be specified and this is usually done for two special cases of interest. In the first case the load is viewed as a variation with x rather than s, with the load/unit length in the x direction being constant. In the second case the constant load is invariant with s and this corresponds to a uniform line supporting its own weight, that is $w(s) = -w$ The negative sign indicating that the weight acts downwards, see Equation (2.8).

In the first case $w(x) = -w$ and so assuming that x varies from 0 to x whilst s varies from 0 to s, substitution for w in Equation (2.21) yields the equivalent expression

$$\frac{dz}{dx} = \frac{-1}{T_x}\int_0^x w dx + \frac{T_z(0)}{T_x},$$

where repeated integration with respect to x gives

$$z(x) = \frac{-wx^2}{2T_x} + \frac{T_z(0)}{T_x}x + z(0) \tag{2.25}$$

where the assumption that $\frac{dz}{dx} = 0$ is a necessary condition.

The second case is very similar to the first case except that the constant load is now with respect to the line parameter s and not the horizontal distance x. As the

pretension is increased so the catenary for the two cases will agree more closely. It is under these conditions that the so called 'catenary equations' are now developed.

2.2.1 Catenary Equations

When considering a mooring problem and the description of this by the catenary equations, it can be seen that there are two distinct cases which need to be considered independently, namely :

- The 'complete' catenary where there is zero slope of the line at the seabed.
- The 'partial' catenary where there is a non-zero slope at the seabed.

Both cases are illustrated in Figures 2.2 and 2.3 respectively. Physically the complete catenary has some portion of the length of the mooring line lying on the seabed and in the case of the partial catenary mooring line is grounded. The two cases are now considered separately:

Complete Catenaries

At the origin ($x = 0$) the following boundary conditions apply

$$\frac{dz}{dx} = 0, \quad s = 0 \text{ and } T_z = 0. \tag{2.26}$$

Therefore with $w(s)$ constant and $T_z = 0$, Equation (2.24) simplifies to

$$x(s) = \int_0^s \frac{ds}{\sqrt{1 + (\frac{ws}{T_x})^2}} \tag{2.27}$$

which can be rearranged as

$$x(s) = \frac{T_x}{w} \int_0^s \frac{ds}{\sqrt{\left(\frac{T_x}{w}\right)^2 + s^2}}$$

which is a standard integral form, the solution of which is

$$x(s) = \left(\frac{T_x}{w}\right) \sinh^{-1}\left(\frac{sw}{T_x}\right).$$

Clearly rearrangement of this solution leads to

$$s = \frac{T_x}{w} \sinh\left(\frac{wx}{T_x}\right). \tag{2.28}$$

Under these same conditions, Equation (2.21) simplifies to

$$\frac{dz}{dx} = \frac{ws}{T_x}, \tag{2.29}$$

and substituting for s using Equation (2.28) leads to

$$\frac{dz}{dx} = \sinh\left(\frac{wx}{T_x}\right)$$

which is directly integrable and yields

$$z = \frac{T_x}{w}\left[\cosh(\frac{wx}{T_x}) - 1\right]. \tag{2.30}$$

The two dimensional vector equation for the tension is

$$\bar{T} = T_x\underline{i} + T_z\underline{k}$$

hence

$$|\bar{T}| = T = \sqrt{T_x^2 + T_z^2}. \tag{2.31}$$

Since the vertical tension component is only dependent upon the weight of the mooring line, Equations (2.20) and (2.29) imply that

$$T = \sqrt{T_x^2 + (ws)^2}. \tag{2.32}$$

In order to make use of the results derived in Equations (2.30) and (2.31), a further relationship is needed and this is derived from Equation (2.22), i.e.

$$\frac{ds}{dz} = \sqrt{1 + \left(\frac{dx}{dz}\right)^2}. \tag{2.33}$$

Substituting for $\frac{dx}{dz}$ from Equation (2.29) and rearranging, leads to the following result

$$dz = \frac{sds}{\sqrt{s^2 + \left(\frac{T_x}{w}\right)^2}}.$$

Integrating over the fluid depth d and mooring line length L leads to

$$\begin{aligned} \int_0^d dz &= \int_0^L \frac{sds}{\sqrt{s^2 + \left(\frac{T_x}{w}\right)^2}} \\ &= \left[\sqrt{s^2 + \left(\frac{T_x}{w}\right)^2}\right]_0^L. \end{aligned} \tag{2.34}$$

Rearrangment of this equation leads to the following result

$$\frac{T_x}{w} = \frac{L^2}{2d} - \frac{d}{2}. \tag{2.35}$$

Thus Equations (2.28), (2.30), (2.31) and (2.35) define all the relevant quantities for specification of the complete catenary problem.

Partial Catenaries

For the case of partial catenaries the boundary conditions at the origin become

$$\frac{dz}{dx} = \tan\beta_o, \text{ and } s = 0 \tag{2.36}$$

Direct application of the first two boundary conditions in Equation (2.21) gives

$$\tan\beta_0 = \frac{T_z(0)}{T_x} \tag{2.37}$$

and hence direct substitution into Equation (2.24) with a constant loading w, yields the following

$$x(s) = \int_0^s \frac{ds}{\sqrt{1 + (\frac{ws}{T_x} + \tan\beta_o)^2}}. \tag{2.38}$$

The form of Equation (2.38) is very similar to Equation (2.27) and so the integration process is also analogous. In particular, using the substitutions

$$p = \frac{ws}{T_x} + tan\beta_0 \text{ and } a = 1 \tag{2.39}$$

it follows that

$$x(s) = \frac{T_x}{w}\left[\sinh^{-1}\left(\frac{ws}{T_x} + \tan\beta_o\right) - \sinh^{-1}(\tan\beta_o)\right] \tag{2.40}$$

and rearranging for s gives

$$s = \frac{T_x}{w}\left[\sinh\left(\frac{wx}{T_x} + \sinh^{-1}(\tan\beta_o)\right) - \tan\beta_o\right]. \tag{2.41}$$

These two equations can be used to calculate s and x, but a value for z is also needed. From Equations (2.20) and (2.21) and the first boundary condition of Equation (2.36), it can be seen that

$$\frac{dz}{dx} = \frac{ws}{T_x} + \tan\beta_o. \tag{2.42}$$

By substituting for ws/T_x from Equation (2.41), and then integrating (implicitly), the equation for z is

$$z = \int_0^x \sinh\left[\frac{wx}{T_x} + \sinh^{-1}(\tan\beta_o)\right] dx. \tag{2.43}$$

Explicit integration then leads to

$$z = \frac{T_x}{w}\left[\cosh\left(\frac{wx}{T_x} + \sinh^{-1}(\tan\beta_o)\right) - \cosh(\sinh^{-1}(\tan\beta_o))\right]. \tag{2.44}$$

To calculate the axial tension at any point s along the line, both T_x and T_z are required. Equation (2.10) is restated

$$T_z(s) = \int_0^s w(s)ds + T_z(0) \tag{2.10}$$

and under the condition of constant loading, $w(s) = w$, it follows that

$$T_z(s) = ws + T_x \tan\beta_0, \tag{2.45}$$

by using Equation (2.20) and the first boundary condition of Equation (2.36). The general expression for axial tension for the case of a partial catenary is now derived from Equation (2.31), that is

$$T(s) = \sqrt{T_x^2 + (T_x \tan\beta_o + ws)^2}. \tag{2.46}$$

Also it follows that $T_x = T\cos\beta = T_o\cos\beta_o$. As before, a further relationship is derived from Equation (2.33), i.e.

$$\frac{ds}{dz} = \sqrt{1 + \left(\frac{dx}{dz}\right)^2}, \tag{2.33}$$

but from Equation (2.21)

$$\frac{dz}{dx} = \frac{ws}{T_x} + \tan\beta_o. \tag{2.47}$$

Rearranging Equation (2.47) to provide $p = \frac{dx}{dz}$, then substitution into Equation (2.33) and some rearranging yields

$$\int_0^d dz = -\frac{T_x}{w}\int_{p_1}^{p_2} \frac{dp}{p^2\sqrt{a^2 + p^2}} \tag{2.48}$$

Following the use of standard integrals, substituting in the limits and some algebraic manipulation, the following results

$$\frac{T_x}{w} = \frac{(L^2 - d^2)\cos\beta_o}{2(d - L\sin\beta_o)}, \tag{2.49}$$

subject to $\cos\beta_0 \neq 0$ and $T_x \neq 0$.

2.2.2 Summary of Theoretical Analysis

This chapter, so far, has primarily been concerned with the general 3D derivation of the equilibrium conditions for a catenary segment subject to arbitrary external loading. Initially equilibrium was expressed through Equations (2.3) and (2.4), with the final forms given by Equations (2.7) and (2.13). Having indicated how this system of 3D equations could be solved, the general 2D solution was explicitly derived, as expressed in Equation (2.24). This solution is dependent upon being able to analytically evaluate the integral in the denominator of Equation (2.24), which, in turn, depends upon the arbitrary loading function $w(s)$. To complete the analytic integration two simple forms of loading were assumed. In the case of $w(s)$ being treated as $w(x) = w$, where w is constant, the analytic expression for $z(x)$ has a parabolic form, see Equation (2.25). The alternative case of $w(s) = w$, where w is constant, leads to the so called catenary equations and these have been discussed in some detail. These equations are developed to analyse two situations; firstly where some part of the mooring line is lying on the seabed, and secondly where all the line is suspended. The former situation corresponds to a 'complete' catenary and the appropriate equations are Equations (2.28), (2.30), (2.32) and (2.35). The latter situation corresponds to a 'partial' catenary and the relevant equations are Equations (2.41), (2.44), (2.46) and (2.49). The solution of these analytic equations is now discussed in the context of the developed software.

2.3 Outline of Analytical Software

With the theory of the catenary equations developed, their solution is now discussed in terms of the role of each equation in the iterative scheme developed.

2.3.1 Complete Catenaries

The governing equations for this case are re-presented here for ease of explanation of the calculation process, that is

$$s = \frac{T_x}{w}\sinh\left(\frac{wx}{T_x}\right), \tag{2.28}$$

$$z = \frac{T_x}{w}\left[\cosh(\frac{wx}{T_x}) - 1\right], \tag{2.30}$$

$$T = \sqrt{T_x^2 + (ws)^2}, \tag{2.32}$$

and

$$\frac{T_x}{w} = \frac{L^2}{2d} - \frac{d}{2}. \tag{2.35}$$

Initially the principal parameters to be specified are, the uniform load w, depth of water d (here it is assumed for convenience that the fairleader is attached to the floater at the undisturbed water line, but this assumption can be changed by making d the height of the fairleader above the seabed), the length of the mooring line L and the horizontal location of the fairleader relative to the origin O, x_p say. In general w is specified by providing the nett weight of the mooring line in the water.

With the principal parameters defined, an iterative scheme is used to calculate the touchdown point of the line on the seabed. Although the vertical height of the upper endpoint position is known, it is now calculated for two possible extreme positions of the touchdown point. The first touchdown point is defined at the anchor, whereas the initial second touchdown point is defined at a position slightly less than x_p, x_{p1} say, from the origin, O. Using Equation (2.30) with $x = x_p$ the vertical position of the fairleader, z_p say, for the first selected touchdown point can be determined. For the second initial touchdown point, the vertical position of the fairleader, z_{p1} say, is determined from Equation (2.30) with $x = x_{p1}$ and Equation (2.35) is used to define T_x using $L = L - x_{p1}$. The required upper endpoint position $z = d$ will then lie between z_p and z_{p1}. Likewise the true position of the touchdown point will lie between x_p and x_{p1}, at x_{td} say. Using

$$x_{td} = \left(\frac{x_p + x_{p1}}{2}\right)$$

to find a new estimate, and using this point as the new 'origin', Equations (2.30) and (2.35) are applied with $x = x_p - x_{td}$ and $L = L - x_{td}$. Depending upon where the value of z calculated for x_{td}, z_{td} say, lies in relation to z_p, the bisection method is used to provide a new estimate of x_{td} according to the following relations:

$$\text{If } z(x_{td}) < z, \text{ then } x_p = x_{td}$$

and

$$\text{If } z(x_{td}) > z, \text{ then } x_{p1} = x_{td}.$$

This process is repeated until z as given by Equation (2.30) lies within an acceptable margin of error. Equation (2.28) should then provide a estimate of the length of the mooring line which is in close agreement with $L = L - x_{td}$. The iterative scheme described is readily appreciated upon studying Figures 2.2 and 2.4 together.

2.3.2 Partial Catenaries

As before the governing equations are re-presented to explain the iterative calculation process. In this case the following are required:

$$s = \frac{T_x}{w}\left[\sinh\left(\frac{wx}{T_x} + \sinh^{-1}(\tan\beta_o)\right) - \tan\beta_o\right], \tag{2.41}$$

$$z = \frac{T_x}{w}\left[\cosh\left(\frac{wx}{T_x} + \sinh^{-1}(\tan\beta_o)\right) - \cosh(\sinh^{-1}(\tan\beta_o))\right], \tag{2.44}$$

$$T(s) = \sqrt{T_x^2 + (T_x\tan\beta_o + ws)^2}, \tag{2.46}$$

$$\frac{T_x}{w} = \frac{(L^2 - d^2)\cos\beta_o}{2(d - L\sin\beta_o)}, \tag{2.49}$$

Here the same principal parameters as for complete catenaries are defined. The depth of the catenary is now calculated from Equation (2.44) subject to $\left(\frac{T_x}{w}\right)$ determined from Equation (2.49). Initially $\beta_0 = 1°$; if for this value of β_0 the catenary depth is greater than the water depth, then this situation is considered to conform to a complete catenary, and the algorithm described previously should be used. Otherwise, the increment in the iteration process is one degree, where with an increasing value of β_0 it is expected that the catenary depth will increase. The increase in β_0 continues until its value is just sufficient for the catenary depth to be greater than the water depth and that for the previous value of β_0 (by definition), the catenary depth is less than the water depth. Linear interpolation is then used to calculate the required β_0 value and this value is used to calculate T_x/w. With the correct values of β_0 and T_x/w having been established, the catenary geometry can now be calculated by taking intervals in x and using Equation (2.44). The flow chart for this process is shown in Figure 2.5.

2.3.3 Iteration and General Solutions

In offshore engineering the catenary equations can be used to provide estimates of the additional stiffness of the moorings in the equations of motion for the floater. This thesis is primarily concerned with the solution of the more general problem

of mooring line dynamics. However, the software developed for the solution of the catenary equations provides some insight regarding the numerical iteration schemes, and in Section 2.6 these solutions will be compared with the predictions derived from another solution method. Prior to this a numerical formulation of the static equations for a mooring line is presented, along with a numerical solution scheme.

2.4 Numerical Formulation

In Figure 2.6 the continuous mooring line is represented as a series of straight line elements with the nodes numbered from zero starting at the anchor point. References to elements is done by taking the 'mean' values of the node numbers bounding the element. Similarly, see Figure 2.7, geometric and element force quantities are subscripted according to the element number. This particular approach to modelling the statics of the line is known as the Lumped Mass (LM) method because the continuous distributions of mass, external forces and geometry is replaced by a discrete distribution of mass and forces acting at the nodes defining the geometry of the line. The nodes are considered to be joined by massless, straight line elements which are treated as springs to simulate the elasticity of the mooring line.

The terminology and nomenclature introduced here is consistent with that used in the formulation of the corresponding dynamic problem in Chapter 3. In particular the following are used:

$T_{j+\frac{1}{2}}$	Tension in element $j+\frac{1}{2}$,
$F_{x(j+\frac{1}{2})}$	Global fluid loading along the x axis for element $j+\frac{1}{2}$,
$M_{j+\frac{1}{2}}$	Net mass of element $j+\frac{1}{2}$, half of which is lumped at node j,
μ_j	Net weight of line attachement at node j,
$\gamma_{j+\frac{1}{2}}$	The angle that element $j+\frac{1}{2}$ makes with the global xy plane,
$\varepsilon_{j+\frac{1}{2}}$	The angle that element $j+\frac{1}{2}$ makes with the global xz plane.

Quantities of a similar form but with a different coordinate dependent subscript, simply relate to these properties acting along different local or global axes. The forces acting on the system of masses are

1. Self weight of the mooring line.

2. The influence of any line attachments which may be present.

3. Fluid loading on the line segments and line attachments.

The self weight of the line must account for the buoyancy of the line segments in order that the total immersed weight of each line segment is used. This is then lumped at the appropriate node and acts negatively along the global z axis. Since at each node the influence of two segments is considered, i.e. the segments above and below the node, then the mass lumped at the node is taken to be an average of the mass of the segments on either side. Modifications of the mass lumped at a node may occur if there are any line attachments present where the points of attachment are always considered to act at a node. These attachments are generally subsurface buoys (SSBs) or clump weights introduced to achieve some desired alteration of the tension distribution or geometry in the line. At all times the line of action of the attachments is parallel to the global z axis. For SSBs the weight of the structure is corrected to account for the associated buoyancy force assumed to act at the node. That is the mass equal to the buoyancy force of the attachment is subtracted from the net mass lumped at the node. The clumped weights are treated similarly.

The calculation of fluid loading on a line segment is considered to be the problem of an arbitrarily oriented smooth cylinder in a uniform ocean current. Morison's equation is used to estimate the drag forces on the cylinder, however the inertial term is not considered because this is a function of relative fluid acceleration which is not applicable in a static formulation. For complete specification of the fluid loading, correct estimation of the normal and tangential drag coefficients is necessary. Although it is recognised that tangential drag is likely to be very small compared to the normal drag, and that the estimation of the tangential drag coefficient is less certain than the determination of the normal drag coefficient, both are included for completeness. In the calculation of the fluid loading acting on line attachments it is assumed that the attachments remain vertical, even in the presence of a current. Furthermore the attachments are assumed to exhibit some form of geometric symmetry, usually spherical, in order to avoid unnecessary complication of the problem. Fluid loading is again calculated from Morison's equation with the drag coefficient estimated as a function of the local Reynold's number.

By resolving the weights and forces along the global axes of Figure 2.7, the conditions of static equilibrium can be expressed as

$$T_{j-\frac{1}{2}} \cos\gamma_{j-\frac{1}{2}} \cos\varepsilon_{j-\frac{1}{2}} = T_{j+\frac{1}{2}} \cos\gamma_{j+\frac{1}{2}} \cos\varepsilon_{j+\frac{1}{2}} + \frac{1}{2}(F_{x(j-\frac{1}{2})} + F_{x(j+\frac{1}{2})}), \quad (2.50)$$

$$T_{j-\frac{1}{2}} \cos\gamma_{j-\frac{1}{2}} \sin\varepsilon_{j-\frac{1}{2}} = T_{j+\frac{1}{2}} \cos\gamma_{j+\frac{1}{2}} \sin\varepsilon_{j+\frac{1}{2}} + \frac{1}{2}(F_{y(j-\frac{1}{2})} + F_{y(j+\frac{1}{2})}), \quad (2.51)$$

$$T_{j-\frac{1}{2}} \sin\gamma_{j-\frac{1}{2}} + \frac{1}{2}(M_{j-\frac{1}{2}} + M_{j+\frac{1}{2}})g + \mu_j = T_{j+\frac{1}{2}} \sin\gamma_{j+\frac{1}{2}} + \frac{1}{2}(F_{z(j-\frac{1}{2})} + F_{z(j+\frac{1}{2})}). \quad (2.52)$$

In continuous mechanics, equilibrium conditions would normally produce six equations. Here, because all the forces are assumed to act at the nodes no corresponding moment equations can be generated. Since the fluid forces acting on an element depend upon the orientation of the element and this, like the tension, is not known *a priori*, a method of satisfying Equations (2.50) to (2.52), is now considered.

2.4.1 Solution Outline

Suppose that all the element properties, masses and fluid forces are known for element $j-\frac{1}{2}$, then Equations (2.50), (2.51) and (2.52) still have six unknowns, namely $T_{j+\frac{1}{2}}$, $\gamma_{j+\frac{1}{2}}$, $\varepsilon_{j+\frac{1}{2}}$, $F_{x(j+\frac{1}{2})}$, $F_{y(j+\frac{1}{2})}$ and $F_{z(j+\frac{1}{2})}$, and hence these equations cannot be solved to yield these unknown values. To solve them an initial solution is calculated where the influence of current forces are omitted, then Equations (2.50), (2.51) and (2.52) reduce to

$$T_{j-\frac{1}{2}} \cos\gamma_{j-\frac{1}{2}} \cos\varepsilon_{j-\frac{1}{2}} = T_{j+\frac{1}{2}} \cos\gamma_{j+\frac{1}{2}} \cos\varepsilon_{j+\frac{1}{2}}, \quad (2.53)$$

$$T_{j-\frac{1}{2}} \cos\gamma_{j-\frac{1}{2}} \sin\varepsilon_{j-\frac{1}{2}} = T_{j+\frac{1}{2}} \cos\gamma_{j+\frac{1}{2}} \sin\varepsilon_{j+\frac{1}{2}}, \quad (2.54)$$

$$T_{j-\frac{1}{2}} \sin\gamma_{j-\frac{1}{2}} = T_{j+\frac{1}{2}} \sin\gamma_{j+\frac{1}{2}} - \frac{1}{2}(M_{j-\frac{1}{2}} + M_{j+\frac{1}{2}})g - \mu_j. \quad (2.55)$$

Under the conditions of the original assumption, all the quantities on the left hand side of these equations are known. Consequently there is now a set of three equations in the three unknowns $T_{j+\frac{1}{2}}$, $\gamma_{j+\frac{1}{2}}$ and $\varepsilon_{j+\frac{1}{2}}$ and hence the equations can now be solved. Clearly once a set of values for the first element have been selected, then this set of equations can be solved successively for each element, resulting in a complete description of the line geometry and the tension distribution. Thus it immediately follows that the final solution depends directly upon the initial values assigned to $T_{\frac{1}{2}}$, $\gamma_{\frac{1}{2}}$ and $\varepsilon_{\frac{1}{2}}$. The boundary condition for the solution at the upper endpoint of the line is that its location must coincide with the preselected position designated (x_p, y_p, z_p). Here without any loss of generality, this point can be located on the undisturbed free surface. In order that the upper endpoint converges to this point a series of iterations as discussed in Section 2.5 must be made with different initial values to achieve the required converged solution. Once convergence is achieved a description of the line geometry and tension distribution

exists and this solution can be designated $\gamma^1_{j+\frac{1}{2}}$, $\varepsilon^1_{j+\frac{1}{2}}$ and $T^1_{j+\frac{1}{2}}$. The next step is to account for any fluid forces which might be present. The manner of including these forces is to formulate a series of approximate solutions which include the fluid forces derived from the displacements of the previous solution. The i^{th} approximation is now determined from the original equations and is written in the form

$$T^i_{j-\frac{1}{2}} \cos\gamma^i_{j-\frac{1}{2}} \cos\varepsilon^i_{j-\frac{1}{2}} = T^i_{j+\frac{1}{2}} \cos\gamma^i_{j+\frac{1}{2}} \cos\varepsilon^i_{j+\frac{1}{2}} + \frac{1}{2}(F^{i-1}_{x(j-\frac{1}{2})} + F^{i-1}_{x(j+\frac{1}{2})}), \quad (2.56)$$

$$T^i_{j-\frac{1}{2}} \cos\gamma^i_{j-\frac{1}{2}} \sin\varepsilon^i_{j-\frac{1}{2}} = T^i_{j+\frac{1}{2}} \cos\gamma^i_{j+\frac{1}{2}} \sin\varepsilon^i_{j+\frac{1}{2}} + \frac{1}{2}(F^{i-1}_{y(j-\frac{1}{2})} + F^{i-1}_{y(j+\frac{1}{2})}), \quad (2.57)$$

$$T^i_{j-\frac{1}{2}} \sin\gamma^i_{j-\frac{1}{2}} = T^i_{j+\frac{1}{2}} \sin\gamma^i_{j+\frac{1}{2}} + \frac{1}{2}(F^{i-1}_{z(j-\frac{1}{2})} + F^{i-1}_{z(j+\frac{1}{2})}) - \frac{1}{2}(M_{j-\frac{1}{2}} + M_{j+\frac{1}{2}}) - \mu_j. \quad (2.58)$$

For this particular problem i not exceeding 4 has been found to provide accurate solutions. Assessment of accuracy and convergence can be monitored through the differences in the nodal displacements predicted by the i^{th} and $(i+1)^{st}$ solutions. With $i = 4$, for example, there will have been three successive solutions which include the effects of fluid loading. Prior to presenting the iterative aspects of the solution technique in any great detail, the methods for evaluating the fluid loading and the tension distribution are discussed. Some further account is also given on how to lump the mass of the mooring line.

2.4.2 Calculation of Fluid Loading and Tension

So far the calculation of the tension and the effects of fluid loading have only been discussed in general terms in the context of the outlined solution procedure, but this is now considered in some detail. In the absence of any tensile forces an element is considered to have an unstretched length of l_o, whereas the new length under tensile loading is $\tilde{l}$. These lengths are now assumed to be related according to Hooke's law, that is

$$\tilde{l} = l_o(1+\epsilon) \quad (2.59)$$

where

$$\epsilon = \frac{4T}{\pi D^2 E}. \quad (2.60)$$

Thus ϵ is the line extension under loading, D is the line diameter with no tension and E is the Young's Modulus of the line material.

In order that the fluid loading forces can be evaluated according to Morison's equation, the value of the line diameter under loading, $\tilde{D}$, is required. This is

related to D, ϵ and Poisson's ratio (ν) for the line material through the following relationship

$$\tilde{D} = D(1 - \nu\epsilon). \tag{2.61}$$

The normal and tangential fluid loading will act respectively over an effective diameter $\tilde{D}$ and a surface area given by

$$A_c = \pi \tilde{l} \tilde{D}. \tag{2.62}$$

Here the fluid loading is assumed to arise from ocean currents, the components of which are usually defined with respect to the global axes. In order to calculate the fluid forces on a line segment, the normal and tangential fluid velocities on a particular element need to be calculated. Since each element has a different orientation defined by $\gamma_{j+\frac{1}{2}}$ and $\varepsilon_{j+\frac{1}{2}}$, then the normal and tangential components need to be calculated for each element. This is achieved by introducing a set of local axes, $p_{j+\frac{1}{2}}$, $q_{j+\frac{1}{2}}$, $r_{j+\frac{1}{2}}$, which are orthogonal to the element orientation (see Figure 2.7). They are also defined as being coincident with the global axes (x, y, z) when $\gamma_{j+\frac{1}{2}}$ and $\varepsilon_{j+\frac{1}{2}}$ are both zero. Dropping the subscripts on ε and γ for convenience, the transformation matrix (see Appendix A) between the two axes systems is given by

$$\begin{pmatrix} p \\ q \\ r \end{pmatrix} = \begin{pmatrix} \cos\gamma\cos\varepsilon & \cos\gamma\sin\varepsilon & \sin\gamma \\ -\sin\varepsilon & \cos\varepsilon & 0 \\ -\cos\varepsilon\sin\gamma & -\sin\gamma\sin\varepsilon & \cos\gamma \end{pmatrix} \begin{pmatrix} x \\ y \\ z \end{pmatrix}. \tag{2.63}$$

Let (Ω) denote the transformation matrix of Equation (2.63). Since the current velocities are also related through the same transformation, then the local current components $\dot{p}$, $\dot{q}$ and $\dot{r}$ satisfy

$$\begin{pmatrix} \dot{p} \\ \dot{q} \\ \dot{r} \end{pmatrix} = (\Omega) \begin{pmatrix} \dot{x} \\ \dot{y} \\ \dot{z} \end{pmatrix}. \tag{2.64}$$

However in the application of Morison's equation the resultant normal velocity defined by

$$u_n = (\dot{q}^2 + \dot{r}^2)^{\frac{1}{2}} \tag{2.65}$$

is used. Also it follows that orientation of the resultant velocity is specified through

$$\phi = \arctan\left(\frac{\dot{r}}{\dot{q}}\right). \tag{2.66}$$

The general form for the drag component of Morison's equation is

$$F = \frac{1}{2}\rho C_d D u|u|, \tag{2.67}$$

where ρ is the density of sea water, C_d is the drag coefficient, D is the characteristic dimension and u is the fluid velocity. Therefore the normal and tangential drag forces acting on a line segment are given respectively by

$$F_n = \frac{1}{2}\rho C d_n \tilde{D} u_n |u_n| \tag{2.68}$$

and

$$F_t = \frac{1}{2}\rho C d_t A u_t |u_t|, \tag{2.69}$$

where A is as defined in Equation (2.62), $\tilde{D}$ is given in Equation (2.61) and $u_t = \dot{p}$. Once the normal and tangential drag forces at any point along the line segment have been determined, they must be integrated to find the total drag forces acting on the element. Since half the total force on each element is lumped at the appropriate nodes, the integration is carried out separately over each half element, as indicated in Figure 2.8. The forces in the local axes are calculated from

$$\begin{pmatrix} F_p \\ F_q \\ F_r \end{pmatrix} = \begin{pmatrix} F_t \\ F_n \cos\phi \\ F_n \sin\phi \end{pmatrix}. \tag{2.70}$$

The forces along the element are integrated according to the 3 point Gauss - Legendre quadrature. The general n point quadrature formulae is defined by

$$\int_{-1}^{1} f(x)dx = \sum_{j=1}^{n} H_j f(a_j), \tag{2.71}$$

where H_j is the j^{th} weighting, and a_j is the j^{th} abscissa of the closed interval $[1, 1]$. With different limits of integration, a and b say, both a_j and H_j would be scaled by $(\frac{b-a}{2})$. Thus for the selected case of $n = 3$ the following apply : $a_1 = -0.77459667$, $a_2 = 0$, $a_3 = 0.77459667$, $H_1 = H_3 = 0.55555...$, and $H_2 = 0.88888....$

The tangential force is integrated by multiplying each of the three values of F_t by the appropriate element length. Once the total force has been calculated for each half element in the local system, it must then be transformed into the global

axes ready for lumping at the appropriate nodes. This is done according to the inverse of the transform of Equation (2.63), that is

$$\begin{pmatrix} F_x \\ F_y \\ F_z \end{pmatrix} = (\Omega)^{-1} \begin{pmatrix} F_p \\ F_q \\ F_r \end{pmatrix}. \tag{2.72}$$

The lumping of the forces at the nodes means that for each element there are six points of integration. However, since the integration is performed by application of the 3-point scheme twice, the maximum order of an exactly integrable polynomial by this scheme is 5. Thus if the actual distribution of the fluid forces over the entire element is represented by a 5^{th} or lower order polynomial, then this method of integrating the fluid forces would have been performed accurately. Since as the current profile is only defined as being piecewise linear, then the above scheme may be considered to provide adequate accuracy.

2.4.3 Mass Distribution

It is seen from Figure 2.9 that half of the mass associated with the first and last elements should, in theory, be lumped at the extremities of the mooring line. However, since the conditions specified at these end points are the required boundary conditions for the solution, they do not enter into the static solution explicitly. Hence the total weight of the mooring line which enters the solution using the mass distribution defined in Figure 2.9 is $M_{T1}g$ say, and is given by

$$M_{T1}g = \sum_{j=1}^{h-1} \frac{1}{2}(M_{j+\frac{1}{2}} + M_{j-\frac{1}{2}})g, \tag{2.73}$$

assuming that there are h elements. However the total weight of the line as expressed at all the nodes, is given by

$$M_{T2}g = \frac{1}{2}(M_{\frac{1}{2}} + M_{h-\frac{1}{2}})g + \sum_{j=1}^{h-1} \frac{1}{2}(M_{j+\frac{1}{2}} + M_{j-\frac{1}{2}})g. \tag{2.74}$$

where h is the total number of elements. To realistically account for the 'extra' mass of $\frac{1}{2}(M_{\frac{1}{2}} + M_{h-\frac{1}{2}})$, this is equally divided between all the 'internal' nodes. Thus the mass at any internal node is now distributed as illustrated in Figure 2.10. That is, it is given by

$$M_j = \frac{1}{2}(M_{j-\frac{1}{2}} + M_{j+\frac{1}{2}}) + \Delta M, \tag{2.75}$$

where

$$\Delta M = \frac{(M_{\frac{1}{2}} + M_{h-\frac{1}{2}})}{2(h-1)}.$$

2.5 Solution Procedure for the Numerical Scheme

The numerical formulation of the static equilibrium problem described earlier is known as an 'initial value' problem, since the solution obtained depends upon the initial values chosen. In this section a description of how the initial values of $T_{\frac{1}{2}}$, $\gamma_{\frac{1}{2}}$ and $\varepsilon_{\frac{1}{2}}$ can be systematically varied to provide a solution which satisfies the upper boundary condition, is presented. A flow chart of the solution procedure is given in Figure 2.11, and is shown in more detail in Figure 2.12. To further clarify these procedures some of the ideas contained in the flow diagrams must be explained. The first concept relates to the definition of a 'convergence line', (C_l). This is a line which lies in a horizontal plane passing through point (x_p, y_p, z_p) and whose horizontal angle is defined between the horizontal line from the origin to the point (x_p, y_p) and the global x axis. The second parameter is the 'radial position' R_p which is the distance along the C_l where the boundary condition (x_p, y_p, z_p) lies. The terms are defined mathematically as

$$C_l = \arctan\left(\frac{y_p}{x_p}\right) \tag{2.76a}$$

and

$$R_p = (x_p^2 + y_p^2)^{\frac{1}{2}}. \tag{2.76b}$$

To start the solution procedure, estimates of the tension and the vertical and horizontal orientation of the first element are needed. For the initial estimate of the tension in the first element the value of the line breaking strength (BS) can be used. Although this will cause the tension in the subsequent elements to be greater than this, when the upper endpoint boundary condition has been satisfied the maximum value of the tension distribution should be less than the breaking force, leading to a safe solution. If it is not then the solution procedure must be repeated with a line material which has a greater breaking strength. Since it is not known *a priori* whether the first element is grounded or not, two angles are to be associated with the vertical orientation of the first suspended element. Firstly a small angle which defines when the element has become 'grounded'; this means that once the element angle has become less than this specified value, the solution procedure will assume that this element is grounded on the seabed. The second

larger angle provides an upper bound for γ. It corresponds to an angle made by a straight line drawn from the anchor position to the free surface, which has a length equal to that of the mooring line. These angular limits are referred to as $\gamma^{\min}$ and $\gamma^{\max}$ and are given by

$$\gamma^{\min} = 0.005^o \text{ (for example)} \tag{2.77a}$$

and

$$\gamma^{\max} = \arcsin\left(\frac{d}{L}\right) \tag{2.77b}$$

where d is the water depth and L is the length of the catenary. When considering the horizontal orientation of the first element the angular definition of the C_l as defined in Equation (2.76a) is used to define maximum and minimum values of ε, that is

$$\varepsilon^{\min} = \varepsilon^{C_l} - 10^\circ \tag{2.78a}$$

and

$$\varepsilon^{max} = \varepsilon^{C_l} + 10^\circ. \tag{2.78b}$$

Before the calculation loop of Figure 2.11 is entered, the following initial conditions to be used are $T_{\frac{1}{2}} = \text{BS}$, $\gamma_{\frac{1}{2}} = \gamma^{\min}$ and $\varepsilon_{\frac{1}{2}} = \varepsilon^{\min}$. The values for the variables $T_{j+\frac{1}{2}}$, $\gamma_{j+\frac{1}{2}}$ and $\varepsilon_{j+\frac{1}{2}}$ for $j = 1, \ldots, h$ are then calculated as described in Section 2.4.1 using the scheme set out in Figure 2.11. The first objective of the iterative solution procedure is to bring the upper endpoint of the line onto the surface defined by z_p. To do this the calculated vertical position (z_c) of the endpoint is compared with z_p; if it is found to be greater than z_p the first element is grounded and the solution is restarted with exactly the same initial conditions but now these are applied to the second element. This process continues until z_c is less than z_p. When this is the case, γ is set to $\gamma^{\max}$ and this is used to provide a value for z_c, designated as z_{c1}, which will lie above the free surface. Interpolation can now be used to establish a value for $\gamma_{j+\frac{1}{2}}$ which causes $z_c \approx z_p$. Because of the nonlinear relationship between $\gamma_{g+\frac{1}{2}}$ and z_p, where the subscript $g+\frac{1}{2}$ denotes the first nongrounded element, the interpolation is an iterative process and so an acceptable error margin for z_p must be defined for z_c to lie within. This error typically has a value of 0.01% of the water depth. When the endpoint lies on the free surface this is the end of the first loop of the solution process.

The second loop of the solution process is intended to bring the catenary endpoint onto the C_l. For the first loop described above, convergence on the free

surface has been achieved for values of $\varepsilon_{g+\frac{1}{2}}$ and $T_{g+\frac{1}{2}}$ which have not been changed from the initial values they were set to. For the start of the second loop new initial values of $T_{\frac{1}{2}} = \text{BS}$, $\gamma_{\frac{1}{2}} = \gamma^{\min}$ and $\varepsilon_{\frac{1}{2}} = \varepsilon^{\max}$, are set and the first loop is then repeated until the solution converges on the free surface for a second time. Now there are two solutions which lie on the horizontal plane defined by z_p and which lie on either side of the C_l. The same interpolative method used in the first loop is now used to alter the horizontal orientation of the first element so that the endpoint converges on the C_l. This is the end of the second loop.

The solution has now been developed to the point where the upper endpoint of the mooring line lies on both the free surface and also on the C_l. At this point in the solution process the tension in the first nongrounded element still has the value of $T_{g+\frac{1}{2}} = \text{BS}$. This value is now reduced to a nominal 10% of this level and the solution is again restarted. When the end of the second loop is reached for the second time there are two solutions which lie on the C_l, but with different radial positions. Again interpolation, as described previously, is used to provide the initial tension required to satisfy the boundary condition, that is the endpoint is located at the requested R_p. This ends the third loop in the solution procedure, and the solution now satisfies the required boundary condition for the case of no fluid loading.

Up to this point the solution has been generated without the application of fluid loading, as discussed in Section 2.4, that is the solution has been obtained for $i = 1$. The fluid loading forces are now calculated for the static geometry obtained from above. Next the entire process is repeated again so that a new solution is obtained which now takes some account of the fluid loading. The fluid loading is then again calculated from the new geometry and the whole process repeated; this is done until the change in the displacements of the solutions obtained for $i - 1$ and i, lies within some predefined tolerance.

With the final solution, the tension distribution along the line can be used to confirm or reject the original choice of line material. With this numerical procedure it is possible to define different material types for each individual element so as to reduce the stresses in areas of high tension. For the practical application of this software error limits are defined on the water depth, the horizontal orientation of the convergence line C_l and the radial position R_p. Note, however, that each time an initial condition is changed, the whole convergence procedure must be repeated up to that point.

2.6 Results

Having developed iterative schemes to solve the analytic catenary equations and indicated how to solve the more general numerical problem, comparisons between the two can now be undertaken. Within the open literature, however, very few published papers provide comparisons of predictions using the catenary equations and the numerical formulation. One such is a paper by Dominguez and Filmer(1971). Although the numerical technique is not explicitly described in the paper, it is based on the equilibrium of forces at each node. Thus the principle, at least, is the same as the formulation presented in Section 2.4. Wang(1975) also presents a comparison between analytical and numerical methods, although there are subtle differences, namely:

1. The analytic form of the catenary equations is not developed, instead the differential equations of equilibrium are directly integrated using numerical methods.

2. Three numerical models are developed but results for the model which corresponds to that in Section 2.4 are not discussed in detail.

3. Both the analytic and numerical models are regarded as initial value problems and not as boundary value problems as formulated in this thesis and in the paper of Dominguez and Filmer(1971).

This means that only the results from Dominguez and Filmer(1971) can be used as a basis for comparison.

Similarly very few papers exist which present the explicit derivation of, or the results from, the numerical method. One paper which does is by Nakajima(1986a). In this case the formulation is presented in some detail, but the required data and the results derived from the method are not clearly given. Consequently validation of the present numerical model with results presented in the literature is not possible. Tables 2.1 and 2.2 illustrate the principal variables required to run the numerical and the analytical programs respectively, together with typical values used. This basic data set is changed as necessary to yield the required results for the different case studies now reported.

Parameter	Symbol	Units	Value
x position of endpoint	x_p	m	1000
y position of endpoint	y_p	m	1000
Water depth	d	m	1000
Line breaking force	BS	N	800000
Length of mooring line	L	m	2000
Number of elements	h	-	20
Water density	ρ	Kg/m^2	1025
Then for each element the following are defined			
Line diameter	D	m	0.07148
Mass per metre in air	m	kg/m	25.5
Young's Modulus	E	MN/m^2	7.848×10^{10}
Poisson's ratio	ν	-	0.3
Normal drag coefficient	Cd_n	-	1.6
Tangential drag coefficient	Cd_t	-	0.03
Radius of SSB	R_{ssb}	m	1.5
Density of SSB material	ρ_{ssb}	kg/m^3	0.0
Drag coefficient of SSB	Cd_{ssb}	-	0.1
Radius of clump weight	R_{cw}	m	0.5
Density of clump weight	ρ_{cw}	kg/m^3	1000
Drag coefficient of clump weight	Cd_{cw}	-	0.4
End of element data			
% error in depth	z_{err}	-	0.001
Angular error on C_l	C_{lerr}	degrees	0.01
% error on R_p	R_{perr}	-	0.01

Table 2.1 — Line Parameters for Numerical Model

Parameter	Symbol	Units	Value
Length of mooring line	L	m	2000
water depth	d	m	1000
Radial position	R_p	m	1414
Second limit	p_1	m	995
% error in depth	z_{err}	-	0.001
Net mass per metre	$w(s)$	Kg/m^3	21.4

Table 2.2 — Line Parameters for the Analytical Method

2.6.1 Comparison of Analytic and Numerical Results

Case Study 1 : Geometric Comparison

The first obvious comparison to be undertaken is the geometry generated by the analytic and numerical models. In general it is expected that the geometries should be the same for the same boundary conditions. Using the catenary equations Figure 2.13 shows the predicted geometry of the complete catenary for different values of R_p, where R_p is the horizontal distance between the anchor position and the endpoint of the line (see Equation (2.76b)). Thus as R_p increases, more of the line is lifted from the seabed and the resulting change in geometry is clearly illustrated.

Figure 2.14 shows the corresponding predictions for a numerical model based on 20 elements. It can be seen that the geometries are almost identical with those of Figure 2.13, including the estimation of the amount of line lying on the seabed. Figures 2.15 and 2.16 show predictions generated when using the same R_p values applied to numerical models of 10 and 3 elements respectively. They show how an increasingly coarse discretisation of the line leads to less accurate predictions of the line geometry. In particular, the 3 element model shows expected inaccuracies in the prediction of the amount of grounded line as the R_p value changes. This is illustrated by comparing the predictions for R_p values of 1500m and 1550m. For the first R_p value it is seen that the first element is grounded, whereas in the second case the solution predicts no grounded line at all. This sudden change in the line geometry has implications regarding the line tension.

A more instructive comparison of the predicted geometries is shown in Figures 2.17 and 2.18. The former shows that the geometries of the 20 element numerical model and the analytic model agree very well for most of the length of the line, only differing slightly in the touchdown region. The geometry of the 3 element model is, as expected, not in good agreement with the other models. Figure 2.18 provides a comparison of the same four models but at values of R_p which correspond to the maximum practical limits allowed in the models. Again the 20 element numerical model and the analytical model agree well, whereas the 3 element numerical model shows the worst comparison at the lower R_p value, but exhibits a much better geometric comparison at the larger R_p value.

Case Study 2 : Tension Variation at Different Excursions

Figure 2.19 indicates how the maximum tension developed in the mooring line varies as a function of R_p for the four different models. Figure 2.20 shows the percentage deviation of the numerical models' maximum tension from the solution obtained from the catenary equations. The location of the maximum tension in a mooring line is normally at the top end, since at this point all the weight of the line is being borne. The position of the maximum tension may change when there is a subsurface buoy (SSB) with a large buoyancy force located at an intermediate position along the line. In this case the maximum tension may be found to be in the element adjoining the SSB. For the present no SSB is assumed so the maximum tension is considered to be located at the top of the line. As the model becomes more coarse, the excursion curve (i.e. the curve of maximum tension versus R_p) becomes more irregular, although the same general trend is maintained. Also the tension developed by the 20 element numerical model very closely matches that developed by the analytical model, but that it diverges slightly at the larger values of R_p. Also the results from the 10 element model closely follow the predictions of the 20 element model, even if they are very slightly greater. This difference increases slightly with R_p.

The excursion curve for the 3 element model is worthy of further discussion, because the coarseness of the model highlights an important feature not immediately apparent in the behaviour of the other numerical models. Firstly, there is the general shape of the excursion curve. The gradient of the curve is shallow at low R_p values, indicating that a large change in R_p produces only a small change in the value of the maximum tension. However the gradient quickly steepens as R_p is increased, until $R_p = 1550$m. Reverting to Figure 2.16 it is observed that at approximately this value of R_p the first element is lifted from the seabed. It

is this which causes a reduction in the gradient of the excursion curve of Figure 2.19. This characteristic can be interpreted in terms of the elastic behaviour of the mooring line. With the first element grounded and the value of R_p increasing, the two freely suspended elements are gradually becoming more taut. Furthermore, any increase in R_p is not only altering the geometry but also is extending the line in a Hookean fashion. As R_p continues to increase the effect is increasingly to stretch the line and not to change the geometry. This is due to a decreasing amount of geometric 'slack'. This effect manifests itself as an increase in the gradient of the excursion curve of Figure 2.19, up to $R_p = 1550$m. Following the lifting of the grounded element, the amount of geometric 'slack' suddenly is increased. This can be thought of as having an effect similar to that of reducing the R_p value when the first element is grounded. That is, this would cause a reduction in the gradient of the excursion curve in Figure 2.19. As the R_p value continues to increase, the gradient of the excursion curve again becomes steeper. Thus it may be concluded that the tension developed in a mooring line is affected by two characteristics of the line, which may be termed the geometric stiffness and the material stiffness.

The above discussion indicates that with a low R_p value a small change in the top tension produces a large change in the R_p. This occurs because at this point on the excursion curve most of the increase in the tension is being absorbed by the geometric stiffness and the contribution of the material stiffness is not as significant. As R_p increases, the amount of geometric slack decreases and hence the ability of the geometric stiffness to absorb the change in the top tension is reduced. Thus the increase in the top tension is increasingly countered by the material stiffness which requires a large change in force to produce a change in displacement. By this reasoning the shape of the excursion curve for the 3 element numerical model is qualitatively explained using concepts of geometric and material stiffness. The same concepts apply to all solutions of mooring lines and act to produce the same effects, but it is only in the 3 element numerical model that these become obvious.

The distribution of tension along the line for the 4 models considered is shown in Figure 2.21. As expected the tension in the grounded elements remains constant, and then gradually increases as the upper endpoint of the mooring line is approached. This is a consequence of there being more line to support and hence a greater tension results.

Case Study 3 : Influence of Water Depth on Maximum Tension

In this study the length of the mooring line is always considered to be twice the water depth, and similarity of catenary shape at different depths is maintained by ensuring that x_p and y_p (the coordinates of the boundary condition) are equal to the water depth. Furthermore, all numerical results are now obtained with the 20 element model unless otherwise stated. The difference between the predicted maximum analytical and numerical tensions are shown in Figure 2.22 for increasing depths. The predicted maximum tensions can be seen to linearly diverge with increasing water depth, suggesting that the analytic results become increasingly inaccurate as water depth increases. The difference between the maximum predicted tension for different numerical models relative to the analytic solution for increasing values of R_p for the same water depth, were presented Figure 2.20. This shows that as R_p increases the difference in the results increases, but even at the maximum practical value of R_p, the difference is not significantly greater than at lower R_p values (for the 20 element model). In both cases the maximum tensions derived from the analytic method are seen to underpredict the maximum tensions derived from the numerical method. This difference, caused by increasing either the water depth or R_p, can be explained on the grounds that the catenary equations are developed for short lines where line stretch is considered relatively unimportant. This is equivalent to demanding that Young's Modulus is infinite which further implies that no line stretch is allowed in the solution generated by the catenary equations. As such this is an effect related to the material stiffness term previously discussed in case study 2 and, as indicated there, this term only becomes important as R_p increases. Therefore in the case of the analytic solution the effect of material stiffness upon the predictions will be unchanging with R_p or water depth. The predictions generated by the numerical model will, however, be subject to the effect of the material stiffness term. As mentioned in case study 2 this effect will increase with increasing R_p values, thus causing the divergence present in Figures 2.20 and 2.22. Therefore the difference in the results is due to having more limiting constraints implicit in the assumptions used to derive the catenary equations.

2.6.2 Properties of the Numerical Model

Case Study 4 : Change of CPU with Number of Elements

Figure 2.23 indicates the computer central processing unit (CPU) time taken to obtain each solution as a function of the number of elements (h). The graphs

are seen to be nonlinear and that within the limits of obtaining an accurate CPU time, the times do not appear to be depth dependent. A rough estimate of the CPU time required as a function of h has the form

$$CPU \approx Ah^B,$$

with $A \approx 5.435$ and $B \approx 1.755$.

Case Study 5 : Change of Maximum Tension with Number of Elements

Figure 2.24 indicates how the maximum tension developed is affected by the number of elements used in the numerical model. This shows that 60 elements would give a very good approximation to the assumed 'true' solution obtained with 100 elements. With 20 elements the solution is over predicted by roughly 1%, but the required CPU time drops from 7000ms (for the 60 element model) to 1000ms. This result is confirmed in the paper of Dominguez and Filmer(1971). Here the right hand side of case III is the relevant result for comparison where an over prediction of approximately 1.5% is found for the 20 element model. However this result is based on comparison with the analytic solution and not to the 'true' numerical solution as assumed here. Figures 2.26 and 2.27 show the percentage deviations of solutions with differing numbers of elements from the solution with 100 elements (100E) and the analytical solution respectively, for three different water depths. What is apparent from Figure 2.26 is that the accuracy is independent of the water depth and it can also be seen that a numerical model with 20 elements only incurs a relative error of 1%. Figure 2.27 shows that the differences are depth dependent, for the reasons given in case study 3, but that for each depth the trends are the same. Additionally a 20 element model is seen to give an error of approximately 1%. Consequently 20 elements may be regarded as a practical number of elements to use with the numerical model with respect to the compromise struck between the accuracy of the predictions and the CPU time required to obtain the solution.

Figure 2.25 is analogous to Figure 2.24, but indicates the sensitivity of the predictions for three different water depths. It may also be concluded that the 20 element model gives increasingly accurate results in shallower waters. This is to be expected since the similarity condition, described in case study 3, means that the length of the catenary, and hence the size of the elements, is being reduced with the water depth. Consequently with the element sizes reducing the answers are increasingly accurate.

Case Study 6 : Influence of A Subsurface Buoy (SSB)

In many practical deep sea mooring applications, the tension at the top end of the mooring line is very large; if the entire line is manufactured to withstand this top tension, then it can become a very costly item. One method of reducing the top tension in the line is to attach SSBs at strategic points along the length of the line, to support part of the line weight. The influence on the maximum tension and the tension distribution, as a result of attaching a SSB at a point along the line is now examined.

Figure 2.28 shows the effect on the tension distribution by attaching a SSB with an equivalent buoyancy force of 200KN at node 15 of a 20 element model. With a SSB this large it is seen that the maximum tension is now located in the element which lies immediately below the buoy, and that the tension immediately above the buoy is almost the same as the tension in the grounded portion of the line. Consequently the tension at the top point of the line is greatly reduced in comparison to the situation when there is no SSB present.

Figure 2.29 shows how the presence of a SSB affects the geometry of the line by measuring the component displacements from the original position of each node. As expected the largest nodal changes occur at the node to which the SSB is attached, whilst it can be seen that there is little effect upon the grounded portion of the line. Because there are no out-of-plane effects present, the displacements in the x and y directions will be the same. Note that although the two curves of x (or y) and z displacements are not identical in magnitude they are very nearly symmetrical about the '0 displacement' line. The graphs indicate that the presence of the SSB increases the z coordinates of all the nodes whilst it decreases the x and y coordinates.

Figure 2.30 shows more readily interpretable data, that is, the percentage changes in the tension and the geometry caused by the presence of a SSB. It can be seen that the SSB causes a large percentage change in the tension distribution over most of the line except at the point of attachment of the SSB. This is to be expected in the situation where the SSB does not cause significant lifting of the grounded portion of the line, since the weight of line supported at the point of attachment will be the same with or without the SSB present. The percentage change in the x and y coordinates is relatively small indicating that the presence of the SSB does not cause a significant horizontal change in the position of the line. The curve which indicates the percentage change in the z coordinates can be

a little misleading. This is because the elements originally forming the grounded portion of the line initially had zero z values, hence any change caused by the presence of the SSB, no matter how small, will produce a large percentage change. Despite this it can still be seen that the percentage change in the z coordinates over most of the rest of the line is generally much larger than the corresponding change in the x and y coordinates. This is to be expected since the action of the SSB is in the z direction.

Figure 2.31 indicates how the tension distribution is affected by locating the SSB at different positions along the length of the line, namely at nodes 8, 10, 12, 14, and 16. With the SSB at different positions the same general shape in the distribution of the tension is present, but each curve has a slight distortion for the different nodal locations of the SSB. But it would seem that having the SSB located at node 10 or 11 would produce the greatest reduction in the tension along the line. This conclusion is more explicitly indicated in Figure 2.32 where a plot of the tension in four 'critical' elements is shown. The four elements under consideration are:

1. The first element of the line (1).
2. The element below the node at which the SSB is located (2).
3. The element above the node at which the SSB is located (3).
4. The last element in the line (4).

As expected the tensions in (2) and (4) are the greatest. As a result the intersection of these two curves indicates the optimum position for the SSB, that is the location which reduces the tension in the line by the greatest amount - in this case node 11.

Figure 2.33 shows excursion curves for the SSB located at different positions along the line length. It confirms the previous conclusion that node 11 is the optimum site for the location of the SSB. Furthermore, it also shows that this conclusion is unaffected by the value of R_p for the line. With the SSB located progressively nearer the line endpoint (i.e. at nodes 14 and 16), it is seen that the beneficial influence of the SSB in reducing the maximum tension is gradually mitigated, until the difference in the tension distribution from the case with no SSB is not discernible. With the SSB located at node 8 the maximum tension is again developed at the top end of the line, since the greatest portion of suspended line is now above the buoy.

2.6.3 Influence of Major Line Parameters

The influence on the maximum tension developed in the line by varying the major line parameters is now investigated. The major line parameters are regarded as Young's Modulus (E), Weight per metre ($w(s)$) and the line diameter D. However, since the latter can be directly transformed into an increase in $w(s)$, results are not explicitly presented for the change in line diameter.

Case Study 7 : Influence of Young's Modulus

Figure 2.34 shows the effect of a percentage change in the value of E, realised as a percentage change in tension. Since E is the ratio of stress and strain it therefore affects the material stiffness and not the geometric stiffness, and since material stiffness is only important at large values of R_p, this graph is for the relatively low R_p value of 1414m. It is expected that a change in E will have a small influence upon the tension distribution. This conclusion is borne in Figure 2.34, however, it is to be noted that a reduction in E produces a larger drop in tension than the equivalent increase in E produces an increase in tension. This can be explained, albeit in rather a convoluted fashion, thus: By decreasing E the material stiffness of the line is reduced and hence under a given constant loading the length of the line will be increased. If the value of E is left unchanged an increase in the length of the line can be effected by increasing the tension in the top element. If an excursion curve is now considered where the usual abscissa of R_p is replaced by the line length L, then it is seen that an increase in L is equivalent to a decrease in R_p - both resulting in a decrease in the tension distribution. Thus the nonlinearity of Figure 2.34 can be explained in the same fashion as the nonlinearities associated with the excursions curves presented earlier. This is more clearly illustrated in Figure 2.35 where the percentage change in tension is plotted against the percentage change in E. This effectively represents the reciprocal of the excursion curves.

Case Study 8 : Influence of Weight per Metre

Figure 2.36 shows the linear influence of changing the $w(s)$ of the line. Here the same percentage change in tension is produced by the same percentage increase and decrease in $w(s)$. Hence the same difference in tension changes against load changes, presented in Figure 2.37, is applicable to all elements.

Case Study 9 : Influence of Depth to Length Ratio

The next investigation examines the relationship between the maximum tension in the line and the water depth to line length ratio, $(\frac{d}{L})$. Figure 2.38 clearly indicates that the changes in tension due to the changes in $(\frac{d}{L})$ depend upon whether d or L is being varied, and the value of the fixed variable. The effect of increasing L when d is constant, and of increasing d when L is constant, is similar to changing the radius of the boundary condition for fixed d and L. Hence it is expected that the resulting curves should be similar to the excursion curves described previously. This is borne out in Figure 2.38. The most important conclusion to be drawn from this figure is that if it is desired to obtain the maximum tension in a mooring line by using the nondimensional ratio of $(\frac{d}{L})$, that no general combination of d and L can be used. Therefore if it is desired to investigate the change in maximum tension caused by, for example, changing the line length at a given water depth, the specific curve appropriate for that depth must be used.

Case Study 10 : Influence of Cd_n and Cd_t

The next investigation concerns the influence of ocean currents and the values assigned to the normal and tangential drag coefficients. Figure 2.39 shows the change in tension distribution which occurs when a vertically uniform in-plane current is introduced. It is clear that magnitude rather than the shape of the excursion curve is affected. Also the increases in the magnitudes of the tensions are nonlinear for linear increases in the current velocity.

The increase in tension relative to the case of the no current situation is presented in Figure 2.40 and the corresponding percentage difference is presented in Figure 2.41. These predictions indicate that when there is a uniform ocean current, the largest increase in the tension is associated with the first nongrounded element, whilst there is a relatively smaller increase in the top tension. For example, with a current of 2.0 m/s there is an increase in tension in the grounded line of approximately 150%, but an increase of only 40% in the tension of the endpoint element.

Figure 2.42 shows the percentage change in the x (and y) coordinates caused by the different vertically uniform currents. As expected the in-plane current causes an increase in the nodal excursions of the elements roughly in the midpoint of the suspended line. What is interesting is the reduction in nodal excursions of the first few nongrounded elements. Also the transition from a reduction to an increase in

nodal excursion occurs at roughly the same position along the line, regardless of the magnitude of this current.

Figure 2.43 shows the corresponding changes in the z coordinates of the nodes. In presenting these results an artificial cut off percentage change of 10% has been used, since any finite change from zero for the grounded elements will produce extremely large percentage changes. The presence of the current causes the line to move in the same plane as the current. There is also a kind of 'pivotal' effect approximately halfway along the suspended part of the line, in the sense that for that portion of the line below the 'pivot' the z coordinate increases, and for that portion of line above the 'pivot' the z coordinate decreases. This is reasonable since the action of the current on the elements forming the top part of the line is to induce a horizontal movement which can only occur when the elements in the lower portion are moving vertically.

Figure 2.44 shows the change in the tension distribution caused by altering the normal drag coefficient of each element by the same amount. The change in the tension for each element for different Cd_n values is nearly, but not quite, linear. Also, as expected, an increase in Cd_n results in a larger fluid loading force and hence a displaced tension distribution curve.

Figure 2.45 shows the percentage change in tension distribution from the case with zero fluid loading, i.e. $Cd_n = 0$.

Figure 2.46 shows the change in the tension distribution caused by a change in the tangential drag coefficient, Cd_t, with Cd_n held constant. As expected the tangential drag force does not have a significant influence upon the tension. This is further confirmed in Figure 2.47 which shows the percentage change in the tensions. From this it is possible to conclude that it is important to use an appropriate value for Cd_n, but that Cd_t can be effectively ignored.

2.7 Summary

This chapter has investigated the analytical and numerical formulation of the static mooring line problem and presents predictions using both methods. The analytical formulation was developed in 3D up to the point where the solution of the resulting equilibrium equations required an iterative scheme. Therefore the more usual 2D form was developed, with the analytic solution dependent upon the assumption made regarding the form of the loading; the two most common

solutions are the 'parabolic' and the 'catenary' equations. The analytical development then continued with the catenary equations by addressing the two particular cases associated with the grounded and nongrounded situations. An outline of the solution method and the developed software is presented. The formulation of the numerical model is then given, where it is explained that this formulation allows for the inclusion of fluid loading and line attachments - in particular subsea buoys. The solution method was then described in detail.

Predictions using both formulations (the catenary equations and the numerical method) were then presented. The following points summarise the main conclusions.

1. Predictions of the line geometry obtained from the analytical and 20 element numerical models are in close agreement. Increasingly coarse numerical meshes (i.e. fewer elements) results in less compatible predictions.

2. Excursion curve predictions are in generally close agreement for the analytical and 20 element numerical models. The predictions however tend to diverge slightly as R_p increases.

3. From the excursion curve of the 3 element numerical model, two contributions to the overall restoring force of the mooring line can be identified. These are termed 'geometric' and 'material' stiffness.

4. Increasing water depth causes a slight divergence in the predictions of the line tensions for the analytical and 20 element numerical models. This is indicated to be a result of the 'infinite' stiffness condition implicit in the development of the catenary equations.

5. Increasing the number of elements used to model the mooring line affects the CPU time for solution in a nonlinear fashion. This is shown to be independent of the water depth used in the simulation.

6. Increasing the number of elements improves the accuracy of the tension predictions. However a 20 element model will only over-predict the 'correct' solution by approximately 1% but this is obtained at a relatively low CPU cost.

7. Subsurface buoys are shown to have a significant influence upon the tension distribution within a mooring line. This can result in a greatly reduced maximum tension.

8. Changes in E produce a nonlinear change in the tension; this can be considered as the reciprocal of the excursion curves. Changing $w(s)$ has a linear influence upon the predicted tensions.

9. The depth to length ratio $\frac{d}{L}$ cannot be used with any general values of d and L. This is because the excursion curves produced are not coincident for different values.

10. Variation Cd_t is shown to have little influence on the results, but the value of Cd_n can have a significant effect.

This validates the use of the catenary equations in situations where fluid loading, line attachments and different line materials are not considered. The numerical formulation has two main advantages over the analytic method, namely : (i) the inclusion of line attachments, and (ii) that arbitrary fluid loading are both handled in a straight forward manner. The drawbacks of the numerical method are (i) the slightly more complicated formulation and (ii) the longer solution times, particularly when fluid loading is included. Even so the numerical formulation is more flexible and can handle situations outside the scope of the catenary equations and most importantly, the numerical static solution is used as the equilibrium position (starting point) for the numerical solution of the dynamics of a mooring line.

CHAPTER 3

Formulation and Solution of Mooring Line Dynamics

3.1 Introduction

This chapter details the presentation of a rigorous and consistent derivation of the equations of motion for a discretised line structure and of the solution of these equations to yield the time domain history of line tension and displacement. The problem may be stated thus: "*Given the initial conditions (i.e. position and velocity at time $t = t_0$) of a line immersed in a fluid, determine its subsequent motions*" (Walton and Polachek(1960)). Apart from the required information about initial and boundary conditions, there are to be no further explicit restrictions on the equations of motion or the adopted solution procedure. Therefore it is a totally general problem to be solved, which allows for:

1. Out of plane longitudinal and transverse motions of the line.
2. Large displacements from the original equilibrium position.
3. General definitions of the boundary conditions.
4. Different line materials along the length of the line.
5. The inclusion of line attachments.

This general statement of the problem also allows for the inclusion of large displacement, low frequency motions as induced by second-order hydrodynamic induced drifting of the vessel, and the high frequency, small displacement motions of the vessel generally associated with the presence of ocean waves. A third possible type of motion is the very high frequency motions induced by the vortex shedding forces around the mooring line. This effect, known as strumming, is only likely to be significant for extremely high line tensions as present, for example, in TLP moorings, and it is therefore not considered further here.

3.2 Equations of Motion for A Mooring Line

In order to derive the numerical formulation of what is in reality a continuous and smooth distribution of line geometry, mass and applied forces, the line must

be 'discretised'. In such a formulation the mooring line is modelled as a series of straight, massless, spring-like elements which are connected at 'nodes'. It is at the nodes that the average of the mass of, and the forces acting on, the adjoining elements are considered to act. The equations of motion can then be formulated for each node, and it is at the nodes that the solution scheme is subsequently applied. Having solved the static problem as described in Chapter 2, the discretisation process has already been applied, hence the static solution is used as the starting point for the dynamic simulation. The most complete presentation of this procedure is given by Walton and Polachek(1960). This may be regarded as the founding paper with regard to the numerical static and dynamic solution of a broad class of "suspended cable" type structures. Several other more concise presentations exist, see, for example, van den Boom(1985), van den Boom *et al.*(1987) and Nakajima *et al.*(1982). However all these papers are deficient in the necessary mathematical detail because of lack of space. Additionally the formulation and solution is only presented in two dimensions (2D) and further, they contain various simplifying assumptions. Although the extension of the 2D problem to three dimensions (3D) is conceptually a relatively easy task, there are a few nuances associated with the 3D solution which have not been presented in the literature.

At this point the difference between longitudinal, transverse and out-of-plane motions is indicated. Consider a line lying totally in the 2D plane defined by the global x and z axes. By increasing the displacement of the mooring line upper endpoint in a direction parallel to the line angle at this endpoint, longitudinal motion will result. However because of the curvature of the line this will also cause transverse motion, that is, motion in a direction which has a component normal to the line axis at any point along the length of the mooring line. Out-of-plane motions are induced by forces which do not act in the (x, z) plane, for example, ocean currents or waves. This produces a component of motion which is normal to the (x, z) plane.

Having established the discretisation presented in Chapter 2, the equations of motion can be formulated explicitly for each node. The forces considered to act on every node in the discretisation, except those nodes which represent the boundary conditions, are:

1. Gravity forces: These include the net self weight of the line in water and the addition of any line attachments, as well as the reaction forces between the seabed and any portion of line which may be grounded.

2. Drag forces: These arise as a result of the drag imposed by the fluid on the line and are directly proportional to the square of the relative fluid velocity between the line and the fluid.

3. Inertial forces: These are the forces caused by the relative acceleration of the node and the surrounding fluid.

Each of these external forces give rise to the internal force of tension. All these forces conspire to make the problem dynamically nonlinear and to couple the transverse and longitudinal degrees of freedom through the resulting line curvature. Effects due to bending are not considered because a mooring cable, and certainly a mooring chain, is deemed flexible enough not to transmit bending moments along its length. Cable kinking should not occur so long as the mean level of the line tension is high enough. Cable rotation is considered to have insignificant effect on the total solution, although it might be important locally, for example at the winch point, but these effects will not be considered here.

Mathematically the equilibrium of forces at each node can be expressed through Newton's second law of motion, namely

$$\underline{G}_j = \underline{M}_j^T \ddot{\underline{U}}_j, \tag{3.1}$$

where the j^{th} node is considered. Each vector has three components, i.e.

$$\underline{G}_j = \begin{pmatrix} G_{xj} \\ G_{yj} \\ G_{zj} \end{pmatrix}, \qquad \underline{M}_j = \begin{pmatrix} M_{xj} \\ M_{yj} \\ M_{zj} \end{pmatrix}, \qquad \ddot{\underline{U}}_j = \begin{pmatrix} \ddot{x}_j \\ \ddot{y}_j \\ \ddot{z}_j \end{pmatrix}.$$

The right hand side of Equation (3.1) is known as the inertial term since it is dependent upon the acceleration vector $\ddot{\underline{U}}_j$. Each of the components in $\underline{M}_j$ has two contributing terms, the actual mass M_j, which is lumped at the node and is acted upon by the nodal accelerations, and the added (or entrained) mass $\underline{m}_j$, which, in this idealisation, depends upon the relative accelerations evaluated at the element midpoints. Therefore Equation (3.1) can be rewritten in the form

$$\underline{G}_j = M_j \ddot{\underline{U}}_j + \underline{P}_j + \underline{P}_j^*, \tag{3.2}$$

where $\underline{P}_j$ is the average of the products of the inertia coefficients and the relative midpoint acceleration for each adjoining element, and $\underline{P}_j^*$ is the added mass of any line attachments at the j^{th} node and is the product of an inertial coefficient for

the line attachment and the acceleration which is assumed to act at node j. The actual mass, M_j, is given by

$$M_j = \frac{1}{2}\left(m_{j-\frac{1}{2}} l_{j-\frac{1}{2}} + m_{j+\frac{1}{2}} l_{j+\frac{1}{2}}\right) + M_j^*, \tag{3.3}$$

where m represents the mass per meter of each element, l is the unstretched length of each element and M_j^* is the additional mass of any line attachments acting at the j^{th} node. It follows from Equation (3.3) that without the presence of line attachments, M_j is the average of the mass of the line elements on either side of node j. Equation (3.2) can now be written as

$$\underline{G}_j = \left[\frac{1}{2}\left(m_{j-\frac{1}{2}} l_{j-\frac{1}{2}} + m_{j+\frac{1}{2}} l_{j+\frac{1}{2}}\right) + M_j^*\right]\underline{\ddot{U}}_j + \underline{P}_j + \underline{P}_j^*. \tag{3.4}$$

In order to evaluate $\underline{P}_j$ the fluid forces acting on each element either side of the node must be considered. Initially the force for element $j+\frac{1}{2}$ is considered in more detail. The transformation matrix $[\Omega]$ has already been defined in Appendix A and this is now used to relate the local coordinate system (p, q, r) to the global coordinate system (x, y, z). The same transformation is used to relate the local and global relative velocities and accelerations. With the element subscript j dropped for convenience, one may write

$$\begin{pmatrix} \ddot{p} \\ \ddot{q} \\ \ddot{r} \end{pmatrix} = (\Omega) \begin{pmatrix} \ddot{x}^r \\ \ddot{y}^r \\ \ddot{z}^r \end{pmatrix}. \tag{3.5}$$

The added mass can now be defined in terms of the inertial forces along each of the three local axes, so that

$$\begin{aligned} P_p &= a_t \ddot{p}, \\ P_q &= a_n \ddot{q}, \\ P_r &= a_n \ddot{r}, \end{aligned} \tag{3.6}$$

where the added mass coefficients a_t and a_n are assumed to remain constant for each element as the solution proceeds. The added mass in the global axes is given by the inverse of the transformation in Equation (3.5), yielding

$$\begin{pmatrix} P_x \\ P_y \\ P_z \end{pmatrix} = (\Omega)^{-1} \begin{pmatrix} P_p \\ P_q \\ P_r \end{pmatrix}. \tag{3.7}$$

The combination of Equations (3.6) and (3.7) is shown in Appendix B and can be reduced to the following form

$$\underline{P}_{j+\frac{1}{2}} = e_{j+\frac{1}{2}}\ddot{\underline{U}}^r_{j+\frac{1}{2}}, \tag{3.8}$$

where the element subscript has now been re-introduced, the superscript r indicates that relative acceleration is to be used and $e_{j+\frac{1}{2}}$ is the global added mass coefficient matrix. The same result also applies for element $j-\frac{1}{2}$, and thus the average of the added masses for the elements on either side of node j, which is considered to act at node j, is given by

$$\underline{P}_j = \frac{1}{2}\left(e_{j-\frac{1}{2}}\ddot{\underline{U}}^r_{j-\frac{1}{2}} + e_{j+\frac{1}{2}}\ddot{\underline{U}}^r_{j+\frac{1}{2}}\right) \tag{3.9}$$

and this becomes

$$\underline{P}_j = \frac{1}{4}\left[e_{j-\frac{1}{2}}(\ddot{\underline{U}}^r_j + \ddot{\underline{U}}^r_{j-1}) + e_{j+\frac{1}{2}}(\ddot{\underline{U}}^r_j + \ddot{\underline{U}}^r_{j+1})\right], \tag{3.10}$$

upon specifying the accelerations at the midpoint of an element as the mean of the accelerations of the nodes defining the element. This formulation leads to an intractable solution since the calculation of $\underline{P}_j$ now involves a knowledge of the relative accelerations at three nodes. Since it is only possible to solve the equations of motion for one node at a time, it is required that the equation for $\underline{P}_j$ involves quantities at that node only. To achieve this it is assumed that the accelerations at the centroids of the neighbouring elements are approximated by the acceleration at the common node, so that Equation (3.9) is then given by

$$\underline{P}_j = \frac{1}{2}\left(e_{j-\frac{1}{2}} + e_{j+\frac{1}{2}}\right)\ddot{\underline{U}}^r_j. \tag{3.11}$$

This means that instead of taking the average of the added masses for the elements on either side of node j, the average of the added mass coefficients for the elements have been used together with the relative nodal accelerations. The added mass, $\underline{P}^*_j$, for any attachment to the line at the j^{th} node is given by

$$\underline{P}^*_j = \rho \underline{V}^*_j \ddot{\underline{U}}^r_j, \tag{3.12}$$

where $\underline{V}^*_j$ is the equivalent volume associated with the added mass for the attachment. Thus Equation (3.2) may be written in the form

$$\begin{aligned}\underline{G}_j = &\left[\frac{1}{2}(m_{j-\frac{1}{2}}l_{j-\frac{1}{2}} + m_{j+\frac{1}{2}}l_{j+\frac{1}{2}}) + M^*_j\right]\ddot{\underline{U}}_j \\ &+ \left[\rho\underline{V}^*_j + \frac{1}{2}(e_{j-\frac{1}{2}} + e_{j+\frac{1}{2}})\right]\ddot{\underline{U}}^r_j.\end{aligned} \tag{3.13}$$

The vector $\underline{G}_j$ therefore now contains all the remaining external forces associated with fluid drag and gravity, as well as the internal force of tension. Resolving these forces into their global component directions in a manner analogous to Equations (2.50) to (2.52), the following are derived

$$\begin{aligned} G_{xj} &= T_{j+\frac{1}{2}} \cos\gamma_{j+\frac{1}{2}} \cos\varepsilon_{j+\frac{1}{2}} - T_{j-\frac{1}{2}} \cos\gamma_{j-\frac{1}{2}} \cos\varepsilon_{j-\frac{1}{2}} + F_{xj} \\ G_{yj} &= T_{j+\frac{1}{2}} \cos\gamma_{j+\frac{1}{2}} \sin\varepsilon_{j+\frac{1}{2}} - T_{j-\frac{1}{2}} \cos\gamma_{j-\frac{1}{2}} \sin\varepsilon_{j-\frac{1}{2}} + F_{yj} \\ G_{zj} &= T_{j+\frac{1}{2}} \sin\gamma_{j+\frac{1}{2}} - T_{j-\frac{1}{2}} \sin\gamma_{j-\frac{1}{2}} - W_j + F_{zj}. \end{aligned} \tag{3.14}$$

This can be expressed more generally as

$$\underline{G}_j = T_{j+\frac{1}{2}}(\alpha_{j+\frac{1}{2}}) - T_{j-\frac{1}{2}}(\alpha_{j-\frac{1}{2}}) + \underline{N}_j, \tag{3.15}$$

where $\underline{N}_j$ contains the fluid drag and gravity forces which act at node j and $\alpha_{j+\frac{1}{2}}$ and $\alpha_{j-\frac{1}{2}}$ define the resolution of the forces acting above and below the node. The gravity force is W_j and this is the net weight of the average of the segment masses lumped at node j, plus the net weight of any attachment. W_j is therefore given by

$$\begin{aligned} W_j = g\Big\{\frac{1}{2}(m_{j-\frac{1}{2}} l_{j-\frac{1}{2}} + m_{j+\frac{1}{2}} l_{j+\frac{1}{2}}) - \frac{\pi\rho}{8}\Big(l_{j-\frac{1}{2}} D^2_{j-\frac{1}{2}} + l_{j+\frac{1}{2}} D^2_{j+\frac{1}{2}}\Big) \\ + (M^*_j - \rho V^*_{j(z)})\Big\}. \end{aligned} \tag{3.16}$$

The drag forces F_{xj}, F_{yj} and F_{zj} are calculated in a similar fashion to the added mass, but with one important difference, viz: The added mass is seen to be linearly proportional to the accelerations in the local component directions and thus it is possible to calculate the added mass in local component form and directly transform these back to global components. However with the drag forces it is seen that they are proportional to the square of the relative fluid velocity across the element and hence are nonlinear. By transforming the global fluid velocity components into local fluid components, there will be two local normal fluid velocities, and one tangential component relative to the line element. The original semi-empirical derivation of Morison's equation referred to a cylinder subject to fluid velocity in one normal direction only and most experimental values for drag coefficients are derived for this case. This situation appears to exclude the possibility of a cross flow which would produce complex fluid interference effects around the cylinder and would apparently make the use of a drag coefficient derived for flow in one direction invalid. Here this difficulty is partially overcome by providing a resultant

normal velocity calculated from the two normal velocity components. This is then used to calculate the velocity squared normal drag which is then resolved back to the two local normal axes. The details of calculating the drag forces are given in Section 2.4 via Equations (2.65) to (2.70). It is assumed that the drag coefficients remain constant during the solution procedure. Thus the definition of $\underline{N}_j$ becomes

$$\underline{N}_j = \frac{1}{2}\left[K_{j+\frac{1}{2}} - K_{j-\frac{1}{2}}\right] - \underline{k}W_j \tag{3.17}$$

where $\underline{k}$ is the unit normal along the z axis and K is defined in Appendix C. All that remains is to define exactly the relative velocities to be used in Equation (3.17) to calculate $\underline{N}_j$. These are the resultant velocities between the mooring line nodal velocities and water particle velocities which may arise from ocean currents or waves or a combination of the two. The current profile vector at the j^{th} node, $\underline{C}_j$, has components C_{xj}, C_{yj} and C_{zj}, and the wave velocity vector $\underline{W}_j^v$ has components W_{xj}^v, W_{yj}^v and W_{zj}^v. These are defined as being positive along the positive global Cartesian axes. The theoretical calculation of the combined wave and current water particle accelerations, $\ddot{\underline{U}}_j^{wc}$, and velocities, $\dot{\underline{U}}_j^{wc}$, is discussed in Section 3.3, here it is simply noted that

$$\dot{\underline{U}}_j^r = \dot{\underline{U}}_j + \dot{\underline{U}}_j^{wc}. \tag{3.18}$$

This concludes the principal part of the derivation of the equations of motion for a mooring line structure. The equations used in the analysis are provided by equating Equations (3.13) and (3.15) and using Equations (3.16) and (3.17) to define $\underline{N}_j$. In the next section two further aspects of the model are examined, namely the calculation of the relative fluid velocities and accelerations and the method of modelling the interaction between the line and the seabed.

3.3 Wave Modification of Velocity and Acceleration Terms

In this section it is shown how the relative fluid accelerations of Equation (3.13) and the relative fluid velocities of Equation (3.17) are determined for a combination of linear waves and an ocean current. More information on this is to be found in Hedges(1983) and Peregrine(1976). By using a relatively simple wave model it is possible to gain some understanding as to whether wave effects are significant or not. If they should prove significant then a more sophisticated wave model should be derived to account for water particle velocities and accelerations in an irregular seaway, see, for example, van den Boom *et al.*(1987). The procedure now outlined is based on developing a description of the wave in the presence of a vertically uniform current profile. First consider Figure 3.1 which shows that the direction

of the wave crests for a monochromatic wave system have a heading of θ' with respect ot the global x axis. Also indicated is the set of local axes (x', y', z') which are used to define the wave quantities. The current velocities U and V along the x' and y' axes are respectively defined as

$$\begin{aligned} U &= C_x \cos\theta' - C_y \sin\theta' \\ V &= C_y \cos\theta' + C_x \sin\theta' \end{aligned} \tag{3.19}$$

The assumption of a monochromatic wave implies that there is no variation in wave properties along the wave crests. It is also assumed that the presence of the ocean current has no effect upon the profile of the wave. Having calculated U, the current velocity in the direction of wave propagation, it is possible to define wave celerity, wave period and wave frequency with respect to either an origin which is fixed in space and time, or to an origin which is steadily advancing with a forward velocity of U in the direction of wave propagation. In the fixed system the apparent quantities of wave celerity, wave period, and wave frequency are designated as C_a, T_a and ω_a respectively. If an observer travels along the x' axis at the current velocity U, then the wave would appear to be propagating on 'still' water and the corresponding relative quantities of C_r, T_r and ω_r are seen. The wave celerities measured in respect to the fixed and relative axes systems are related according to

$$C_a = C_r + U, \tag{3.20}$$

where

$$C_a = \frac{\lambda_w}{T_a} \tag{3.21}$$

and

$$C_r = \frac{\lambda_w}{T_r}. \tag{3.22}$$

Clearly Equation (3.20) describes a linear combination of wave and current effects. Also note that the wavelength λ_w is assumed to be the same in both reference systems. Both of these assumptions are to be considered as approximations to the real situation. In reality the presence of a current will have a nonlinear effect on the wave profile and thus nonlinearly affect the water particle velocities and accelerations. This is due to the nonlinear kinematic and dynamic free surface boundary conditions which control the wave propagation, see Stoker(1957).

Similarly there are definitions of apparent and relative wave frequency, viz

$$\omega_a = \frac{2\pi}{T_a}, \tag{3.23}$$

and

$$\omega_r = \frac{2\pi}{T_r}. \tag{3.24}$$

Therefore Equations (3.21) and (3.22) become

$$C_a = \frac{\lambda_w \omega_a}{2\pi} \qquad \text{and} \qquad C_r = \frac{\lambda_w \omega_r}{2\pi},$$

and hence Equation (3.20) can be rewritten in the form

$$\omega_a = \omega_r + \frac{2\pi}{\lambda_w} U.$$

The quantity $2\pi/\lambda_w$ is the wave number, k, and so

$$\omega_a = \omega_r + kU. \tag{3.25}$$

From basic linear water wave theory there is the dispersion relationship which relates the wave frequency to the wave number, i.e.

$$\omega_r^2 = gk \tanh(kd), \tag{3.26}$$

where d is the water depth. Substituting for ω_r from Equation (3.25) in Equation (3.26), leads to

$$(\omega_a - kU)^2 = gk \tanh(kd). \tag{3.27}$$

With ω_a, U, g and d known, Equation (3.27) can be iteratively solved for k, as indicated in Appendix D. Then Equation (3.26) will yield a value for ω_r. With k and ω_r known, it is now possible to calculate the associated water particle velocities and accelerations from the definition of the velocity potential for a linear wave. With respect to a fixed reference system, (x', z'), the associated velocity potential has the form

$$\Phi(x', z', t) = \frac{gH}{2\omega} \frac{\cosh(k(\bar{z} + d))}{\cosh(kd)} \sin(k\bar{x} - \omega t), \tag{3.28}$$

where $\bar{x}$ is the distance from the origin of this reference system to the point of interest and $\bar{z}$ is the distance from the mean free surface to the same point. Now with a forward velocity of U towards the point of interest, then at any time t the separation between the moving origin and the point of interest is given by

$$\bar{x}_r = \bar{x} - Ut, \tag{3.29}$$

where $\bar{x}_r = \bar{x}$ at time $t = t_0 = 0$. As stated previously, with reference to the moving axes system, the wave profile appears to be propagating on 'still' water, and hence the corresponding velocity potential will have the same form as Equation (3.28), but this time $\bar{x}$ and ω are expressed in terms of their relative quantities, that is

$$\Phi(x', z', t) = \frac{gH}{2\omega_r} \frac{\cosh(k(\bar{z} + d))}{\cosh(kd)} \sin(k\bar{x}_r - \omega_r t). \tag{3.30}$$

It is from Equation (3.30) that the relevant expressions for the water particle velocities and accelerations are now derived.

3.3.1 Water Particle Velocities

The horizontal and vertical water particle velocities are denoted by $V_{rx'}$ and $V_{rz'}$ respectively and are calculated by differentiating Equation (3.30) with respect to $\bar{x}_r$ and $\bar{z}$ respectively, to yield

$$V_{rx'} = \frac{\partial \Phi}{\partial \bar{x}} = \frac{kgH}{2\omega_r} \frac{\cosh(k(\bar{z} + d))}{\cosh(kd)} \cos(k\bar{x}_r - \omega_r t) \tag{3.31}$$

and

$$V_{rz'} = \frac{\partial \Phi}{\partial \bar{z}} = \frac{kgH}{2\omega_r} \frac{\sinh(k(\bar{z} + d))}{\cosh(kd)} \sin(k\bar{x}_r - \omega_r t). \tag{3.32}$$

Since Equations (3.31) and (3.32) provide velocities with respect to the moving observer, the equivalent for a stationary observer is derived directly from Equation (3.20) to yield

$$V_{ax'} = U + \frac{kgH}{2\omega_r} \frac{\cosh(k(\bar{z} + d))}{\cosh(kd)} \cos(k\bar{x}_r - \omega_r t), \tag{3.33}$$

and, by analogy,

$$V_{az'} = C_z + \frac{kgH}{2\omega_r} \frac{\sinh(k(\bar{z} + d))}{\cosh(kd)} \sin(k\bar{x}_r - \omega_r t), \tag{3.34}$$

where C_z is the current component along the z' axis. $V_{ax'}$ and $V_{az'}$ thus defined are the horizontal and vertical water particle velocities for a linear wave which accounts for the presence of a vertically uniform ocean current. Note that they are defined in an axis system which is parallel to the direction of wave propagation. Their corresponding values in the global axes system are given by

$$\underline{\dot{U}}_j^{wc} = \begin{pmatrix} \dot{x}_j^{wc} \\ \dot{y}_j^{wc} \\ \dot{z}_j^{wc} \end{pmatrix} = \begin{pmatrix} V_{ax'} \cos\theta' \\ -V_{ax'} \sin\theta' \\ V_{az'} \end{pmatrix}. \tag{3.35}$$

3.3.2 Water Particle Accelerations

To derive the water particle accelerations, it is assumed that the current velocity is time invariant, i.e. that it makes no contribution to the inertia forces. The substantive (or total) derivatives of Equations (3.33) and (3.34) are taken to yield the accelerations. The substantive derivative is generally defined as

$$\frac{D()}{Dt} = \frac{\partial()}{\partial t} + u\frac{\partial()}{\partial x} + v\frac{\partial()}{\partial y} + w\frac{\partial()}{\partial z}. \tag{3.36}$$

Thus the x and z acceleration components are respectively given by

$$A_{ax'} = \frac{D}{Dt}(V_{ax'}) = \frac{\partial}{\partial t}(V_{ax'}) + V_{ax'}\frac{\partial}{\partial x'}(V_{ax'}) + V_{ay'}\frac{\partial}{\partial y'}(V_{ax'}) + V_{az'}\frac{\partial}{\partial z'}(V_{ax'}) \tag{3.37}$$

and

$$A_{az'} = \frac{D}{Dt}(V_{az'}) = \frac{\partial}{\partial t}(V_{az'}) + V_{ax'}\frac{\partial}{\partial x'}(V_{az'}) + V_{ay'}\frac{\partial}{\partial y'}(V_{az'}) + V_{az'}\frac{\partial}{\partial z'}(V_{az'}) \tag{3.38}$$

where

$$V_{ax'} = V_{rx'} + U,$$

$$V_{ay'} = V, \text{ and}$$

$$V_{az'} = V_{rz'} + C_{z'},$$

where U and V are defined in Equation (3.19). By carrying out the differentiation and applying the assumptions made in Appendix E, the following results are derived

$$A_{ax'} = \frac{\varepsilon}{\beta}\left[\omega_r \sin\delta - \frac{\varepsilon k}{\beta}\sin\delta\cos\delta + C_z k\gamma\cos\delta\right] \tag{3.39}$$

and

$$A_{az'} = \frac{\varepsilon}{\beta}\left[C_z k\alpha\sin\delta + \frac{\varepsilon k}{\beta}\alpha\gamma - \omega_r\gamma\cos\delta\right] \tag{3.40}$$

where α, β, γ, δ and ε are defined in Appendix E. The vertical and horizontal accelerations for a wave in the presence of a vertically uniform current have now been derived, but because $A_{ax'}$ and $A_{az'}$ are defined relative to the direction of wave propagation, they must be resolved along the global axes thus

$$\underline{\ddot{U}}_j^{wc} = \begin{pmatrix} \ddot{x}_j^{wc} \\ \ddot{y}_j^{wc} \\ \ddot{z}_j^{wc} \end{pmatrix} = \begin{pmatrix} A_{ax'}\cos\theta' \\ -A_{ax'}\sin\theta' \\ A_{az'} \end{pmatrix}. \tag{3.41}$$

Therefore the relative nodal accelerations $\underline{\ddot{U}}_j^r$ of Equation (3.13) are given by the following vector combination

$$\underline{\ddot{U}}_j^r = \underline{\ddot{U}}_j + \underline{\ddot{U}}_j^{wc}. \tag{3.42}$$

3.4 Mooring Line / Seabed Interaction

Due to the nature of the Lumped Mass method adopted here, there are a series of nodes at which the mass of the line is concentrated and where the forces are assumed to act. Each node is then considered to be joined by straight, massless segments. If any of these masses should lift from, or ground on, the seabed during the dynamic simulation, then unrealistically large shock loads will be introduced into the solution. Therefore a manner of reducing the shock loads should be included in the mathematical model in order that the resulting solution of the tension history should not contain spurious peaks. To this end, three basic approaches seem to have been adopted in the literature, viz:

1. Linear springs with critical damping are used to model the seabed. This is the most widely adopted approach. See, for example, Larsen and Fylling (1982) and van den Boom(1985).

2. To set the velocities and accelerations of the nodes to zero when they reach the seabed. See, for example, Wilhelmy and Fjeld(1981) and Hwang(1984).

3. To reduce the mass of the first freely suspended node as it approaches the seabed. See, for example, Nakajima *et al.*(1982).

Each of the three methods have difficulties associated with their implementation, but apart from the paper of Larsen and Fylling(1982), where these problems are highlighted, none of the other references make mention of any mathematical or numerical difficulties in applied analyses. In fact throughout most of the literature associated with lumped mass models of mooring line dynamics, the interaction between the line and the seabed is rarely indicated by more than a passing comment. With method (1) the problem lies in the correct selection of the stiffness constants for the springs, since these values will depend upon the mass and velocity characteristics of each node. This means that not only will each node have a stiffness value associated with it because of its (possibly different) mass, but this value also depends upon the motion of the node and hence is time dependent. In method (2) the problem of preventing shock loading is not really addressed. By setting

the velocity and acceleration to zero when the node reaches the seabed, all that is achieved is prevention of the node passing through the seabed. Shock loading will still be introduced because the node has been suddenly prevented from moving. For method (3) the problem rests with how to reduce the mass in a consistent manner - in fact this procedure is directly analogous with method (1), since a reduction in node mass corresponds to a reduction in the downward force associated with that node, and this is exactly the desired effect of using the springs in method (1).

Of these three approaches, method (3) models most closely what happens physically as a real line is laid down or picked up from the seabed. It is seen that the mass of the suspended part of the line is gradually reduced as the grounded portion of the line is increased, and vice versa. Therefore the usual numerical formulation of the line still applies, but now the mass assigned to the first suspended element varies according to its distance from the seabed. The mass distribution of the line is shown in Figure 2.10. It can be seen that as the first suspended node approaches the seabed, the amount of line which in reality contributes mass to that node is constantly being reduced. Hence in the limiting case it is expected that just before the node grounds, its mass should be equal to half the mass of the next element, plus ΔM. Therefore because of the physical basis for the method and because of its direct analogy with method (1), it has been adopted here. The details of this procedure are presented in Appendix F, but will be briefly described here. Essentially a parabola is constructed through the first suspended and the last grounded nodes, with the straight line between the nodes used as the reference axis. The distance from the last grounded node to the intersection of the parabola and the seabed is calculated. This is then used as a proportion of the element length in order to reduce the mass associated with the first suspended node.

Other seabed effects which are present include friction and suction on the grounded portion of the line. In the tangential (or axial) direction along the line it is supposed that frictional effects are not large, but ground suction may be important. The effects of both normal and tangential soil friction forces, together with the instabilities introduced by the nodal grounding and lifting procedure, are further examined in some detail in Chapter 8.

3.5 Solution Procedure

The equations of motion which have been formulated are essentially stated through Equations (3.13) and (3.14), and these are to be solved in the time domain

using direct integration schemes. With a complete solution known at a particular instance, the use of time integration schemes allows the calculation of a trial solution for the next time step which is then subject to correction by the application of an appropriate constraint equation. The use of direct time integration schemes enables accurate answers to be obtained, since all the nonlinearities inherent in the formulation are preserved. However, the limitations of the schemes must be well understood in order that a sensible interpretation of the results can be made.

3.5.1 Overview of Time Integration Schemes

An investigation into the numerical properties of the direct time integration schemes used here is undertaken in Chapter 5. Here the forms of the four different schemes selected are stated, without the inclusion of the element subscripts, as:

Central Difference Scheme

$$\ddot{\underline{U}}^n = \frac{1}{\Delta t^2}\left(\underline{U}^{n+1} - 2\underline{U}^n + \underline{U}^{n-1}\right) \tag{3.43}$$

$$\dot{\underline{U}}^n = \frac{1}{2\Delta t}\left(\underline{U}^{n+1} - \underline{U}^{n-1}\right). \tag{3.44}$$

Houbolt Scheme

$$\ddot{\underline{U}}^{n+1} = \frac{1}{\Delta t^2}\left(2\underline{U}^{n+1} - 5\underline{U}^n + 4\underline{U}^{n-1} - \underline{U}^{n-2}\right) \tag{3.45}$$

$$\dot{\underline{U}}^{n+1} = \frac{1}{6\Delta t}\left(11\underline{U}^{n+1} - 18\underline{U}^n + 9\underline{U}^{n-1} - 2\underline{U}^{n-2}\right). \tag{3.46}$$

Wilson-θ Scheme

$$\ddot{\underline{U}}^{n+\theta} = \frac{6}{(\theta\Delta t)^2}\left(\underline{U}^{n+\theta} - \underline{U}^n\right) - \frac{6}{\theta\Delta t}\dot{\underline{U}}^n - 2\ddot{\underline{U}}^n \tag{3.47}$$

$$\dot{\underline{U}}^{n+\theta} = \frac{3}{\theta\Delta t}\left(\underline{U}^{n+\theta} - \underline{U}^n\right) - 2\dot{\underline{U}}^n - \frac{\theta\Delta t}{2}\ddot{\underline{U}}^n. \tag{3.48}$$

Newmark Scheme

$$\underline{\dot{U}}^{n+1} = \underline{\dot{U}}^{n} + \Delta t\left[(1-\delta)\underline{\ddot{U}}^{n} + \delta\underline{\ddot{U}}^{n+1}\right] \tag{3.49}$$

$$\underline{U}^{n+1} = \underline{U}^{n} + \Delta t\underline{\dot{U}}^{n} + \Delta t^{2}\left[(0.5-\alpha)\underline{\ddot{U}}^{n} + \alpha\underline{\ddot{U}}^{n+1}\right]. \tag{3.50}$$

Note the slight difference in the notation associated with the Wilson-θ scheme. This is introduced because the size of the time step is now considered as non-integer and so cannot be denoted by integer increments as with the other schemes. The variable θ measures the size of the time step, so that $n+1 = n+\theta$ when $\theta = 1$ (θ is usually taken as being equal to 1.4 for reasons which are explained in Chapter 5). The principal difference between the Central Difference (CD) scheme and the three remaining schemes can be seen from the functional dependence of the solution at the next time step upon the previous solutions. The CD scheme can be rearranged in the form

$$\underline{U}^{n+1} = f\left(\underline{U}^{n}, \underline{U}^{n-1}, \underline{\ddot{U}}^{n}\right), \tag{3.51}$$

where the displacement at the next time step $(n+1)$ is calculated from the solutions up to, and including n only. The remaining schemes can be rearranged in the form

$$\underline{U}^{n+1} = f_1\left(\underline{U}^{n}, \underline{U}^{n-1}, \underline{U}^{n-2}, \underline{\ddot{U}}^{n+1}\right), \tag{3.52}$$

where it is seen that the displacement at the next time step, $\underline{U}^{n+1}$, is related to the solutions up to and including time step $n+1$. Hence it is possible to define two general families of time integration schemes, namely 'explicit' and 'implicit' schemes. The CD scheme is a member of the former, whilst the remaining schemes belong to the latter. The most important difference between these two families is that for explicit schemes to remain numerically stable there is a maximum limit on the size of the time step which can be used, whilst, in theory at least, the implicit schemes are applicable with any size of time step. This point is further expounded in Chapter 5.

In order to use the time integration schemes described in Equations (3.43) to (3.50), the equations of motion must be rearranged into a more amenable form, and this is shown next.

3.5.2 Rearranged Equations of Motion

The aim of this section is to rearrange the equations of motion, as given by Equation (3.13) and (3.14), into the following functional form

$$\begin{aligned}\ddot{x}_j &= f\Big(\gamma_j, \varepsilon_j, T_j, F_{xj}, a_{tj}, a_{nj}\Big),\\ \ddot{y}_j &= f\Big(\gamma_j, \varepsilon_j, T_j, F_{yj}, a_{tj}, a_{nj}\Big),\\ \ddot{z}_j &= f\Big(\gamma_j, \varepsilon_j, T_j, F_{zj}, W_j, a_{tj}, a_{nj}\Big).\end{aligned} \tag{3.53}$$

The general form of the equations of motion as expressed by Equation (3.13), is given by

$$\underline{G}_j = M_j \ddot{\underline{U}}_j + \underline{P}_j, \tag{3.54}$$

where M_j now represents the mass of the elements and the attachments, and $\underline{P}_j$ is the added mass of the elements as well as the added mass of any line attachments, and is given by Equation (3.11), viz

$$\underline{P}_j = \frac{1}{2}\big(e_{j+\frac{1}{2}} + e_{j-\frac{1}{2}}\big)\ddot{\underline{U}}_j^r,$$

where it is assumed that there are no line attachments present. First consider the $e_{j+\frac{1}{2}}\ddot{\underline{U}}_j^r$ term, where the expanded components of this are given in Appendix B in Equations (B.6), (B.7) and (B.8). These further reduce to the following forms

$$\begin{aligned}P_{x(j+\frac{1}{2})} = {}& \ddot{x}_j^r\Big[a_t\cos^2\gamma\cos^2\varepsilon + a_n(\sin^2\varepsilon + \cos^2\varepsilon\sin^2\gamma)\Big]_{j+\frac{1}{2}}\\ &+ \ddot{y}_j^r\Big[(a_t - a_n)\cos^2\gamma\cos\varepsilon\sin\varepsilon\Big]_{j+\frac{1}{2}}\\ &+ \ddot{z}_j^r\Big[(a_t - a_n)\sin\gamma\cos\gamma\cos\varepsilon\Big]_{j+\frac{1}{2}}\end{aligned} \tag{3.55}$$

$$\begin{aligned}P_{y(j+\frac{1}{2})} = {}& \ddot{x}_j^r\Big[(a_t - a_n)\cos^2\gamma\sin\varepsilon\cos\varepsilon\Big]_{j+\frac{1}{2}}\\ &+ \ddot{y}_j^r\Big[a_t\cos^2\gamma\sin^2\varepsilon + a_n(\cos^2\varepsilon + \sin^2\varepsilon\sin^2\gamma)\Big]_{j+\frac{1}{2}}\\ &+ \ddot{z}_j^r\Big[(a_t - a_n)\sin\gamma\cos\gamma\sin\varepsilon\Big]_{j+\frac{1}{2}}\end{aligned} \tag{3.56}$$

$$P_{z(j+\frac{1}{2})} = \ddot{x}_j^r\Big[(a_t - a_n)\sin\gamma\cos\gamma\cos\varepsilon\Big]_{j+\frac{1}{2}} + \ddot{y}_j^r\Big[(a_t - a_n)\sin\gamma\cos\gamma\sin\varepsilon\Big]_{j+\frac{1}{2}} + \ddot{z}_j^r\Big[a_t\sin^2\gamma + a_n\cos^2\gamma\Big]_{j+\frac{1}{2}}. \tag{3.57}$$

It can also be seen that $P_{x(j-\frac{1}{2})}$, $P_{y(j-\frac{1}{2})}$ and $P_{z(j-\frac{1}{2})}$ will have the same form as the three equations above. Hence with the fluid added mass vector $\underline{P}_j$ described as

$$\underline{P}_j = \begin{pmatrix} P_{xj} \\ P_{yj} \\ P_{zj} \end{pmatrix} = \frac{1}{2}\begin{pmatrix} P_{x(j+\frac{1}{2})} + P_{x(j-\frac{1}{2})} \\ P_{y(j+\frac{1}{2})} + P_{y(j-\frac{1}{2})} \\ P_{z(j+\frac{1}{2})} + P_{z(j-\frac{1}{2})} \end{pmatrix},$$

it can be seen that the components are given as

$$P_{xj} = \frac{\ddot{x}_j^r}{2}\Big[a_t\cos^2\gamma\cos^2\varepsilon + a_n(\sin^2\varepsilon + \cos^2\varepsilon\sin^2\gamma)\Big]_{j-\frac{1}{2}}^{j+\frac{1}{2}} + \frac{\ddot{y}_j^r}{2}\Big[(a_t - a_n)\cos^2\gamma\cos\varepsilon\sin\varepsilon\Big]_{j-\frac{1}{2}}^{j+\frac{1}{2}} + \frac{\ddot{z}_j^r}{2}\Big[(a_t - a_n)\sin\gamma\cos\gamma\cos\varepsilon\Big]_{j-\frac{1}{2}}^{j+\frac{1}{2}} \tag{3.58}$$

$$P_{yj} = \frac{\ddot{x}_j^r}{2}\Big[(a_t - a_n)\cos^2\gamma\sin\varepsilon\cos\varepsilon\Big]_{j-\frac{1}{2}}^{j+\frac{1}{2}} + \frac{\ddot{y}_j^r}{2}\Big[a_t\cos^2\gamma\sin^2\varepsilon + a_n(\cos^2\varepsilon + \sin^2\varepsilon\sin^2\gamma)\Big]_{j-\frac{1}{2}}^{j+\frac{1}{2}} + \frac{\ddot{z}_j^r}{2}\Big[(a_t - a_n)\sin\gamma\cos\gamma\sin\varepsilon\Big]_{j-\frac{1}{2}}^{j+\frac{1}{2}} \tag{3.59}$$

$$P_{zj} = \frac{\ddot{x}_j^r}{2}\Big[(a_t - a_n)\sin\gamma\cos\gamma\cos\varepsilon\Big]_{j-\frac{1}{2}}^{j+\frac{1}{2}} + \frac{\ddot{y}_j^r}{2}\Big[(a_t - a_n)\sin\gamma\cos\gamma\sin\varepsilon\Big]_{j-\frac{1}{2}}^{j+\frac{1}{2}} + \frac{\ddot{z}_j^r}{2}\Big[a_t\sin^2\gamma + a_n\cos^2\gamma\Big]_{j-\frac{1}{2}}^{j+\frac{1}{2}}, \tag{3.60}$$

where the notation introduced above should be interpreted thus

$$\Big[x\Big]_{j-\frac{1}{2}}^{j+\frac{1}{2}} = x_{j+\frac{1}{2}} + x_{j-\frac{1}{2}}.$$

Equation (3.54) is now written in component form as

$$\begin{aligned} G_{xj} &= P_{xj} + M_j \ddot{x}_j \\ G_{yj} &= P_{yj} + M_j \ddot{y}_j \\ G_{zj} &= P_{zj} + M_j \ddot{z}_j, \end{aligned} \tag{3.61}$$

where $\underline{G}_j$ now contains all the remaining external forces indicated in Equation (3.14). Therefore Equation (3.61) can finally be expressed in the following form

$$\begin{aligned} &\left\{\left(M_j + M_j^*\right)\ddot{x}_j + \frac{\ddot{x}_j^r}{2}\left[a_t \cos^2\gamma\cos^2\varepsilon + a_n(\sin^2\varepsilon + \cos^2\varepsilon\sin^2\gamma)\right]_{j-\frac{1}{2}}^{j+\frac{1}{2}} + \ddot{x}_j^r \rho V_x^*\right\} \\ &\quad + \frac{\ddot{y}_j^r}{2}\left[(a_t - a_n)\cos^2\gamma\cos\varepsilon\sin\varepsilon\right]_{j-\frac{1}{2}}^{j+\frac{1}{2}} \\ &\quad + \frac{\ddot{z}_j^r}{2}\left[(a_t - a_n)\sin\gamma\cos\gamma\cos\varepsilon\right]_{j-\frac{1}{2}}^{j+\frac{1}{2}} \\ &\quad = \left[T\cos\gamma\cos\varepsilon\right]_{j-\frac{1}{2}}^{j+\frac{1}{2}} + F_{xj} \end{aligned} \tag{3.62}$$

$$\begin{aligned} &\frac{\ddot{x}_j^r}{2}\left[(a_t - a_n)\cos^2\gamma\sin\varepsilon\cos\varepsilon\right]_{j-\frac{1}{2}}^{j+\frac{1}{2}} \\ &+\left\{\left(M_j + M_j^*\right)\ddot{y}_j + \frac{\ddot{y}_j^r}{2}\left[a_t\cos^2\gamma\sin^2\varepsilon + a_n(\cos^2\varepsilon + \sin^2\varepsilon\sin^2\gamma)\right]_{j-\frac{1}{2}}^{j+\frac{1}{2}} + \ddot{y}_j^r\rho V_y^*\right\} \\ &\quad + \frac{\ddot{z}_j^r}{2}\left[(a_t - a_n)\sin\gamma\cos\gamma\sin\varepsilon\right]_{j-\frac{1}{2}}^{j+\frac{1}{2}} \\ &\quad = \left[T\cos\gamma\sin\varepsilon\right]_{j-\frac{1}{2}}^{j+\frac{1}{2}} + F_{yj} \end{aligned} \tag{3.63}$$

$$\begin{aligned} &\frac{\ddot{x}_j^r}{2}\left[(a_t - a_n)\sin\gamma\cos\gamma\cos\varepsilon\right]_{j-\frac{1}{2}}^{j+\frac{1}{2}} \\ &\quad + \frac{\ddot{y}_j^r}{2}\left[(a_t - a_n)\sin\gamma\cos\gamma\sin\varepsilon\right]_{j-\frac{1}{2}}^{j+\frac{1}{2}} \\ &+\left\{\left(M_j + M_j^*\right)\ddot{z}_j + \frac{\ddot{z}_j^r}{2}\left[a_t\sin^2\gamma + a_n\cos^2\gamma\right]_{j-\frac{1}{2}}^{j+\frac{1}{2}} + \ddot{z}_j^r\rho V_z^*\right\} \\ &\quad = \left[T\sin\gamma\right]_{j-\frac{1}{2}}^{j+\frac{1}{2}} + F_{zj} - W_j. \end{aligned} \tag{3.64}$$

These three equations can be rearranged to give

$$\begin{aligned}\ddot{x}_j &= \hat{R}_j T_{j+\frac{1}{2}} + \hat{S}_j T_{j-\frac{1}{2}} + \hat{T}_j \\ \ddot{y}_j &= \hat{U}_j T_{j+\frac{1}{2}} + \hat{V}_j T_{j-\frac{1}{2}} + \hat{W}_j \\ \ddot{z}_j &= \hat{O}_j T_{j+\frac{1}{2}} + \hat{P}_j T_{j-\frac{1}{2}} + \hat{Q}_j,\end{aligned} \tag{3.65}$$

where the rearrangement and the coefficients in Equation (3.65) are shown in Appendix G. Examination of these coefficients shows that Equation (3.65) has now been arranged in the required form specified by Equation (3.53). It is now possible to apply the direct time integration schemes to these forms.

3.5.3 Application of Time Integration Schemes

In this section the application of the two families of integration schemes (i.e. the implicit and explicit methods) are considered separately, since the methodology of solution differs slightly in each case.

Implicit Schemes

Here the three implicit schemes, namely the Houbolt, Wilson-θ, and Newmark methods are considered. The implicit nature of these schemes means that the solution, $\underline{U}_j^{n+1}$, is required at time $t = (n+1)\Delta t$ and is therefore dependent not only upon past displacements, but is also dependent upon the acceleration at time $t = (n+1)\Delta t$, i.e. $\ddot{\underline{U}}_j^{n+1}$. This displacement is generally expressed by Equation (3.52) where the function f_1 is defined for each of the individual schemes and the subscript j is omitted for convenience. Since the correct value of $\underline{U}^{n+1}$ is dependent upon the correct value of $\ddot{\underline{U}}^{n+1}$, and the latter is not yet known, a trial or tentative estimate of this acceleration vector must be made, which is denoted by $\tilde{\ddot{\underline{U}}}^{n+1}$, in order to calculate a tentative estimate of $\underline{U}^{n+1}$, namely $\tilde{\underline{U}}^{n+1}$. Therefore, Equation (3.52) can be rewritten as

$$\tilde{\underline{U}}^{n+1} = f(\tilde{\ddot{\underline{U}}}^{n+1}, \underline{U}^n, \underline{U}^{n-1}, ..., \underline{U}^1). \tag{3.66}$$

By application of the constraint equation (explained later) to the solution of tentative displacements, $\tilde{\underline{U}}^{n+1}$, a correction can be calculated which is to be applied to $\tilde{\ddot{\underline{U}}}^{n+1}$ so that the distance between the predicted nodal displacements matches the distance predicted through Hooke's law. The correction process is then continued until $\tilde{\underline{U}}^{n+1}$ is deemed to have converged. At this point it is worth noting that an

examination of the coefficients in Appendix G for Equation (3.65), shows that the tentative accelerations are dependent upon both the tentative tensions and the tentative displacements, thus

$$\underset{\sim}{\tilde{\ddot{U}}}^{n+1} = f(\underset{\sim}{\tilde{U}}^{n+1}, \tilde{T}^{n+1}). \tag{3.67}$$

Thus the constraint equation may be satisfied with any non-unique pairing of $\underset{\sim}{\tilde{U}}^{n+1}$ and $\tilde{T}^{n+1}$, which means that there are potentially an infinite number of solutions. A unique solution can only be obtained when either the tentative displacements or the tentative tensions of Equation (3.67) are held constant, the choice of which depends upon the form of the rearranged equations of motion. Following the rearrangement adopted here, as indicated by Equation (3.53), the displacements are maintained constant whilst the values for the tensions are used for the iteration. Thus Equation (3.67) becomes

$$\underset{\sim}{\tilde{\ddot{U}}}^{n+1} = f(\underset{\sim}{U}^{n+1}, \tilde{T}^{n+1}). \tag{3.68}$$

The foregoing discussion indicates in general terms the solution procedure using implicit schemes. This is now considered in more detail for one scheme, the Houbolt method. Results for the Wilson-θ and Newmark schemes can then be drawn from the general conclusions obtained with the Houbolt scheme and although subtle differences exist, these will be explained at the end of this section. Once the relations in Equation (3.65) have been substituted into the rearranged component form of Equation (3.45), and bearing in mind the result of Equation (3.68), it can be shown that

$$\begin{aligned}
\tilde{x}_j^{n+1} &= \frac{1}{2}\Big\{5x_j^n - 4x_j^{n-1} + x_j^{n-2} + \Delta t^2\big[\hat{R}_j^n \tilde{T}_{j+\frac{1}{2}}^{n+1} + \hat{S}_j^n \tilde{T}_{j-\frac{1}{2}}^{n+1} + \hat{T}_j^n\big]\Big\} \\
\tilde{y}_j^{n+1} &= \frac{1}{2}\Big\{5y_j^n - 4y_j^{n-1} + y_j^{n-2} + \Delta t^2\big[\hat{U}_j^n \tilde{T}_{j+\frac{1}{2}}^{n+1} + \hat{V}_j^n \tilde{T}_{j-\frac{1}{2}}^{n+1} + \hat{W}_j^n\big]\Big\} \\
\tilde{z}_j^{n+1} &= \frac{1}{2}\Big\{5z_j^n - 4z_j^{n-1} + z_j^{n-2} + \Delta t^2\big[\hat{O}_j^n \tilde{T}_{j+\frac{1}{2}}^{n+1} + \hat{P}_j^n \tilde{T}_{j-\frac{1}{2}}^{n+1} + \hat{Q}_j^n\big]\Big\}.
\end{aligned} \tag{3.69}$$

The subsequent computational procedure can now be split into three main steps:

1. Find a set of tensions and coordinates at time $t = n\Delta t$, i.e. $T_{j+\frac{1}{2}}^n$ and $\underset{\sim}{U}_j^n$. These must represent a correct or consistent solution from which it is possible to extrapolate forward in time; for the first time step ($t = t_0$) the solution is taken to be the static solution obtained in Chapter 2.

2. Now a set of tentative displacements are determined for the next time step through the relations in Equations (3.69) using tentative estimates for the tensions at the next time step. For a first estimate these are considered to be the tensions at the previous time step.

3. In general the tentative displacements obtained at time $t = (n+1)\Delta t$ will not satisfy the condition that the distance between the nodes predicted by Equation (3.69), be the same as the distance calculated from Hooke's law. This requirement forms the constraint equation, and from this a set of corrections $\delta\tilde{T}^{n+1}$ can be calculated and applied to $\tilde{T}^{n+1}$ so that the constraint equation will be satisfied. Letting k indicate the iteration index, the new tension can be expressed as

$$ {}^{k+1}\tilde{T}^{n+1} = {}^{k}\tilde{T}^{n+1} + \delta T^{n+1}, \tag{3.70} $$

and for $k = 0$

$$ {}^{1}\tilde{T}^{n+1} = \tilde{T}^{n}. \tag{3.71} $$

At this point the distinction between keeping the displacements constant and iterating with the tensions can be more clearly made. From Equations (3.69) and (3.70) it is seen that a new tentative value for the displacements is calculated so that they are not strictly maintained constant as previously suggested. However, if it were necessary to calculate two or more iterations for tentative displacements, each new value is only dependent upon the past displacement solutions and not upon the past iterative value of the displacements. With the tension iteration indicated in Equation (3.70), it can be seen that each new iterative tension value is dependent upon the previous iterative value, hence it is by definition the tensions which are being used in the iteration. The main difficulty in the solution scheme is the determination of the set of corrections, δT^{n+1}, which are to be used. The constraint equation can be mathematically formulated as

$$ \begin{aligned} {}^{k}\Omega^{n+1}_{j-\frac{1}{2}} = &\left({}^{k+1}\tilde{x}^{n+1}_{j} - {}^{k+1}\tilde{x}^{n+1}_{j-1}\right)^2 + \left({}^{k+1}\tilde{y}^{n+1}_{j} - {}^{k+1}\tilde{y}^{n+1}_{j-1}\right)^2 \\ &+ \left({}^{k+1}\tilde{z}^{n+1}_{j} - {}^{k+1}\tilde{z}^{n+1}_{j-1}\right)^2 - l^2_{j-\frac{1}{2}}\left[1 + \frac{{}^{k}\tilde{T}^{n+1}_{j-\frac{1}{2}}}{EA}\right]^2, \end{aligned} \tag{3.72} $$

where the variable ${}^{k}\Omega^{n+1}_{j-\frac{1}{2}}$ is sometimes known as the segment error function. By substituting Equation (3.69) into Equation (3.72), it can be seen that the following

functional dependence exists

$$ {}^{k}\Omega^{n+1}_{j-\frac{1}{2}} = f({}^{k}\tilde{T}^{n+1}_{j+\frac{1}{2}}, {}^{k}\tilde{T}^{n+1}_{j-\frac{1}{2}}, {}^{k}\tilde{T}^{n+1}_{j-\frac{3}{2}}) \tag{3.73} $$

since the general form of Equation (3.69), without element subscripts, is given by

$$ {}^{k+1}\underline{\tilde{U}}^{n+1} = f\left(\underline{U}^{n}, \underline{U}^{n-1}, ..., {}^{k}\tilde{T}^{n+1}\right). $$

If, for example, the three tensions in Equation (3.73) are to be determined at iteration $k+1$, then by substituting Equation (3.70) into Equation (3.73) the following functional dependence exists

$$ {}^{k+1}\Omega^{n+1}_{j-\frac{1}{2}} = f({}^{k}\tilde{T}^{n+1}_{j+\frac{1}{2}} + \delta T^{n+1}_{j+\frac{1}{2}}, {}^{k}\tilde{T}^{n+1}_{j-\frac{1}{2}} + \delta T^{n+1}_{j-\frac{1}{2}}, {}^{k}\tilde{T}^{n+1}_{j-\frac{3}{2}} + \delta T^{n+1}_{j-\frac{3}{2}}). \tag{3.74} $$

Furthermore, Equation (3.74) can be expanded in a Taylor series about the point $({}^{k}\tilde{T}^{n+1}_{j+\frac{1}{2}}, {}^{k}\tilde{T}^{n+1}_{j-\frac{1}{2}}, {}^{k}\tilde{T}^{n+1}_{j-\frac{3}{2}})$ to give

$$ \begin{aligned} {}^{k+1}\Omega^{n+1}_{j-\frac{1}{2}} = {}^{k}\Omega^{n+1}_{j-\frac{1}{2}} &+ \frac{\partial^{k}\Omega^{n+1}_{j-\frac{1}{2}}}{\partial {}^{k}\tilde{T}^{n+1}_{j-\frac{3}{2}}}\delta T^{n+1}_{j-\frac{3}{2}} + \frac{\partial^{k}\Omega^{n+1}_{j-\frac{1}{2}}}{\partial {}^{k}\tilde{T}^{n+1}_{j-\frac{1}{2}}}\delta T^{n+1}_{j-\frac{1}{2}} \\ &+ \frac{\partial^{k}\Omega^{n+1}_{j-\frac{1}{2}}}{\partial {}^{k}\tilde{T}^{n+1}_{j+\frac{1}{2}}}\delta T^{n+1}_{j+\frac{1}{2}} + \text{H.O.T}, \end{aligned} \tag{3.75} $$

where 'H.O.T.' represents the neglected higher order terms. So to first order, Equation (3.75) may be expressed as

$$ {}^{k+1}\Omega^{n+1}_{j-\frac{1}{2}} = {}^{k}\Omega^{n+1}_{j-\frac{1}{2}} + A^{n+1}_{j-\frac{1}{2}}\delta T^{n+1}_{j-\frac{3}{2}} + B^{n+1}_{j-\frac{1}{2}}\delta T^{n+1}_{j-\frac{1}{2}} + C^{n+1}_{j-\frac{1}{2}}\delta T^{n+1}_{j+\frac{1}{2}} \tag{3.76} $$

where $A^{n+1}_{j-\frac{1}{2}}$, $B^{n+1}_{j-\frac{1}{2}}$ and $C^{n+1}_{j-\frac{1}{2}}$ represent the partial derivatives of Equation (3.75). Hence for the segment error function to vanish, it is necessary that there is a zero difference between the nodal distances predicted from Equation (3.69) and the nodal distances obtained from Hooke's law. The evaluation of the derivatives in Equation (3.76) is given in Appendix H. Equation (3.76) and the requirement that ${}^{k+1}\Omega^{n+1}_{j-\frac{1}{2}} = 0$ can be seen to represent a system of linear equations which can be

written in the following matrix form

$$\begin{pmatrix} B_{\frac{1}{2}}^{n+1} & C_{\frac{1}{2}}^{n+1} & 0 & 0 & \dots & 0 \\ A_{\frac{3}{2}}^{n+1} & B_{\frac{3}{2}}^{n+1} & C_{\frac{3}{2}}^{n+1} & 0 & \dots & 0 \\ 0 & A_{\frac{5}{2}}^{n+1} & B_{\frac{5}{2}}^{n+1} & C_{\frac{5}{2}}^{n+1} & \dots & 0 \\ \vdots & \vdots & \ddots & \ddots & \ddots & \vdots \\ 0 & 0 & 0 & A_{h-\frac{3}{2}}^{n+1} & B_{h-\frac{3}{2}}^{n+1} & C_{h-\frac{3}{2}}^{n+1} \\ 0 & 0 & 0 & 0 & A_{h-\frac{1}{2}}^{n+1} & B_{h-\frac{1}{2}}^{n+1} \end{pmatrix} \begin{pmatrix} \delta T_{\frac{1}{2}}^{n+1} \\ \delta T_{\frac{3}{2}}^{n+1} \\ \delta T_{\frac{5}{2}}^{n+1} \\ \vdots \\ \delta T_{h-\frac{3}{2}}^{n+1} \\ \delta T_{h-\frac{1}{2}}^{n+1} \end{pmatrix} = \begin{pmatrix} -{}^{k}\Omega_{\frac{1}{2}}^{n+1} \\ -{}^{k}\Omega_{\frac{3}{2}}^{n+1} \\ -{}^{k}\Omega_{\frac{5}{2}}^{n+1} \\ \vdots \\ -{}^{k}\Omega_{h-\frac{3}{2}}^{n+1} \\ -{}^{k}\Omega_{h-\frac{1}{2}}^{n+1} \end{pmatrix}. \tag{3.77}$$

This can be solved by standard matrix inversion routines to yield the set of tension corrections $\delta\tilde{T}_{j+\frac{1}{2}}^{n+1}$. These are then used with Equation (3.70) to gain a better estimate of ${}^{k+1}\tilde{T}_{j+\frac{1}{2}}^{n+1}$ which is then used with Equation (3.69) to provide a new set of tentative displacements. Thus the improved estimate of tentative tensions is acting to reduce the segment error function. This iterative process continues until convergence is deemed to have been achieved which is when the segment error function is less than some predefined (small) percentage of each element length. It is worth noting here that the segment error function must be satisfied for all the elements simultaneously. If, for example, all but one of the elements satisfy this condition, then the whole iterative cycle must be repeated again involving all the elements. This could quite possibly mean that an element which had previously satisfied the condition might not do so on the next iteration.

Up to this point only the acceleration form of the Houbolt scheme and not the velocity form has been used. Implicit in the coefficients of the rearranged form of the equations of motion, given by Equation (3.65), are the drag terms. The method of calculating and integrating the drag forces over each element is exactly the same as described in Section 2.4, with the exception that there is now a component due to the nodal velocity of the line as given in Equation (3.18). The velocity form of the Houbolt scheme, Equation (3.46), is used to calculate the relative velocity, $\dot{\underline{U}}_j^r$. However, examination of Equation (3.46) shows that it is not possible to evaluate $\dot{\underline{U}}^{n+1}$ at the same time as trying to evaluate $\underline{U}^{n+1}$. Therefore the nodal velocities and hence the drag forces are evaluated at the previous time step, and this is used as the closest approximation to the drag forces at the current time step.

The details of the solution process based on the Houbolt scheme has now been presented. The differences in the solution technique when implementing either of the remaining two implicit methods is now indicated. First considered is the

Wilson-θ scheme. Here the new tentative displacements are not sought at time $t = (n+1)\Delta t$, but at a multiple of this, i.e. $t = (n+\theta)\Delta t$, where $\theta > 1$. Therefore

$$\begin{aligned} \underline{U}^{n+\theta} &= \underline{U}^n + \dot{\underline{U}}^n \theta\Delta t + \frac{(\theta\Delta t)^2}{6}\left(\ddot{\underline{U}}^{n+\theta} + 2\ddot{\underline{U}}^n\right) \\ \dot{\underline{U}}^{n+\theta} &= \frac{3}{\theta\Delta t}\left(\underline{U}^{n+\theta} - \underline{U}^n\right) - 2\dot{\underline{U}}^n - \frac{\theta\Delta t}{2}\ddot{\underline{U}}^n, \end{aligned} \tag{3.78}$$

where the derivation of this is given in Chapter 5. Once the solution is obtained at time $t = (n+\theta)\Delta t$, the following set of equations are used to interpolate in order gain the solution at the correct point in time, i.e. at $t = (n+1)\Delta t$

$$\begin{aligned} \underline{U}^{n+1} &= \underline{U}^n + \dot{\underline{U}}^n \Delta t + \ddot{\underline{U}}^n \frac{\Delta t^2}{2} + \frac{\Delta t^2}{6\theta}\left(\ddot{\underline{U}}^{n+\theta} - \ddot{\underline{U}}^n\right) \\ \dot{\underline{U}}^{n+1} &= \dot{\underline{U}}^n + \ddot{\underline{U}}^n \Delta t + \frac{\Delta t}{2\theta}\left(\ddot{\underline{U}}^{n+\theta} - \ddot{\underline{U}}^n\right) \\ \ddot{\underline{U}}^{n+1} &= \ddot{\underline{U}}^n + \frac{1}{\theta}\left(\ddot{\underline{U}}^{n+\theta} - \ddot{\underline{U}}^n\right). \end{aligned} \tag{3.79}$$

The boundary condition for the top point of the mooring line must also be handled in a slightly different manner. Since this is given as a predefined displacement with time, then the calculation of velocity and acceleration at the line endpoint is easily accomplished using the Houbolt Scheme. With the Wilson-θ scheme, the displacement at time step $n+\theta$ for the upper endpoint is required so that the total solution is obtained at this point, prior to using Equation (3.79) to interpolate for the solution at the correct point. The first relation of Equation (3.78) is used to obtain $\underline{U}^{n+\theta}$, however since the upper endpoint is a boundary condition it does not explicitly enter into the solution process and therefore the value of $\ddot{\underline{U}}^{n+\theta}$ is not calculated. Hence the approximation of $\ddot{\underline{U}}^{n+\theta} \approx \ddot{\underline{U}}^n$ is used and substituted into the first relation of Equation (3.78) to yield

$$\underline{U}^{n+\theta} = \underline{U}^n + \dot{\underline{U}}^n \theta\Delta t + \frac{(\theta\Delta t)^2}{2}\ddot{\underline{U}}^n. \tag{3.80}$$

Equation (3.80) is recognised as a Taylor series expansion of the displacement about the point $\underline{U}^n$. As with the Houbolt scheme the velocity form of the Wilson-θ method is used to calculate the drag forces at time $t = n\Delta t$, which is one time step behind the solution point.

The Newmark scheme is relatively easier to apply than the Wilson-θ scheme in so far as the solution point is at time $t = (n+1)\Delta t$ and not at time $t = (n+\theta)\Delta t$.

Equation (3.50) is used to gain the displacements of all of the nodes, but there is a problem in the calculation of the velocity and acceleration for the mooring line endpoint. The acceleration is gained by rearranging Equation (3.50) and this is then substituted into Equation (3.49) to obtain the velocity of the endpoint.

Explicit Schemes

The explicit scheme studied here is the familiar Central Difference (CD) scheme represented by Equations (3.43) and (3.44). However, some confusion seems to exist within the literature regarding how the scheme is applied to the solution of nonlinear equations. In Bathe(1982) it is stated that: "*The solution therefore simply corresponds to a forward marching in time...*", with the tacit assumption that no iteration is performed at each time step, in order to satisfy a constraint equation. Wood(1990) does not clarify whether iteration is necessary or not. At one stage he describes the solution at time step n as an approximate solution, subject to the correct solution at time step $n+1$ being obtained. Later he describes the comparison of explicit schemes with the iterative methods necessary for use with the implicit schemes - with the tacit implication that there is no iteration involved with the CD scheme. Only in the Walton and Polachek(1960) paper is a solution of mooring line dynamics with the CD scheme presented and they very definitely undertake iteration at each time step. In the present study both approaches, i.e. with and without iteration, were employed. This conclusively showed that iteration at each time step is essential to prevent the solution collapsing.

By taking Equation (3.51) and the relations in Equation (3.53), the following functional dependence is seen

$$\underline{U}^{n+1} = f(\underline{U}^n, \underline{U}^{n-1}, T^n), \tag{3.81}$$

indicating that the displacement at the next time step is dependent upon the tension at the previous time step. This means that the constraint equation for the tentative values at the next time step is being satisfied using the tension at time step n. Since any value at time step n is a solution which cannot be changed, then these tensions cannot be used for the iteration otherwise the solution procedure would be solving for the tensions one step behind the displacements. However rewriting Equation (3.81) in the form

$$\underline{U}^{n+1} = f(\underline{U}^n, \underline{U}^{n-1}, T^{n+1}), \tag{3.82}$$

leads to an 'implicit type' scheme. Hence the solution procedure is now identical to that of the implicit schemes described previously because now the constraint equation must be satisfied at $n+1$ using values at $n+1$. However it is to be noted that by rewriting the explicit form of Equation (3.81) as an 'implicit' type form (as given in Equation (3.82)), the numerical properties of the explicit nature of the scheme are preserved. The adoption of Equation (3.82) is only done to facilitate the solution procedure.

With the methodology for the solution with both the implicit and explicit schemes being identical, the general solution procedure can be outlined as indicated in Figure 3.2 where the iterative process necessary at each time step is shown.

3.6 Starting Procedures and Initial Conditions

3.6.1 Houbolt Scheme

The Houbolt scheme always requires a knowledge of the solution at the previous two time steps in order to be able to calculate the next one. Therefore at times $t = 0$ and $t = \Delta t$ the scheme cannot be used to calculate $\underline{U}^{n+1}$ for $n = 0$ or $n = 1$. In this case a Taylor series expansion of the displacement about the initial position is used, that is

$$\underline{\tilde{U}}^{n+1} = \underline{U}^0 + \Delta t \dot{\underline{U}}^0 + \frac{\Delta t^2}{2} \ddot{\underline{U}}^0 + \text{H.O.T.} \tag{3.83}$$

With the initial velocity assumed to be zero, Equation (3.83) can then be used to calculate the displacements at times $t = \Delta t$ and $t = 2\Delta t$. It should be noted that dynamic solutions are 'path dependent', which means that the final solution can be significantly affected by the initial conditions and consequently may be significantly affected by the starting procedure. Thus it might be prudent to use the CD scheme, with a much smaller time step than that used in the implicit scheme, to generate the solutions at the first two time steps. Thereafter, the solution can be advanced with the implicit scheme.

3.6.2 Central Difference Scheme

For the first time step the Taylor series expansion as given by Equation (3.83) is again used with the assumption that the initial velocity is zero. Although the solution is still path dependent, the effect of using a different starting procedure is mitigated by the use of a time step with the CD algorithm which is generally much smaller than that used with the implicit schemes. Also the path dependency is reduced because the Taylor series acts over one time step only.

3.6.3 Wilson-θ and Newmark Schemes

These schemes are attractive to use because they require no special starting procedure, except that the initial velocity is still set to zero.

3.7 Summary

This chapter has dealt with the derivation of the equations of motion for a 'suspended cable' type structure and explains how these equations are to be solved using direct time integration schemes. For the first part, the use of the static solution and discretisation as a starting point for the dynamic procedure is indicated. The equations of motion are stated as they apply to each node in the discretisation by equating the inertial (acceleration dependent) terms with the remaining external and internal forces. The manner of calculating the added mass was presented in detail so that the final representation of the inertial terms used is as given in Equation (3.13). With the remaining forces acting on the system of nodes identified, the basic model for the equations of motion for a mooring line structure has been developed. These equations are then slightly modified to account for the presence of ocean waves and currents, and to model the interaction of the line with the seabed. For the former, the linear velocity potential for a wave is modified to take into account the presence of a vertically uniform current. From the modified velocity potential it is possible to derive the associated water particle velocities and accelerations. These are then combined with the mooring line motions to yield the relative velocities and accelerations from which the added mass and drag forces are calculated. Modelling the interaction of the cable and the seabed is more imprecise, but essentially involves trying to reduce the downward force of the first suspended node as it approaches the seabed. This is done so that when the node reaches the seabed it will have no subsequent motion until there is sufficient resolved upward force to lift it again. The more important reason for doing this is to reduce the shock loadings induced by the lifting or grounding of the mass which has been lumped at the nodes.

The second half of the chapter was concerned with the solution of the equations of motion by the use of direct time integration schemes; these are also more generally referred to as finite difference (FD) expressions. The general functional form of implicit and explicit FD schemes were indicated and the rearrangement of the equations of motion to a form indicated by Equation (3.53) is shown. A complete statement of the equations of motion is given by Equations (3.62), (3.63) and (3.64) and it is these which are rearranged to the form given by Equation (3.66).

Next the FD expressions were applied to these equations; because the general solution procedure is the same for all the four integration schemes considered here, only a detailed description of the solution using the Houbolt scheme is given. The differences in the solution procedure which arise from using either the Wilson-θ or the Newmark schemes, were indicated. In particular, the additional complexity introduced by the use of the Wilson-θ scheme is discussed. The use of both of these schemes must be modified when applied to the upper endpoint of the cable and this is also indicated. The solution utilising the CD scheme is then demonstrated, and in particular the 'implicit' type representation of the explicit CD scheme which must be adopted to make the solution 'sensible', is given. For all the methods the velocity forms of the schemes are applied one step behind the solution, so that the drag forces are always calculated for the previous solution. This must be done because the drag forces cannot be calculated at the current solution point, as this would involve variables which are not known until the solution at the current time step has been determined.

This chapter concludes with an indication of the manner by which the solution with each scheme is started. With the Houbolt and CD schemes a Taylor series expansion of the displacement is used to start, since solution advancement relies upon past displacements which are not available at the start of the simulation. The Wilson-θ and Newmark methods require no special starting procedures. The initial conditions needed to start the dynamic solution are also indicated.

CHAPTER 4

Modal Methods and Mooring Line Dynamics

4.1 Introduction

This chapter indicates how the equations of motion for a mooring line are solved by modal methods.

The application of the modal method essentially involves the rewriting of the equations of motion in matrix form and then finding the $2h$ eigenvalues and eigenvectors, where h is the number of elements used to model the system. Each solution, that is an eigenvalue and its associated eigenvector, is called a mode, and the total solution is gained by the appropriate summation of the solutions for each mode. The eigenvectors are assembled into the 'modal' matrix $\underline{A}$ and this is then used to uncouple the equations of motion. The equations of motion are more efficiently solved in their uncoupled form than in their coupled form. However, in the application of modal analysis techniques to more common structural dynamics problems, the dynamic displacements of the structure are considered to be small. Therefore $\underline{A}$ has only to be calculated once and can then be used, unmodified, throughout the rest of the solution.

In the situation where the displacements cannot be considered small, as is the case with mooring line dynamics, then $\underline{A}$ must be recalculated periodically throughout the solution, ideally at every time step. It is the application of this method to the solution of problems involving large displacements which distinguishes it from the many solution cases presented in the literature which are relevant only for small displacement problems.

It is surmised that a solution accurate enough for engineering purposes may be obtained by the summation of relatively few modes and by recalculating $\underline{A}$ only at a predetermined multiple of the time step, every 10 time steps, say. This approach might therefore yield a solution technique which is more efficient in terms of computation time than the direct integration methods alluded to in Chapter 3, whilst still providing sufficient accuracy. As indicated in Chapter 1, the theoretical analysis in this chapter was implemented in a computer program, but there was insufficient time to debug the code and generate any results.

Only a few references to this method of solution as applied to large displacement dynamics, exist in the literature. Most of these papers omit the details of the solution process and the necessary matrix manipulations, and give only brief accounts of how the nonlinearities are dealt with in the solution process. Whilst details are discussed in Section 4.6, here a short description of the contributions made in two references which examine this subject is given. Johansson(1978) formulates the equations of motion in a matrix form in the usual fashion, however the description of the solution method is a little confusing. The same forces are considered to act on the line as here, but it is not clear whether $\underline{A}$ is calculated once only or periodically as the solution advances. Further, it is stated that all modes of the solution must be considered, although the heuristic argument presented to justify this does not seem to precisely address this point. Dominguez and Smith(1972) uncouple the equations of motion by the application of a method due to Foss(1958) and then find the eigensolutions for the resulting set of first order equations. Here the mooring line is assumed to undergo small displacements about the initial equilibrium position, and therefore it is tacitly assumed that the determination of $\underline{A}$ only needs to be carried out once.

4.2 Recasting of the Equations of Motion in Matrix Form

Here it is shown how the original three dimensional (3D) form of the equations of motion are reduced to a two dimensional (2D) form and then how these 2D equations are cast into a matrix form by way of a four element example. This method is only applied in 2D to establish the validity, or otherwise, of this approach and to develop a solution methodology. In particular the problems addressed are simplified by neglecting the influence of line attachments and the presence of ocean waves so that $\ddot{\underline{U}}_j^r = \ddot{\underline{U}}_j$. The 3D equations of motion expressed in Equations (3.62), (3.63) and (3.64) are reduced to their 2D form by setting $\varepsilon = 0$ and ignoring all terms pertaining to the y direction, thus

$$\left\{M_j\ddot{x}_j + \frac{\ddot{x}_j}{2}\left[a_t\cos^2\gamma + a_n\sin^2\gamma\right]_{j-\frac{1}{2}}^{j+\frac{1}{2}}\right\} + \frac{\ddot{z}_j}{2}\left[(a_t - a_n)\sin\gamma\cos\gamma\right]_{j-\frac{1}{2}}^{j+\frac{1}{2}} = \left[T\cos\gamma\right]_{j-\frac{1}{2}}^{j+\frac{1}{2}} + F_{xj} \tag{4.1a}$$

and

$$\frac{\ddot{x}_j}{2}\left[(a_t - a_n)\sin\gamma\cos\gamma\right]_{j-\frac{1}{2}}^{j+\frac{1}{2}} + \left\{M_j\ddot{z}_j + \frac{\ddot{z}_j}{2}\left[a_t\sin^2\gamma + a_n\cos^2\gamma\right]_{j-\frac{1}{2}}^{j+\frac{1}{2}}\right\} = \left[T\sin\gamma\right]_{j-\frac{1}{2}}^{j+\frac{1}{2}} + F_{zj} - W_j. \tag{4.1b}$$

The expansion of the tension related terms in Equations (4.1a) and (4.1b), yields

$$\left[T\cos\gamma\right]_{j-\frac{1}{2}}^{j+\frac{1}{2}} = \frac{1}{l}\left[x_{j+1}T_{j+\frac{1}{2}} - x_j(T_{j+\frac{1}{2}} + T_{j-\frac{1}{2}}) + x_{j-1}T_{j-\frac{1}{2}}\right] \tag{4.2a}$$

and

$$\left[T\sin\gamma\right]_{j-\frac{1}{2}}^{j+\frac{1}{2}} = \frac{1}{l}\left[z_{j+1}T_{j+\frac{1}{2}} - z_j(T_{j+\frac{1}{2}} + T_{j-\frac{1}{2}}) + z_{j-1}T_{j-\frac{1}{2}}\right] \tag{4.2b}$$

upon assuming that $\tilde{l}_{j+\frac{1}{2}} = \tilde{l}_{j-\frac{1}{2}} = l$. That is, it is to be assumed that the elemental lengths are the same and remain constant throughout the solution. Substituting Equations (4.2a) and (4.2b) into Equations (4.1a) and (4.1b), then these equations can be explicitly written in matrix form for a four element model as an example, i.e.

$$\begin{pmatrix} M_1^1 & M_1^2 & 0 & 0 & 0 & 0 \\ M_1^2 & M_1^3 & 0 & 0 & 0 & 0 \\ 0 & 0 & M_2^1 & M_2^2 & 0 & 0 \\ 0 & 0 & M_2^2 & M_2^3 & 0 & 0 \\ 0 & 0 & 0 & 0 & M_3^1 & M_3^2 \\ 0 & 0 & 0 & 0 & M_3^2 & M_3^3 \end{pmatrix} \begin{pmatrix} \ddot{x}_1 \\ \ddot{z}_1 \\ \ddot{x}_2 \\ \ddot{z}_2 \\ \ddot{x}_3 \\ \ddot{z}_3 \end{pmatrix}$$

$$= \frac{1}{l}\begin{pmatrix} T_1^1 & 0 & T_1^2 & 0 & 0 & 0 & 0 & 0 \\ 0 & T_1^1 & 0 & T_1^2 & 0 & 0 & 0 & 0 \\ T_1^2 & 0 & T_2^1 & 0 & T_2^2 & 0 & 0 & 0 \\ 0 & T_1^2 & 0 & T_2^1 & 0 & T_2^2 & 0 & 0 \\ 0 & 0 & T_2^2 & 0 & T_3^1 & 0 & T_3^2 & 0 \\ 0 & 0 & 0 & T_2^2 & 0 & T_3^1 & 0 & T_3^2 \end{pmatrix} \begin{pmatrix} x_1 \\ z_1 \\ x_2 \\ z_2 \\ x_3 \\ z_3 \\ x_4 \\ z_4 \end{pmatrix} + \begin{pmatrix} F_{x1} \\ F_{z1} - W_1 \\ F_{x2} \\ F_{z2} - W_2 \\ F_{x3} \\ F_{z3} - W_3 \end{pmatrix}, \tag{4.3}$$

where

$$M_j^1 = M_j + \frac{1}{2}\left[a_t \cos^2\gamma + a_n \sin^2\gamma\right]_{j-\frac{1}{2}}^{j+\frac{1}{2}+}$$

$$M_j^2 = \frac{1}{2}\left[(a_t - a_n)\sin\gamma\cos\gamma\right]_{j-\frac{1}{2}}^{j+\frac{1}{2}+}$$

$$M_j^3 = M_j + \frac{1}{2}\left[a_t \sin^2\gamma + a_n \cos^2\gamma\right]_{j-\frac{1}{2}}^{j+\frac{1}{2}+}$$

$$T_j^1 = -(T_{j+\frac{1}{2}} + T_{j-\frac{1}{2}})$$

$$T_j^2 = T_{j+\frac{1}{2}}.$$

Whereas the matrix representation of Equations (4.1a) and (4.1b) given in Equation (4.3) is correct, it is not directly solvable since the accelerations are only defined at nodes 1, 2, and 3, but the displacements are defined at nodes 1, 2, 3 and 4. This situation arises because the displacement at node 4 is explicitly included in the formulation through the specification of the 'forcing function' (or boundary condition) of the dynamic solution. As such, terms related to the boundary condition can be partitioned from the stiffness matrix, which yields the following matrix representation of Equations (4.1a) and (4.1b)

$$\begin{pmatrix} M_1^1 & M_1^2 & 0 & 0 & 0 & 0 \\ M_1^2 & M_1^3 & 0 & 0 & 0 & 0 \\ 0 & 0 & M_2^1 & M_2^2 & 0 & 0 \\ 0 & 0 & M_2^2 & M_2^3 & 0 & 0 \\ 0 & 0 & 0 & 0 & M_3^1 & M_3^2 \\ 0 & 0 & 0 & 0 & M_3^2 & M_3^3 \end{pmatrix} \begin{pmatrix} \ddot{x}_1 \\ \ddot{z}_1 \\ \ddot{x}_2 \\ \ddot{z}_2 \\ \ddot{x}_3 \\ \ddot{z}_3 \end{pmatrix} + \begin{pmatrix} F_{x1} \\ F_{z1} - W_1 \\ F_{x2} \\ F_{z2} - W_2 \\ F_{x3} \\ F_{z3} - W_3 \end{pmatrix}$$

$$-\frac{1}{l}\begin{pmatrix} T_1^1 & 0 & T_1^2 & 0 & 0 & 0 \\ 0 & T_1^1 & 0 & T_1^2 & 0 & 0 \\ T_1^2 & 0 & T_2^1 & 0 & T_2^2 & 0 \\ 0 & T_1^2 & 0 & T_2^1 & 0 & T_2^2 \\ 0 & 0 & T_2^2 & 0 & T_3^1 & 0 \\ 0 & 0 & 0 & T_2^2 & 0 & T_3^1 \end{pmatrix} \begin{pmatrix} x_1 \\ z_1 \\ x_2 \\ z_2 \\ x_3 \\ z_3 \end{pmatrix} = \frac{T_{3.5}}{l} \begin{pmatrix} 0 \\ 0 \\ 0 \\ 0 \\ x_4 \\ z_4 \end{pmatrix}, \tag{4.4}$$

upon noting that $T_3^2 = T_{3.5}$, the tension in the last element. Since x_4 and z_4 are known, the matrix problem has been reduced to a solvable form. Equation (4.4) can be expressed more generally as

$$\underline{M}\,\ddot{\underline{U}} + \underline{D}\,\dot{\underline{U}} + \underline{K}\,\underline{U} = \underline{F}_n \tag{4.5}$$

where the current induced drag matrix from Equation (4.4) is now expressed as the product of a matrix of damping coefficients and the relative velocity vector, and the elements in the stiffness matrix contain the common factor of $\frac{1}{7}$.

Prior to undertaking the solution of Equation (4.5) some preliminaries related to matrix methods are now presented.

4.3 The Free Undamped Equations of Motion

For the free undamped equations of motion there are no terms relating to the drag or to the boundary condition, therefore under these conditions Equation (4.5) becomes

$$\underline{M}\,\ddot{\underline{U}} + \underline{K}\,\underline{U} = 0, \tag{4.6}$$

where both $\underline{M}$ and $\underline{K}$ are defined in Equation (4.4) and are noted to be real symmetric matrices. The implication of excluding a damping term from Equation (4.6) is that any external force introduced to the system will produce an oscillatory motion that will not decay with time as it would with damped systems. By excluding the forcing function from the solution of Equation (4.6), the 'natural' modes of Equation (4.6) are obtained. It is now assumed that the natural modes of Equation (4.6) will have a solution of the form

$$\underline{U} = \sum_{i=1}^{2h} \underline{A}_i \sin(p_i t + \phi_i), \tag{4.7}$$

where

- $\underline{U}$ is the matrix of displacements,
- $\underline{A}_i$ is the column modal matrix of nodal x and z displacements for the i^{th} mode, hence the upper limit of summation of $2h$,
- p_i is the frequency of oscillation for the i^{th} mode,
- ϕ_i is the phase of the i^{th} mode.

By differentiating Equation (4.7) twice with respect to time, the acceleration vector is

$$\ddot{\underline{U}} = -\sum_{i=1}^{2h} \underline{A}_i p_i^2 \sin(p_i t + \phi_i). \tag{4.8}$$

Substitution of Equations (4.7) and (4.8) for the i^{th} mode only, into Equation (4.6), yields

$$\underline{K}\,\underline{A}_i = p_i^2 \underline{M}\,\underline{A}_i. \tag{4.9}$$

This represents what is called the eigenproblem where the eigenvalues are p_i^2 and the associated eigenvectors are $\underline{A}_i$. However the eigenproblem of Equation (4.9) is in nonstandard form because of the presence of $\underline{M}$ on the right hand side. It is possible to premultiply both sides of Equation (4.9) by $\underline{M}^{-1}$, yielding

$$\underline{M}^{-1}\,\underline{K}\,\underline{A}_i = p_i^2 \underline{A}_i, \tag{4.10}$$

which now represents the standard form of the eigenproblem. However the matrix defined by $\underline{M}^{-1}\,\underline{K}$ will be unsymmetric. Because the maintenance of symmetry is an important consideration for the efficient solution of matrix problems, the form given by Equation (4.10) is not preferred for solution. The alternative is to perform a Cholesky decomposition of $\underline{M}$ into the form

$$\underline{M} = \underline{V}^T\,\underline{V}. \tag{4.11}$$

By premultiplying both sides of Equation (4.9) by $(\underline{V}^{-1})^T$, and noting that $\underline{K} = \underline{K}\underline{I} = \underline{K}\,\underline{V}^{-1}\underline{V}$ and the results in Equation (4.11), it follows that

$$(\underline{V}^{-1})^T\,\underline{K}\,\underline{V}^{-1}\,\underline{V}\,\underline{A}_i = p_i^2 (\underline{V}^{-1})^T\,\underline{V}^T\,\underline{V}\,\underline{A}_i. \tag{4.12}$$

This can be reduced to

$$\underline{K}_v\,\underline{A}_i^v = p_i^2 \underline{A}_i^v \tag{4.13}$$

upon defining the equivalences

$$\underline{K}_v = (\underline{V}^{-1})^T\,\underline{K}\,\underline{V}^{-1}$$

$$\underline{A}_i^v = \underline{V}\,\underline{A}_i$$

and noting that

$$(\underline{V}^{-1})^T\,\underline{V}^T = (\underline{V}\,\underline{V}^{-1})^T = \underline{I}.$$

Equation (4.13) now represents the standard form of the eigenproblem where $\underline{K}_v$ has been preserved as a symmetric matrix. This can be solved using standard routines to calculate the eigenvalues and eigenvectors of Equation (4.13). The eigenvalues are generally returned in ascending order, so that

$$[p_i^2] = \left[p_1^2, p_2^2, p_3^2, \ldots, p_{2h}^2\right] \quad \text{where} \quad p_{i+1}^2 \geq p_i^2. \tag{4.14}$$

If there are h nodes in the discretisation there will be $2h$ eigenvalues and eigenvectors returned from the solution of Equation (4.13) since each node in the discretisation has two degrees of freedom associated with it. The eigenvectors are then assembled into what is called the modal matrix, $\underline{A}$, where each column is the eigenvector associated with each eigenvalue of Equation (4.14), thus $\underline{A}$ is given by

$$\begin{aligned}\underline{A} &= \left[\underline{A}_1, \underline{A}_2, \underline{A}_3, \ldots, \underline{A}_r\right] \\ &= \left(\begin{pmatrix} A_{11} \\ A_{21} \\ \vdots \\ A_{r1} \end{pmatrix} \begin{pmatrix} A_{12} \\ A_{22} \\ \vdots \\ A_{r2} \end{pmatrix} \begin{pmatrix} A_{13} \\ A_{23} \\ \vdots \\ A_{r3} \end{pmatrix} \begin{pmatrix} \ldots \\ \ldots \\ \ddots \\ \ldots \end{pmatrix} \begin{pmatrix} A_{1r} \\ A_{2r} \\ \vdots \\ A_{rr} \end{pmatrix} \right)\end{aligned} \tag{4.15}$$

with $r = 2h$. For the i^{th} mode the eigenvalue is p_i^2 and the eigenvector is given by the i^{th} column of the modal matrix. The eigenvectors are determined to within an arbitrary constant which depends upon the initial conditions of the problem under consideration. Thus when the initial conditions are not specified, the eigenvectors can be normalised in any fashion required, the most common is such that the sum of the squares of all the elements equals 1. Therefore if the original eigenvector is given by

$$\underline{A}_i = \begin{pmatrix} A_{1i} \\ A_{2i} \\ \vdots \\ A_{ri} \end{pmatrix},$$

then the scaling factor is gained by the Euclidean norm, that is $N_i = (A_{1i}^2 + A_{2i}^2 + \ldots + A_{ri}^2)^{\frac{1}{2}}$, and the normalised eigenvector $\underline{A}^{\text{norm}}$, say, is given by

$$\underline{A}_i^{\text{norm}} = \frac{1}{N_i} \begin{pmatrix} A_{1i} \\ A_{2i} \\ \vdots \\ A_{ri} \end{pmatrix}. \tag{4.16}$$

Next it is shown how the initial conditions can be used to determine the 'true' modal matrix. With the general solution given by Equation (4.7), the total displacement at each node is defined as the sum of the displacements at each node for each mode. Thus, for example, at time $t = 0$ and for a two node problem Equation

(4.7) reduces to

$$\begin{aligned} x_1 &= A_{11}\sin\phi_1 + A_{12}\sin\phi_2 + A_{13}\sin\phi_3 + A_{14}\sin\phi_4 \\ z_1 &= A_{21}\sin\phi_1 + A_{22}\sin\phi_2 + A_{23}\sin\phi_3 + A_{24}\sin\phi_4 \\ x_2 &= A_{31}\sin\phi_1 + A_{32}\sin\phi_2 + A_{33}\sin\phi_3 + A_{34}\sin\phi_4 \\ z_2 &= A_{41}\sin\phi_1 + A_{42}\sin\phi_2 + A_{43}\sin\phi_3 + A_{44}\sin\phi_4. \end{aligned} \tag{4.17}$$

For one of the component directions, x say, this can be expressed more generally as

$$x_i = \sum_{j=1}^{r} A_{ij}\sin\phi_j, \tag{4.18}$$

thus the relationship presented in Equation (4.17) can be expressed in the matrix form

$$\underline{U} = \underline{A}\,\underline{S} \tag{4.19}$$

where

$$\underline{S} = \begin{pmatrix} \sin\phi_1 \\ \sin\phi_2 \\ \sin\phi_3 \\ \sin\phi_4 \end{pmatrix}. \tag{4.20}$$

As already noted since the evaluation is for the initial conditions, i.e at time $t = 0$, the elements of $\underline{S}$ are written as $\sin\phi_i$ and not as $\sin(p_i t + \phi_i)$. It can also be deduced from Equation (4.17) that all the elements of each eigenvector can be expressed relative to the elements of the first eigenvector, so that Equation (4.17) can be expressed in the alternative form

$$\begin{pmatrix} x_1 \\ z_1 \\ x_2 \\ z_2 \end{pmatrix} = \begin{pmatrix} 1 & 1 & 1 & 1 \\ \alpha_1 & \beta_1 & \gamma_1 & \delta_1 \\ \alpha_2 & \beta_2 & \gamma_2 & \delta_2 \\ \alpha_3 & \beta_3 & \gamma_3 & \delta_3 \end{pmatrix} \begin{pmatrix} A_{11}\sin\phi_1 \\ A_{12}\sin\phi_2 \\ A_{13}\sin\phi_3 \\ A_{14}\sin\phi_4 \end{pmatrix}. \tag{4.21}$$

The analogous matrix form to Equation (4.21) for the initial velocities is also required for the complete specification. This is simply the time derivative of Equation (4.21) but with the ϕ_i replaced with $(p_i t + \phi_i)$ to facilitate the differentiation, hence

$$\begin{pmatrix} \dot{x}_1 \\ \dot{z}_1 \\ \dot{x}_2 \\ \dot{z}_2 \end{pmatrix} = \begin{pmatrix} p_1 & p_2 & p_3 & p_4 \\ \alpha_1 p_1 & \beta_1 p_2 & \gamma_1 p_3 & \delta_1 p_4 \\ \alpha_2 p_1 & \beta_2 p_2 & \gamma_2 p_3 & \delta_2 p_4 \\ \alpha_3 p_1 & \beta_3 p_2 & \gamma_3 p_3 & \delta_3 p_4 \end{pmatrix} \begin{pmatrix} A_{11}\cos\phi_1 \\ A_{12}\cos\phi_2 \\ A_{13}\cos\phi_3 \\ A_{14}\cos\phi_4 \end{pmatrix}. \tag{4.22}$$

With the initial conditions for the displacements and velocities known, Equations (4.21) and (4.22) can be solved for the eight unknowns defined by

$$\begin{aligned} J_1 &= A_{11}\sin\phi_1 & J_5 &= A_{11}\cos\phi_1 \\ J_2 &= A_{12}\sin\phi_2 & J_6 &= A_{12}\cos\phi_2 \\ J_3 &= A_{13}\sin\phi_3 & J_7 &= A_{13}\cos\phi_3 \\ J_4 &= A_{14}\sin\phi_4 & J_8 &= A_{14}\cos\phi_4. \end{aligned} \tag{4.23}$$

where J_i are the solutions to Equations (4.21) and (4.22). By solving the set of simultaneous equations in Equation (4.23), the true values of the elements of the modal matrix A_{ij} are obtained as well the phase angles of each mode ϕ_i. The values for the displacement at each node is then given by Equation (4.19) but with the 'true' modal matrix instead of $\underline{A}$ and with $\underline{S}$ given by

$$\underline{S} = \begin{pmatrix} \sin(p_1 t + \phi_1) \\ \sin(p_2 t + \phi_2) \\ \sin(p_3 t + \phi_3) \\ \sin(p_4 t + \phi_4) \end{pmatrix}. \tag{4.24}$$

4.4 Undamped Arbitrarily Excited Systems

The equations of motion for an undamped arbitrarily excited system is given generally by

$$\underline{M}\,\ddot{\underline{U}} + \underline{K}\,\underline{U} = \underline{Q}(t), \tag{4.25}$$

where $\underline{Q}(t)$ is a column vector describing the time varying forces applied in each direction to each node, that is with $r = 2h$, i.e.

$$\underline{Q}(t) = \begin{pmatrix} q_1 \\ q_2 \\ q_3 \\ \vdots \\ q_r \end{pmatrix} = \begin{pmatrix} f_1(t) \\ f_2(t) \\ f_3(t) \\ \vdots \\ f_r(t) \end{pmatrix}. \tag{4.26}$$

As revealed by the original re-casting of the equations of motion into a matrix form, there is excitation only at the last node of the discretisation, i.e. at the point of attachment to the floater. Hence $f_r(t) \neq 0$ and $f_{(r-1)}(t) \neq 0$, but $f_j(t) = 0$ for

$j = 1, ..., (r-2)$, therefore

$$\underline{Q}(t) = \begin{pmatrix} 0 \\ 0 \\ \vdots \\ f_{(r-1)}(t) \\ f_r(t) \end{pmatrix}. \tag{4.27}$$

The diagonalisation of the matrices in Equation (4.25) would result in an uncoupled form of the equations of motion and this form is more efficient for advancement by the direct time integration schemes discussed in Chapters 3 and 5. To reduce the matrices to a diagonal form an orthogonal transformation is required, that is a matrix with property that $\underline{P}^{-1} = \underline{P}^T$. Here diagonalisation is achieved using the transpose of the modal matrix of 'true' values, as derived in the previous section, to premultiply Equation (4.25) to yield

$$\underline{A}^T \underline{M}\, \ddot{\underline{U}} + \underline{A}^T \underline{K}\, \underline{U} = \underline{A}^T \underline{Q}(t). \tag{4.28}$$

Now define $\underline{U}_p$ through the following relationships

$$\begin{aligned} \underline{U} &= \underline{A}\, \underline{U}_p \\ \ddot{\underline{U}} &= \underline{A}\, \ddot{\underline{U}}_p \end{aligned} \tag{4.29}$$

so that Equation (4.28) reduces to

$$\underline{M}_p \ddot{\underline{U}}_p + \underline{K}_p \underline{U}_p = \underline{Q}_p(t) \tag{4.30}$$

where

$$\begin{aligned} \underline{M}_p &= \underline{A}^T \underline{M}\, \underline{A} \\ \underline{K}_p &= \underline{A}^T \underline{K}\, \underline{A} \\ \underline{Q}_p(t) &= \underline{A}^T \underline{Q}(t). \end{aligned}$$

The equations of motion given by Equation (4.30) are now defined in what are called principal coordinates. Under the transformations performed on the original mass and stiffness matrices, both $\underline{M}_p$ and $\underline{K}_p$ are now diagonal. As a result the equations of motion are now described as being uncoupled. This means that when

written in principal coordinates, they have neither inertial or elastic coupling. Furthermore $\underline{Q}_p(t)$ is given by

$$\underline{Q}_p(t) = \underline{A}^T \underline{Q}(t) = \begin{pmatrix} A_{11} & A_{12} & \dots & A_{1r} \\ A_{21} & A_{22} & \dots & A_{2r} \\ \vdots & \vdots & \ddots & \vdots \\ A_{r1} & A_{r2} & \dots & A_{rr} \end{pmatrix}^T \begin{pmatrix} 0 \\ \vdots \\ f_{(r-1)}(t) \\ f_r(t), \end{pmatrix} \tag{4.31}$$

where expansion of Equation (4.31) leads to the simpler form

$$\underline{Q}_p(t) = f_{(r-1)}(t) \begin{pmatrix} A_{(r-1)1} \\ A_{(r-1)2} \\ \vdots \\ A_{(r-1)r} \end{pmatrix} + f_r(t) \begin{pmatrix} A_{r1} \\ A_{r2} \\ \vdots \\ A_{rr} \end{pmatrix}. \tag{4.32}$$

Thus any constituent equation which forms part of the system described in Equation (4.30), has the form

$$m_{pi}\ddot{x}_{pi}(t) + k_{pi}x_{pi}(t) = f_{(r-1)}(t)A_{(r-1)i} + f_r(t)A_{ri}, \tag{4.33}$$

where x_{pi} and $\ddot{x}_{pi}$ are the general coordinates defined by Equation (4.29). Using the same notation as adopted in Chapter 3, Equation (4.33) can be expressed in the time domain in the form

$$m^n_{pi}\ddot{x}^{n+1}_{pi} + k^n_{pi}x^{n+1}_{pi} = f^{n+1}_{(r-1)}A^n_{i(r-1)} + f^{n+1}_r A^n_{ir}. \tag{4.34}$$

This equation can be solved using one of the direct integration schemes described in Chapter 3, such as the Houbolt method given by Equations (3.45) and (3.46). In this case

$$\ddot{x}^{n+1} = \frac{1}{\Delta t^2}\left[2x^{n+1} - 5x^n + 4x^{n-1} - x^{n-2}\right],$$

and substitution into Equation (4.34) and following the usual iterative procedure described in Chapter 3, allows x^{n+1}_{pi} to be evaluated. However, since x^{n+1}_{pi} corresponds to the solution in principal coordinates, the 'true' displacements are derived from the first relationship presented in Equation (4.29). For example, for a 2 node problem, Equation (4.29) is explicitly written as

$$\begin{pmatrix} x_1 \\ z_1 \\ x_2 \\ z_2 \end{pmatrix} = \begin{pmatrix} A_{11} & A_{12} & A_{13} & A_{14} \\ A_{21} & A_{22} & A_{23} & A_{24} \\ A_{31} & A_{32} & A_{33} & A_{34} \\ A_{41} & A_{42} & A_{43} & A_{44} \end{pmatrix} \begin{pmatrix} x_{p1} \\ z_{p1} \\ x_{p2} \\ z_{p2} \end{pmatrix} \tag{4.35}$$

and minor manipulation yields

$$\begin{pmatrix} x_1 \\ z_1 \\ x_2 \\ z_2 \end{pmatrix} = x_{p1} \begin{pmatrix} A_{11} \\ A_{21} \\ A_{31} \\ A_{41} \end{pmatrix} + z_{p1} \begin{pmatrix} A_{12} \\ A_{22} \\ A_{32} \\ A_{42} \end{pmatrix} + x_{p2} \begin{pmatrix} A_{13} \\ A_{23} \\ A_{33} \\ A_{43} \end{pmatrix} + z_{p2} \begin{pmatrix} A_{14} \\ A_{24} \\ A_{34} \\ A_{44} \end{pmatrix}.$$

This can be written in a general form for one component, x say, as

$$x_i = \sum_{j=1}^{r} (x_{pj} A_{ij}). \tag{4.36}$$

It should be noted that the initial conditions and starting procedure is the same as described for the Houbolt method as presented in Section 3.4.4. The real advantage of uncoupling the equations of motion is now clear. That is that the response in each mode is decoupled from the response in any of the other modes and so different time step sizes can be used to integrate each equation of Equation (4.30). If all these equations were to be integrated with the same time step size, then this procedure would be identical to using the direct integration schemes of Chapter 3 on the original coupled equations of motion. However, the method of determining the size of each time step for each mode, and the number of modes to be used when integrating the equations of motion to provide an accurate solution, can only be gauged through a systematic numerical investigation.

4.5 Damped Arbitrarily Excited Systems

The equations of motion for a damped arbitrarily excited dynamic system can be expressed as

$$\underline{M}\,\ddot{\underline{U}} + \underline{D}\,\dot{\underline{U}} + \underline{K}\,\underline{U} = \underline{Q}(t). \tag{4.37}$$

Before looking at how to include the damping effects, the equations are transformed into what are called normal coordinates. To do this the modal matrix $\underline{A}$, as derived for the free undamped equations of motion in Section 4.3 is again used, but it is now normalised with respect to the mass matrix. In particular, each column of $\underline{A}$ is modified according to

$$\underline{B}_i = \frac{\underline{A}_i}{C_i} \tag{4.38}$$

where the scalar C_i is given by

$$C_i = \pm\sqrt{\underline{A}_i^T \underline{M}\,\underline{A}_i} = \pm\sqrt{\sum_{j=1}^{r} A_{ji} (\sum_{l=1}^{r} M_{jl} A_{li})}. \tag{4.39}$$

A_{ji} is defined by Equation (4.15). If the mass matrix contains diagonal terms only, then C_i is given by

$$C_i = \pm\sqrt{\sum_{j=1}^{r}(M_j A_{ji}^2)}. \tag{4.40}$$

Defining $\underline{B}$ to consist of columns defined by $\underline{B}_j$, and $\underline{U}_n$ as satisfying the following relationships

$$\underline{U} = \underline{B}\,\underline{U}_n$$

$$\dot{\underline{U}} = \underline{B}\,\dot{\underline{U}}_n$$

$$\ddot{\underline{U}} = \underline{B}\,\ddot{\underline{U}}_n,$$

then premultiplication of Equation (4.37) by $\underline{B}^T$ leads to

$$\underline{B}^T\underline{M}\,\underline{B}\,\ddot{\underline{U}}_n + \underline{B}^T\underline{D}\,\underline{B}\,\dot{\underline{U}}_n + \underline{B}^T\underline{K}\,\underline{B}\,\underline{U}_n = \underline{B}^T\underline{Q}(t). \tag{4.41}$$

Because of the normalisation performed by Equation (4.38), $\underline{B}^T\underline{M}\,\underline{B} = I$. Also rewriting Equation (4.9) with this transformation, yields

$$\underline{B}_i^T\underline{K}\,\underline{B}_i = p_i^2\underline{B}_i^T\underline{M}\,\underline{B}_i, \tag{4.42}$$

where $\underline{A}_i$ has been replaced by its normalised form, $\underline{B}_i$. Hence $\underline{B}_i^T\underline{K}\,\underline{B}_i = p_i^2$, and thus Equation (4.41) can be written as

$$\ddot{\underline{U}}_n + \underline{B}^T\underline{D}\,\underline{B}\,\dot{\underline{U}}_n + p_i^2\underline{U}_n = \underline{Q}_n(t) \tag{4.43}$$

where $\underline{Q}_n(t) = \underline{B}^T\underline{Q}(t)$. If the damping term were to be removed from any equation of Equation (4.43), then that equation would become identical in form to Equation (4.33) except that having written Equation (4.43) in Normal coordinates, the mass terms are now unity and the stiffness terms are the eigenvalues. Equation (4.43) represents the equations of motion for a damped arbitrarily excited structure which are written in Normal coordinates. However there is still the problem of how to include the damping term $\underline{B}^T\,\underline{D}\,\underline{B}$ into the solution. An excellent account of the influence of damping in multidegree systems can be found in Timoshenko, Young and Weaver(1974), where three methods are proposed to assimilate the damping matrix into the solution. Two of these are obtained through an estimation of the amount of damping in the system and the other assumes proportional damping. These procedures are now outlined.

4.5.1 Proportional Damping

In this case the damping matrix $\underline{D}$ is considered to be linearly proportional to some linear combination of the mass and stiffness matrices, thus

$$\underline{D} = a\,\underline{M} + b\,\underline{K}, \quad \text{say.} \tag{4.44}$$

Substitution into Equation (4.43) yields

$$\ddot{\underline{U}}_n + \underline{B}^T(a\,\underline{M} + b\,\underline{K})\,\underline{B}\,\dot{\underline{U}}_n + p_i^2\underline{U}_n = \underline{Q}_n(t).$$

Remembering that $\underline{B}^T\underline{M}\,\underline{B} = I$, and bearing in mind Equation (4.42), the above reduces to

$$\ddot{\underline{U}}_n + (a + bp_i^2)\dot{\underline{U}}_n + p_i^2\underline{U}_n = \underline{Q}_n(t).$$

Thus it can be seen that the resulting equations have been uncoupled with the modal matrix $\underline{A}$ derived for the undamped class of problems. This form of damping is alternatively known as classical or Rayleigh damping. The problem with this method lies in the selection of a and b to give a good approximation to the total damping. As stated by Bathe(1982): *"In general the damping matrix cannot be constructed from element damping matrices, such as the mass and stiffness matrices of the element assemblage..."*. In other words the correct selection of a and b for Equation (4.44) is not straightforward and would require a certain amount of numerical experimentation and calibration with the direct methods of Chapter 3. Any scalar equation of Equation (4.44) is expressed as

$$\ddot{x}_{ni} + (a + bp_i^2)\dot{x}_{ni} + p_i^2 x_{ni} = q_{ni}(t)$$

The modal damping ratio is ξ_i and is thus defined as

$$\xi_i = \frac{a + bp_i^2}{2p_i}. \tag{4.45}$$

This relationship is introduced because it is useful in studying the effect of varying the constants a and b upon the amount of damping which is admitted into the system.

4.5.2 Highly Damped Equations

If it is expected that the amount of damping present in the equations of motion is likely to be large, then it is proposed to use the method due to Foss(1958).

Although the title of this paper implies that the solution method is used only for linear systems, it is supposed that it is applicable in this situation as the solution can be thought of being essentially linear over each time step. The reason for this is thus: The main contribution to the nonlinearities inherent in the formulation of the equations of motion are the nonlinear influence of the geometry, and the variable nature of the coefficients of the second order differential equation being solved. The effect of the geometry is particularly significant at large excursion values, but even so the influence of a change in geometry over one time step could be considered linear. The second order differential equation being solved is the matrix representation of the equations of motion formulated in the preceeding sections, and hence the coefficients are the mass, damping and stiffness matrices. It is evident from Equation (4.3) that the mass matrix only changes because the added mass changes as a function of geometry. The stiffness matrix comprises the tension in each element and this too changes as a consequence of the geometric changes. The drag force, although nonlinear, is often linearised by some method, hence together with the geometric change over one time step considered as linear, it is proposed that the solution process can be considered as a series of approximate linear solutions. This then allows the method of Foss(1958) to be applied. This method involves the transformation of the h coupled second order equations into $2h$ first order equations, from which the homogeneous and the nonhomogeneous solutions are derived.

4.5.3 Lightly Damped Equations

Here it is assumed that the damped equations of motion are uncoupled by the modal matrix $\underline{A}$ obtained for the undamped solution. This means that $\underline{A}$ is not only orthogonal with the mass and stiffness matrices, but that it is assumed to be orthogonal with the damping matrix, $\underline{D}$. As stated in Timoshenko *et al.*(1974): *"This assumption implies that any off diagonal terms resulting from the operation* $\underline{B}^T \underline{D}\, \underline{B}$ *are small and can be neglected."* Furthermore, the values of the damping ratios ξ_i must be experimentally determined, or assumed, before the solution can commence. This leaves the familiar scalar equation for the undamped equations of motion, namely

$$\ddot{x}_{ni} + 2p_i\xi_i\delta_{ii}\dot{x}_{ni} + p_i^2 x_{ni} = \underline{B}_i^T q_i(t) \tag{4.46}$$

where δ_{ij}, the kroneker delta, is present to ensure that only terms on the diagonal enter the solution. The solution procedure for Equation (4.46) is identical to that for the undamped equations of motion as described in Section 4.3, except that now the velocity relation from the Houbolt time integration scheme is also needed.

4.6 Discussion of Nonlinearities

Modal analysis is usually applied to systems of linear equations, where it proves to be particularly effective if only a few modes are excited. A linear system is one where the amplitude of the response is proportional to the amplitude of the exciting force and the coefficients of the differential equation being solved must be constant. Clearly the equations of motion as formulated for a mooring line are nonlinear, where the contributions to the nonlinearity arise from four main sources: (i) Geometric nonlinearity, (ii) seabed interaction, (iii) quadratic fluid drag forces, and (iv) time dependent coefficients. The first contribution is clearly shown in the excursion curve results of Chapter 2, where the tension-displacement curves are nonlinear. The second contribution is more subtle and is a less significant effect, as discussed in Section 3.4 and further in Chapter 8. Fluid drag forces are modelled through the use of Morison's equation which contains a nonlinear effect through the velocity squared term. The fourth effect arises because the coefficients of acceleration, velocity and displacement represented by the mass, damping and stiffness matrices, are time dependent as can be seen from Equations (4.1) and (4.2). This occurs because as the displacements of the nodes change with time, so do the angles of inclination of the elements. It can therefore be seen that the time varying contributions to the mass matrix are the added mass terms. This is not usually a consideration in normal structural analysis, since the added mass of air is neglected. This results in a diagonal mass matrix which, in turn, implies that there is no inertial coupling. The stiffness matrix is also time dependent but for two reasons. Firstly, the change in element orientation, γ, and secondly the changes in nodal displacements cause the element tensions to change. The tension part of the equations of motion is totally analogous to the expression: force = stiffness $\times$ displacement, which is more usual in structural analysis. For linear problems the stiffness (or slope of the force-displacement graph) is constant, but for a nonlinear problem, the stiffness changes with the displacement, which implies that it also changes with time.

From the above discussion of nonlinearities, the difference in the application of modal techniques when applied to linear and nonlinear equations becomes clear. For linear equations once the modal matrix $\underline{A}$ has been determined it remains unchanged and hence it is used to uncouple the equations of motion only once and thereafter the uncoupled form of the governing equations are integrated. With nonlinear equations the coefficient matrices are time dependent and hence so is the modal matrix. This means that the mass and stiffness matrices are updated at

each time step and hence the modal matrix $\underline{A}$ must also be constantly recalculated before use. Physically this implies that the nonlinearities present are causing the mode shapes and frequencies of the solution to change with time. Thus at each time step it is required that the mass and stiffness matrices are updated and that the eigenvalues and eigenvectors are calculated from the free undamped equations of motion. These are used to calculate the modal matrix $\underline{A}$, which is then used to uncouple the damped equations of motion as described in the previous section. These are then integrated using the Houbolt scheme, say. At this new time step, both the mass and stiffness matrices must be updated and the whole process, as illustrated in Figure 4.1, must be repeated.

It is clearly a time consuming process to find the eigensolutions for a matrix of $2h$ at each time step. However, when considered in the context of the iterative process necessary at each time step, which might involve the inversion of a matrix of order h typically three times per time step, this process might not prove such a penalty. Additional computational savings may be gained by being able to assume that the mass, stiffness and hence modal matrices remain constant over a number of time steps so that the amount of updating necessary is reduced to a minimum. As mentioned previously, modal analysis is most effective for problems where only a few mode shapes need to be evaluated to provide an accurate solution. In particular, if less than 25% of the eigenvalues (and therefore the associated eigenvectors) are needed, then more efficient matrix solvers can be used.

With the preceding theory and discussion presented, a more detailed appraisal of the few relevant papers in the open literature can now be made.

Johansson(1978) finds the solutions for a linearised form of the free, undamped equations of motion and uses this to uncouple the equations so that they are written in normal coordinates. In the discussion of the solution procedure it is not clear whether the modal matrix is determined at each time step, although this could be inferred from the information given. The formulation of the equations of motion is different to that presented here, although the same forces are indicated as being included in his model. The solution procedure is also different but again corresponds, in principle, to the solution methods proposed here. The drag force is linearised by assuming that the nodal velocity is small compared to the fluid velocity. However the paper does not provide any insight into the effect of not updating the modal matrix at every time step; also it is indicated that all modes are used to provide the solution, but there is no mention of the degree of approximation that can be expected if only a few modes are used. Therefore it seems that this

paper is describing the same solution process as proposed here but does not provide any discussion of the potential numerical advantages or disadvantages inherent in the formulation.

Nuckolls and Dominguez(1977) use modal methods to determine the natural frequencies of a particular mooring configuration and then uncouple the equations of motion using the modal matrix. The solution is gained through the use of the 'Phase-Plane δ' method, and not the more usual time integration methods.

Dominguez and Smith(1972) formulate a linearly damped set of equations which they then solve using the method of Foss(1958). Here the original $2h$ coupled second order differential equations are reduced to $4h$ uncoupled first order equations for which the eigensolutions are determined and then used to uncouple the equations of motion. The solution is then carried out in Normal coordinates and utilises a particular convolution integral technique. Because of the assumption of small displacements about the initial equilibrium position, the calculation of the modal matrix $\underline{A}$ only needs to be done once. No mention is made of the fact that it is possible to integrate each uncoupled mode with different time step sizes, and so the potential computational saving inherent in the modal method has not been fully realised.

4.7 Preliminary Results

In this section the eigenvalues for the free undamped equations of motion (see Equation (4.3)) are obtained. These are then used to assess the minimum value of the time step to be used in the direct integration method. In order to prepare the mass and stiffness matrices, the static numerical model described in Section 2.4 is used in conjunction with the values in Table 4.1. In addition to these values the normal and tangential added mass coefficients were taken as 1.98 and 0.0 respectively. With this 20 element model there will be 38 modes in the solution; approximately, the first 19 will represent the transverse modes, whilst the remainder are essentially the longitudinal modes. Half of the natural frequencies for the first 19 modes are shown in Figure 4.2 as the endpoint of the mooring line is moved further away from the anchor position. As would be intuitively expected the natural frequencies of the transverse modes increase as the line becomes more taut. However, the natural frequencies of the longitudinal modes remain essentially constant - typical values are shown in Table 4.2:

Quantity	2D static values
x displacement of endpoint	1000 m
y displacement of endpoint	1000 m
z displacement of endpoint	1000 m
Length of mooring line	1790 m
Number of elements	20
Water density	1025 kg/m^3
Diameter of mooring line	0.07148 m
Mass per meter in air	25.493 kg/m
Young's modulus	7.848×10^{10}N/m^2
Cd_n, Cd_t	1.6, 0.03

Table 4.1 — Static Input Parameters

Mode	Natural Frequency (rads/sec)
20	6.0
22	17.63
24	28.88
26	29.4
28	48.97
30	57.33
32	64.28
34	69.65
36	73.3
38	75.16

Table 4.2 — Natural Frequencies for Higher Modes

In order to incorporate all the modes into a time stepping dynamic solution, experience suggests that a time step of approximately $\frac{1}{10}^{th}$ of the period of the

highest mode should be used. In this case a time step of 0.0084 seconds would be needed; this compares with the "minimum practicable value" of 0.001 seconds used in the results presented in Chapter 6.

4.8 Summary

In this chapter the method of solving the equations of motion for a mooring line by modal techniques is discussed. The importance of deciding whether the solution is required for small or large displacement problems is indicated. With the former, the modal matrix $\underline{A}$ need only be determined once; with the latter, $\underline{A}$ should be determined periodically - the regularity of which affects the efficiency of the solution. In particular, how the simplified 2D equations are assembled into the necessary mass and stiffness matrices. Then details of the matrix manipulations required for the solution are presented. In particular how the equations may be uncoupled by using the modal matrix derived from the undamped free oscillation equation. The manner of including the damping is extensively discussed since this presents the one obstacle to the uncoupling of the damped equations of motion. Finally there is a discussion of the nonlinearities present and how these have been accounted for during the suggested solution process. Also a selection of the relevant literature is discussed in the light of the theory presented in this chapter.

CHAPTER 5

Numerical Properties of Time Integration Schemes

5.1 Introduction

This chapter is intended to be a guide to the finite difference (FD) time integration schemes presented in Chapter 3. It is essential to have an understanding of the numerical properties of these schemes and how these properties can be expected to affect the solution. This enables features of the solution to be correctly ascribed to either the equations being solved or the numerical procedure being used to solve them. This chapter starts with a statement of the four FD schemes proposed for use in the solution of the equations of motion. This is then followed by a brief introduction to some of the numerical terms and definitions used in the analysis of FD schemes. The next section presents the derivation of the Central Difference (CD) and Houbolt schemes from consideration of general expressions for first and second order linear multistep methods. The Wilson-θ and Newmark schemes are derived in a straightforward manner from the assumption of linear acceleration over a time interval. The next section then examines the stability of these methods when applied to linear equations. The stability of the schemes is demonstrated through the numerical analysis of the resulting amplification matrices. This is followed by a section on numerical accuracy, again for the schemes applied in the solution of linear equations. The chapter concludes with estimations of the minimum time step size to ensure accurate results and the 'critical' time step size for the CD scheme.

Whilst many texts and papers exist on this subject, the work in this chapter is largely based on one or two works most commonly cited. Books by Wood(1990) and Ritchmyer and Morton(1967) form as complete a mathematical treatise on the subject as is usually required, but many of the points of interest to the practicing engineer are couched in complex mathematical verbage. The paper of O'Brien, Morton and Kaplan(1950) details many of the terms most commonly used in a fashion that is less rigorous and therefore more understandable. The book of Bathe(1982) gives a brief but succinct account of the stability and accuracy of these schemes.

5.2 Brief Presentation of Finite Difference Schemes

Here the FD schemes which have been adopted for study in this thesis are briefly presented in the forms in which they most commonly appear in the literature. The origins of each scheme are also indicated.

5.2.1 Central Difference Method

The Central Difference (CD) scheme has been used in one form or another for many years, having been often developed in many branches of engineering from an intuitive understanding of the problem being considered. As such the scheme does not have an 'originator', but the first reported use of the CD method for the numerical solution of problems in mooring line dynamics was by Walton and Polachek in their well established paper of 1960. Since then the CD method does not seem to have been widely adopted for the solution of this class of problem, mainly because the unconditional stability of alternative FD schemes has made these alternatives more attractive. The identities for the CD scheme are

$$\ddot{\underline{U}}^n = \frac{1}{\Delta t^2}\left(\underline{U}^{n-1} - 2\underline{U}^n + \underline{U}^{n+1}\right) \tag{5.1}$$

and

$$\dot{\underline{U}}^n = \frac{1}{2\Delta t}\left(\underline{U}^{n+1} - \underline{U}^{n-1}\right), \tag{5.2}$$

where $\underline{U}^n$ is the general displacement vector at time n. It is called the Central Difference method because the differences are centred at time n and the solution is required at time $(n+1)$. This is known as an explicit integration scheme because the solution at $(n+1)$ depends only upon the solution at n and $(n-1)$. By substituting Equations (5.1) and (5.2) into the standard form of the equations of motion given by

$$\underline{M}\,\ddot{\underline{U}} + \underline{D}\,\dot{\underline{U}} + \underline{K}\,\underline{U} = f(t), \tag{5.3}$$

it is seen that the stiffness matrix $\underline{K}$ does not appear as a factor of the required solution ($\underline{U}^{n+1}$). This is another way of defining an explicit scheme. One of the most important features of this explicit scheme is that it is conditionally stable. This means that a critical time step limit, Δt_{cr}, exists and if this value is exceeded, the numerical solution becomes unstable. This instability manifests itself either as an unfeasible solution, or, as in the case of line dynamics, the collapse of the solution procedure caused by the uncontrolled growth of numerical errors.

5.2.2 Houbolt Scheme

The Houbolt method was first presented in 1950 (Houbolt(1950)) in a paper dealing with the dynamic response of elastic aircraft. The scheme was developed from consideration of a cubic curve passing through four displacement points and obtaining the derivatives at the last point. This results in the following expressions for acceleration and velocity

$$\underline{\ddot{U}}^{n+1} = \frac{1}{\Delta t^2}\left\{2\underline{U}^{n+1} - 5\underline{U}^{n} + 4\underline{U}^{n-1} - \underline{U}^{n-2}\right\} \tag{5.4}$$

and

$$\underline{\dot{U}}^{n+1} = \frac{1}{6\Delta t}\left\{11\underline{U}^{n+1} - 18\underline{U}^{n} + 9\underline{U}^{n-1} - 2\underline{U}^{n-2}\right\}. \tag{5.5}$$

Since its introduction this method has been frequently used in the solution of dynamic equations and seems to be particularly popular in the field of mooring line dynamics. By substituting the above expressions into Equation (5.3), the resulting equations can be solved for dynamic equilibrium at time $(n+1)$, rather than at time n as in the CD method. For this reason the Houbolt method is called an implicit scheme; this is also illustrated by the stiffness matrix now appearing as a factor of $\underline{U}^{n+1}$ (the required solution) and thus it has to be inverted during the solution process. The advantage of this scheme, and the remaining two implicit schemes considered here, is that there is no limit, in the context of numerical stability, upon the permissible size of the time step which can be used. This means that in general the time step can be much larger for these three implicit methods than the time step used with the explicit CD scheme. However, the size will eventually be constrained by consideration of the required solution accuracy.

5.2.3 The Newmark Algorithm

The Newmark algorithm was first presented in 1959 (Newmark(1959)) in connection with the estimation of structural response to earthquake loadings and has subsequently become established as probably the most popular method of predicting the response of dynamic systems. It is not however, frequently used in the field of mooring line dynamics, where only a few papers exist detailing its use in this context. This algorithm is defined by

$$\underline{\dot{U}}^{n+1} = \underline{\dot{U}}^{n} + \Delta t\left\{(1-\delta)\underline{\ddot{U}}^{n} + \delta\underline{\ddot{U}}^{n+1}\right\} \tag{5.6}$$

and

$$\underline{U}^{n+1} = \underline{U}^{n} + \Delta t\underline{\dot{U}}^{n} + \Delta t^2\left\{(0.5-\beta)\underline{\ddot{U}}^{n} + \beta\underline{\ddot{U}}^{n+1}\right\}. \tag{5.7}$$

The parameters δ and β are introduced to allow control over how much of the acceleration at the end of each time interval enters the solution. They also control other aspects of the scheme such as stability and accuracy and with certain choices of these parameters, other FD expressions are obtained. For example with $\delta = \frac{1}{2}$ and $\beta = \frac{1}{6}$, the Newmark algorithm reduces to the 'linear acceleration' method (not considered here) and with $\delta = 0.5$ and $\beta = 0$ the algorithm reduces to the explicit CD scheme. With $\delta = \frac{1}{2}$ and $\beta = \frac{1}{4}$ it becomes the 'unconditionally' stable method originally proposed by Newmark. This is alternatively known as the constant-average-acceleration method or the trapezoidal rule. The scheme is implicit and therefore has properties similar to those discussed for the Houbolt method.

5.2.4 The Wilson-θ Method

The Wilson-θ method was first presented in 1968 (Wilson(1968)) as an extension of the linear acceleration method. The algorithm is defined by the following approximations of acceleration and velocity, namely

$$\underline{\ddot{U}}^{n+\theta} = \frac{6}{(\theta\Delta t)^2}\left(\underline{U}^{n+\theta} - \underline{U}^{n}\right) - \frac{6}{\theta\Delta t}\underline{\dot{U}}^{n} - 2\underline{\ddot{U}}^{n} \tag{5.8}$$

and

$$\underline{\dot{U}}^{n+\theta} = \frac{3}{\theta\Delta t}\left(\underline{U}^{n+\theta} - \underline{U}^{n}\right) - 2\underline{\dot{U}}^{n} - \frac{\theta\Delta t}{2}\underline{\ddot{U}}^{n}. \tag{5.9}$$

The linear acceleration method (not considered here) can be derived from these equations by setting $\theta = 1$; this scheme will be shown to be conditionally stable in Section 5.7. By establishing dynamic equilibrium at time $(n+\theta)\Delta t$ with $\theta \geq 1.37$, this becomes an unconditionally stable implicit method. Once the total solution is obtained at time $(n+\theta)\Delta t$, interpolation is used for the required solution at time $(n+1)\Delta t$.

5.3 Numerical Terms and Background

The formulation of an equation or a set of equations which describe a physical process is, in most cases, a relatively straightforward task in comparison to the problems which can be encountered in the solution of these equations. Often analytical solutions cannot be derived unless various simplifying assumptions are made during the derivation. Without simplification, recourse must be made to various numerical solution techniques which are now widely available. However the choice of which methods are the most applicable, and under which circumstances,

and how best to optimise the solution has become a separate subject of study in itself. In the case of mooring line dynamics an analytical solution does not exist for the full nonlinear second order partial differential equations (PDEs) which govern the physics. To preserve the inherent nonlinearities a numerical solution has been derived which involves a discretisation of the space and time dimensions. This means that the original PDEs are now replaced by a set of ordinary differential equations (ODEs) which are second order and have variable coefficients. Next the derivatives of the ODEs are represented by equivalent numerical difference equations. The numerical representation to be adopted is hereafter referred to as a finite difference equation (FDE). In the context of the time domain, these difference equations are sometimes called Time Integration schemes. It then follows, by definition, that the solutions obtained subsequently will only be an approximation to the 'true' solution obtained, if it were possible, from the PDEs. There are two main reasons for needing a FD representation of a derivative:

1. Because the derivative cannot be evaluated analytically.

2. If it can be evaluated analytically this might require much greater effort than numerical evaluation.

If, for example, the velocity derivative $d\underline{U}/dt$ (where $\underline{U}$ is displacement and t is time) is to be evaluated, then a relationship between $\underline{U}$ and t must be known if the differentiation is to be carried out. An equivalent FD representation of this particular derivative might be $\frac{1}{2\Delta t}(\underline{U}^{n+1} - \underline{U}^{n-1})$. This expression corresponds to the velocity form of the Central Difference scheme, and it can be seen that the derivative is now expressed as a function of known past displacements. It is the study of FD representations of continuous derivatives and the subsequent implications for the accuracy and stability of the solution which is the subject of this chapter.

In order to discuss these concepts further an initial introduction is made using the notation of O'Brien *et al.*(1950). This is then slightly more formalised using a notation due to Lambert(1973) and Richtmyer and Morton(1967). The following terms are defined

1. P is the exact solution of the PDEs.

2. N is the exact solution of the FDEs.

3. Δ is the numerical solution of the FDEs.

Note the distinction between the exact (to infinite precision) and the numerical (to finite precision) solutions. In the discussion of FDEs three main error terms arise, and these are:

1. The Global Truncation Error (GTE).
2. The Local Truncation Error (LTE).
3. The Global Rounding Error (GRE).

The GTE is also known as the 'discretisation error' and measures the difference between P and N at any point during the solution, thus

$$\mathrm{GTE}^n = \mathrm{P}^n - \mathrm{N}^n.$$

A more useful concept is the LTE which may be considered as a local measure of the GTE. By considering the GTE defined at time steps n and $n+1$, then the LTE can be thought of as being the difference between these two, namely

$$\begin{aligned}\mathrm{LTE}^n &= \mathrm{GTE}^{n+1} - \mathrm{GTE}^n \\ &= (\mathrm{P}^{n+1} - \mathrm{N}^{n+1}) - (\mathrm{P}^n - \mathrm{N}^n).\end{aligned}$$

To illustrate this consider the general point (i, j) in space and or space/time. That is, for example, i might represent a general space coordinate and j might represent position in time. Thus the LTE at this point can be seen to be a measure of the GTE at the point $(i, j+1)$ when the FDEs are applied once only to the exact solutions of the PDEs.

The GRE is a numerical error which is derived only from the practical considerations of computing the required values. This means that it arises from the inability of the computer to calculate numbers to infinite precision. The GRE is therefore defined as N - Δ, which is the difference between the exact solution of the FDEs and the actual answers returned by the computer. Maintaining a bound on the GRE is the subject of numerical stability, which is dealt with in more detail later. The stability of a FDE requires that any error introduced during the solution will decay at an acceptable rate with time.

Having given an intuitive definition of these terms a slightly more formal approach is now adopted. Consider the FD representation

$$E_1 \underline{U}^{n+1} = E_0 \underline{U}^n \tag{5.10}$$

with $\underline{U}$ denoting the displacements, $E_i (i = 0, 1)$ represent the FDE coefficients and n indicates the time level as before. Note that this is a one step FD scheme, since only the time levels n and $n + 1$ are involved. However this form will be used for the introduction of the concepts of *consistency*, *convergence* and *stability*. A multistep formula is not used here since it can be reduced to an equivalent set of one step formulae through the introduction of dependent variables. Equation (5.10) can also be written in the form

$$\underline{U}^{n+1} = C(\Delta t)\underline{U}^n, \tag{5.11}$$

where $C(\Delta t) = E_1^{-1} E_0$. Now introduce the definition

$$\frac{d\underline{U}(t)}{dt} = A\underline{U}(t), \tag{5.12}$$

so that A represents the form of the differentiation to be undertaken on the variable $U(t)$ to provide the required derivative. It can be seen that

$$\frac{\underline{U}^{n+1} - \underline{U}^n}{\Delta t} \tag{5.13}$$

represents a simple approximation to the time derivative of $\underline{U}$. Use of the FD representation in Equation (5.11) leads to

$$\frac{C(\Delta t)\underline{U} - \underline{U}}{\Delta t} \approx A\underline{U}. \tag{5.14}$$

Following Richtmyer and Morton(1967) the concept of consistency is expressed through the requirement that "*the family of operators $C(\Delta t)$ provides a consistent approximation for the initial value problem if*

$$\left\| \left\{ \frac{C(\Delta t) - I}{\Delta t} - A \right\} \underline{U}(t) \right\| \to 0 \quad \text{as} \quad \Delta \text{t} \to 0, \tag{5.15}$$

where I is the identity operator. In Equation (5.15) the quantity represented by $||M||$ is called the 'norm of M' and merely represents a measure of the magnitude of

the difference. It can therefore be seen that the consistency condition as expressed by Equation (5.15) requires the FD representation ($C(\Delta t)$) of the derivative operator A, to be exactly equal to A as the time interval Δt tends to zero. Hence the consistency condition is actually independent of the initial value problem being solved. An alternative equivalent form of this consistency condition is that

$$\left\| \frac{\underline{U}(t+\Delta t) - C(\Delta t)\underline{U}(t)}{\Delta t} \right\| \to 0 \quad \text{as} \quad \Delta t \to 0 \tag{5.16}$$

where the term under the norm is called the local truncation error and is the mathematical equivalent of the verbal definition given previously. Therefore the LTE measures how closely the genuine solution of the initial value problem matches the numerical solution of the FD equations. It can therefore be seen that if the LTE tends to zero as $\Delta t \to 0$ the FD expression is consistent with the original PDE.

The concept of convergence can now be introduced. This too is associated with the GTE defined previously. If the initial value $\underline{U}_0$ is operated on n times by the FDE then

$$\underline{U}^n = [C(\Delta t)]^n \underline{U}_0. \tag{5.17}$$

The equivalent analytical solution is given by $\underline{U}(\underline{U}\Delta t) = D\underline{U}_0$, say. Then $C(\Delta t)$ is said to be a convergent approximation to the PDE if

$$\|[C(\Delta t)]^n \underline{U}_0 - D\underline{U}_0\| \to 0 \quad \text{as} \quad \Delta t \to 0. \tag{5.18}$$

This means that for $C(\Delta t)$ to be a convergent approximation to A, the GTE must vanish as $\Delta t \to 0$.

These definitions of consistency along with the briefly mentioned concept of stability, allows for the introduction of the Equivalence Theorem due to Lax which states: "*Given a properly posed initial value problem and a FD approximation to it that satisfies the consistency condition, stability is the necessary and sufficient condition for convergence*", see Richtmyer and Morton(1967, pg. 45). In other words given that the FD scheme is consistent with the initial value problem in the sense of Equation (5.15), then if it can be shown that the FD scheme is stable, this will guarantee that it is also convergent. The converse is also true, i.e. by establishing the convergence of a FD approximation this guarantees the stability of the numerical expression.

As mentioned at the start of this section, all these remarks apply to one step FD schemes. However, the practical differences between these definitions and those for multilevel schemes arise in the mathematical rigour of the derivations. Thus when multilevel schemes are employed the following difference must be noted: For one step schemes, vanishing of the truncation error as $\Delta t \rightarrow 0$ implies consistency, whereas for multilevel schemes consistency also depends upon the schemes being stable.

5.4 Derivation of the FD Schemes

The four schemes alluded to have been widely used in the solution of dynamic problems, but as yet a comprehensive derivation of all of these schemes has not been presented. In this section the CD and Houbolt schemes are derived from methods in numerical analysis, whereas the derivations of the Wilson-θ and the Newmark schemes are based on the linear acceleration concept. Before undertaking the derivation of each scheme a few preliminary concepts are introduced to provide relevant background. In particular, the local truncation error of general first and second order differential equations will be considered in some detail. On route the concept of order of accuracy and its relation to the consistency of approximation will be introduced.

A Second Order Differential Equation

From numerical analysis (see Lambert(1973)), a linear, k-step solution scheme for the general second order problem of $\ddot{y} = f(x, y)$ is defined as having the form

$$\sum_{j=0}^{k} \alpha_j \underline{U}^{n+j} = h^2 \sum_{j=0}^{k} \beta_j f^{n+j}, \tag{5.19}$$

where α_j and β_j are suitably selected coefficients and h is the step size. This is the definition of the form of a multistep FD scheme. The associated LTE is a function of the step size and the behaviour of $\underline{U}$ and its derivative. This can be estimated using

$$\mathcal{L}\big[\underline{U}(x); h\big] = \sum_{j=0}^{k} \big[\alpha_j \underline{U}(x + jh) - h^2 \beta_j \ddot{\underline{U}}(x + jh)\big], \tag{5.20}$$

where the coefficients of the FD scheme are used with the analytic solutions for one time step only. Since an approximation to $\ddot{\underline{U}}$ is not possible with less than three values, k must be at least 2. Equation (5.19) is introduced with the differential equation $\ddot{\underline{U}} = f(x, y)$ so that the order of accuracy of the Linear Multistep Method

(LMM) may be formally defined without having to solve for the required derivatives of the initial value problem, which, in any case, may not exist. Expanding Equation (5.20) in a Taylor series about x yields

$$\mathcal{L}[\underline{U}(x); h] = C_0\underline{U}(x) + C_1 h\underline{U}^{(1)}(x) + ... + C_q h^q \underline{U}^{(q)}(x) + ... \tag{5.21}$$

where C_q are constants which are obtained by expanding each term in Equation (5.20) as a Taylor series about x and then collecting coefficients of the same power, to give

$$\begin{aligned}
C_0 &= \alpha_0 + \alpha_1 + \alpha_2 + ... + \alpha_k \\
C_1 &= \alpha_1 + 2\alpha_2 + ... + k\alpha_k \\
C_2 &= \frac{1}{2!}(\alpha_1 + 2^2\alpha_2 + ... + k^2\alpha_k) - (\beta_0 + \beta_1 + \beta_2 + ... + \beta_k) \\
&\vdots \qquad\qquad \vdots \qquad\qquad \vdots \\
C_q &= \frac{1}{q!}(\alpha_1 + 2^q\alpha_2 + ... + k^q\alpha_k) - \frac{1}{(q-2)!}(\beta_1 + 2^{q-2}\beta_2 + ... + k^{q-2}\beta_k).
\end{aligned} \tag{5.22}$$

The LMM defined in Equation (5.19), is said to have an order of accuracy of p if

$$C_0 = C_1 = ... = C_p = C_{p+1} = 0, \text{ and } C_{p+2} \neq 0. \tag{5.23}$$

The LMM is said to be a consistent method if it has an order of at least 1. Consistency defined in this sense indicates that the order of accuracy in the Taylor series expansion of the LTE must be at least $O(h^2)$, i.e. the same as the order of accuracy of the difference equation.

A First Order Differential Equation

The form of a linear k-step solution scheme for the general first order problem $\dot{\underline{U}} = f(x, y)$ is considered as

$$\mathcal{L}\big[\underline{U}(x); h\big] = \sum_{j=0}^{k}\big[\alpha_j\underline{U}(x + jh) - h\beta_j\dot{\underline{U}}(x + jh)\big]. \tag{5.24}$$

The use of a Taylor series expansion about the point x leads to a relationship of

the same form as Equation (5.21), but the coefficients are now defined by

$$\begin{aligned} C_0 &= \alpha_0 + \alpha_1 + \alpha_2 + ... + \alpha_k \\ C_1 &= \alpha_1 + 2\alpha_2 + ... + k\alpha_k - (\beta_0 + \beta_1 + \beta_2 + ... + \beta_k) \\ &\vdots \qquad\qquad \vdots \qquad\qquad \vdots \\ C_q &= \frac{1}{q!}(\alpha_1 + 2^q\alpha_2 + ... + k^q\alpha_k) - \frac{1}{(q-1)!}(\beta_1 + 2^{q-1}\beta_2 + ... + k^{q-1}\beta_k). \end{aligned} \tag{5.25}$$

The LMM defined by Equation (5.24) is also said to have an order of accuracy of p if

$$C_0 = C_1 = ... = C_p = 0, \text{ and } C_{p+1} \neq 0. \tag{5.26}$$

The two LMM formulations defined in Equations (5.20) and (5.24), together with the coefficients of the associated Taylor series expansion defined in Equations (5.22) and (5.25) are now used to derive the FD equations for the CD and the Houbolt schemes.

5.4.1 Derivation of the CD Scheme

Acceleration Expression

An explicit scheme is required to operate over 3 time levels in order to provide a representation of the acceleration. This implies that $k = 2$ in Equation (5.19). Advantages will also occur if the scheme minimises the number of functional evaluations involved. The expansion of Equation (5.19) with $k = 2$ yields

$$\alpha_0\underline{U}^n + \alpha_1\underline{U}^{n+1} + \alpha_2\underline{U}^{n+2} = h^2(\beta_0 f^n + \beta_1 f^{n+1} + \beta_2 f^{n+2}). \tag{5.27}$$

To minimise the number of functional evaluations, $\beta_0 = \beta_2 = 0$ and $\beta_1 = 1$, hence

$$\alpha_0\underline{U}^n + \alpha_1\underline{U}^{n+1} + \alpha_2\underline{U}^{n+2} = h^2 f^{n+1} \tag{5.28}$$

where α_0, α_1 and α_2 are yet to be specified. Here f^{n+1} denotes that the acceleration is evaluated at time step $n+1$. The Taylor series expansion of the LTE provided in Equations (5.21) and (5.22), for $k = 2$ assumes the form

$$\mathcal{L}[\underline{U}(x); h] = \sum_{j=0}^{k} C_j h^{(j)} \underline{U}^{(j)}(x) = C_0\underline{U}(x) + C_1 h\dot{\underline{U}}(x) + C_2 h^2\ddot{\underline{U}}(x). \tag{5.29}$$

It is required that the error in the expansion is of order $O(h^2)$, hence from Equation (5.23), $p = 2$ so that $C_0 = C_1 = C_2 = C_3 = 0$. This also satisfies the consistency requirement, namely that $p \geq 1$. Therefore the coefficients C_q, defined in Equation (5.22), become

$$\begin{aligned} C_0 &= 0 = \alpha_0 + \alpha_1 + \alpha_2 \\ C_1 &= 0 = \alpha_1 + 2\alpha_2 \\ C_2 &= 0 = \frac{1}{2}(\alpha_1 + 4\alpha_2) - 1 \\ C_3 &= 0 = \frac{1}{6}(\alpha_1 + 8\alpha_2) - 1. \end{aligned}$$

Taking any three of the four equations defined above and solving, yields $\alpha_0 = 1, \alpha_1 = -2$ and $\alpha_2 = 1$. This shows that there are only 3 independent equations. Substitution of these values into Equation (5.28), and noting that the interval h is in fact the time step Δt, the following representation of acceleration is derived

$$\underline{\ddot{U}}^{n+1} = \frac{1}{\Delta t^2}(\underline{U}^n - 2\underline{U}^{n+1} + \underline{U}^{n+2}) \tag{5.30}$$

which is the acceleration form of the CD scheme.

Velocity Expression

The equivalent form to Equation (5.28) for the velocity expression is derived through Equation (5.24), and is

$$\alpha_0 \underline{U}^n + \alpha_1 \underline{U}^{n+1} + \alpha_2 \underline{U}^{n+2} = h f^{n+1}, \tag{5.31}$$

where f^{n+1} is now velocity. The coefficients from the Taylor series expansion are presented in Equation (5.25). For the order of the error in the expansion again to be $O(h^2)$, $p = 2$ and hence from Equation (5.26) $C_0 = C_1 = C_2 = 0$, therefore

$$\begin{aligned} C_0 &= 0 = \alpha_0 + \alpha_1 + \alpha_2 \\ C_1 &= 0 = \alpha_1 + 2\alpha_2 - 1 \\ C_2 &= 0 = \frac{1}{2}(\alpha_1 + 4\alpha_2) - 1. \end{aligned} \tag{5.32}$$

Thus, it follows that

$$\begin{aligned} \alpha_0 &= -(\alpha_1 + \alpha_2) \\ \alpha_1 &= 1 - 2\alpha_2 \\ \alpha_1 &= 2 - 4\alpha_2. \end{aligned} \tag{5.33}$$

The solution for the last two equations yields $\alpha_1 = 0$ and $\alpha_2 = 1/2$, and hence $\alpha_0 = -1/2$, so that Equation (5.31) becomes

$$\dot{\underline{U}}^{n+1} = \frac{1}{2\Delta t}(\underline{U}^{n+2} - \underline{U}^{n}), \tag{5.34}$$

which is the velocity form for the CD method.

5.4.2 Derivation of the Houbolt Method

Acceleration Term

The Houbolt scheme is a four step method and this implies that $k = 3$. Hence Equation (5.19) assumes the form

$$\alpha_0\underline{U}^{n}+\alpha_1\underline{U}^{n+1}+\alpha_2\underline{U}^{n+2}+\alpha_3\underline{U}^{n+3} = h^2(\beta_0 f^{n}+\beta_1 f^{n+1}+\beta_2 f^{n+2}+\beta_3 f^{n+3}). \tag{5.35}$$

If the method is to be implicit and the number of functional evaluations is to minimised, then $\beta_0 = \beta_1 = \beta_2 = 0$, and $\beta_3 = 1$, hence

$$\alpha_0\underline{U}^{n} + \alpha_1\underline{U}^{n+1} + \alpha_2 U^{n+2} + \alpha_3\underline{U}^{n+3} = h^2 f^{n+3}, \tag{5.36}$$

where $h = \Delta t$ as before, and f^{n+3} is the acceleration at time $t = n+3$. The Taylor series expansion of the LTE now assumes the form

$$\begin{aligned}\mathcal{L}\left[\underline{U}(x); h\right] &= \sum_{j=0}^{k} C_j h^{(j-1)}\underline{U}^{(j)}(x) \\ &= C_0\underline{U}(x) + C_1 h\dot{\underline{U}}(x) + C_2 h^2\ddot{\underline{U}}(x) + C_3 h^3\dddot{\underline{U}}\end{aligned} \tag{5.37}$$

with the coefficients satisfying

$$\begin{aligned} C_0 &= \alpha_0 + \alpha_1 + \alpha_2 + \alpha_3 \\ C_1 &= \alpha_1 + 2\alpha_2 + 3\alpha_3 \\ C_2 &= \frac{1}{2}(\alpha_1 + 4\alpha_2 + 9\alpha_3) - 1 \\ C_3 &= \frac{1}{6}(\alpha_1 + 8\alpha_2 + 27\alpha_3) - 3. \end{aligned} \tag{5.38}$$

For the order of the error in the expansion to be $O(h^2)$ $p = 2$ and hence $C_0 = C_1 = C_2 = C_3 = 0$, which reduces Equations (5.38) to

$$\alpha_0 = -(\alpha_1 + \alpha_2 + \alpha_3)$$

$$\alpha_1 = -(2\alpha_2 + 3\alpha_3)$$

$$\alpha_1 = 2 - (4\alpha_2 + 9\alpha_3)$$

$$\alpha_1 = 18 - (8\alpha_2 + 27\alpha_3).$$

The simultaneous solution of these equations yields $\alpha_3 = 2, \alpha_2 = -5, \alpha_1 = 4$ and $\alpha_0 = -1$. Thus Equation (5.36) becomes

$$\ddot{\underline{U}}^{n+3} = \frac{1}{\Delta t^2}(2\underline{U}^{n+3} - 5\underline{U}^{n+2} + 4\underline{U}^{n+1} - \underline{U}^n), \tag{5.39}$$

which is the acceleration form for the Houbolt scheme.

Velocity Term

The equivalent form of Equation (5.36) for the velocity expression, is gained through Equation (5.24) and is given by

$$\alpha_0\underline{U}^n + \alpha_1\underline{U}^{n+1} + \alpha_2\underline{U}^{n+2} + \alpha_3\underline{U}^{n+3} = hf^{n+3}$$

where $h = \Delta t$ and f^{n+3} is the velocity term. The relevant coefficients of the Taylor series expansion of the LTE are given by

$$C_0 = \alpha_0 + \alpha_1 + \alpha_2 + \alpha_3$$

$$C_1 = \alpha_1 + 2\alpha_2 + 3\alpha_3 - 1$$

$$C_2 = \frac{1}{2}(\alpha_1 + 4\alpha_2 + 9\alpha_3) - 3$$

$$C_3 = \frac{1}{6}(\alpha_1 + 8\alpha_2 + 27\alpha_3) - \frac{9}{2}.$$

For the expansion in the LTE to have an order of accuracy of $O(h^2)$, $p = 2$ and hence $C_0 = C_1 = C_2 = 0$ and $C_3 \neq 0$ although its precise form is not defined. Solving the first three relations allows α_0, α_1 and α_2 to be expressed in terms of α_3 only.

$$\alpha_0 = \frac{3}{2} - \alpha_3$$

$$\alpha_1 = 3\alpha_3 - 4$$

$$\alpha_2 = \frac{5}{2} - 3\alpha_3.$$

It can be seen that there is not enough information to completely define the velocity form of the Houbolt scheme. This means that a family of velocity relations can be derived according to the value selected for α_3. To precisely derive the Houbolt form, the order of accuracy demanded of the scheme should be increased, therefore $p = 3$ and hence solution of $C_3 = 0$ yields $\alpha_3 = 11/6$. The relations above then give $\alpha_0 = -2/6$, $\alpha_1 = 3/2$ and $\alpha_2 = -6/2$. Substitution of these values yields

$$\underline{\dot{U}}^{n+3} = \frac{1}{6\Delta t}(11\underline{U}^{n+3} - 18\underline{U}^{n+2} + 9\underline{U}^{n+1} - 2\underline{U}^{n}), \tag{5.40}$$

which is the velocity form of the Houbolt scheme.

5.4.3 Derivation of the Wilson-θ Method

The underlying assumption of this method is that the acceleration varies linearly over each time step, as in the linear acceleration method, but in this case the size of the time step is taken to be θ where $\theta \geq 1$. Therefore at any time τ on the interval, the acceleration is given by

$$\underline{\ddot{U}}^{n+\tau} = \underline{\ddot{U}}^{n} + \frac{\tau}{\theta\Delta t}\left\{\underline{\ddot{U}}^{n+\theta} - \underline{\ddot{U}}^{n}\right\}, \tag{5.41}$$

i.e. straightforward linear interpolation. With $\theta = 1$ this scheme reduces to the linear acceleration method which is only conditionally stable. In order to make this method unconditionally stable it is required that $\theta \geq 1.37$. This result is seen from the numerical study of the stability of these schemes carried out in section 5.7. Thus the solution is sought at time $(n+\theta)\Delta t$ and interpolation is then used to determine the relevant quantities at time $(n+1)\Delta t$. Integration of Equation (5.41) with respect to τ, yields the following expressions for velocity and displacements respectively, namely

$$\underline{\dot{U}}^{n+\tau} = \underline{\ddot{U}}^{n}\tau + \frac{\tau^2}{2\theta\Delta t}\left\{\underline{\ddot{U}}^{n+\theta} - \underline{\ddot{U}}^{n}\right\} + A$$

and

$$\underline{U}^{n+\tau} = \frac{\underline{\ddot{U}}^{n}\tau^2}{2} + \frac{\tau^3}{6\theta\Delta t}\left\{\underline{\ddot{U}}^{n+\theta} - \underline{\ddot{U}}^{n}\right\} + A\tau + B.$$

Setting $\tau = 0$, the constants of integration are $A = \underline{\dot{U}}^{n}$ and $B = \underline{U}^{n}$, hence

$$\underline{\dot{U}}^{n+\tau} = \underline{\dot{U}}^{n} + \underline{\ddot{U}}^{n}\tau + \frac{\tau^2}{2\theta\Delta t}\left\{\underline{\ddot{U}}^{n+\theta} - \underline{\ddot{U}}^{n}\right\} \tag{5.42}$$

and,

$$\underline{U}^{n+\tau} = \underline{U}^n + \dot{\underline{U}}^n \tau + \frac{\ddot{\underline{U}}^n \tau^2}{2} + \frac{\tau^3}{6\theta\Delta t}\left\{\ddot{\underline{U}}^{n+\theta} - \ddot{\underline{U}}^n\right\}. \tag{5.43}$$

When evaluated with $\tau = \theta$, these last two equations yield

$$\dot{\underline{U}}^{n+\theta} = \dot{\underline{U}}^n + \frac{\theta\Delta t}{2}\left\{\ddot{\underline{U}}^{n+\theta} + \ddot{\underline{U}}^n\right\}, \tag{5.44}$$

and

$$\underline{U}^{n+\theta} = \underline{U}^n + \dot{\underline{U}}^n \theta\Delta t + \frac{\theta^2\Delta t^2}{6}\left\{\ddot{\underline{U}}^{n+\theta} + 2\ddot{\underline{U}}^n\right\}. \tag{5.45}$$

Rearranging Equation (5.45) yields

$$\ddot{\underline{U}}^{n+\theta} = \frac{6}{\theta^2\Delta t^2}\left\{\underline{U}^{n+\theta} - \underline{U}^n\right\} - 2\ddot{\underline{U}}^n - \frac{6}{\theta\Delta t}\dot{\underline{U}}^n, \tag{5.46}$$

the acceleration form for the Wilson-θ method. Rearranging Equation (5.44) for $\ddot{\underline{U}}^{n+\theta}$, and substituting this into Equation (5.45), yields

$$\dot{\underline{U}}^{n+\theta} = \frac{3}{\theta\Delta t}\left\{\underline{U}^{n+\theta} - \underline{U}^n\right\} - 2\dot{\underline{U}}^n - \frac{\theta\Delta t}{2}\ddot{\underline{U}}^n, \tag{5.47}$$

the velocity form for the Wilson-θ method. Thus Equations (5.46) and (5.47) are used to establish the solution at time $(n+\theta)\Delta t$, with unconditional stability, then Equations (5.42) and (5.43) are used with $\tau = 1(= \Delta t)$ to establish the solution at the correct position in time.

5.4.4 Derivation of the Newmark Algorithm

This scheme is also based on the linear acceleration assumption which underlies the Wilson-θ method. The latter can therefore be used as a convenient starting point. Consider Equation (5.42) with $\theta = 1$ and $\tau = 1$, i.e.

$$\dot{\underline{U}}^{n+1} = \dot{\underline{U}}^n + \Delta t\ddot{\underline{U}}^n + \frac{\Delta t}{2}\left\{\ddot{\underline{U}}^{n+1} - \ddot{\underline{U}}^n\right\}. \tag{5.48}$$

The premise of this scheme is that it is possible to introduce artificial variables which control how much of the increase in the acceleration, at the end of the time interval, will enter the expressions for velocity and displacement. Thus Equation (5.48) may be written as

$$\dot{\underline{U}}^{n+1} = \dot{\underline{U}}^n + \Delta t\ddot{\underline{U}}^n + \phi\frac{\Delta t}{2}\left\{\ddot{\underline{U}}^{n+1} - \ddot{\underline{U}}^n\right\}.$$

Alternatively this can be expressed in the form

$$\underline{\dot{U}}^{n+1} = \underline{\dot{U}}^{n} + \Delta t\left\{\delta\underline{\ddot{U}}^{n+1} + (1-\delta)\underline{\ddot{U}}^{n}\right\}, \tag{5.49}$$

which is the velocity form for the Newmark method.

Now consider the displacement from the Wilson-θ method, as given by Equation (5.43), but with $\theta = 1$ and $\tau = 1$, then

$$\underline{U}^{n+1} = \underline{U}^{n} + \underline{\dot{U}}^{n}\Delta t + \underline{\ddot{U}}^{n}\frac{\Delta t^2}{2} + \frac{\Delta t^2}{6}\left\{\underline{\ddot{U}}^{n+1} - \underline{\ddot{U}}^{n}\right\}. \tag{5.50}$$

By introducing the variable ε, it is again possible to control the amount of increase in acceleration influencing the updated displacement, thus

$$\underline{U}^{n+1} = \underline{U}^{n} + \underline{\dot{U}}^{n}\Delta t + \underline{\ddot{U}}^{n}\frac{\Delta t^2}{2} + \varepsilon\frac{\Delta t^2}{6}\left\{\underline{\ddot{U}}^{n+1} - \underline{\ddot{U}}^{n}\right\}, \text{ say,}$$

and this can be manipulated to give

$$\underline{U}^{n+1} = \underline{U}^{n} + \underline{\dot{U}}^{n}\Delta t + \Delta t^2\left\{(0.5-\beta)\underline{\ddot{U}}^{n} + \beta\underline{\ddot{U}}^{n+1}\right\}. \tag{5.51}$$

This is the displacement form for the Newmark Method.

The selection of the values for the parameters θ, δ and β are discussed in Section 5.7 after the concepts of stability and accuracy have been introduced.

5.5 Numerical Stability

The essence of numerical stability (hereafter referred to as stability) is that there should be a limit to the extent to which any component of the initial function can be amplified by the numerical procedure as the solution is advanced. This means that the solution should, in some as yet undefined sense, remain bounded throughout the solution time. It should be noted that the concept of stability does not depend upon the original PDEs which are being solved, but is solely a property of the FD scheme used to approximate the derivatives of the PDEs. With $\underline{U}_j^n$ representing the numerical solution at time $t = n\Delta t$ and $\underline{U}_j(n\Delta t)$ representing the (presumably unknown) analytical solution at the same point in time then the GTE is defined as $\underline{U}_j^n - \underline{U}_j(n\Delta t)$. In order to gain an insight into the stability of a particular scheme two questions about the behaviour of the scheme must be asked, namely:

1. What happens to |GTE| as $n \rightarrow \infty$ with Δt fixed, and

2. What happens to |GTE| as $\Delta t \rightarrow 0$ with $n\Delta t$ fixed?

In both cases it can be seen that in the limit the number of time steps n tends to infinity. Therefore there is a possibility of an unlimited amplification of any errors which may be introduced during the numerical solution. The answers to both these questions are addressed in the next section.

5.5.1 von Neumann Stability

It is possible to postulate that two types of stability exist, weak and strong. If the overall numerical error, as defined by $P-\Delta$, grows, then this is defined as strong instability and if it decays this is strong stability. If an individual component of the error grows, then this is weak instability, and vice versa. The assumption that weak stability implies strong stability and that weak instability implies strong instability, is the underlying premise of the von Neumann (VN) stability analysis method. This assumption allows the investigation of the simpler problem of weak (in)stability and hence allows information to be inferred about the strong (in)stability of the scheme being considered. The following functional form of a FD equation can be defined

$$F_1 = F(\underline{U}_j^n) \tag{5.52}$$

where n indicates the time differences and j the space differences. The function defined in Equation (5.52) allows all values of n and j to be considered. If the exact solution of the FDEs is represented by Equation (5.52), then an error parameter, $\underline{\varepsilon}$, can be defined which allows the derived solution to be represented as

$$F_2 = F\left(\underline{U}_j^n + \underline{\varepsilon}_j^n\right). \tag{5.53}$$

The difference of Equations (5.53) and (5.52) leaves the variational form of the FDE, namely

$$F_3 = F\left(\underline{\varepsilon}_j^n\right). \tag{5.54}$$

It is to be noted that the form of the variational equation is the same as the original FD expression. This indicates that the transient part of the solution, as defined by $\underline{\varepsilon}$, usually has the same growth characteristics as the total FD expression. As previously implied, this is not always the case since the initial conditions and boundary conditions only act on $\underline{U}$ and not on $\underline{\varepsilon}$, because so far as the actual computation is concerned, $\underline{\varepsilon}$ is a nonexistant abstract quantity.

Strictly speaking this method only applies to linear Differential Equations (DEs) which have constant coefficients. The linear nature of the FDEs means that the corresponding variational equation will also be linear, regardless of the form of the original PDE. However if the PDE is nonlinear, the coefficients of the variational equation will depend upon the functional dependence on space and time of the original PDE. Hence the coefficients of the variational equation are no longer constant, and the application of this method becomes invalid. When confronted with this situation, the usual procedure is to consider only a small area of the space-time plane (see Walton and Polachek(1960)), over which it may be assumed that the coefficients of the variational function are invariant and then proceed with the analysis as for constant coefficients.

The application of the VN stability method involves introducing a set of errors at each stage of the computation, which are expressed as a finite Fourier series. This implies that a harmonic decomposition of the errors can be made so that each error harmonic can grow or decay independently of the other harmonics, depending upon the associated growth factor. The harmonic decomposition of the errors can be represented by

$$\varepsilon_j^n = \sum_{m=0}^{\infty} A_m exp(i\beta_m x). \tag{5.55}$$

The procedure just described has effectively linearised the variational problem, hence the growth of only one term in the above series needs to be examined to determine the stability of the scheme. The specific term which needs to be considered is

$$e^{i\beta x}. \tag{5.56}$$

In order that this term can represent any error harmonic which is potentially present, β is to be any member of the set $\{\beta_m\}$. Without loss of generality, Equation (5.56) can be studied at time $n = 0$. Hence an expression is required which reduces to Equation (5.56) at this time, and this is given by

$$e^{\alpha n\Delta t}e^{i\beta x}. \tag{5.57}$$

It is seen from Equation (5.57) that to prevent the original error, as defined in Equation (5.56) from growing, a bound on $e^{\alpha n\Delta t}$ is required and this is given by

$$|e^{\alpha n\Delta t}| \leq 1, \tag{5.58}$$

where this is the basis of the VN stability criterion. This condition is necessary for all FD schemes, and it is also sufficient for schemes of only two time levels.

If this condition is satisfied, then no error harmonic is amplified. If it is violated then any harmonic may potentially grow without bound as n increases and could eventually swamp the solution.

5.5.2 The Generous von Neumann Condition

Consider the following where $\underline{U}^0$ is the initial solution, and $\underline{U}^1$ is the solution at the next time step,

$$\underline{U}^1 = \underline{G}\,\underline{U}^0. \tag{5.59}$$

Then $\underline{G}$ is the amplification matrix associated with the FD scheme being used (see Section 5.5.4). It also follows that

$$\underline{U}^2 = \underline{G}(\underline{G}\underline{U}^0) \tag{5.60}$$

so that in general

$$\underline{U}^{n+1} = \underline{G}^{n+1}\underline{U}^0. \tag{5.61}$$

The spectral radius of $\underline{G}$ is denoted as R, where this is defined as the largest of all the eigenvalues of the matrix. Hence the spectral radius associated with $\underline{G}^{n+1}$ is R^{n+1}. A necessary condition for stability is that there exists a constant B_1 such that

$$R^n \leq B_1 \quad \text{for} \quad 0 \leq \mathrm{n}\Delta\mathrm{t} \leq \mathrm{T}. \tag{5.62}$$

This condition implies that the spectral radius of the solution remains bounded for all n since T is the solution time. Taking natural logs of Equation (5.62) leads to

$$n\log_{\mathrm{e}}\mathrm{R} = \log_{\mathrm{e}}\mathrm{B}_1,$$

or

$$R = B_1^{\frac{1}{n}} \quad \text{for} \quad 0 \leq \mathrm{n} \leq \frac{\mathrm{T}}{\Delta\mathrm{t}}. \tag{5.63}$$

From the condition that $0 \leq n\Delta t \leq T$ cited with Equation (5.63), it can be seen that because $\Delta t \leq T$, then $n \geq 1$. Without loss of generality, B_1 can be taken to be greater than or equal to unity. A plot of $B_1^{\frac{\Delta t}{T}}$ against Δt is shown in Figure 5.1. It is seen from this figure that regardless of the values of B_1 or T, that as $\Delta t \to 0$, then $B_1^{\frac{\Delta t}{T}} \to 1$. Furthermore, the curve has a very shallow exponential shape which means that it can be approximately bounded by a linear expression of the form $1 + B_2\Delta t$. The spectral radius for this 'generous' VN stability condition is therefore

$$R \leq 1 + O(\Delta t) \tag{5.64}$$

The relevance of this definition of the VN stability condition is that for some problems the solution may contain legitimate exponential growth; these would not be permitted by the more stringent condition of $R \leq 1$ which was defined previously, but are allowed by the condition in Equation (5.64).

5.5.3 Application of the VN Method to Mooring Line Dynamics

The stability analysis presented in Walton and Polachek(1960) for the stability of the CD scheme, uses the concept of VN stability to demonstrate the conditional nature of this scheme. Further, because the CD scheme operates over two time levels only, the stability condition can be used to derive an expression for the size of the critical time step. However it is important to note that this analysis applies only in the case of a inelastic line.

The present analysis differs from that of Walton and Polachek(1960) in that the equations of motion are formulated to include the elasticity of the mooring line, and that the Houbolt scheme is to be used for the solution. Because this scheme operates over more than two time levels it must be remembered that satisfaction of the VN stability criterion would only demonstrate satisfaction of the necessary stability condition and not the sufficient stability condition.

In order to reduce the considerable amount of algebraic manipulation required for the stability analysis, the equations of motion are reduced from their 3D form to their 2D form. This process is shown in Section 4.2; the 2D form is restated here as

$$M_j \ddot{x}_j = T_{j+\frac{1}{2}} \cos\gamma_{j+\frac{1}{2}} - T_{j-\frac{1}{2}} \cos\gamma_{j-\frac{1}{2}} - \frac{1}{2}(F_{n(j+\frac{1}{2})} \sin\gamma_{j+\frac{1}{2}} + F_{n(j-\frac{1}{2})} \sin\gamma_{j-\frac{1}{2}}) \tag{5.65}$$

and

$$M_j \ddot{z}_j = T_{j+\frac{1}{2}} \sin\gamma_{j+\frac{1}{2}} - T_{j-\frac{1}{2}} \sin\gamma_{j-\frac{1}{2}} + \frac{1}{2}(F_{n(j+\frac{1}{2})} \cos\gamma_{j+\frac{1}{2}} + F_{n(j-\frac{1}{2})} \cos\gamma_{j-\frac{1}{2}}). \tag{5.66}$$

In this form of the equations of motion the added mass terms have been neglected. Also the drag components F_{xj} and F_{zj} have been expanded using the 2D form of the transformation matrix $[\Omega]$ derived in Appendix A, where the contribution from the tangential drag is assumed to be negligible. The details of the derivation of

Equations (5.65) and (5.66) and the remaining derivation of the stability condition is contained in Appendix I, only a summary of which is presented here. The first step in the process is to derive the variational form of Equations (5.65) and (5.66), along with the variational form of the constraint equation. The constraint equation is defined in Equation (3.72), the 2D form of which is given by

$$\text{constant} = (x_{j+1} - x_j)^2 + (z_{j+1} - z_j)^2 - l_{j+\frac{1}{2}}^2 \left[1 + \frac{T_{j+\frac{1}{2}}}{EA}\right]^2 \tag{5.67}$$

which can be alternatively expressed as

$$0 = \cos^2 \gamma_{j+\frac{1}{2}} + \sin^2 \gamma_{j+\frac{1}{2}} - \left[1 + \frac{2T_{j+\frac{1}{2}}}{EA} + \frac{T_{j+\frac{1}{2}}^2}{(EA)^2}\right]. \tag{5.68}$$

The variational form of these equations are derived by assuming that there is an error associated with each term, so that

$$\begin{aligned} T_{j+\frac{1}{2}} &= T_{j+\frac{1}{2}} + \delta T_{j+\frac{1}{2}} \\ x_j &= x_j + \delta x_j \\ z_j &= z_j + \delta z_j. \end{aligned} \tag{5.69}$$

These are substituted into Equations (5.65), (5.66) and (5.67) so that when the original forms of these equations are subtracted the variational equations result. These are given in Equations (I.11), (I.12) and (I.13). The errors in the solution are then assumed to have the following harmonic forms

$$\begin{aligned} \delta x_j &= a exp(i\beta j + \alpha n \Delta t) \\ \delta z_j &= b exp(i\beta j + \alpha n \Delta t) \\ \delta T_j &= c exp(i\beta j + \alpha n \Delta t), \end{aligned} \tag{5.70}$$

where a, b and c represent the differing amplitudes of the error functions. Substituting in the relationships in Equation (5.70) into the variational equations and following a considerable amount of algebraic manipulation, a matrix representation of these equations can be derived and is given by

$$\begin{pmatrix} F - A\sin\gamma & D + B\sin\gamma & H\cos\gamma \\ -D + A\cos\gamma & F - B\cos\gamma & H\sin\gamma \\ G\cos\gamma & G\sin\gamma & I \end{pmatrix} \begin{pmatrix} a \\ b \\ c \end{pmatrix} = 0 \tag{5.71}$$

or $[P][a] = 0$. Examining the coefficients of Equation (5.71), as defined in Equation (I.26), it is seen that the P_{33} element represents the elasticity of the mooring line. It is shown in Appendix I that if the mooring line is assumed to be inelastic then $P_{33} = 0$.

The next step in the derivation of the stability condition is to calculate the characteristic equation, or determinant, of the coefficient matrix $[P]$, since for a non-trivial solution of Equation (5.71) it is required that

$$|P| = 0. \tag{5.72}$$

Examination of the magnitudes of the roots of the characteristic equation will then indicate the stability, or otherwise, of this system of equations. For an inelastic mooring line the resulting polynomial is of order 3 (since $P_{33} = 0$), but for the elastic case the polynomial has an order of 6. Therefore a numerical algorithm is used to obtain the roots, the theory of which is presented in Grant and Hitchins(1971). They state that the determination of the roots of a polynomial using this method can be problem dependent and as a consequence the algorithm may fail. However, this did not appear to be a problem for the polynomials solved here.

A slight complication arises in the selection of the values of β_m. In the analysis of stability presented by Walton and Polachek(1960), this problem does not arise since the VN condition is both necessary and sufficient. As a result β_m can be easily selected to yield the largest estimate of the size of time step. In the present case, the selection of a value of β_m to derive a limiting criteria for the time step size is not obvious and therefore values for β_m must be explicitly assigned.

In order to do this, careful consideration must be given to what the harmonic composition of the errors (as given by Equation (5.55)) actually represents. The variable ε_j^n is to represent any error variable in the variational form of the equations (i.e ε represents δT or δx or δz etc.) at the mesh point n in time and j in space. This is equivalent to identifying all the variables at node j in the mooring line at time n. Then for any one of these error variables, assume that it can be expanded in a finite Fourier series represented by the right hand side of Equation (5.55). For example this means that the error variable δT_j^n is considered to be composed of a series of components (harmonics), each of which has a different amplitude (A_m) and frequency (β_m) associated with it. From Equation (5.71) it is seen that the amplitudes A_m do not enter into the solution of the determinant of $[P]$ since they have been factored out as the variables to be solved for.

However the problem of selecting the number of terms in the series, m, and the frequencies β_m still remains. To the author's knowledge there is no guiding principle available in the literature for the selection of these values, consequently there is a certain amount of arbitrariness involved. However, certain convenient choices can be made which help to simplify the problem. For example if the length of the mooring line is L and it is divided into h elements each of length l (i.e. $L = hl$), then it is convenient to introduce the same number of terms in the series as there are elements in the space dimension. From the theory of Fourier series, the general frequency is

$$\beta = \frac{n\pi}{L} \; : \; n = 0, 1, 2, ..., h.$$

Therefore, for the maximum value of β, $n = h$ and with $L = hl$, the range of β becomes

$$0 \leq |\beta| \leq \frac{\pi}{l_m}, \tag{5.73}$$

where $l_m = \text{Min } |l|$, since this will allow for the largest error frequency which can enter the system. Therefore the stability of the scheme can only be assessed by using this range of the β values in the stability polynomial.

Following the extensive derivation of the characteristic polynomial associated with the elastic and inelastic equations (shown in Appendix I), it is possible to show that the VN necessary stability condition is satisfied. Due to the large amount of algebraic manipulation needed to establish the VN condition, the proof was not extended to include the Newmark or Wilson-θ methods. The stability of all the schemes is now presented in the next section which deals with amplification matrices.

5.5.4 The Method of Amplification Matrices

The principle behind the derivation of amplification matrices is that it is possible to establish a recursive relationship between the solutions at two adjoining time steps. This relationship is unique to each particular FD scheme under consideration and has the following general form

$$\underline{U}^{n+1} = \underline{G}\,\underline{U}^{n} + \underline{L} r^{n+\gamma} \tag{5.74}$$

where $\gamma = 0$, Δt or $\theta \Delta t$ according to which integration scheme is being used. The matrix $\underline{G}$ is then defined as the amplification matrix, and the vector $\underline{L}$ is the

load operator. By substituting the acceleration and velocity expressions of each integration scheme, $\underline{G}$ and $\underline{L}$ can be derived in a relatively straightforward manner as shown in Appendix J. However, the analysis of stability can be undertaken with arbitrary initial conditions, therefore Equation (5.74) can be considered with no load, and hence becomes

$$\underline{U}^{n+1} = \underline{G}\,\underline{U}^{n}. \tag{5.75}$$

The variational form of Equation (5.75) is derived in the same manner as the variational equations of motion (given in Equations (I.11) and (I.12)) and is seen to be

$$\underline{\varepsilon}^{n+1} = \underline{G}\,\underline{\varepsilon}^{n}. \tag{5.76}$$

The characteristic equation (or determinant) of $\underline{G}$ is called the stability polynomial and this may be expressed as

$$\sum_{a=0}^{p} x_a \lambda_a^a = x_0 + x_1\lambda_1 + x_2\lambda_2^2 + x_p\lambda_p^p = 0$$

where λ_a^a are the roots of the polynomial. These are also the eigenvalues of the amplification matrix. In order to prevent the unbounded growth of errors in the solution of Equation (5.75), it is required that the spectral radius of $\underline{G}$ as denoted by R, should be less than, or equal to, unity, i.e.

$$\rho(\underline{G}) = R \leq 1 \tag{5.77}$$

where

$$R = \mathrm{Max}(|\lambda_i|)$$

and where λ_i are the eigenvalues of the amplification matrix $\underline{G}$.

In order to explicitly derive the amplifications matrices for each FD scheme, a form of the equations of motion must be assumed, to which the velocity and acceleration expressions of the integration scheme can be applied. The form used is given by Equation (4.46) which represents the uncoupled modal form of the equations of motion with the assumption that they are lightly damped. This is restated here in vector form as

$$\ddot{\underline{U}} + 2p\xi\dot{\underline{U}} + p^2\underline{U} = r \tag{5.78}$$

where the various subscripts and the Kronecker delta are omitted for clarity. Thus stability and accuracy of the FD schemes can be studied as a function of $\Delta t/T$, ξ

and r, rather than as a function of the mass, damping and stiffness matrices. Given that the physical parameters of the equation remain constant, it can be seen from an examination of the amplification matrices in Appendix J, that R is a function of the frequency ω. Because $\omega = 2\pi/T$ where T is the natural period of the system, it is possible to plot R against $\Delta t/T$ for each time integration scheme. This will illustrate the conditional stability of the CD scheme and the unconditional stability of the Houbolt, Wilson-θ and Newmark schemes.

Having determined the amplification matrices as shown in Appendix J, it is relatively straightforward to calculate the spectral radius of each matrix for given values of Δt, T, ξ, θ, δ and β. Stability curves for each scheme are shown in Figures 5.2, 5.3, 5.4 and 5.5, where for each scheme the damping ratio has the following range: $0 \leq \xi \leq 1$. All the graphs indicate that the same trend of the curves R vs. $(\Delta t/T)$ is maintained for each scheme, regardless of the damping ratio. They also show that the inclusion of damping does not alter the conditional or unconditional nature of the scheme. It should be remembered that in general this is not true. In most analyses of numerical stability, it is assumed that an equation of the form of Equation (4.34) (i.e. with damping neglected) is sufficient to determine the stability characteristics of the particular scheme being considered. This is based on the assumption that the inclusion of physical damping, as present in the equations of motion, will improve the stability of the solution. Whilst this assumption has been shown to hold true for the numerical schemes considered here, it cannot be said to be generally true, since the inclusion of damping may in fact change a scheme from being unconditionally stable to one which is only conditionally stable, Wood(1990, pg. 126).

Figure 5.2 clearly shows the conditional nature of the stability of the CD method and hence the importance of selecting a time step which is less than a critical time step limit, Δt_{cr}. Figures 5.3, 5.4 and 5.5 show the unconditional stability of the Houbolt, Wilson-θ and Newmark methods. This means that regardless of the size of the time step (Δt) which is used, the spectral radius of the amplification matrix is never greater than unity. A cursory examination of these three graphs indicates that as the damping ratio increases uniformly, the resulting stability curves tend to limiting values.

5.5.5 The Routh-Hurwitz Conditions

Before considering the Routh-Hurwitz (RH) conditions, there is an important concept associated with the roots of the second order differential equation (i.e. the

equations of motion) which should be introduced here. Consider the homogeneous scalar form given by

$$m\ddot{x} + c\dot{x} + kx = 0. \tag{5.79}$$

Following the usual procedure for obtaining the solution of a second order differential equation, it will be seen that for any of the three cases associated with the conditions of the roots, the solution will contain terms of the following form

$$\exp\left\{\frac{-c \pm \sqrt{c^2 - 4km}}{2m}\right\}. \tag{5.80}$$

From Equation (5.80) it will be seen that if $c^2 \leq 4km$ the two roots will be complex and hence the solution will contain sine and cosine terms and is therefore oscillatory. If $c^2 > 4km$ then the roots will be real and consequently the solution will exponentially increase or decrease and therefore represents an unbounded solution. Since from the the physics of the problem it is expected that the solution will remain bounded, it is a requirement that the roots of the differential equation remain complex. The condition for this is that

$$c^2 < 4km. \tag{5.81}$$

This condition can only be implemented for two step FD formulae; the reason for this is now made clear. In the previous section the amplification matrices were used with numerical values to yield the spectral radii. If the characteristic determinant (or stability polynomial) of the amplification matrix is explicitly derived it will have the following functional form

$$f_1(\xi, p, \Delta t) + f_2(\xi, p, \Delta t)\lambda + f_3(\xi, p, \Delta t)\lambda^2 + \ldots + f_{k+1}(\xi, p, \Delta t)\lambda^k = 0 \tag{5.82}$$

where k indicate a k-step formula. It can then be seen that the condition in Equation (5.81) can only be applied when $k = 2$, where it results in the following

$$f_2(\xi, p, \Delta t)^2 < 4 f_1(\xi, p, \Delta t) f_3(\xi, p, \Delta t). \tag{5.83}$$

Equation (5.83) will usually provide a limiting condition for Δt, but in the case of an unconditionally stable scheme this condition will illustrate this. This indicates that the roots of an unconditionally stable scheme always remain complex. For conditionally stable schemes it indicates the regions where the complex and real roots occur, but then the RH conditions have to be applied to yield stability

conditions. Therefore for schemes where $p > 2$ or which are conditionally stable use must be made of the RH transformation (Wood(1990), pg 536) where the transformation is to be applied to Equation (5.82) and is given by

$$\lambda = \frac{1+z}{1-z}. \tag{5.84}$$

This results in an equation of the following form

$$a_0 z^p + a_1 z^{p-1} + \ldots + a_{p-1} z + a_p = 0 \tag{5.85}$$

where $a_i = f_i(\xi, p, \Delta t)$ for $i = 0, 1, \ldots, p$. The RH conditions are

$$\begin{aligned} a_i &> 0 \quad \text{for} \quad i = 0 \\ a_i &\geq 0 \quad \text{for} \quad i = 1, \ldots, p. \end{aligned} \tag{5.86}$$

These conditions ensure that $|R| \leq 1$ which is the requirement for the scheme to be stable. Application of the inequalities in Equation (5.86) to conditionally stable FD schemes will then produce a set of inequalities which provide a limit on the time step to be used. When applied to unconditionally stable schemes it will merely demonstrate the unconditional nature of the schemes.

By requiring the spectral radius of an amplification matrix to always be less than or equal to unity, what is being demanded is called the necessary condition for stability. This means that if a scheme is stable then this condition will always be satisfied, however to guarantee the stability of a scheme there are, in general, further sufficient conditions. These might require, for example, that $R < \eta$ where $\eta \leq 1$, hence it is seen that the necessary condition is satisfied for this further sufficient condition. The derivation of the necessary condition is relatively straight forward and intuitive, however the derivation of sufficient conditions is more complex and will not be considered here.

5.6 Numerical Accuracy

As well as an investigation into the stability of FD schemes, an assessment of the accuracy must also be made, in order that the validity of the solution for the particular problem under consideration can be gauged. With the CD scheme the maximum size of the time step is limited by stability considerations where this limit is then small enough so that in general it will provide accurate results. With the unconditionally stable implicit methods, the size of the time step is unrestricted

from the stability point of view, however it will be realised that there must be a limit in order to provide an accurate solution. The most effective and illustrative way in which to demonstrate the accuracy of different time integration schemes, is to apply them to a simple equation, the solution to which is known analytically. Bathe(1982) uses the following equation

$$\ddot{x} + \omega^2 x = 0 \tag{5.87}$$

and indicates that it is sufficient to illustrate the concepts. Wood(1981) prefers the following equation

$$\ddot{x} + 2\nu\omega\dot{x} + \omega^2 x = pe^{ist} \tag{5.88}$$

in order that some insight may be gained as to the effect of damping and a periodic forcing function upon the numerical accuracy of the solution.

Before continuing it will be useful to now define what is meant by an accurate solution. Obviously the reason for employing numerical techniques to solve a particular problem, is because of the inability to derive a tractable analytic solution. Hence, once the numerical solution has been obtained, there are only two ways of judging whether or not it is accurate:

1. To see if the trend of the results conform to what is expected - obviously not a good measure of the accuracy, just an indication of the general validity.

2. To have established the accuracy of a particular integration scheme on either Equation (5.87) or Equation (5.88), where it can be compared to the analytical result.

Accuracy, as defined through the second approach, is gauged by two measures, the period elongation (PE) and the amplitude decay (AD), of the numerical solution relative to the analytical result, see Figure 5.6. In Bathe(1982), each of the integration schemes under consideration were applied in turn to Equation (5.87) and the results for PE and AD derived. Wood(1990) employs a more rigorous approach by assuming a general form for a FD expression and substitutes this into Equation (5.88). The exact solution to the homogeneous form of Equation (5.88) is given by $\exp(\gamma t)$, where

$$\gamma = -\nu\omega \pm i\omega\sqrt{1-\nu^2} \tag{5.89}$$

hence

$$e^{\gamma t} = e^{\omega(-\cos\alpha \pm i\sin\alpha)t} \tag{5.90}$$

where $\nu = \cos\alpha$ so that the damping is always less than critical, i.e. $\nu < 1$. After substituting the general form of the FD expression into Equation (5.88), the principal root of the resulting polynomial is given by $e^{(\gamma+\eta)\Delta t}$, where η is the error in the numerical solution. Assuming that this error has the form $\eta = \delta + i\varepsilon$, the principal root becomes

$$e^{(\nu+\xi)\Delta t} = e^{-\Delta t(\omega\cos\alpha+\delta)+i\Delta t(\pm\omega\sin\alpha+\varepsilon)}. \tag{5.91}$$

It can be clearly seen from Equation (5.91) that it has been assumed that the error in the numerical solution will have a twofold influence. Firstly it is considered to have the effect of increasing the damping by δ, resulting in the AD already referred to, and, secondly, of increasing the frequency by an amount ε, which manifests itself as the PE. Wood(1990) uses this result to derive general formulae for the PE and AD for a particular FD expression. These two effects upon a total solution are illustrated in Figure 5.7.

Using either the approach of Bathe(1982), or of Wood(1990), graphs of PE and AD against $\frac{\Delta t}{T}$ can be determined and a comparison of the two approaches shows that they give the same trends and very close answers for the same schemes. Figures 5.8 and 5.9 show the graphs of AD and PE quoted from Bathe(1982). They can be used to determine how much PE and AD can be expected for a given $\Delta t/T$ ratio, and thus determine whether a particular scheme and / or a particular time step are suitable. Note that these results are only given for the three implicit schemes considered. Also note that the Newmark scheme will introduce no amplitude decay when used with $\delta = \frac{1}{2}$ and $\beta = \frac{1}{4}$.

5.7 A Further Discussion of Accuracy and Stability

The selection of the Wilson-θ and the Newmark scheme parameters (θ, δ, β), are made to enhance particular aspects of numerical stability and accuracy. For θ a value of 1.4 is usually selected since a plot of the spectral radius against θ shows that the scheme is only conditionally stable for $\theta < 1.37$ and that it is unconditionally stable for $\theta \geq 1.37$; see Figure 5.10. This is then usually rounded up to 1.4 for convenience; larger values are not usually used since this increases the time for convergence at each step. The choice of parameters for the Newmark scheme is more complicated, but for the scheme to be unconditionally stable it is required that

$$2\beta \geq \delta \geq 0.5. \tag{5.92}$$

It can be shown that no 'algorithmic' damping is introduced when $\delta = 0.5$; that is there is no amplitude decay in the solution caused by the numerical scheme being used. This means that all the modes present in the solution are being preserved. It has been suggested (Wood(1990)) that the higher frequency modes become increasingly inaccurate and because of this that a value for δ should be selected which is slightly greater than 0.5. This would then damp out the higher modes in the solution whilst still preserving the more accurate lower modes.

In engineering applications however it is more common to keep the value of δ equal to 0.5 and then to rewrite the Newmark scheme (Equation (5.49) and (5.51)) with this value to derive the one parameter Newmark-β family of schemes. The value of β for most purposes is set equal to 0.25 since from Equation (5.92) this is the minimum value to ensure unconditional stability. Newmark (Newmark(1959)) remarks that this value will ensure that the maximum velocity response is correct. A value of $\beta = 1/12$ would yield a better convergence rate and a more accurate solution but the scheme then becomes only conditional in nature. Therefore the following parameters are used

$$\theta = 1.4, \quad \delta = 0.5 \text{ and } \beta = 0.25. \tag{5.93}$$

Having discussed the selection of θ, δ and β, a further discussion of the stability and accuracy of each scheme can now be undertaken. As pointed out in Chapter 4, the total solution can be expressed as a summation of solutions in different modes, i.e.

$$\underline{U} = \sum_{i=1}^{h} \underline{U}_i$$

where h is the total number of modes and $\underline{U}_i$ represents the solution for the i^{th} mode. For each solution (eigenvector) there is an associated distinct frequency (eigenvalue) p_i and the solution procedure usually orders the eigensolutions from the largest to the smallest frequencies, i.e. $p_{i+1} > p_i$. Hence the term 'higher modes' refers to those modes with high frequencies and vice versa. When it is realised that the response in the lower modes change more slowly than the response in the higher modes, it can be seen that a larger time step may be used to integrate the lower modes, whilst for the higher modes, successively smaller time steps will have to be used to integrate each mode accurately. Thus the two advantages of using the modal analysis technique presented in Chapter 4 are:

1. Different time step sizes can be used to integrate the different modes. This is in contrast to the direct integration methods of Chapter 3 where one time step is used to integrate all modes present in the solution.

2. Generally only the first b modes need to be summed to provide an accurate solution, where $b < h$.

Intuitively it is to be expected that the lower modes contribute most significantly to the solution since they are associated with the low frequencies where their slowly varying nature means that the associated amplitudes dominate the solution. Thus the higher modes are seen to increasingly contribute less to the solution since the high frequencies present mean that the amplitudes of the oscillations must be necessarily smaller than those of the lower modes. Thus for modes higher than b it is assumed that the contribution to the total solution is negligible, i.e.

1. For modes $1 \rightarrow b$, where $b < h$, it is considered that they contribute significantly to the solution.

2. For modes $b \rightarrow h$, their contribution to the total solution is assumed to be negligible.

Now consider the graphs of AD and PE indicated in Figures 5.8 and 5.9. These have been calculated when each of the three implicit schemes have been applied to Equation (5.87) where both the forcing function and the damping have been neglected. The abscissa in both cases is the nondimensional time step to period ratio ($\Delta t/T$). For a fixed value of Δt, an increasing value for this ratio implies that T is decreasing and hence that the frequency is increasing, i.e. larger time step to period ratios apply to the higher modes present in the solution. It can be seen that if $\Delta t/T$ is less than approximately 0.01 then all the modes in the solution are integrated accurately. However an increasing value for Δt means that the higher modes present in the solution will not be accurately integrated.

With the preceding remarks in mind, first consider what happens if the same time step size is used to integrate all the modes present in the solution. Define T_l as that value of period for which $\frac{\Delta t}{T} = 0.01$ and T_b as being the period of the mode b. As long as $T_b < T_l$ then an accurate solution will result, but if $T_b > T_l$ then some errors will be introduced since some of the modes which are required in the sum for the total solution will be integrated inaccurately. The assessment of these errors is the basis of the accuracy analysis for FD schemes.

When different time step sizes are used to integrate each mode separately then as long as Δt_i is selected so that $\Delta t_i/T_i < 0.01$ then the i^{th} mode will be integrated accurately. This can be seen to imply that the higher the mode which needs to be integrated, the smaller the time step which is required which is also what is intuitively expected. Also if $\Delta t/T_l < 0.01$ then the value of Δt will also integrate all the modes up to and including T_l accurately and its only for higher modes that the value of Δt needs to be reduced. Examining the curves of spectral radius, R, against $\Delta t/T$ for zero damping as shown in Figure 5.11, it becomes clear why errors are introduced into the solution. For a value of $\Delta t/T < 0.01$ it is noted that $R = 1$ and therefore that the solution is not amplified at all. With increasing values of $\Delta t/T$ the solution will be multiplied by a value which is less than unity and hence this introduces the AD which is seen to be present.

Now attention is turned to a description of the characteristics of the curves in Figures 5.8 and 5.9. In both graphs the Houbolt method is seen to produce greater AD and PE when compared to either the Wilson-θ or the Newmark methods. Also the Newmark method produces less PE than the Wilson-θ method, but no AD as can be seen from the spectral radius in Figure 5.11, which is unity. As indicated in Wood(1990, pg120) the unconditional nature of stability will always introduce a certain amount of PE and this error cannot be continuously controlled by altering the parameters in the schemes. In contrast, AD can be systematically controlled in the Newmark method by selecting a value for δ which is greater than 0.5 (where the unconditional nature of the scheme is now maintained by setting $\beta = 0.25(\delta+0.5)^2$). Increasing the numerical dissipation (AD) for the higher modes in the solution is actually a desirable property for a FD scheme to possess, see, for example, Hilber and Taylor(1978), as long as it can be continuously controlled. The AD in the Wilson-θ with $\theta = 1.4$ is already very high and is considered to damp out modes which may contribute significantly to the total solution. Increasing the value of θ allows for a systematic increase in the AD, but in this case this is not desirable because of the high dissipation already present. Reducing the value of θ is not possible since for $\theta \leq 1.37$ the scheme becomes only conditionally stable. Therefore the only scheme where the amount of numerical dissipation can be controlled is the Newmark method, however to introduce AD here it is required that δ be greater than 0.5 and this then means that the scheme becomes less than second order accurate and it is for this reason that introducing numerical dissipation is not one of the desirable properties listed by Hilber and Taylor(1978) which a FD scheme should contain.

5.8 Estimation of Time Step Size

From the modal analysis of Chapter 4, there are a set of h equations which represent the h different modal solutions corresponding to the different frequencies of the solution. To obtain a correct total solution, each modal equation is integrated with an appropriate time step size. However, with the direct methods of Chapter 3, only one time step is used, therefore the 'correct' solution is only obtained by integrating all the equations with a time step small enough to accurately assess the contribution of the higher frequencies. The minimum time step size is therefore related to the minimum period of the mesh. Consider the equation

$$P = \frac{\lambda_w}{C} \tag{5.94}$$

where

P is the period,
λ_w is the wavelength,
C is the wave speed.

There are two modes of wave propagation in a line element, transverse and longitudinal and, following Ractliffe(1984), they are denoted by

$$C_T = \sqrt{\frac{\sigma}{\rho_m}} \quad \text{and} \quad C_L = \sqrt{\frac{E}{\rho_m}} \tag{5.95}$$

where

σ is the stress in the line element,
ρ_m is the line material density,
E is Young's Modulus.

Clearly $C_L > C_T$ and because the minumum mesh period is required, C_L is used in Equation (5.94), i.e.

$$P_{min} = \lambda_w \sqrt{\frac{\rho_m}{E}}.$$

From experience Bathe(1982) suggests that Δt should be equal to $P_{min}/10$, but Ractliffe(1984) suggests it should be $P_{min}/5$. In connection with the present study the former seems to be more applicable, hence

$$\Delta t = \frac{l_m}{10}\sqrt{\frac{\rho_m}{E}} \tag{5.96}$$

where l_m is the minimum size of any of the elements. Equation (5.96) can be used to establish a time step size for which all h modal equations are integrated

accurately. However, as pointed out previously, it can be considered that the modes associated with higher frequencies contribute little to the total solution. This means that by using a time step size which is small enough to accurately evaluate the modes associated with the higher frequencies, little is been gained as far as the accuracy of the total solution is concerned but at the expense of excessive computing time. Thus it is proposed that the size of Δt can be much larger (of the order of 100 times) where this will still allow the accurate integration of the more important lower modes with the advantage of greatly reduced computing time.

One point for further consideration is the estimation of the critical value of Δt for use with the explicit Central Difference scheme. From Figure 5.2 the following empirical relationship is derived

$$\frac{\Delta t}{P} = \frac{1}{\pi} \tag{5.97}$$

hence

$$\Delta t = \frac{P}{\pi} \tag{5.98}$$

where P is given in Equation (5.94). In order to calculate the maximum Δt, the maximum wave period and hence wave celerity, is required. This is given by C_T in Equation (5.95); hence it can be shown that

$$\Delta t = \frac{\sqrt{mg}}{10\pi} \frac{l_{max}}{\sqrt{T}} \tag{5.99}$$

where

m	is the mass per meter,
l_{max}	is the maximum mesh length,
T	is line tension.

The question then arises as to what value of T should be used, the minimum dynamic tension, or the maximum static tension. The results are further discussed in Chapters 6 and 7.

5.9 Summary

This chapter is intended to give what can only be considered as an introduction to the complex subject of the stability and accuracy of FD schemes. The chapter begins with a brief statement of the four FD schemes which are used in this study and indicates the original references where they were first presented. This is then followed by a section which verbally indicates the errors which are to be

expected when a numerical solution of this type is used. This is then slightly more formalised with the use of notation derived from Richtmyer and Morton(1967) and Lambert(1973). Following this the four schemes are derived from first principles. The Central Difference and the Houbolt scheme are derived from direct consideration of the Linear Multistep Methods for first and second order differential equations. The Wilson-θ and the Newmark methods are derived from the assumption of a linearly varying acceleration over each time interval.

The numerical stability of these FD expressions are investigated through the use of the von Neumann stability condition, the method of amplification matrices and the Routh-Hurwitz conditions. The first and last methods produce inequalities which allow the time step size to be selected so as to guarantee the stability of the scheme, whilst the second method is a numerical way of demonstrating the stability. Given that a particular FD scheme will be stable, the accuracy of the results must then be assessed. This is measured through the amplitude decay and the period elongation of the numerical solution when compared to a known analytical solution. Finally an indication is given of how to determine a time step size which will integrate all modes present in the solution in order to obtain an accurate answer. Also included is another method for the determination of the limiting time step size to ensure the stability of the Central Difference algorithm.

It must be stated now, as a conclusion to this chapter, that all the preceding remarks about the stability and accuracy of FD schemes only strictly apply to the analysis of equations which are linear. However this discussion of the linear case is still of importance since it may illustrate the possible errors which arise and how they might occur, when these schemes are applied to nonlinear equations. It would seem that it is not possible to provide an analytic analysis of the stability and accuracy of the solution of nonlinear equations using FD schemes. The only method of gaining this is by actually solving the equations in question and then examining the numerical properties of the scheme used. As pointed out in the introduction, no published study of the numerical properties of these time integration schemes as applied to mooring line dynamics, seems to exist.

CHAPTER 6

Numerical Investigation of Time Integration Schemes

6.1 Introduction

The first section of this chapter indicates how the reduction of the equations of motion from a three dimensional (3D) form to a 2D form is achieved. These are then compared with published sets of equations to establish any discrepancies which might be present. The next section demonstrates the validity of the 2D equations of motion by comparing the results obtained through the use of four different time integration schemes. Also shown is how the dynamic results reduce to the static results (as predicted by the numerical method in Chapter 2) in the limiting excitation cases. The final section of this chapter provides a comprehensive numerical investigation and comparison of the predictions derived using the four time integration schemes as they are applied in the solution of the 2D form of the equations of motion. For this study the effects of nodal grounding and lifting are ignored as this will be studied in greater detail in Chapter 8. Next, a short section detailing the setting up of "benchmark" tests for mooring line dynamics is introduced. These would then allow for the assessment of the use of different time integration schemes or of new theoretical developments relative to some commonly acceptable "benchmark" results. Finally a brief summary of the main points from the results of the comparative study is presented.

6.2 2D Form of the Equations of Motion

The reduction of the 3D equations of motion, as represented by Equations (3.62), (3.63) and (3.64), to their 2D form has been demonstrated in Section 4.2. This was achieved by ignoring all the terms pertaining to the y direction and by setting $\varepsilon_{j+\frac{1}{2}} = 0°$ for $j = 0, 1, ..., (h-1)$. The 2D equations are then given by Equations (4.1a) and (4.1b), where the influence of line attachements and the wave particle velocity and acceleration terms are neglected. These equations, restated

here, are of the form

$$\left\{M_j\ddot{x}_j + \frac{\ddot{x}_j}{2}\left[a_t\cos^2\gamma + a_n\sin^2\gamma\right]_{j-\frac{1}{2}}^{j+\frac{1}{2}}\right\} + \frac{\ddot{z}_j}{2}\left[(a_t - a_n)\sin\gamma\cos\gamma\right]_{j-\frac{1}{2}}^{j+\frac{1}{2}} = \left[T\cos\gamma\right]_{j-\frac{1}{2}}^{j+\frac{1}{2}} + F_{xj} \tag{6.1}$$

and

$$\frac{\ddot{x}_j}{2}\left[(a_t - a_n)\sin\gamma\cos\gamma\right]_{j-\frac{1}{2}}^{j+\frac{1}{2}} + \left\{M_j\ddot{z}_j + \frac{\ddot{z}_j}{2}\left[a_t\sin^2\gamma + a_n\cos^2\gamma\right]_{j-\frac{1}{2}}^{j+\frac{1}{2}}\right\} = \left[T\sin\gamma\right]_{j-\frac{1}{2}}^{j+\frac{1}{2}} + F_{zj} - W_j. \tag{6.2}$$

6.2.1 Comparison with Nakajima(1982)

Equations (1) and (2) in the paper of Nakajima (1982) correspond to a 2D set of equations of motion derived for a mooring line. The differences between these and Equations (6.1) and (6.2) are:

1. A slight difference in notation. A reference to element $j+\frac{1}{2}$ in this thesis would be referred to as element $j+1$ in the Nakajima paper.

2. In this thesis the normal (or tangential) added mass to be lumped at node j is calculated as being the average of the product of the normal (or tangential) added mass and a function of the element angles for those elements which adjoin node j, for example the term $\left[a_n\sin^2\gamma\right]_{j-\frac{1}{2}}^{j+\frac{1}{2}}$. In Nakajima's paper the average of the normal (or tangential) added masses are calculated, as well as the average of the functions of the element angles and then the product of these is calculated. This is represented by

$$A_{nj} = \frac{1}{2}\left[a_{n(j+1)} + a_{n(j)}\right]$$

to denote the average of the normal added massses, and

$$\bar{\gamma}_j = \frac{1}{2}\left[\gamma_{j+1} + \gamma_j\right]$$

to denote the mean angle. Hence the normal added mass to be lumped at node j is given by $A = A_{nj}\sin^2\bar{\gamma}_j$. The principal difference between the two

approaches readily explained. In this thesis all the forces are expressed in a global cartesian coordinate system, i.e. (x, y, z), before they are lumped at the appropriate nodes. In the approach of Nakajima(1982) these quantities are not resolved globally until they have been lumped at the nodes. This different approach will result in a slight difference in the predictions.

3. The only other difference is in the remaining drag and tension forces expressed by Equations (3) and (4) of Nakajima(1982). Here the drag terms are incorrectly subtracted from the right hand side when they should be added. In Nakajima(1986b) these drag forces are added which implies a typographic error in the earlier paper.

6.2.2 Comparison with van den Boom(1985)

The equations of motion are represented in matrix form by Equation (1) of the van den Boom(1985) paper. It appears that the same general approach is adopted as that of Nakajima(1982), with the functions of the element angles based on the average of the element angles on either side of the node in question. However, it is not particularly clear how the local normal and tangential added masses are incorporated into the added mass matrix. In the van den Boom approach, this is given by

$$\left[m_j(\tau)\right] = a_{nj}\left[\Lambda_{nj}(\tau)\right] + a_{tj}\left[\Lambda_{tj}(\tau)\right]$$

where $[\Lambda_{nj}(\tau)]$ and $[\Lambda_{tj}(\tau)]$ represent the transformation matrices which relate the local and global added masses in the normal and tangential directions respectively. As previously indicated, the angles in these transformations are the average of the angles of the adjoining elements. However, the notation in this paper implies that a_{nj} and a_{tj} are the local normal and tangential added masses which are assumed to be lumped at node j, and therefore correspond to some averaging principle, as used by Nakajima(1982). Furthermore, the added mass quantities are indicated as being calculated thus

$$a_{nj} = \rho Ci_n \frac{\pi}{4} D_j^2 l_j$$

and

$$a_{tj} = \rho Ci_t \frac{\pi}{4} D_j^2 l_j$$

where D_j and l_j represent the diameter and length of element j and Ci_n and Ci_t denote the normal and tangential added mass coefficients respectively. In order

for this formulation to be consistent with that of Nakajima(1982) the calculation of a_{nj} and a_{tj} given above would have to be given by

$$a_{nj} = \rho\frac{\pi}{8}\Big\{Ci_{n(j+1)}D_{j+1}^2 l_{j+1} + Ci_{n(j)}D_j^2 l_j\Big\}$$

and

$$a_{tj} = \rho\frac{\pi}{8}\Big\{Ci_{t(j+1)}D_{j+1}^2 l_{j+1} + Ci_{t(j)}D_j^2 l_j\Big\},$$

where j and j+1 refer to the element quantities above and below node j respectively.

6.2.3 Comparison with Walton and Polachek(1960)

In this paper the equations of motion are represented in the matrix form given by Equation (2.1), where the tangential added mass and drag effects have been neglected. Thus the equations of motion used in this thesis are directly comparable with those of Walton and Polachek(1960).

6.2.4 General Observations Deduced From Comparative Study

It would seem, therefore, from the different models considered above, that two basic procedures have been adopted in the development of a lumped mass method, namely:

1. To express all forces acting on the elements in global coordinates and then lump them at the appropriate nodes. This is the procedure adopted in this thesis.

2. To average and lump the local values of fluid inertia and drag at the node before evaluating the global components, whilst the remaining forces are handled as in (1).

The differences between the two formulations are expected to be small. However, the first approach has the advantage of being consistent, but the disadvantage of slightly more involved encoding in the associated software.

6.2.5 Benchmarks With McNamara(1993)

A simulation run based on the parameters indicated in Table 6.1 (see over) was undertaken and compared with the results generated by McNamara(1993, Figures 6.0A and 6.0B) in order that independent corroboration could be obtained. The results of this comparison are shown in Table 6.0:

	Present Method	McNamara(1993)		% Differences	
	20 Elements	CABLE-3D (30E)	FLEXCOM-3D (86E)	30E	86E
Static	495.3kN	478.9kN	479.2kN	3.42%	3.36%
Dynamic	884.7kN	904.1kN	825.0kN	2.15%	7.2%

Table 6.0 - Benchmark Comparison

Note that the values indicated in Table 6.1 for the static analysis are given in 3D, whilst the dynamic quantities are specified in 2D; also the amplitude of excitation in the x direction is 10m for this case. The formulation and discussion of the FLEXCOM-3D program is described in O'Brien and McNamara(1989). Although this is a FE formulation which includes bending stiffness, with the latter set to a small value, the program can be used to analyse mooring situations. The results seem to offer an acceptable degree of comparison.

6.3 Comparison of Dynamic and Static Results

In this section an attempt is made to correlate the predictions based on the limiting excitation cases of the dynamic model (i.e. situations for which there is no endpoint excitation) with comparable results derived from the static numerical model described in Chapter 2. The principal input parameters and the numerical values assigned to them for this study, for both the static and dynamic models, are shown in Table 6.1.

Since the software for the numerical static model is written for the 3D case, the input data specified is 3D. However, for the purposes of the comparisons in this chapter, the four different time integration schemes have been encoded only for the 2D equations of motion. Hence in this study the upper endpoint excitation is restricted to the initial static plane of the mooring line. The endpoint excitation function is defined by

$$\underline{U}_j^n = \underline{U}_j^0 + (1 - e^{\zeta n\Delta t})\underline{A}_e \sin(\underline{\omega}_e n\Delta t + \underline{\varepsilon}_e). \tag{6.3}$$

where

$\underline{A}_e$ is the amplitude of the excitation function.

$\underline{\omega}_e$ is the frequency of the excitation function.

$\underline{\varepsilon}_e$ is the phase of the excitation function.

and the term $(1-e^{\zeta n\Delta t})$ allows the excitation to be gradually introduced to prevent possible numerical start up errors.

When referring to the 3D static or dynamic quantities, the normal reference system is the Cartesian system. However for the 2D programs the x direction refers to an axis which lies horizontally in the plane of the mooring line with the origin coincident with the anchor point. Therefore endpoint excitation might be thought of as corresponding to a surge excitation in the case of a mooring line being attached to a floating body. Throughout Sections 6.3 and 6.4 the influence of changing the various parameters in Table 6.1 is examined. Each variable is examined in isolation, unless otherwise stated, from the remaining variables. Unless indicated otherwise, the variables always have the same values as indicated in Table 6.1.

6.3.1 Case Study 1: No Dynamic Excitation

In the first case study the four dynamic models are run with no endpoint excitation. The static value for the tension in the last (uppermost) element is $T_s = 495336.993N$. The mean uppermost element tensions for the dynamic solutions are calculated over two time periods, $0-350$ seconds and $100-350$ seconds. The latter is used to ensure that any numerical irregularities from the start up procedure do not affect the calculation of the mean. The results are shown in Table 6.2 where "% Diff." denotes the percentage difference of the dynamic tension from T_s relative to T_s. From these results it is possible to see that the solution obtained from each of the schemes with no endpoint excitation represents very closely the static solution. Furthermore, it can be said that the solution obtained from the Central Difference (CD) scheme is more accurate than the remaining three schemes. However, these differences are only of interest from an academic point of view, since they all lie well within the limits of engineering accuracy.

Static		Dynamic	
Quantity	Value	Quantity	Value
x Endpoint displacement	1000.0 (m)	Time increment(Δt)	0.02 (secs)
y Endpoint displacement	1000.0 (m)	Simulation time(T)	255 (secs)
Water depth (d)	1000.0 (m)	θ	1.4
Length of line(L)	1790.0 (m)	β	0.25
Number of elements(h)	20	δ	0.5
Sea water density(ρ)	1025 (kg/m^3)	μ	0.5
Line diameter(D)	0.07148 (m)	Amp. x	0.0
Mass per metre in air	25.493 (kg/m)	Amp. z	0.0
Young's modulus(E)	7.848×10^{10}	x Freq.	$\frac{\pi}{10}$
Poisson's ratio(ν)	0.0	z Freq.	$\frac{\pi}{10}$
Normal drag coeff.(Cd_n)	1.6	x Phase	0.0
Tangential drag coeff.(Cd_t)	0.03	z Phase	0.0
-	-	Growth factor(ζ)	0.05
-	-	Tan. AM. Coeff.(Ca_t)	0.0
-	-	Nor. AM. Coeff.(Ca_n)	1.98

Table 6.1 — Principal Static and Dynamic Input Parameters

Scheme	Mean 1	% Diff.	Mean 2	% Diff.	CPU (secs.)
Houbolt	495338.223	-0.000248	495338.735	-0.000351	330.723
CD	495337.026	-0.000008	495337.046	-0.000012	411.472
Wilson-θ	495338.259	-0.000256	495338.769	-0.000359	387.977
Newmark	495337.346	-0.000073	495337.493	-0.000101	430.491

Table 6.2 — Mean of Solutions with no Excitation.

6.3.2 Case Study 2: Decayed Dynamic Excitation

In the next part of the study the four schemes are run with a sinusoidal excitation in the 2D x direction. This oscillation is introduced at the upper endpoint position indicated in Table 6.1 and is allowed to gradually grow to a maximum amplitude of 10m with a growth factor, ζ, of 0.05 (see Equation (6.3)). This excitation is then allowed to decay back to the original point with the same (but negative) growth factor once the maximum amplitude has been reached. A steady decayed solution is only obtained after 250 seconds and therefore the mean tension is calculated between 250 and 350 seconds only. The results are summarised in Table 6.3.

Scheme	Mean(250 – 350)	% Diff. From T_s	CPU (secs.)
Houbolt	495072.393	0.0534	341.245
CD	495075.519	0.0528	510.445
Wilson-θ	495069.875	0.0539	517.263
Newmark	495091.284	0.0496	447.680

Table 6.3 — Means of Decayed Sinusoidal Solutions.

Table 6.3 shows that the accuracy of the four scheme are now comparable, but that the relative errors are worse than for the case with no excitation, see Table 6.2. This suggests that once numerical oscillations are introduce through endpoint excitation, they become established and do not entirely decay out as the solution proceeds following the termination of the endpoint excitation. However, although the error is of the order of 100 times larger than the case of no excitation, in engineering terms the decayed dynamic solution and the static solution are essentially the same.

6.3.3 Case Study 3: Influence of Total Simulation Time

To see if the total simulation time affects the results, each of the four models are run with a regular sinusoidal excitation in the 2D x direction for simulation times (T) of 350 and 1000 seconds. In addition to the overall mean ($\bar{T}_m$) being calculated for both simulation times, the means of the tension peaks ($\bar{T}_p$) and of the tension troughs ($\bar{T}_t$) for the region containing the last five peaks of the solution

are also calculated. The results for the 350 second simulation are shown in Table 6.4, whereas the 1000 second simulation results are in Table 6.5. The percentage differences in the results obtained for the two different simulation times are given in Table 6.6.

Scheme	$\bar{T}_p$(N)	$\bar{T}_m$(N)	$\bar{T}_t$(N)	CPU (secs.)
Houbolt	885723.69	508968.55	175344.243	337.01
CD	885362.47	508913.78	175622.45	558.55
Wilson-θ	888632.04	508943.99	165704.72	572.58
Newmark	886024.66	509794.17	177694.86	462.096

Table 6.4 — Tension Means for 350 Second Simulation.

Scheme	$\bar{T}_p$(N)	$\bar{T}_m$(N)	$\bar{T}_t$(N)	CPU (secs.)
Houbolt	885699.96	508972.16	175340.97	962.05
CD	885358.36	508917.99	175624.13	1613.59
Wilson-θ	888630.53	508944.72	165702.91	1636.72
Newmark	886021.07	509798.43	177696.50	1320.84

Table 6.5 — Tension Means for 1000 Second Simulation.

Scheme	Peaks	Overall Means	Troughs
Houbolt	0.00268%	-0.00071%	0.00186%
CD	0.00046%	-0.00083%	-0.00096%
Wilson-θ	0.00017%	-0.00014%	0.00109 %
Newmark	0.00041%	-0.00084%	-0.000923%

Table 6.6 — % Differences in Tensions.

The percentage differences are so negligible it may be considered reasonable to assume that, for the problem considered, short simulation times will be representative of the results obtained from longer simulations.

6.3.4 Case Study 4: Influence of Irregular Endpoint Excitation

Having examined the influence of a regular upper endpoint excitation, each scheme is now subject to an irregular endpoint excitation. This is also allowed to grow and decay over 250 seconds as in Case Study 2. The irregularity is introduced by selecting, at random, values for the amplitude, phase and frequency of the governing excitation function (see Equation (6.3)). The randomness is generated from a pseudo random number generator and limits are imposed upon the ranges which the randomised variables can attain. The total simulation time is 350 seconds so the mean of the decayed result is calculated for the last 100 seconds. The results are indicated in Table 6.7.

Scheme	Mean(250 – 350)	% Diff. from T_s	CPU Times (secs.)
Houbolt	495337.322	-0.000067	342.76
CD	495335.17	0.000367	757.06
Wilson-θ	495335.09	0.000384	560.59
Newmark	495346.45	-0.001910	551.32

Table 6.7 — Decayed Mean Tensions for Irregular Excitation.

These results are analogous to those given for the case of decayed regular excitation presented in Table 6.3. However, the accuracy obtained in the present case is better than that for the case of decayed regular excitations This implies that spurious numerical oscillations generated by the solution, die out more readily for irregular excitation than for regular excitation. Also note that the CPU times for the Houbolt scheme (see Tables (6.3) and (6.4)) are comparable for the two cases of excitation. However, for the remaining three schemes the CPU times with irregular excitation are 48%, 8% and 23%, respectively for the CD, Wilson-θ and Newmark schemes, greater.

6.3.5 Case Study 5: Different Excitation Amps. and Freqs.

Finally each of the four models are now run with different amplitudes and frequencies of excitation in the 2D x direction. These regular excitations are then allowed to decay away so that the effects of different endpoint excitations can be examined. The percentage differences between the average dynamic tensions of the decayed solution and the static tension T_s, and the CPU times are shown in Table 6.8.

Scheme	Freq.	$\text{Amp}_1 = 5\text{m}$		$\text{Amp}_2 = 15\text{m}$		$\text{Amp}_3 = 25\text{m}$	
	(rads./s.)	% Diff.	CPU (secs.)	% Diff.	CPU (secs.)	% Diff.	CPU (secs.)
Houbolt	$\frac{2\pi}{5}$	0.05324	338.84	0.05313	352.71	0.05396	376.89
CD		0.05307	733.241	0.05207	914.573	0.05213	1001.686
Wilson-θ		0.04912	539.642	0.05045	584.789	0.05066	632.652
Newmark		0.05424	532.457	0.05197	611.064	0.05108	664.472
Houbolt	$\frac{2\pi}{17}$	0.05357	338.934	0.05446	339.358	0.05443	339.332
CD		0.05272	472.120	0.05275	587.570	0.05236	695.632
Wilson-θ		0.05276	509.328	0.05102	508.751	0.04993	543.662
Newmark		0.05097	442.266	0.05095	480.968	0.05233	526.908
Houbolt	$\frac{2\pi}{30}$	0.05093	338.937	0.05051	338.838	0.04950	342.301
CD		0.05183	437.946	0.05198	493.562	0.05177	584.061
Wilson-θ		0.05000	507.281	0.05095	516.517	0.05151	519.734
Newmark		0.05355	447.671	0.05349	452.263	0.05417	475.284

Table 6.8 — % Differences for Different Amplitudes and Frequencies of Excitation.

From Table 6.8 it follows that the amplitude and frequency of the endpoint excitation has, once the excitation has died away, a negligible influence upon the percentage difference between the static solution and the means of the decayed tensions.

In conclusion, it is clear that once the dynamic solutions (by any of the four schemes) have reached a point where there is no longer any excitation present,

then the resulting endpoint tension is, for all practical purposes, identical to the static solution. This is as far as the self validation of the dynamic model with the static model can be carried. A more detailed numerical comparison of the solutions generated using the four different time integration schemes is presented in the next section.

6.4 Numerical Study of Four Time Integration Schemes

6.4.1 Case Study 6: Maximum Permissible Δt Values

In this case study the influence of the amplitude and frequency of the endpoint excitation is examined with regard to the maximum permissible value of the time step, Δt, which can be used to obtain a valid solution. The three implicit schemes (the Houbolt, Wilson and Newmark) will, in theory, provide a solution regardless of the size of Δt. However the solutions obtained with these schemes do eventually collapse at a certain maximum value of Δt. The reason for this is that for larger values of Δt the 'basin of attraction' of the Taylor series expansion used in the iterative process, see Equation (3.76), is exceeded. Thus it can be seen that it is not the implicit nature of the scheme which is causing the collapse of the solutions, but rather it is the restriction imposed by the use of the first order Taylor Series expansion. This is clearly not a limitation in the integration of linear equations since no iterative procedure is employed in this situation.

In principle it is expected that increasing either, or both, the amplitude and frequency of excitation will result in a smaller permissible value for the maximum value of Δt. This supposition is clearly borne out in Figure 6.1 generated using the Houbolt scheme. It can be seen that for any given amplitude, increasing the frequency has the effect of reducing the maximum permissible value of Δt. Similarly it can also be seen that at any given frequency, increasing the amplitude has the same effect. Note that both are nonlinear effects.

The features present in the results for the (CD) scheme - as illustrated in Figure 6.2 - are not so easily explained. For the portion of the graph prior to a frequency of approximately 0.3 rads/s., the behaviour is as expected. For frequency values greater than this it appears that any subsequent increase in the frequency results in an increase in the maximum permissible value of Δt. It is not possible to directly attribute this effect to a particular cause, but it can be hypothesised that some 'resonance' effect is present which, for certain combinations of excitation amplitude and frequency, enhance the stability properties of the CD scheme. However this

can only be a 'localised' effect since, as indicated above, increasing the amplitude and frequency of excitation in the extreme must reduce the size of the maximum permissible Δt.

It is seen from Figure 6.2 that the result for an excitation amplitude of 5m does illustrate a local peak at approximately 0.48 rads/s. After this peak the trend for a decreasing maximum value of Δt is again established. As the amplitude of excitation is increased it seems that the 'local' peak becomes larger in the sense that it applies over a greater range of frequency values. The supposition previously mentioned suggests that at higher frequencies than used here, the decreasing trend ought to again reappear. If this is infact true, then this means that increasing the amplitude acts to increase the 'size' of the peaks for the larger Δt values.

Figure 6.3 shows the results for the Wilson-θ scheme. It is again evident that certain combinations of frequency and amplitude produce slight increases in the maximum value of Δt. However the broader picture confirms the initial hypothesis that the maximum permissible value of Δt decreases as the amplitude and frequency increases. The results in Figure 6.3 also exhibit some local effects analogous to those described for the CD scheme, namely an increase in the maximum permissible value of Δt with increasing excitation frequency at the lower end of the frequency range. However the trend at the higher frequencies is opposite to that demonstrated with the CD scheme meaning that as the amplitude is increased, the size of the local peak decreases.

Figure 6.4. shows the results for the Newmark scheme. Again a local peak in the results is present, and the characteristics of the peak follow precisely the same trends identified for the Wilson-θ scheme in Figure 6.3.

6.4.2 Case Study 7: Influence of Excitation Ramping Function

In this case study the influence of the growth factor ζ in Equation (6.3) is examined. The growth factor is applied to the sinusoidal excitation function which governs the endpoint motion. This allows the excitation to be gradually introduced rather than starting suddenly and risk the possibility of introducing numerical shocks.

Examination of Equation (6.3) shows that as n, the number of time steps so far, increases, so the function $(1 - e^{\zeta n \Delta t})$ will tend to unity. This will then yield the correct amplitude, $\underline{a}_e$, for the endpoint excitation. The practical upper limit

imposed by the computer system on the calculation of $e^{\zeta n\Delta t}$ is 174, i.e.

$$e^{\zeta n\Delta t} \leq 174, \qquad \text{hence} \qquad \zeta \leq \frac{\ln(174)}{n\Delta t}.$$

If, instead of using $n\Delta t$, the value of the simulation time, T, is used, then it is possible to obtain the smallest possible value of ζ. With $T = 250$ seconds, the range of permissible values for ζ obtained for the four schemes are shown in Table 6.9.

Scheme	ζ range
Houbolt	$0.02 \leq \zeta \leq 17.2$
CD	$0.02 \leq \zeta \leq 123$
Wilson-θ	$0.02 \leq \zeta \leq 17.2$
Newmark	$0.02 \leq \zeta \leq 15$

Table 6.9 — Range of Growth Factors for Each Scheme.

If, however, the values for Δt are taken from Figures 6.1 to 6.4 for an excitation amplitude of 10m and a frequency of $\frac{\pi}{10}$, as an example, then Figure 6.5 shows ζ plotted against the maximum permissible value of Δt. Note that the Δt values for the CD scheme have been scaled up by a factor of 10 and the growth factors by 0.15 to provide values comparable with the results for the other schemes. For the three implicit schemes it seems that once the value of ζ is greater than approximately 0.5 the maximum permissible value of Δt remains constant. Remembering the scaling of the results for the CD scheme, it can be seen that they are not as variable as they appear on the graph. It also seems possible to identify a 'critical' value of ζ, for all the schemes, beyond which the maximum value of Δt is invariant.

These comments also apply to Figure 6.6 where ζ is plotted against the means of the tension peaks, $\bar{T}_p$. Here the critical limit would seem to be approximately 1.0, rather than the value of 0.25 for the determination of a maximum value of Δt. Again the the abscissa for the CD scheme has been scaled by a factor of 0.15. Figure 6.7 shows ζ plotted against the overall mean of the tensions, $\bar{T}_m$, and Figure 6.8 shows the same graph but for a smaller range on the x axis. It is difficult to make generalized comments applicable to these graphs other than to say that for

$\zeta > 1$ both the CD and Wilson-θ schemes produce means which are invariant of ζ. The Newmark scheme exhibits the greatest variation (of approximately $\frac{1}{2}\%$), whilst the Houbolt scheme seems to be tending towards a limiting value.

6.4.3 Case Study 8: Influence of Vertical Excitation upon Δt

So far the endpoint excitation has been limited to the horizontal (2D x) direction. In this case study the influence of simultaneous motion in both the horizontal (2D x) and vertical (z) directions upon the maximum value of Δt is investigated. An initial amplitude of 10m is maintained in the x direction, whilst the amplitude of the motion in the z direction lies in the range $0.0 \leq A_z \leq 10.0$. The motion in the z direction is selected to be 90° out of phase with the motion in the x direction, i.e. $\varepsilon_z = \frac{\pi}{4}$. This is to obtain elliptical, and not linear, endpoint motion. The frequency of oscillation in both directions was maintained at $\pi/10$ and the same ramping function of $\zeta = 0.05$ was used in both directions. With $A_z < 10.0$, the resultant endpoint motion will be truly elliptical, whilst when $A_z = 10.0$ the resultant motion will be circular. It is expected that with increasing A_z, the maximum permissible value of Δt should decrease since the excitation is becoming more extreme. This is borne out in Figure 6.9, but the effect is not as great as might initially have been supposed. The maximum reductions in the maximum permissible value of Δt being 33%, 3%, 20%and13% for the Houbolt, CD, Wilson-θ and Newmark schemes respectively.

6.4.4 Case Study 9: Irregular Endpoint Motion upon Max. Δt

Here the influence of the irregularity of the endpoint motion in the 2D x direction, upon the maximum value of Δt, is investigated. The irregular motion is composed of a specified number of sinusoidal components which have randomly assigned amplitudes, frequencies and phases as in Case Study 4. Figure 6.10 shows the maximum attainable value of Δt plotted against the number of components used to generate the irregular motion. Precisely because of the irregularity of the endpoint motion, it is not possible to generalize comments about this graph. However, it does appear that the more components which are used to generate the endpoint motion, the smaller the maximum value of Δt becomes.

Generally speaking it would be expected that the effects produced by the irregular excitation would cancel out. However, were this always true then the occasional spurious component of endpoint excitation caused by reinforcement of

the different components would not occur. Spurious values for the endpoint excitation will result in maximum permissible value of Δt and maximum predicted tensions which could be greatly different to those normally expected. Figures 6.11, 6.12 and 6.13 show plots of the number of components against the maximum, mean and variance of the resulting tension time history. It will be noted that the behaviour of the four schemes seem to separate into two groups. Both the CD and the Houbolt schemes appear to react more dramatically to produce wider variations in the maximum Δt, the maximum tension and the mean tension than either the Wilson-θ or the Newmark schemes.

6.4.5 Case Study 10: Relationship Between Δt and Mesh Size

In this case study one of the most important features of finite difference (FD) schemes is examined, namely the relationship between the maximum permissible value of Δt and the number of elements (h) used, i.e. the mesh size. Figure 6.14 indicates, as expected from the analysis in Chapter 5, that the value of the maximum permissible Δt decreases as the number of elements increases. In particular, in Section 5.8 the maximum time step size was shown to be proportional to the minimum period of the mesh. Therefore as the number of elements increase, so the minimum period decreases, and hence so does the allowable time step size. Also indicated in Figure 6.14 is the theoretical limit for the CD scheme (note that the ordinates for both CD curves have been scaled up by a factor of 10) as given by Equation (5.99). To estimate Δt_{cr} as given by Equation (5.99), a value for the tension T needs to be defined. For this case this is taken to be the maximum value of tension from the static analysis. This theoretical limit is well below the curve of actual maximum permissible values of Δt showing that at least for this nonlinear problem, the theoretical limit for the CD scheme is conservative.

6.4.6 Case Study 11: Solution Histories for Different Δt and h

Here the effects of using different values of Δt and h upon the actual tension time history is examined for each of the four time integration schemes. In all cases the excitation is in the 2D x direction only. This has an amplitude of 10.0m and a fixed frequency of $\pi/10$ rads/s. The value of h ranges between 10 and 30 (inclusive) with an interval of 5, whilst the range of Δt for each scheme is shown in Table 6.10. The minimum practical value for Δt was taken as 0.001 seconds because for smaller values the program execution times became intolerably long. The maximum values were chosen to be 'sensibly' less than the permissible maximum Δt values obtained in the previous case study for 30 elements, see Figure 6.14. Also the maximum

Δt values were selected so as to easily divide to give an appropriate range. Each scheme was run with $\Delta t = 0.001$ seconds and then at multiples of the intervals as indicated in Table 6.10.

Scheme	Range of Δt (secs.)	interval (secs.)	Range of h	Interval
Houbolt	$0.001 \leq \Delta t \leq 0.20$	0.04	$10 \leq h \leq 30$	5
CD	$0.001 \leq \Delta t \leq 0.025$	0.005	$10 \leq h \leq 30$	5
Wilson-θ	$0.001 \leq \Delta t \leq 0.15$	0.03	$10 \leq h \leq 30$	5
Newmark	$0.001 \leq \Delta t \leq 0.20$	0.04	$10 \leq h \leq 30$	5

Table 6.10 — Δt and h Used for Each Scheme Considered.

To plot the full range of the solution, i.e. to show the peaks, troughs and everything in between, produces a graph where no distinction can be made between solutions obtained with different values of Δt and h. For this reason the extreme sections of the peaks and troughs of the tension time history have been isolated and then separately plotted so that the differences become clear. A simulation time of 250 seconds was used throughout and only the results for the last five peaks and troughs of the simulation were plotted.

Results from the Houbolt Scheme

The results for the Houbolt scheme are shown in Figures 6.15 to 6.24. For a given value of h the tension time histories are plotted for the different values of Δt. Apart from the graphs corresponding to $h = 30$, the others clearly show a trend of reduced amplitudes with increasing values of Δt. With $h = 30$ the tension peaks obtained for the two largest time steps (0.16 and 0.2) are very erratic, whilst the solution for the remaining four values of Δt produce regular and smooth responses for the tension peaks. The results for the tension troughs with $h = 30$ are totally erratic. The remaining solutions for different numbers of elements and values of Δt are generally smooth and regular. Even those which are not regular, e.g. for $h = 25$ and $\Delta t = 0.2$ seconds, the mean trend of the irregularities are consistent with the regular results. Furthermore, these irregularities also die out as the solution proceeds.

The percentage deviations from the solution with $\Delta t = 0.001$ seconds of the solutions obtained with the remaining values of Δt are indicated in Table 6.11. The

indicated percentage differences are greater for the troughs than for the peaks. This is to be expected since the absolute value with which the percentage relative error is being calculated is much lower for the troughs. However, closer examination of the associated computer output (not presented) indicates that the absolute differences at the peaks and troughs are nearly equal. Therefore it is not meaningful to attach any significance to the differences in the percentage errors between peaks and troughs for any given value of h. Rather, it is more instructive to simply compare the percentage differences for peaks (or troughs) only for different values of h. If the entries in Table 6.11 corresponding to $h = 30$ and $\Delta t = 0.16$ and 0.20 are neglected because of the unacceptable irregular oscillations already indicated, then as previously mentioned for a given value of h it can be seen that increasing the value of Δt reduces the amplitude of the results.

For the case where Δt is fixed and the variation of the solution with increasing h is examined, it can be seen that there is no clear trend regarding the results of the peaks. If there is any trend it is not monotonic but oscillatory, and not always diminishing in amplitude. In contrast the results for the troughs show a clear trend, i.e. that increasing the number of elements for any given value of Δt reduces the percentage differences from the 'accurate' solution.

The plot of troughs for $h = 30$ is very irregular with no semblance of order until the last two peaks of the time history and even these are still fairly erratic. The reason for this is not obvious, but clearly the irregularities in the solution manifest themselves first at the lower tensions present in the time history, i.e. the equivalent peaks are more smooth. To summarise the results for the Houbolt scheme, the following points are made:

- For any given value of h, increasing Δt increases the deviation of the results from the 'accurate' solution.
- For any given value of Δt, increasing h reduces the deviation of the results from the 'accurate' solution.
- For certain combinations of h and Δt irregular results will arise.
- There is Period Elongation (PE) present in the solution but this only appears at low tensions (i.e. at the troughs) and for the case of higher element numbers.

h		Δt (secs.)				
		0.04	0.08	0.12	0.16	0.20
10	Peaks	0.25846	0.45137	0.69313	0.92488	1.15418
15		0.27669	0.48138	0.73745	0.96550	1.21146
20		0.19895	0.37244	0.63485	0.87766	1.11313
25		0.23749	0.49363	0.74139	0.95510	1.07855
30		0.17934	0.32847	0.55554	0.20366	-0.17045
10	Troughs	-2.05888	-3.84874	-5.66534	-7.63957	-9.72212
15		-1.67186	-2.91125	-4.42944	-6.05168	-7.59973
20		-1.39027	-2.54198	-3.94135	-5.43076	-6.72520
25		-1.23533	-2.28871	-3.63527	-4.66045	-2.52475
30		-1.21205	-2.29210	-1.73907	4.50663	6.51207

Table 6.11 — % Deviations of Peaks and Troughs for Houbolt Scheme.

Results from the CD scheme

The corresponding sets of results for the CD scheme are shown in Figures 6.25 to 6.34 and Table 6.12. Basically the same trends are evident here as for the equivalent results of the Houbolt scheme, however, the most noticeable difference is that the CD scheme produces no irregularities over the range of Δt and h values considered. Additionally, there is a noticeable amount of PE produced by using increasing values of Δt, and this becomes more pronounced for the solutions with more elements. The percentage deviations from the 'accurate' solution (i.e. the CD solution with $\Delta t = 0.001$) are shown in Table 6.12.

h		Δt (secs.)				
		0.005	0.010	0.015	0.020	0.025
10	Peaks	0.04780	0.10287	0.15529	0.12320	0.25721
15		0.04305	0.09724	0.15101	0.20483	0.25837
20		0.00802	0.03795	0.07897	0.12569	0.17526
25		0.05195	0.11043	0.16543	0.21906	0.27212
30		0.00580	0.03399	0.07355	0.11868	0.16724
10	Troughs	-0.27785	-0.66920	-1.08161	-3.94454	-1.92798
15		-0.18908	-0.45599	-0.74761	-1.05176	-1.36573
20		-0.21772	-0.45618	-0.70464	-0.96355	-1.23252
25		-0.18200	-0.41056	-0.64634	-0.88728	-1.13528
30		-0.24799	-0.50402	-0.74482	-0.98118	-1.21922

Table 6.12 — % Deviations of Peaks and Troughs for CD Scheme.

A study of Table 6.12 indicates that increasing Δt for a given value of h increases the percentage deviation from the 'accurate' solution. However, for a given value of Δt the effect of increasing the number of elements is not immediately clear. A trend for the peaks cannot be discerned, but for the troughs it appears that an increase in h causes a reduction in the deviations up to a certain point, i.e. for 30 elements the deviations start increasing again. A summary of the results for the CD scheme are as follows:

- No case of irregular solutions.
- Discernible amounts of PE exists and this increases with increasing h and Δt.
- For a given value of h, increasing Δt increases the deviation of the solution from the 'accurate' solution.
- For a fixed value of Δt, no consistent trend is identifiable in the deviations of the peaks or troughs with increasing h is evident.
- For all combinations of Δt and h considered here, extremely smooth and regular solutions were obtained.

Results from the Wilson-θ scheme

The Wilson-θ scheme results are shown in Figures 6.35 to Figure 6.44, and in Table 6.13. What is immediately obvious from these results is the existence of more irregular solutions for much lower values of Δt and h irrespective of whether the comparison is with the Houbolt or CD results. An increase in irregularity is apparent when increasing both Δt and h. The solutions obtained when $h = 30$ for both peaks and troughs show no semblance of regularity at all, see Figure 6.43 and 6.44. The solutions obtained with the smallest time step of 0.001 seconds seem regular for any value of h except 30. For any other combination of Δt and h the solutions are irregular and not particularly pleasing for engineering applications.

h		Δt (secs.)				
		0.03	0.06	0.09	0.12	0.15
10	Peaks	0.18291	0.33712	0.48648	0.53198	0.60837
15		0.16543	0.30965	0.47131	0.51426	0.63984
20		0.20726	0.32564	0.46320	0.48344	0.60677
25		0.21414	0.35604	0.49344	0.49365	0.43279
30		0.23809	0.35094	0.26005	-6.01958	-28.58870
10	Troughs	-2.80331	-5.13665	-7.31494	-9.19764	-10.20959
15		-1.95354	-3.54515	-4.98693	-6.50764	-7.75304
20		-1.50725	-2.81252	-4.14949	-5.18531	-5.70435
25		-1.38008	-2.42457	-3.34438	-4.56348	-2.76595
30		-0.93274	-1.93308	-3.96353	10.48312	15.21909

Table 6.13 — % Deviations of Peaks and Troughs for Wilson-θ Scheme.

The percentage deviations from the 'accurate' solution are shown in Table 6.13 which suggests more regularity than is present in the Figures. This is readily explained thus : The percentage deviations are calculated using the means of the last five solution peaks and troughs from the means of the 'accurate' solution peaks and troughs. Therefore the averages of the irregular solutions are lending themselves to produce an indication of regularity in Table 6.13. The main points to be summarised for the Wilson-θ scheme are:

- Markedly more irregular tension time histories.
- No viable solution for any value of Δt at $h = 30$.
- In the more regular plots, Figure 6.35 for example, there is a noticeable amount of PE (negative in this case) produced by increasing the value of Δt.

Results from the Newmark scheme

The results for the Newmark scheme are shown in Figures 6.45 to Figure 6.52 and Table 6.14. The figures presented show the most complicated set of features, where no solution for $h = 30$ is plotted since the time histories for this case were so irregular they made the plots unintelligible. If Figures 6.45 and 6.46 are first examined, the regularity in the solutions is to be noted, but it is also apparent that the solution with $\Delta t = 0.001$ seconds has been markedly offset from the remaining solutions. The behaviour of this offset with increasing values of h is not regular, since increasing h seems to introduce different amounts of offset for the peaks and the troughs. If the solution with $\Delta t = 0.001$ seconds is ignored, then the remaining solutions can be judged as well behaved, regular and follow the trends previously indicated for the other procedures. However when large numbers of elements are combined with larger time steps, irregularity is evident yet again. The percentage deviations presented in Table 6.14 are included for completeness. However, given the behaviour of the solution with $\Delta t = 0.001$ seconds the relevance of the inclusion of this table has to be questioned. The main points to be summarised in this case are:

- The main trends as previously identified for other schemes are observed, except for the solution with $\Delta t = 0.001$ seconds which behaves quite differently.
- Irregularity is very pronounced for $h = 30$ and leads to a non-viable solution.
- Period elongation is again evident, but to a lesser extent than for the other schemes.

h		Δt (secs.)				
		0.04	0.08	0.12	0.16	0.20
10	Peaks	-0.94913	-0.70932	-0.46115	-0.23775	-0.02806
15		-1.03280	-0.79276	-0.54984	-0.31925	-0.07390
20		-0.65479	-0.40004	-0.14333	0.09145	0.31424
25		-0.60606	-0.35002	-0.10103	0.07700	-0.68254
30		-0.43123	-0.19969	-0.05306	-10.16856	-31.34569
10	Troughs	-17.14541	-19.63783	-22.33766	-24.97102	-27.61055
15		-1.22756	-2.73982	-4.60053	-6.44855	-8.32078
20		10.71017	9.38077	7.89400	6.41231	4.98713
25		17.04024	15.87448	14.62463	14.17566	21.67207
30		19.80074	18.78001	20.50214	29.82369	34.80034

Table 6.14 — % Deviations of Peaks and Troughs for Newmark Scheme.

6.4.7 Case Study 12: Further Analysis of Solution Histories

In this case study a further analysis of the graphs presented in Figures 6.15 to 6.52, i.e. the peak and trough tension time histories for different combinations of Δt and h, is undertaken. The means of the tension peaks and troughs respectively are presented for the Houbolt scheme, plotted against Δt, in Figures 6.53 and 6.54. Again the smooth reduction in the means of the peaks as the time step size increases is shown, and the irregularity present in the graph for $h = 30$ is highlighted.

Figures 6.55 and 6.56 provide the corresponding results for the CD scheme. There is a linear reduction (or increase) in the peaks (or troughs) again evident as the time step size increases for any value of $h > 10$.

Figures 6.57 and 6.58 demonstrate the same results for the Wilson-θ scheme. Here the irregularity of the method is again apparent; also note that the increase (decrease) of the peaks (troughs) with increasing Δt for the lower h values is not

linear. For higher values of h (25 and 30) the troughs switch from near linear increases in the mean tension to near linear decreases.

Figures 6.59 and 6.60 show corresponding results for the Newmark scheme. The curious behaviour noted earlier for the case of the solution with $\Delta t = 0.001$ seconds has a marked effect on the initial parts of the graph - as might be expected. Subsequent to this and prior to the onset of any irregularity, the graphs display the same relationship as noted before.

6.4.8 Case Study 13: CPU Timings for Simulations

The influence of the selection of Δt and h can now be made with reference to the plots of Case Study 11. In selecting values for Δt and h, solutions are required which exhibit smooth and regular time histories. Furthermore, it is also desirable that the computational effort required is not to great. Given this, then it is also of interest to examine the Central Processing Unit (CPU) time required for the execution of the different simulations. CPU time is, of course, dependent upon the computer system used, but the figures given here will allow a comparison of the relative efficiency of the four time integration schemes used.

Up to the point of writing it has not been possible to obtain a concensus of opinion as to whether the CPU times obtained here are influenced by the load on the system. It is the authors experience that they are and therefore have to be considered as values subject to an error of approximately $\pm 10\%$. Rather than present the total CPU time for execution, it is more instructive to show the CPU values for the time spent executing the Newton-Raphson iterative solver (CPU_2), and the time for the execution of the rest of the code (CPU_1) - their sum giving the total CPU time for the simulation.

Results for the Houbolt scheme are presented in Figures 6.61 and 6.62 and show the expected trends for all values of h. Namely, that as the time step increases, both CPU_1 and CPU_2 decrease. It should be noted that the CPU times for $\Delta t = 0.001$ are not presented since to include them would cause the scale to eliminate the detail for the remaining values of Δt. These graphs show that for a given value of Δt there is a linear decrease in CPU_1, see Figure 6.61, and a nonlinear decrease in CPU_2, see Figure 6.62. Thus it can be seen that the total CPU time will decrease nonlinearly with a reduction in the numbers of elements used, and that this is directly attributable to the nonlinear decrease in CPU_2. The order of magnitude of the values of CPU_1 and CPU_2 remain roughly comparable over the range of

Δt and h considered. Thus approximately half the solution time is spent in the iterative portion of the code.

The corresponding graphs for the CD scheme are presented in Figures 6.63 and 6.64. Again it is clear that CPU_1 decreases linearly and CPU_2 non-linearly with decreasing h for any given value of Δt. Figure 6.64 shows an additional feature, namely an increase in CPU_2 for certain cases where a decrease is expected. For $\Delta t \leq 0.01$ the nonlinear decrease in CPU_2 with decreasing h follows the expected trend, however for the remaining portion of the graph, particularly at larger values of h, an increase in CPU_2 is observed with increasing values of Δt. This implies that in terms of CPU timing, the CD scheme has an optimum value for Δt for execution, and that this value is less than the 'critical' value. This is important to realise since it means that a more accurate solution will be obtained, and that this more accurate solution will be derived more efficiently than a solution gained with larger values of Δt. The reason for this effect is explained later in Section 6.4.11. Whilst for $\Delta t \leq 0.01$, CPU_1 and CPU_2 again remain roughly comparable, for the case of $h = 30$, for example, it can be seen that when $\Delta t = 0.025$ seconds, CPU_2 is seven times greater than CPU_1.

The results for the Wilson-θ scheme are shown in Figures 6.65 and 6.66. The same trends as for the Houbolt scheme can be identified, namely a linear decrease in CPU_1 with decreasing h, and an associated nonlinear decrease in CPU_2. The most important point to note here is that the ratio of CPU_2 to CPU_1 is much greater for larger values of h. For example, with $h = 30$, the ratio with $\Delta t = 0.04$ is 4.8, whilst the comparable ratio for the Houbolt scheme is 1.1. This indicates that the Wilson-θ scheme spends a greater proportion of its execution time in the iterative part of the code. This difference can be partially accounted for on looking at the details of the procedure, see Section 3.5. In particular this scheme requires an additional interpolation in order to establish the solution at time $t = (n+1)\Delta t$ rather than at the solution point of time $t = (n+\theta)\Delta t$, where $\theta > 1.37$. The latter is required to provide the scheme with unconditional stability. However the effect of this additional interpolation on the CPU time is not thought to be significant enough to cause the noted disparity seen in the CPU ratios.

The CPU times for the Newmark scheme are shown in Figures 6.67 and 6.68 where the same trends as noted earlier are again clearly visible. The CPU ratio is 3.43 at $\Delta t = 0.04$, which indicates that, in common with the Wilson-θ scheme, the Newmark method spends a disproportionate amount of time in the iterative cycle. There is a slight increase in CPU_2 as Δt increases for the 25 and 30 element models.

This can be seen to be insignificant in relation to the same effect associated with the CD scheme. In light of the fact that this does not increase the total CPU time, as happens for the CD scheme, it can be considered insignificant here. The following points summarise this case study:

- Generally the total CPU time decreases with increasing Δt.
- CPU_1 decreases linearly with decreasing element numbers.
- CPU_2 decreases nonlinearly with decreasing h.
- An optimum Δt value can be identified for the CD scheme which is less than the maximum permissible value.

6.4.9 Case Study 14: Direct Comparison of Solution Histories

Now that the results for the CPU times have been plotted on the same graph for direct comparison, the solution peaks for the different integration schemes are now plotted on the same graph for a common value of Δt. Figures 6.69, 6.70 and 6.71 show the solution peaks for $\Delta t = 0.001$, 0.021 and 0.042 seconds respectively. It is suggested that if the time step restriction on the CD scheme can be accommodated, that this scheme models more appropriately what happens in reality. This is because the implicit nature of the Houbolt, Wilson-θ and Newmark schemes, see Section 3.5, means that a solution which is derived at time $t = (n+1)\Delta t$ depends upon knowing what has already happened at that instant in time and intuitively this can be seen not to be physically correct. In contrast, the solution for the explicit CD scheme at time $t = (n+1)\Delta t$ depends only upon the solutions at time $t = n\Delta t$ and earlier, and is therefore a more consistent scheme to use. With this in mind, it can be said that the solution for the CD scheme with the smallest time step would be expected to yield the most accurate and physically appropriate results for any given number of elements.

With $\Delta t = 0.001$ seconds (Figure 6.69) it can be seen that the Houbolt and CD schemes are virtually identical, apart from the high frequency oscillations at the peaks of the Houbolt scheme. The amount of high frequency oscillation appears to decay as the solution proceeds. As mentioned in Case Study 11, and seen clearly here in Figure 6.69, the mean trend of the high frequency oscillation closely follows the solutions for the remaining three schemes. This is evident because, at least visually, the solution obtained from the CD scheme appears to represent a mean of the solution obtained from the Houbolt scheme. This numerical instability

probably has its origins at the instant in time when the ramped growth of the endpoint function is terminated, which is just prior to these results. If this is the case then it is significant to note that the remaining schemes seem unaffected. The CD scheme has a very smooth solution free of any such numerical instabilities. Figure 6.69 also shows the over and under prediction of the solutions generated by the Newmark and Wilson-θ schemes respectively, relative to the CD scheme. However, the maximum range of the discrepancy is only of the order of 1%.

Figure 6.70 shows the corresponding results for the solutions generated with $\Delta t = 0.021$ seconds. There is now a slight difference between the solutions generated by the Houbolt and CD schemes, although the numerical instabilities present in Figure 6.69 for the Houbolt scheme are no longer seen. For this time step both the Wilson-θ and the Newmark schemes overpredict the results of the CD method by approximately 0.5% and 0.26% respectively. However, the overprediction is smaller than that for the smaller value of Δt.

Figure 6.71 shows the same trends as established in Figure 6.70, with the discrepancy between the Houbolt and the CD solutions continuing to increase. The overpredictions of the Wilson-θ and the Newmark schemes are now approximately 0.6% and 0.4% respectively. A summary of these results is given in Table 6.15.

Δt (secs.)	CD Value (N)	%Δ CD	%Δ Houbolt	%Δ Wilson-θ	%Δ Newmark
0.001	888600.0	-	0.0	-0.52	0.61
0.021	887350.0	0.14	-0.04	-0.27	-0.27
0.042	885450.0	0.36	-0.19	-0.59	-0.38

Table 6.15 — % Deviations of Schemes from CD with $\Delta t = 0.001$.

Table 6.15 indicates several points of interest. Firstly, the percentage change in the peak tension produced by the CD scheme with the smallest practicable time step of $\Delta t = 0.001$ and the largest possible time step of $\Delta t = 0.042$ is only 0.36%. Secondly, each row of the table shows the percentage change of the three implicit schemes relative to the CD scheme and these demonstrate that the maximum discrepancy is only 0.61%. The value of $\Delta t = 0.042$ has been used as the maximum time step for the previous three figures since it represents the critical time step limit associated with the CD scheme.

Figures 6.72, 6.73, and 6.74 provide comparisons of the three implicit schemes for time steps larger than, and including, $\Delta t = 0.042$. It is immediately apparent that the same relative predictions of the Wilson-θ, Newmark and Houbolt schemes (i.e. that the predicted magnitudes of the solutions descend in that order) are preserved regardless of the size of the time step. Also the peak magnitudes for the Wilson-θ scheme become less uniform as Δt increases. With reference to the previous graphs, it appears that the regularity of the Wilson-θ solutions improve at the extremes of the Δt range considered, but deteriorate for the middle Δt values. Table 6.16 shows the percentage differences of the three implicit schemes relative to the explicit CD solution with $\Delta t = 0.001$.

Δt	%Δ Houbolt	%Δ Wilson-θ	%Δ Newmark
0.042	0.16	-0.25	-0.04
0.15	0.79	0.12	0.64
0.29	1.77	-	0.81

Table 6.16 — % Deviations of Schemes from CD with $\Delta t = 0.001$.

It is evident from Table 6.16 that as Δt increases and approaches the point at which all the schemes collapse, that the undershoot becomes more significant. That is, as Δt increases, the peaks of the solution decrease. It can also be seen that the Houbolt scheme is the most significant underpredictor and this confirms the often cited result that the Houbolt scheme produces the greatest amount of AD of the the three implicit schemes considered. Also note that the last value for the Wilson-θ scheme was too erratic to present. To summarise :

- The CD scheme gives smooth results which remain essentially constant over the whole practical range of Δt.
- For all values of Δt considered, the predicted tension peaks decrease according to the following order, the Wilson-θ, Newmark, Houbolt and CD schemes respectively. The Newmark scheme predictions lay between the predictions of the Wilson-θ and the Houbolt schemes when $\Delta t > 0.021$.
- As Δt increases, the magnitudes predicted by the Wilson-θ scheme improve in consistency, for those values of Δt providing a solution.

6.4.10 Case Study 15: Influence of $\frac{\Delta t}{h}$ Ratio

In this case study the effect of the ratio of $\Delta t/h$ is investigated as it applies to the quantities already examined. The study is undertaken with the weak supposition that results are dependent upon the $\Delta t/h$ ratio rather than the absolute values of Δt and h. Figures 6.75 to 6.82 show the means of the tension peaks and troughs plotted against this ratio for different meshes. Again the irregularities clearly show up as deviations from what are otherwise reasonably linear graphs. These graphs also serve to demonstrate that these quantities are very dependent upon the absolute values of Δt and h, and that they are essentially independent of the $\Delta t/h$ ratio. For dependence upon this ratio to be in evidence, it is expected that the curves for different values of h would be coincident. For example, for a ratio of 0.008 there are three different values of the mean tensions according to the numbers of elements used and this shows that the results are independent of $\Delta t/h$.

Figures 6.83 to 6.86 demonstrate the total CPU time plotted against the $\Delta t/h$ ratio, and again indicate that the results for CPU depend upon the absolute values of Δt and h and not their ratio.

6.4.11 Case Study 16: Direct Comparison of CPU Times

So far all of the CPU results for the four schemes have been plotted independently of one another. Here the CPU time breakdowns for each scheme are plotted on the same graph to enable direct comparison. Note that in all cases the abscissa values associated with the CD scheme have been scaled up by a factor of 10, whereas the CD ordinates have been divided by 10 for most cases.

Figures 6.87 to 6.91 show the total CPU time required by each scheme for different numbers of elements. Of the three implicit schemes the Houbolt method consistently provides the lowest total CPU time. As expected the results for the CD scheme are greater by virtue of the fact that a small value of Δt must be used to ensure stability. As pointed out earlier, the total CPU of the CD scheme can be seen to increase in certain circumstances as Δt increases - this is in contradiction to the general expectation in the trend of the results. This situation occurs as the number of elements are increased. The reason for this is as follows: The Newton-Raphson iterative solver employed in the solution of these non-linear equations, is essentially a first order truncated Taylor Series, see Equation (3.76), which depends upon the value of the step size (Δt in this case) for its accuracy. As Δt increases

the point at which the solution is sought moves further away from the last known solution point and starts approaching the limits of the 'basin of attraction'. As this happens the number of iterations necessary to obtain the solution increases and it is this effect which causes the total CPU time for the CD scheme to start to rise as Δt approaches its limit.

The formulations for the Wilson-θ and the Newmark schemes are in essence very similar, and consequently similar values for the total CPU time would be expected. However the results show that the Wilson-θ scheme always takes slightly longer for execution and, as suggested before, this can be attributed to the extra interpolation necessary for a solution obtained using the Wilson-θ scheme. What is also evident, as expected, is the increase in total CPU time, for all the schemes, with an increase in the number of elements used to model the mooring line.

Results are now presented for the CPU breakdowns described in Case Study 13. Figures 6.92 to 6.96 show the variation of CPU_1 with Δt and for different numbers of elements. Again notice that the results for the CD scheme have been appropriately scaled to fit the graphs. As expected the values of CPU_1 for the CD scheme are much higher than the remaining three implicit schemes, where the results are more or less equal. The values for CPU_1 for the Newmark and the Houbolt methods are so similar that it is hard to distinguish one from the other. These graphs also show that the values of CPU_1, for each of the four schemes, increase almost linearly with the number of elements. This is to be expected since increasing the number of elements will only increase the upper bounds of the loops in the computer code and hence result in a linear increase in the CPU time.

Figures 6.97 to 6.101 illustrate the variations in CPU_2 as a function of Δt and for different numbers of elements. In this case only the abscissa values for the CD scheme have been scaled. Bearing this in mind this shows that CPU_2 for the CD scheme is more comparable with the three remaining schemes, than for either CPU_1 or the total CPU. Whilst examining earlier results for the CD scheme (see Figures 6.63 and 6.64), it was noted that the iterative part of the code, as measured by CPU_2, is responsible for the increase in total CPU as Δt increases. This nonlinear variation in CPU_2 means that at larger values of Δt, the amount of CPU time spent in executing the iterative part of the code dominates and this starts to outweigh the savings derived from using a larger value of Δt. This same trend is also apparent, but to a lesser extent, in the results of the Newmark scheme, although they do not manifest themselves in the graphs of total CPU. For both the Houbolt and the Wilson-θ schemes this trend is not present, where the total CPU

results in both these cases are seen to tend to limiting values. It can also be seen for any one scheme that the value of CPU_2 increases nonlinearly as the number of elements are increased; hence it can be seen that it is the iterative part of the code which generates the nonlinearity in the total CPU times. To summarise:

- As expected the general trend is for decreasing CPU times with increasing values of Δt - except in the case of the CD scheme where an increase in CPU time can result under certain circumstances.
- Total CPU time increases nonlinearly as the number of elements increases; CPU_1 increases linearly, but CPU_2 increases nonlinearly.

6.4.12 Case Study 17: Investigation of Varying θ

Here an investigation of the effect of varying θ in the Wilson-θ scheme is made. Figure 6.102 shows a plot of the tension peaks for increasing values of θ, where θ is greater than 1.37, the value necessary to ensure unconditional stability. Increasing θ seems to have a twofold effect upon the solution:

1. To slightly increase the numerical instabilities present in the peaks.
2. To increase the maximum value of the tension peaks.

Bearing in mind that the Wilson-θ scheme already overpredicts the results given by the other schemes, see Case Study 14, any increase in the overprediction is undesirable. Table 6.17 shows the percentage deviations of the solutions for $\theta =$ 2.0, 2.5 and 3.0 relative to the solution obtained with $\theta = 1.4$, and the percentage deviation of all these solutions relative to the CD scheme solution with $\Delta t = 0.001$.

	$\theta = 1.4$	$\theta = 2.0$	$\theta = 2.5$	$\theta = 3.0$
% Dev. from $\theta = 1.4$	-	-0.17	-0.26	-0.39
% Dev. from CD	-0.46	-0.64	-0.72	-0.86

Table 6.17 — % Deviations with θ.

Figure 6.102 also clearly shows the presence of PE effects and how these change with θ. It is seen that the solution for peak tension gained through the use of the CD scheme introduces very little PE. From Figure 6.70 it can be seen that the

Wilson-θ scheme has introduced a small amount of (negative) PE for $\Delta t = 0.021$ seconds and $\theta = 1.4$. Figure 6.102 therefore shows that the effect of increasing θ beyond the value of 1.4 acts to increase the amount of PE present in the solution. Figure 6.103 shows how the value of θ affects the maximum size of the time step which can be used. This figure illustrates that an optimum value of θ may be defined with respect to the CPU time. In this case it appears to be quite close to the value of $\theta = 1.4$ which is usually selected to ensure unconditional stability. The latter is more precisely obtained with $\theta = 1.37$ but for most purposes this is taken as 1.4. It would therefore seem that the value of $\theta = 1.4$ is the most suitable for several reasons:

1. It ensures the unconditional stability of the scheme.

2. It has a near optimum value in terms of the maximum size of Δt which may be used.

3. Increasing the value of θ increases the overprediction of the results obtained from the Wilson-θ scheme when compared with the results for the CD scheme.

Figures 6.104 to 6.115 illustrate the effect of θ upon the tension peaks and troughs generated. With $\Delta t = 0.001$ the solutions are smooth and regular, and the magnitude of the peaks continually increase as θ increases. The troughs, however, illustrate a slightly different behaviour, in that both the amplitude and PE do not change in a regular manner. With $\Delta t = 0.025$, see Figures 6.106 and 6.107, there is a great increase in the irregularity of the solutions for the peaks and the troughs, although closer examination of these figures reveals that there is a 'regular' change in both the amplitude and the PE of the predicted troughs and peaks. This 'regularity' is lost with further increases in Δt. Some of the solutions for the conditionally stable schemes ($\theta \leq 1.37$) are lost due to time step restrictions. It can be said, as a general comment, that the solutions obtained for the peaks show a degree more regularity than those obtained for the troughs. This is in keeping with previous observation of time histories for peaks and troughs.

Also of interest is the influence of θ upon the CPU times required to generate the solutions. Here the same notation is used as in Case Study 13. The total CPU time shown in Figure 6.116 indicates that there is an optimum value of θ with respect to the solution time. Unfortunately the best that can be said is that the optimum value of θ lies somewhere in the range of $1.6 < \theta < 2.0$. Figure 6.117 indicates that there is virtually no variance of CPU_1 with θ. This is to be expected

since changing the value of θ is not increasing the upper bound on the program loops and the variation displayed is well within the possible 10% variation of CPU times due to the computer system load.

Figure 6.118 shows how CPU_2 varies with θ and it is clearly this component which generates the shape of the total CPU curve. The optimum value of θ with respect to CPU time can therefore be seen to be related to the number of iterations needed for the solution. The increase in total CPU with increases in θ is analogous to the total CPU increase with increasing Δt for the CD scheme. This is because increasing θ is establishing the required solution at a point further away from the last known solution point and this causes an increase in the number of iterations needed for the Newton-Raphson scheme to converge.

6.4.13 Case Study 18: Effects of Different Starting Procedures

In this case study the influence of different starting procedures upon the time history results gained using the Houbolt scheme is examined. It will be recalled from Section 3.6.1 that a truncated Taylor Series (TS) expansion of the displacement which neglects velocity terms, Equation (3.83), is used over the first two time steps of the solution to provide $\underline{U}^1$ and $\underline{U}^2$. These values of displacement, together with $\underline{U}^0$, are enough for the Houbolt scheme to proceed. However, as stated in Bathe(1982, pg 506) : *"it is more accurate to calculate* ${}^{\Delta t}\underline{U}$ *and* ${}^{2\Delta t}\underline{U}$ *by some other means; i.e. we employ special starting procedures. One way of proceeding.....is to use the CD scheme with a fraction of the* Δt *value used for the Houbolt scheme, as the time step".*

Before identifying the different starting procedures adopted it is instructive to define two distinct time step values. As before, let Δt denote the value of the time step which is to be used for most of the solution, except for the first two values over which the starting procedures are defined. The suggestion of Bathe is to subdivide the first two time steps ($2\Delta t$) into a number of smaller time step values which are denoted here as Δt_1. Therefore, for example, if $\Delta t_1 = 0.1\Delta t$ then $2\Delta t = 20\Delta t_1$, that is, the two solution points of interest (Δt and $2\Delta t$) are given by $10\Delta t_1$ and $20\Delta t_1$ respectively. Four different starting methods are now described and compared :

1. A TS is used over the first two time steps ($2\Delta t$) in which the velocity terms are neglected. Thereafter the Houbolt scheme is used to generate the rest of

the solution. That is, a single common time step of Δt is used throughout. This is the method already adopted and will be called the 'usual' procedure.

2. The region of $2\Delta t$ is divided into a number of Δt_1 values. A TS approach, as described in method 1, is then used to obtain the solutions at the first two points, i.e. at Δt_1 and $2\Delta t_1$, and thereafter the Houbolt scheme is used for the remaining Δt_1 values. Then Δt is used for the remainder of the solution.

3. A TS is again used over the first two time steps ($2\Delta t$) with a time step, Δt_1, set to a fraction of the time step (Δt) to be used with the Houbolt scheme for the rest of the solution. After the solution has been obtained for Δt_1 and $2\Delta t_1$, the velocity terms are included in the TS expansion, see Equation (3.83), for generating the remainder of the solution to be obtained with Δt_1. Then Δt is used for the remainder of the solution.

4. The CD scheme is used over the interval $2\Delta t$ with a time step (Δt_1) which is a fraction of that to be used later with the Houbolt scheme.

The values of the time steps used and the CPU time breakdowns for the execution times are shown in Table 6.18. The fifth starting procedure indicated in the table is the solution obtained with the CD scheme where $\Delta t = 0.001$. This is included for comparative purposes.

Starting Proc.	Δt(secs.)	Δt_1(secs.)	CPU_1 (secs.)	CPU_2 (secs.)
1	0.1	0.001	70.93	92.65
2	0.1	0.001	70.04	91.90
3	0.1	0.001	79.14	104.67
4	0.1	0.001	78.33	102.91
5	0.001	-	-	-

Table 6.18 — Δt and CPU for Houbolt Starting Procedures.

The solutions are plotted in Figures 6.119 and 6.120 where it can be seen that there are only two discernible curves representing the four different starting procedures. In order to distinguish them, recourse is made to the original computer output

data files (not presented). It then transpires that the first two starting procedures (1 and 2) are virtually identical to the last two starting procedures (3 and 4). Both sets predict the same maximum and minimum for the tension peaks and troughs, but the second set have a constant amount of PE which displaces them from the first set. There is also a difference between the two groups with regard to CPU_1 and CPU_2, with both CPU values exhibiting an approximate 10% increase for starting procedures 3 and 4 over starting procedures 1 and 2.

From this it can be concluded that the difference between the first two starting procedures is negligible, which implies that there is no difference between starting with the TS which uses Δt and ignores velocity, and starting with the Houbolt scheme which uses Δt_1. It can also be seen that for the second set there is no practical difference between using the TS or the CD method as starting procedures. It can also be concluded from consideration of the relative errors, that the differences between the two sets are also negligible. It would therefore seem that any of the starting procedures considered here can be used to provide an accurate solution to this non-linear problem.

It seems quite clear from these results that the tension time histories are, for all practical purposes, independent of the starting procedure used. This is contrary to the initial hypothesis of Bathe, however, his comments were aimed toward the solution of linear systems of equations. The conclusion would seem to be that the sensitivity to the starting procedures is not a property inherent to nonlinear systems in which iterative techniques have been employed.

Finally an investigation was carried out to see whether the size of Δt_1 has any influence on the results when starting procedure 4 is used. The range of Δt_1 considered was $0.001 \leq \Delta t_1 \leq 0.025$. The solutions generated proved identical. It should be noted here that the maximum value of Δt which could be used when the CD scheme is employed on its own is 0.042 but this value cannot be used in this case. It seems that by coupling two time integration schemes together, as done in this case study, the maximum time step value which can be used is affected.

6.4.14 Case Study 19: Influence of Newmark Parameters

In this case study the influence of varying δ and β in the Newmark scheme, see Equations (3.49) and (3.50), is examined. Firstly the effect of increasing δ is studied. It should be noted that with $\delta = 0.5$ the Newmark scheme introduces no algorithmic damping into the solution, Newmark(1959). Thus increasing δ will

increase the algorithmic damping and hence reduce the predicted maxima and minima of the solution. For the Newmark scheme to be unconditionally stable, it is required that $2\beta \leq \delta \leq 0.5$. In this part of the case study the following is adopted, namely, $2\beta = \delta$. Figure 6.121 shows the variation in the mean of the peaks ($\bar{T}_p$) and the mean of the troughs ($\bar{T}_t$), with δ having the following range $0.5 \leq \delta \leq 1.0$. Note that the results for the troughs have been scaled up by a factor of 5 so that both the results for the peaks and the troughs could be presented on the same graph. It is clear that the increased algorithmic damping affects the $\bar{T}_t$ values more significantly than the $\bar{T}_p$ values. This might be explained as follows: As the mooring line is excited, the stiffness of the line (and hence of the equations of motion) is constantly changing. The stiffness of the equations are at their greatest when at the tension peaks and at its lowest when at the tension troughs. It is known that Time Integration schemes can have different stability properties depending upon the 'stiffness' of the equations being solved, see Park(1975). It is therefore suggested here that the stiffness also affects the amount of AD present in the solution. The conclusion to be drawn from these results is that when the stiffness is high the algorithmic damping introduced has a less significant effect on the solution than for the case when the stiffness is low.

An attempt was also made to study the effect of β when the $2\beta = \delta$ relationship was not maintained. However, no combination of δ, β, and Δt would provide a solution for this case. The conclusion here must be that for this particular nonlinear problem the relationship $2\beta = \delta$ must always be employed. It is also interesting to note that $2\beta = \delta = 0.5$ is almost universally used in the engineering literature even if no explanation is given.

6.4.15 Case Study 20: Inclusion of Sub Surface Buoys (SSBs)

Here the influence of including a Sub Surface Buoy (SSB) at some point along the mooring line is examined. In the present 20 element model, node 14 was used as the location for the SSB. The radius (R_b) of the SSB was gradually increased from 0.0m (obviously the case with no SSB) and the results for the maximum time step, the CPU times and the tension histories were noted. Figure 6.122 shows the variation of the maximum obtainable value of Δt with R_b. It is interesting to note that for the three implicit schemes the presence of the SSB actually improves the stability of the solutions (apart from one spurious point on the Newmark curve). In contrast the stability of the CD scheme is virtually unaffected over the same range of R_b values.

However, although the maximum permissible values of Δt will initially increase with R_b, there exists a value of R_b at which the schemes completely collapses and the equations of motion cannot be integrated even with the smallest practical time step of $\Delta t = 0.001$. These two effects can be explained through the following reasoning :

1. The whole objective in including a SSB along the length of a mooring line is to reduce the maximum tension, or stiffness, which the line develops. Because a slack system (low tension) transmits information more slowly than a taut one, it can be seen that a larger value of Δt can be used in the integration of the equations of motion because the quantities are changing less rapidly.

2. The cause of the total collapse is less clear but it is possible that at certain values of R_b a resonance is set up which causes the collapse of the solution procedure for all Δt. This hypothesis would need to be further tested with numerical experimentation not undertaken here.

Figures 6.123 and 6.124 show the effect of R_b upon the tension time histories for the Houbolt scheme. Increasing the value of R_b is seen to have a nonlinear effect in reducing the peak tensions predicted. For the troughs, apart from the case of $R_b = 1.0$, increasing R_b reduces the tension troughs; therefore the overall effect of including a SSB is to cause a reduction in the mean tension value of the time history, or, a bodily (but not necessarily linear) reduction in the tension values. The case of $R_b = 1.0$ for the troughs demonstrates an increase in the tension and this cannot be explained.

Figures 6.125 and 6.126 indicate the equivalent results for the CD scheme. It will be noted that although the maximum values of Δt have been obtained for the CD scheme for $0.0 \leq R_b \leq 1.7$, for values of $R_b > 0.6$ the solutions exhibit a high degree of nonlinearity and are therefore not included. However for $0.0 \leq R_b \leq 0.6$ exactly the same trends can be identified for the CD scheme as for the Houbolt scheme.

Figures 6.127 and 6.128 show the same results for the Wilson-θ scheme as for the Houbolt scheme, including the 'rogue' behaviour of the trough for $R_b = 1.0$. It is interesting to note that as R_b increases the magnitudes of the peaks and troughs change, but the minor peaks and troughs are preserved in trend, but not in magnitude.

Figures 6.129 and 6.130 show the equivalent results for the Newmark scheme. These results display the same trends as observed for the other schemes.

6.4.16 Case Study 21: Influence of the Convergence Parameter η

As explained in Section 3.5, the Newton-Raphson iterative process is continued at each time step until a certain convergence limit called the segment error function (here denoted by η) is satisfied. This limit is defined in this thesis in terms of a percentage of the unstretched length of each element; for all the data generated in the Case Studies up to now η has always been set to 0.0001%. In this case study an investigation is carried out to assess the influence of altering η upon the following quantities of the tension time history : CPU_1, CPU_2, (see Case Study 13), $\bar{T}_p$, $\bar{T}_t$ and $\bar{T}_m$. The values of η used in this study are 0.0001, 0.001, 0.01, 0.1, 1.0 and 10.0.

As expected the influence of η upon CPU_1 is negligible, or at least within the $\pm 10\%$ variation possible due to system load, since this measures the amount of time spent outside the iterative process. The effect upon CPU_2 is more significant and this is illustrated in Figure 6.131. It can be seen that, as would be expected, CPU_2 decreases with increasing η and rapidly reaches a limiting value, i.e. beyond a value of $\eta = 1\%$, CPU_2 is essentially invariant.

Scheme	$\%\Delta CPU_2$	$\%\Delta\bar{T}_p$	$\%\Delta\bar{T}_t$	$\%\Delta\bar{T}_m$
Houbolt	25.6	-9.4	23.1	-2.5
CD	57.1	-4.5	2.2	-1.8
Wilson-θ	82.7	-2.1	7.0	-0.3
Newmark	22.7	-17.5	-15.4	-19.0

Table 6.19 — The Influence of η upon Output Parameters.

Table 6.19 shows the percentage change in CPU_2, $\bar{T}_p$, $\bar{T}_t$ and $\bar{T}_m$ when the value of η is changed from 0.0001% to 10.0%. The influence of η upon $\bar{T}_p$, $\bar{T}_t$ and $\bar{T}_m$ is shown in Figures 6.132, 6.133 and 6.134 respectively. These figures together with Table 6.19 show an interesting variation in results. For example the Wilson-θ scheme shows a reduction in CPU_2 of 83% when η is changed from 0.0001% to 10.0%, but this change has a minimal effect on the statistics of the tension time

history. The Houbolt scheme shows only a 25% saving in CPU_2, but the change in η causes a relatively large change in the tension statistics. The Newmark scheme exhibits the least CPU_2 saving and demonstrates the most change in the tension statistics. The CD scheme shows the second greatest saving in CPU_2, which is accompanied by only a moderate change in the tension peaks and troughs.

6.5 Benchmark Tests

In many Finite Element (FE) applications, so-called "Benchmark" tests have been developed. These allow new solution developements to be compared with existing and accepted (benchmark) solutions. The latter may be analytical solutions to a particular structural problem (for example) or they maybe well tried and reliable numerical results which have been successfully reproduced by a number of researchers. These then allow an interpretation of the accuracy of the new techniques and would also quickly allow an investigator to identify whether the correct "ballpark" results were being obtained during the software development.

It is the intention of this section of the thesis to suggest a number of benchmark tests to which the results from all dynamic mooring line models should aspire to conform to. As mentioned in Section 6.4.9, of the four time integration schemes considered here, the CD scheme is physically the most appropriate method to use and is to be the preferred method if the small size of the time step can be accommodated. It is also considered reasonable that the benchmark tests should be considered under the headings of the accuracy and the efficiency of the solution. Because of the appropriateness and the consistently regular results generated under all conditions examined in this thesis, it is suggested that the CD scheme be used to generate the "accurate" benchmarks results.

In Section 6.4.11 the Houbolt scheme was shown to consistently provide the most efficient solutions, and it is therefore proposed that this scheme be used to generate the "efficiency" benchmark results. These tests, and an indication of which scheme should be used to derive them, are shown in Table 6.22.

Benchmark tests	Accuracy (CD)	Efficiency (Houbolt)
1.Decay tests	•	
2.Simulation time effects	•	
3."Regularity" of solution	•	
4.Max. value of Δt		•
5.CPU times		•

Table 6.20 — Benchmark Tests.

The results should be presented for all five tests for both schemes although the bulletpoints indicate which are the preferred schemes for each test. The benchmarks tests are to be obtained for a standard set of physical parameters. The actual values would not be of importance as long as they remained constant for the generation of the benchmark results and for each comparative study. Therefore, the values established in Table 6.1 would form a convenient set of starting values. The suggested benchmark tests are now detailed further.

6.5.1 Decay Tests

Here a small software program can be used to calculate the various statistical quantities of the solution history between certain pre-specified limits in the solution time. In this case the mean of the solution history is to calculated for the last 100 seconds of a 350 second simulation time. The means are to be calculated for two cases of endpoint excitation:

1. No endpoint excitation.
2. Endpoint excitation which is allowed to grow and decay out before 250 seconds.

More details are given in Case Studies 1 and 2 of Section 6.3. Since the mean is calculated for the last 100 seconds of a 350 second simulation, then in both the cases indicated above it will be seen that the mean is calculated for the case of zero endpoint excitation.

6.5.2 Influence of Length of Simulation Time

If the endpoint excitation being used is regular, then it is desirable to determine the shortest possible time which may be considered representative of much longer simulations. The details of this are given in Case Study 3 of Section 6.3. Essentially a sinusoidal endpoint function is defined and allowed to run for two simulation times, one short and one long. The solution history - maximum mooring line tension in this case - will therefore be sinusoidal. The means of the last five occuring peaks and troughs, as well as the overall solution mean, are calculated for the two solution times. It must be ensured that the effects of any excitation ramping (if used) have decayed before the means are calculated.

6.5.3 "Regularity" of Solution History

This is a more subjective criteria since there can be no clear measure of regularity other than a subjective visual inspection. The results obtained from the new scheme/method should, for a perfect sinusoidal excitation, generate a perfect sinusoidal solution, such as illustrated, for example, in Figures 6.29 and 6.30. The extent of the irregularities (see, for example, Figure 6.39 and 6.40) can then be assessed relative to the perfect sinusoidal solution. As discussed in Section 6.5.2 the following statistics, the mean of the troughs, means of peaks and the overall mean, can be calculated for the last five peaks of the solution history. This can also be done for the new scheme/method and the results compared.

6.5.4 Maximum Permissible Value of Δt

Although the CD scheme is limited by a maximum value of Δt, the explicit nature of this scheme means that this must be very small in comparison with the values of Δt used with implicit schemes. Therefore it is proposed that the value of the maximum permissible Δt is to be taken from the results obtained through the use of the Houbolt scheme since of the schemes considered in this thesis, these provide the best results, see Figures 6.1 to 6.4. However, comparisons between the implementations of different schemes/methods are difficult to make on the basis of this benchmark. The reason for this is thus: Although a scheme may successfully integrate the equations of motion for a large value of Δt, the results might be unacceptably irregular - see Section 6.5.3. A different scheme/method might also integrate successfully but produce a more regular solution. Therefore it is the assessment of the regularity of the solution for different values of Δt which forms the subjective assessment involved with this benchmark test.

6.5.5 CPU Times

Again, because of the relative efficiency of the Houbolt scheme, it is proposed to use the results gained from it in this benchmark description. Here a common value of Δt is used for a simulation time of, say, 250 seconds, for both the Houbolt scheme and the new scheme/method. A comparison of the two CPU values will then give a assessment of the relative efficiency of the new scheme/method.

6.5.6 Benchmark Sheet

The indicated series of benchmark tests are now presented in the tabular form given by Table 6.20. The benchmark test numbers are given in Table 6.20.

Benchmark Test	Notes	CD Scheme	Houbolt Scheme	New Scheme
1	1. No Endpoint Excitation	0.00001%	0.0004%	
	2. Decayed Excitation	0.06%	0.06%	
2	$T_1 = 350$s., $T_2 = 1000$s.	0.0009%	0.0008%	
3	See indicated Figures:	6.25 to 6.34	6.15 to 6.24	
	$\Delta\bar{T}_p$	0.175%	1.113%	
	$\Delta\bar{T}_t$	-1.233%	-6.725%	
4	$A = 10$m, $\omega = 0.2$rads.	0.0435s.	0.4s.	
5	$\Delta t = 0.001$ secs.	2208s.	3233s.	
	$\Delta t = 0.001$ secs.	-	21.46s.	

Table 6.21 — Benchmark Test Values

The terms $\Delta\bar{T}_p$ and $\Delta\bar{T}_t$ are the percentage changes in the means of the peaks and troughs relative to these values when obtained from the CD scheme with $\Delta t = 0.001$. The percentages indicated in Table 6.21 are to be considered as positive or negative error bounds.

6.6 Summary

To bring together all the different aspects of the analysis studied in this chapter a brief summary of the main points considered is stated prior to summarising the findings. The principal aspects studied were:

- The reduction of the 3D equations of Motion to a 2D form. These were then compared with other published sets of equations to highlight any differences.

- A short section was presented which derives the limiting results for the dynamic models (i.e. results with no endpoint excitation, or with decayed endpoint excitation) and then compares these with static results.

- Then a major section of work is presented in which results obtained from the four different time integration schemes are compared so that an assessment of which scheme is more appropriate for the investigation of mooring dynamics can be made.

The last section presents many results from the numerical experimentation. From these, the main points of interest have been distilled and are presented below :

1. For all practical purposes (and certainly within the limits of engineering accuracy), it can be said that if there is no endpoint excitation (or even if this has been allowed to decay out), then all the schemes predict a maximum tension which is identical to that predicted by the static numerical procedure described in Chapter 2.

2. Generally it can be said that, as expected, increasing the amplitude and frequency of the endpoint excitation will cause a reduction in the size of the maximum permissible value of Δt which can be used to integrate the equations of motion.

3. The growth factor used to ramp the endpoint excitation does not have a significant effect upon the final solution; therefore the excitation can be ramped up quite quickly.

4. The maximum value of Δt which can be used, decreases as the mesh size decreases.

5. Certain combinations of Δt and h will produce irregular time histories, whilst other combinations will produce smooth results. This does not depend upon the ratio of $\Delta t/h$ but rather upon the absolute values of Δt and h. Of the four schemes, for the ranges of Δt and h considered, the following generalities are observed:

    - The CD scheme produces very regular and smooth solutions.

- The Houbolt scheme also gives smooth solutions over most of the range of Δt and h but can generate irregularities at the larger values of Δt and h values.

- The Newmark and Wilson-θ schemes are notably worse, generating irregular solutions at lower values of Δt and h than for the Houbolt scheme. Also the solutions which are regular overpredicted the 'accurate' solution gained from the CD scheme when $\Delta t = 0.001$ seconds.

6. Generally the total CPU time needed for execution decreases nonlinearly with increasing values of Δt. There is an optimum value of Δt which can be identified for the CD scheme, and this is less than the maximum value.

7. Of the three implicit schemes, the Houbolt scheme always provides the closest approximation to the 'accurate' solution (from the CD scheme). The other two implicit schemes show relatively greater error.

8. A value of $\theta = 1.4$ used with the Wilson-θ scheme, represents a near optimum value with regard to both numerical accuracy and stability, although not with respect to CPU times.

9. Four different starting procedures are used with the Houbolt scheme to see if this will significantly affect the resulting time histories. All predict the same peak tensions but two have a slight, but constant, amount of Period Elongation which can be considered negligible. Therefore it seems that the resulting solutions are essentially independent of the starting procedure used, at least when the Houbolt scheme is used.

10. When considering the Newmark scheme a solution cannot be obtained when the minimum condition for unconditional stability ($2\beta = \delta$) is violated.

11. The presence of a Sub Surface Buoy reduces the maximum tension and, up to a point, increases the size of the maximum time step which can be used. Beyond this point a solution cannot be obtained for any value of the time step.

12. It seems that the value of the segment error function, η, can have a profound effect upon the solutions gained from different schemes. In particular the Newmark and the Houbolt schemes show relatively little

saving of CPU_2, but a large degradation in the statistics of the the tension time histories when η is changed from 0.0001% to 10.0%. The CPU_2 saving of the Wilson-θ scheme is significant with relatively little change in the predicted values; the same is true but to a lesser extent for the CD scheme.

As a final conclusion and to answer the main aim of this study, it would appear that if the time step restriction (Δt_{cr}) imposed on the CD scheme cannot be accommodated, then of the three remaining implicit schemes, the Houbolt method is to be preferred. If it is necessary to use a value of Δt which allows the inclusion of the CD scheme for consideration, then the CD scheme should be used in preference to the three implicit methods. In general, however, a time step which is larger than Δt_{cr} is usually employed.

CHAPTER 7

3D Dynamic Results

7.1 Introduction

The preceding chapter gave a detailed numerical comparison of four of the most commonly used time integration schemes (namely the Houbolt, Central Difference, Wilson-θ and Newmark schemes) as applied to the solution of the 2D equations of motion for a mooring line structure. The conclusion drawn from this comparative study is that the Houbolt and CD schemes have a number of advantages over the Wilson-θ and Newmark methods. Furthermore, the ability of the Houbolt scheme to generate 'regular' time histories at much larger time steps than the critical time step limit associated with the CD scheme, makes the former method more attractive to use. With this justification of the appropriateness of the Houbolt scheme, it is thus used to obtain the solution for the 3D equations of motion of a mooring line. This chapter describes a series of studies which examine various aspects of the results generated by a 3D mooring line model starting with a validation of the 3D model along similar lines to that undertaken in the beginning of Chapter 6.

Often in this chapter reference is made to the 3D model being run 'in-plane'. This means that the amplitudes and frequencies specified in the global x and y directions are equal and hence the mooring line is restricted to move in the vertical plane defined by the anchor and the line endpoint. Running the 3D model in-plane allows direct comparison with results generated from the 2D model which utilises the Houbolt scheme.

7.2 3D Mooring Line Results

Unless otherwise stated, all the values used to run the dynamic model are given in Table 6.1. As before, these values are maintained as constant unless they are being systematically varied in one of the case studies.

Out of plane results are generated and compared with those of McNamara(1993, Figure 7.0). The static parameters are shown in Table 6.1 and the dynamic parameters in Table 7.0A:

Parameter	3D o.p.v.
Excitation amp. in x	7.07107m
Excitation amp. in y	7.07107m
Excitation amp. in z	0.0m
Excitation freq. in x	$\frac{\pi}{10}$
Excitation freq. in y	$\frac{\pi}{10}$
Excitation freq. in z	0.0
Excitation phase in x	0.0
Excitation phase in y	$\frac{\pi}{2}$
Excitation phase in z	0.0

Table 7.0A - Dynamic Excitation Values

The results of the comparison are shown in Table 7.0B:

	Present Method	McNamara(1993)	% Difference
	20 Elements	FLEXCOM-3D (90E)	
Dynamic	717.0kN	664.78kN	7.85%

Table 7.0B - Benchmark Comparison

The difference in these results is comparable to the difference indicated in Table 6.0 for the in plane situation. This indicates that the present method appears to be consistent, in the sense that the differences in the results remain very similar for the two situations considered.

Validation of the 3D Model

Initially the 3D model is run with no endpoint excitation. Consequently the mean of the tension time history ($\bar{T}_m$) is expected to be close to the maximum static value T_s. It is found that $T_s = 495337$N and that $\bar{T}_m(0 - 350 \text{ seconds}) = \bar{T}_m(133 - 350 \text{ seconds}) = 495337$N. This demonstrates the accuracy of the 3D solution technique for the case of no endpoint excitation. This also shows close comparison with the results in Table 6.2.

As in Case Study 2 of Section 6.3, a regular in-plane sinusoidal endpoint exci-

tation is defined which is allowed to grow and decay so that there is no excitation after 250 seconds. The resulting mean for the last 100 seconds of the simulation is $\bar{T}_m(250-350) = 495343$N. This indicates that the numerical transients die away much more readily for the 3D solution than for the same results generated with the 2D scheme, see Table 6.3.

By running the 3D program in-plane a direct comparison with the 2D model can be made. A sinusoidal endpoint excitation is defined, thus allowing the calculation of the means of the solution peaks ($\bar{T}_p$) and troughs ($\bar{T}_t$), as well as the overall mean($\bar{T}_m$) in addition to CPU_1 and CPU_2 (see Case Study 13 of Chapter 6 for the definitions of CPU_1 and CPU_2). The percentage differences between the 2D and 3D solutions are calculated with respect to the 2D results, and these are illustrated in Figures 7.1 and 7.2. It can be seen that the differences in the tension results are, from an engineering point of view, negligible. However the differences in the CPU times are very much more significant. The 3D version requires approximately twice the amount of CPU_1 time and 2.5 times the amount of CPU_2 time than required in the 2D model.

Next the effect of out-of-plane motions is investigated. This is done by prescribing the endpoint excitation to be at 90° to the static equilibrium plane of the mooring line. This is achieved by setting the amplitudes in the global x and y directions to be equal, but setting the phase of the y component to be $\pi/2$. Table 7.1 summarises the overall means, $\bar{T}_m$, obtained with different forms for the endpoint excitation and over different parts of the simulation time:

The term $\%\Delta T$ denotes the percentage change in the overall mean tension ($\bar{T}_m$) from the static value T_s. Again it can be clearly seen that the results show that the means of the dynamic results as indicated in Table 7.1 are essentially the same as the maximum static tension T_s.

Time [secs.]	$\bar{T}_m$[N]	$\%\Delta T(T_s = 495337)$[N]	Motion
0-250	498066	-0.55	Sinusoidal only
133-250	498463	-0.63	Sinusoidal only
0-350	496637	-0.26	Sinusoidal growth and decay
250-350	405339	-0.0004	Sinusoidal growth and decay

Table 7.1 — $\bar{T}_m$ for Out of Plane Motions with Different Excitations.

The results of this case study can be summarised thus:

- The results (tension means) for the 3D problem when run in-plane compare very closely with the corresponding 2D results.
- CPU times are at least twice as great for the 3D in-plane model as for the 2D model.
- The results derived from running the 3D model out of plane are essentially the same as the static result T_s.

7.2.1 Brief Parametric Investigation of 3D Model

Here a brief parametric investigation is carried out along lines similar to the static parametric study undertaken in Chapter 2.

Variation of Maximum Δt

The first topic of interest is identification of the maximum time step which can be used with the 3D Houbolt scheme. The results shown in Figure 7.3 are generated for 3 cases and present the maximum attainable value of Δt as a function of the amplitude of the endpoint excitation. The 3D scheme is run with both in-plane and circular excitation functions, where the results for the 2D scheme, run under the same conditions, are also included for comparison. Figure 7.3 shows that there is little difference between the results of the 2D model and the 3D in-plane model - as would be expected. However, when the 3D model is run with a circular endpoint excitation function in the horizontal plane the maximum value of Δt which can be used increases. It can be shown that the distance traversed in one time step for the in-plane motion is greater than the distance moved in one time step for circular motion, hence the maximum attainable values of Δt are greater for this case than for the in-plane case.

Normal and Tangential Drag Coefficients

Next an investigation into the influence of the normal and tangential drag coefficients, Cd_n and Cd_t respectively, upon the tension time history is carried out. The range of Cd_n considered is $0.3 < Cd_n < 3.0$ and it is assumed that Cd_t can be calculated as 2% of the Cd_n value, see Berteaux(1976). A sinusoidal in-plane excitation is prescribed and the means of the peaks $\bar{T}_p$, troughs $\bar{T}_t$ and the overall mean, $\bar{T}_m$, are calculated. These values are first established with a series of Cd_n values where the Cd_t values have been set to zero. The means are

then established with both Cd_n and Cd_t assigned non-zero values; the percentage differences in the means are then calculated relative to the case with no tangential drag. The results are shown in Figure 7.4. This figure shows that the inclusion of tangential drag has a negligible influence on $\bar{T}_m$, a slightly larger influence upon $\bar{T}_p$ and causes the maximum differences in $\bar{T}_t$. It can be seen that the maximum differences occur for a range of Cd_n of approximately $1.2 < Cd_n < 2.5$. The differences for values of Cd_n outside this range are seen not to be as significant.

The influence of Cd_n and Cd_t upon the peak and trough tension time histories are shown in Figures 7.5 and 7.6. These figures indicate that increasing the value of Cd_n without limit starts to have a detrimental effect upon the solution. In particular with $Cd_n = 3.0$ the solution for both the peaks and troughs shows an increasing amount of irregularity, compared to the solution with $Cd_n = 1.65$, say. These figures also show a significant decrease in the amplitudes of the peak and trough tension values as Cd_n is increased. Relative to the tension values with $Cd_n = 1.65$ there is a 10% (57%) increase in the peaks (troughs) when $Cd_n = 0.3$ and a 38% (117%) decrease in the peaks (troughs) when $Cd_n = 3.0$.

A solution cannot be obtained with $Cd_n = Cd_t = 0$; this means that physical damping must be present to stabilise the solution.

Normal and Tangential Added Mass Coefficients

A similar investigation is now carried out into the influence of the normal and tangential added mass coefficients, Ca_n and Ca_t. The range of Ca_n which is considered is $0.0 \leq Ca_n \leq 3.0$ and Ca_t is calculated as being 16% of the Ca_n values. This value is a little higher than the value of 12.5% used in van den Boom(1984), but the percentage used here is still considered representative. As with the drag investigation, $\bar{T}_p$, $\bar{T}_t$ and $\bar{T}_m$ are established for the range of Ca_n values indicated but with tangential added mass neglected; then the values are re-calculated with both normal and tangential added mass coefficients and the percentage differences relative to the values with Ca_n only are calculated. The differences are plotted in Figure 7.7 and it is clearly seen that tangential added mass has a negligible influence upon the tension means. The percentage changes in $\bar{T}_p$, $\bar{T}_t$ and $\bar{T}_m$ when Ca_n is changed from 0.0 to 3.0 are $-1.8\%, -4.53\%$ and -0.85% respectively. Therefore it can be seen that increasing Ca_n acts to increase the amplitude of the tension time history.

Influence of Line Diameter, Young's Modulus and Weight/m

Now the influence of three major line parameters are investigated. These are the line diameter, D, the Young's modulus, E, and the weight per metre of the line material. It is expected that increasing any of these parameters will result in an increase in the amplitude of the resulting tension history. The results are shown in Figures 7.8, 7.9 and 7.10 and they show that the initial expectation is broadly confirmed.

Figure 7.8 shows the change in $\bar{T}_p$ and $\bar{T}_t$ as the mooring line diameter is increased. The diameter increase is expressed as a percentage of the reference diameter which is 0.07148m. The trend is almost, but not quite, linear; the deviation is caused by an alteration in the nonlinear drag forces as the line diameter changes. It is also seen that increasing the diameter increases the amplitude of the solution, that is the tension peaks increase whilst the tension troughs decrease.

Figure 7.9 shows the effect of increasing the stiffness (i.e. Young's modulus E) of the line material, not only upon $\bar{T}_p$ and $\bar{T}_t$ but also upon the maximum attainable value of Δt. Note that the values on the abscissa of Figure 7.9 refer to the exponent of E, i.e. this is 10 for the value of E given on Table 6.1. As with a change in the line diameter, increasing E increases the amplitudes of the peaks and troughs of the tension history. However, there is a limiting value of E where the values of $\bar{T}_p$ and $\bar{T}_t$ remain essentially constant as E is further increased. It can also be seen that increasing E acts to decrease the maximum attainable value of Δt. With a stiff set of equations of motion (corresponding to large value of E) information is transmitted more rapidly along the line and therefore a smaller time step is necessary to adequately represent the changes occuring. Slack systems (corresponding to low values of E) transmit changes much more slowly and therefore larger time steps can be used for the integration of the equations of motion. As with $\bar{T}_p$ and $\bar{T}_t$, a limiting value of E can be identified beyond which Δt remains essentially constant - this limit is very close to the limit to achieve constant values of $\bar{T}_p$ and $\bar{T}_t$.

Figure 7.10 shows the changes in $\bar{T}_p$ and $\bar{T}_t$ as the weight per metre increases. Over the lower portion of the graph both $\bar{T}_p$ and $\bar{T}_t$ increase more or less linearly. After a multiplier of approximately 6, the curves become more irregular but the overall trend is still increasing. The point to note is that both $\bar{T}_p$ and $\bar{T}_t$ are increasing which means that increasing the weight per metre increases the peak

tension which can be expected as well as increasing the troughs - in contrast to Figure 7.8 where the troughs decrease.

The results for this case study can be summarised thus:

- The maximum value of Δt which can be used with the 3D in-plane and the 2D models is roughly the same. Elliptical endpoint motions for the 3D model increases the maximum value of Δt which can be used.
- The inclusion of tangential drag and tangential added mass forces have a negligible influence upon the results.
- The correct selection of the normal drag coefficient, Cd_n, is imperative to ensure accurate values of the peak and trough tension.
- The exclusion of drag forces leads to the breakdown of the solution.
- An 'optimum' value of Cd_n may be identified from the point of view of the numerical irregularities introduced into the solution time histories.
- The inclusion of Ca_n has a marginal influence upon the results.
- Increasing line diameter alone, increases the amplitudes of the solution in a nearly linear fashion.
- Increasing the weight per metre alone, increases both the peak and trough means in a nearly linear fashion.
- A 'critical' value of E can be identified beyond which the values of $\bar{T}_p$, $\bar{T}_t$ and the maximum value of Δt remain essentially constant.

7.2.2 Dynamic Tension Amplification Factors

In this case study one of the more directly relevant quantities obtainable from a dynamic analysis, the dynamic tension amplification (DTA) factor, is derived. This is then used to show how mooring line dynamics are affected by different input parameters. The DTA is usually defined as

"The ratio of the maximum dynamic tension to the maximum static tension",

and hence is used to measure the increase (or amplification) of the static tension value caused by the inclusion of dynamic effects in the model.

Some discussion of the reasons for calculating the DTA in this fashion is necessary before considering the results. The maximum dynamic tension can be easily obtained from the tension time history of a dynamic simulation. As long as it is clear that this is a true maximum and not one introduced by the numerical irregularities already discussed in Chapter 6, or by the process of nodal grounding or lifting to be considered in Chapter 8, then there is no problem. The point of discussion arises in the choice of which value of static tension is to be used as the divisor in the calculation of the DTA. A slightly better definition of the DTA should read thus:

"The ratio of the dynamic tension at any point in the solution time, to the static tension at that point".

The introduction of this DTA definition leads directly to the idea of a time history of DTAs. However, the work involved in calculating the static tension at each point in time makes this an infeasible definition. It is, however, the strictly correct definition since from the DTA time history it is possible to obtain the maximum DTA. This maximum would not necessarily be the same as the DTA calculated from the first definition. Despite this, the first definition of the DTA is a more practical one, however a problem arises in the determination of the maximum static value. From the point of view of the theoretical model if the endpoint excitation is defined as a simple sinusoid, then the maximum excursion of the line is given as

$$(x, y, z)_e = \left[(x_o + A_x), (y_o + A_y), (z_o + A_z)\right]. \tag{7.1}$$

The subscript e is to represent the point of maximum excursion, the subscript o indicates the original equilibrium position of the line structure and A_x, A_y and A_z represent the amplitudes of the sinusoidal endpoint excitation in the global x, y and z directions respectively. Thus for a simple endpoint excitation the maximum static tension can be calculated at $(x, y, z)_e$ and the DTA values obtained without a problem. The real problem lies in the calculation of the maximum static tension when the endpoint excitation is defined as the sum of two or more sinusoids. If, for example, two sinusoidal components were to be defined in the surge direction (i.e. in the plane of the mooring line), one a low frequency (LF) sinusoid and the other a high frequency (HF) component, then, unless the HF is an exact multiple of the LF, the maximum excursion will not occur at the sum of these two amplitudes. The

problem is further compounded when more than two components are introduced and excitation in the vertical direction is considered. At this point it can be seen precisely how difficult the calculation of the maximum static tension can be and how it is important to appreciate how the DTA is to be calculated.

To remain consistent with the literature the point of maximum excursion is defined as the sum of the amplitudes of each component in each direction, and hence the endpoint position at which the static tension is calculated is given by

$$(x, y, z)_e = \left[\left(x_o + \sum_{i=1}^{n_c} A_{xi}\right), \left(y_o + \sum_{i=1}^{n_c} A_{yi}\right), \left(z_o + \sum_{i=1}^{n_c} A_{zi}\right)\right], \tag{7.2}$$

where n_c is the number of components used to define the endpoint motion. Although this excursion point may never be reached because of the different frequencies and phasings of the components, it represents the maximum theoretically attainable displacement of the endpoint. The maximum static tension at this point is denoted by T_o^+ and the static tension at the original equilibrium position is denoted by T_o.

Given the potential difficulty of obtaining T_o^+ and the inherent possibility of then misunderstanding how a given DTA is calculated, it would seem that there is a strong argument for using two DTA values during the design and construction phases of a moored floating structure. During the design phase it would be easy to establish a value for T_o once the length and material type for the mooring line have been determined, as well as the operating water depth. This value can then be used in the calculation of DTA values for different endpoint excitations whether these be defined theoretically or from a time series of fairleader motions. Thus it would be straight forward to see under which conditions the largest (worst) values of the DTA would be obtained. In terms of the construction of the mooring line, T_o^+ can be calculated according to Equation (7.2) for the conditions which produced the worst DTA during the design phase, and this can be used to establish a 'construction' DTA.

By taking the tensions at the peaks and the troughs of the solutions these can be used to define peak and trough DTA values. These prove useful in studying the results of the simulations. Figures 7.11 and 7.12 show the changes in the peak and trough DTA values when the amplitude and frequency of the endpoint excitation is varied. As expected the largest dynamic tension (and hence DTA values) arise with the greatest endpoint amplitude (a_i) and frequency (ω_i). Except for one spurious

point in Figure 7.12 the same trends are observed regardless of the values of a_i and ω_i. It is interesting to note in Figure 7.12 the decrease in the DTA values at higher values of ω_i and how this decrease becomes more prominent at larger values of a_i. This shows that the worst dynamic tensions cannot be assumed to occur when the largest excitation amplitudes and frequencies are used simultaneously. The maximum DTA can be seen to occur with the largest amplitude of excitation, but in general the DTA will have to be calculated for a wide range of possible excitation frequencies, so that the maximum may be correctly identified.

Figures 7.13 and 7.14 show the effect of pre-tension (i.e. T_o) upon the peak and trough DTA values for a given value of a_i. These figures show that, contrary to expectations, slack lines can develop DTA values which are comparable to those developed at larger values of T_o. From Figure 7.14 where the troughs in the DTA values can again be identified, it can be seen that the effect of increasing the pre-tension is to move the troughs towards the lower end of the frequency range considered. A similar, although not as distinct, trend can be identified in Figure 7.13 for the peak DTA values.

Figures 7.15, 7.16, 7.17 and 7.18 show the peak and trough DTA values for four directions of motion, i.e. in surge (in-plane), sway (90° out-of-plane), heave (vertical) and axial motion. The last direction is defined as being tangential to the orientation of the top element in the line when at the equilibrium position. An initial glance at the four figures indicates that the DTA values decrease in the following order of motions: axial, heave, surge and sway. Apart from a couple of spurious results in Figure 7.18, the effects of pre-tension and increasing ω_i are as previously identified. Table 7.2 gives a brief summary of the peak DTA values at different frequencies for the middle of the three pre-tension values. This table clearly shows the negligible effect which sway motion has upon the dynamic tension and this provides a strong justification for developing only 2D mooring line models to be used to analyse deep water moorings.

ω_i (rads.)	Surge	Sway	Heave	Axial
0.3	1.287	1.002	1.504	2.027
1.05	1.885	1.061	2.382	3.257
1.8	1.993	1.028	2.655	3.638

Table 7.2 — Peak DTA Values for Selected Frequencies.

In contrast, the effect of axial motion can be seen to be very significant in magnifying the static value of the tension. Remembering that axial motion must, by definition, be composed of the three axial components, it follows that pure heave has the largest influence upon the DTA values.

Another important concept which needs to be introduced here, and that is the definition of safety factors (SF). In Macdonald(1984) mooring line SFs are defined for 5 operating conditions; these definitions are reproduced in the table below:

Case	Condition	SF
1	Operating	3.0
2	Damaged operating	2.0
3	Survival	2.0
4	Damaged survival	1.4
5	Damaged survival(c.p.)	2.0

Table 7.3 — Mooring Line Safety Factors - After Macdonald(1984)

Cases 1 and 3 are for the intact mooring system, cases 2, 4 and 5 refer to the mooring system after the failure of one line and case 5 is intended for vessels operating in close proximity to other installations. It will be seen that the SFs of Table 7.3 are exceeded in many cases by the DTA values of Table 7.2, and this serves to highlight the important difference between the two concepts. In Macdonald(1984), the SF is defined as:

"mooring line breaking strength over the maximum tension."

Or,

$$\mathrm{SF} = \frac{\mathrm{BS}}{T_0^+}, \tag{7.3}$$

with,

$$\mathrm{BS} = ID^2(44.0 - 0.08D) \tag{7.4}$$

where

$D =$ Mooring chain diameter in mm,

$I =$ 1.4 - chain grade U2,

2.0 - chain grade UB,

2.15 - oil rig quality,

2.8 - chain grade 4.

The above definitions apply for mooring chain only and not for wire rope. It is not made clear in Macdonald(1984) whether the maximum tension defined above is the maximum dynamic tension, the maximum static tension (T_0) at the original equilibrium position or the maximum static tension (T_0^+) at the position of maximum excursion. From the context of the paper it is assumed to be T_0^+, particularly in the light of conclusion 5.2.a where it is suggested that work on the dynamic aspect of mooring lines needs to be carried out.

In the present analysis $D = 71.48$mm, therefore BS becomes

$$\text{BS} = 195596I. \tag{7.5}$$

If it is assumed that oil rig quality chain is used, then $I = 2.15$ and hence BS= 420531N. With reference to Figure 7.11, the value of T_0^+ used to define the DTA values for an excitation amplitude of 10m is 520817N, and hence the SF according to Equation (7.5) is 1.24 - much lower than the DTA values associated with this excitation amplitude, namely in the range 1.85 to 3.0. Using selected results from Figure 7.11, Table 7.4 gives a more comprehensive comparison between DTA values and safety factors for different values of T_0^+.

Amp.[m]	T_0^+[N]	SF	ω_i[rads/s.]	DTA
2.0	500048.0	1.19	0.6	1.123
			1.2	1.291
			1.8	1.362
6.0	509953.0	1.213	0.6	1.659
			1.2	1.933
			1.8	1.993
10.0	520817.0	1.24	0.6	2.367
			1.2	2.632
			1.8	3.014

Table 7.4 — Comparisons of DTA Values and SFs

It is clear from this table that the SFs are much lower than the DTA values, thus underlying the importance of distinguishing between the two definitions.

The main points can be summarised thus:

- A clear understanding of which static value is used in the calculation of the DTA values is needed. Due to the possible confusion which may arise it is suggested that T_o should be used for the design comparisons.
- DTA increases with increasing endpoint amplitude, but the greatest DTA value does not occur for the largest endpoint frequency.
- The order for ranking the importance of the influence of the direction of excitation upon the dynamic tensions is axial, heave, surge and sway.
- An important distinction between the safety factors and the DTA factors needs to be made, since they measure different quantities.

7.2.3 Dynamic Line Geometry

Figures 7.19, 7.20 and 7.21 show the mooring line geometries for pure surge, heave and sway respectively. In each case the geometries are calculated for four points during one period of excitation after the start up transients have died away. The points are:

1. At the endpoint equilibrium position.
2. At 100% of the endpoint amplitude.
3. Again at the endpoint equilibrium position.
4. At -100% of the endpoint amplitude.

Figures 7.19 and 7.20 show a very interesting feature near the anchor end of the line, and that is apparent geometric discontinuities. Closer inspection shows these to occur when the endpoint is returning from its point of maximum excursion and tending towards the point of minimum excursion. Although the majority of the geometry behaves in an expected manner, the discontinuities are redolent of what happens if compression is applied to a series of links. Hence it can be concluded that this is what is happening for this portion of the geometry. This is

in violation of the original assumptions used in the derivation of the lumped mass method, in particular the assumption that the elements will not support compression. However, this does not appear to cause the invalidation of the method, but an awareness that the results are subject to this effect is needed. The whole question of grounding or lifting of the elements from the seabed is further investigated in Chapter 8.

Figure 7.21 shows the geometry of the mooring line in the horizontal plane for one sway cycle. Even graphically it can be seen that the same amplitude of endpoint excitation used for sway as for surge and heave produces much less variation in line geometry. This confirms the markedly lower DTA values obtained for sway in the previous case study.

Figure 7.22 illustrates the variations in the dynamic tension time history for surge, sway and heave for the same cycle for which the line geometries have been produced in Figures 7.19 and 7.20. The most obvious point to note is the clear asymmetry of the tension time history for surge and heave. This asymmetry reflects the discontinuous geometry of the mooring line near the seabed as previously identified, and the the negative tension confirms that compression is occuring in the line. However these irregularities in geometry and tension histories are not seen to occur for combinations of a_i and ω_i which produce less rapid changes in the geometry. Therefore for any given situation which is to be analysed with this method, critical combinations of a_i and ω_i should be identified at which such irregularities start to occur. This is only an important consideration if the total tension time history needs to be known. If the peak values only are required then this method can still be used because the geometries show no signs of irregularities around the point of maximum excursion and the tension time history is regular.

The main points arising from this study are:

- Large values of excitation amplitude and frequency can produce geometric discontinuities in the mooring line near the seabed.
- The tension history is significantly affected by the geometric discontinuities, but it is thought that the peak values are unaffected.

7.2.4 High and Low Frequency Excitations

In this case study combinations of low frequency (LF) and high frequency (HF) endpoint excitations are analysed by means of calculating the DTA values and the

energy expended during one cycle of excitation. The reason behind an analysis of this kind is that it gives an insight into the effect of LF motions in the horizontal plane (surge and sway) when they are coupled with HF heave motions. The former is intended to simulate the slow drift oscillation of a vessel induced by the effects of a wave train, whilst the latter is intended to simulate the HF heave motion induced by waves. Figures 7.23 and 7.24 illustrate the excursion of the endpoint (in metres) when pure sinusoidal motion is applied to give LF surge and HF heave respectively.

Figure 7.25 shows the complete tension time history for HF heave motion only. As an aside, this figure illustrates two points: (a) Why the complete tension time histories are not used for the graphical comparisons presented in Chapter 6, and (b) the near symmetry of the tension history when the combination of a_i and ω_i is not enough to produce geometric irregularities. Figure 7.26 shows the effect of a combined combined LF surge and HF heave motion upon the tension time history. Both components are clearly visible. Figures 7.27 and 7.28 further illustrate the tension time histories obtained for combinations of LF and HF heave.

Table 7.5 shows more useful quantities for comparative purposes.

Motion	Energy (150-200 secs.)	DTA
1. LF Surge	4.85641×10^{12}	1.373
2. LF Sway	5.94592×10^{12}	1.010
3. LF Heave	5.58039×10^{12}	1.676
4. HF Heave	8.45079×10^{12}	1.827
1+4	6.81266×10^{12}	2.481
2+4	8.52708×10^{12}	1.048
3+4	7.69331×10^{12}	1.916

Table 7.5 — Energy and DTA Values for HF and LF Motions.

The term "energy" used in Table 7.5 is defined as

$$\text{Energy} = \int_{t_1}^{t_2} T_{(h-\frac{1}{2})} \dot{x}_h . dt \tag{7.6}$$

where $\dot{x}_h$ is the vector velocity of the mooring line endpoint and $T_{(h-\frac{1}{2})}$ is the tension in the upper element. From Table 7.5 it can be clearly seen that the energies in the system under the different endpoint excitations can be split into two groups according to the relative magnitudes. The two groups are defined by the presence or absence of HF heave motion in the endpoint excitation. Those with HF heave have greater energy than the results with no HF heave. This indicates that HF heave motion makes the most significant contribution to the damping of the vessel caused by the dynamics of mooring lines.

Also of significance is the magnitude of the energy in the system induced by LF sway motion. This is the largest of the LF motions, however it also produces the lowest DTA value. This difference is important to note in the context of assessing the influence of the mooring line damping upon the motions of the floating structure. If the influence of mooring line damping were to be judged by comparing the relative magnitudes of the DTA values only, then sway motion would be deemed the least significant. However, the energy expended during one cycle clearly shows that pure sway gives rise to the largest contribution to the damping of vessel motion by the mooring lines.

This table also shows that the energy contained in one combined cycle of high and low frequency heave motion is lower that the LF motion alone. This is in contrast to the remaining combinations of high and low frequency motions which are always larger than for the LF motion alone. This suggests that in the case of the combined heave motions that "interference" of the two excitations leads to a slight cancellation of the resulting energy in the system.

The main points arising from this case study are:

- In the calculation of the contribution of mooring line damping to vessel motions, the sway direction must be included.
- Combined HF and LF excitation should be considered in the calculation of the DTA values.

7.2.5 SSBs, Ocean Currents and Waves

In this case study the influence of the following parameters upon the peak and trough DTA values is investigated:

1. The inclusion of subsea buoys (SSB).

2. The inclusion of ocean current.

3. The effect of wave induced water particle velocity and acceleration.

The Inclusion of SSB's

Here the standard 20 element model is used and the peak and trough DTA values are calculated with a SSB of radius 1.0m located at different nodes along the length of the mooring line. The influence of the frequency of excitation is also investigated and as expected both the peak and trough DTA values decrease as the excitation frequency decreases. Note that the value of T_o^+ used in the calculation of the DTA values is the maximum static tension at the maximum excursion with the SSB included in the line. The DTA curves are presented in Figure 7.29. It can be seen that they follow very similar trends and that these are nearly symmetrical about the condition corresponding to the SSB being located at the middle node of the line. The peak DTA values are a maximum at this point and the trough DTA values are a minimum.

The Inclusion of Ocean Current

Figure 7.30 shows the effect of an in-plane, vertically uniform horizontal current (U) upon the peak and trough DTA values. The expected trends are clear, namely that an increase in ocean current velocity increases the peak and trough DTA values. T_o^+ is calculated in the usual fashion, i.e. with the value of T_o^+ being taken as the maximum static value at the extreme excursion point, but with no current loading. However, also included for the purposes of comparison, are the peak and trough DTA values (denoted as $\mathrm{DTA_1}$) for a positive current U when T_o^+ is calculated as a function of U. These show that a maximum $\mathrm{DTA_1}$ value is reached and that the $\mathrm{DTA_1}$ values decrease with increasing values of U.

The Inclusion of Wave Effects

Figure 7.31 shows the effect of the inclusion of wave induced water particle velocities and accelerations upon the DTA values. To allow the peak and trough DTA values to be presented on the same graph with sufficient detail, the trough DTA values have been scaled up by a factor of 5. It can be seen that the inclusion of these effects is negligible; this is perhaps to be expected since the influence of surface waves decrease exponentially with depth. However some point of inflexion is clear at the wave frequency of 0.6 radians, where the peak DTA values are a maximum and the trough DTA values are a minimum, but this is still relatively

insignificant. It can thus be concluded that the influence of wave particle velocity and accelerations upon the dynamic tension developed in a deep water mooring line is negligible and should therefore not be included in the theoretical model.

To summarise the main points of these studies:

- The inclusion of SSBs induces the maximum peak and minimum trough DTA values when the SSB is located halfway along the mooring line.
- Ocean current has a significant effect upon the DTA values and an assessment should always be made with potential ocean currents included.
- The influence of wave induced water particle velocities and acceleration is negligible.

7.2.6 Excitation and Response Timelag

Also of interest is the time difference between the excitation and the response - the maximum dynamic tension in this case. This would then provide a qualitative understanding of the point in the excitation cycle at which the maximum mooring line tension would be expected to occur. Figure 7.32 shows the variation in the time difference as the frequency of endpoint excitation is changed and clearly indicates a decrease with increasing frequency. Figures 7.33 and 7.34 compare the time histories of the maximum dynamic tension and the endpoint excursion for two different frequencies. In order that the endpoint displacement caused by the excitation function and the tension time history can be directly compared, the displacements are illustrated with a scale which is deliberately not indicated. It can be seen that the tension time history 'lags' the excitation and that this decreases with excitation frequency. This is to be expected since at the point of maximum excursion there is very little line motion and this is reflected by a tension value which is not a maximum. For example for the excitation frequency of 0.3 rads. shown in Figure 7.33, the timelag is 2.9 secs. Since the period of excitation is approximately 20.9 secs., it can be seen that the maximum tension is developed at 55% of the quatre period. This means that the maximum tension occurs when the endpoint is approximately half way between the equilibrium position and the point of maximum excursion.

7.3 Summary

The main results from this chapter may be summarised thus:

1. Dynamic tensions predicted with the 3D model for the case of no and decayed excitations agree very well with the maximum static value.

2. The values for $\bar{T}_p$, $\bar{T}_t$ and $\bar{T}_m$ agree very closely between the in-plane 3D model and the 2D model.

3. For the case investigated the total CPU time for the 3D model was approximately $2\frac{1}{4}$ times the total CPU time for the 2D model. This means that for situations when the out of plane effects can be neglected, the 2D model should be used in preference to the 3D model.

4. The maximum value of Δt which can be used is nearly identical for the 2D and 3D models.

5. The inclusion of tangential drag has a negligible effect upon the tension peaks but is slightly more significant in influencing the tension troughs.

6. Physical drag is required to stabilise the solution, but too much can cause irregularities to be introduced in the time history.

7. The inclusion of tangential added mass has a negligible effect on both the peak and trough tension.

8. Heave is the most significant motion in producing the maximum DTA values; sway is the least significant.

9. A distinction between safety factors and DTA values need to be made.

10. Large amplitudes and / or frequencies for the endpoint excitation can produce geometric irregularities which manifest themselves as reduced tension troughs.

11. LF sway produces the largest energy dissipation and therefore makes the largest contribution to the damping of vessel motion despite the fact that sway motion produces the lowest DTA values.

12. In-plane ocean currents can significantly affect the DTA values.

13. Wave induced water particle velocity and acceleration have a negligible effect upon the solution.

14. The tension time history always 'lags' the endpoint excitation; this lag decreases as the excitation frequency increases.

The results from the studies carried out in this chapter have several important implications regarding the original development of the model. In particular it can be seen that the inclusion of tangential drag and tangential added mass can be neglected thus considerably simplifying the derivation. Also the water particle velocities and accelerations induced by the action of surface waves can be neglected in all but the shallowest of water situations, again resulting in a further simplification in the derivation of the model. This chapter has also highlighted the inconsistencies in the derivation of the dynamic tension amplification factor and suggests the use of two DTA values; one for design comparisons and the other for construction. Furthermore, the differences between the definitions of the safety factors and the DTA values have been emphasised.

CHAPTER 8

Mooring Line and Seabed Interactions

8.1 Introduction

This chapter examines the effects of the interaction between the sea bed and the mooring line, with particular reference to two aspects:

1. Frictional and suction effects.

2. Problems associated with the lifting and grounding of the nodes.

The latter has been briefly mentioned with in Section 3.4 and a formulation to account for this is given in Appendix F. The effects of seabed friction and suction have not been accounted for, so this chapter opens with a description of a model designed to include these effects, in a static fashion, for both the normal and tangential directions. Results are then generated using this model to illustrate the influence of these effects upon the peaks, troughs and means of the resulting tension time histories. Following this, an extensive examination of the lifting and grounding model proposed in Appendix F is undertaken, and an explanation of the irregularities caused by a grounding node is offered. It is important to realise at this point that the effects due to lifting and grounding are present only because of the discretisation employed to describe a physically continuous system. Therefore this work is not an extension of theoretical mooring line analysis, but is rather an attempt to contain the irregularities introduced through the use of a numerical model.

8.2 Seabed Frictional Effects

8.2.1 General Considerations

The assessment of frictional effects falls into four categories, two for the direction considered and for each of these, consideration must be given as to whether the mooring line is lying on the seabed or is 'submerged' therein. The two directions are:

- Tangential motion, i.e. the sliding of the line on or through the seabed soil in the same direction as the orientation of the last grounded element, and
- Normal motion, i.e. the sliding of the line on or through the seabed soil in a direction which is at 90° to the orientation of the last grounded element.

There are three sources of pertinent literature :

1. Discussions of pipeline on-bottom-stability.
2. Discussions of the final configuration of the anchor chain which is submerged because of attachment to a submerged anchor pile.
3. Literature dealing directly with the problem in hand.

There are very few references in the last category; the first category contains an extremely large body of material and although the physical processes are the same for pipelines as for mooring lines, the differences in diameter and flexural rigidity makes the results for pipelines less applicable for the present problem. Category 2 contains the most useful references with regard to the movement of the mooring line on or through the seabed soil. Although there are only a few references in this field they are concisely summarised in a paper by Dutta(1988) where the methods for estimating the soil forces (both normally and tangentially) are adopted here. In reviewing the literature in these categories, the following assumptions which apply to the problem in hand are worth noting:

1. The same physical effects apply to both chain and wire rope, although the relative magnitudes will be different.
2. The mooring line will be considered to lie on, or just below, the surface of the seabed.
3. The anchor point is assumed to be on the seabed surface.

With reference to literature in Category 3 it will be seen that the frictional interaction of the mooring line with the seabed is considered in very few papers which deal with mooring line dynamics. One such paper is that of Kwan and Bruen(1991) where the inclusion of frictional effects is implemented through the classical (or Coulomb) friction law of $F = \mu R$, but this is not further expanded upon in this paper.

A brief review of pipeline/soil interaction (Category 1) yields many papers examining aspects of this topic. Some selected references are: Hale *et al.*(1991), Allen *et al.*(1989), Wagner *et al.*(1987), Hale *et al.*(1989), Lammert *et al.*(1989), Brennodden *et al.*(1989) and Karal and Halvorsen(1982). Successive researchers in this field have come to the conclusion that the simple Coulomb friction model is not suitable for use in pipeline analysis. As a result of these deficiencies a detailed pipeline dynamics model has been developed, see, for example, Lammert *et al.*(1989). Here the equations of motion are formulated through the finite element method and are solved in the time domain. However it is reported that these types of theoretical models are not well suited to pipeline design purposes because information regarding the weight requirements for the pipeline coating cannot be readily derived from the results. Also, the nature of engineering design in general, requires a method which is quick and easy to use which these types of theoretical models are clearly not. Because of this efforts have been made to derive simplified models which are seen to be extensions of the Coulomb friction law where some account is taken of the dynamic effects between the pipe and the soil. Attention is largely concentrated on cyclic hydrodynamic loadings (e.g. those induced by waves and tides) leading to pipe embedment. This increases the soil resistance and therefore the new empirical models take the form

$$F_t = F_c + F_e, \tag{8.1}$$

where F_t is the total soil friction force, F_c is the soil frictional force due to the usual Coulomb law and F_e is the increase in the soil friction force due to the embedment of the pipe in the soil.

For the second category, namely static mooring line behaviour when submerged in seabed soils, analysis techniques have developed and culminated with a static finite difference representation of the part of the mooring line in the seabed soil. Using an iterative procedure and appropriate boundary conditions the distribution of geometry and hence line tension can be derived. This is clearly explained in Dutta(1988) where a brief but concise review of previous efforts to solve this problem can also be found. In this work the soil forces which are considered to act on a segment of the submerged line are divided up in to normal and tangential components in the following manner

$$f_n = K S_u A_b \tag{8.2}$$

and

$$f_t = \alpha S_u A_s, \tag{8.3}$$

where:

f_n, f_t	normal and tangential soil resistance per unit length,
K	soil bearing capacity factor ($9 \leq K \leq 11$),
S_u	undrained soil shear strength,
A_b, A_s	effective sliding/bearing area per unit length,
α	tangential sliding friction factor.

Both these soil forces apply to the mooring line moving through the seabed soil. Dutta(1988) also identifies a third soil resistance force which is considered to act in lieu of the previous two when the mooring line lies on, or is partially embedded in the seabed. This is expressed as a Coulomb friction model of the form

$$f = \eta W_s. \tag{8.4}$$

However, no attempt is made in this paper to indicate how A_b and A_s should be calculated or what the typical values of the coefficients K, α and η might be.

8.2.2 Lateral Formulation

Consider Figure 8.1 which shows a plan view of the last grounded and first suspended elements in the discretisation of a mooring line, and their angles relative to each other in the horizontal plane. The normal soil friction force at any point along the element $(j-\frac{1}{2})$ is f_n. The total normal soil resistance is therefore $f_n l_{j-\frac{1}{2}}$ where $l_{j-\frac{1}{2}}$ is the length of element $(j-\frac{1}{2})$. It is assumed that all of the soil resistance is lumped at node j; therefore this node will only move if

$$T_{j+\frac{1}{2}} \cos\gamma_{j+\frac{1}{2}} \sin(\varepsilon_{j+\frac{1}{2}} - \varepsilon_{j-\frac{1}{2}}) > f_n l_{j-\frac{1}{2}}. \tag{8.5}$$

Once the node moves, the angles $\varepsilon_{j+\frac{1}{2}}$ and $\varepsilon_{j-\frac{1}{2}}$ will change and the new angles are denoted by $\varepsilon'_{j+\frac{1}{2}}$ and $\varepsilon'_{j-\frac{1}{2}}$. The node will move in the normal direction until the resolved tension force is equal to the normal soil resistance, i.e. until

$$T_{j+\frac{1}{2}} \cos\gamma_{j+\frac{1}{2}} \sin(\varepsilon'_{j+\frac{1}{2}} - \varepsilon'_{j-\frac{1}{2}}) - f_n l_{j-\frac{1}{2}} = 0, \tag{8.6}$$

hence

$$\varepsilon'_{j+\frac{1}{2}} - \varepsilon'_{j-\frac{1}{2}} = \sin^{-1}\left[\frac{f_n l_{j-\frac{1}{2}}}{T_{j+\frac{1}{2}} \cos\gamma_{j+\frac{1}{2}}}\right]. \tag{8.7}$$

Now assume that $\varepsilon_{j+\frac{1}{2}}$ and $\varepsilon_{j-\frac{1}{2}}$ have changed by the same amount, i.e. that

$$\begin{aligned} \varepsilon'_{j+\frac{1}{2}} &= \varepsilon_{j+\frac{1}{2}} - \Delta\varepsilon \\ \varepsilon'_{j-\frac{1}{2}} &= \varepsilon_{j-\frac{1}{2}} + \Delta\varepsilon. \end{aligned} \tag{8.8}$$

Substituting Equation (8.8) into Equation (8.7) the following results

$$\Delta\varepsilon = \left|\frac{1}{2}\{\varepsilon_{j+\frac{1}{2}} - \varepsilon_{j-\frac{1}{2}} - \sin^{-1}\left[\frac{f_n l_{j-\frac{1}{2}}}{T_{j+\frac{1}{2}}\cos\gamma_{j+\frac{1}{2}}}\right]\}\right|. \tag{8.9}$$

The estimation of f_n follows Dutta(1988); for this it is required to know before the start of the simulation whether the mooring line is (a) resting on the seabed, or (b) totally submerged in the seabed soil. For (a) the Coulomb friction model may be applied, i.e. $f_n = \eta_n W_s$ where η_n is the normal surface friction coefficient. For case (b) it is more appropriate to use Equation (8.2).

8.2.3 Tangential Formulation

Consider Figure 8.2 which shows a mooring line discretisation and the touchdown forces in the vertical plane. The touchdown node will only move tangentially if the following inequality is satisfied

$$T_{j+\frac{1}{2}}\cos\gamma_{j+\frac{1}{2}} > f_t l_g, \tag{8.10}$$

where l_g is the length of grounded line. It is assumed that the mooring line will stretch according to Hooke's law, so that the new length of the grounded line is given by

$$l'_g = \left[\frac{T_{j+\frac{1}{2}}\cos\gamma_{j+\frac{1}{2}} - f_t l_g}{AE}\right] l_g, \tag{8.11}$$

where A and E are the cross sectional area and Young's modulus for the grounded line and these are assumed to be the same for all the grounded elements. Effects due to Poisson's ratio are ignored and f_t is calculated according to Equation (8.3) or Equation (8.4) depending upon whether the line is assumed to lying on, or submerged in, the seabed soil.

8.3 Results for Seabed Interactions

8.3.1 Case Study 1: Seabed Friction

Sinusoidal excitation which causes motion in the tangential direction was examined first. Figures 8.3 and 8.4 show the results with in-plane excitation amplitudes of 14.14m and 21.21m respectively, both with a frequency of $\frac{\pi}{10}$ rads/s and with some portion of the mooring line lying on the seabed, (L=2000m). The results shown are the means of the peaks and troughs ($\bar{T}_p, \bar{T}_t$) as well as the overall mean ($\bar{T}_m$), of the sinusoidal tension time history once the ramping function used to start the solution no longer has any effect. The lines indicated by the box markers are the same means as described above but as derived by neglecting the seabed interactions, both frictional and lifting. Thus for the latter there are only three values, one each for the overall mean and the means of the peaks and troughs. It should be noted that these are not function of η_t but are plotted as such to show the differences when seabed interactions are considered.

It is clear from these figures that once the tangential soil force becomes large by increasing the values of η_t, the inequality of Equation (8.10) is not satisfied and there is then no change in the geometry of the grounded line. Increasing the excitation amplitude as shown in Figure 8.4 means that a larger value of η_t is needed before the inequality is no longer satisfied - as would be expected. From both figures it can be seen that the effect of tangential soil friction on $\bar{T}_t$ and $\bar{T}_p$ may be relatively small, but that the effects upon $\bar{T}_p$ is more significant. The percentage differences (relative to the case where no seabed interactions are considered) with $\eta_t = 0.2$ are 1.63% and 4.95% respectively for the two endpoint amplitudes considered.

Figures 8.5 and 8.6 show the same set of results but repeated for the case where the line is assumed to be submerged in the seabed soil. With the undrained soil shear strength taken to be 1000N/m^2 (1KPa) it can be seen that even with α (the tangential submerged friction coefficient) taken to be 1.0, the inequality of Equation (8.10) is always satisfied, i.e. the grounded portion of the line is always modified by the resolved tension in the first suspended element. However in both figures the means are seen to tend towards the limiting case of the means calculated without the seabed interaction effects (again denoted by the lines with the box markers). The percentage difference relative to the case with no interactions for the means of the peaks with $\alpha = 0.5$ is 3.2% and 3.63% respectively for the two different excitation amplitudes considered. Hence it can be seen that the inclusion

of tangential seabed friction effects can have a significant effect upon the magnitude of the predicted response; but it also shows how sensitive to the correct selection of the friction coefficients the procedure is.

For the case of normal motions it was not possible with any combination of a_i and w_i to produce enough resolved tension in the normal direction to cause any change in $\bar{T}_p$, $\bar{T}_t$ and $\bar{T}_m$. However, a closer examination of the computer output (not presented), showed that the last grounded element was in fact moving according to the procedure described in Section 8.2.2. This was not large enough, however, to register a change in the tension means. This result confirms the previous work in Chapter 6 where it is shown that the DTA values for pure sway are only marginally greater than unity.

8.3.2 Case Study 2: Introduction to Nodal Lifting/Grounding

Figure 8.7 shows a sinusoidal solution where no lifting or grounding is allowed. Figure 8.8 shows the result for the same situation except now with the inclusion of nodal lifting/grounding. It can be seen that the result for the latter case is generally more irregular, but more importantly note that the magnitude of the peaks and troughs have been reduced. The results of Figure 8.8 are compared with results of McNamara(1993, Figure 8.8A) analysed for the same situation. Here the average of the the last five tension peaks are found to be 420kN which compares with a value of 400kN (McNamara(1993)), a difference of 5%. The significant differences in the two tension time histories (Figures 8.7 and 8.8) provides the justification for the investigation into the lifting and grounding of nodes. Figure 8.9 again illustrates the same situation as previously, but now both nodal lifting and grounding as well as seabed friction effects are included. Note the greatly increases irregularity; this is clearly not an acceptable situation.

In order to investigate the effect of nodal lifting/grounding in a more systematic manner, two types of endpoint excitation were defined:

1. Where the endpoint moves from a predetermined maximum excursion to a predefined minimum excursion, (to examine grounding only).

2. The reverse of the above to investigate nodal lifting only.

These are illustrated in Figures 8.10 and 8.11 respectively; also shown next to the irregularities are the nodes which upon grounding or lifting have caused these. Note the initial irregularity at the beginning of both simulations. This is caused

because, unlike the sinusoidal excitation, no ramping function has been applied at the start. Once the increment in endpoint displacement has been determined at the first time step this is applied unmodified throughout the simulation meaning that the endpoint goes from rest at time $t = 0$, to moving with a constant acceleration and velocity for all subsequent time steps. The reason for doing this is to allow the full extent of the grounding irregularities to be shown, i.e. unmodified by the ramping function.

To examine in more detail what is happening, only the case of nodal lifting is considered. Further, the results for node 5 only are identified and isolated. Firstly a free body analysis of the moving node shows that the vertical force which the node experiences can be expressed thus

$$M_j(\ddot{z}_j - g) + D_{zj} + (T_{j+\frac{1}{2}} \sin\gamma_{j+\frac{1}{2}} - T_{j-\frac{1}{2}} \sin\gamma_{j-\frac{1}{2}}) = F, \qquad (8.12)$$

where each term represents the inertia, drag and stiffness forces respectively and F is the exciting force. Figure 8.12 shows F plotted against the total simulation time for node 5 only. Clearly visible are the start up irregularities and the influence of the groundings of nodes 3 and 4 prior to the grounding of node 5 which occurs at approximately 40 seconds into the simulation. Note that the total force is always negative since the node is moving towards the seabed. After the grounding of node 5 both the velocity and acceleration of this node are zero so there will be no drag or inertial terms in Equation (8.12) except for the (negative) weight of the node. The stiffness term continues to make a contribution but this is reduced as the vertical orientation of element 6 reduces. This eventually becomes zero when node 6 is grounded at approximately 65 seconds into the simulation. Therefore the only contribution to F after 65 seconds is the $-M_j g$ term of Equation (8.12) and this remains invariant for the rest of the solution as confirmed by Figure 8.12.

Subsequent graphs now show each component in Equation (8.12) for node 5 for the total simulation. Figure 8.13 shows the inertial term (i.e. $M_j(\ddot{z}_j - g)$) which is clearly constant after the grounding of node 5. Figure 8.14 shows the vertical drag force on the node; again this is clearly zero after the node grounds. Figure 8.15 shows the variation in vertical stiffness and how this becomes zero at approximately 65 seconds when node 6 grounds. Figure 8.16 shows the addition of vertical drag and stiffness terms for node 5 and illustrates a very interesting feature. It can be seen from Figure 8.14 and 8.15 that prior to the grounding of the node, the variation in the graphs is not regular, however Figure 8.16 shows that the addition of these two components prior to grounding is virtually constant (except

when nodes 3 and 4 ground). This can be seen to be the primary contribution to the near constant value F in Figure 8.12 prior to grounding. Upon reflection a constant value of F is to be expected since with a uniform endpoint velocity and acceleration each node will also possess a near constant velocity and acceleration until such time as it grounds. From an examination of these figures it can be seen that the inertial force makes the largest contribution to F, then vertical stiffness and then the drag forces; the last two being positive whilst the first is negative.

8.3.3 Case Study 3: Influence of h and Δt

The next investigation examines the influence upon the total grounding history of:

1. The number of elements (h) with a constant value of Δt.
2. Size of the the time step for a constant value of h.

For (1), h took on the following values: $10, 20, 30, 40, 50$ and the grounding histories for these are shown in Figures 8.17, 8.18, 8.19, 8.20 and 8.21 respectively. These show that up to a certain point, increasing the number of elements acts to reduce the numerical irregularities associated with the successive grounding of the nodes. This is to be expected since increasing the number of elements will reduce the mass 'lumped' at each node thus reducing the impact forces as it grounds. However the solutions for $h = 40$ and $h = 50$ and to a certain extent the solution for $h = 30$ show a degree of irregularity. Figure 8.22 shows the grounding history for $h = 50$ but with a reduced value of Δt. From this it is clear that the irregularities associated with the larger values of h are caused by the use of an inappropriate value for Δt being used.

For a value of $h = 20$ the grounding histories for different values of Δt are shown in Figures 8.23, 8.24, 8.25, 8.26 and 8.27 for values of Δt which are $0.35, 0.25, 0.15, 0.05$ and 0.001 respectively. The largest value of Δt which could be used was numerically determined to be 0.388 seconds. It can be seen that with $\Delta t = 0.35$ secs. (Figure 8.23) a solution is obtained where the groundings can be identified but in between these irregularity is evident. The irregularity is reduced with $\Delta t = 0.25$ secs. (Figure 8.24) and is almost completely eliminated with $\Delta t = 0.15$ (Figure 8.25). However, further reduction in Δt causes a reappearance of irregularity and an increase in both the magnitude and duration of the irregularities associated with each grounding. With $\Delta t = 0.001$ (Figure 8.27) although the groundings can still be identified, the irregularities all but swamp the solution.

For a more detailed view of the tension variation as the node grounds, Figure 8.28 presents the isolated tension time history as node 5 grounds for $\Delta t = 0.35, 0.25, 0.15$ and 0.05. The solution for $\Delta t = 0.001$ was not included in Figure 8.28 since the oscillations associated with this value obscured the other results. What is clear from this figure is that the solutions with the extreme values of the time step always contain oscillations, but it is not clear whether these are caused by the grounding of the nodes or by numerical problems inherent in the solution technique. If the curve for $\Delta t = 0.15$ is examined it will be seen that prior to the grounding there are no oscillations in the solution; then as the node grounds some oscillations are set up but these immediately start to decay so that by approximately 4 seconds after grounding the solution again shows no oscillations. With a smaller value of Δt the magnitude of the oscillations caused by the grounding increases and, more importantly, the oscillations never completely die away. As mentioned before the numerical oscillations produced with $\Delta t = 0.001$ obscures the solution. It therefore seems that there are two intertwined effects which need to be separated out, and they are:

1. The numerical oscillations inherent in the solution procedure and which directly depend upon the $\frac{\Delta t}{h}$ ratio where it seems that an optimum value can be identified.

2. The oscillations caused by the grounding process alone.

In order to isolate the second effect which is the one of interest, a value of Δt should be selected which allows for a smooth and continuous variation of the tension time history away from the areas of grounding. For the remaining case studies Δt was taken as 0.1 seconds unless otherwise stated.

8.3.4 Case Study 4: Influence of Grounding Angle

The grounding angle, γ_g, is used in conjunction with the length of the first suspended element to calculate a distance above the seabed, z_g, i.e.

$$z_g = l_{j+\frac{1}{2}} \sin \gamma_g. \tag{8.13}$$

When the vertical height of the first suspended node above the seabed is less than z_g then the node is deemed to have grounded and the acceleration and velocity of the node are set to zero. It then takes no further part in the dynamic solution

unless the resolved vertical tension in the first suspended element is greater than the weight of the grounded node, i.e. unless

$$T_{j+\frac{1}{2}} \sin \gamma_{j+\frac{1}{2}} > M_j g, \tag{8.14}$$

when the node will then rejoin the solution procedure. This case study investigates the influence of varying γ_g. Table 8.1 shows the effect of different values of γ_g upon the time at which the node grounds, t_g:

γ_g (degs.)	z_g (m)	t_g (secs.)
1.00	1.745	38.7
0.75	1.309	38.8
0.50	0.873	39.2
0.25	0.436	39.7
0.00	0.000	40.1

Table 8.1 — Grouding Information as γ_g Varies.

The column headed by t_g indicates the time at which node 5 grounds; it can be seen that as the value of γ_g is decreased the time at which node 5 is grounded is increased. This is to be expected since decreasing γ_g decreases z_g and hence the simulation must proceed for longer before the vertical height of node 5 is less than z_g. The tension time history is shown in Figure 8.29 for $t_g - 4 \leq t \leq t_g + 8$; close examination of this figure shows that apart from the different t_g values, the magnitudes and number of oscillations of the solution after grounding is virtually identical for all values of γ_g.

8.3.5 Case Study 5: Influence of Mass Modifiers

The derivation of the mass modifiers is shown in Appendix F and are shown to be

$$\begin{aligned} MM_1 &= C_1 - \frac{\Delta l}{l} \\ MM_2 &= C_2 - \frac{\Delta l}{l}, \end{aligned} \tag{8.15}$$

where MM_1 and MM_2 are used to premultiply the masses of the first and second suspended nodes respectively. C_1 and C_2 are the variables used to control the

magnitudes of MM_1 and MM_2, l is the length of the first suspended element and Δl is defined in Appendix F. For all the numerical examples so far presented $MM_1 = MM_2 = 1.0$. An indication of the influence of Equations (8.15) can be gained by setting $C_1 = 1.5$ and keeping $MM_2 = 1.0$. It can be seen from Figure 8.30 that there is a greater discontinuity than with $MM_1 = MM_2 = 1.0$ but that the number of oscillations after the grounding has been reduced.

The next step is to carry out an investigation of the effects of different values of MM_1 and MM_2 through a systematic variation of C_1 and C_2. This is shown graphically as in Figure 8.30 by isolating the tension time history for $t_g - 4 \leq t \leq t_g + 8$. Before further detailing the influence of C_1 and C_2, a discussion of the physical changes which occur during the grounding process is made. In this, particular reference is made to the tension in the elements in the touchdown area and the masses of the first two suspended nodes.

Initially assume that $MM_1 = MM_2 = 1.0$ then the results are given as the solid line of Figure 8.30. The increase in the tension evident between the groundings (clearly seen in Figure 8.25) is difficult to account for, although one possible explanation might be as follows: The prescribed excitation allows for the endpoint to have zero acceleration and a constant velocity for the simulation time. However it will be realised that nodes further away from the endpoint will develop a finite amount of acceleration because of the increasing influence of drag effects. It is therefore suggested that a vertical acceleration develops for the nodes away from the endpoint and that this increases with the simulation time. This acts directly to alter the relative displacements of the nodes and therefore (through Hooke's law) alters the tension distribution. If nodal separation increases then the associated values of the tension time history will also increase. This explanation is rather heuristic but at the same time justifiable not by the physics of the real life situation but by the physics of the Lumped Mass method adopted for the solution.

Once the vertical distance of a node is less than or equal to z_g, the z coordinate of the node is maintained at this value and the acceleration and velocity associated with that node are set to zero - in effect the node is stopped dead. This information cannot be instantly transmitted to all other points along the line and so the remaining part of the mooring line is still behaving as if the node had not grounded. In particular, the node which is now the first suspended one is still moving towards the seabed in an unchanged fashion. However, because the grounded node is now 'fixed' the motion of the node above causes the first suspended element to 'compress', directly resulting in a reduction in the tension of the line. The

subsequent oscillations after grounding are due to the solution procedure trying to re-establish dynamic equilibrium across all the nodes where the initial out of balance has been caused by the compression in the first suspended element. This involves the tension oscillating about the new 'correct' value until that value is attained.

The effect of a systematic variation of the C_1 coefficient is shown in Figures 8.31 and 8.32 where MM_2 is maintained at unity. In Figure 8.31 the effect of increasing C_1 is seen to result in two major features in the solution. Firstly the level of the tension before grounding increases as C_1 increases; this is to be expected since Equation (8.15) indicates that the value of the mass multiplier associated with the first suspended node will increase with C_1. An increase in the mass of any node in the line will obviously result in an increased value of the maximum tension level since the line is now 'heavier'. The second effect is more significant and that is the reduction in the tension trough which immediately follows the grounding of the node. This is explained thus: If the first and second suspended nodes are denoted as node A and node B respectively, then it will be seen that just prior to node A being grounded the mass modifier (MM_1) will be approximately 0.5 (see Equation (8.15), since $\frac{\Delta l}{l} \approx 1.0$) and for node B the mass multiplier (MM_2) will be 1.0. As soon as node A grounds the mass lumped here is no longer explicitly pre-multiplied by a mass modifier and therefore returns to the original value. However, node B, instead of being multiplied by $MM_2(=1)$, is now multiplied by MM_1 whose value in this case is of the order of 0.6 (when $C_1 = 1.5$). In effect the mass modifier associated with node B has changed from 1.0 to 0.6 over the time step in which node A has grounded. It can therefore be seen that the drop in tension just after node A has grounded is due to two effects :

1. The stopping 'dead' of node A whilst node B continues downwards.

2. The sudden change in the mass of node B since it is now premultiplied by a constant other than 1.0

When the mass modifier applied to node B is less than 1.0 the downward motion of node B is reduced because the mass has been reduced (see Equation (8.12)), hence resulting in compression in the element above node B. As C_1 increases (see Equation (8.15)), the value of MM_1 will also increase. For example, in the case where $C_1 = 1.5$ as shown in Figure 8.30, it is found that at the moment of grounding for node A, $MM_1 = C_1 - \frac{\Delta l}{l} \approx 0.6$, therefore $\frac{\Delta l}{l} \approx 0.9$. Hence if $C_1 = 1.9$ it is seen that MM_1 will be 1.0 at the time of grounding. This will reduce the amount of

compression which occurs in the element above node B and thus reduces the trough in the maximum tension after node A grounds. However, close examination of Figure 8.31 shows that an optimum value of C_1 can be identified. In this example, $C_1 = 1.7$ seems to provide the minimum trough after grounding; increasing C_1 further starts to yield a deeper trough. This is clearly seen in Figure 8.32 where the effect of using much larger values of C_1 is examined.

The reason for this 'optimum' value of C_1 is clear. By increasing the mass of node B (after node A has grounded) as C_1 increases past the optimum, there is a relatively greater effect on the compression of the element below node B than on the tensioning of the element above. This would result in an increased trough after grounding. With reference to Figure 8.32, for values of C_1 greater than 2.5, it can be seen that the solution following the grounding is more irregular. Closer examination of the output information (not presented) shows that these irregularities are caused by a subsequent lifting and regrounding of the node which has just grounded. Increasing the value of C_1 increases the weight of the node and causes it to ground sooner than a 'lighter' node and at a point when the inequality of Equation (8.14) is still satisfied.

A similar investigation was also carried out into the effect of varying C_2 whilst maintaining $MM_1 = 1.0$. The results are shown in Figures 8.33 and 8.34. The minimum value of C_2 which could be used without the solution collapsing was determined to be 1.25. All the trends as observed for the variation of C_1 are present in these figures but to a different extent. Therefore it is logical to assume that the same processes are at work - the difference being that they are being applied to the second suspended node and therefore will have different absolute values.

Figure 8.35 shows what happens when both C_1 and C_2 were varied simultaneously but maintaining the same value. The same broad trends as shown for the individual variation of either C_1 or C_2 can be identified. A 'best' solution, at least graphically, would appear to be when $C_1 = C_2 = 1.5$ or when $C_1 = C_2 = 1.9$; note that these values are just either side of the 'optimum' value identified for the variation of C_1 or C_2 alone.

Table 8.2 shows that the greatest variation in t_g is when C_1 and C_2 are varied simultaneously whilst minimal variation occurs when C_2 is varied alone. Note that for the purposes of plotting the graphs in Figures 8.32 through to 8.36 the shift

in the grounding history (i.e. the variation in t_g) caused by different nodal masses has been removed so that a more direct comparison may be made.

C_1	t_g (secs.)	C_2	t_g (secs.)	$C_1 = C_2$	t_g (secs.)
1.3	57.3	1.25	44.6	1.3	77.1
1.5	50.7	1.45	42.6	1.5	56.3
1.7	45.2	1.65	41.3	1.7	46.2
1.9	40.9	1.85	40.2	1.9	40.9
2.0	39.0	2.0	39.3	2.0	38.7
2.1	37.6	2.05	39.4	2.1	36.9
2.5	33.3	2.5	38.2	2.5	32.2
3.0	30.2	3.0	37.1	3.0	28.4
3.5	28.0	3.5	36.4	3.5	26.0
4.0	26.5	4.0	35.5	4.0	24.1

Table 8.2 — Influence of C_1 and C_2 Upon Grounding Time

8.3.6 Case Study 6: Mass Reduction by Increasing h

In this case study an attempt is made to investigate the influence that changing the node mass by increasing the number of elements (h) has upon the irregularities caused by nodal grounding. The increase in the number of elements is done in such a manner that there is always a node at the same point of interest along the line. As previously (see Section 8.3.2), the position in the mooring line for the new discretisation, which corresponds most closely to node 5 is isolated and examined in more detail. However by changing the length of the elements the accuracy of the solution will be affected and hence a direct and meaningful comparison is hard to gain. As a result two cases are considered :

1. Where the $\frac{\Delta t}{T}$ ratio is maintained.
2. $\Delta t = 0.001$ for all values of h.

Details for both cases are given in Tables 8.3 and 8.4 respectively. For either case the solution when $h = 72$ was extremely erratic and therefore not included.

The only point of interest to note from these tables is that the time of nodal grounding, t_g, is significantly influenced by the number of elements used to model the mooring line. This is part of the modelling error introduced by using a discrete model to account for a physically continuous situation. It will be seen therefore, that not only does the number of elements affect the magnitude of the grounding irregularities, but it also affects the position of the nodal grounding in the solution time.

h	Δt(secs.)	$\frac{\Delta t}{T}$	Node	t_g(secs.)
9	0.100	0.00045	3	23.8
18	0.050	0.00045	6	51.8
36	0.025	0.00045	12	72.85

Table 8.3 — Mass Changes Whilst Maintaining $\frac{\Delta t}{T}$ Ratio

h	Δt(secs.)	Node	t_g(secs.)
8	0.001	3	23.68
18	0.001	6	51.77
36	0.001	12	72.84

Table 8.4 — Mass Changes Whilst Maintaining Δt

Figure 8.37 shows the results for the case where the ratio of $\Delta t/h$ is maintained at a constant value. Note that the t_g values are all shifted so that they coincide with the t_g value for $h = 8$. It is clear that reducing the mass of the nodes has a very significant effect upon the grounding irregularities, to the point that for $h = 36$ the irregularities are insignificant compared to those for $h = 9$. Therefore there is clearly an improvement caused by increasing the number of elements, but this must be weighed against the increase in the CPU time which this entails. The initial percentage drops in the tensions relative to those immediately prior to grounding are $20\%, 11\%$ and 3% respectively for $h = 9, 18$ and 36. This is a significant reduction in the magnitude of the initial tension drop. This is caused

by both the reduction in the mean level of the tension prior to grounding and the reduction in the node mass introduced by the use of a finer mesh.

Figure 8.38 shows the results for the case where Δt is maintained at 0.001 seconds. Whilst significant drops in mean tension are found for $h = 9$ and 18, the change for $h = 36$ is barely perceptible. What is apparent is the increased numerical irregularities caused by using such a small time step, but also that the magnitude of the irregularities is reduced by using a finer mesh. It can be seen that the means of the irregularities apparent here correspond very closely with those of Figure 8.37. Figure 8.38 illustrates the dangers inherent in using a value of Δt which is to small, on the assumption that greater accuracy will result.

8.3.7 Case Study 7: Effect of Ramping Mass Modifier Changes

Consider the first three suspended nodes in a discrete model of a mooring line, nodes A, B and C say. Now assume that node A is about to ground, therefore its mass multiplier is MM_1, that of node B is MM_2 and for node C the mass multiplier is 1.0, the default value for all the nodes in the discretisation. As explained in Section 8.3.5 at the point of grounding $\Delta l/l \approx 1.0$ therefore $MM_1 \approx C_1 - 1.0$ and $MM_2 \approx C_2 - 1.0$. In this case study the following values are used : $C_1 = 1.5$ and $C_2 = 1.8$, therefore $MM_1 \approx 0.5$ and $MM_2 \approx 0.8$. However after node A grounds, the value of the mass multiplier for node B changes from approximately 0.8 to $1.5 - \frac{\Delta l}{l}$; similarily that for node C changes from 1.0 to approximately $1.8 - \frac{\Delta l}{l}$, where $\frac{\Delta l}{l}$ now applies to the element between nodes A and B. Table 8.5 illustrates these concepts with a numerical example. Therefore, for example, when node 5 grounds, the mass multiplier of node B changes from 0.8 to 0.643, and that of node C from 1.0 to 0.943 in the space of one time step.

It is suggested in this case study that as a node grounds it is the rapidity of the change of the mass multipliers during one time step which causes the initial drastic change in tension. The ensuing oscillations are a result of the solution procedure trying to re-establish dynamic equilibrium across the remaining suspended nodes. Therefore a remedy might be to gradually introduce the changes in the mass modifiers over a number of time steps, N_s. The method for doing this is simple and is now briefly described: As soon as node A grounds, two values for the mass multiplier applied a node B (also for node C since the same procedure applies) are retained, B_1 and B_2 say. B_1 is the value of MM_2 immediately before node A grounds and B_2 is the value of MM_1 immediately node A has grounded. Therefore $B_1 - B_2$ represents the change in the mass modifier applied at node B

as indicated in Table 8.5. By calculating $\Delta B = (B_1 - B_2)/N_s$, then the change is gradually applied over N_s steps to give $B' = B_1 \Delta B$. However one problem with this procedure is that at the end of the ramping time (i.e. after N_s steps), $B' \neq B_2$ because the solution has advanced and the ratio $\Delta l/l$ will have changed.

		Before Grounding			After Grounding		
t_g(secs.)	Node	A	B	C	A	B	C
5.0	2	0.50070	0.80070	1.0	-	0.58064	0.88064
14.5	3	0.50042	0.80042	1.0	-	0.61500	0.91500
30.1	4	0.50001	0.80001	1.0	-	0.63325	0.93325
52.0	5	0.50040	0.80040	1.0	-	0.64305	0.94305
81.6	6	0.50012	0.80012	1.0	-	0.64328	0.94328
117.2	7	0.50004	0.80004	1.0	-	0.65862	0.95862

Table 8.5 — Mass Modifiers Before and After Grounding

Table 8.6 shows the values of the mass modifiers as node 5 grounds at four points of interest in the solution, namely :

1. The values just before node 5 grounds.
2. The values immediately after grounding.
3. The values at the end of the ramping period.
4. The values immediately after the end of ramping.

It is noted that the quantities in (1) and (2) are the same as the values indicated in the columns headed A and B of Table 8.5. Table 8.6 shows the results. Note that the first run maintains MM_1 and MM_2 as unity throughout the solution, and that the second run introduces the changes over one time step which is the original procedure. The solution histories for the grounding of node 5 are shown in Figure 8.39 but in the interests of clarity the histories for runs 4 and 6 have been omitted. The result for run 1 shows a significant initial drop - of the order of 7.5%. Solutions for the remaining runs have noticeably lower levels of tension prior to the grounding of node 5.

Point			1		2		3		4	
Run	t_g(secs.)	N_s	MM_1	MM_2	MM_1	MM_2	MM_1	MM_2	MM_1	MM_2
1	40.1	-	1.0	1.0	1.0	1.0	-	-	-	-
2	52.0	0	0.50040	0.80040	0.64305	0.94305	-	-	-	-
3	52.1	10	0.50001	0.80001	0.78580	0.98421	0.67208	0.85793	0.65787	0.85793
4	52.0	20	0.50042	0.80042	0.79329	0.99213	0.66493	0.85050	0.65780	0.84263
5	51.9	30	0.50039	0.80039	0.79563	0.99476	0.66246	0.84793	0.65770	0.84269
6	51.9	40	0.50028	0.80028	0.79690	0.99608	0.66073	0.84705	0.65715	0.84313
7	51.3	50	0.50022	0.80022	0.79730	0.99692	0.65720	0.84902	0.65429	0.84593

Table 8.6 — Ramped Mass Modifiers at the Four Points of Interest

Table 8.7 shows the initial percentage changes which occur in the tension where ΔT represents the change in tension over the initial tension drop, and Max. ΔT is the maximum change of tension relative to any of the ensuing oscillations. The result for run 7 cannot be determined since the level of tension prior to grounding is not clearly defined. It can be seen from Table 8.7 that the percentage change in tensions decreases as the time over which the mass modifiers are ramped increases.

The large difference between run 1 and the remaining cases is not only explained by the reduction in the tension drop after grounding but also by the lower value of the tension prior to the grounding. Additionally, however, the greatest differences between the tensions prior to and after grounding actually increases, despite the fact that the initial tension drop is decreasing.

Run	N_s	$\%\Delta T$	% Max. ΔT
1	-	7.5	7.5
2	0	3.6	3.6
3	10	1.6	3.5
5	30	1.3	4.2
7	50	-	5.17

Table 8.7 — $\%\Delta T$ at Grounding for Ramped Mass Modifiers

It also appears that as the value of N_s increases so does the amount of irregularity which is present immediately after the initial tension drop. With $N_s = 50$ it appears that this irregularity does not die out and is present in the solution as indicated by the irregular tension prior to grounding in Figure 8.39.

8.3.8 Case Study 8 : Attempts to Improve 'Overall' Response

In this case study an attempt is made to reduce the numerical irregularities associated with the grounding and lifting of nodes for a more realistic (sinusoidal) endpoint excitation than considered in the previous case studies. Figure 8.40 shows the tension time history for a sinusoidal excitation of amplitude 15m and frequency $\pi/10$ rads/s, a time step of 0.1 seconds and $C_1 = C_2 = 1.0$; this is a reproduction of Figure 8.8 and is included here for ease of comparison with subsequent attempts to improve the response. Although a steady state appears to have been reached after approximately 150 seconds, the irregularities associated with nodal lifting / grounding (l/g) are clearly visible especially after comparison with Figure 8.7 where no l/g is allowed. Examination of the output files (not presented) indicates that for the l/g associated with the peak tensions, there is a brief period of time when the node oscillates between a lifted and grounded condition. This change between the lifted and grounded condition takes place over the interval of one time step. With the smooth sinusoidal excitation used it is to be expected that when a node lifts that it will remain lifted and not demonstrate the aforementioned oscillatory behaviour.

A first attempt to reduce this behaviour was made by marginally increasing the mass of the last grounded node. To this end a multiplier of 1.1 was used and the results are shown in Figure 8.41. As expected the values of the tension peaks increase due to the greater 'weight' of the line caused by the multiplier. It is also apparent that a greater regularity is now present and that a steady state is reached shortly after the growth in excitation amplitude - at approximately 103 seconds - has stopped. The tension troughs have the same values whether the mass multiplier is 1.0 or 1.1. Increasing the value of the multiplier only results in an increase in the peak tensions; a steady state is reached at the same time.

Examination of the output files, however, indicates that oscillation in l/g is still taking place even with the introduced multiplier. To eliminate this effect the computer code was modified to accept a variable which allows the user to specify how many time steps after l/g that the code controlling the l/g portion of the program should be ignored. This effectively 'fixes' the node in question in a lifted

or grounded condition, thereby manually eliminating the oscillation effect and the distortion in the results which this causes. The results are shown in Figure 8.42 with the multilpier described above reset to 1.0. A marked change in the magnitude and form of the tension peaks is clearly in evidence. It can also be seen that there is a slight irregularity present just prior to the maximum tension value and this is seen from the output files to be caused by node lifting. Again the troughs remain unaffected.

This represents the 'best' response for the tension peaks and is therefore sufficient if only the peak tension values are required, for example to facilitate mooring line design purposes. However for the requirement of the coupled simulations motivating this study, the total solution history is important and therefore the irregularities associated with the grounding oscillation in the region of the tension troughs must be reduced. The only method found to achieve this was by selecting different values for the variables C_1 and C_2; Figure 8.43 shows the results with $C_1 = 1.5$ and $C_2 = 1.8$ and no 'fixing' to reduce the l/g irregularities. This figure shows a slight reduction in the peak tension values, but a notable increase in the irregularity just prior to the peaks when compared with Figure 8.42. The irregularities near the tension troughs are greatly reduced in magnitude. Figure 8.44 shows the effect of ramping in the changes in the mass modifiers (as described in Case Study 7) and 'fixing' the node concerned to eliminate l/g oscillations. This represents an 'optimum' solution history for this case but it is noted that there are still irregularities associated with the l/g of the nodes.

The maximum changes in the tension (ΔT) at the point of lifting or grounding were calculated from the output files and are indicated in Table 8.8:

Run	C_2	N_s	ISET	ΔT@140secs.	ΔT@151secs.	Figure No.
1	1.8	0	0	31988	7013	8.43
2	1.8	30	10	-22025	7510	8.44
3	1.7	30	10	-17237	7694	-
4	1.6	20	10	-21755	4692	-

Table 8.8 — ΔT for the Lifting and Grounding of Nodes

Note that ΔT@140secs. corresponds to a node being lifted and ΔT@151secs. corresponds to a node being grounded. N_s controls over how many time steps the changes in C_1 and C_2 are ramped in and ISET is the number of time steps for which the node remains 'fixed' - a value of 0 indicates no 'fixing'. It is clear from Table 8.8 that and adjustment of C_2, 'ramping' and 'fixing' has a significant effect upon the maximum changes in the tension when a node lifts or grounds. However it must be stressed that the improvement in the results illustrated here was gained only through an approach of trial and error in the variation of the relevant parameters.

8.4 Summary

The first part of this chapter deals with the development of a model to account for tangential and normal seabed friction effects. This is essentially a static based procedure with motion only allowed if the resolved tension in the mooring line exceeds the static friction forces. Different formulations are required according to whether the grounded portion of the mooring line is assumed to lie on, or to be submerged in, the seabed soil.

The second part is an account of the results gained for both frictional and lifting/grounding effects. For the former a clear conclusion was that motion in the tangential direction occurs and therefore should be taken into account, whilst for the normal direction it was not possible to produce any movement. This indicates that a formulation to account for normal seabed friction, either with the line on or submerged in the seabed soil, is not necessary. In the case of nodal lifting/grounding effects a standard endpoint motion was defined where the mooring line endpoint moves from a maximum to a minimum excursion value. To examine in greater detail what is happening during this endpoint motion, the tension time histories for one node (node 5 in all the examples presented) are isolated for different grounding conditions and presented. The following points succinctly summarise these results:

1. The components of the dynamic vertical force are, in decreasing order of magnitude: Inertial force, vertical stiffness and then the drag forces.

2. Variations in h and Δt show that, generally, increasing h or reducing Δt reduces the irregularities associated with the grounding of nodes. Beyond certain values, however, the 'usual' numerical irregularities reappear.

3. Changing the value of the grounding angle, γ_g, produces virtually no discernible differences in the magnitude and number of oscillations after grounding, but does affect the timing of the grounding.

4. The effects of C_1 and C_2 used in the mass modifiers can significantly affect the irregularities after grounding. It is clear however that values selected for one node under a prescribed endpoint excitation cannot be applied to any other node.

5. The effect of increasing h is to reduce the node mass and hence the impact irregularities.

6. Ramping the changes to the mass modifiers over a number of time steps will, generally speaking, improve the initial tension drop. However ramping over longer times will actually have a detrimental effect upon the solution after grounding.

7. The 'optimum' overall solution can be obtained from combining N_s, ISET and C_2 in a manner which can only be determined through trial and error.

The last point is important and must be stressed. It means that there is no known method available to select these values before a simulation is started and so they can only be determined through numerical experimentation. Also once these values have been determined for a particular node to yield an 'optimum' grounding history, they will not be generally applicable to other nodes. However, it is suggested that with the magnitude of endpoint amplitudes and frequencies normally encountered, that unless a particularly fine mesh is being used, only one node is likely to be lifted and grounded during any given simulation.

CHAPTER 9

Concluding Remarks

9.1 Summary and Conclusion

The problem of a static analysis of a mooring line is considered from two perspectives in Chapter 2. Firstly the analytic catenary equations are developed. This is done in a rigorous fashion and also shows why they cannot be developed in three dimensions (3D). Flow charts and a brief explanation of the arrangement of the software is given and the differences between the theory for grounded and non-grounded situations is highlighted. The chapter then continues by developing a 3D numerical model which is used to determine the equilibrium position for the dynamic situation to be considered later. It is explained how this formulation allows for the inclusion of fluid loading as a straightforward addition to the theory, as well as allowing for the inclusion of sections of different materials and line attachments. Because the static work is relatively distinct from the remaining part of the thesis, results are also presented here. Generally very close agreement between the catenary equations and the numerical method is found, demonstrating the validity of the catenary equations in situations where no fluid loading, line attachments or different materials are considered. The numerical formulation has the two distinct advantages that it can allow for out of plane situations, i.e. 3D, and that it is needed as the starting point for the dynamic solutions.

Chapter 3 is the principal theory chapter; it deals not only with the formulation but also the solution of the equations of motion for a mooring line. In the numerical static procedure described in Chapter 2, the mooring line is divided into a number of straight line, massless elements which are connected by nodes at the points of the element discontinuities. All the mass of, and forces which act on, the mooring line are assumed to be concentrated at these nodes and this then allows the equations of motion to be explicitly formulated for each node. This formulation is given in some detail and also includes an introduction to the problem of the lifting and grounding of the nodes on the seabed. A method for including the wave induced water particle velocity and acceleration is also presented. The second half of this chapter deals with the solution of the equations of motion by finite difference schemes. To facilitate this the equations must be rearranged into a form where the

components of nodal acceleration are calculated as a function of mass , added mass, drag and stiffness forces. This then allows the application of the Central Difference, Houbolt, Wilson-θ and Newmark finite difference schemes, where acceleration and velocity are expressed as functions of past (and hence known) displacements. Four programs have been developed where the equations of motion are solved by the four schemes already alluded to; the special starting procedures and initial conditions for each scheme are also indicated.

Modal analysis provides an alternative method of solution to the direct approach of using the finite difference schemes alluded to in Chapter 3. Chapter 4 indicates how the 3D equations of motion are reduced to a 2D form and how these are recast into a standard matrix form. A form more efficient for direct time integration is obtained when the equations of motion are uncoupled (i.e. no cross terms). This is achieved through the use of the 'modal' matrix which is derived from the eigensolutions of the free undamped equations of motion. Methods to include damping which still allow the equations to be uncoupled are examined. The inclusion of nonlinearities which are inherent in the equations of motion for a mooring line have important implications for the solution of the equations and these seem to have been ignored in the relevant literature. The main point to note is that, as with the direct methods of Chapter 3, iterations must be undertaken at each time step to satisfy a predetermined constraint equation.

The four finite difference (or time integration) schemes used in Chapter 3, poses distinct and important characteristics with regard to their numerical stability and accuracy. Chapter 5 presents an introduction to the theory associated with these topics. The four schemes used here are derived from first principles and the stability aspects as applied to linear equations are investigated through the use of the von Neumann condition, the Routh-Hurwitz conditions and the method of amplification matrices. The first two methods allow inequalities to be derived which place restrictions on the size of the time step which can be used, whilst the latter is a numerical way of demonstrating stability. The accuracy of the results obtained from these schemes is assessed by the amount of amplitude decay and period elongation present in the numerical solution of an equation to which the analytic solution is known. A method of determining apriori a value for the size of the time step whereby all modes present in the solution will be accurately integrated is given, as well as a method of estimating the critical time step limit used with the Central Difference scheme. A great deal of theoretical analysis is possible when the equations being solved are linear. If the equations of motion

are nonlinear then both the stability and accuracy have to be investigated by examining the limiting tendencies of a number of solutions for different conditions of interest. This means that the stability and accuracy characteristics have to be determined by conducting a series of numerical 'experiments' and cannot be calculated theoretically.

Chapter 6 is the first of the results chapters. It provides an extensive comparison of the numerical properties of the four time integration schemes used as applied to the 2D equations of motion for a mooring line. This chapter presents three sections of work:

2. The reduction of the equations of motion from a 3D to a 2D form, which are then compared to published sets of equations to highlight any differences.

3. A short section which derives limiting results for the dynamic models, i.e. results where the endpoint excitation has died out or is non-existent.

4. A major section comparing the results gained from the four time integration schemes.

The main aspects of interest for each scheme is the comparison between the size of the time step which will give a stable and accurate solution and the desire not to incur excessive CPU times. From these results it has been possible to produce a recommendation as to the 'best' scheme to be employed in the solution of mooring dynamics. The major conclusions which have been found from this investigation are :

- Increasing the amplitude and frequency of endpoint excitation reduces the maximum value of Δt which can be used.

- The maximum value of Δt decreases as the mesh size l decreases.

- Stability and accuracy are functions of the absolute value of Δt and l and are independent of the ratio $\frac{\Delta t}{l}$.

- The Central Difference scheme has a critical value of Δt beyond which the solution is impossible to gain.

- Total CPU time decreases nonlinearly with increasing values of Δt. There is an optimum value of Δt for the Central Difference scheme which is less than the critical value.

- Different starting procedures implemented with the Houbolt scheme have a negligible effect.

- The value of $\theta = 1.4$ is a near optimum value with respect to the stability and accuracy of the scheme.

The recommendation as to which scheme should be used depends upon the value of Δt which can be used. If this is to be less than the critical value identified for the Central Difference scheme then this is the scheme recommended for use. If this is not the case then it is recommended that the Houbolt scheme be used.

The results from the preceding chapter are not directly useful for mooring line design purposes. The aim of Chapter 7 is to provide a method of calculating dynamic tension amplification (DTA) factors and to present a parametric study of the main factors affecting mooring line dynamics. The DTA values cannot be directly compared with the safety factors specified by the classification societies, because they measure different aspects of mooring dynamics. It is shown that the manner of calculating the DTA can differ according to how the maximum static tension is defined; this is clearly pointed out and two types of DTA values are identified, tentatively referred to as design and construction DTA values. The former is suggested for use in the design phase of a floating production system, whilst the latter should be used for the design and construction of the mooring lines only. The main conclusions to be drawn from this chapter are :

- The CPU time for the 3D model is approximately twice that for the 2D model run under the same circumstances. Thus if out of plane effects can be ignored, the 2D model should be used in preference.

- Physical drag is required to stabilise the solution, but too much can cause irregularities.

- Tangential added mass and drag forces are generally negligible.

- Heave motion produces the largest DTA; sway the smallest.

- Wave induced water particle velocity and acceleration is negligible.

Chapter 8 is an investigation into the interaction of the mooring line with the seabed. The two effects considered are the soil frictional forces and the lifting and grounding of the nodes in the Lumped Mass discretisation. The frictional effects need to be considered for two cases : (i) When the line is assumed to be lying on

the seabed, and (ii) when the line is considered to be submerged in the seabed soil. It was shown that no movement of the grounded portion of the line could be effected for any combination of endpoint amplitude and frequency. Therefore the tangential effects only need to be considered. The principal conclusions are :

- Changing the grounding angle γ_g has no influence except on the time of nodal grounding.
- The effect of increasing the number of elements is to reduce the mass concentrated at each node and hence to reduce the irregularities caused by impact of the nodes on the seabed.
- Ramping the changes in the mass modifiers over several time steps, which otherwise would take place over one time step, can improve the grounding irregularities.
- An 'optimum' solution can be gained from numerical experimentation with certain factors, but these are then only applicable for a particular node under the prescribed endpoint excitation.

9.2 Recommendations for Further Work

In this section a distinction is made between further work relevant to the work already undertaken and further work which is an extension of the existing effort.

9.2.1 Recommendations for Existing Work

- A further and more detailed parametric study for the work carried out in Chapters 6 and 7 but related to 'real' mooring situations so that experience through case studies can be built up.
- The most obvious recommendation is the full implementation of the modal theory described in Chapter 4 so that comparisons of the effectiveness (or otherwise) can be made with the direct methods of Chapter 3.
- The four time integration schemes used here are only examined because they are the most popular schemes used in the solution of structural dynamics. In reality they represent a small fraction of the total number of schemes available. Therefore the possibility exists that a scheme which has not been considered here might be more suited to the specific problem of mooring line dynamics.

- In the solution scheme adopted here the mass and damping matrices remain constant during the iterative procedure whilst the stiffness (tension) is used as the iteration parameter. An investigation should be carried out as to the effect on the solution efficiency of allowing the mass and damping terms to be updated at the end of each iteration.

- In the present implementation of the solution, the matrix inversion method used to calculate the tension corrections (see Equation (3.77) of Chapter 3) takes no advantage of the tridiagonal nature of the coefficient matrix. More effective methods exist for the inversion of matrices with this characteristic and these should be implemented to improve the efficiency of the solution.

9.2.2 Recommendations for Future Work

- Further software should be developed which handles a spread of mooring lines as attached to a rigid floater. Endpoint motions can then be specified for each line in order that the fairleaders remain in the same relative positions. This would allow for a global analysis of the dynamics of a realistic mooring arrangement.

- More advanced than the previous point is the coupling of the mooring line dynamics with a time domain analysis of the motions of the floater. Software exists for both analyses separately and although several efforts have been made towards full coupling, various simplifications have usually been employed to make the problem more tractable. The full coupling would allow very detailed analysis of the total system and in particular the effects of line failure could be assessed.

- In Chapters 7 the calculation of the dynamic tension amplification (DTA) factors is demonstrated. In the light of this work, an assessment of the validity of the safety factors issued by the certifying authorities can be made and compared with the results from operational experience.

- Hooke's law is used to model the stress-strain relationship, however this is only applicable when chain and/or wire rope is being analysed. Neither of these materials are ideal for use in the deep waters proposed for the exploitation of marginal oil and gas fields where the use of synthetic rope has been suggested. This material type has a nonlinear stress-strain relationship and this should be incorporated into the present analysis.

- Following the previous point a natural extension to the proposed work program is the analysis of fatigue failure of mooring lines. As far as can be ascertained there is a dearth of test data available for both chains and wire ropes and none for synthetic materials. If exploitation of the marginal fields continues then it is suggested that extensive fatigue analysis of synthetic materials is needed.

As a final comment, it may be said that the broad objective outline in the introduction, namely an assessment of the numerical efficacy of different time integration schemes as applied to the solution of mooring line dynamics, has been achieved. The variation of the schemes to input parameters such as the time step size and the element length has been shown and this has highlighted some important aspects not previously demonstrated in the literature.

Appendices

Appendix A

Rotational Coordinate Transformations

The general rotational coordinate transformation matrix is derived for a right handed coordinate system. This is then tailored to suit the requirements of this work. If the original axis system is defined as being (x, y, z), then a complete general finite rotational transformation is defined by the three following Eulerian rotations:

1. Rotate anticlockwise about z by an angle ε to give a new axis system defined by (x', y', z).

2. Rotate anticlockwise about y' by an angle γ to give a new axis system defined by (x'', y', z').

3. Rotate anticlockwise about x'' by an angle β to give a new axis system defined by (x'', y'', z'').

These individual rotations are shown in Figure A1. Figure A2 shows the first of these three transformations, i.e. the rotation about the z axis and from this it is seen that

$$x = r\cos(\theta + \varepsilon), \quad y = r\sin(\theta + \varepsilon)$$

and

$$x' = r\cos\theta, \quad y' = r\sin\theta.$$

By expanding $\cos(\theta + \varepsilon)$ and $\sin(\theta + \varepsilon)$ and using the equations for x' and y' the following matrix form (which also includes the unmodified z coordinate)

$$\begin{pmatrix} x' \\ y' \\ z \end{pmatrix} = \begin{pmatrix} \cos\varepsilon & \sin\varepsilon & 0 \\ -\sin\varepsilon & \cos\varepsilon & 0 \\ 0 & 0 & 1 \end{pmatrix} \begin{pmatrix} x \\ y \\ z \end{pmatrix} . \tag{A.1}$$

can be derived after some matrix inversion. By applying the same derivation process to the next two rotations the following two matrices result

$$\begin{pmatrix} x'' \\ y' \\ z' \end{pmatrix} = \begin{pmatrix} \cos\gamma & 0 & \sin\gamma \\ 0 & 1 & 0 \\ -\sin\gamma & 0 & \cos\gamma \end{pmatrix} \begin{pmatrix} x' \\ y' \\ z \end{pmatrix} \tag{A.2}$$

and

$$\begin{pmatrix} x'' \\ y'' \\ z'' \end{pmatrix} = \begin{pmatrix} 1 & 0 & 0 \\ 0 & \cos\beta & \sin\beta \\ 0 & -\sin\beta & \cos\beta \end{pmatrix} \begin{pmatrix} x'' \\ y' \\ z' \end{pmatrix}. \tag{A.3}$$

If each of the transformation matrices defined above are denoted by $\mathbf{T_1}$, $\mathbf{T_2}$ and $\mathbf{T_3}$ respectively, then the total transformation is defined by

$$\begin{pmatrix} x'' \\ y'' \\ z'' \end{pmatrix} = \mathbf{T_3 T_2 T_1} \begin{pmatrix} x \\ y \\ z \end{pmatrix} \tag{A.4}$$

where the transformation matrix, $\mathbf{T}$, is given by

$$\begin{pmatrix} 1 & 0 & 0 \\ 0 & \cos\beta & \sin\beta \\ 0 & -\sin\beta & \cos\beta \end{pmatrix} \begin{pmatrix} \cos\gamma & 0 & \sin\gamma \\ 0 & 1 & 0 \\ -\sin\gamma & 0 & \cos\gamma \end{pmatrix} \begin{pmatrix} \cos\varepsilon & \sin\varepsilon & 0 \\ -\sin\varepsilon & \cos\varepsilon & 0 \\ 0 & 0 & 1 \end{pmatrix}.$$

Note that the order in which the rotations are defined controls the order of the matrix multiplication in the resulting transformation matrix $\mathbf{T}$. This results in the total transformation matrix $\mathbf{T}$ being defined as

$$\mathbf{T} = \begin{pmatrix} \cos\gamma\cos\varepsilon & \cos\gamma\sin\varepsilon & \sin\gamma \\ (-\sin\gamma\sin\beta\cos\varepsilon - \cos\beta\sin\varepsilon) & (-\sin\gamma\sin\beta\sin\varepsilon + \cos\beta\cos\varepsilon) & \sin\beta\cos\gamma \\ (-\sin\gamma\cos\beta\cos\varepsilon + \sin\beta\sin\varepsilon) & (-\sin\gamma\cos\beta\sin\varepsilon - \sin\beta\cos\varepsilon) & \cos\beta\cos\gamma \end{pmatrix}.$$

Since for this application $\beta = 0$, the transformation matrix $\mathbf{T}$ becomes (Ω), say, and is defined by

$$(\Omega) = \begin{pmatrix} \cos\gamma\cos\varepsilon & \cos\gamma\sin\varepsilon & \sin\gamma \\ -\sin\varepsilon & \cos\varepsilon & 0 \\ -\sin\gamma\cos\varepsilon & -\sin\gamma\sin\varepsilon & \cos\gamma \end{pmatrix}, \tag{A.5}$$

and if the local axis system is now defined as (p, q, r), then

$$\begin{pmatrix} p \\ q \\ r \end{pmatrix} = \begin{pmatrix} \cos\gamma\cos\varepsilon & \cos\gamma\sin\varepsilon & \sin\gamma \\ -\sin\varepsilon & \cos\varepsilon & 0 \\ -\sin\gamma\cos\varepsilon & -\sin\gamma\sin\varepsilon & \cos\gamma \end{pmatrix} \begin{pmatrix} x \\ y \\ z \end{pmatrix}. \tag{A.6}$$

Now the same form of transformation matrix is also used to relate the local and global velocities and accelerations, although this is not strictly correct for the following reason. Consider the local displacement p, as given in Equation (A.6), i.e.

$$p = \cos\gamma\cos\varepsilon(x) + \cos\gamma\sin\varepsilon(y) + \sin\gamma(z). \tag{A.7}$$

Then the velocity is strictly given by

$$\begin{aligned}\dot{p} =& \frac{d\cos\gamma}{dt}\cos\varepsilon(x) + \cos\gamma\frac{d\cos\varepsilon}{dt}(x) + \cos\gamma\cos\varepsilon\frac{dx}{dt} \\ &+ \frac{d\cos\gamma}{dt}\sin\varepsilon(y) + \cos\gamma\frac{d\sin\varepsilon}{dt}\cos\varepsilon(y) + \cos\gamma\sin\varepsilon\frac{dy}{dt} \\ &+ \frac{d\sin\gamma}{dt}(z) + \sin\gamma\frac{dz}{dt}.\end{aligned} \tag{A.8}$$

The assumption used in this work is that the contributions from the angular velocities are negligible so that $\dot{p}$ is assumed to be given by

$$\dot{p} = \cos\gamma\cos\varepsilon(\dot{x}) + \cos\gamma\sin\varepsilon(\dot{y}) + \sin\gamma(\dot{z}). \tag{A.9}$$

Thus it is seen that the velocities are related by

$$\begin{pmatrix}\dot{p}\\ \dot{q}\\ \dot{r}\end{pmatrix} = (\Omega)\begin{pmatrix}\dot{x}\\ \dot{y}\\ \dot{z}\end{pmatrix}. \tag{A.10}$$

If Equation (A.8) were again to be differentiated with respect to time to obtain the acceleration $\ddot{p}$, and all the first and second derivatives of functions of γ and ε are assumed negligible, then the global and local accelerations are also related through the same transform, namely

$$\begin{pmatrix}\ddot{p}\\ \ddot{q}\\ \ddot{r}\end{pmatrix} = (\Omega)\begin{pmatrix}\ddot{x}\\ \ddot{y}\\ \ddot{z}\end{pmatrix}. \tag{A.11}$$

Appendix B

Derivation of The Added Mass Coefficient Matrix

From Equation (3.6)

$$\begin{pmatrix} P_p \\ P_q \\ P_r \end{pmatrix} = \begin{pmatrix} a_t\ddot{p} \\ a_n\ddot{q} \\ a_n\ddot{r} \end{pmatrix} \tag{B.1}$$

where $\ddot{p}$, $\ddot{q}$ and $\ddot{r}$ are given from Equation (3.5), hence Equation (B.1) becomes

$$\begin{pmatrix} P_p \\ P_q \\ P_r \end{pmatrix} = \begin{pmatrix} a_t & 0 & 0 \\ 0 & a_n & 0 \\ 0 & 0 & a_n \end{pmatrix} (\Omega) \begin{pmatrix} \ddot{x}^r \\ \ddot{y}^r \\ \ddot{z}^r \end{pmatrix}. \tag{B.2}$$

Explicitly inserting (Ω) from Equation (A.5) of Appendix A, Equation (B.2) reduces to

$$\begin{pmatrix} P_p \\ P_q \\ P_r \end{pmatrix} = \begin{pmatrix} a_t \cos\gamma\cos\varepsilon & a_t\cos\gamma\sin\varepsilon & a_t\sin\gamma \\ a_n\sin\varepsilon & a_n\cos\varepsilon & 0 \\ a_n\cos\varepsilon\sin\gamma & -a_n\sin\gamma\sin\varepsilon & a_n\cos\gamma \end{pmatrix} \begin{pmatrix} \ddot{x}^r \\ \ddot{y}^r \\ \ddot{z}^r \end{pmatrix}, \tag{B.3}$$

but from Equation (3.7) the following result holds

$$\begin{pmatrix} P_x \\ P_y \\ P_z \end{pmatrix} = (\Omega)^{-1} \begin{pmatrix} P_p \\ P_q \\ P_r \end{pmatrix}. \tag{B.4}$$

Due to the orthogonal nature of (Ω), its inverse is equal to its transform so substituting this and Equation (B.3) into Equation (B.4) results in the following identity

$$\begin{pmatrix} P_x \\ P_y \\ P_z \end{pmatrix} = \begin{pmatrix} \cos\gamma\cos\varepsilon & -\sin\varepsilon & -\cos\varepsilon\sin\gamma \\ \cos\gamma\sin\varepsilon & \cos\varepsilon & -\sin\varepsilon\sin\gamma \\ \sin\gamma & 0 & \cos\gamma \end{pmatrix} \times \tag{B.5}$$

$$\begin{pmatrix} a_t\ddot{x}^r\cos\gamma\cos\varepsilon + a_t\ddot{y}^r\cos\gamma\sin\varepsilon + a_t\ddot{z}^r\sin\gamma \\ -a_n\ddot{x}^r\sin\varepsilon + a_n\ddot{y}^r\cos\varepsilon \\ -a_n\ddot{x}^r\sin\gamma\cos\varepsilon - a_n\ddot{y}^r\sin\gamma\sin\varepsilon + a_n\ddot{z}^r\cos\gamma \end{pmatrix}.$$

By expanding and collecting terms for each component acceleration, the following

equations result

$$\begin{aligned} P_x = &\left(a_t \cos^2\gamma\cos^2\varepsilon + a_n(\sin^2\varepsilon + \cos^2\varepsilon\sin^2\gamma)\right)\ddot{x}^r \\ &+ \left(a_t\cos^2\gamma\cos\varepsilon\sin\varepsilon + a_n\sin\varepsilon\cos\varepsilon(\sin^2\gamma - 1)\right)\ddot{y}^r \\ &+ \left(a_t\sin\gamma\cos\gamma\cos\varepsilon - a_n\sin\gamma\cos\gamma\cos\varepsilon\right)\ddot{z}^r \end{aligned} \tag{B.6}$$

$$\begin{aligned} P_y = &\left(a_t\cos^2\gamma\cos\varepsilon\sin\varepsilon + a_n\sin\varepsilon\cos\varepsilon(\sin^2\gamma - 1)\right)\ddot{x}^r \\ &+ \left(a_t\cos^2\gamma\sin^2\varepsilon + a_n(\cos^2\varepsilon + \sin^2\varepsilon\sin^2\gamma)\right)\ddot{y}^r \\ &+ \left(a_t\sin\gamma\cos\gamma\sin\varepsilon - a_n\sin\gamma\cos\gamma\sin\varepsilon\right)\ddot{z}^r \end{aligned} \tag{B.7}$$

$$\begin{aligned} P_z = &\left(a_t\sin\gamma\cos\gamma\cos\varepsilon - a_n\sin\gamma\cos\gamma\cos\varepsilon\right)\ddot{x}^r \\ &+ \left(a_t\sin\gamma\cos\gamma\sin\varepsilon - a_n\sin\gamma\cos\gamma\sin\varepsilon\right)\ddot{y}^r \\ &+ \left(a_t\sin^2\gamma + a_n\cos^2\gamma\right)\ddot{z}^r. \end{aligned} \tag{B.8}$$

When assembled back into matrix form, with a_t and a_n separated out, the final form for the global added mass is

$$\begin{pmatrix} P_x \\ P_y \\ P_z \end{pmatrix} = \left[a_t(\Omega_1) + a_n(\Omega_2)\right]\begin{pmatrix} \ddot{x}^r \\ \ddot{y}^r \\ \ddot{z}^r \end{pmatrix} \tag{B.9}$$

where

$$(\Omega_1) = \begin{pmatrix} \cos^2\gamma\cos^2\varepsilon & \cos^2\gamma\cos\varepsilon\sin\varepsilon & \sin\gamma\cos\gamma\cos\varepsilon \\ \cos^2\gamma\sin\varepsilon\cos\varepsilon & \cos^2\gamma\sin^2\varepsilon & \sin\gamma\cos\gamma\sin\epsilon \\ \sin\gamma\cos\gamma\cos\varepsilon & \sin\gamma\cos\gamma\sin\varepsilon & \sin^2\gamma \end{pmatrix}$$

and

$$(\Omega_2) = \begin{pmatrix} (\sin^2\varepsilon + \cos^2\varepsilon\sin^2\gamma) & -\sin\varepsilon\cos\varepsilon\cos^2\gamma & -\sin\gamma\cos\gamma\cos\varepsilon \\ -\sin\varepsilon\cos\varepsilon\cos^2\gamma & (\cos^2\varepsilon + \sin^2\gamma\sin^2\varepsilon) & -\sin\gamma\cos\gamma\sin\varepsilon \\ -\sin\gamma\cos\gamma\cos\varepsilon & -\sin\gamma\cos\gamma\sin\varepsilon & \cos^2\gamma \end{pmatrix}.$$

By reintroducing the element subscript $j+\frac{1}{2}$, Equation (B.9) can be expressed as

$$\underline{P}_{j+\frac{1}{2}} = e_{j+\frac{1}{2}}\ddot{\underline{U}}^r_{j+\frac{1}{2}} \tag{B.10}$$

where the global added mass term $e_{j+\frac{1}{2}}$ is defined as the matrix which premultiplies $\underline{\ddot{U}}^r_{j+\frac{1}{2}}$, and $\underline{\ddot{U}}^r$ is the vector containing all the relative fluid accelerations. Therefore $e_{j+\frac{1}{2}}$ is given by

$$e_{j+\frac{1}{2}} = \Big[a_t(\Omega_1) + a_n(\Omega_2)\Big]. \tag{B.11}$$

Appendix C

Derivation of the Fluid Drag Matrix, K

Equations (2.70) and (2.72) can be combined to give

$$\begin{pmatrix} F_x \\ F_y \\ F_z \end{pmatrix} = (\Omega)^T \begin{pmatrix} F_t \\ F_n \cos\phi \\ F_n \sin\phi \end{pmatrix}. \tag{C.1}$$

Expanding this into component parts results in

$$\begin{aligned} F_x &= F_t\big[\cos\gamma\cos\varepsilon\big] - F_n\big[\sin\varepsilon\cos\phi + \cos\varepsilon\sin\gamma\sin\phi\big] \\ F_y &= F_t\big[\cos\gamma\sin\varepsilon\big] - F_n\big[\sin\gamma\sin\varepsilon\sin\phi - \cos\varepsilon\cos\phi\big] \\ F_z &= F_t\big[\sin\gamma\big] - F_n\big[-\cos\gamma\sin\phi\big], \end{aligned}$$

and this can be expressed in the following matrix form

$$\begin{pmatrix} F_x \\ F_y \\ F_z \end{pmatrix} = F_t \begin{pmatrix} \cos\gamma\cos\varepsilon \\ \cos\gamma\sin\varepsilon \\ \sin\gamma \end{pmatrix} - F_n \begin{pmatrix} \sin\varepsilon\cos\phi + \cos\varepsilon\sin\gamma\sin\phi \\ \sin\gamma\sin\varepsilon\sin\phi - \cos\varepsilon\cos\phi \\ -\cos\gamma\sin\phi \end{pmatrix}. \tag{C.2}$$

Letting $K = (F_x, F_y, F_z)^T$ and if the element subscript is reintroduced, then Equation (C.2) can be re-expressed as

$$K_{j+\frac{1}{2}} = \Big\{F_t[\Omega_3] - F_n[\Omega_4]\Big\}_{j+\frac{1}{2}} \tag{C.3}$$

where $\{\}_{j+\frac{1}{2}}$ implies that all the angles within the braces have the subscript $j+\frac{1}{2}$. Similarily for the other element attached to the node the same form of the Equation (C.3) is present but now with the subscript $j-\frac{1}{2}$. Thus the total fluid loading force to be concentrated at node j is given by

$$\underline{N}_j = \frac{1}{2}\big[K_{j+\frac{1}{2}} - K_{j-\frac{1}{2}}\big] \tag{C.4}$$

Appendix D

Solution of the Dispersion Equation

The dispersion equation presented in Equation (3.27) of Chapter 3, is

$$\left(\omega_a - kU\right)^2 = gk\tanh(kd) \tag{D.1}$$

where

- ω_a is apparent wave frequency,
- k is wave number,
- U is current velocity coplanar with the wave heading,
- g is gravitational constant,
- d is water depth.

All the variables in Equation (D.1) are known except for the wave number k. The value of this has to be determined implicitly since k appears on both sides of Equation (D.1) and on the right hand side k occurs in a transcendental function. It is therefore not possible to rearrange the equation to solve directly for k.

The method of determining k is iterative, therefore a value of k is selected and used to evaluate both sides of Equation (D.1). These two values are then compared and if they agree the value of k is correct. If not then the value of k is modified and the process is repeated until the difference between the left and right hand sides of Equation (D.1) is negligible.

The largest possible starting value for k can be determined from the asymptotic behaviour of $\tanh(kd)$, that is, since

$$\tanh(kd) = 1 \text{ for } \mathrm{kd} \geq 11.9, \tag{D.2}$$

then let

$$k_1 = \frac{11.9}{d}. \tag{D.3}$$

Rearranging Equation (D.1) yields the following alternative estimate of k, namely

$$k_2 = \frac{(\omega_a - k_1 U)^2}{g\tanh(k_1 d)}. \tag{D.4}$$

If $(k_2 - k_1)$ is less than some limit, then $k_2 = k_1 = k$ and the wave number has been determined. If $(k_2 - k_1)$ is greater than this limit then a new estimate of k_1 can be made from

$$k_1 = \frac{(k_1 + k_2)}{2} \tag{D.5}$$

and this value is then substituted into Equation (D.4). This process is repeated until $(k_2 - k_1)$ is less than the required limit.

It should be mentioned that Equation (D.1) is not the most common form of the dispersion equation used in the forward speed ship hydrodynamic problems. For such ship problems it is normal to assume deep water so that Equation (D.1) reduces to a quadratic equation in k since $\tanh(kd) = 1$ and in this case there will always be two solutions. For the case $U = 0$ and $\omega_a = \omega$ the dispersion relationship for a regular wave is again solved in the manner described above.

In this study Equation (D.1) is the forward speed dispersion equation for a finite water depth of d. Because of the forward speed term, which in this case corresponds to the uniform current velocity U, there are four possible solutions to Equation (D.1). These solutions depend upon the relative magnitude of U to the wave velocity and are described in Hedges(1983) and in more detail by Peregrine(1976).

Appendix E

Wave Particle Acceleration

Upon substituting Equation (3.29) into Equations (3.31) and (3.32) the following are derived

$$V_{rx'} = \frac{kgH}{2\omega_r}\frac{\cosh(k(z+d))}{\cosh(kd)}\cos(kx' - t(kU+\omega_r)) \tag{E.1}$$

and

$$V_{rz'} = \frac{kgH}{2\omega_r}\frac{\sinh(k(z+d))}{\cosh(kd)}\sin(kx' - t(kU+\omega_r)). \tag{E.2}$$

For the x Component:

For the x component of water particle acceleration we appeal to Equation (3.37), that is

$$A_{ax'} = \frac{D}{Dt}(V_{ax'}) = \frac{\partial}{\partial t}(V_{ax'}) + V_{ax'}\frac{\partial}{\partial x'}(V_{ax'}) + V_{ay'}\frac{\partial}{\partial y'}(V_{ax'}) + V_{az'}\frac{\partial}{\partial z'}(V_{ax'}) \tag{E.3}$$

where $V_{ax'} = V_{rx'} + U$ and $V_{ay'} = V$. Therefore the above equation becomes

$$\begin{aligned} A_{ax'} = {} & \frac{\partial}{\partial t}(V_{rx'}+U) + (V_{rx'}+U)\frac{\partial}{\partial x'}(V_{rx'}+U) \\ & + V\frac{\partial}{\partial y'}(V_{rx'}+U) + (V_{rz'}+C_z)\frac{\partial}{\partial z'}(V_{rx'}+U). \end{aligned} \tag{E.4}$$

Since the current is steady, $\frac{\partial U}{\partial t} = 0$ and since the current is assumed to be horizontally uniform, $\frac{\partial U}{\partial x'} = \frac{\partial U}{\partial y'} = 0$. Also for a monochromatic wave there is no variation in the properties of the wave along the wave crest and so $\frac{\partial}{\partial y}(V_{ry'}) = 0$. Therefore Equation (E.4) reduces to

$$A_{ax'} = \frac{\partial}{\partial t}(V_{rx'}) + (V_{rx'}+U)\frac{\partial}{\partial x'}(V_{rx'}) + (V_{rz'}+C_z)\frac{\partial}{\partial z'}(V_{rx'}+U). \tag{E.5}$$

From Equation (E.1), the following results are derived

$$\frac{\partial}{\partial t}(V_{rx'}) = (kU+\omega_r)\frac{kgH}{2\omega_r}\frac{\cosh(k(z+d))}{\cosh(kd)}\sin(kx' - t(kU+\omega_r)),$$

$$\frac{\partial}{\partial x'}(V_{rx'}) = \frac{-k^2gH}{2\omega_r}\frac{\cosh(k(z+d))}{\cosh(kd)}\sin(kx' - t(kU+\omega_r)),$$

$$\frac{\partial}{\partial z'}(V_{rx'}) = \frac{k^2 gH}{2\omega_r}\frac{\sinh(k(z+d))}{\cosh(kd)}\cos(kx' - t(kU+\omega_r)).$$

Therefore Equation (E.5) can be written as

$$\begin{aligned} A_{ax'} =& (kU+\omega_r)\frac{kgH}{2\omega_r}\frac{\cosh(k(z+d))}{\cosh(kd)}\sin(kx' - t(kU+\omega_r)) \\ &- (V_{rx'}+U)\left[\frac{k^2 gH}{2\omega_r}\frac{\cosh(k(z+d))}{\cosh(kd)}\sin(kx' - t(kU+\omega_r))\right] \\ &+ (V_{rz'}+C_z)\left[\frac{k^2 gH}{2\omega_r}\frac{\sinh(k(z+d))}{\cosh(kd)}\cos(kx' - t(kU+\omega_r)) + \frac{\partial U}{\partial z'}\right]. \end{aligned} \tag{E.6}$$

Defining the following terms

$$\begin{aligned} \alpha &= \cosh(k(z+d)), \\ \beta &= \cosh(kd), \\ \gamma &= \sinh(k(z+d)), \\ \delta &= kx' - t(kU+\omega_r), \\ \varepsilon &= \frac{kgH}{2\omega_r}, \end{aligned}$$

and assuming that there is a vertically uniform current (i.e. $\frac{\partial U}{\partial z'} = 0$), then the following is derived from Equation (E.6) once the substitutions for $V_{rx'}$ and $V_{rz'}$ are made form Equations (E.1) and (E.2)

$$\begin{aligned} A_{ax'} = \left[(kU+\omega_r)\varepsilon\frac{\alpha}{\beta}\sin\delta\right] - \left[Uk\varepsilon\frac{\alpha}{\beta}\sin\delta + \varepsilon^2 k\frac{\alpha^2}{\beta^2}\sin\delta\cos\delta\right] \\ + \left[C_z k\varepsilon\frac{\gamma}{\beta}\cos\delta + \varepsilon^2 k\frac{\gamma^2}{\beta^2}\sin\delta\cos\delta\right]. \end{aligned} \tag{E.7}$$

Rearranging and cancelling leads to

$$A_{ax'} = \frac{\varepsilon}{\beta}\left[\alpha\omega_r\sin\delta - \frac{\varepsilon k}{\beta}\sin\delta\cos\delta + C_z k\gamma\cos\delta\right]. \tag{E.8}$$

For the z Component:

In this case Equation (3.38) provides the expression

$$A_{az'} = \frac{\partial}{\partial t}(V_{az'}) + V_{ax'}\frac{\partial}{\partial x'}(V_{az'}) + V_{ay'}\frac{\partial}{\partial y'}(V_{az'}) + V_{az'}\frac{\partial}{\partial z'}(V_{az'})$$

where $V_{az'} = V_{rx'} + C_{z'}$ and $V_{ax'} = V_{rx'} + U$. Also $\frac{\partial C_z}{\partial x'} = \frac{\partial C_z}{\partial y'} = 0$ since C_z is the same at any point, $\frac{\partial C_z}{\partial t} = 0$ since C_z is assumed to be time invariant, and $\frac{\partial}{\partial y}(V_{rz'} + C_z) = 0$ since there is no variation in the properties of the wave along the wave crest. Therefore the above equation reduces to

$$A_{az'} = \frac{\partial}{\partial t}(V_{rz'}) + (V_{rx'} + U)\frac{\partial}{\partial x'}(V_{rz'}) + (V_{rz'} + C_z)\frac{\partial}{\partial z'}(V_{rz'} + C_z). \tag{E.9}$$

From Equation(E.2), the following results are obtained

$$\frac{\partial}{\partial t}(V_{rz'}) = -(kU + \omega_r)\frac{kgH}{2\omega_r}\frac{\sinh(k(z+d))}{\cosh(kd)}\cos(kx' - t(kU + \omega_r)),$$

$$\frac{\partial}{\partial x'}(V_{rz'}) = \frac{k^2gH}{2\omega_r}\frac{\sinh(k(z+d))}{\cosh(kd)}\cos(kx' - t(kU + \omega_r)),$$

$$\frac{\partial}{\partial z'}(V_{rz'}) = \frac{k^2gH}{2\omega_r}\frac{\cosh(k(z+d))}{\cosh(kd)}\sin(kx' - t(kU + \omega_r)).$$

Therefore Equation (E.9) can be written as

$$\begin{aligned} A_{az'} = &-(kU + \omega_r)\frac{kgH}{2\omega_r}\frac{\sinh(k(z+d))}{\cosh(kd)}\cos(kx' - t(kU + \omega_r)) \\ &+ (V_{rz'} + U)\left[\frac{k^2gH}{2\omega_r}\frac{\sinh(k(z+d))}{\cosh(kd)}\cos(kx' - t(kU + \omega_r))\right] \\ &+ (V_{rz'} + C_z)\left[\frac{k^2gH}{2\omega_r}\frac{\cosh(k(z+d))}{\cosh(kd)}\sin(kx' - t(kU + \omega_r)) + \frac{\partial U}{\partial z'}\right]. \end{aligned} \tag{E.10}$$

Defining the same variables as before, and making the substitutions for $V_{rx'}$ and $V_{rz'}$ given in Equations (E.1) and (E.2), leads to

$$\begin{aligned} A_{az'} = &\left[-(kU + \omega_r)\varepsilon\frac{\gamma}{\beta}\cos\delta\right] + \left[Uk\varepsilon\frac{\gamma}{\beta}\cos\delta + \varepsilon^2k\frac{\alpha\gamma}{\beta^2}\cos^2\delta\right] \\ &+ \left[C_zk\varepsilon\frac{\alpha}{\beta}\sin\delta + \varepsilon^2k\frac{\gamma\alpha}{\beta^2}\sin^2\delta\right], \end{aligned} \tag{E.11}$$

where $\frac{\partial U}{\partial z'}$ is assumed to be zero. Rearranging and cancelling leads to

$$A_{az'} = \frac{\varepsilon}{\beta}\left[C_zk\alpha\sin\delta + \varepsilon k\frac{\alpha\gamma}{\beta} - \omega_r\gamma\cos\delta\right]. \tag{E.12}$$

Appendix F

Derivation of Mass Modifiers

Consider Figure F1 where this diagram shows the geometry of the grounding area with a parabolic profile between the last grounded and first non-grounded nodes. Here it is shown in two dimensions, for the benefit of clarity, but the subsequent derivation is easily generalised to three dimensions. The purpose here is to try and reduce the mass of the first suspended node as it approaches the seabed, in order to reduce the associated impact forces. The actual mass lumped at node j is given by

$$M_{aj} = \frac{1}{2}\left[m_{j-\frac{1}{2}} l_{j-\frac{1}{2}} + m_{j+\frac{1}{2}} l_{j+\frac{1}{2}}\right], \tag{F.1}$$

and it is this term which is to be modified. In terms of Figure 2.8b, the mass at any node j is given by

$$\begin{aligned} M_j &= \frac{1}{2}\left[M_{j+\frac{1}{2}} + M_{j-\frac{1}{2}}\right] + \Delta M \\ &= \frac{1}{2}\left[(M_{j-\frac{1}{2}} + \Delta M) + (M_{j+\frac{1}{2}} + \Delta M)\right]. \end{aligned} \tag{F.2}$$

Mass modifiers are to be applied to the masses lumped at both the first and second nodes. These are denoted by MM_1 and MM_2 respectively and they are applied to both the first and second lifted nodes, i.e.

$$\begin{aligned} M_{L1} &= M_{L1} \times \mathrm{MM}_1 \\ M_{L2} &= M_{L2} \times \mathrm{MM}_2. \end{aligned} \tag{F.3}$$

The modifiers are defined by

$$\mathrm{MM}_1 = C_1 - \frac{\Delta l_{j-\frac{1}{2}}}{l_{j-\frac{1}{2}}} \tag{F.4}$$

and

$$\mathrm{MM}_2 = C_2 - \frac{\Delta l_{j-\frac{1}{2}}}{l_{j-\frac{1}{2}}} \tag{F.5}$$

If the constants C_1 and C_2 are taken to be unity, then in the limit as the node grounds, $\Delta l_{j-\frac{1}{2}} \rightarrow l_{j-\frac{1}{2}}$, so that $M_j \rightarrow 0$ which, in theory, is what is required.

C_1 and C_2 are introduced to facilitate the numerical study of this phenomenon carried out in Chapter 8. The next problem is how to determine the length $\Delta l_{j-\frac{1}{2}}$. Consider Figures F2 and F3; O is defined to be midway along the first suspended element and has coordinates (a, b, c) in the global (x, y, z) axis system. In order to construct the parabola as indicated in Figure F1, a local set of axes, (x'', y'', z''), must be defined, with the x'' axis coincident with the the first suspended element, and y'' and z'' are normal to it. The definition of the required parabola is achieved through the following steps:

1. Transform the coordinates of nodes j and j+1, from the (x, y, z) to the (x', y', z') system by using the following translation

$$\begin{aligned} x' &= (x - a) \\ y' &= (y - b) \\ z' &= (z - c). \end{aligned} \tag{F.6}$$

2. Now rotate the axes (x', y', z') by $\varepsilon_{j+\frac{1}{2}}$ and $\gamma_{j+\frac{1}{2}}$ in order to obtain the new axis system (x'', y'', z''), that is

$$\begin{pmatrix} x'' \\ y'' \\ z'' \end{pmatrix} = (\Omega_{j+\frac{1}{2}}) \begin{pmatrix} x' \\ y' \\ z' \end{pmatrix}, \tag{F.7}$$

where $(\Omega_{j+\frac{1}{2}})$ is the rotational transformation matrix defined by Equation (A.5) of Appendix A.

3. Calculate the distance r from the node j, (or j+1), to the origin of the (x'', y'', z'') axis system. Following the transforms defined in Equations (F.6) and (F.7), it follows that r is equivalent to x''_j.

4. Next the parabola is defined. Consider the Figure F4. A parabola defined about the point A has the following form

$$z = \frac{x^2}{2r}. \tag{F.8}$$

Therefore the origin of the (x'', y'', z'') axis system (defined at O) must be shifted to the origin of the parabola defined at A. This accomplished by increasing all the z'' coordinates by an amount $\frac{r}{2}$, i.e

$$z''' = z'' + \frac{r}{2}. \tag{F.9}$$

5. By selecting a series of positive and negative x'' values, which range evenly from zero (at A) to r, z''' can be calculated and hence there are now a series of points on the parabola defined $(x'', y'', z''')_p$.

6. Now the local $(x'', y'', z''')_p$ coordinates must be transformed back to the global axes. This is done by reversing all the coordinate transformations described above, namely

$$(x'', y'', z''')_p \rightarrow (x'', y'', z'') \text{ by } z'' = z''' - \frac{r}{2}, \tag{F.10}$$

$$\begin{pmatrix} x' \\ y' \\ z' \end{pmatrix} = (\Omega_{j+\frac{1}{2}})^T \begin{pmatrix} x'' \\ y'' \\ z'' \end{pmatrix}, \tag{F.11}$$

and then

$$\begin{aligned} x &= x' + a \\ y &= y' + b \\ z &= z' + c. \end{aligned} \tag{F.12}$$

7. Now the intersection of the parabola with the seabed must be determined. This is done by finding the two points on the parabola which lie on either side of the seabed; this is straightforward since the point above the seabed will be the first point with a positive z coordinate. Linear interpolation is used between these two points to find the x coordinate of the intersection with the seabed, designated x_{gi}, and hence the length $\Delta l_{j+\frac{1}{2}}$, see Figure F1, is given by

$$\Delta l_{j+\frac{1}{2}} = x_{gi} - x_j. \tag{F.13}$$

Appendix G

Rearrangement of the Equations of Motion

The equations of motion are defined in Equations (3.14) and (3.54) and are represented here as

$$M_j\ddot{x}_j + P_{xj} = \left[T\cos\gamma\cos\varepsilon\right]_{j-\frac{1}{2}}^{j+\frac{1}{2}} + F_{xj} \tag{G.1}$$

$$M_j\ddot{y}_j + P_{yj} = \left[T\cos\gamma\sin\varepsilon\right]_{j-\frac{1}{2}}^{j+\frac{1}{2}} + F_{yj} \tag{G.2}$$

$$M_j\ddot{z}_j + P_{zj} = \left[T\sin\gamma\right]_{j-\frac{1}{2}}^{j+\frac{1}{2}} + F_{zj} - W_j. \tag{G.3}$$

Rearranging Equation (G.1) yields

$$\ddot{x}_j = T_{j+\frac{1}{2}}\left\{\frac{\cos\gamma_{j+\frac{1}{2}}\cos\varepsilon_{j+\frac{1}{2}}}{M_j}\right\} - T_{j-\frac{1}{2}}\left\{\frac{\cos\gamma_{j-\frac{1}{2}}\cos\varepsilon_{j-\frac{1}{2}}}{M_j}\right\} + \left\{\frac{F_{xj}-P_{xj}}{M_j}\right\}$$

and this is then defined as

$$\ddot{x}_j = \hat{R}_jT_{j+\frac{1}{2}} + \hat{S}_jT_{j-\frac{1}{2}} + \hat{T}_j. \tag{G.4}$$

Rearranging Equation (G.2) in the same manner, yields

$$\ddot{y}_j = T_{j+\frac{1}{2}}\left\{\frac{\cos\gamma_{j+\frac{1}{2}}\sin\varepsilon_{j+\frac{1}{2}}}{M_j}\right\} - T_{j-\frac{1}{2}}\left\{\frac{\cos\gamma_{j-\frac{1}{2}}\sin\varepsilon_{j-\frac{1}{2}}}{M_j}\right\} + \left\{\frac{F_{yj}-P_{yj}}{M_j}\right\}$$

and this is then defined as

$$\ddot{y}_j = \hat{U}_jT_{j+\frac{1}{2}} + \hat{V}_jT_{j-\frac{1}{2}} + \hat{W}_j. \tag{G.5}$$

Similarly rearranging Equation (G.3) yields

$$\ddot{z}_j = T_{j+\frac{1}{2}}\left\{\frac{\sin\gamma_{j+\frac{1}{2}}}{M_j}\right\} - T_{j-\frac{1}{2}}\left\{\frac{\sin\gamma_{j-\frac{1}{2}}}{M_j}\right\} + \left\{\frac{F_{zj}-W_j-P_{zj}}{M_j}\right\}$$

which then becomes

$$\ddot{z}_j = \hat{O}_jT_{j+\frac{1}{2}} + \hat{P}_jT_{j-\frac{1}{2}} + \hat{Q}_j. \tag{G.6}$$

Where the following apply

$$\hat{R}_j = M_j^{-1}\left[\cos\gamma_{j+\frac{1}{2}}\cos\varepsilon_{j+\frac{1}{2}}\right]$$

$$\hat{S}_j = -M_j^{-1}\left[\cos\gamma_{j-\frac{1}{2}}\cos\varepsilon_{j-\frac{1}{2}}\right]$$

$$\hat{T}_j = M_j^{-1}\left[F_{xj} - P_{xj}\right]$$

$$\hat{U}_j = M_j^{-1}\left[\cos\gamma_{j+\frac{1}{2}}\sin\varepsilon_{j+\frac{1}{2}}\right]$$

$$\hat{V}_j = -M_j^{-1}\left[\cos\gamma_{j-\frac{1}{2}}\sin\varepsilon_{j-\frac{1}{2}}\right]$$

$$\hat{W}_j = M_j^{-1}\left[F_{yj} - P_{yj}\right]$$

$$\hat{O}_j = M_j^{-1}\left[\sin\gamma_{j+\frac{1}{2}}\right]$$

$$\hat{P}_j = -M_j^{-1}\left[\sin\gamma_{j-\frac{1}{2}}\right]$$

$$\hat{Q}_j = M_j^{-1}\left[F_{zj} - W_j - P_{zj}\right].$$

The fluid loads P_{xj}, P_{yj} and P_{zj} are defined in Equations (3.58), (3.59) and (3.60) where, with the addition of the fluid loads on the line attachments, they become

$$\begin{aligned}P_{xj} = \frac{\ddot{x}_j^r}{2}\Big\{&\left[a_t\cos^2\gamma\cos^2\varepsilon + a_n(\sin^2\varepsilon + \cos^2\varepsilon\sin^2\gamma)\right]_{j-\frac{1}{2}}^{j+\frac{1}{2}} + \rho V_{jx}^*\Big\}\\ &+ \frac{\ddot{y}_j^r}{2}\Big\{\left[(a_t - a_n)\cos^2\gamma\cos\varepsilon\sin\varepsilon\right]_{j-\frac{1}{2}}^{j+\frac{1}{2}} + \rho V_{jy}^*\Big\}\\ &+ \frac{\ddot{z}_j^r}{2}\Big\{\left[(a_t - a_n)\sin\gamma\cos\gamma\cos\varepsilon\right]_{j-\frac{1}{2}}^{j+\frac{1}{2}} + \rho V_{jz}^*\Big\},\end{aligned}$$

$$\begin{aligned}P_{yj} = \frac{\ddot{x}_j^r}{2}\Big\{&\left[(a_t - a_n)\cos^2\gamma\sin\varepsilon\cos\varepsilon\right]_{j-\frac{1}{2}}^{j+\frac{1}{2}} + \rho V_{jx}^*\Big\}\\ &+ \frac{\ddot{y}_j^r}{2}\Big\{\left[a_t\cos^2\gamma\sin^2\varepsilon + a_n(\cos^2\varepsilon + \sin^2\varepsilon\sin^2\gamma)\right]_{j-\frac{1}{2}}^{j+\frac{1}{2}} + \rho V_{jy}^*\Big\}\\ &+ \frac{\ddot{z}_j^r}{2}\Big\{\left[(a_t - a_n)\sin\gamma\cos\gamma\sin\varepsilon\right]_{j-\frac{1}{2}}^{j+\frac{1}{2}} + \rho V_{jz}^*\Big\},\end{aligned}$$

and

$$\begin{aligned}P_{zj} = \frac{\ddot{x}_j^r}{2}\Big\{&\left[(a_t - a_n)\sin\gamma\cos\gamma\cos\varepsilon\right]_{j-\frac{1}{2}}^{j+\frac{1}{2}} + \rho V_{jx}^*\Big\}\\ &+ \frac{\ddot{y}_j^r}{2}\Big\{\left[(a_t - a_n)\sin\gamma\cos\gamma\sin\varepsilon\right]_{j-\frac{1}{2}}^{j+\frac{1}{2}} + \rho V_{jy}^*\Big\}\\ &+ \frac{\ddot{z}_j^r}{2}\Big\{\left[a_t\sin^2\gamma + a_n\cos^2\gamma\right]_{j-\frac{1}{2}}^{j+\frac{1}{2}} + \rho V_{jz}^*\Big\}.\end{aligned}$$

Appendix H

Matrix Coefficients for the Segment Error Function

Firstly Equation (3.76) of Chapter 3 is restated, that is

$$ {}^{k+1}\Omega^{n+1}_{j-\frac{1}{2}} = {}^{k}\Omega^{n+1}_{j-\frac{1}{2}} + A^{n+1}_{j-\frac{1}{2}}\delta\tilde{T}^{n+1}_{j-\frac{3}{2}} + B^{n+1}_{j-\frac{1}{2}}\delta\tilde{T}^{n+1}_{j-\frac{1}{2}} + C^{n+1}_{j-\frac{1}{2}}\delta\tilde{T}^{n+1}_{j+\frac{1}{2}} \tag{H.1} $$

where $A^{n+1}_{j-\frac{1}{2}}$, $B^{n+1}_{j-\frac{1}{2}}$ and $C^{n+1}_{j-\frac{1}{2}}$ are defined by

$$ A^{n+1}_{j-\frac{1}{2}} = \frac{\partial}{\partial^k\tilde{T}^{n+1}_{j-\frac{3}{2}}}({}^{k}\Omega^{n+1}_{j-\frac{1}{2}}), \quad B^{n+1}_{j-\frac{1}{2}} = \frac{\partial}{\partial^k\tilde{T}^{n+1}_{j-\frac{1}{2}}}({}^{k}\Omega^{n+1}_{j-\frac{1}{2}}) \text{ and } \mathrm{C}^{\mathrm{n+1}}_{\mathrm{j-\frac{1}{2}}} = \frac{\partial}{\partial^{\mathrm{k}}\tilde{\mathrm{T}}^{\mathrm{n+1}}_{\mathrm{j+\frac{1}{2}}}}({}^{\mathrm{k}}\Omega^{\mathrm{n+1}}_{\mathrm{j-\frac{1}{2}}}), $$

and where

$$ \begin{aligned} {}^{k}\Omega^{n+1}_{j-\frac{1}{2}} = &\left({}^{k+1}\tilde{x}^{n+1}_{j} - {}^{k+1}\tilde{x}^{n+1}_{j-1}\right)^2 + \left({}^{k+1}\tilde{y}^{n+1}_{j} - {}^{k+1}\tilde{y}^{n+1}_{j-1}\right)^2 \\ &+ \left({}^{k+1}\tilde{z}^{n+1}_{j} - {}^{k+1}\tilde{z}^{n+1}_{j-1}\right)^2 - l^2_{j-\frac{1}{2}}\left[1 + \frac{{}^{k}\tilde{T}^{n+1}_{j-\frac{1}{2}}}{E_{j-\frac{1}{2}}A_{j-\frac{1}{2}}}\right]^2. \end{aligned} \tag{H.2} $$

First consider the evaluation of $B^{n+1}_{j-\frac{1}{2}}$, which is given by direct differentiation of Equation (H.2) thus

$$ \begin{aligned} B^{n+1}_{j-\frac{1}{2}} = &2\left({}^{k+1}\tilde{x}^{n+1}_{j} - {}^{k+1}\tilde{x}^{n+1}_{j-1}\right)\frac{\partial}{\partial^k\tilde{T}^{n+1}_{j-\frac{1}{2}}}\left({}^{k+1}\tilde{x}^{n+1}_{j} - {}^{k+1}\tilde{x}^{n+1}_{j-1}\right) \\ &+ 2\left({}^{k+1}\tilde{y}^{n+1}_{j} - {}^{k+1}\tilde{y}^{n+1}_{j-1}\right)\frac{\partial}{\partial^k\tilde{T}^{n+1}_{j-\frac{1}{2}}}\left({}^{k+1}\tilde{y}^{n+1}_{j} - {}^{k+1}\tilde{y}^{n+1}_{j-1}\right) \\ &+ 2\left({}^{k+1}\tilde{z}^{n+1}_{j} - {}^{k+1}\tilde{z}^{n+1}_{j-1}\right)\frac{\partial}{\partial^k\tilde{T}^{n+1}_{j-\frac{1}{2}}}\left({}^{k+1}\tilde{z}^{n+1}_{j} - {}^{k+1}\tilde{z}^{n+1}_{j-1}\right) \\ &- \frac{\partial}{\partial^k\tilde{T}^{n+1}_{j-\frac{1}{2}}}\left\{l^2_{j-\frac{1}{2}}\left(1 + \frac{{}^{k}\tilde{T}^{n+1}_{j-\frac{1}{2}}}{E_{j-\frac{1}{2}}A_{j-\frac{1}{2}}}\right)^2\right\}. \end{aligned} \tag{H.3} $$

Next, using Equation (3.69) with Equation (H.3), this yields

$$
\begin{aligned}
B_{j-\frac{1}{2}}^{n+1} = {} & 2\left({}^{k+1}\tilde{x}_j^{n+1} - {}^{k+1}\tilde{x}_{j-1}^{n+1}\right) \\
& \frac{\partial}{\partial {}^{k}\tilde{T}_{j-\frac{1}{2}}^{n+1}}\left\{\left[\frac{5}{2}x_j^n - 2x_j^{n-1} + \frac{1}{2}x_j^{n-2} + \frac{\Delta t^2}{2}(\hat{R}_j^n\, {}^{k}\tilde{T}_{j+\frac{1}{2}}^{n+1} + \hat{S}_j^n\, {}^{k}\tilde{T}_{j-\frac{1}{2}}^{n+1} + \hat{T}_j^n)\right]\right. \\
& \left. - \left[\frac{5}{2}x_{j-1}^n - 2x_{j-1}^{n-1} + \frac{1}{2}x_{j-1}^{n-2} + \frac{\Delta t^2}{2}(\hat{R}_{j-1}^n\, {}^{k}\tilde{T}_{j-\frac{1}{2}}^{n+1} + \hat{S}_{j-1}^n\, {}^{k}\tilde{T}_{j-\frac{3}{2}}^{n+1} + \hat{T}_{j-1}^n)\right]\right\} \\
& + 2\left({}^{k+1}\tilde{y}_j^{n+1} - {}^{k+1}\tilde{y}_{j-1}^{n+1}\right) \\
& \frac{\partial}{\partial {}^{k}\tilde{T}_{j-\frac{1}{2}}^{n+1}}\left\{\left[\frac{5}{2}y_j^n - 2y_j^{n-1} + \frac{1}{2}y_j^{n-2} + \frac{\Delta t^2}{2}(\hat{U}_j^n\, {}^{k}\tilde{T}_{j+\frac{1}{2}}^{n+1} + \hat{V}_j^n\, {}^{k}\tilde{T}_{j-\frac{1}{2}}^{n+1} + \hat{W}_j^n)\right]\right. \\
& \left. - \left[\frac{5}{2}y_{j-1}^n - 2y_{j-1}^{n-1} + \frac{1}{2}y_{j-1}^{n-2} + \frac{\Delta t^2}{2}(\hat{U}_{j-1}^n\, {}^{k}\tilde{T}_{j-\frac{1}{2}}^{n+1} + \hat{V}_{j-1}^n\, {}^{k}\tilde{T}_{j-\frac{3}{2}}^{n+1} + \hat{W}_{j-1}^n)\right]\right\} \\
& + 2\left({}^{k+1}\tilde{z}_j^{n+1} - {}^{k+1}\tilde{z}_{j-1}^{n+1}\right) \\
& \frac{\partial}{\partial {}^{k}\tilde{T}_{j-\frac{1}{2}}^{n+1}}\left\{\left[\frac{5}{2}z_j^n - 2z_j^{n-1} + \frac{1}{2}z_j^{n-2} + \frac{\Delta t^2}{2}(\hat{O}_j^n\, {}^{k}\tilde{T}_{j+\frac{1}{2}}^{n+1} + \hat{P}_j^n\, {}^{k}\tilde{T}_{j-\frac{1}{2}}^{n+1} + \hat{Q}_j^n)\right]\right. \\
& \left. - \left[\frac{5}{2}z_{j-1}^n - 2z_{j-1}^{n-1} + \frac{1}{2}z_{j-1}^{n-2} + \frac{\Delta t^2}{2}(\hat{O}_{j-1}^n\, {}^{k}\tilde{T}_{j-\frac{1}{2}}^{n+1} + \hat{P}_{j-1}^n\, {}^{k}\tilde{T}_{j-\frac{3}{2}}^{n+1} + \hat{Q}_{j-1}^n)\right]\right\} \\
& - \frac{\partial}{\partial\, {}^{k}\tilde{T}_{j-\frac{1}{2}}^{n+1}}\left\{l_{j-\frac{1}{2}} + \frac{l_{j-\frac{1}{2}}\, {}^{k}\tilde{T}_{j-\frac{1}{2}}^{n+1}}{E_{j-\frac{1}{2}}A_{j-\frac{1}{2}}}\right\}^2 .
\end{aligned}
\tag{H.4}
$$

Carrying out the differentiation indicated in Equation (H.4) yields

$$
\begin{aligned}
B_{j-\frac{1}{2}}^{n+1} = {} & \Delta t^2\left\{\left({}^{k+1}\tilde{x}_j^{n+1} - {}^{k+1}\tilde{x}_{j-1}^{n+1}\right)\left(\hat{S}_j^n - \hat{R}_{j-1}^n\right)\right. \\
& + \left({}^{k+1}\tilde{y}_j^{n+1} - {}^{k+1}\tilde{y}_{j-1}^{n+1}\right)\left(\hat{V}_j^n - \hat{U}_{j-1}^n\right) \\
& \left. + \left({}^{k+1}\tilde{z}_j^{n+1} - {}^{k+1}\tilde{z}_{j-1}^{n+1}\right)\left(\hat{P}_j^n - \hat{O}_{j-1}^n\right)\right\} \\
& - \frac{2l_{j-\frac{1}{2}}^2}{E_{j-\frac{1}{2}}A_{j-\frac{1}{2}}}\left(1 + \frac{{}^{k}\tilde{T}_{j-\frac{1}{2}}^{n+1}}{E_{j-\frac{1}{2}}A_{j-\frac{1}{2}}}\right).
\end{aligned}
\tag{H.5}
$$

The derivative $A_{j-\frac{1}{2}}^{n+1}$ has almost the same form as Equation (H.4), except that the explicit derivatives are now taken with respect to ${}^{k}\tilde{T}_{j-\frac{3}{2}}^{n+1}$, rather than with respect to ${}^{k}\tilde{T}_{j-\frac{1}{2}}^{n+1}$. Hence

$$
\begin{aligned}
A_{j-\frac{1}{2}}^{n+1} = -\Delta t^2\left\{\left({}^{k+1}\tilde{x}_j^{n+1} - {}^{k+1}\tilde{x}_{j-1}^{n+1}\right)\hat{S}_{j-1}^n + \left({}^{k+1}\tilde{y}_j^{n+1} - {}^{k+1}\tilde{y}_{j-1}^{n+1}\right)\hat{V}_{j-1}^n \right. \\
\left. + \left({}^{k+1}\tilde{z}_j^{n+1} - {}^{k+1}\tilde{z}_{j-1}^{n+1}\right)\hat{P}_{j-1}^n\right\}.
\end{aligned}
\tag{H.6}
$$

Similarily the derivative $C_{j-\frac{1}{2}}^{n+1}$ is obtained from Equation (H.4) by replacing the explicit derivatives with respect to ${}^{k}\tilde{T}_{j-\frac{1}{2}}^{n+1}$ by ${}^{k}\tilde{T}_{j+\frac{1}{2}}^{n+1}$, to yield

$$C_{j-\frac{1}{2}}^{n+1} = \Delta t^2 \Big\{ ({}^{k+1}\tilde{x}_j^{n+1} - {}^{k+1}\tilde{x}_{j-1}^{n+1})\hat{R}_j^n + ({}^{k+1}\tilde{y}_j^{n+1} - {}^{k+1}\tilde{y}_{j-1}^{n+1})\hat{U}_j^n + ({}^{k+1}\tilde{z}_j^{n+1} - {}^{k+1}\tilde{z}_{j-1}^{n+1})\hat{O}_j^n \Big\}. \tag{H.7}$$

Appendix I

VN Stability for Mooring Line Dynamics

In this appendix the important details in establishing that the VN stability condition is satisfied when the Houbolt scheme is applied to the problem of mooring line dynamics are presented. To simplify the algebraic manipulation, the proof is only established for the 2D form of the equations of motion. The derivation is further simplified by neglecting terms related to added mass, tangential fluid drag and line attachements. Despite these assumptions the amount of algebraic manipulation is considerable and therefore only the principle points in the solution are indicated.

The 2D form of the equations of motion are given in Equations (4.1a) and (4.1b) which, under the assumption that terms related to the added mass are neglected, are written as

$$M_j \ddot{x}_j = [T \cos\gamma]_{j-\frac{1}{2}}^{j+\frac{1}{2}} + F_{xj} \tag{I.1}$$

and

$$M_j \ddot{z}_j = [T \sin\gamma]_{j-\frac{1}{2}}^{j+\frac{1}{2}} + F_{zj} - W_j. \tag{I.2}$$

The constraint equation, as expressed in Equation (3.72), is also required. The 2D form of this is

$$\text{constant} = (x_{j+1} - x_j)^2 + (y_{j+1} - y_j)^2 - l_{j+\frac{1}{2}}\left[1 + \frac{T_{j+\frac{1}{2}}}{EA}\right]^2. \tag{I.3}$$

The drag terms F_{xj} and F_{zj} in Equations (I.1) and (I.2) are derived from consideration of the 2D form of the transformation matrix $[\Omega]$, which is derived in Appendix A. The 2D form is obtained by setting $\varepsilon = 0$ and ignoring all the terms related to the global y direction, so that

$$[\Omega]_{2D} = \begin{pmatrix} \cos\gamma & \sin\gamma \\ -\sin\gamma & \cos\gamma \end{pmatrix}. \tag{I.4}$$

The relationship between the global and local fluid loads on element $j+\frac{1}{2}$, for example, is then

$$\begin{pmatrix} F_x \\ F_z \end{pmatrix}_{j+\frac{1}{2}} = \begin{pmatrix} \cos\gamma & -\sin\gamma \\ \sin\gamma & \cos\gamma \end{pmatrix}_{j+\frac{1}{2}} \begin{pmatrix} F_t \\ F_n \end{pmatrix}_{j+\frac{1}{2}}. \tag{I.5}$$

With $F_{xj} = \frac{1}{2}(F_{x(j+\frac{1}{2})} + F_{x(j-\frac{1}{2})})$ and $F_{zj} = \frac{1}{2}(F_{z(j+\frac{1}{2})} + F_{z(j-\frac{1}{2})})$, the following are derived

$$F_{xj} = -\frac{1}{2}(F_{n(j+\frac{1}{2})} \sin\gamma_{j+\frac{1}{2}} + F_{n(j-\frac{1}{2})} \sin\gamma_{j-\frac{1}{2}}) \tag{I.6}$$

and

$$F_{zj} = \frac{1}{2}(F_{n(j+\frac{1}{2})} \cos\gamma_{j+\frac{1}{2}} + F_{n(j-\frac{1}{2})} \cos\gamma_{j-\frac{1}{2}}) \tag{I.7}$$

with the assumption that the tangential fluid drag force, F_t, is negligible. Therefore the expanded forms of Equations (I.1) and (I.2) are

$$\begin{aligned} M_j\ddot{x}_j = {} & T_{j+\frac{1}{2}} \cos\gamma_{j+\frac{1}{2}} - T_{j-\frac{1}{2}} \cos\gamma_{j-\frac{1}{2}} \\ & - \frac{1}{2}(F_{n(j+\frac{1}{2})} \sin\gamma_{j+\frac{1}{2}} + F_{n(j-\frac{1}{2})} \sin\gamma_{j-\frac{1}{2}}) \end{aligned} \tag{I.8}$$

and

$$\begin{aligned} M_j\ddot{z}_j = {} & T_{j+\frac{1}{2}} \sin\gamma_{j+\frac{1}{2}} - T_{j-\frac{1}{2}} \sin\gamma_{j-\frac{1}{2}} \\ & + \frac{1}{2}(F_{n(j+\frac{1}{2})} \cos\gamma_{j+\frac{1}{2}} + F_{n(j-\frac{1}{2})} \cos\gamma_{j-\frac{1}{2}}). \end{aligned} \tag{I.9}$$

From basic trigonometry it will be seen that Equation (I.3) can be re-expressed in the following equivalent form

$$0 = \cos^2\gamma_{j+\frac{1}{2}} + \sin^2\gamma_{j+\frac{1}{2}} - \left[1 + \frac{2T_{j+\frac{1}{2}}}{EA} + \frac{T^2_{j+\frac{1}{2}}}{(EA)^2}\right]. \tag{I.10}$$

Equations (I.8), (I.9) and (I.10) form the starting set of equations for this derivation. The 'variational' forms of these equations are now derived. This is done by assuming that each variable has an associated error, for example the error in the tension $T_{j+\frac{1}{2}}$ is denoted by $\delta T_{j+\frac{1}{2}}$, so that the total tension term is now expressed as $T_{j+\frac{1}{2}} + \delta T_{j+\frac{1}{2}}$. Similarily the total acceleration and angle terms are denoted by $\ddot{U}_j + \delta\ddot{U}_j$ and $\cos\gamma_{j+\frac{1}{2}} + \delta\cos\gamma_{j+\frac{1}{2}}$ respectively. By subtracting the original form of the equations, the variational forms are derived and are given by

$$\begin{aligned} M_j\delta\ddot{x}_j = {} & T_{j+\frac{1}{2}}\delta\cos\gamma_{j+\frac{1}{2}} \delta T_{j+\frac{1}{2}} \cos\gamma_{j+\frac{1}{2}} - T_{j-\frac{1}{2}}\delta\cos\gamma_{j-\frac{1}{2}} \delta T_{j-\frac{1}{2}} \cos\gamma_{j-\frac{1}{2}} \\ & - \frac{1}{2}\Big[\delta F_{n(j+\frac{1}{2})} \sin\gamma_{j+\frac{1}{2}} + F_{n(j+\frac{1}{2})}\delta\sin\gamma_{j+\frac{1}{2}} + \delta F_{n(j-\frac{1}{2})} \sin\gamma_{j-\frac{1}{2}} \\ & + F_{n(j-\frac{1}{2})}\delta\sin\gamma_{j-\frac{1}{2}}\Big] \end{aligned} \tag{I.11}$$

$$M_j\delta\ddot{z}_j = T_{j+\frac{1}{2}}\delta\sin\gamma_{j+\frac{1}{2}}\delta T_{j+\frac{1}{2}}\sin\gamma_{j+\frac{1}{2}} - T_{j-\frac{1}{2}}\delta\sin\gamma_{j-\frac{1}{2}}\delta T_{j-\frac{1}{2}}\sin\gamma_{j-\frac{1}{2}}$$
$$-\frac{1}{2}\Big[\delta F_{n(j+\frac{1}{2})}\cos\gamma_{j+\frac{1}{2}} + F_{n(j+\frac{1}{2})}\delta\cos\gamma_{j+\frac{1}{2}} + \delta F_{n(j-\frac{1}{2})}\cos\gamma_{j-\frac{1}{2}} \quad \text{(I.12)}$$
$$+ F_{n(j-\frac{1}{2})}\delta\cos\gamma_{j-\frac{1}{2}}\Big]$$

$$0 = 2\delta\cos\gamma_{j+\frac{1}{2}}\cos\gamma_{j+\frac{1}{2}} + 2\delta\sin\gamma_{j+\frac{1}{2}}\sin\gamma_{j+\frac{1}{2}} - \frac{2\delta T_{j+\frac{1}{2}}}{EA}\Big[1 - \frac{T_{j+\frac{1}{2}}}{EA}\Big]. \quad \text{(I.13)}$$

In this it is assumed that only errors of first order are significant, that is terms such as $\delta T_{j+\frac{1}{2}}\delta\cos\gamma_{j+\frac{1}{2}}$ are considered negligible. The normal drag component $F_{n(j+\frac{1}{2})}$ is represented by

$$F_{n(j+\frac{1}{2})} = -\frac{1}{2}\rho C d_{j+\frac{1}{2}} D_{j+\frac{1}{2}}\dot{r}^2_{j+\frac{1}{2}} \quad \text{(I.14)}$$

or,

$$F_{n(j+\frac{1}{2})} = -\frac{1}{2}\rho C d_{j+\frac{1}{2}} D_{j+\frac{1}{2}}|\dot{r}_{j+\frac{1}{2}}|\dot{r}_{j+\frac{1}{2}}. \quad \text{(I.15)}$$

The variational form of this is derived from Equation (I.14), so that

$$\delta F_{n(j+\frac{1}{2})} = \rho C d_{j+\frac{1}{2}} D_{j+\frac{1}{2}}|\dot{r}_{j+\frac{1}{2}}|\delta\dot{r}_{j+\frac{1}{2}}. \quad \text{(I.16)}$$

The normal velocity component $\dot{r}_{j+\frac{1}{2}}$ is derived from $[\Omega]_{2D}$ and is

$$\dot{r}_{j+\frac{1}{2}} = -\dot{x}_{j+\frac{1}{2}}\sin\gamma_{j+\frac{1}{2}} + \dot{z}_{j+\frac{1}{2}}\cos\gamma_{j+\frac{1}{2}}. \quad \text{(I.17)}$$

The velocity in the global x direction is also considered to include the effects of ocean currents, therefore

$$\dot{x}_{j+\frac{1}{2}} = \frac{1}{2}\Big[(\dot{x}_{j+1} - C_{x(j+1)}) + (\dot{x}_j - C_{xj})\Big]$$

and hence Equation (I.17) becomes

$$\dot{r}_{j+\frac{1}{2}} = -\frac{1}{2}\Big[(\dot{x}_{j+1} - C_{x(j+1)}) + (\dot{x}_j - C_{xj})\Big]\sin\gamma_{j+\frac{1}{2}} + \dot{z}_{j+\frac{1}{2}}\sin\gamma_{j+\frac{1}{2}} \quad \text{(I.18)}$$

and the variational form is

$$\delta\dot{r}_{j+\frac{1}{2}} = -\frac{1}{2}\Big[(\delta\dot{x}_{j+1} - \delta C_{x(j+1)}) + (\delta\dot{x}_j - \delta C_{xj})\Big]\sin\gamma_{j+\frac{1}{2}}$$
$$-\frac{1}{2}\Big[(\dot{x}_{j+1} - C_{x(j+1)}) + (\dot{x}_j - C_{xj})\Big]\delta\sin\gamma_{j+\frac{1}{2}} \quad \text{(I.19)}$$
$$+ \delta\dot{z}_{j+\frac{1}{2}}\cos\gamma_{j+\frac{1}{2}} + \dot{z}_{j+\frac{1}{2}}\cos\gamma_{j+\frac{1}{2}}.$$

Additionally, the variational forms of the velocity and acceleration forms (Equations (3.46) and (3.45) respectively) of the Houbolt scheme are needed. These are, simply,

$$\delta\ddot{\underline{U}}_j^{n+1} = \frac{1}{(\Delta t)^2}\left\{2\delta\underline{U}_j^{n+1} - 5\delta\underline{U}_j^{n} + 4\delta\underline{U}_j^{n-1} - \delta\underline{U}_j^{n-2}\right\} \tag{I.20}$$

and

$$\delta\dot{\underline{U}}_j^{n+1} = \frac{1}{6\Delta t}\left\{11\delta\underline{U}_j^{n+1} - 18\delta\underline{U}_j^{n} + 9\delta\underline{U}_j^{n-1} - 2\delta\underline{U}_j^{n-2}\right\}. \tag{I.21}$$

The variational forms of the cosine and sine terms are represented in terms of nodal displacements, to yield

$$\delta\cos\gamma_{j+\frac{1}{2}} = \frac{\delta x_{j+1} - \delta x_j}{l_{j+\frac{1}{2}}} \tag{I.22}$$

and

$$\delta\sin\gamma_{j+\frac{1}{2}} = \frac{\delta z_{j+1} - \delta y_j}{l_{j+\frac{1}{2}}}. \tag{I.23}$$

Substitution of Equations (I.15) to (I.23) into the variational Equations (I.11), (I.12) and (I.13) and, following some manipulation, it will be seen that the variational terms in these three equations are only δx, δz and δT, with the appropriate subscripts. The error terms are assumed to have the following form

$$\begin{aligned}
\delta x_j &= a.\exp(i\beta j + \alpha n\Delta t) \\
\delta z_j &= b.\exp(i\beta j + \alpha n\Delta t) \\
\delta T_j &= c.\exp(i\beta j + \alpha n\Delta t).
\end{aligned} \tag{I.24}$$

It is to noted that there will be terms of the form $\exp(i\beta j)$ and $\exp(\alpha n\Delta t)$ which are common to all terms and therefore cancel. After some further considerable algebraic manipulation, the terms may be grouped as coefficients of a, b and c, to yield the following matrix representation of the three equations

$$\begin{pmatrix} F - A\sin\gamma & D + B\sin\gamma & H\cos\gamma \\ -D + A\cos\gamma & F - B\cos\gamma & H\sin\gamma \\ G\cos\gamma & G\sin\gamma & I \end{pmatrix} \begin{pmatrix} a \\ b \\ c \end{pmatrix} = 0 \tag{I.25}$$

where

$$
\begin{aligned}
A &= \frac{\rho C d D|\dot{r}|}{4}\left\{2i\dot{z}\sin\beta - \frac{l\sin\gamma}{6\Delta t}(1+\cos\beta)(11\lambda - 18 + 9\lambda^{-1} - 2\lambda^{-2})\right\} \\
B &= \frac{\rho C d D|\dot{r}|}{4}\left\{2i(\dot{x} - C_x)\sin\beta - \frac{l\cos\gamma}{6\Delta t}(1+\cos\beta)(11\lambda - 18 + 9\lambda^{-1} - 2\lambda^{-2})\right\} \\
D &= iD_n \sin\beta \\
F &= \frac{Ml}{(\Delta t)^2}(2\lambda - 5 + 4\lambda^{-1} - \lambda^{-2}) + 4T\sin^2\left(\frac{\beta}{2}\right) \\
H &= 2i\sin\left(\frac{\beta}{2}\right) \\
I &= \frac{-2}{EA}\left(\cos\left(\frac{\beta}{2}\right) + i\sin\left(\frac{\beta}{2}\right)\right)\left[1 + \frac{T}{EA}\right] \\
G &= \frac{2}{l}\left(\cos\beta + i\sin\beta - 1\right).
\end{aligned}
\tag{I.26}
$$

During the manipulation the variational equations, given by Equations (I.11), (I.12) and (I.13), into the matrix form of Equation (I.25), several assumptions and simplifications have been made. These are:

1. All coefficients of the variational quantities are assumed to be constant over a small area of the space-time region. This means that terms such as $T_{j+\frac{1}{2}}\delta\cos\gamma_{j+\frac{1}{2}} - T_{j-\frac{1}{2}}\delta\cos\gamma_{j-\frac{1}{2}}$ for example, becomes $T(\delta\cos\gamma_{j+\frac{1}{2}} - \delta\cos\gamma_{j-\frac{1}{2}})$.

2. The following are employed

$$
\begin{aligned}
\lambda &= \exp(\alpha\Delta t) \\
\exp(i\beta) &= \cos\beta + i\sin\beta \\
\exp(-i\beta) &= \cos\beta - i\sin\beta.
\end{aligned}
$$

3. The subscripts have been omitted for clarity and ease of presentation.

Equation (I.25) is more succinctly expressed as

$$[P][a] = 0 \tag{I.27}$$

and it will be seen from the definitions of the coefficients given in Equation (I.26) that the P_{33} element is the only term which includes the elasticity of the mooring line. For an inelastic line, the constraint equation expressed by Equation (I.3) becomes

$$l_{j+\frac{1}{2}}^2 = (x_{j+1} - x_j)^2 + (z_{j+1} - z_j)^2$$

or,

$$1 = \cos^2 \gamma_{j+\frac{1}{2}} + \sin \gamma_{j+\frac{1}{2}}. \tag{I.28}$$

Following the usual procedure, the variational form of Equation (I.28) is

$$0 = \delta \cos \gamma_{j+\frac{1}{2}} \cos \gamma_{j+\frac{1}{2}} + \delta \sin \gamma_{j+\frac{1}{2}} \sin \gamma_{j+\frac{1}{2}}. \tag{I.29}$$

When the solutions for the error terms given by the relationships in Equation (I.24) are substituted in Equation (I.29), it is seen that the coefficient of c will be zero since there is no tension term present. Hence $P_{33} = 0$ for an inelastic mooring line.

The stability of the set of equations expressed in Equation (I.27) is examined by calculating the roots of the characteristic equation (or determinant) of the coefficient matrix $[P]$. For a non-trivial solution it is required that

$$|P| = 0. \tag{I.30}$$

The complexity of the resulting characteristic equation is governed by whether the case of an inelastic or elastic mooring line is considered. The characteristic equation for the inelastic case is a 3^{rd} order polynomial in λ, whilst for the elastic case the characteristic equation is 6^{th} order polynomial in λ. The initial expansion for the determinant in Equation (I.30), for an elastic mooring line, is given by

$$\begin{aligned}(F - A\sin\gamma)\begin{pmatrix} F - B\cos\gamma & H\sin\gamma \\ G\sin\gamma & I \end{pmatrix} - (D + B\sin\gamma)\begin{pmatrix} -D + A\cos\gamma & H\sin\gamma \\ G\cos\gamma & I \end{pmatrix} \\ + (H\cos\gamma)\begin{pmatrix} -D + A\cos\gamma & F - B\cos\gamma \\ G\cos\gamma & G\sin\gamma \end{pmatrix} = 0.\end{aligned} \tag{I.31}$$

Making the substitutions given by the relationships in Equation (I.26) and following some extensive manipulation, the coefficients of the powers of λ can be determined. These coefficients are further arranged into their real and imaginary parts. From this it transpires that the greatest power of λ is 6; because of this, a general analytic solution cannot be used to obtain the roots of the polynomial and consequently a numerical solution technique developed by NAG was used. The routine selected was C02ADF; the theory is described in Grant and Hitchins(1971) but briefly, the method determines one root at a time and then divides this out from the polynomial using the technique of 'composite deflation' to minimise the errors.

Appendix J

Derivation of Amplification Matrices

Here the Finite Difference schemes are applied to the uncoupled scalar form of the Equations of Motion as derived in Chapter 4. For this purpose it is assumed that the equations are lightly damped and that there is no forcing function, i.e.

$$\ddot{\underline{U}} + 2p\xi\dot{\underline{U}} + p^2\underline{U} = 0. \tag{J.1}$$

Central Difference Scheme

By application of the CD equations as given by Equations (3.43) and (3.44) of Chapter 3, a matrix recursion expression of the following form is obtained

$$\begin{pmatrix} \underline{U}^{n+1} \\ \underline{U}^{n} \end{pmatrix} = (A) \begin{pmatrix} \underline{U}^{n} \\ \underline{U}^{n-1} \end{pmatrix} \tag{J.2}$$

and the resulting amplification matrix is defined by

$$(A) = \begin{pmatrix} \frac{2-p^2\Delta t^2}{1+\Delta t\xi p} & \frac{\Delta t\xi p-1}{1+\Delta t\xi p} \\ 1 & 0 \end{pmatrix}. \tag{J.3}$$

Houbolt Scheme

Application of the equations for the Houbolt scheme, as given in Equations (3.45) and (3.46) in Chapter 3, to Equation (J.1), yields a recurrence form thus

$$\begin{pmatrix} \underline{U}^{n+1} \\ \underline{U}^{n} \\ \underline{U}^{n-1} \end{pmatrix} = (A) \begin{pmatrix} \underline{U}^{n} \\ \underline{U}^{n-1} \\ \underline{U}^{n-2} \end{pmatrix} \tag{J.4}$$

and the resulting amplification matrix is given by

$$(A) = \begin{pmatrix} (\frac{5\beta}{\Delta t^2p^2} + 6\kappa) & -(\frac{4\beta}{\Delta t^2p^2} + 3\kappa) & (\frac{\beta}{\Delta t^2p^2} + \frac{2\kappa}{3}) \\ 1 & 0 & 0 \\ 0 & 1 & 0 \end{pmatrix} \tag{J.5}$$

where

$$\beta = \left(\frac{2}{\Delta t^2p^2} + \frac{11\xi}{3\Delta tp} + 1\right)^{-1}. \tag{J.6}$$

Wilson-θ Scheme

By applying the equations of the Wilson-θ scheme, as given by Equations (3.47) and (3.48) of Chapter 3, a recursion equation of the following form is required

$$\begin{pmatrix} \underline{\ddot{U}}^{n+\theta\Delta t} \\ \underline{\dot{U}}^{n+\theta\Delta t} \\ \underline{U}^{n+\theta\Delta t} \end{pmatrix} = (A) \begin{pmatrix} \underline{\ddot{U}}^{n} \\ \underline{\dot{U}}^{n} \\ \underline{U}^{n} \end{pmatrix} \tag{J.7}$$

hence

$$(A) = \begin{pmatrix} (1-\theta\kappa-\frac{\theta^2\beta}{3}-\frac{1}{\theta}) & -\frac{1}{\Delta t}(2\kappa+\theta\beta) & -(\frac{\beta}{\Delta t^2}) \\ \Delta t(1-\frac{\kappa\theta}{2}-\frac{\theta^2\beta}{6}-\frac{1}{2\theta}) & (1-\kappa-\frac{\theta\beta}{2}) & -(\frac{\beta}{2\Delta t}) \\ \Delta t^2(\frac{1}{2}-\frac{\kappa\theta}{6}-\frac{\theta^2\beta}{18}-\frac{1}{6\theta}) & \Delta t(1-\frac{\kappa}{3}-\frac{\theta\beta}{6}) & (1-\frac{\beta}{6}) \end{pmatrix} \tag{J.8}$$

where

$$\beta = \left(\frac{2}{p^2\Delta t^2} + \frac{11\xi}{3\Delta t p} + 1\right)^{-1}. \tag{J.9}$$

Newmark Scheme

By applying the equations of the Newmark Scheme, as given by Equations (3.49) and (3.50) in Chapter 3, to Equation (J.1), a recurrence equation of the following form is derived

$$\begin{pmatrix} \underline{\ddot{U}}^{n+1} \\ \underline{\dot{U}}^{n+1} \\ \underline{U}^{n+1} \end{pmatrix} = (A) \begin{pmatrix} \underline{\ddot{U}}^{n} \\ \underline{\dot{U}}^{n} \\ \underline{U}^{n} \end{pmatrix} \tag{J.10}$$

and the resulting amplification matrix is

$$(A) = \begin{pmatrix} -(2\kappa(1-\delta)+\beta(\frac{1}{2}-\alpha)) & -(\frac{2\kappa}{\Delta t}+\frac{\beta}{\Delta t}) & -(\frac{\beta}{\Delta t^2}) \\ \Delta t(1-\delta-2\kappa\delta(1-\delta)-\beta\delta(\frac{1}{2}-\alpha)) & (1-2\kappa\delta-\beta\delta) & -(\frac{\beta\delta}{\Delta t}) \\ \Delta t^2(\frac{1}{2}-\alpha-2\alpha\kappa(1-\delta)-\alpha\beta(\frac{1}{2}-\alpha) & \Delta t(1-2\kappa\alpha-\alpha\beta) & (1-\alpha\beta) \end{pmatrix} \tag{J.11}$$

where

$$\beta = \left(\frac{1}{\Delta t^2 p^2} + \frac{2\xi\delta}{\Delta t p} + \alpha\right)^{-1}. \tag{J.12}$$

The expression for κ is the same for all the matrices and is given by

$$\kappa = \frac{\xi\beta}{p\Delta t}. \tag{J.13}$$

References

Allen,D. W., Lammert,W. F., Hale,J. R., and Jacobsen,V. (1989) "Submarine Pipeline On-Bottom Stability: Recent AGA Research", *Proceedings of the 21st Offshore Technology Conference*, May, Paper No. 6055, pp. 121-132.

Ansari, K. A. and Khan, N. U., (1986) "The Effect Of Cable Dynamics On The Station-Keeping Response Of A Moored Offshore Vessel", *Proceedings Of The Fifth Symposium On Offshore Mechanics And Arctic Engineering*, pg. 514.

Bathe, K. J., (1982) "Finite Element Procedures In Engineering Analysis", Prentice - Hall.

Berteaux, H. O., (1976) "Buoy Engineering", *A Wiley-Interscience Publication.*

Boom, H. J. J., (1984) "Mooring Line Dynamics", *MARIN Report No. 45064-3-RD*, Phase II - Part 1, November.

Boom, H. J. J., (1985) "Dynamic Behaviour Of Mooring Lines", 4th *Intl. Conf. On The Behaviour Of Offshore Structures*, Delft, July, pg. 359.

Boom, H. J. J., Dekker, J. N. and Van Elsacker, A. W., (1987) "Dynamic Aspects Of Offshore Riser And Mooring Concepts", *Proceedings of the 19th Offshore Technology Conference*, Vol. III, April, pg. 405.

Brennodden,H., Liegn,J. T., Sotberg, T., and Verley,R. L. P. (1989) "An Energy-Based Pipe-Soil Interaction Model", *Proceedings Of The 21st Offshore Technology Conference*, May, Paper No. 6057, pp. 147-158.

Chen, M. C. and Chou, F., (1986) "Dynamic Mooring System Comparison for a Deepwater Semisubmersible", *Proceedings Of The Fifth Symposium On Offshore Mechanics And Arctic Engineering*, pp. 479-486.

Dominguez, R. F. and Filmer, R. W., (1971) "Discrete Paramter Analysis as a Practical Means For Solving Mooring Behaviour Problems", *Proceedings Of The 3rd Offshore Technology Conference*, April, Paper No. OTC 1505.

Dominguez, R. F. and Smith, C. E., (1972) "Dynamic Analysis of Cable Systems", *Journal of the Structural Division, Proc. ASME*, August, pp. 1817-1834.

Dutta,A., (1988) "A Simple Method of Analyzing Mooring Chains With Embedded Anchor Point", *Journal of Offshore Mechanics And Arctic Engineering*, February 1988, Vol. 110, pp. 71-73.

Foss, K. A., (1958) "Co-Ordinates Which Uncouple the Equations of Motion of Damped Linear Dynamic Systems", *Journal of Applied Mechanics*, Vol. 25.

Goodman, T. R. and Breslin, J. P., (1976) "Statics And Dynamics Of Anchoring Cables In Waves", *Journal Of Hydronautics*, No. 4, October, pg. 112.

Ghosh, P. K., (1980) "Discrete Lumped Mass Modelling for the Time Domain Structural Dynamic Simulation of Cable Systems Immersed in a Fluid", *Internal Progress Report, Department of Naval Architecture and Shipbuilding, University of Newcastle upon Tyne, England*, December.

Ghosh, P. K., (1981) "Direct time integration Method for Nonlinear Hydroelastic Analysis of Marine Cables - Results and Proposals for Alternative Numerical Integration Methods With Improved Stability Characteristics", *Internal Progress Report, Department of Naval Architecture and Shipbuilding, University of Newcastle upon Tyne, England*, Project 3.4, April.

Grant, J. A., and Hitchins, G. D., (1971) "An Always Convergent Minimization Technique for the Solution of Polynomial Equations", *J. Inst. Maths Applics*, Vol. 8, pp. 122-129.

Hairston, D. E., (1979) "Dynamics Of Vessels Moored By Multiple Cables In Deep Water", *Marine Technology*, Vol. 16, No. 2, April, pg. 156.

Hale,J. R., Lammert,W. F., and Jacobsen,V. (1989) "Improved Basis for Static Stability Analysis and Design of Marine Pipelines", *Proceedings Of The 21st Offshore Technology Conference*, May, Paper No. 6059, pp. 171-180.

Hale,J. R., Lammert,W. F., and Allen,D. W. (1991) "Pipeline On-Bottom Stability Calculations: Comparison of Two State-of-the-Art Methods and Pipe-Soil Interaction," *Proceedings Of The 23rd Offshore Technology Conference*, May, Paper No. 6761, pp. 567-582.

Hearn, G. E., Lau, S. M. and Tong, K. C., (1988) "Wave Drift Damping Influence Upon The Time Domain Simulation Of Moored Structures", *Proceedings Of The 20th Offshore Technology Conference*, May.

Hedges, T, S., (1983) "Effects of Currents on Wave Drag and Inertia Loads", Private Communication.

Hilber, H. M. and Taylor, T. J. R., (1978) "Collocation, Dissapation and 'Overshoot' for Time Integration Schemes in Structural Dynamics", *Earthquake Engineering and Structural Dynamics*, Vol. 6, pp. 99-117.

Houbolt, J. C., (1950) "A Recurrence Matrix Solution for the Dynamic Response of Elastic Aircraft", *Journal of Aeronautical Science*, Vol 17.

Huse, E., (1986) "Influence of Mooring Line Damping Upon Rig Motions", *Proceedings Of The 18th Offshore Technology Conference*, May, Paper No. 5204.

Huse, E., and Matsumoto, K., (1989) "Mooring Line Damping Due To First-And Second-Order Vessel Motion", *Proceedings Of The 21st Offshore Technology Conference*, May, Paper No. 6137.

Hwang, Y. L., (1984) "Nonlinear Dynamic Analysis of Mooring Lines".

Jennings, A. J., (1962) "The Free Cable", *The Engineer*, Dec.

Johansson, P. I., (1978) "Non-Linear Dynamic Response of A Mooring Line", *Det Norske Veritas*, Publication No. 106, March.

Karel,K., and Halvorsen,S. A., (1982) "Dynamics of the Water-Pipeline-Soil Interaction", *Proceedings Of The First Symposium On Offshore Mechanics And Arctic Engineering*, Vol. II, pp. 41-48.

Kwan,C. T., and Bruen,F. J., (1991) "Mooring Line Dynamics: Comparison of Time Domain, Frequency Domain, and Quasi-Static Analysis", *Proceedings Of The 23rd Offshore Technology Conference*, May, Paper No. 6657, pp. 95-108.

Lambert, J. D., (1973) "Computational Methods in Ordinary Differential Equations", Chapters 2 and 5.

Lammert,W. F., Hale,J. R., and Jacobsen,V. (1989) "Dynamic Response of Submarine Pipelines Exposed to Combined Wave and Current Action", *Proceedings Of The 21st Offshore Technology Conference*, May, Paper No. 6058, pp. 159-170.

Larsen, C. M. and Fylling, I. J., (1982) "Dynamic Behaviour Of Anchor Lines", *Intl. Conf. On The Behaviour of Offshore Structures*, pg. 651.

Leonard, J. W., (1979) "Newton-Raphson Iterative Method Applied to Circularly Towed Cable-Body Systems", *Engineering Structures*, Vol. 1, Jan., pp. 73-78.

Macdonald, R. C., (1984) "Positional Mooring Offshore", *Lloyd's Register Technical Association*, Paper No. 4, Session 1984-1985.

Mchlachlan, N. W., (1961) "Bessel Functions For Engineers", *Oxford University Press*, London, England, pp. 106-109.

McNamara, J. F., (1993) *Private Communication.*

Nakajima, T., Motora, S. and Fujino, M., (1982) "On The Dynamic Analysis Of Multi-Component Mooring Lines", *Proceedings Of The 14th Offshore Technology Conference*, May, Paper No. OTC 4309.

Nakajima, T., (1986a) "A New Three Dimensional Quasi-Static Solution For The Multi-component Mooring Systems", *Proceedings Of The Fifth Symposium On Offshore Mechanics And Arctic Engineering*, Vol. III, pg. 487.

Nakajima, T., (1986b) "Time Domain Simulations of Coupled Responses of a Moored Buoy and Mooring Lines in Deep Water", *Proc. Intl. Symp. Developments in Deeper Water*, RINA. London, October.

Newmark, N. M., (1959) "A Method of Computation for Structural Dynamics", *Journal of the Engineering Mechanics Division , Proc. A.S.M.E*, July, pg. 67.

Nuckolls, C. E. and Dominguez, R. F., (1977) "Large Displacement Mooring Dynamics", *Proceedings Of The* 9^{th} *Offshore Technology Conference*, May, Paper No. OTC 2880.

O'Brien, G. G., Morton, H. A. and Kaplan, S., (1950) "A Study of the Numerical Solution of Partial Differential Equations", *Journal of Mathematics and Physics*, Vol 29.30, pg. 223.

O'Brien, P. J., and McNamara, J. F., (1989) "Significant Characteristics of Three-Dimensional Flexible Riser Analysis", *Engineering Structures*, Vol. 11, October, pp. 223-233.

O'Brien, W. T., (1967), "General Solution of Suspended Cable Problems", *J. of the Structural Division*, ASCE, Vol. 93, ST!, Feb.

Oden, J. T., (1972) "Finite Elements in Nonlinear Continua", *McGraw-Hill*, Inc., New York.

Oppenheim, B. W., and Wilson, P. A., (1982) "Static 2-D Solution of A Mooring Line of Arbitrary Composition in the Vertical and Horizontal Operating Modes", *International Shipbuilding Progress*, June.

Park, K. C., (1975) "An Improved Stiffly Stable Method for Direct Integration of Nonlinear Structural Dynamics", *Trans. of the ASME*, June, pp. 464-470.

Peregrine, D, H., (1976) "Interaction of Water Waves and Current", *Advances in Applied Mechanics*, Vol. 16, pg. 9.

Peyrot, A. H., (1980) "Marine Cable Structures", *J. of the Structural Division*, ASCE, Vol. 106, No. ST12, Dec., pp. 2391-2404.

Polacheck, H., Walton, T. S., Mejia, R. and Dawson, C., (1963) "Transient Motion Of A Cable Immersed In A Fluid", *Mathematics Of Computation*, Vol. 17, No. 81, January, pg. 60.

Ractliffe, A. T., (1984) "Dynamic Response of Flexible Catenary Risers", *Int. Symp. on Developments in Floating Production Systems*, London, March, Paper No. 15.

Ramzan, F. A. and Mitchell, N. D., (1985) "Design Considerations And Behaviour Of Moored Offshore Vessels", *Intl. Conf. On The Behaviour Of Offshore Structures*, pg. 973.

Ramzan, F. A. and Robinson, R. W., (1986) "An Engineering Assessment Of The Validity Of The Quasi-Static Approach To Semisubmersible Mooring Design", *Proceedings Of The* 18^{th} *Offshore Technology Conference*, May, Paper No. OTC 5203.

Richtmyer, R. D., and Morton, K. W., (1967) "Difference Methods for Initial Value Problems", *Interscience Publishers (John Wiley and Sons).*

Seidl, L. H., Foreman, R. D., Beynet, P. A. and Singhal, S. N., (1987) "Prediction Of Stability, Mooring Load and Motion Aboard Floating Platforms", *Proceedings Of The* 19^{th} *Offshore Technology Conference*, May, Paper No. 5447.

Skop, R. A. and O'Hara, G. J., (1970) "The method of Imaginary reactions - A New Technique for Analysing Structural Cable Systems", *Marine Technology Society Journal*, Vol. 4, No. 1, pp. 21-30.

Skop, R. A. and O'Hara, G. J., (1972) "A Method for the Analysis of Internally Redundant Structural Cable Arrays", *Marine Technology Society Journal*, Vol. 6, Part 1, Jan./Feb., pp. 6-18.

Sparks, C. P., (1983) "The Influence of Tension, Pressure and Weight on Pipe and Riser Deformations and Stresses", *Proceedings Of The Second Symposium On Offshore Mechanics And Arctic Engineering*, pp. 443-452.

Stoker, J. J., (1957) *Water Waves*, Interscience Publishers Inc., New York.

Tein, Y. S. D., Cantrel, J. M., Marol., P. and Huang, K., (1987) "A Rational Dynamic Analysis Procedure for Turret Mooring Systems", *Proceedings of the* 19^{th} *Offshore Technology Conference*, Paper No. OTC 5527.

Timoshenko, S., Young, D. H., and Weaver, D. H., (1974) "Vibration Problems in Engineering", 4^{th} *ed. John Wiley and Sons.*

Wagner,D. A., and Murff,J. D. (1987) "Pipe-Soil Interaction Model", *Proceedings of the* 19^{th} *Offshore Technology Conference*, May, Paper No. 5504, pp. 181-190.

Walton, T. S. and Polacheck, H., (1960) "Calculation Of Transient Motion Of Submerged Cables",*Mathematics Of Computation*, Vol. 14, pg. 27.

Wang, H. T., (1975) "Determination of the Accuracy of Segmented Representations of Cable Shape", *Petroleum Division of the ASME*, Paper No. 74-Pet-52, pg. 472-478.

Webster, R. L., (1975a) "Non-Linear Static and Dynamic Response of Underwater Cable Structures Using the Finite Element Approach", *Proceedings of the* 7^{th} *Offshore Technology Conference*, Paper No. 2322, pp. 753-764.

Webster, R. L., (1975b) "Structural Response of Arbitrary Underwater Cable Systems", *Ocean Engineering Mechanics, ASME*, Vol. 1.

Wichers, J. E. W., and Sluijs, M. F., (1979) "The Influence of Waves on the Low-Frequency Hydrodynamic Coefficients of Moored Vessels", *Proceedings of the* 11^{th} *Offshore Technology Conference*, April, Paper No. OTC 3625.

Wichers, J. E. W., (1982) "On the Low Frequency Surge Motions of Vessels Moored in High Seas", *Proceedings of the* 14^{th} *Offshore Technology Conference*, May, Paper No. OTC 4437.

Wichers, J. E. W. and Huijsmans, R. H. M., (1990) "The Contribution of Hydrodynamic Damping Induced by Mooring Chains on Low Frequency Vessel Motions", *Proceedings of the* 22^{nd} *Offshore Technology Conference*, May, Paper No. OTC 6218.

Wilhelmy, V. and Fjeld, S., (1981) "Non-Linear Response Analysis of Anchorage Systems for Compliant Deep Water Plateforms", *Proceedings of the* 13^{th} *Offshore Technology Conference*, May, Paper No. OTC 4051.

Wilhelmy, V. and Fjeld, S., (1982) "Assessment of Deep-Water Anchorings Based on Their Dynamic Behaviour", *Proceedings of the* 14^{th} *Offshore Technology Conference*, May, Paper No. OTC 4174.

Wilson, E. L., (1968) "A Computer Program for the Dynamic Stress Analysis of Underground Structures", *SESM Report No. 68-1, Division of Structural Engineering and Structural Mechanics, Univ. of California, Berkeley.*

Wood, W. L., (1981) "Numerical Integration of Structural Dynamics Equations Including Natural Damping and Periodic Forcing Terms", *International Journal for Numerical Methods in Engineering*, Vol. 17, pp. 281-289.

Wood, W. L., (1990) "Practical Time Stepping Schemes", *Oxford Applied Mathematics and Computing Science Series*, Clarendon Press, Oxford.

Zienkiewicz, O. C., (1971) "The Finite Element Method in Engineering Science", *McGraw-Hill*, Inc., London.

Figures

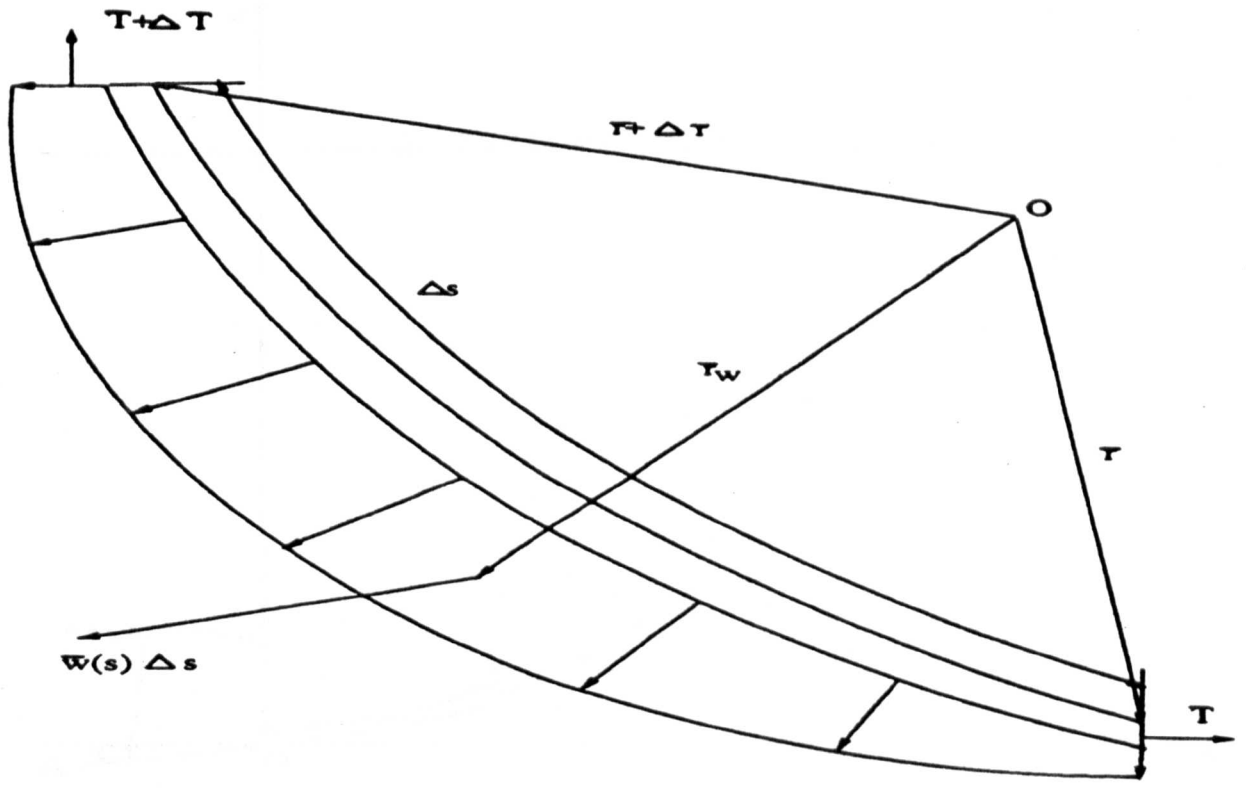

Figure 2.1 — Geometry For A Catenary Element

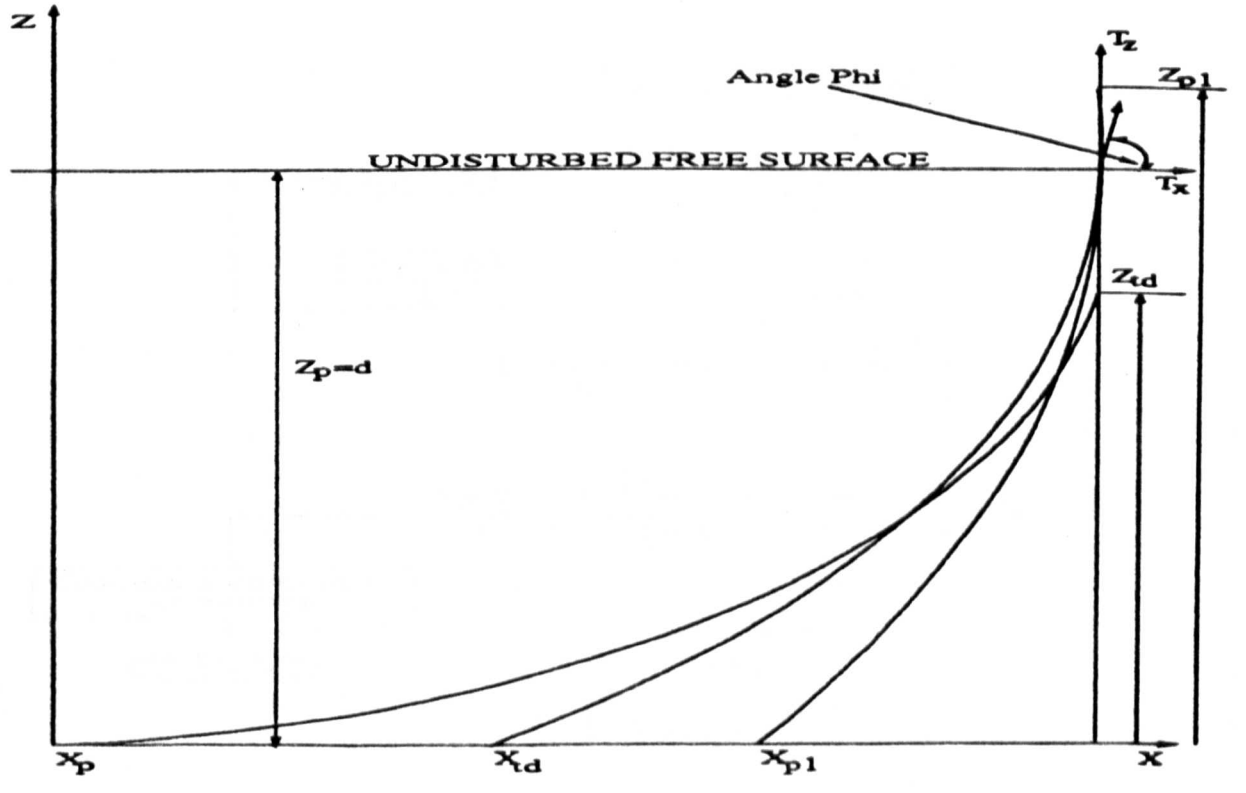

Figure 2.2 — Definition of A Complete Catenary

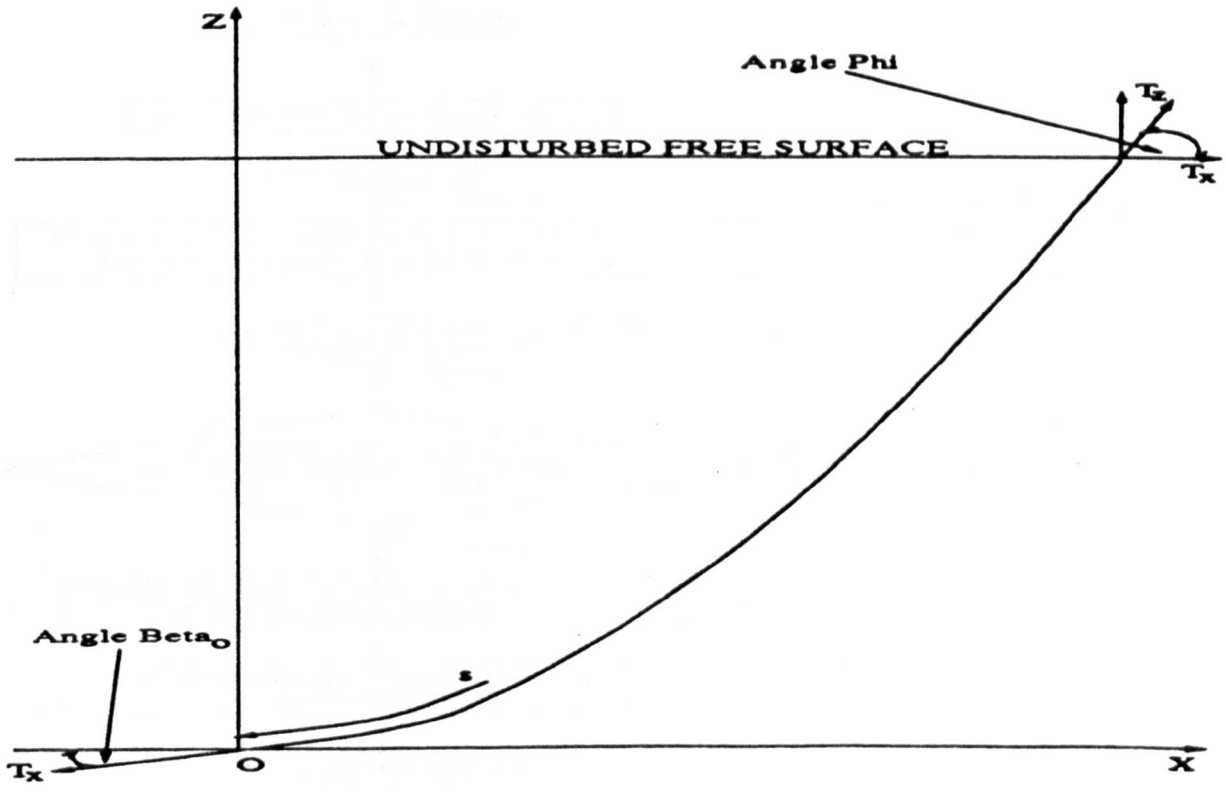

Figure 2.3 — Definition of A Partial Catenary

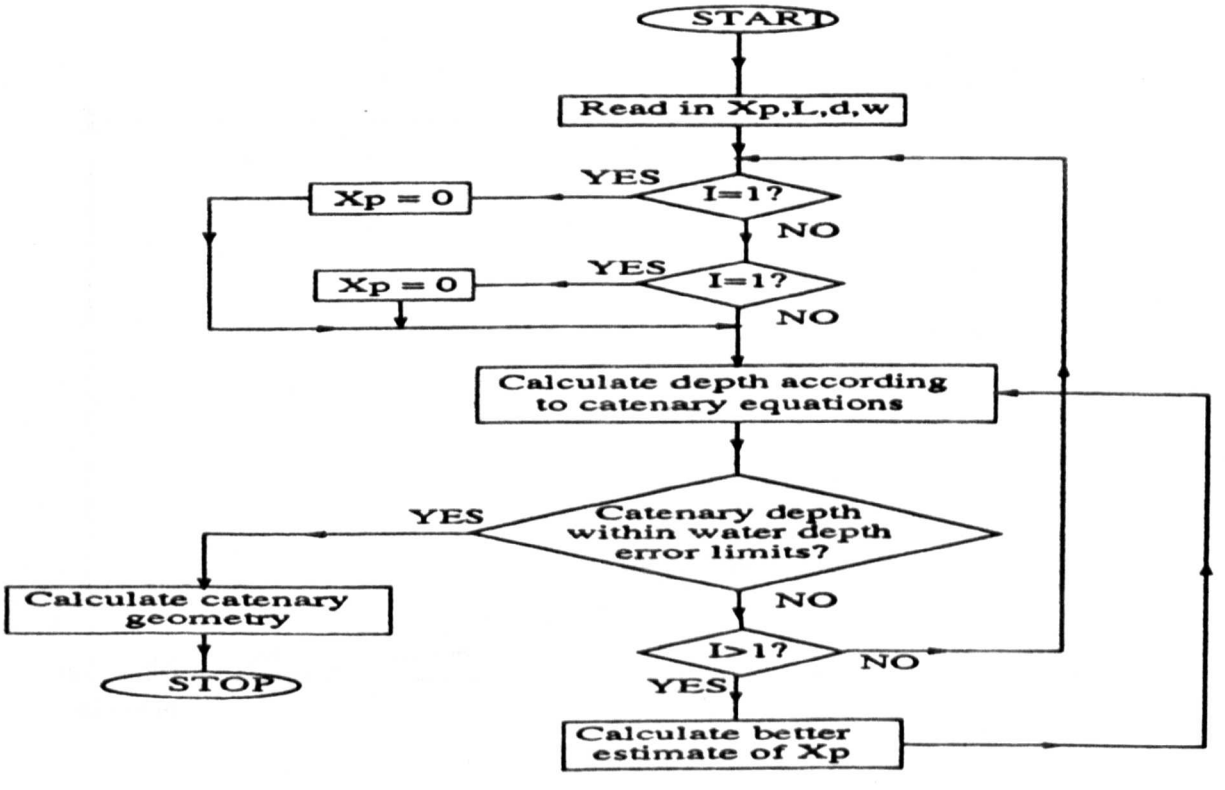

Figure 2.4 — Flow Chart for Solution of A Complete Catenary

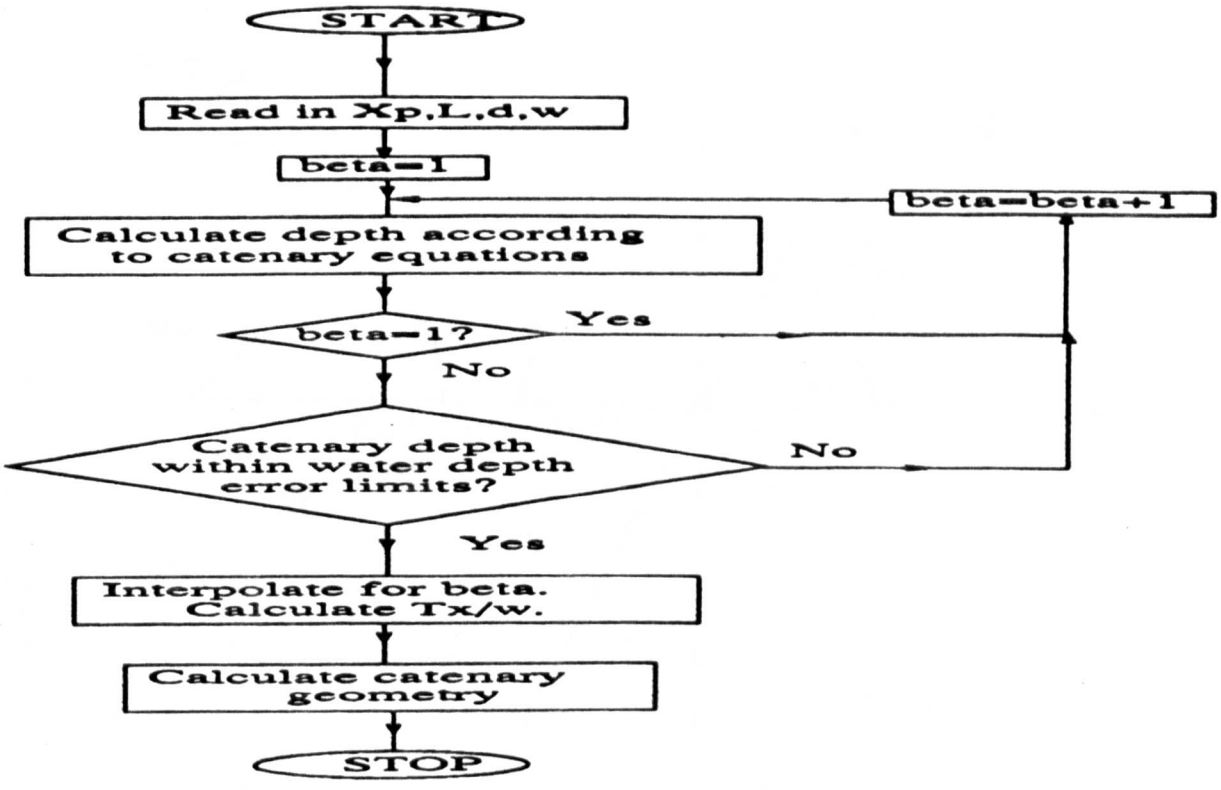

Figure 2.5 — Flow Chart for Solution of A Partial Catenary

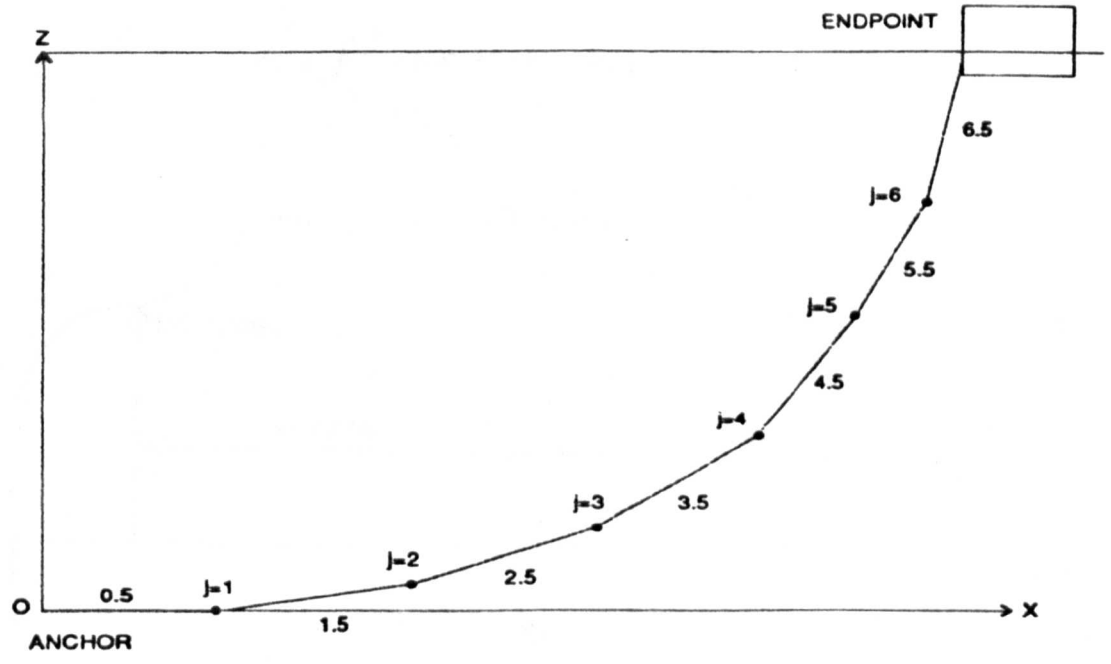

Figure 2.6 — Definitions of Element and Node Numbering

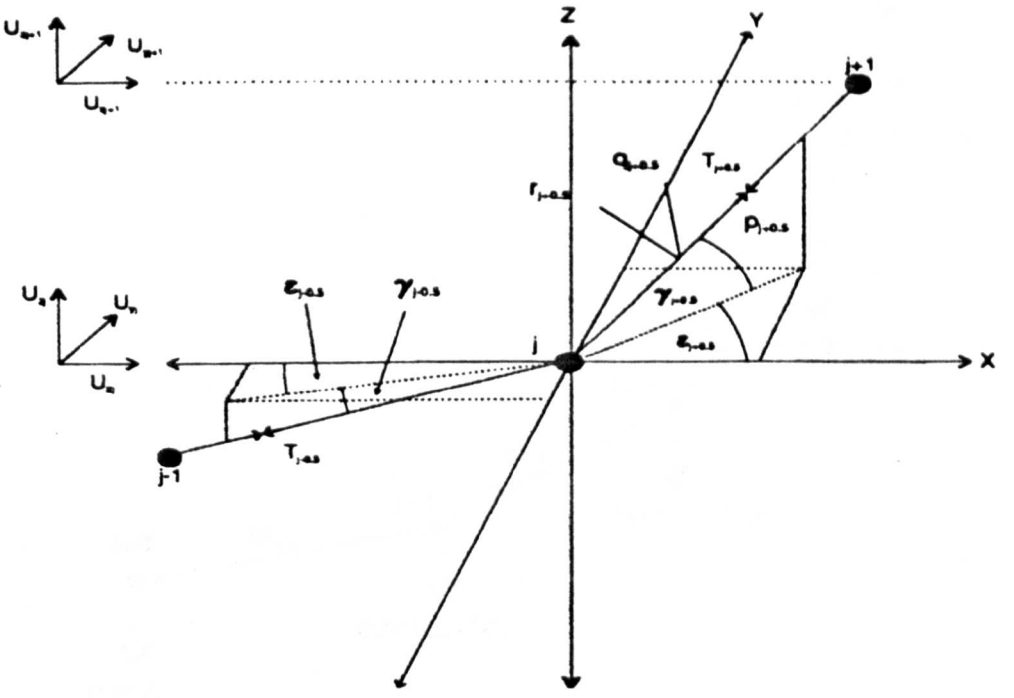

Figure 2.7 — Definition Nodes, Elements and Orientation in 3D

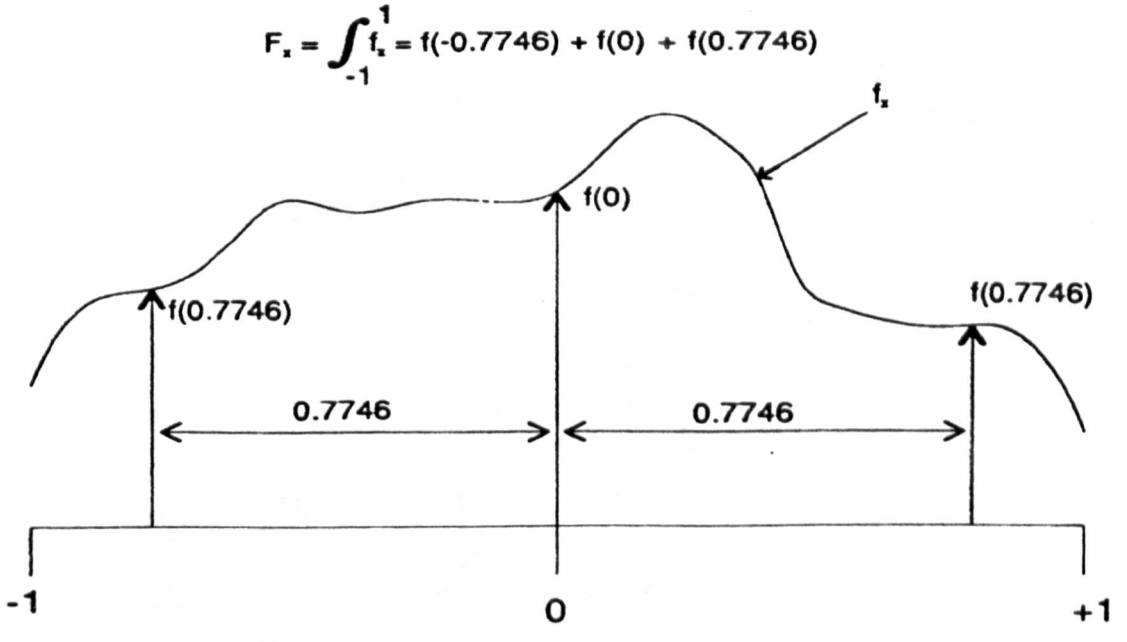

Figure 2.8 — Integration Scheme for Fluid Loading

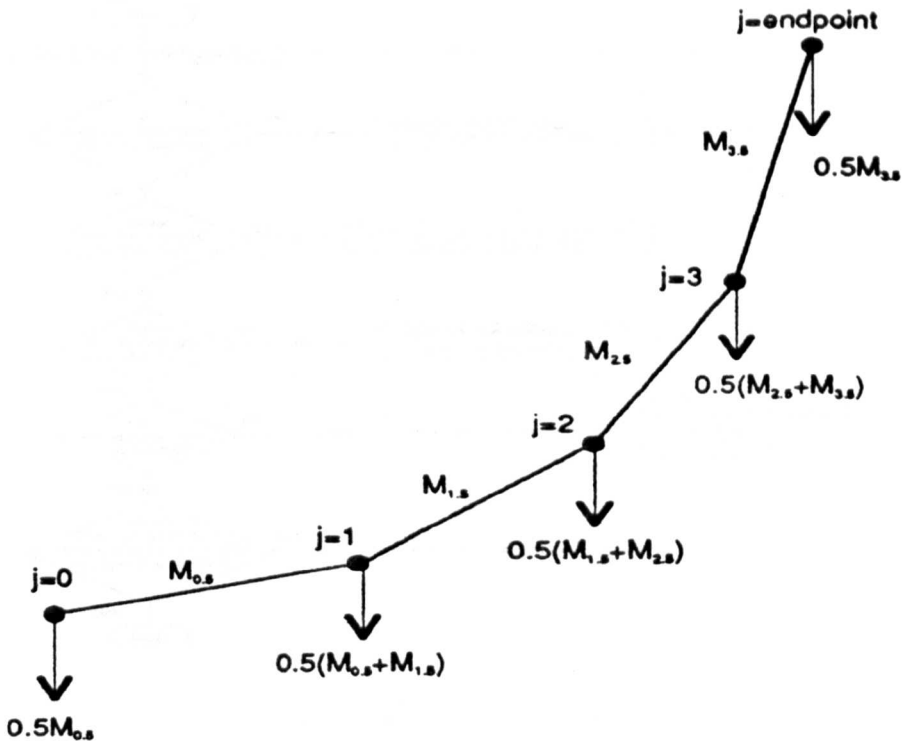

Figure 2.9 — First Mass Distribution

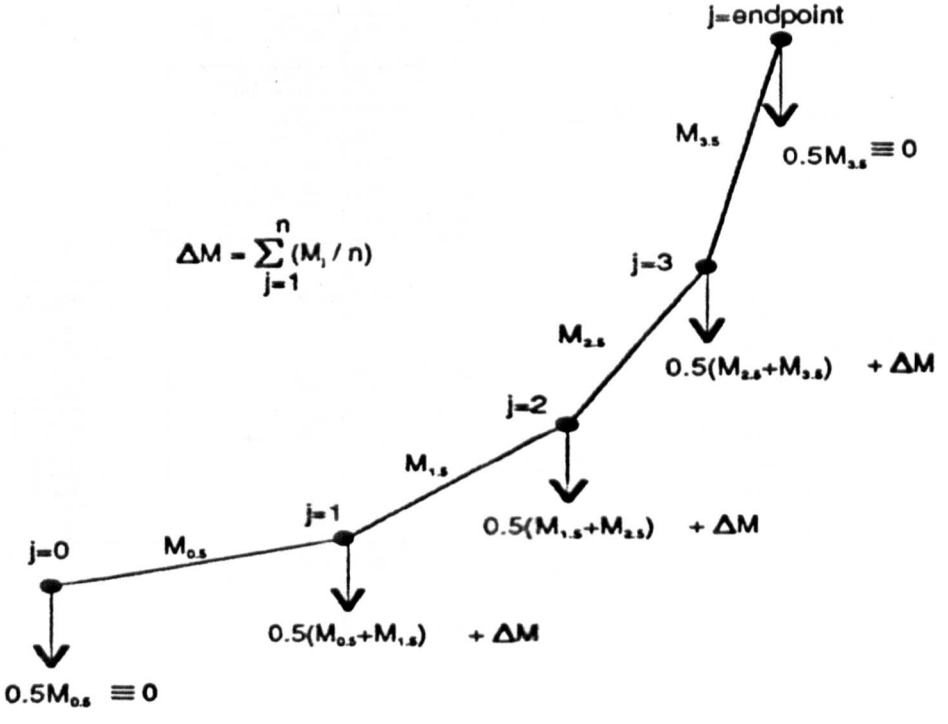

Figure 2.10 — Second Mass Distribution

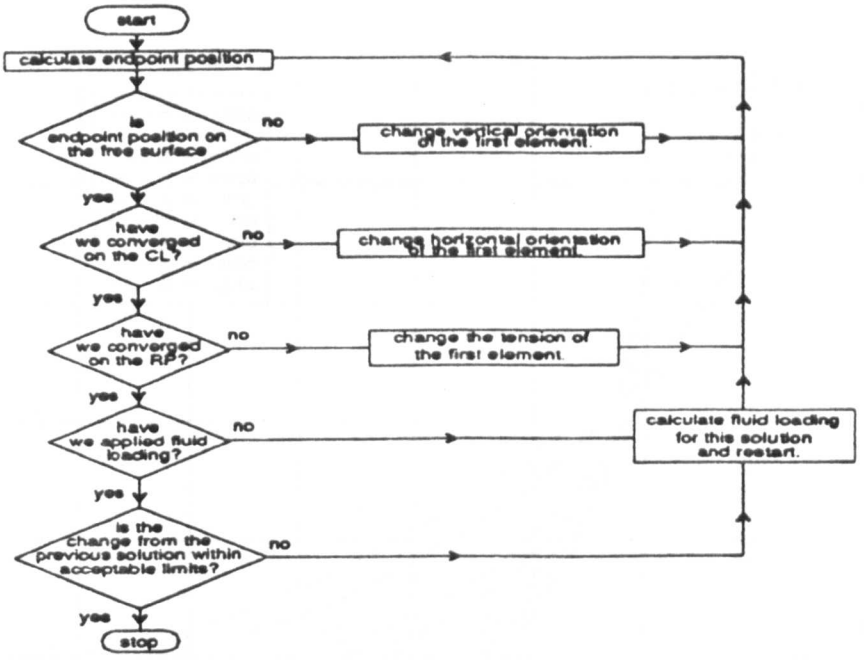

Figure 2.11 — Flow Chart for the Static Numerical Procedure

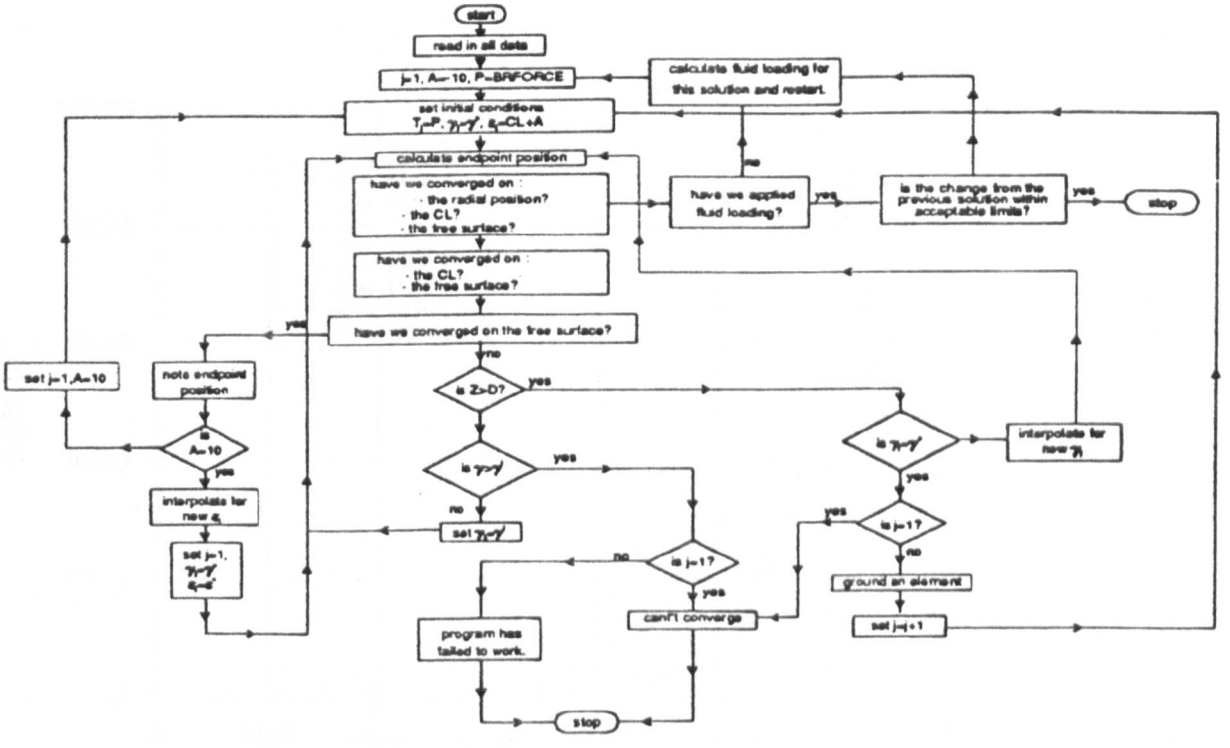

Figure 2.12 — Detailed Flow Chart for the Static Numerical Procedure

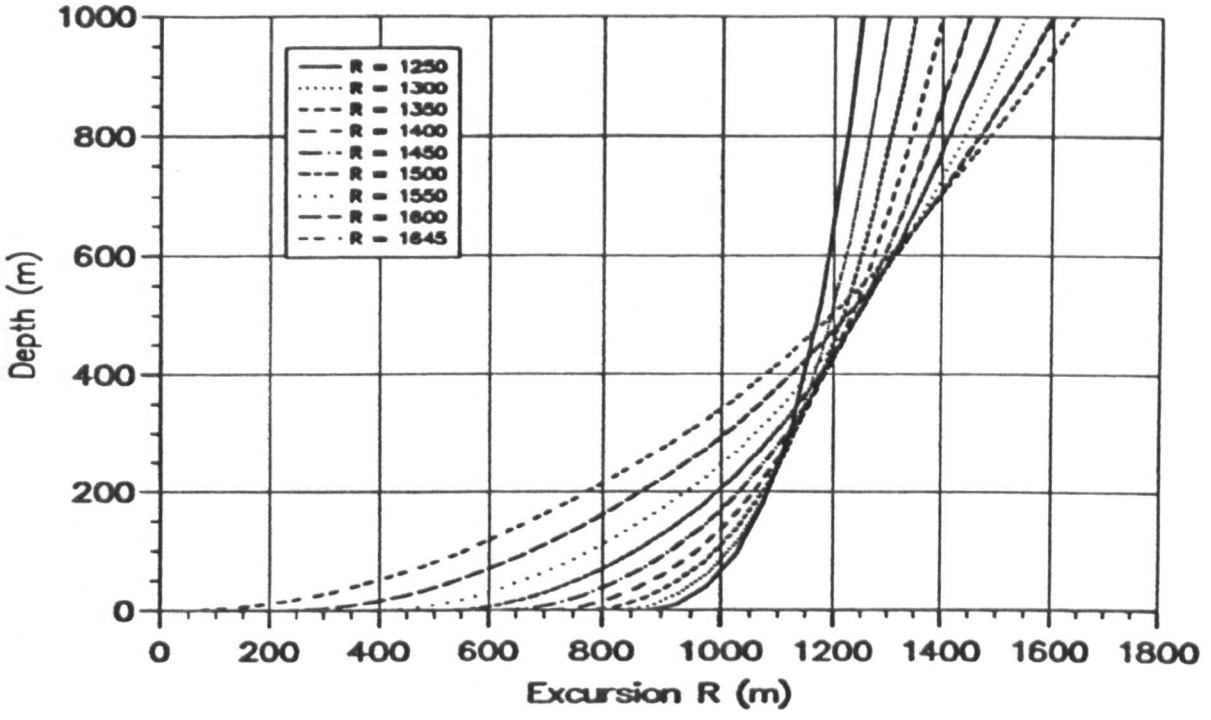

Figure 2.13 — Catenary Cable Geometry At Different Excursions

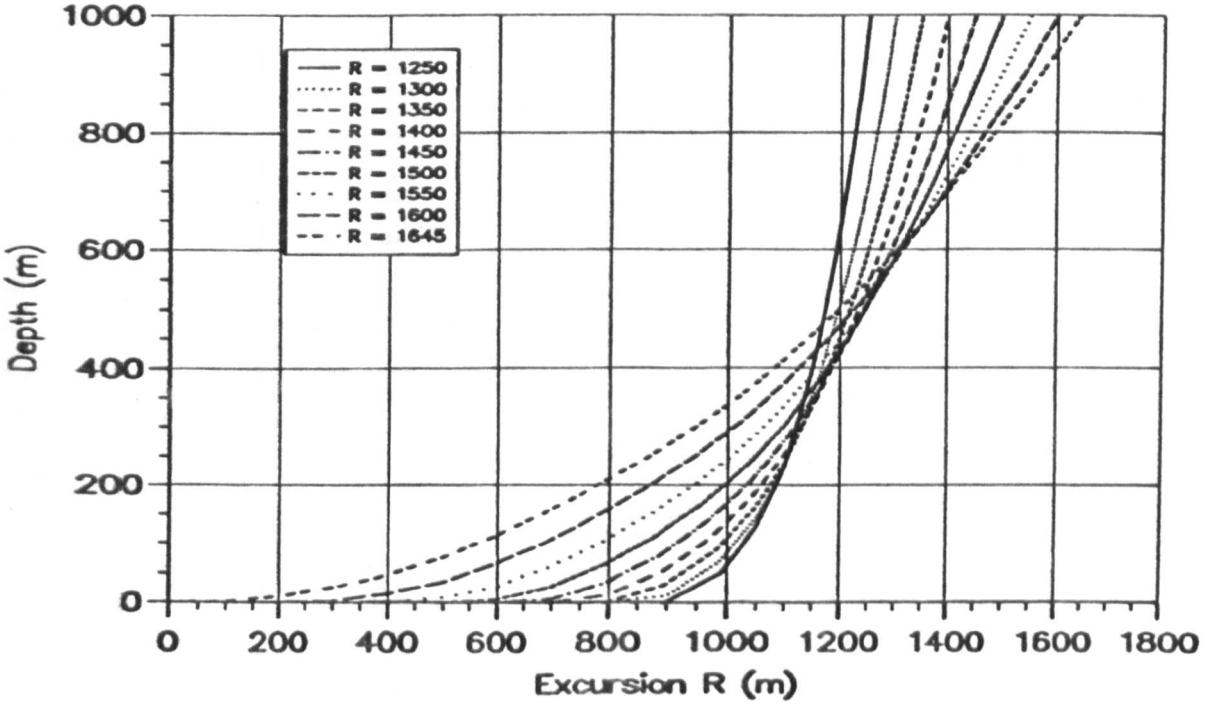

Figure 2.14 — Cable Geometry At Different R_p With 20 Elements

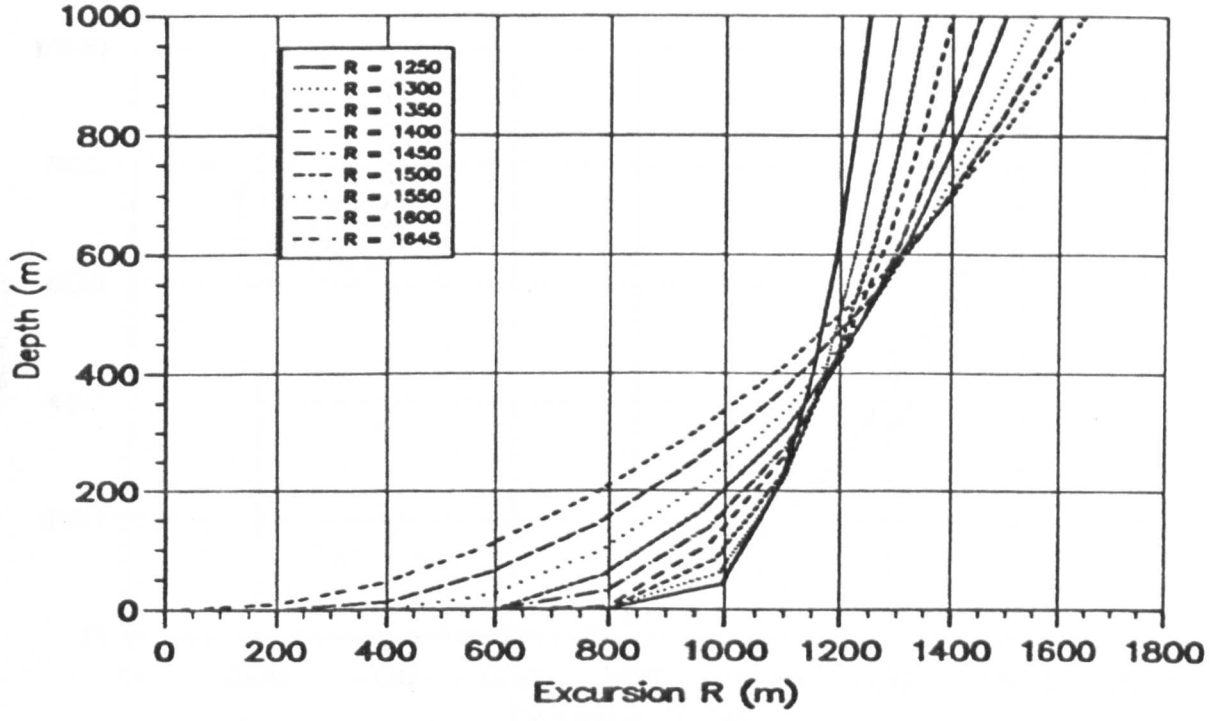

Figure 2.15 — Cable Geometry At Different R_p With 10 Elements

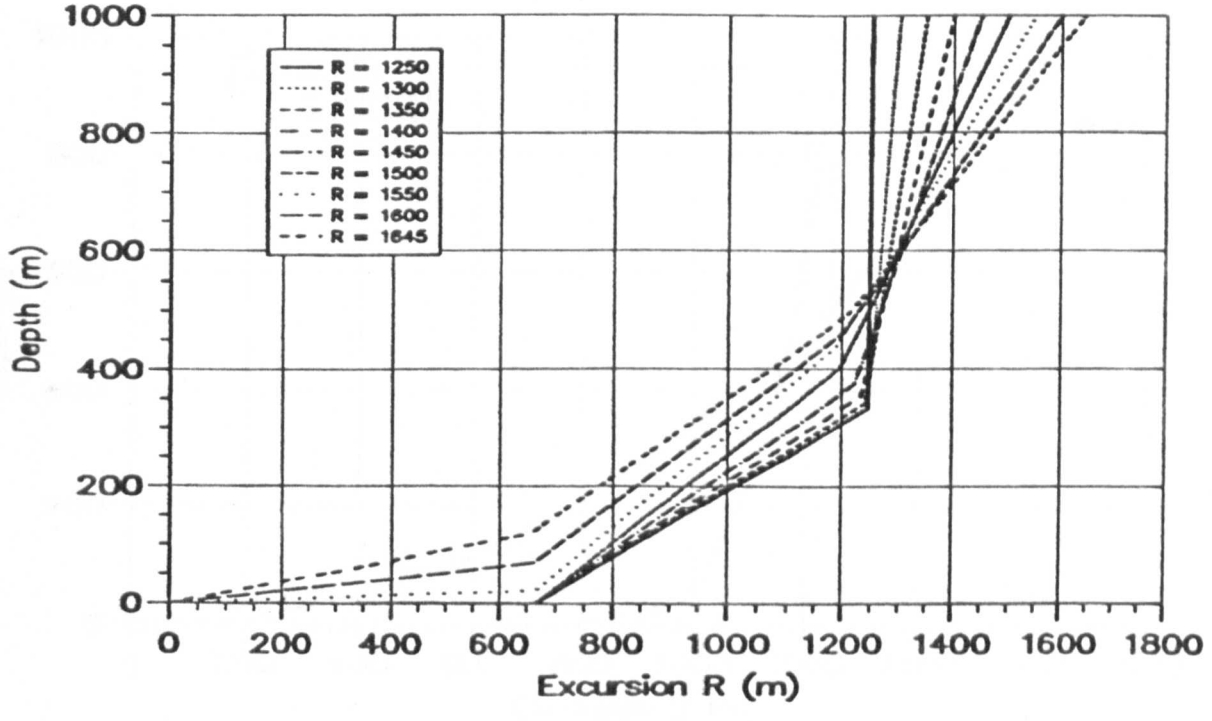

Figure 2.16 — Cable Geometry At Different R_p With 3 Elements

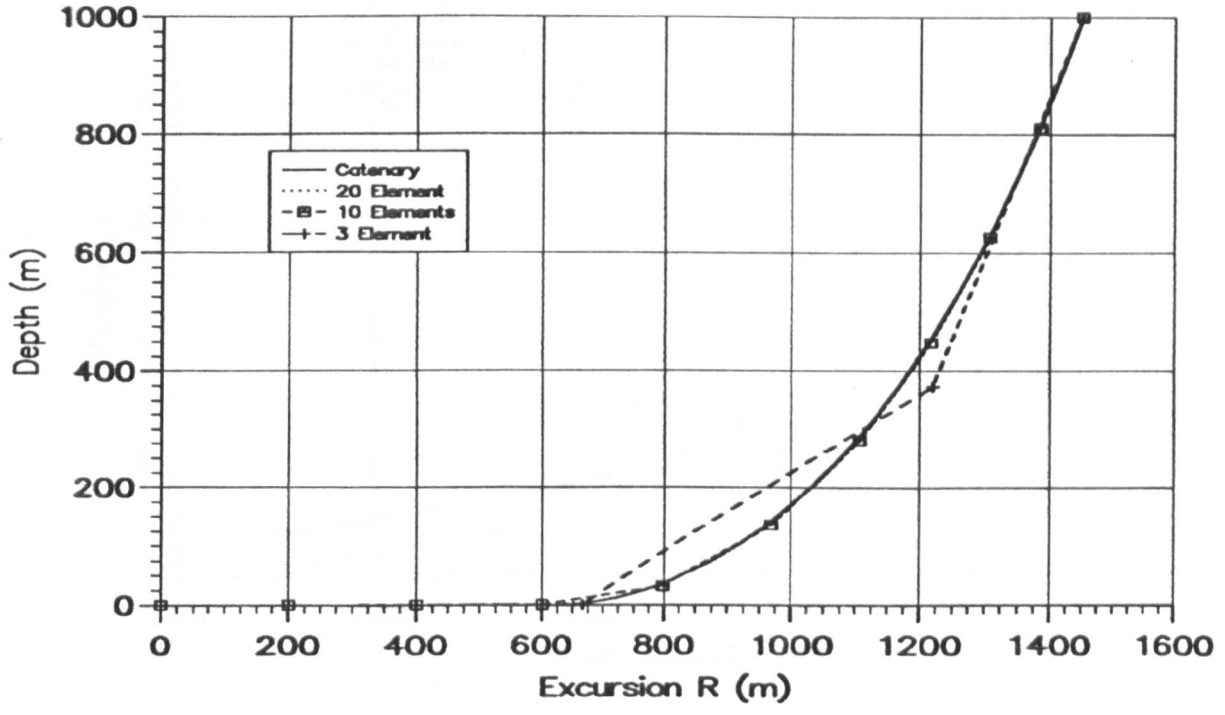

Figure 2.17 — Comparative Geometries at A Common Excursion

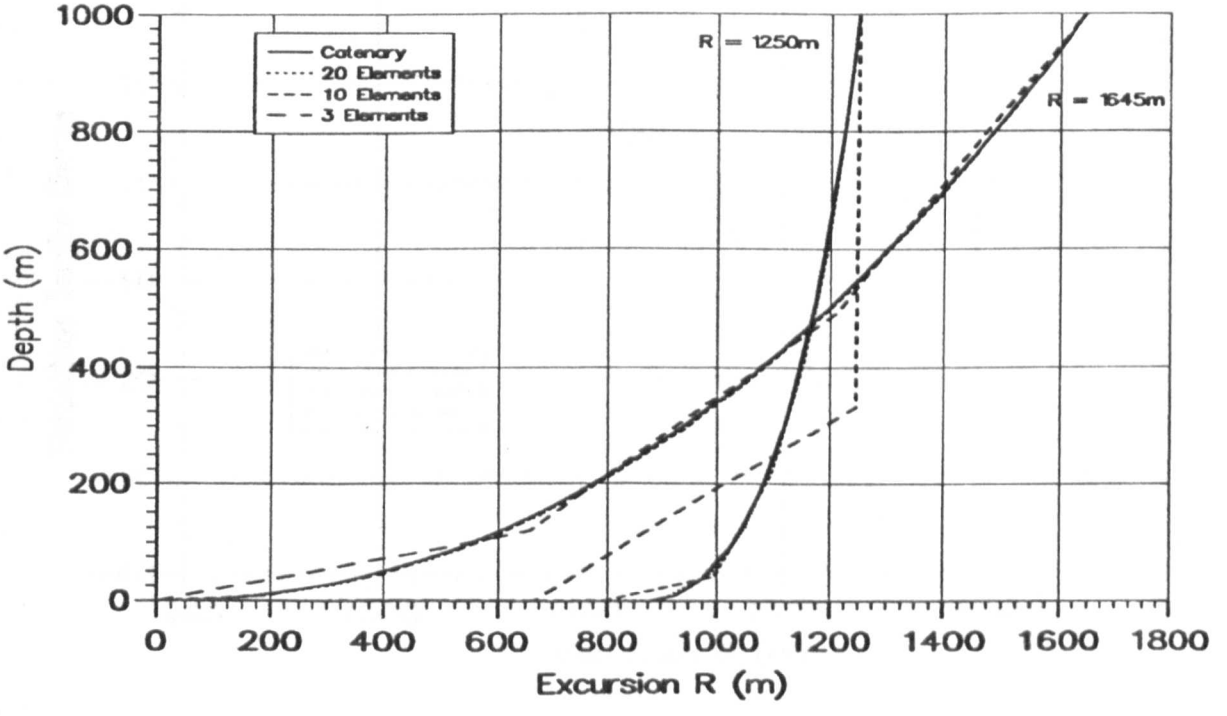

Figure 2.18 — Comparative Geometries at 2 Excursions

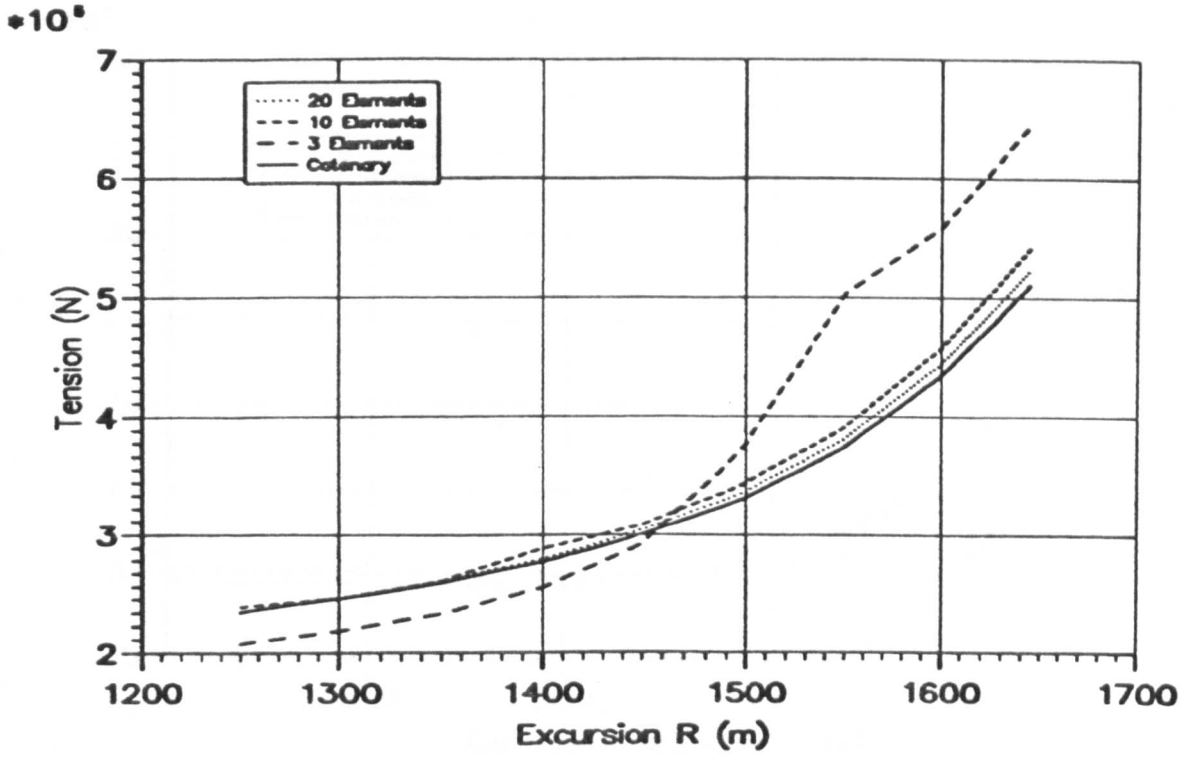

Figure 2.19 — Max. Tension vs. Excursion For the 4 Models

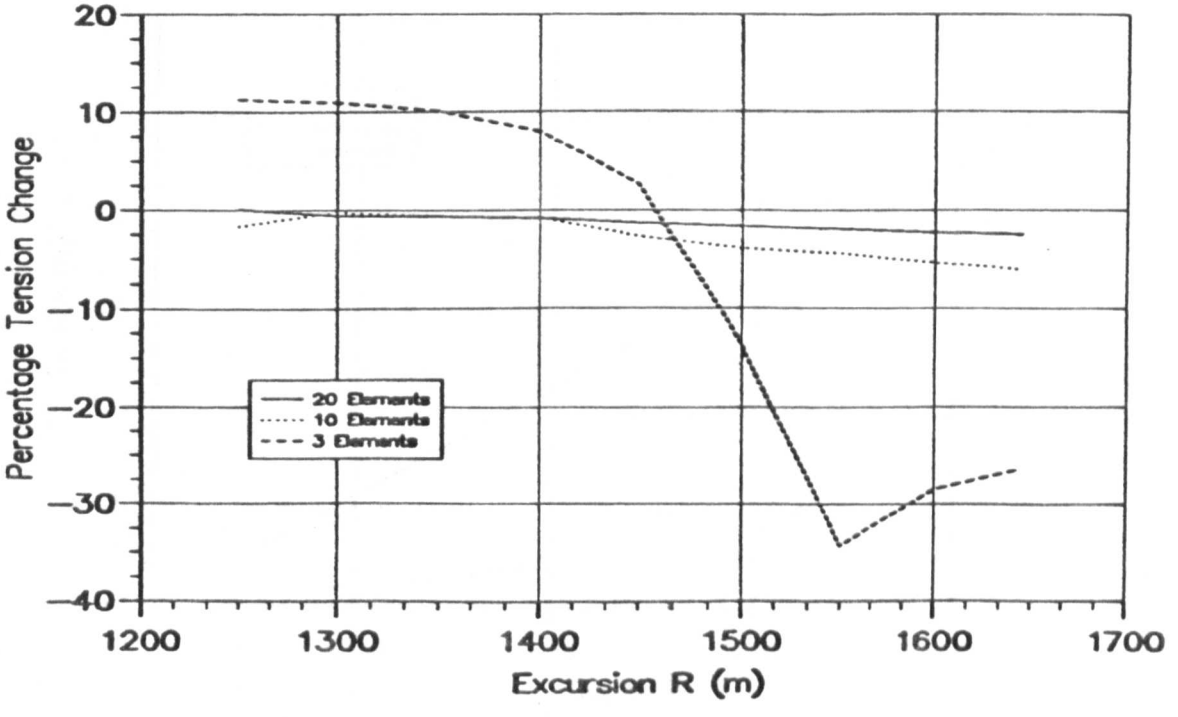

Figure 2.20 — % Deviation of Models From Catenary Solution

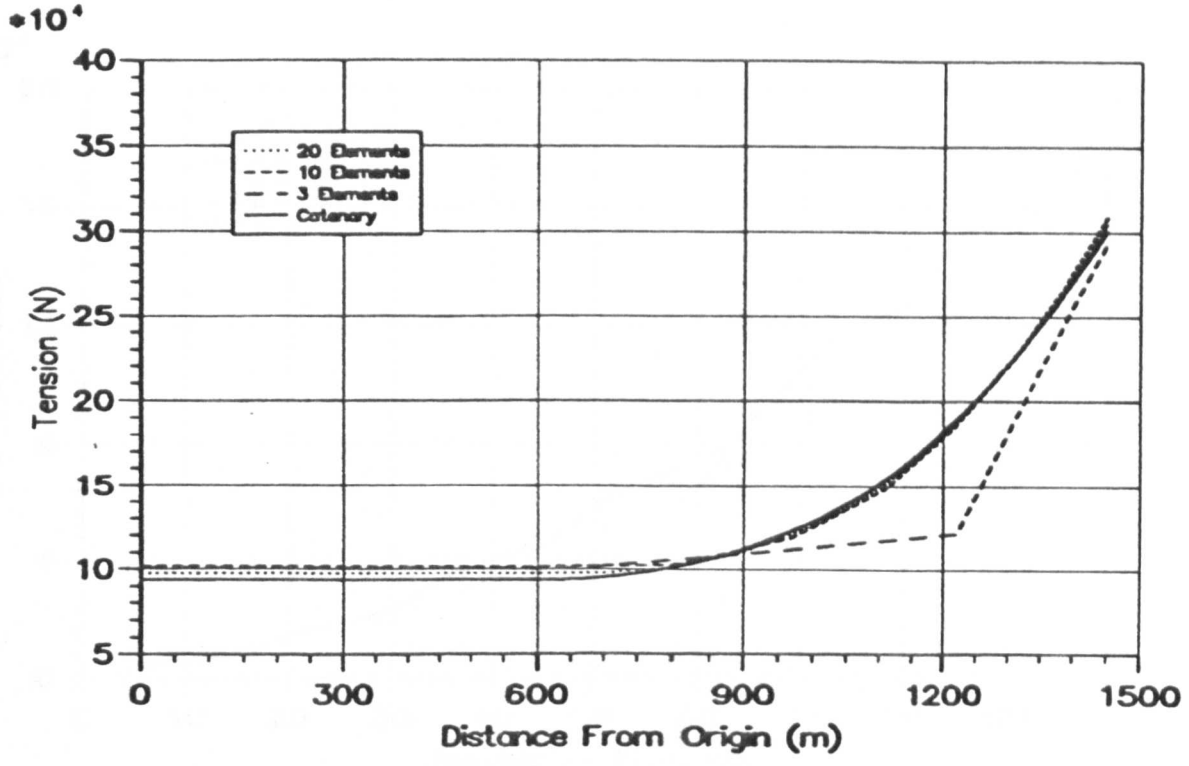

Figure 2.21 — Tension Distribution for the 4 Models

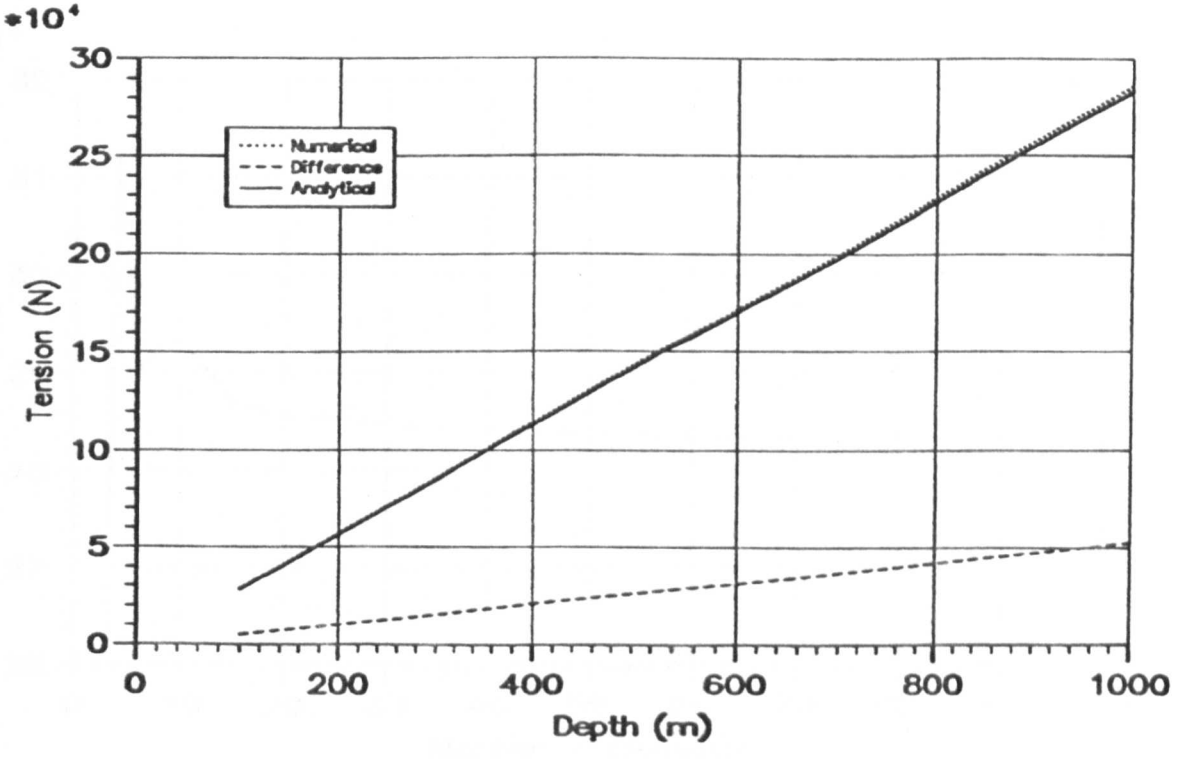

Figure 2.22 — Max. Static Tension vs. Water Depth

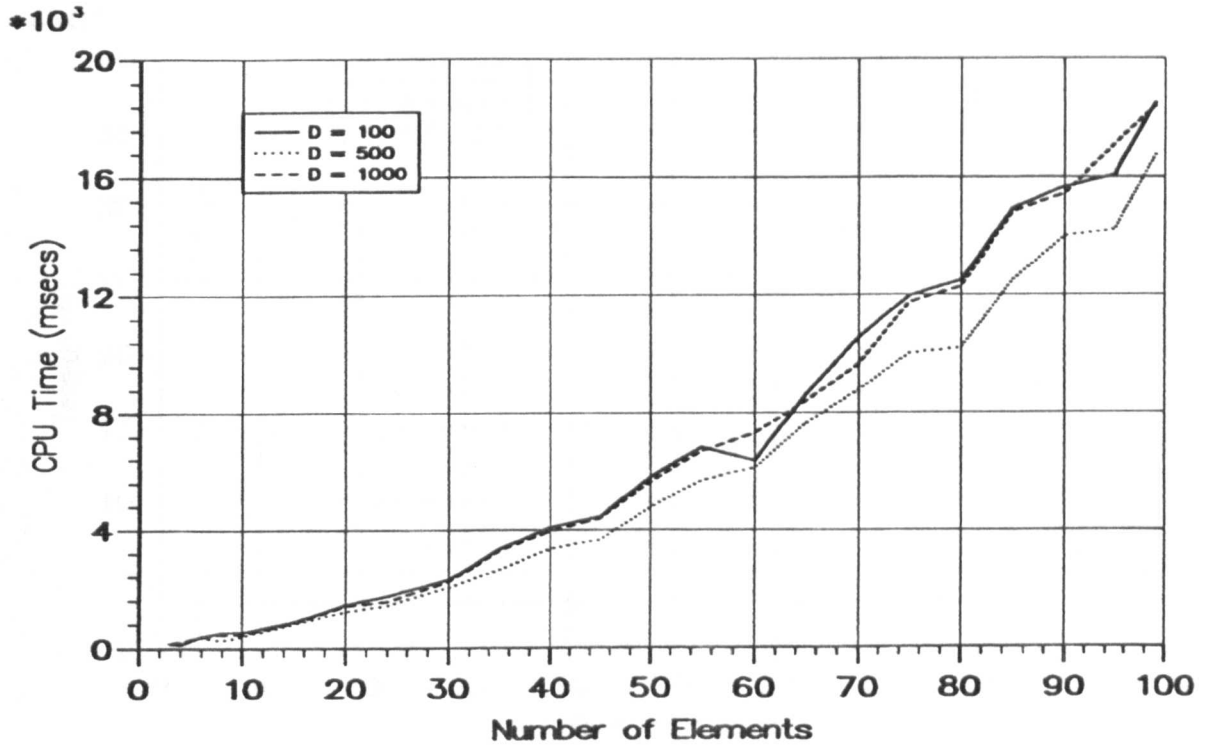

Figure 2.23 — CPU Times vs. h at Different Water Depths

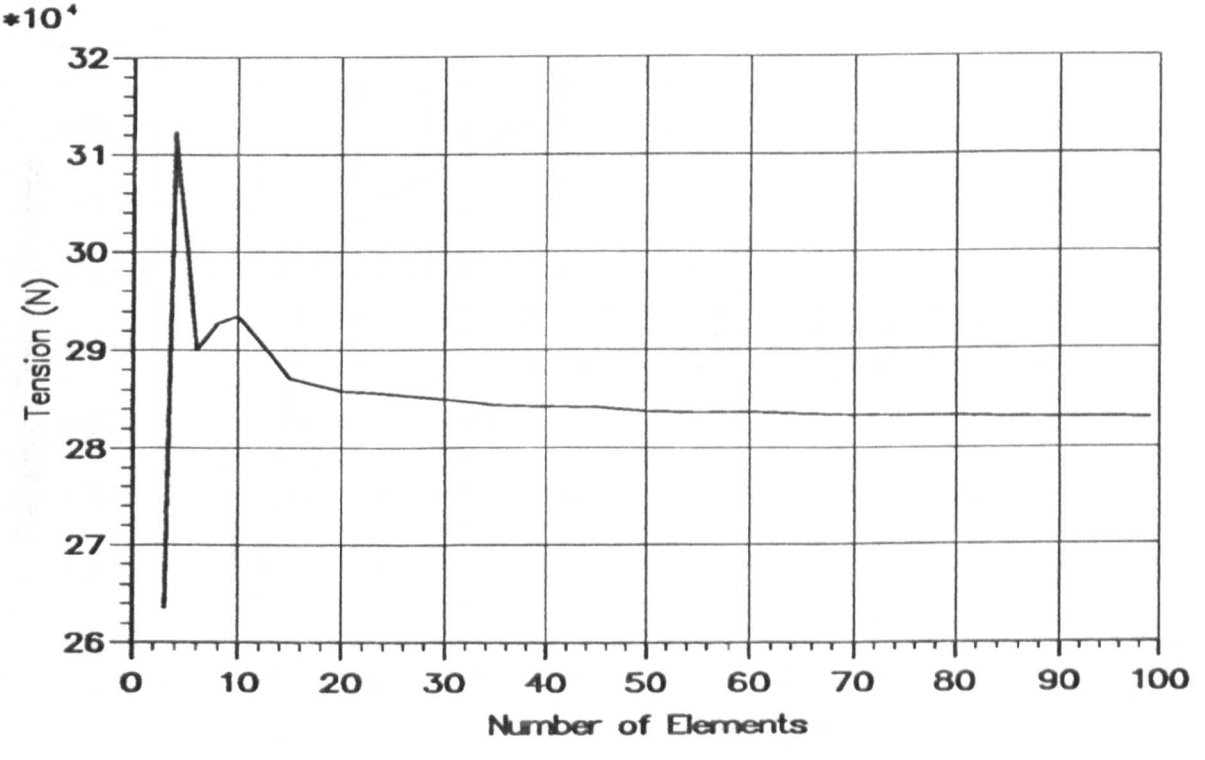

Figure 2.24 — Maximum Tension vs. h

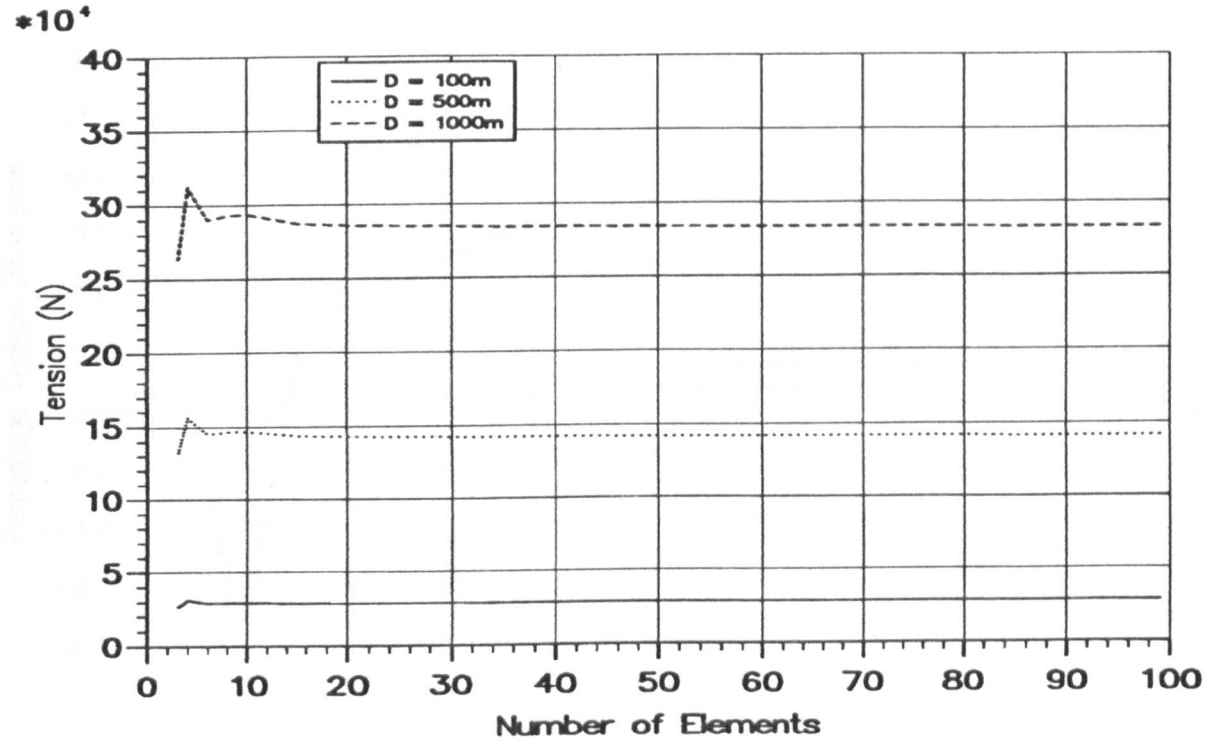

Figure 2.25 — Maximum Tension vs. h at Different Water Depths

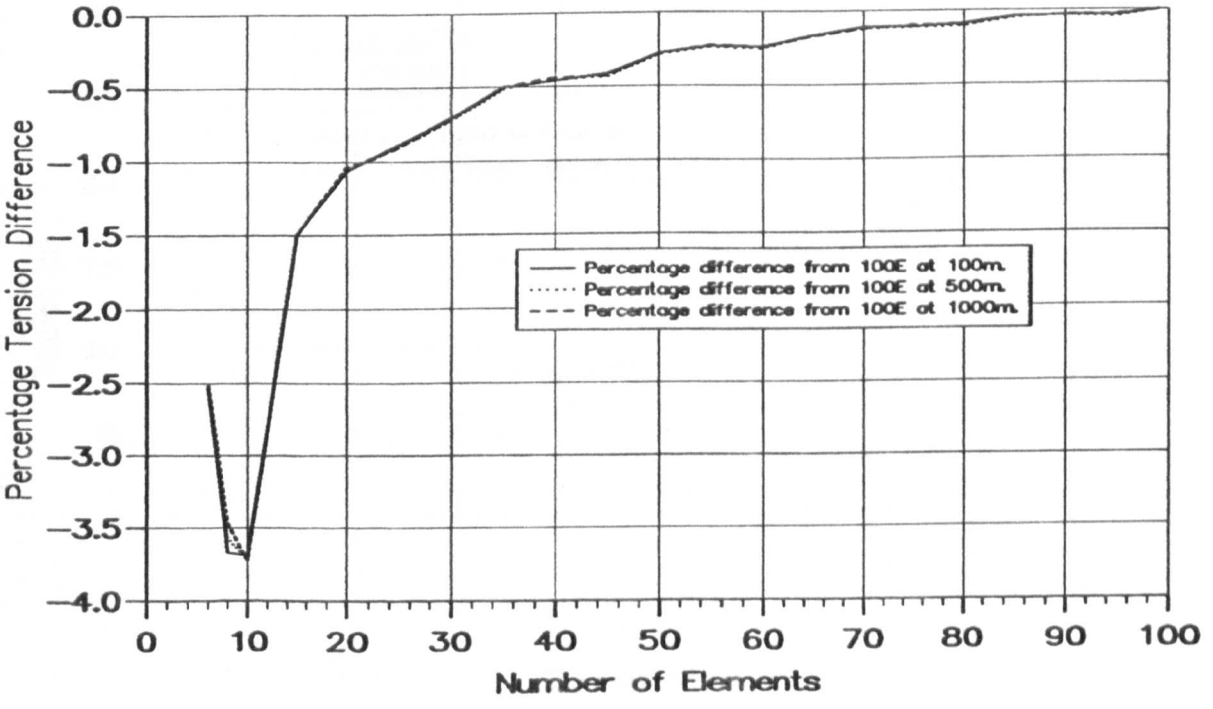

Figure 2.26 — % Deviation from 'true Numerical solution'

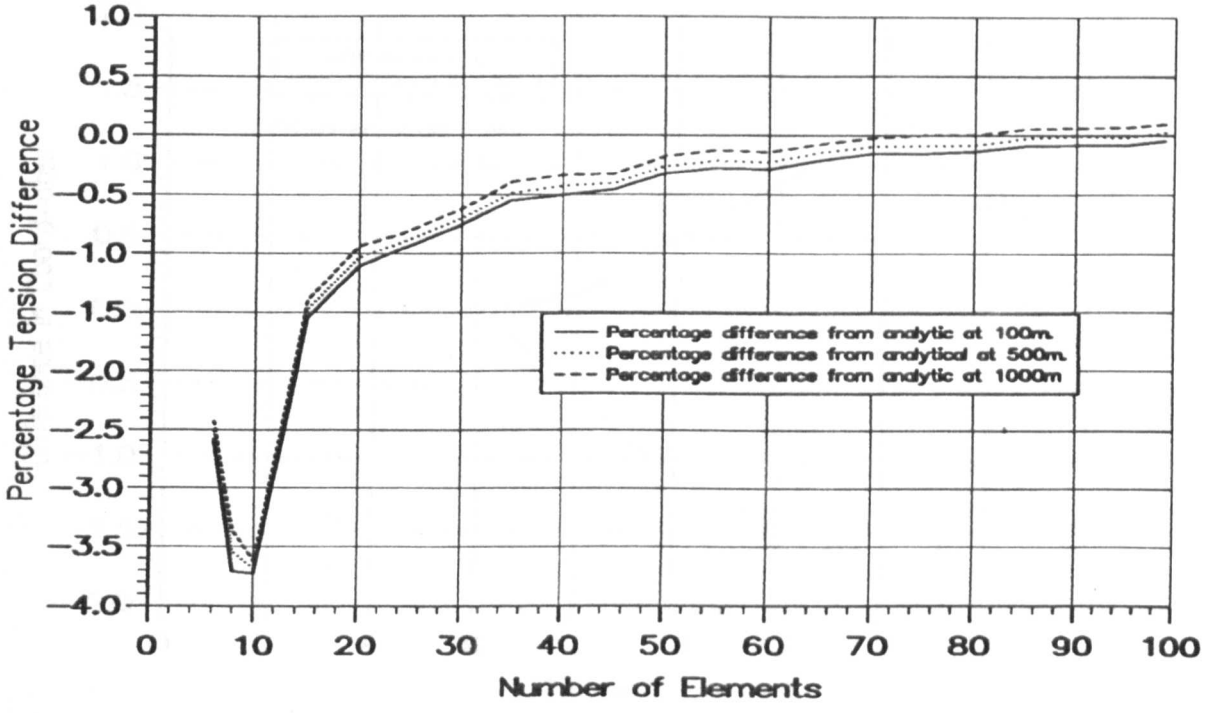

Figure 2.27 — % Deviation from Analytic Solution

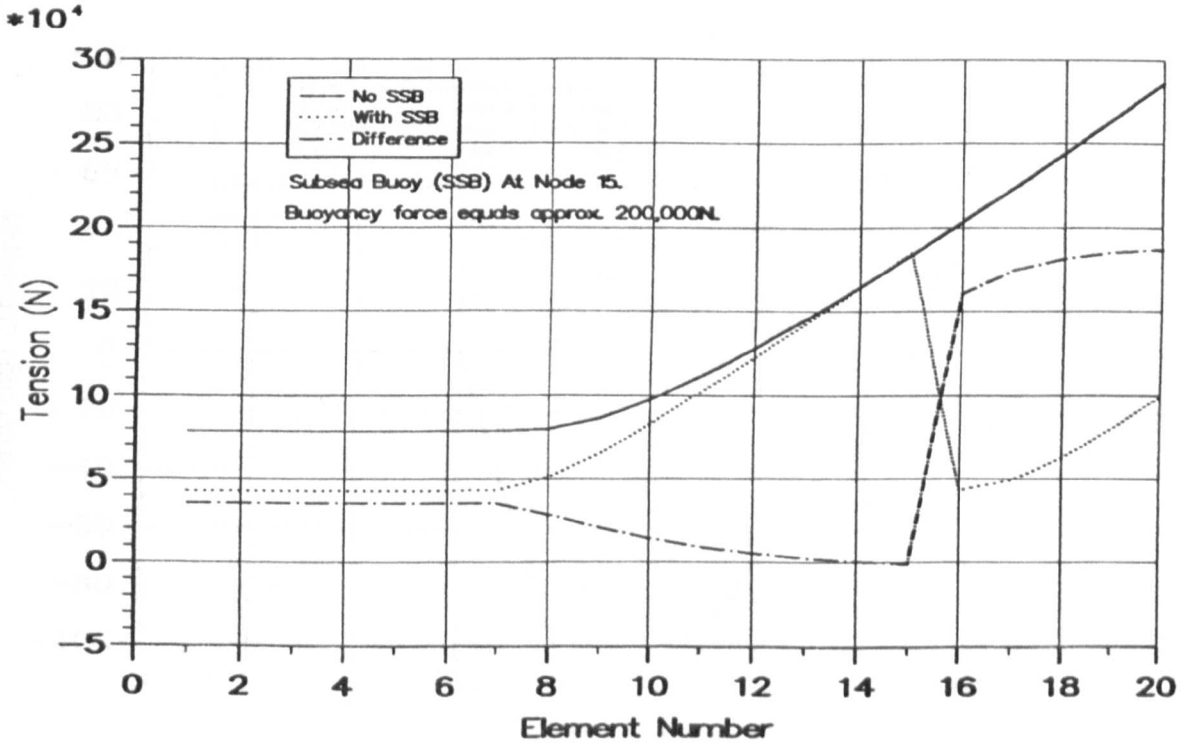

Figure 2.28 — Variation in Tension Distribution With A SSB Present

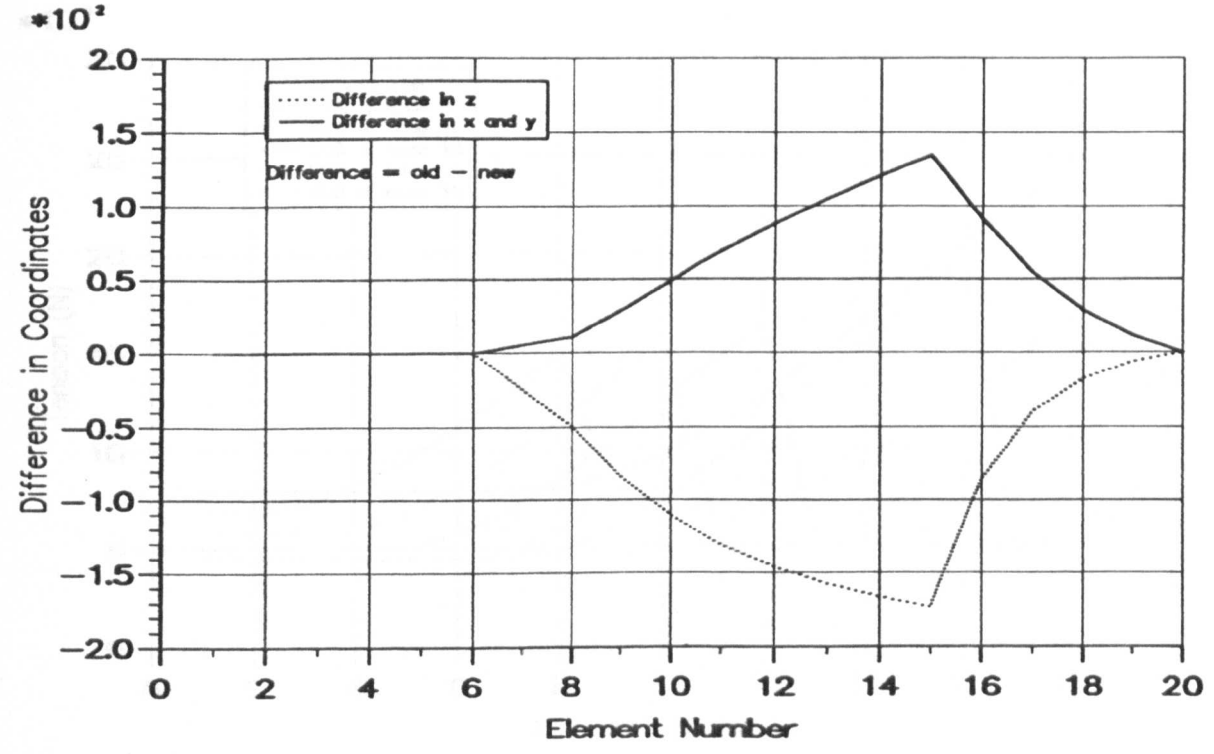

Figure 2.29 — Change in Geometry With A SSB Present

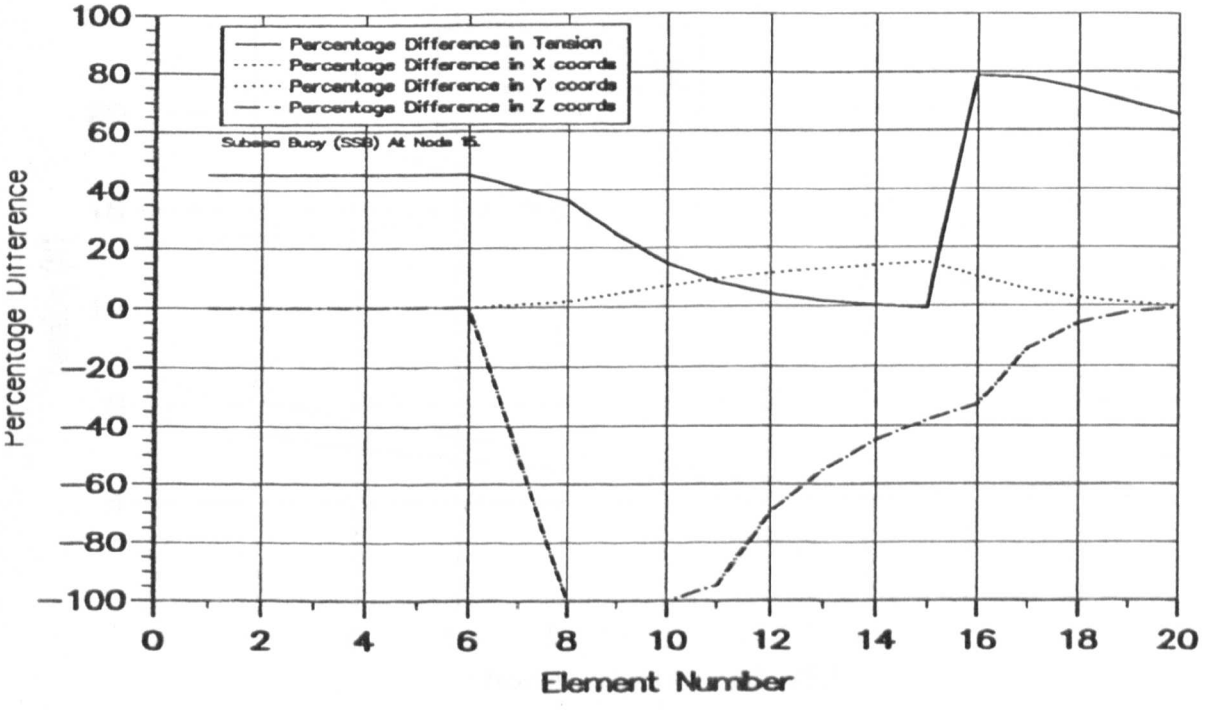

Figure 2.30 — % Differences With and Without a SSB

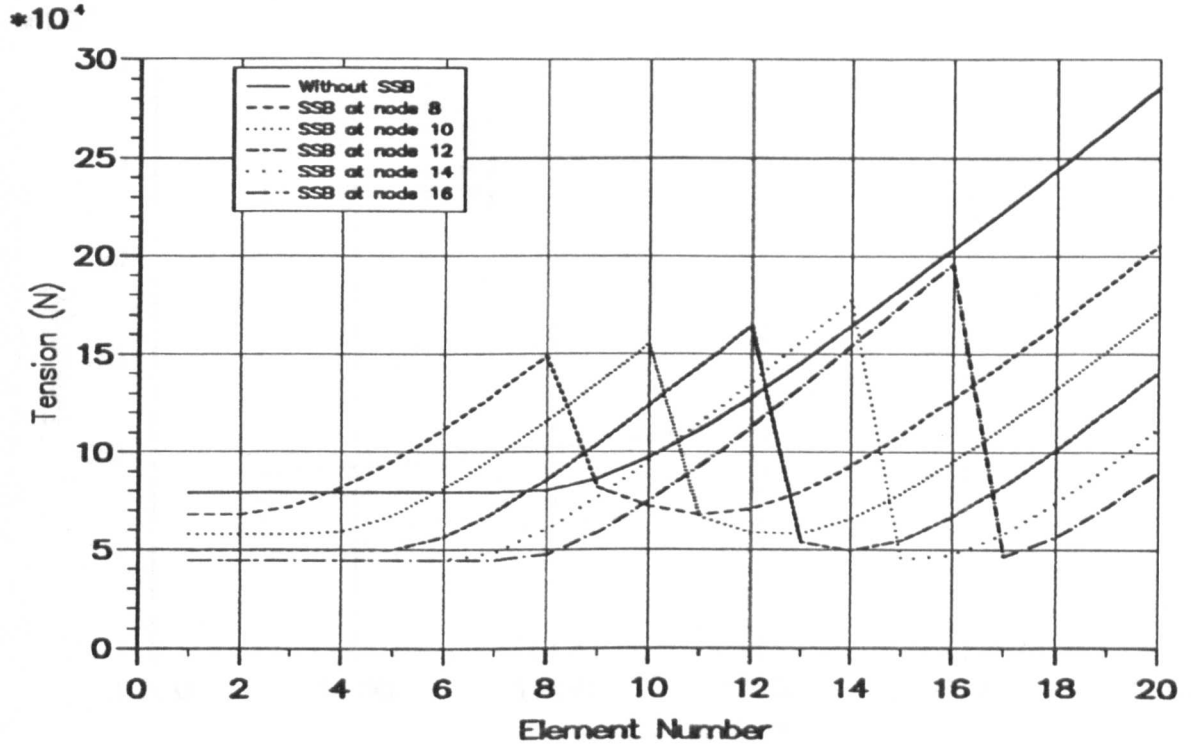

Figure 2.31 — Tension Distribution With SSB at Different Nodes

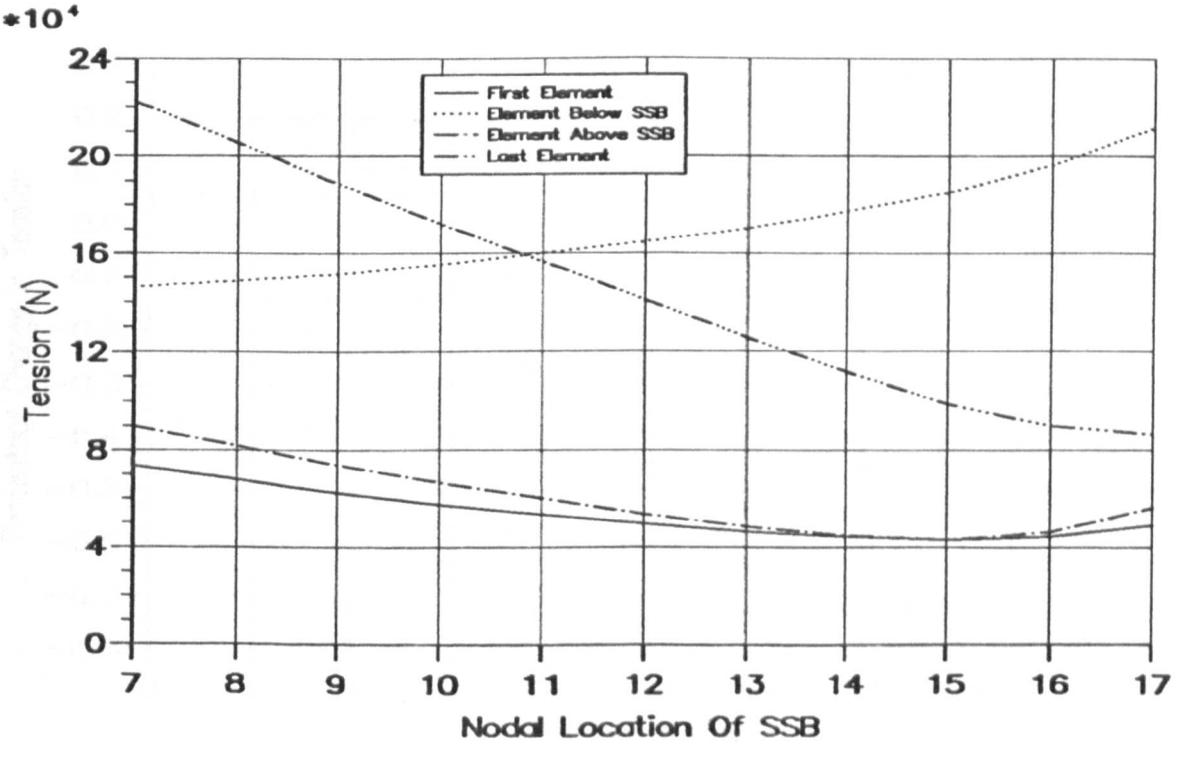

Figure 2.32 — 'Critical' Element Tensions vs. SSB Position

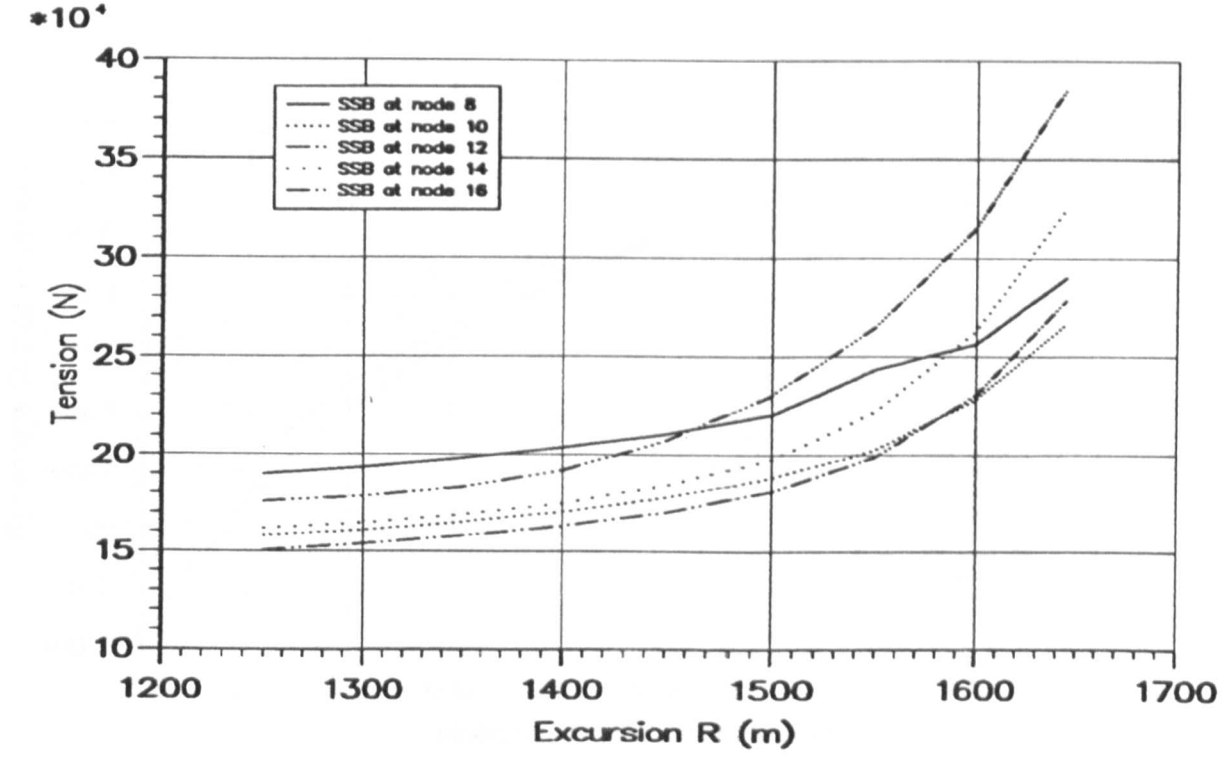

Figure 2.33 — Max. Tension vs. R_p With SSB at Different Nodes

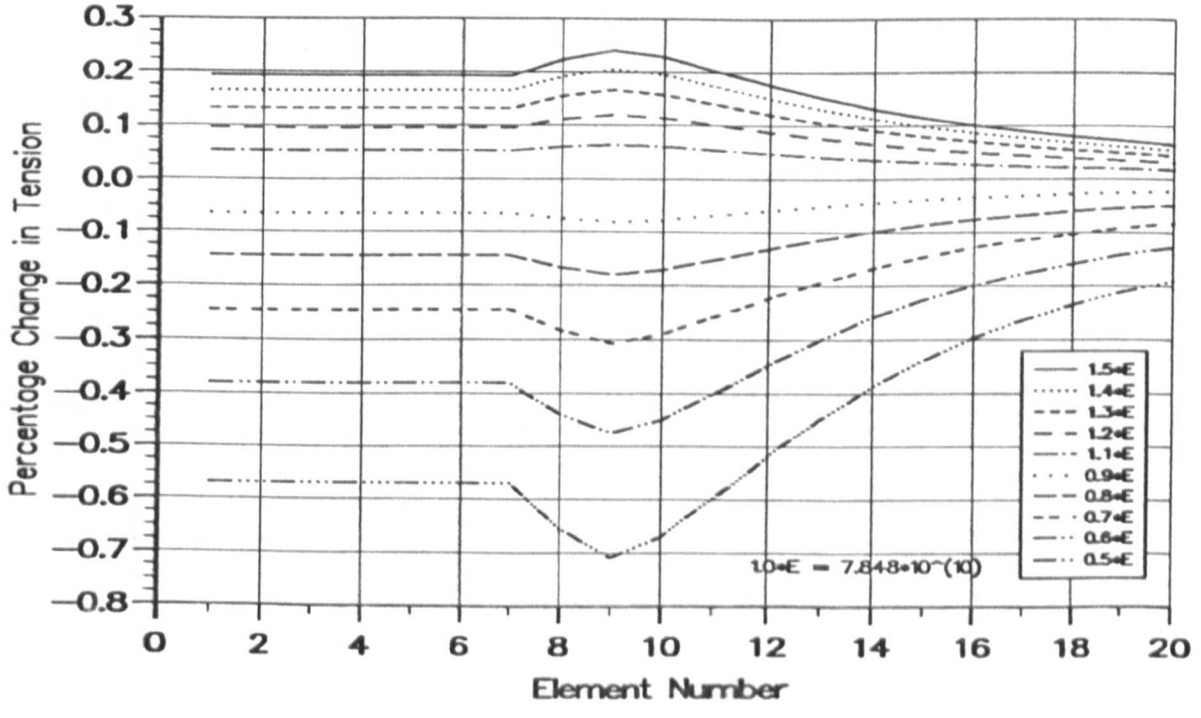

Figure 2.34 — Influence of % Change in E Upon Tension Distribution

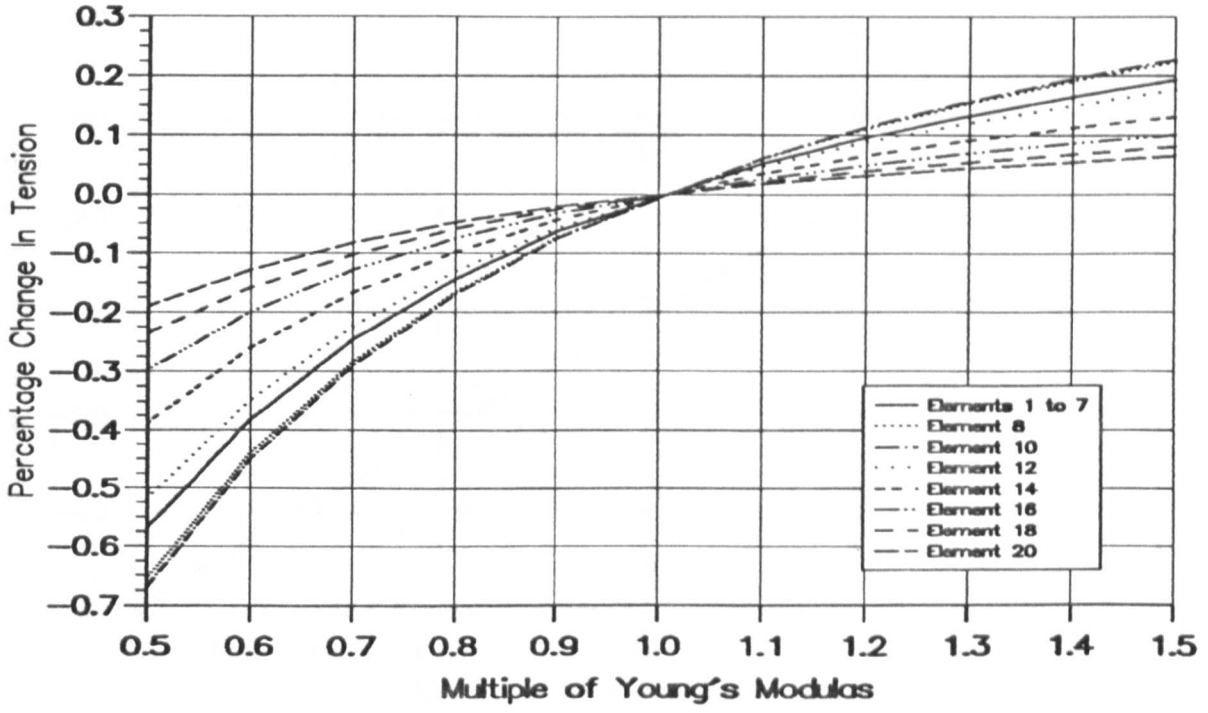

Figure 2.35 — % Change in Tension Caused By a % Change in E

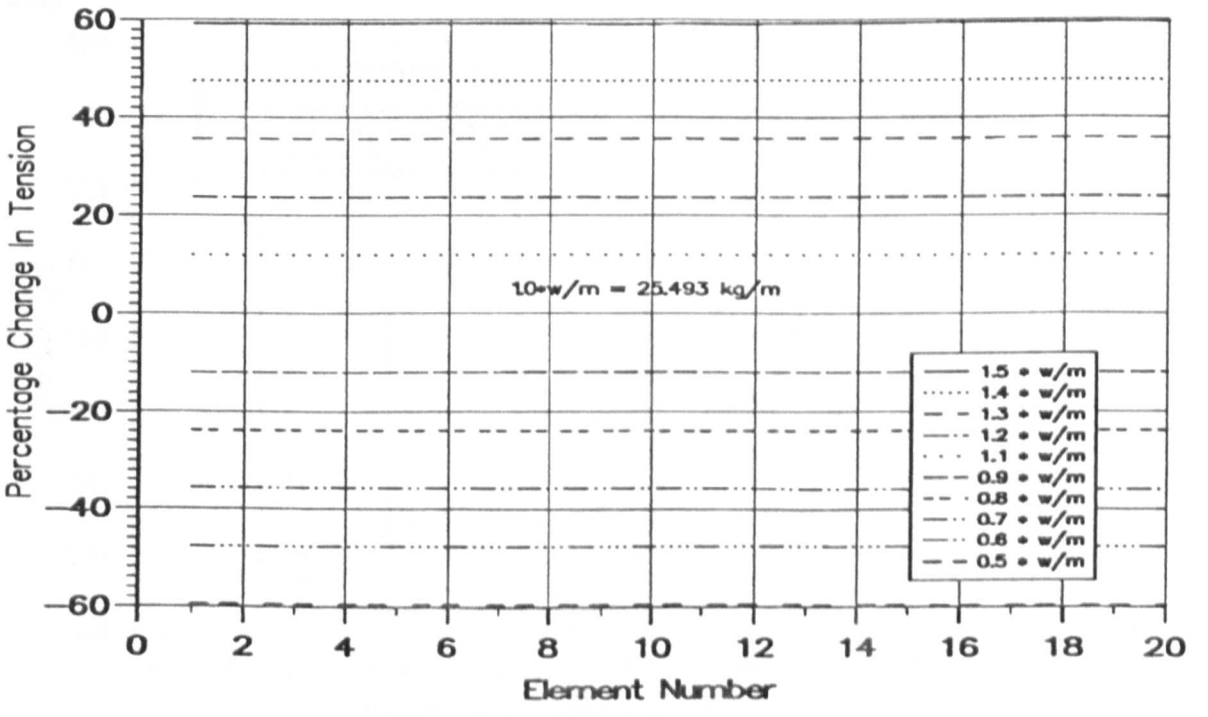

Figure 2.36 — Influence of % Change in W/m on Tension Distribution

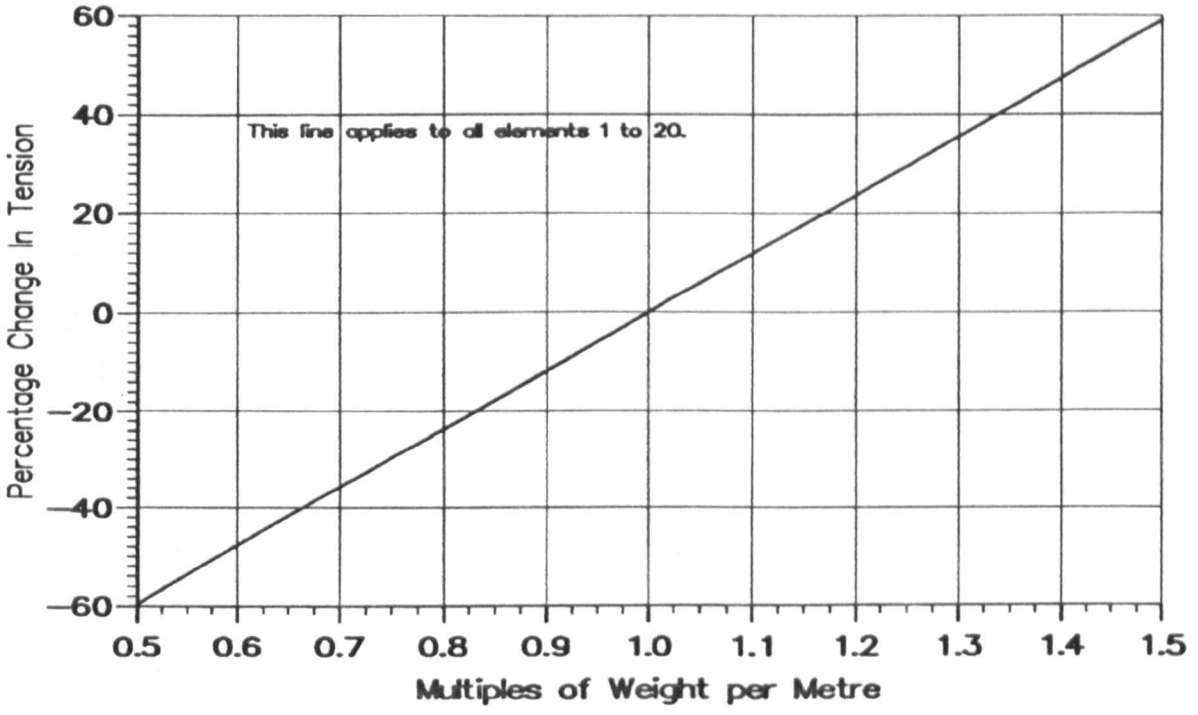

Figure 2.37 — % Change in Tension Caused By a % Change in W/m

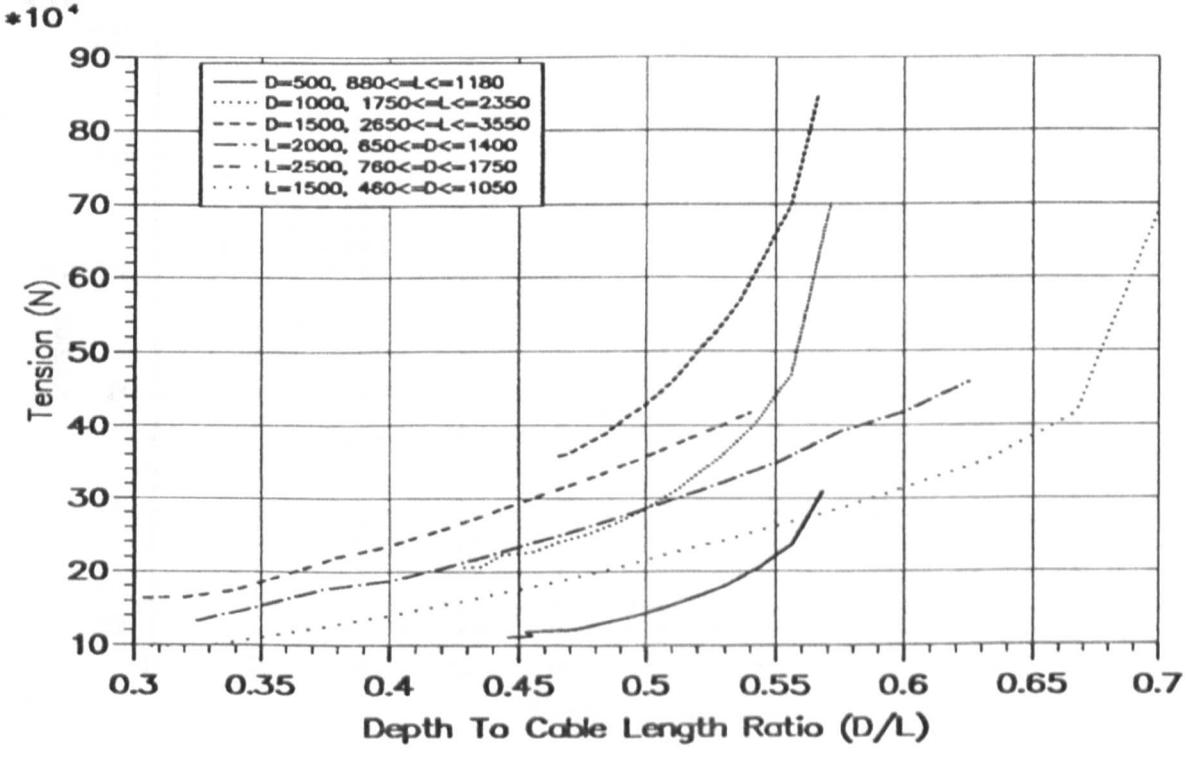

Figure 2.38 — Max. Tension vs. Depth to Length Ratio

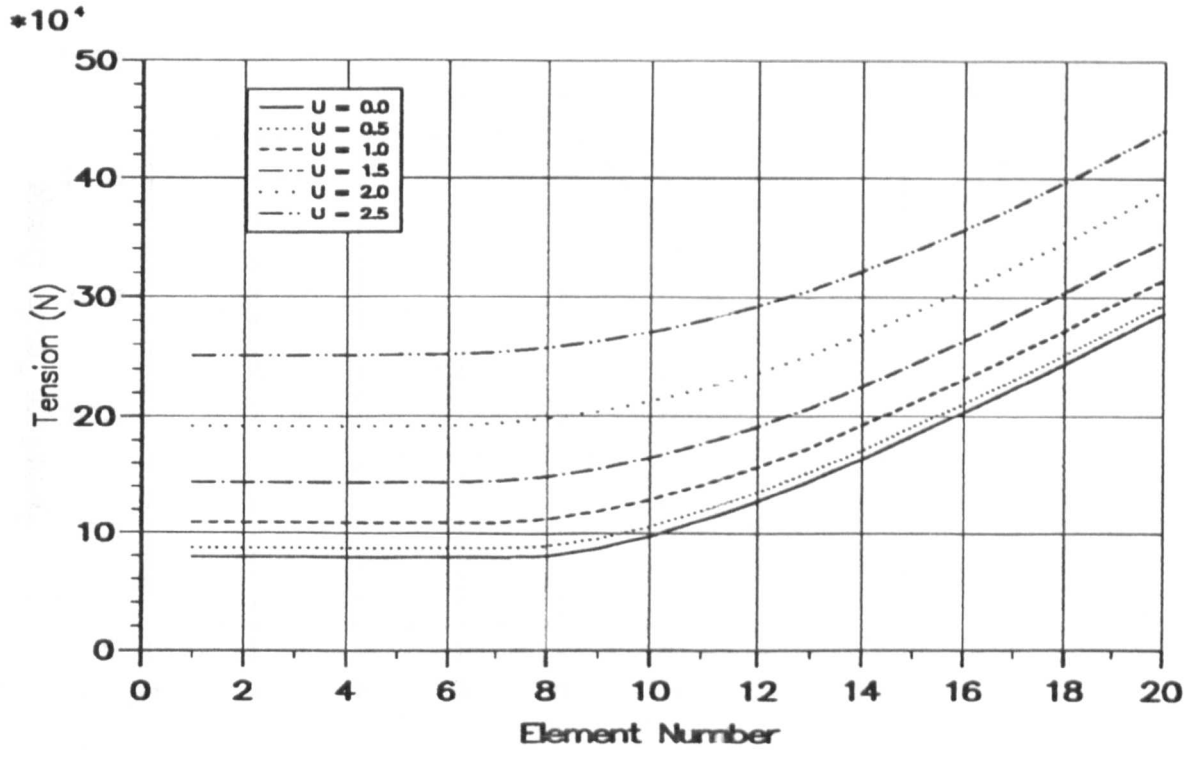

Figure 2.39 — Tension Distribution vs. U

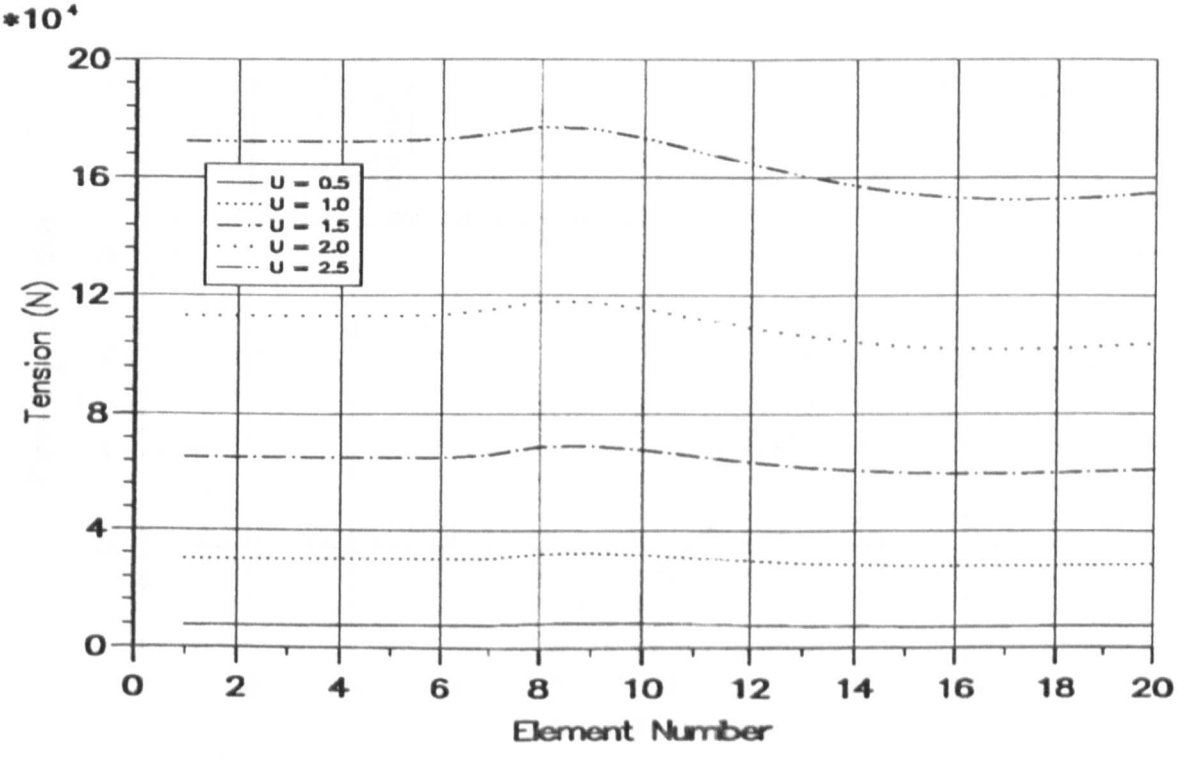

Figure 2.40 — Tension Difference From $U = 0$ For Different U

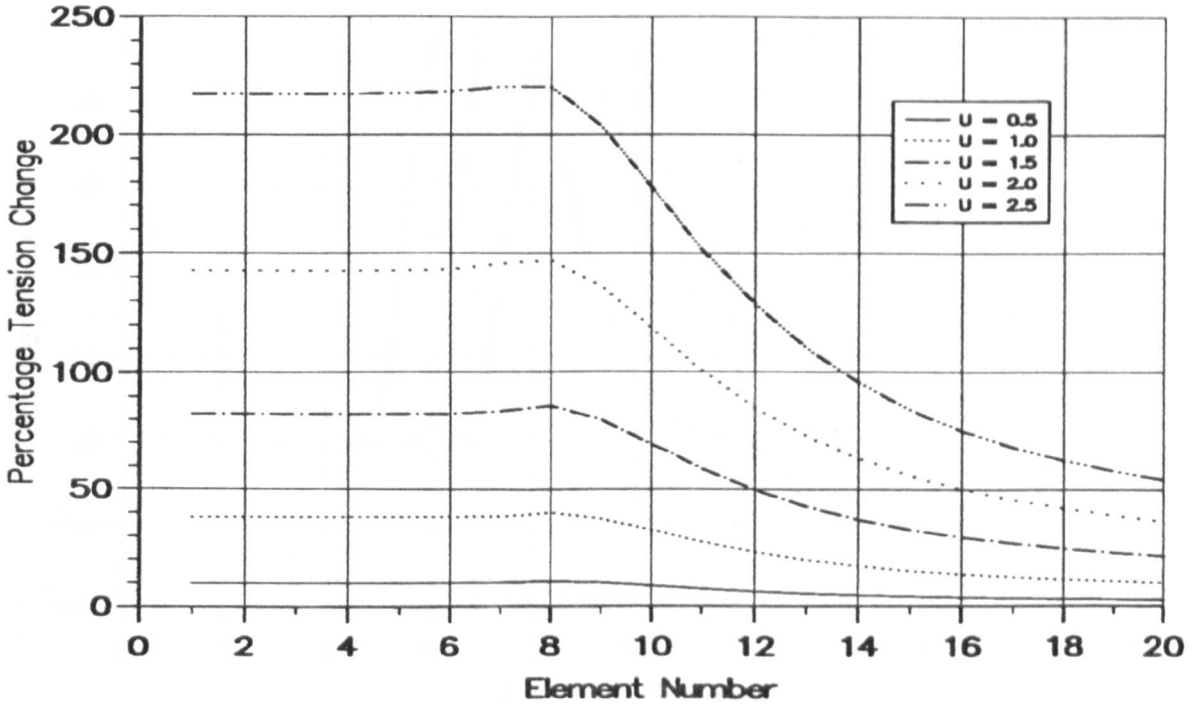

Figure 2.41 — % Change in Tension Distribution For Different U

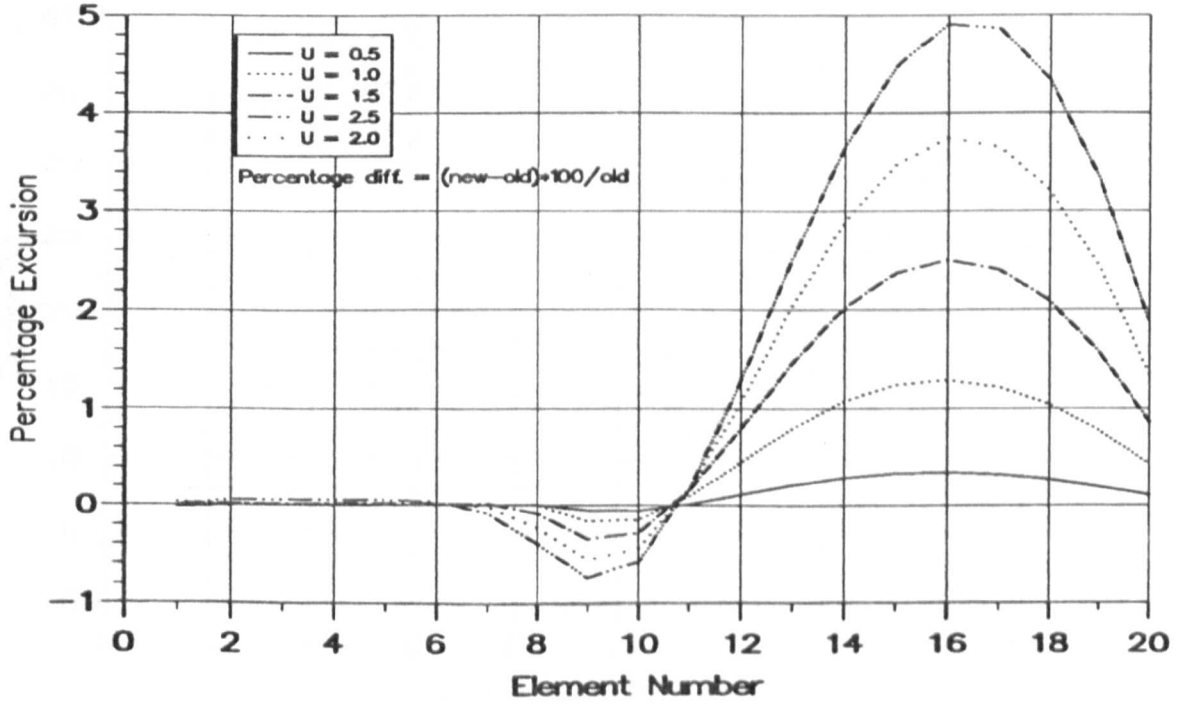

Figure 2.42 — % Change in Geometry For Different U

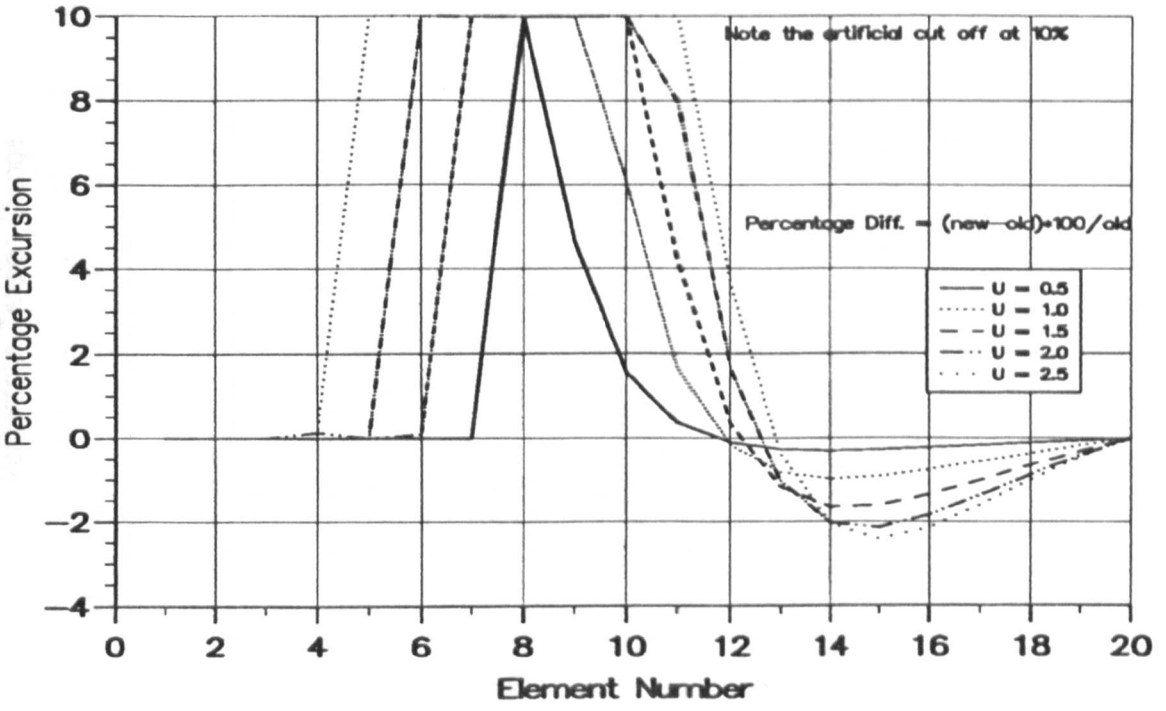

Figure 2.43 — % Change in z Coords. For Different U

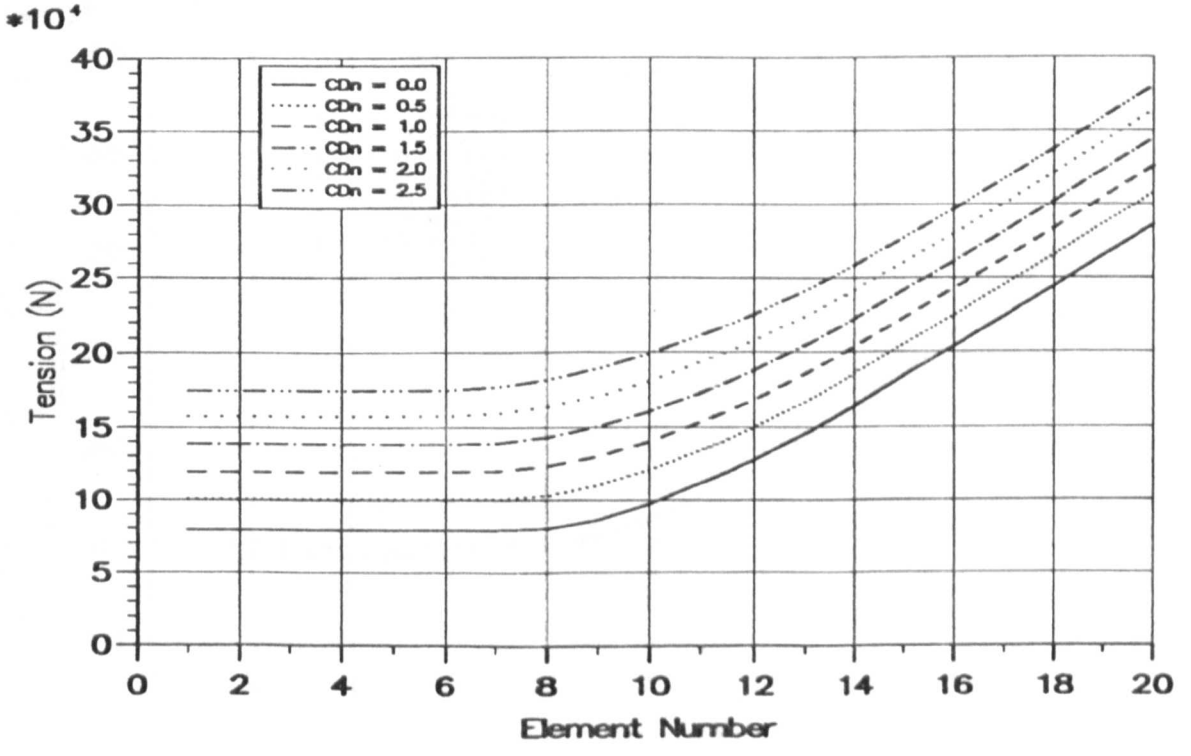

Figure 2.44 — Tension Distributions vs. Cd_n

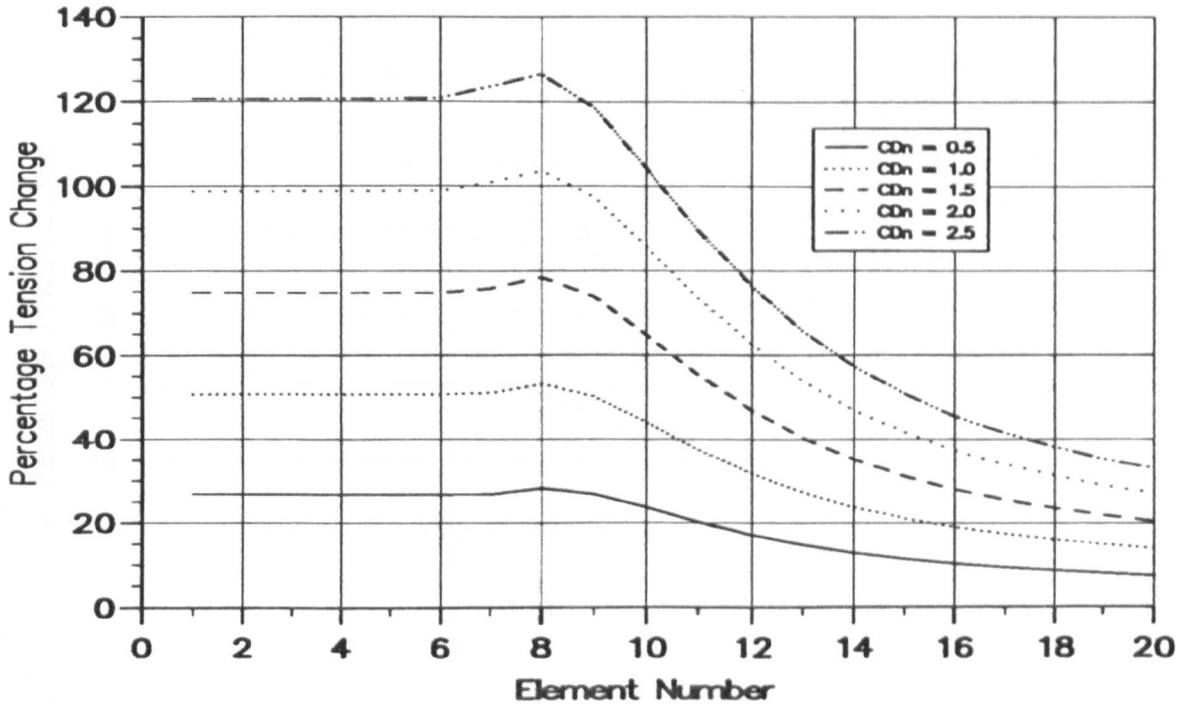

Figure 2.45 — % Change in Tension Distribution vs. Cd_n

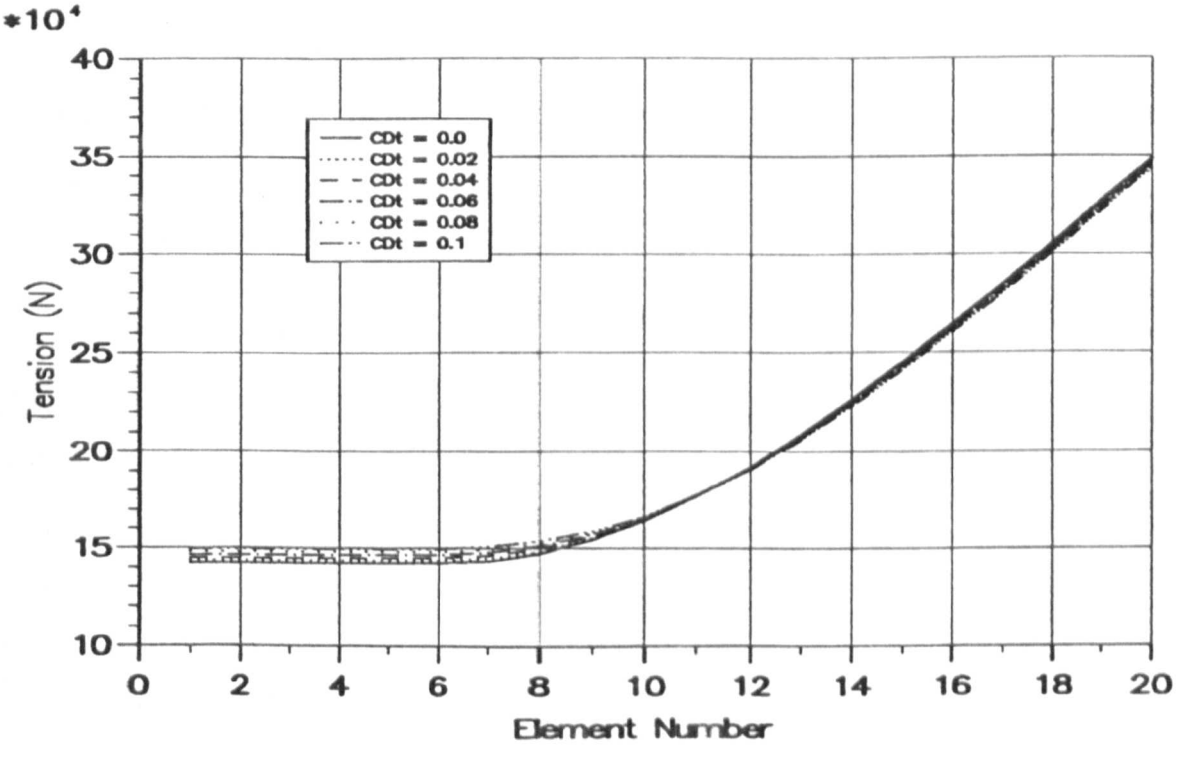

Figure 2.46 — Tension Distributions vs. Cd_t

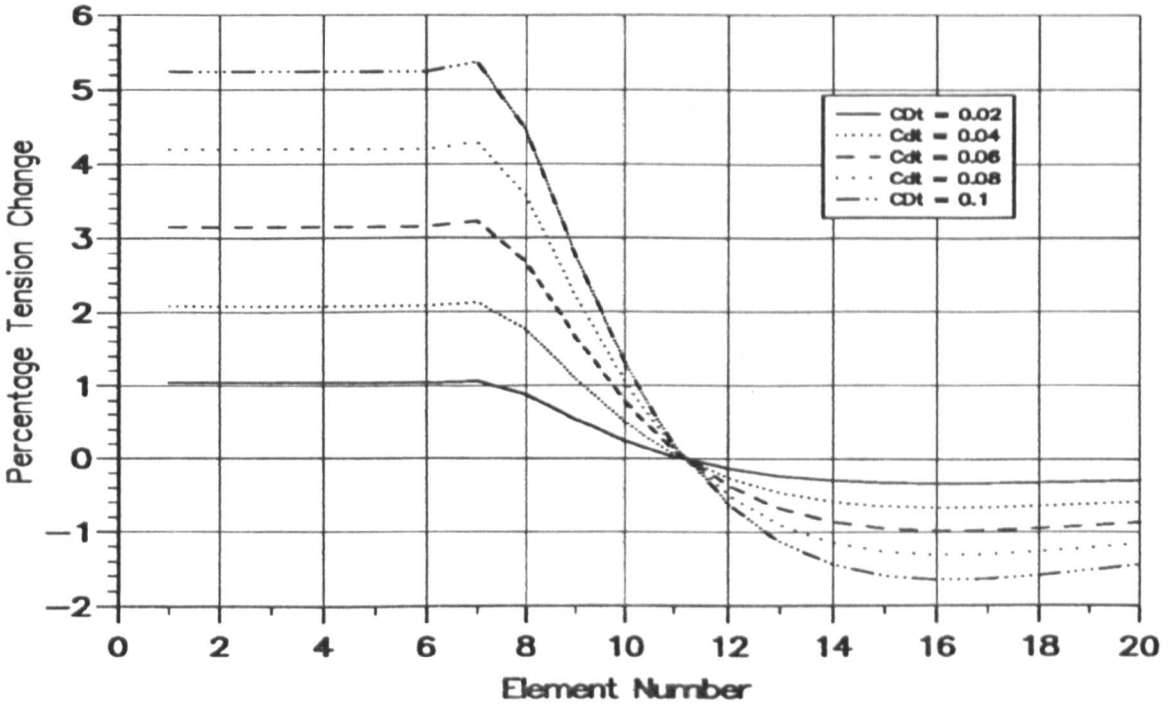

Figure 2.47 — % Change in Tension Distribution vs. Cd_t

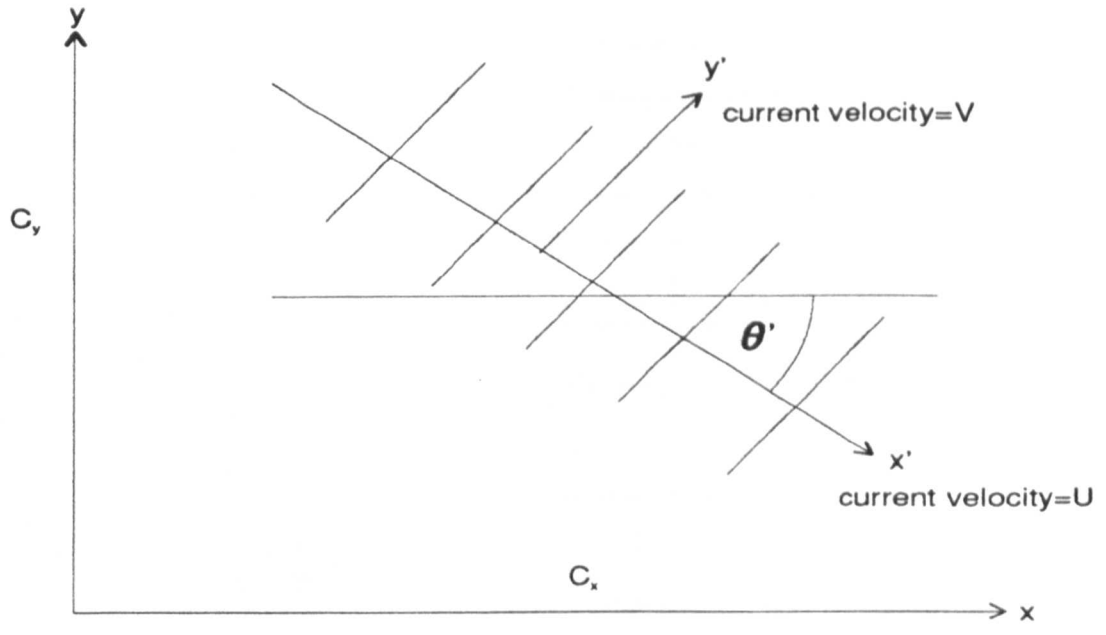

Figure 3.1 — Monochromatic Wave in Global Axes

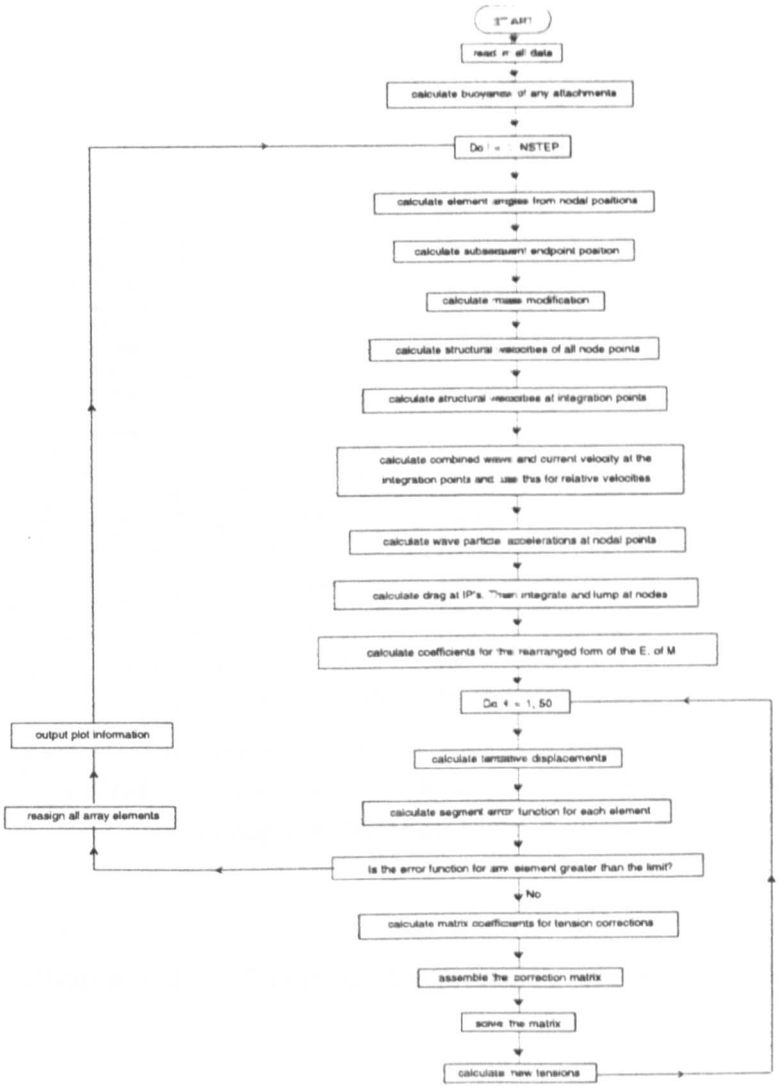

Figure 3.2 — Flow Chart for the Dynamic Solution

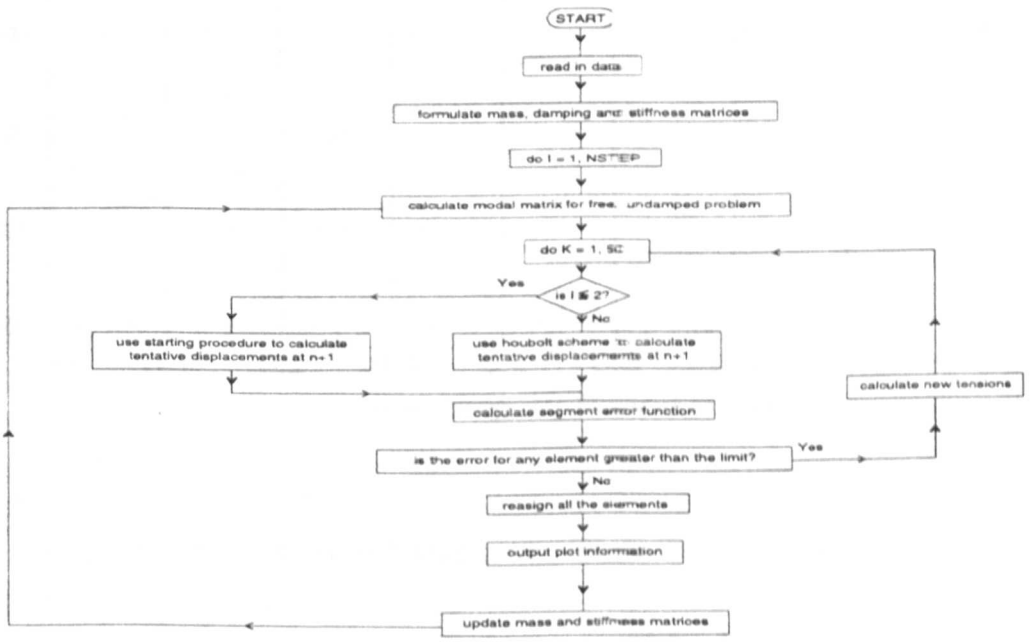

Figure 4.1 — Flow Chart for Modal Analysis

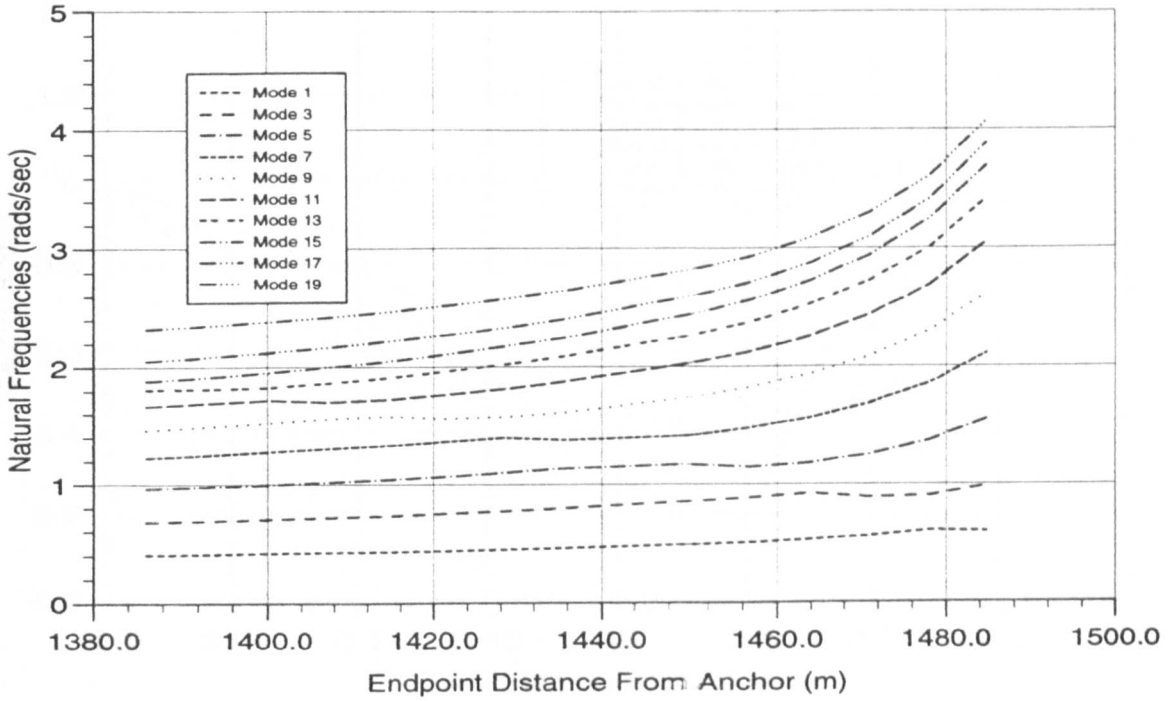

Figure 4.2 — Natural Frequencies vs. Excursion

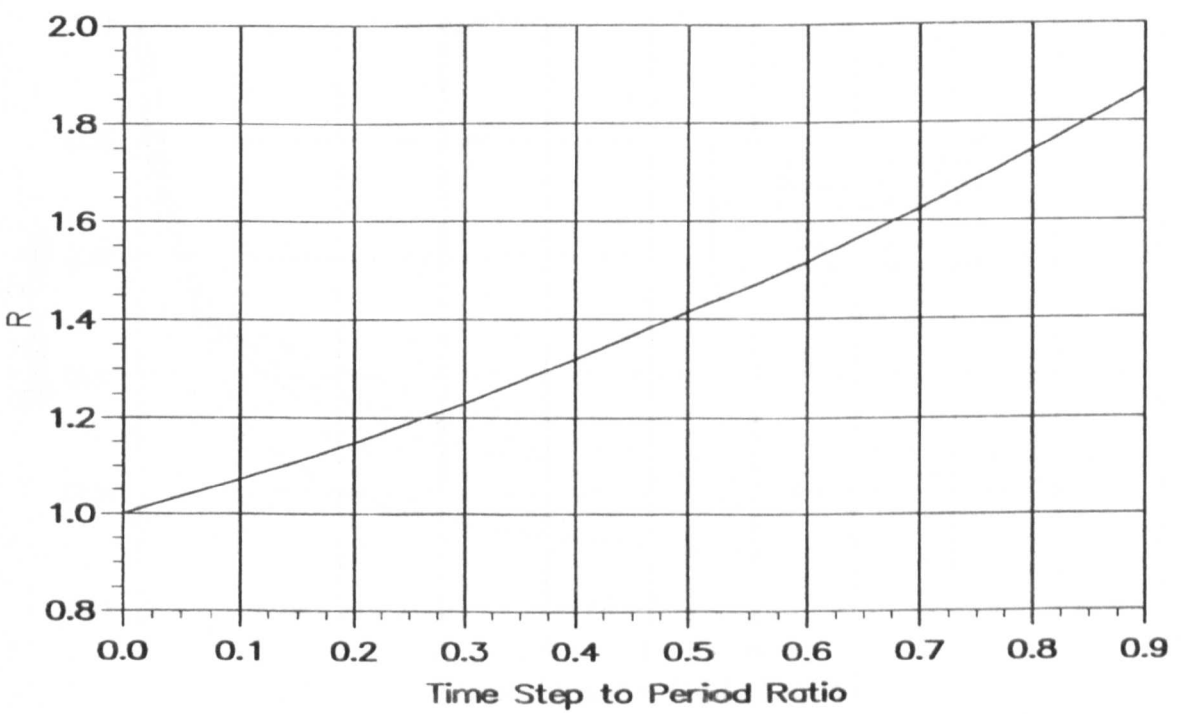

Figure 5.1 — Spectral Ratio vs. Time Step to Period Ratio

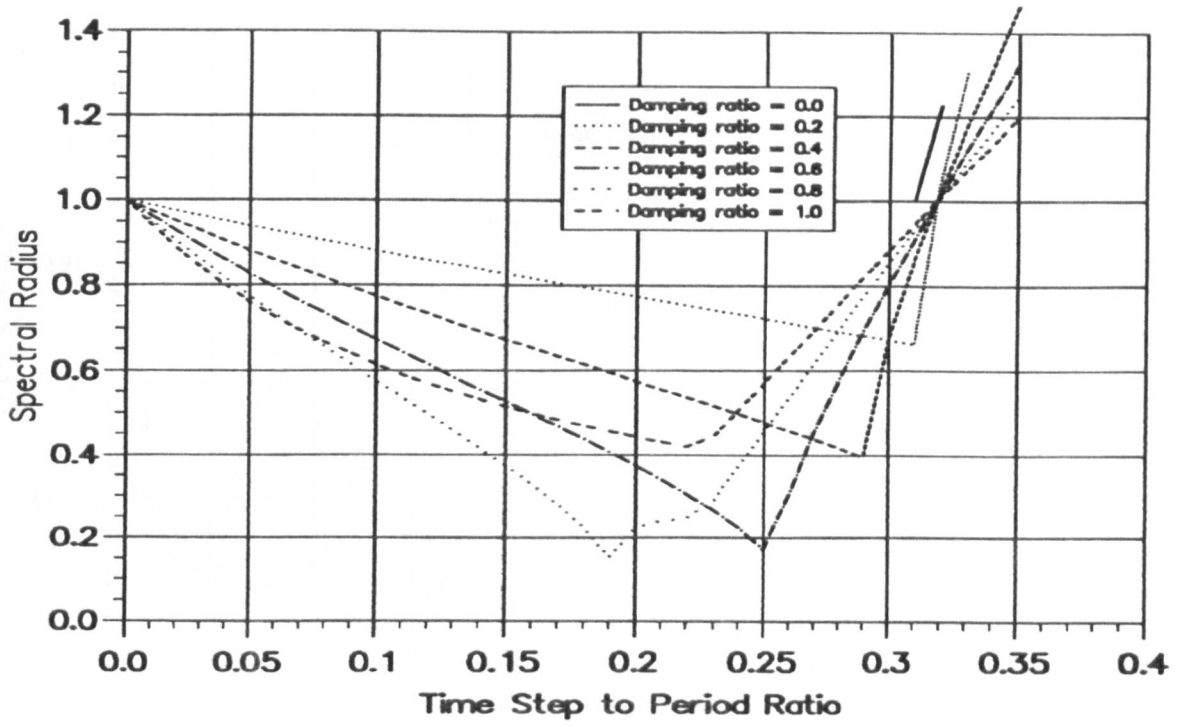

Figure 5.2 — Spectral Radius for CD Scheme

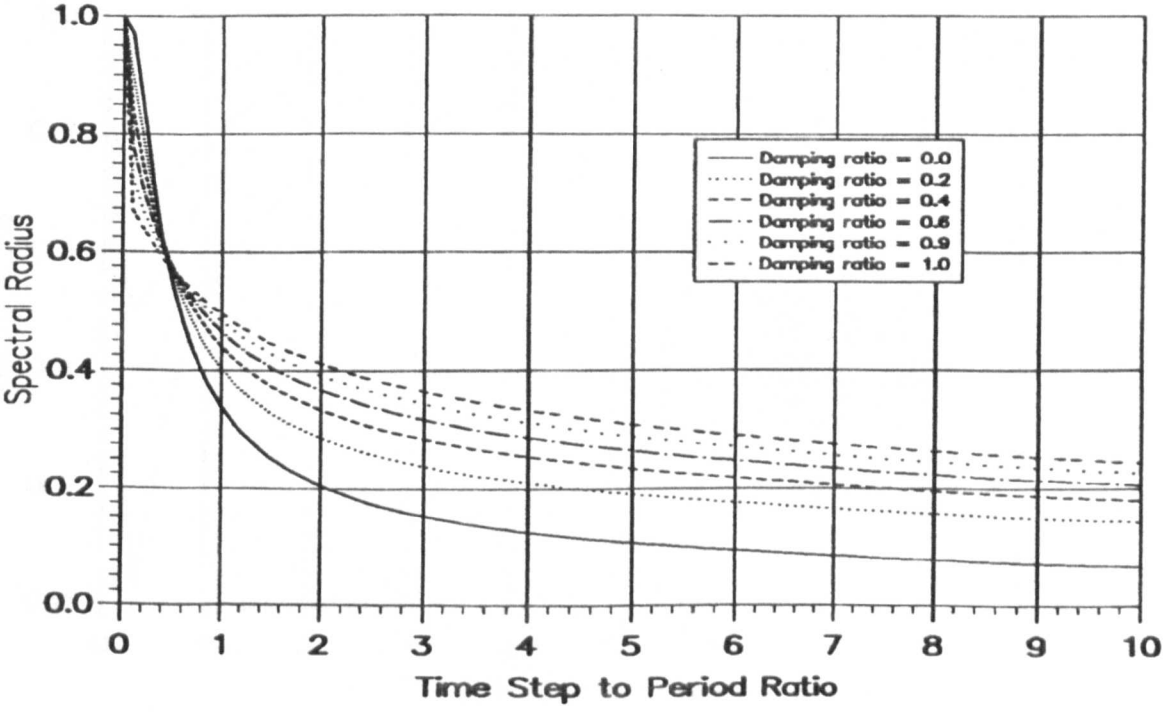

Figure 5.3 — Spectral Radius for Houbolt Scheme

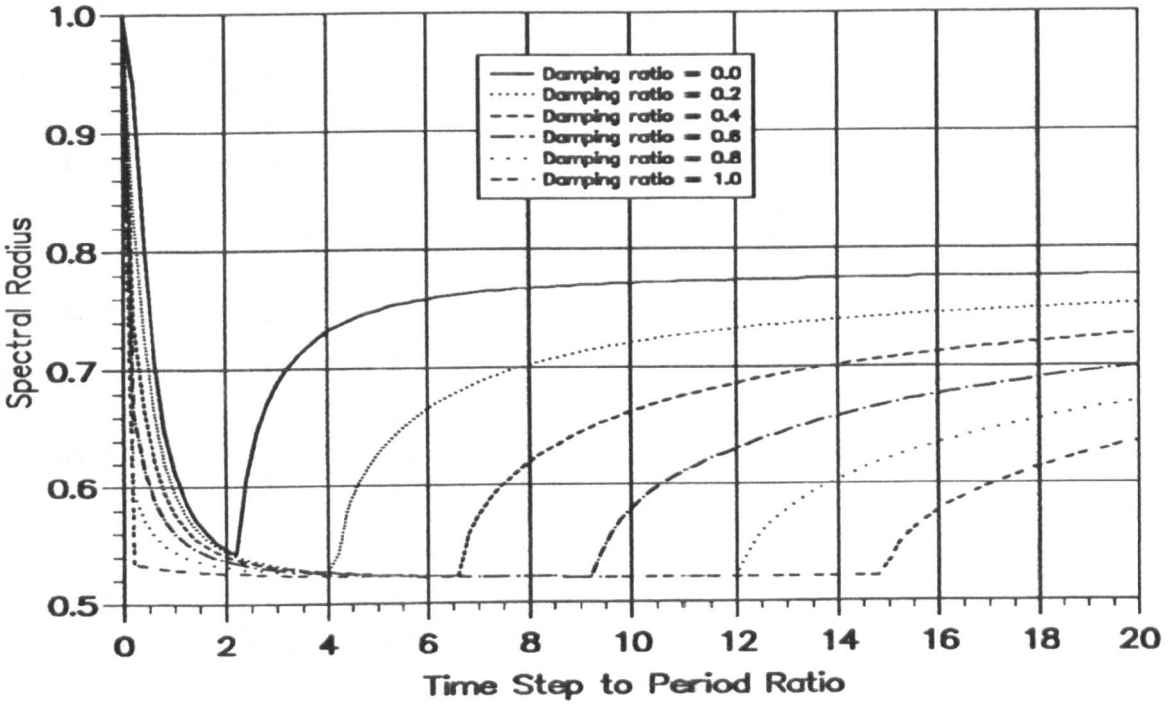

Figure 5.4 — Spectral Radius for Wilson Scheme ($\theta = 1.4$)

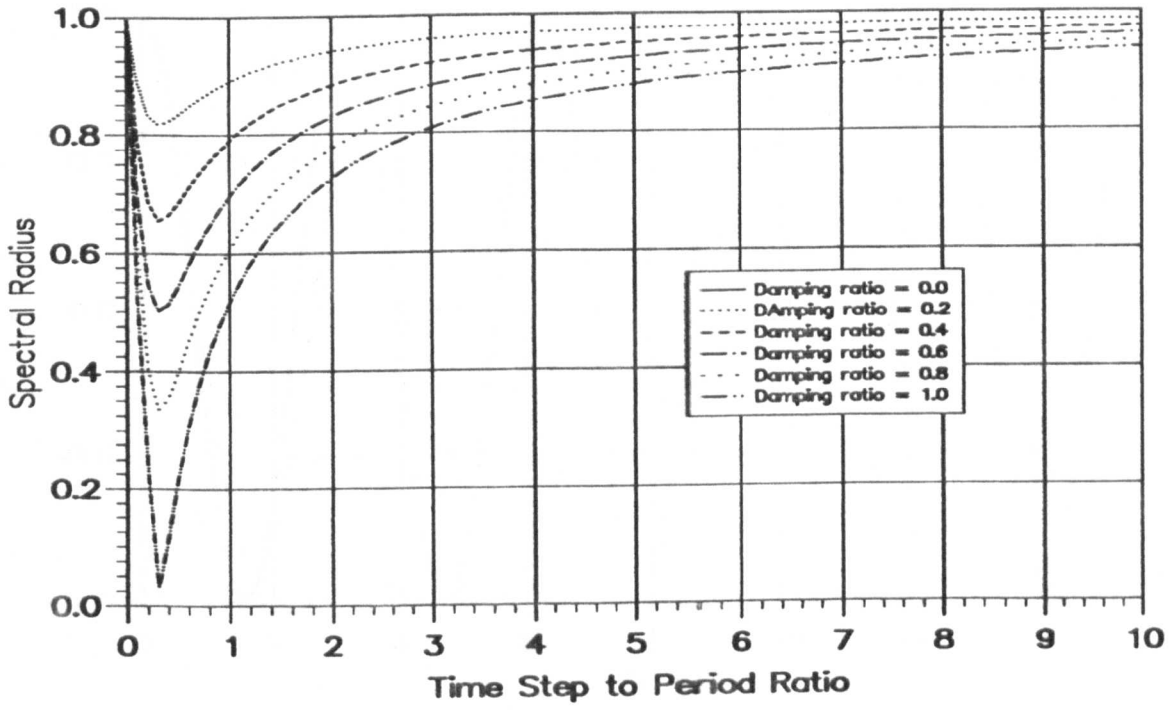

Figure 5.5 — Spectral Radius for Newmark Scheme

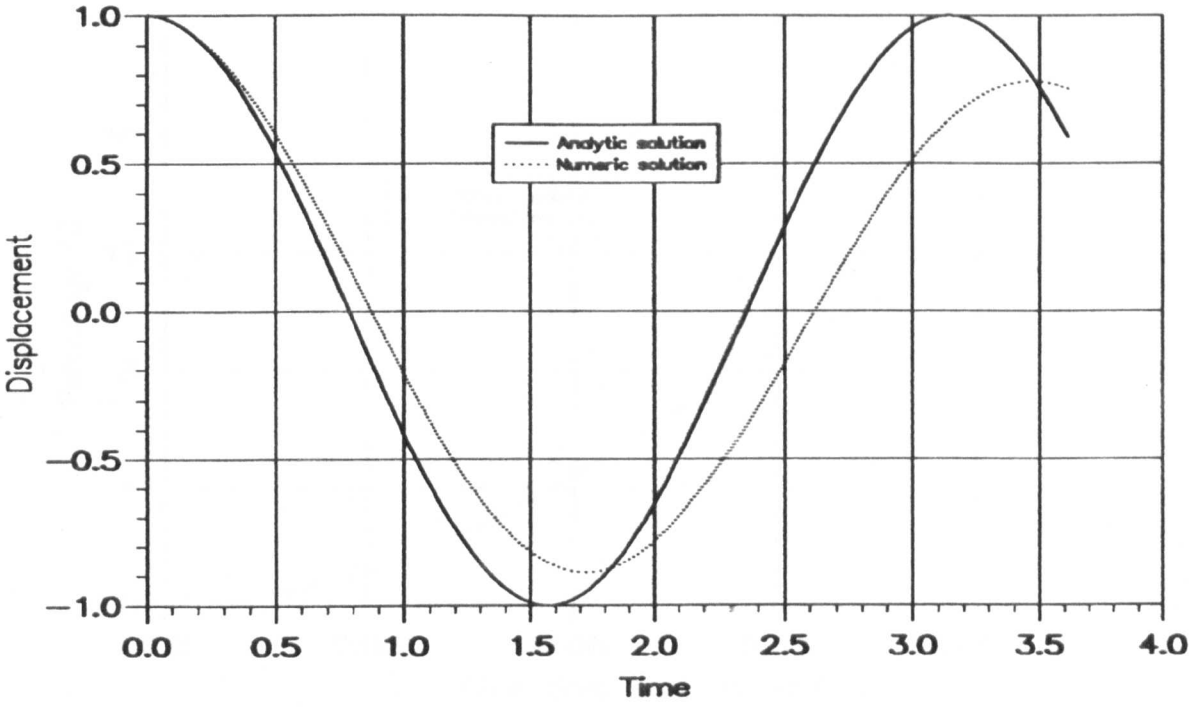

Figure 5.6 — Illustration of Amplitude Decay and Period Elongation

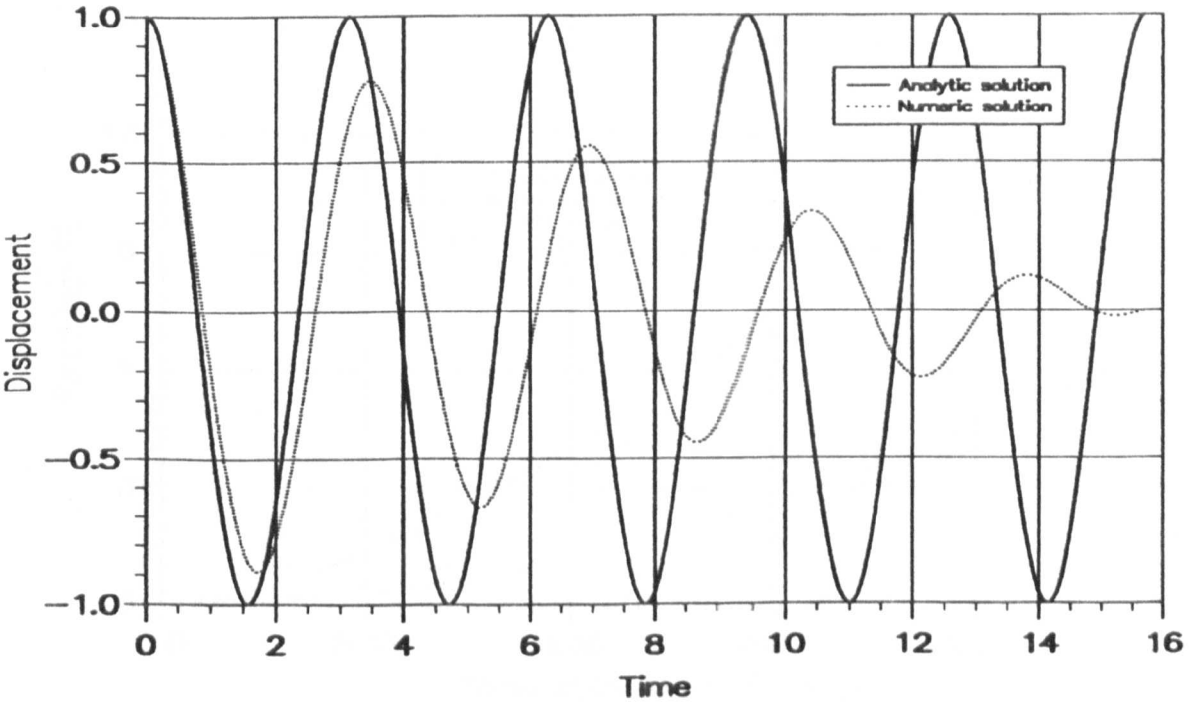

Figure 5.7 — Effect of AD and PE Upon Total Solution

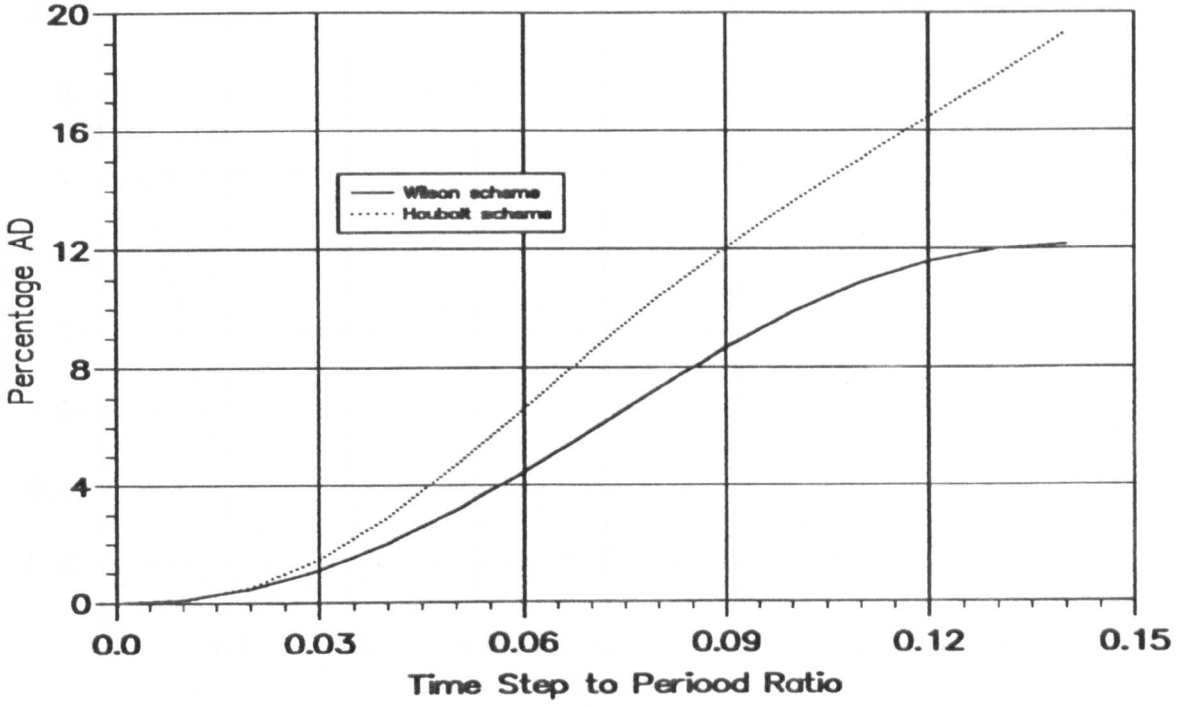

Figure 5.8 — Percentage Amplitude Decay

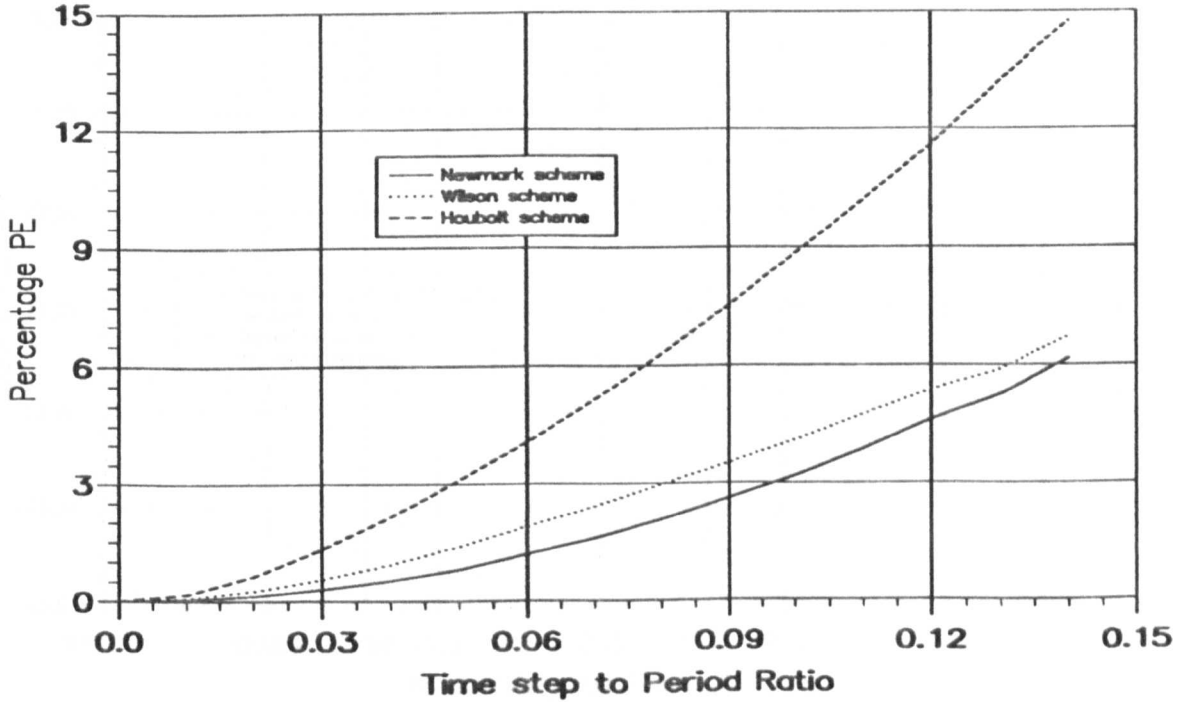

Figure 5.9 — Percentage Period Elongation

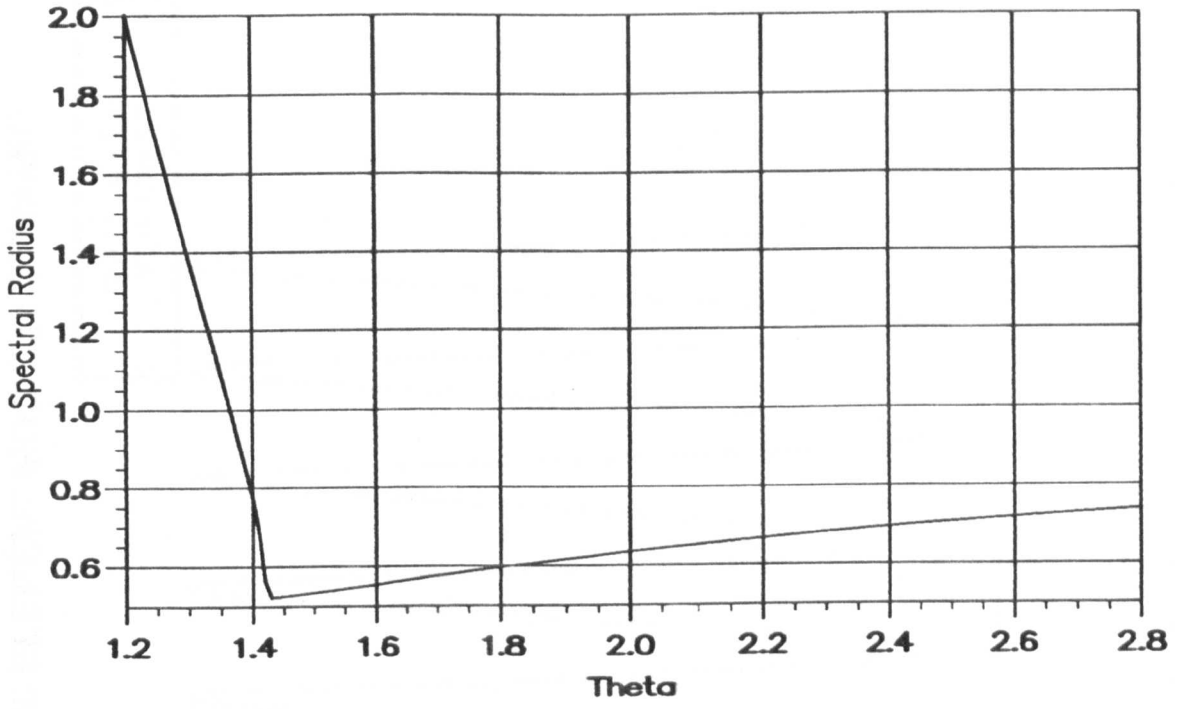

Figure 5.10 — Spectral Radius vs. θ for Wilson Scheme

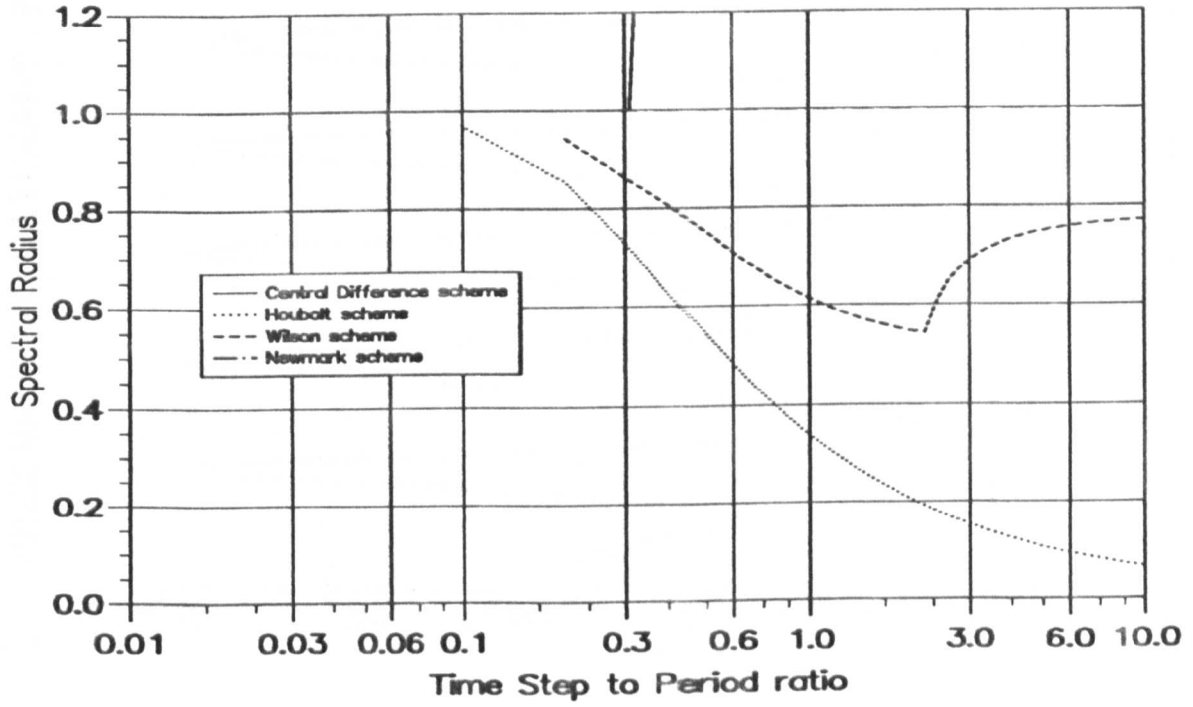

Figure 5.11 — Spectral Radius With Zero Damping

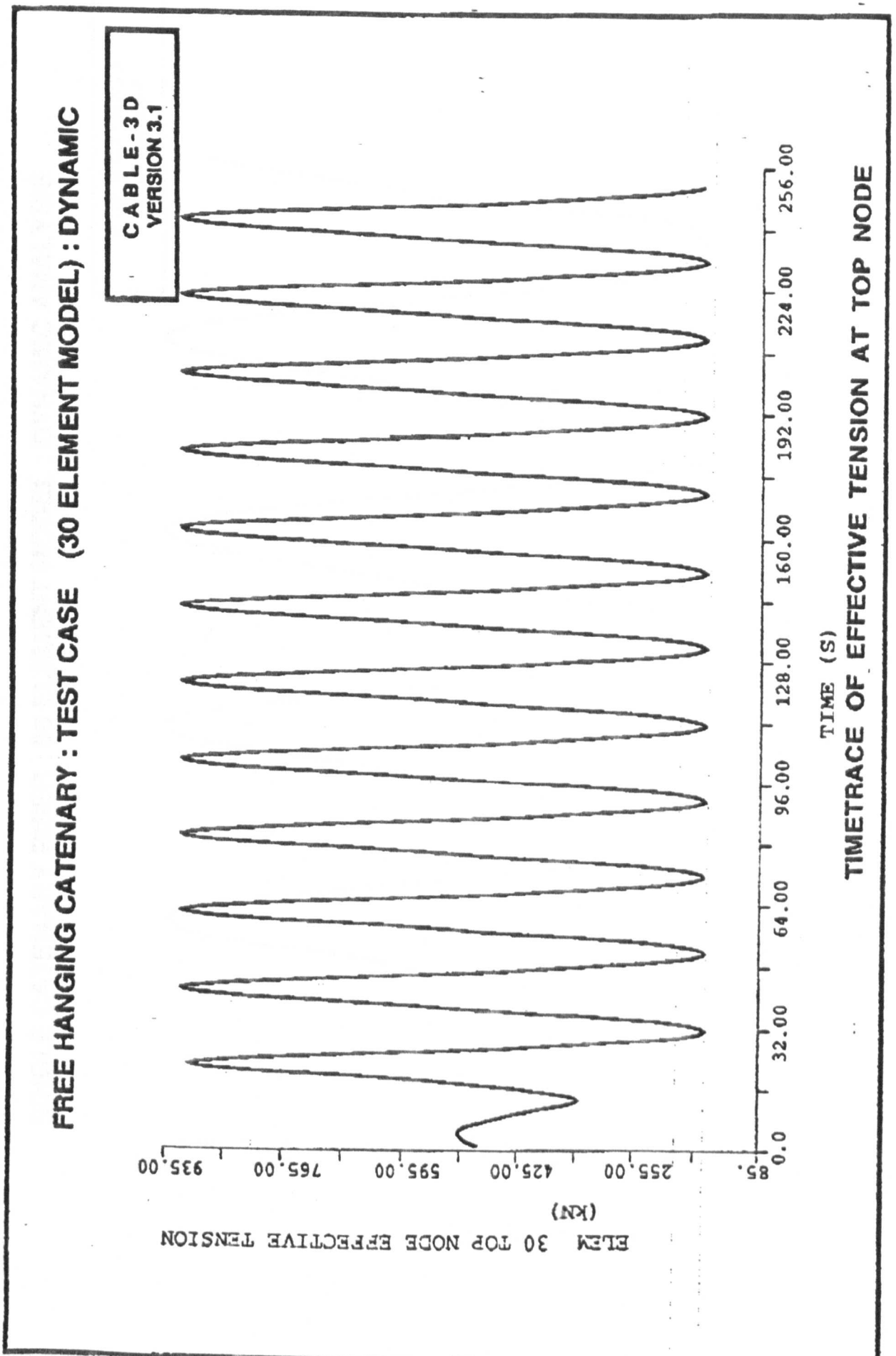

Figure 6.0A - CABLE-3D (30E), McNamara(1993)

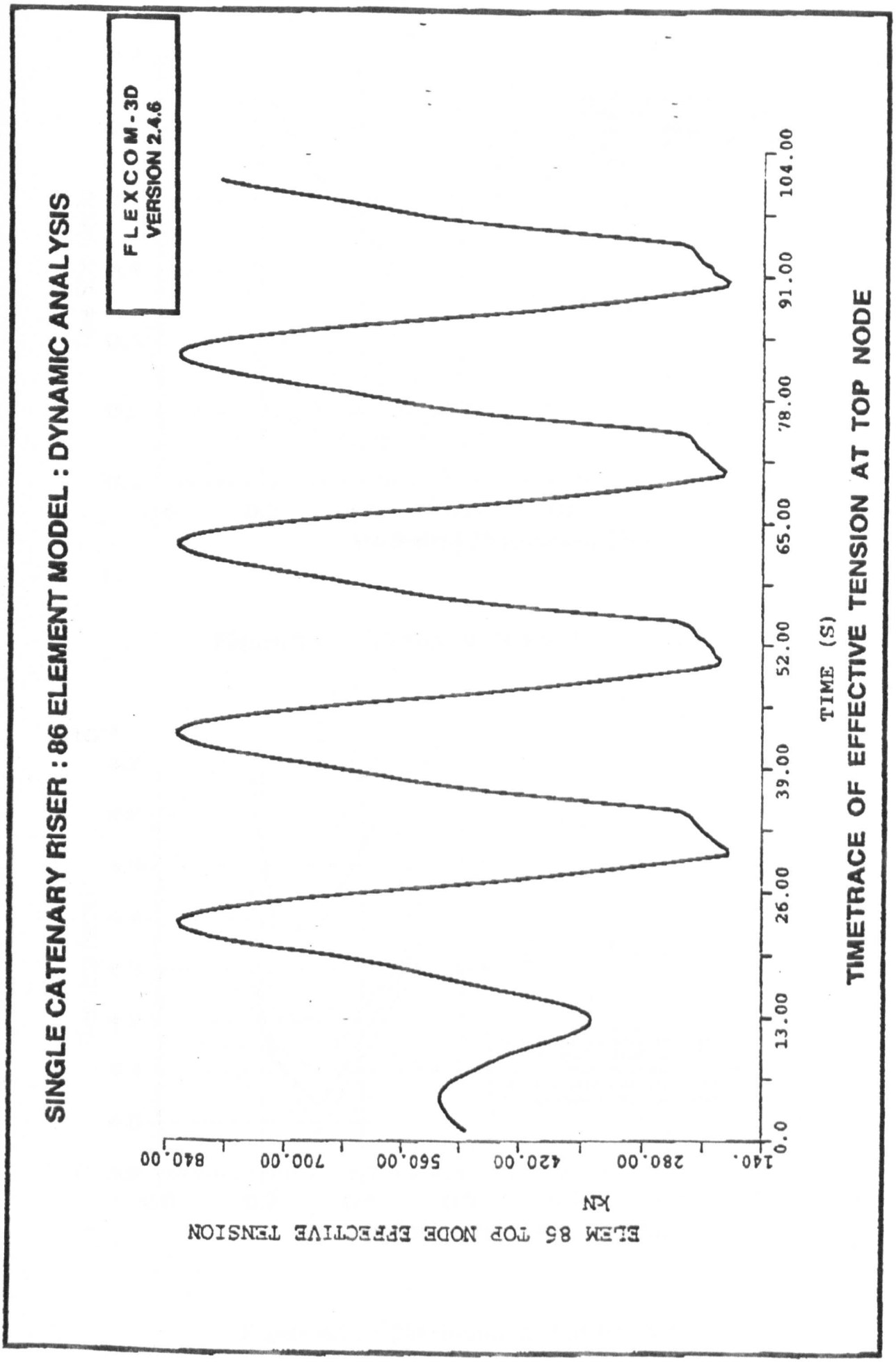

Figure 6.0B - FLEXCOM-3D (86E), McNamara(1993)

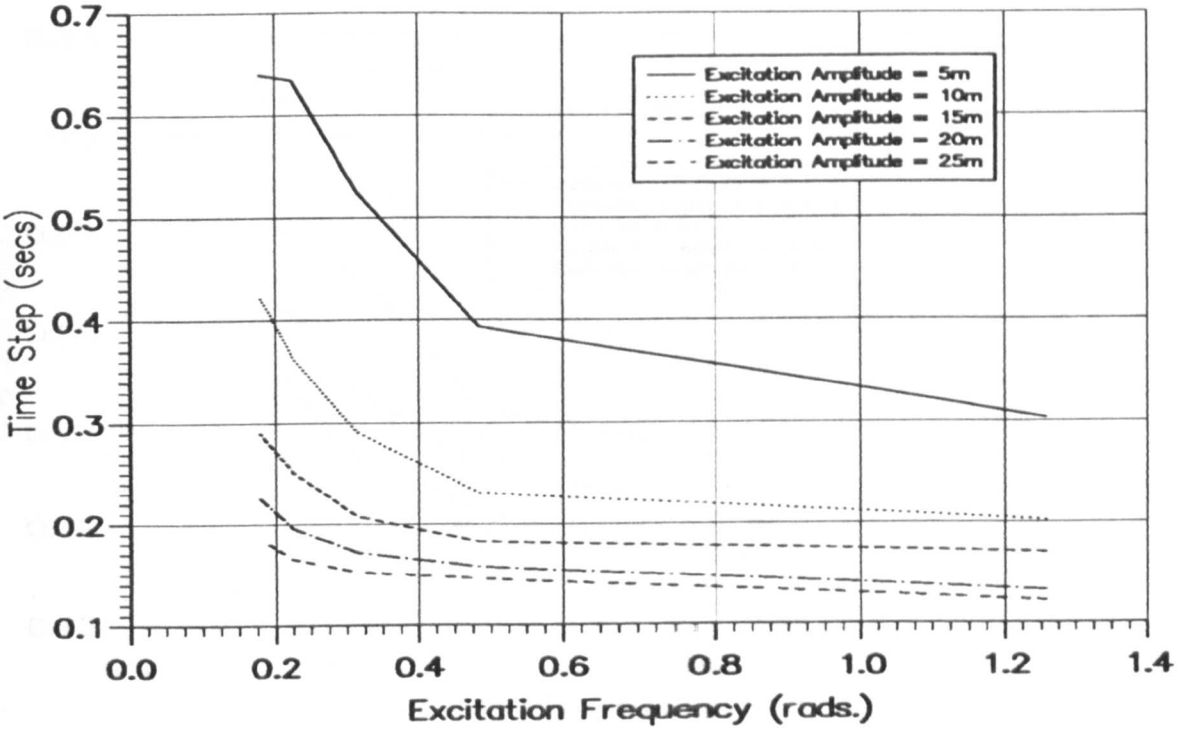

Figure 6.1 — Maximum Δt For Houbolt Scheme.

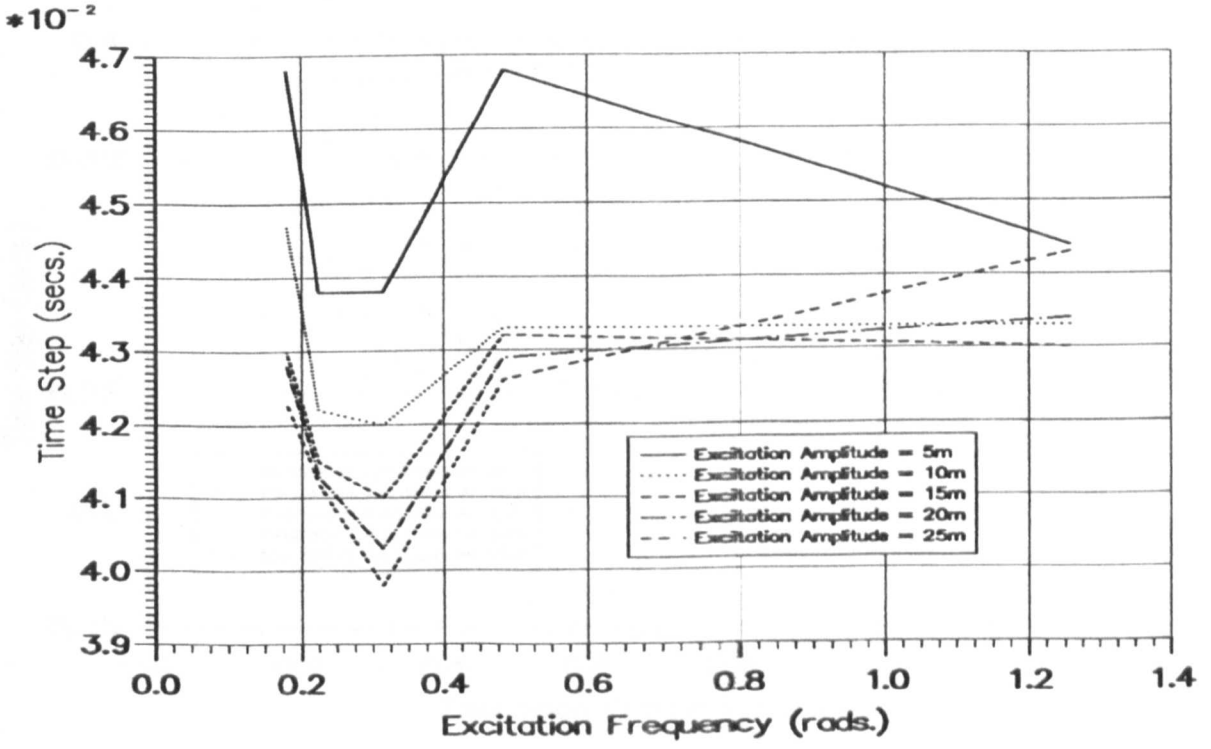

Figure 6.2 — Maximum Δt For CD Scheme.

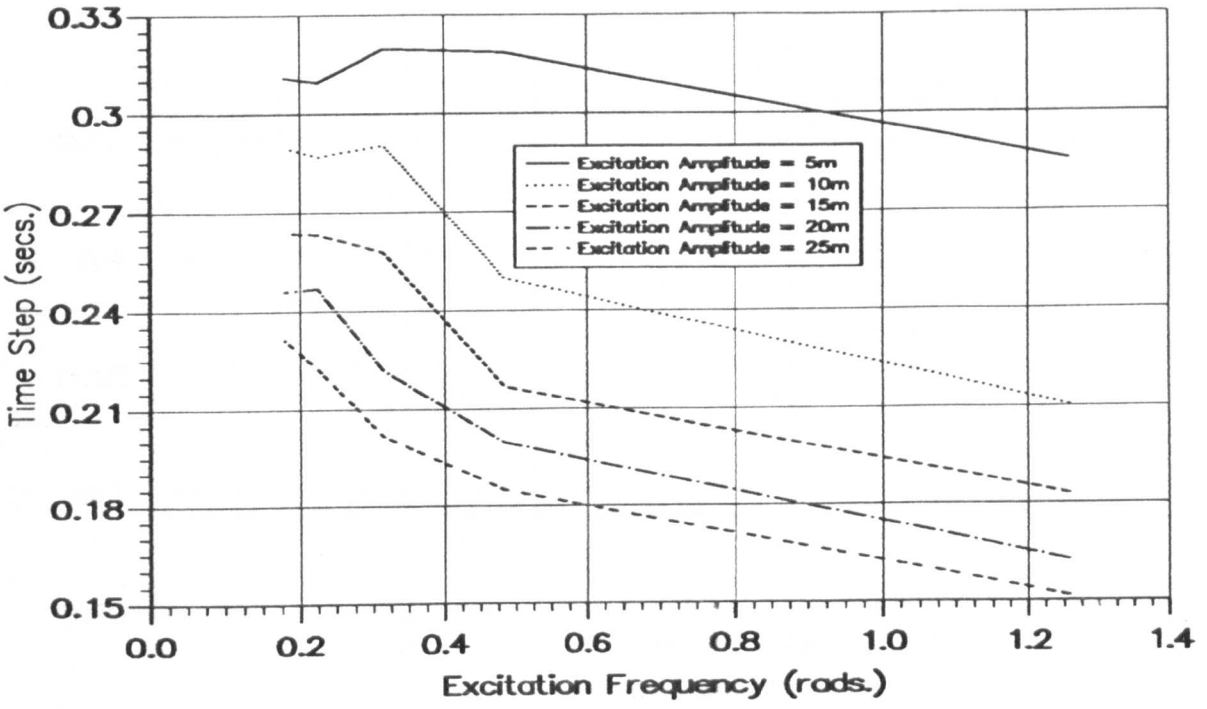

Figure 6.3 — Maximum Δt For Wilson Scheme.

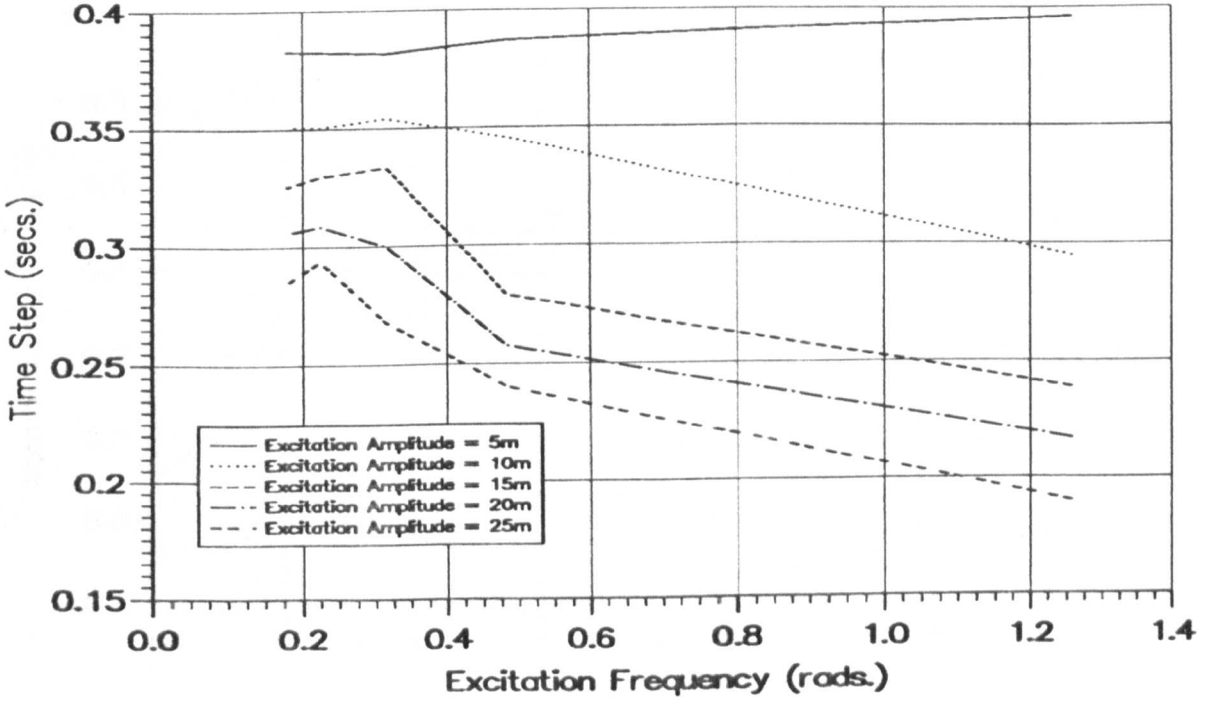

Figure 6.4 — Maximum Δt For Newmark Scheme.

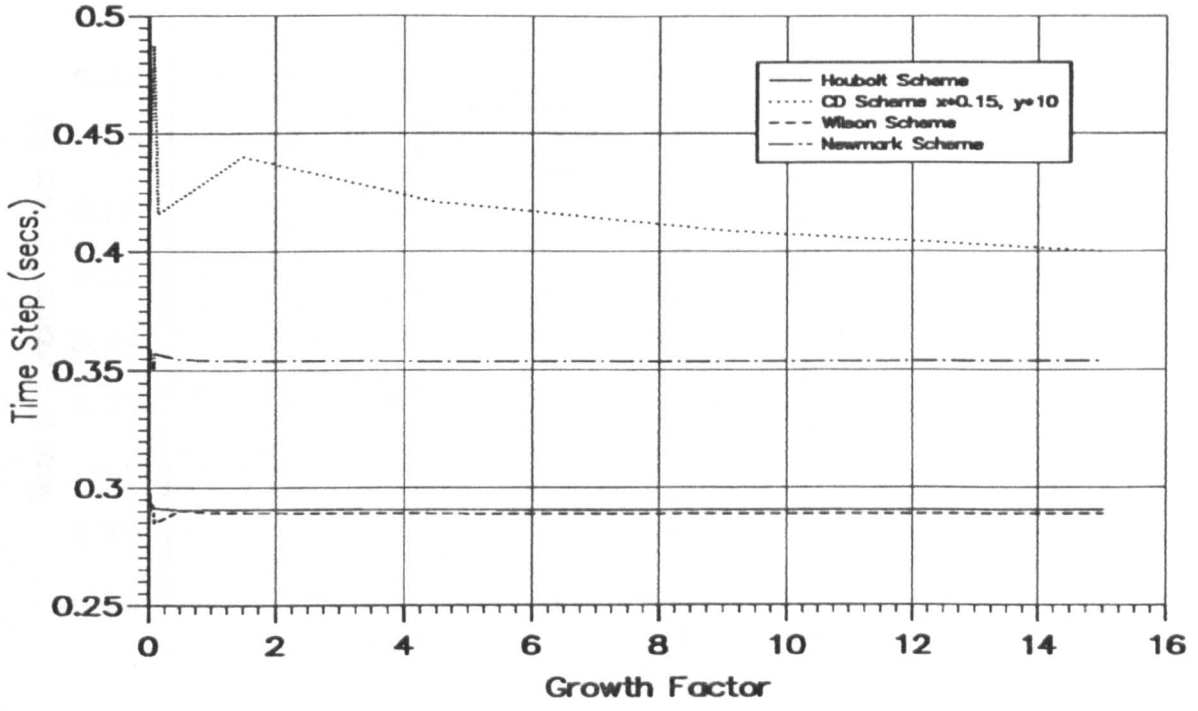

Figure 6.5 — Growth Factor, ζ, Vs. Maximum Δt.

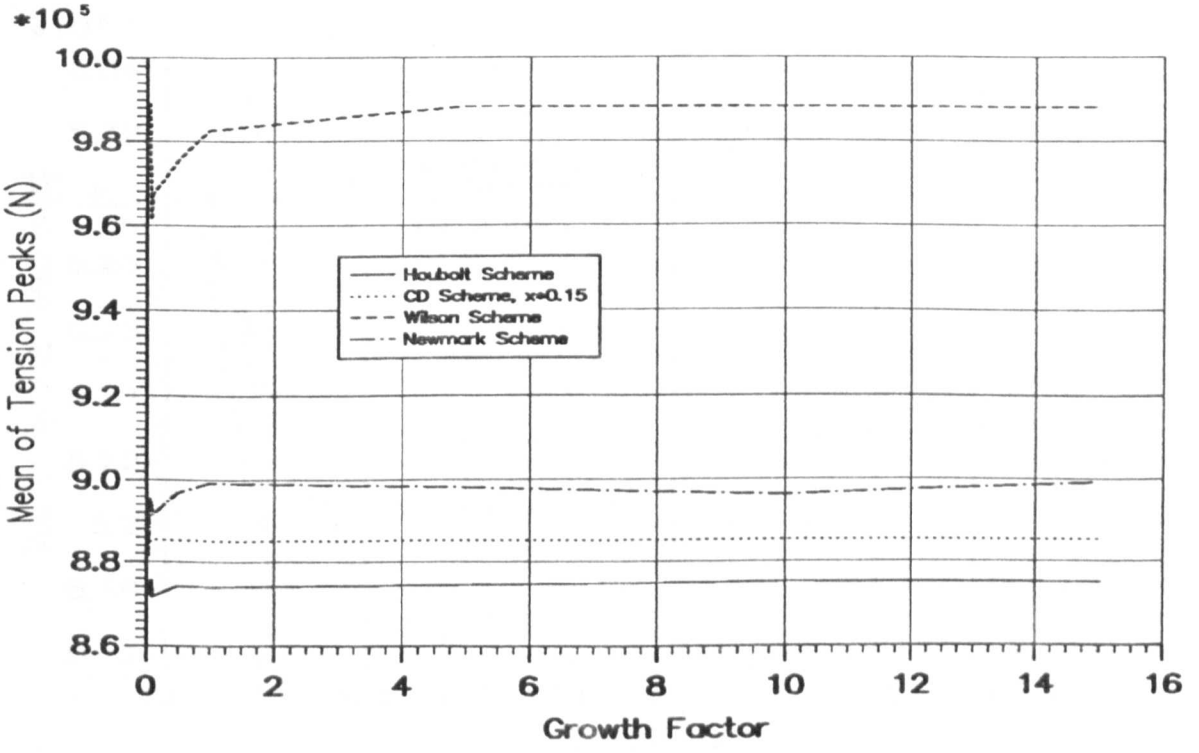

Figure 6.6 — Growth Factor Vs. Mean of Tension Peaks.

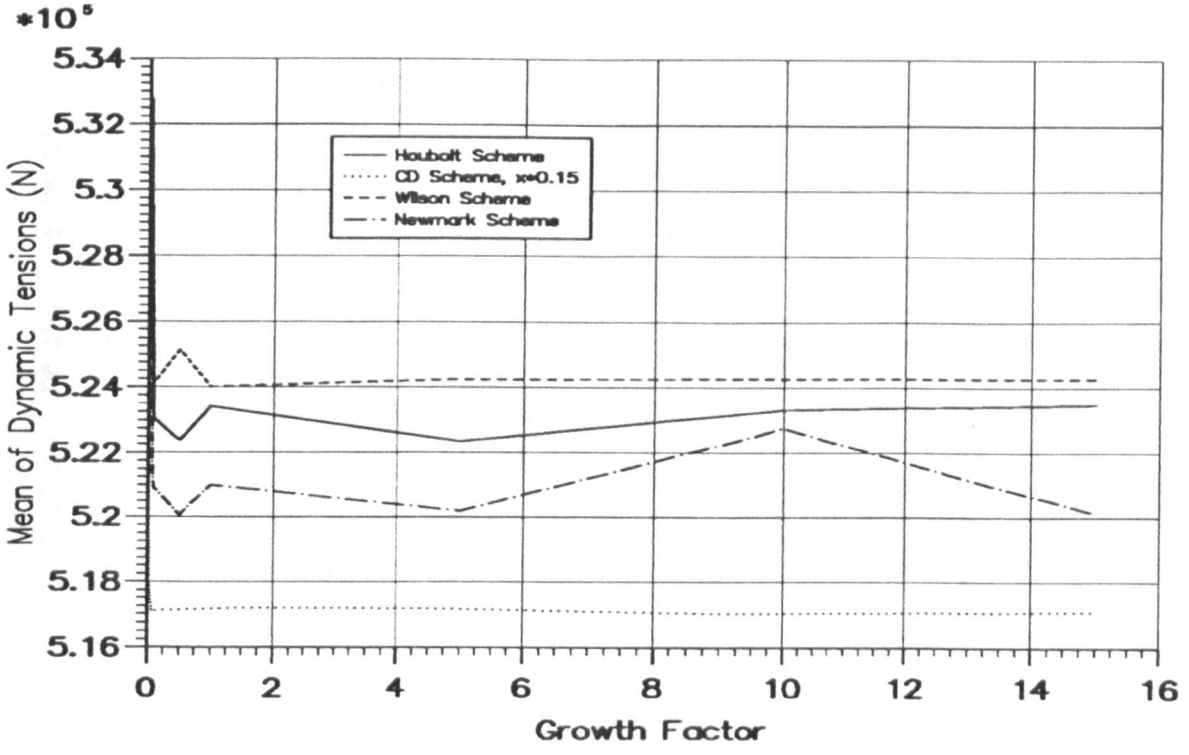

Figure 6.7 — Growth Factor Vs. Mean of Dynamic Tensions.

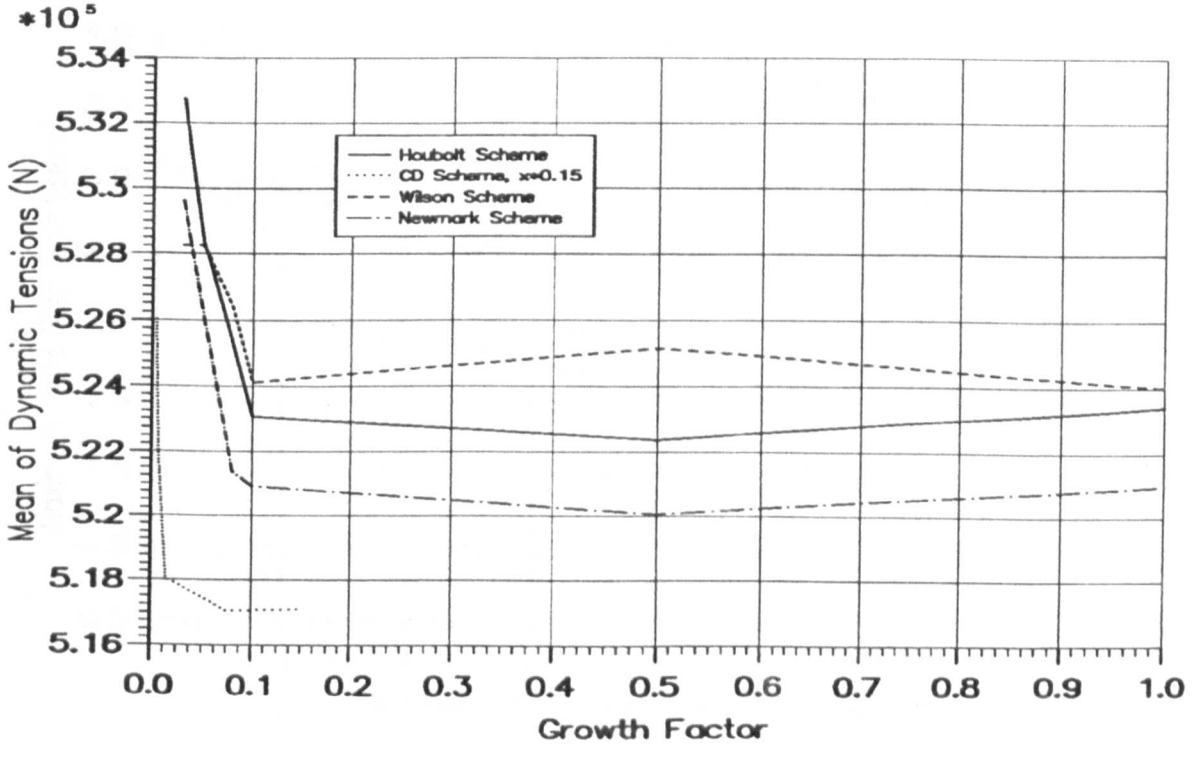

Figure 6.8 — Growth Factor Vs. Mean of Tensions For $0.0 \leq x \leq 1.0$

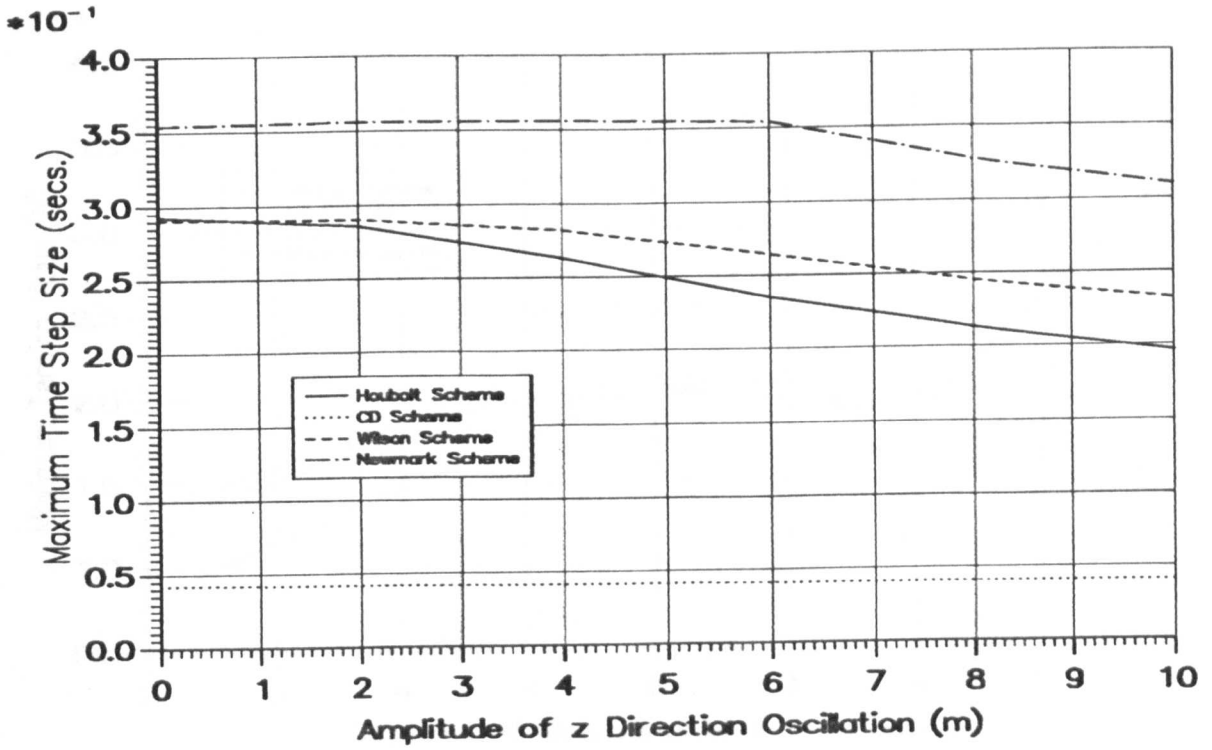

Figure 6.9 — Influence of Elliptical Endpoint Motion on Max. Δt.

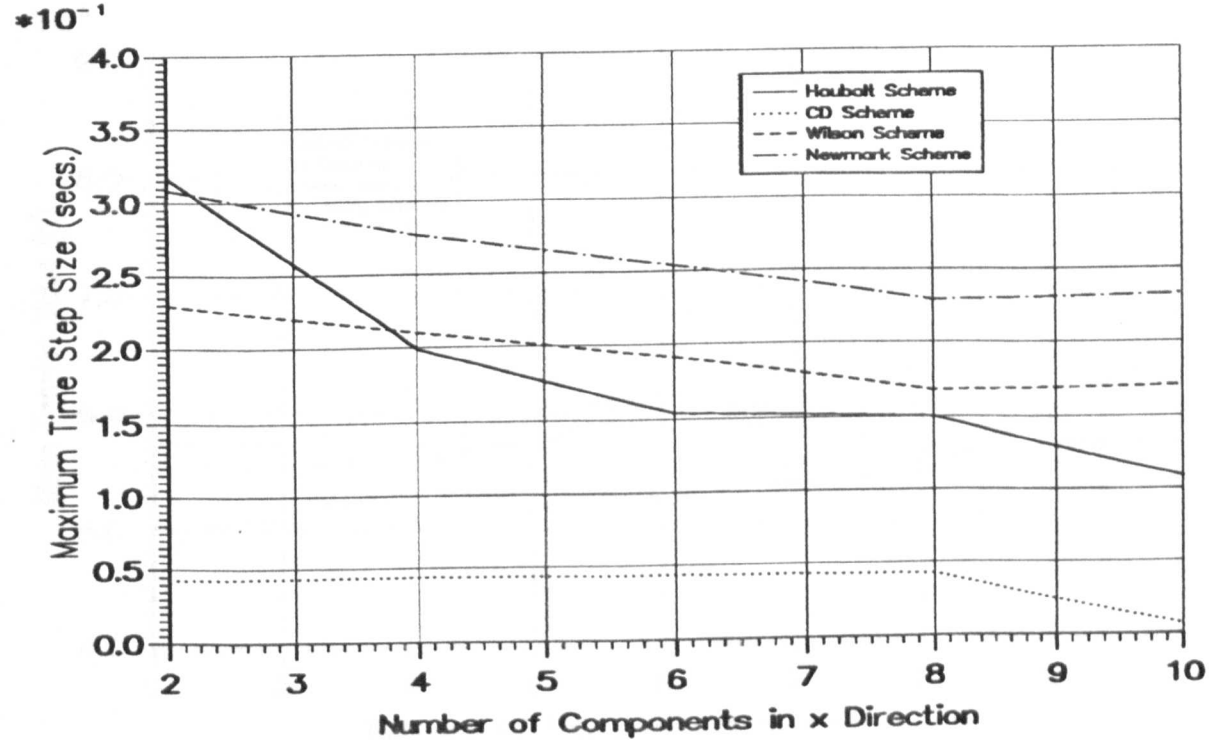

Figure 6.10 — Max. Δt For Irregular Endpoint Excitations.

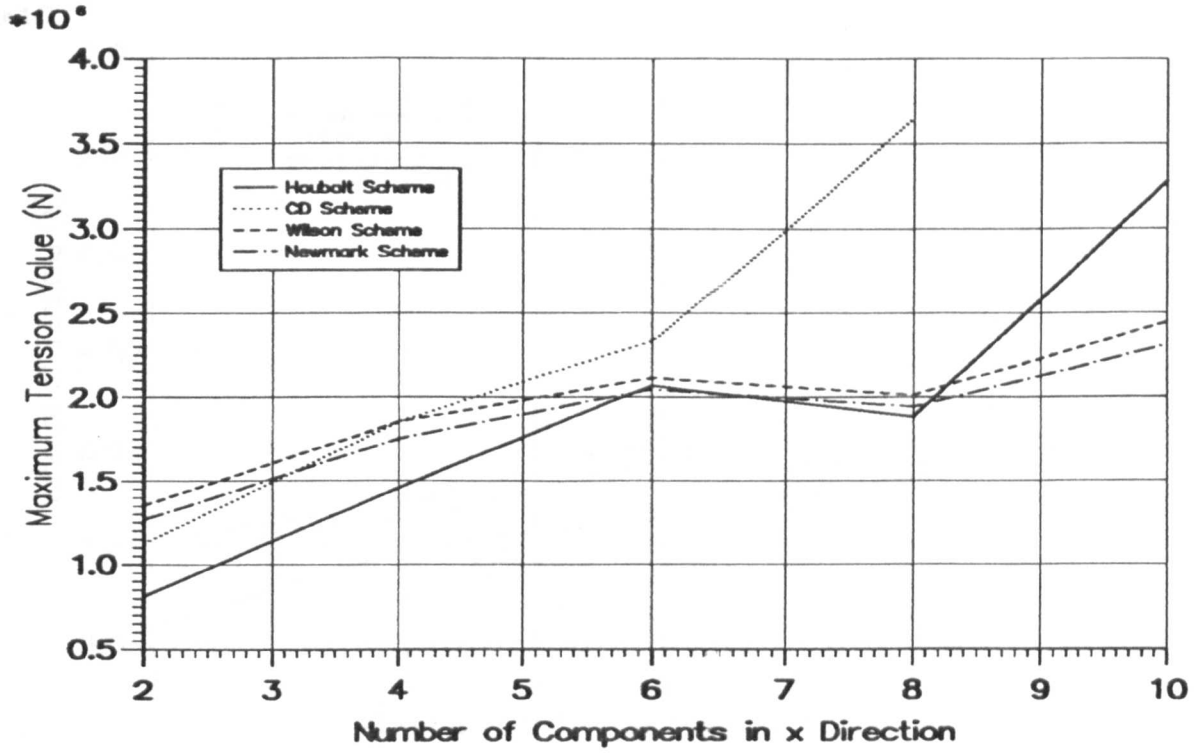

Figure 6.11 — Different Irregular Motion Vs. Max. Tension Values.

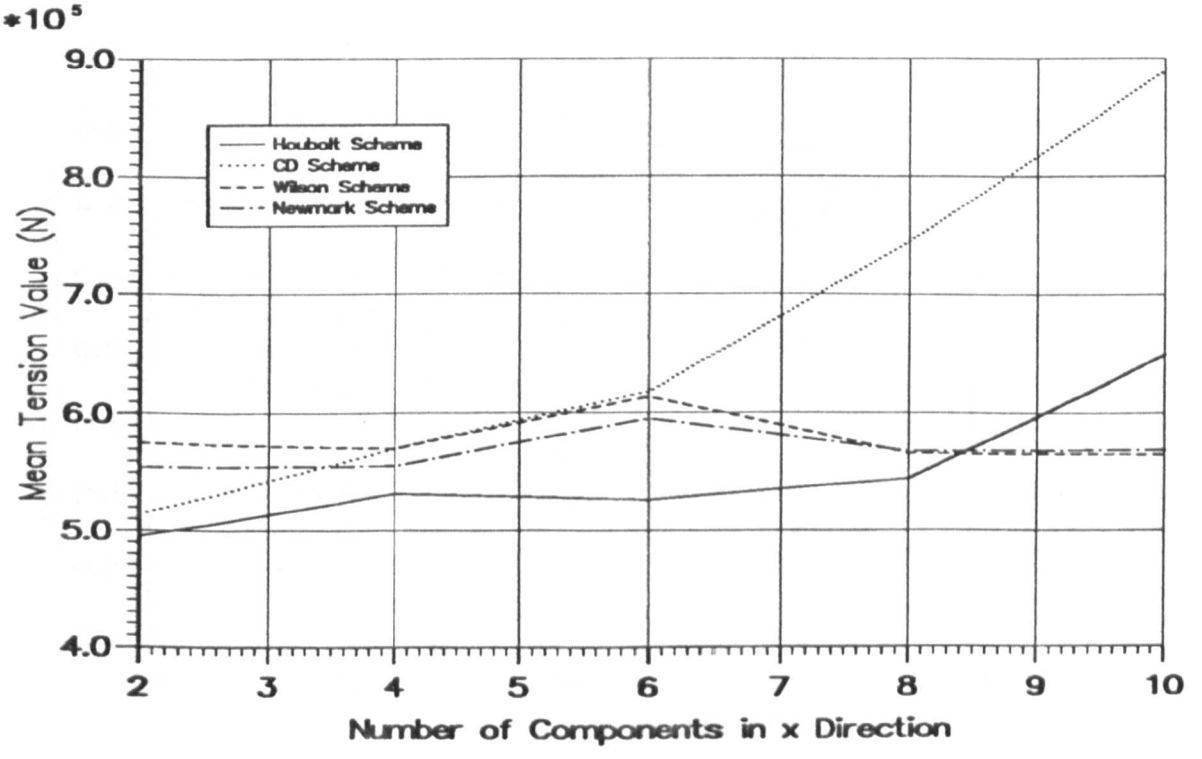

Figure 6.12 — Different Irregular Motion Vs. Mean Tension Values.

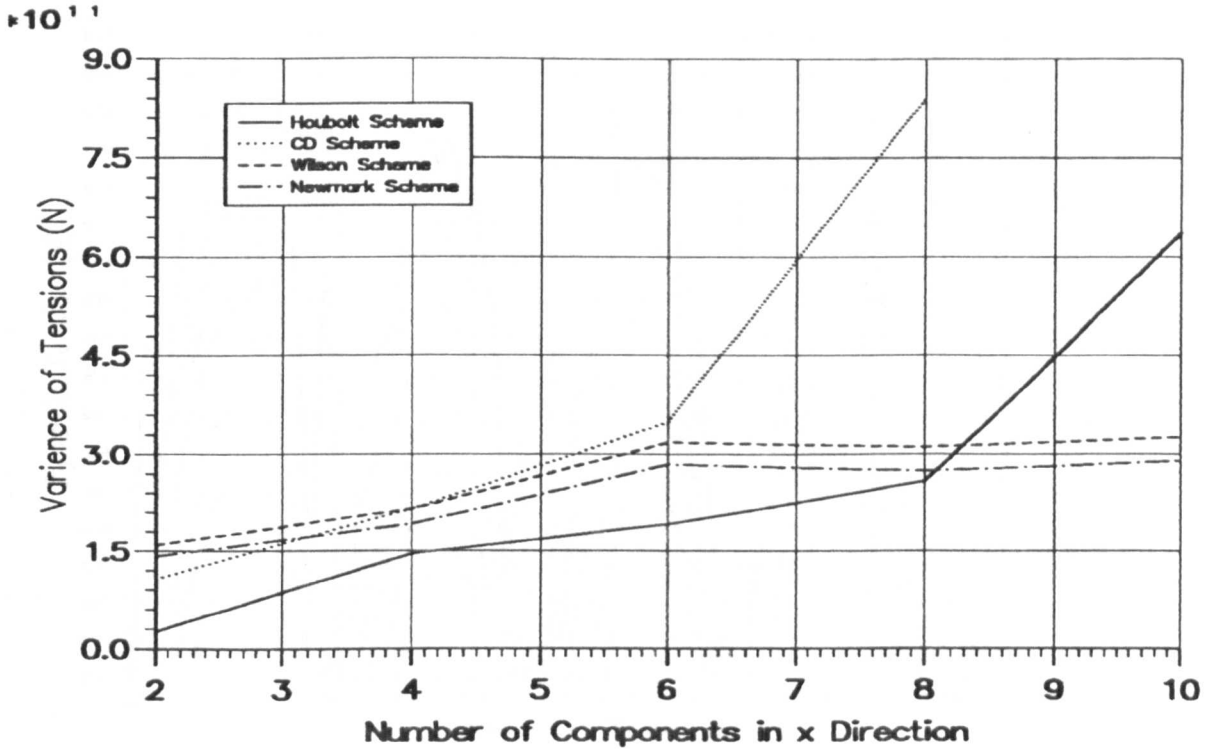

Figure 6.13 — Different Irregular Motion Vs. Varience of Tension.

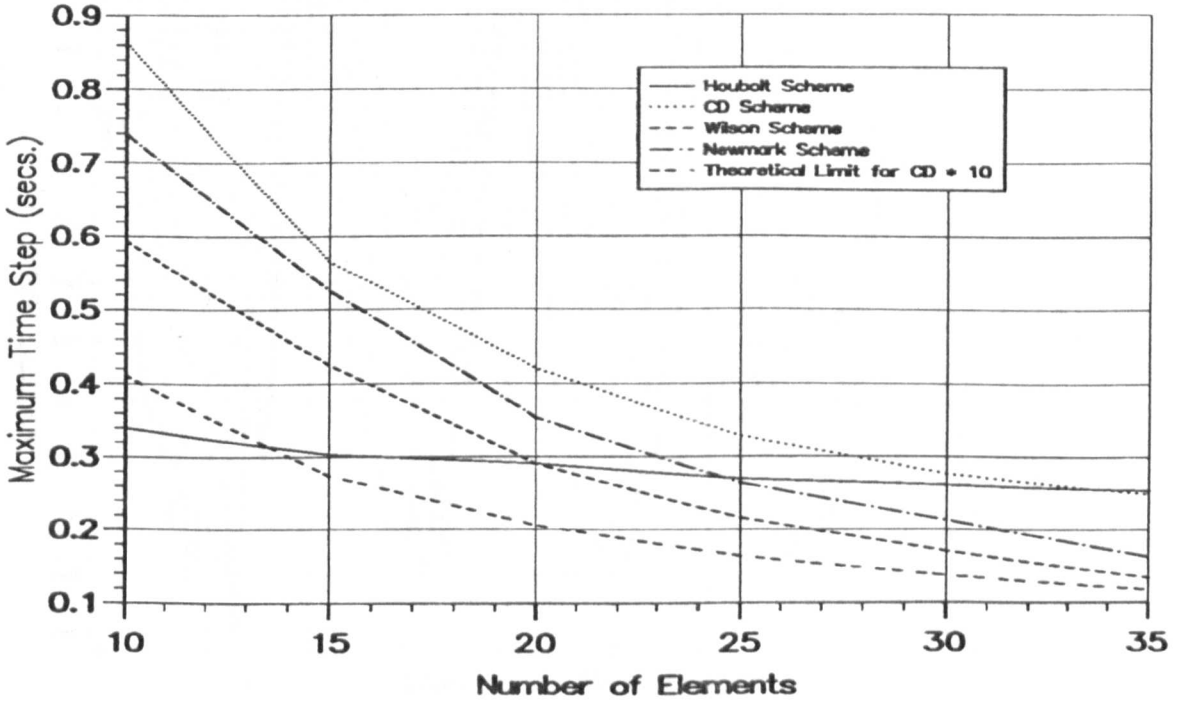

Figure 6.14 — Maximum Δt Vs. The Number of Elements.

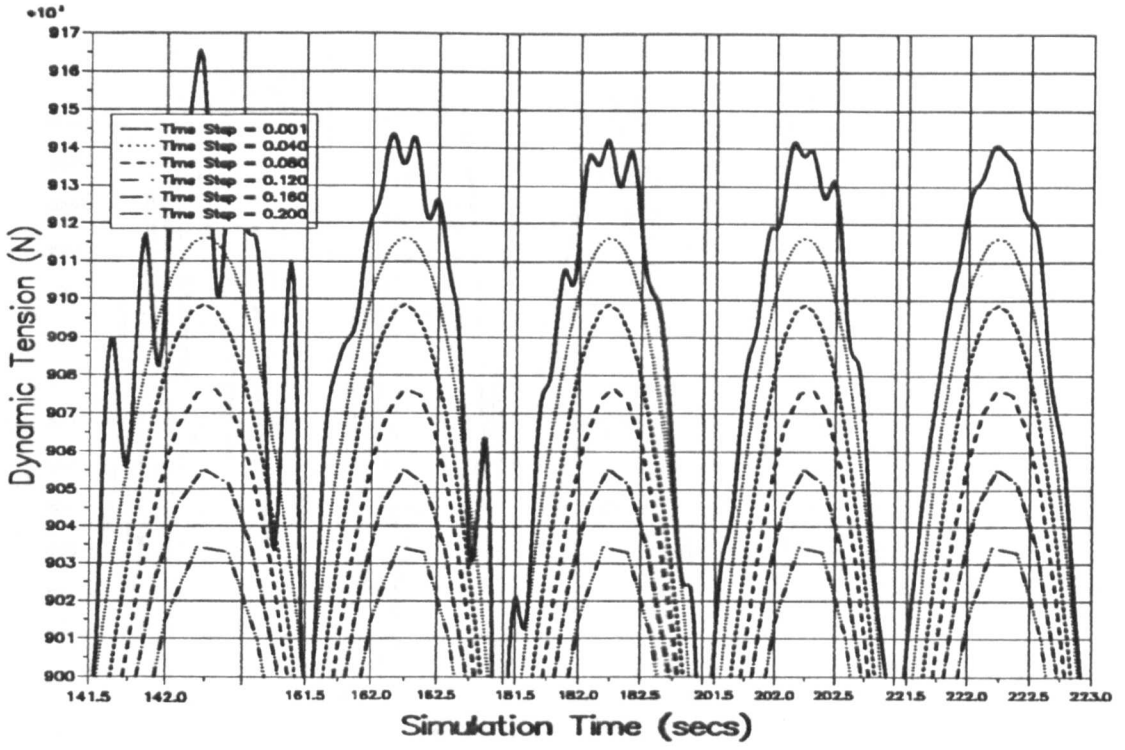

Figure 6.15 — Houbolt Scheme Tension Peaks For $h = 10$.

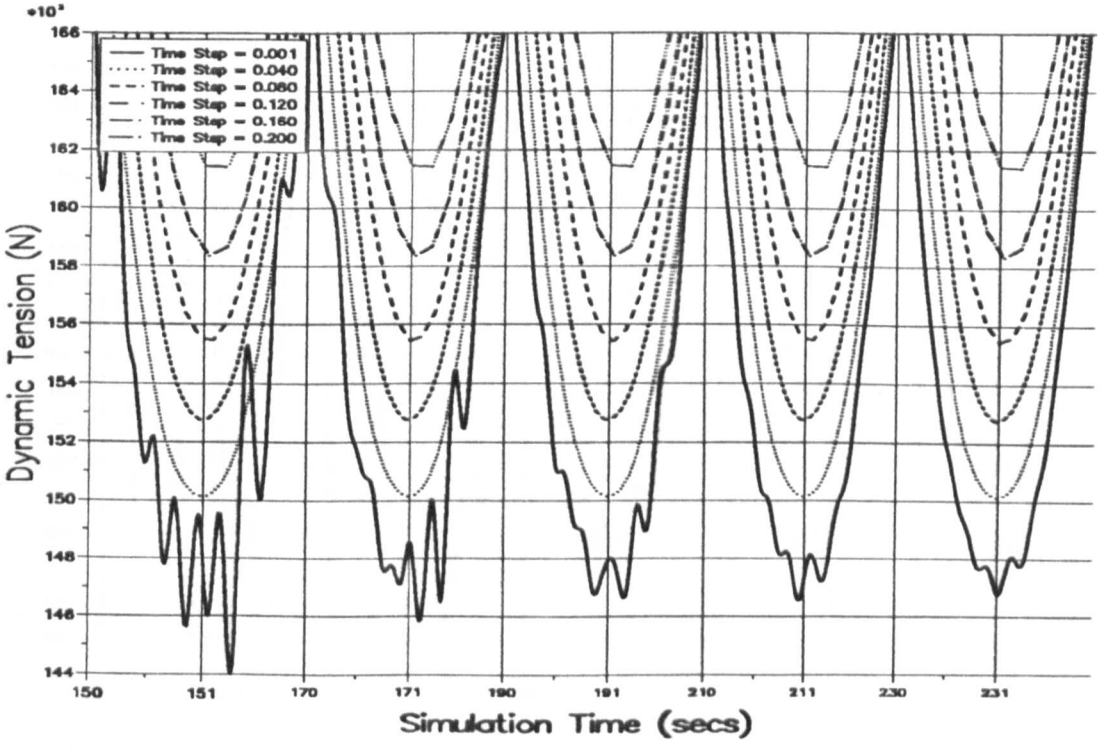

Figure 6.16 — Houbolt Scheme Tension Troughs For $h = 10$.

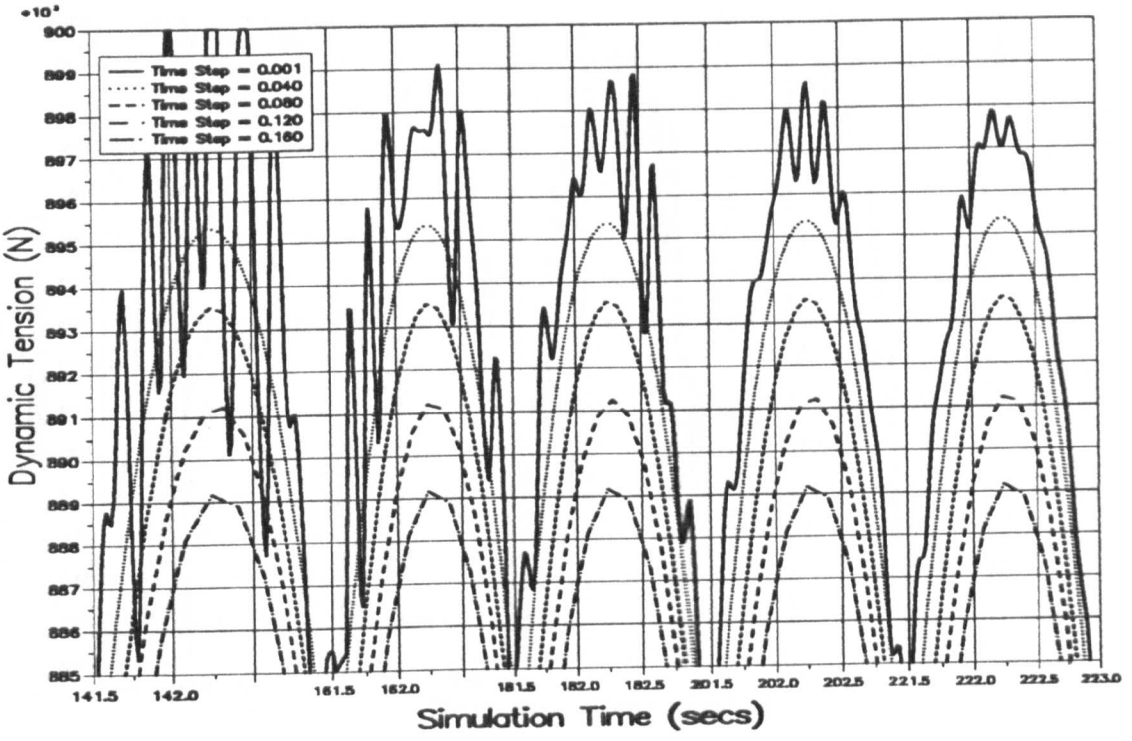

Figure 6.17 — Houbolt Scheme Tension Peaks For $h = 15$.

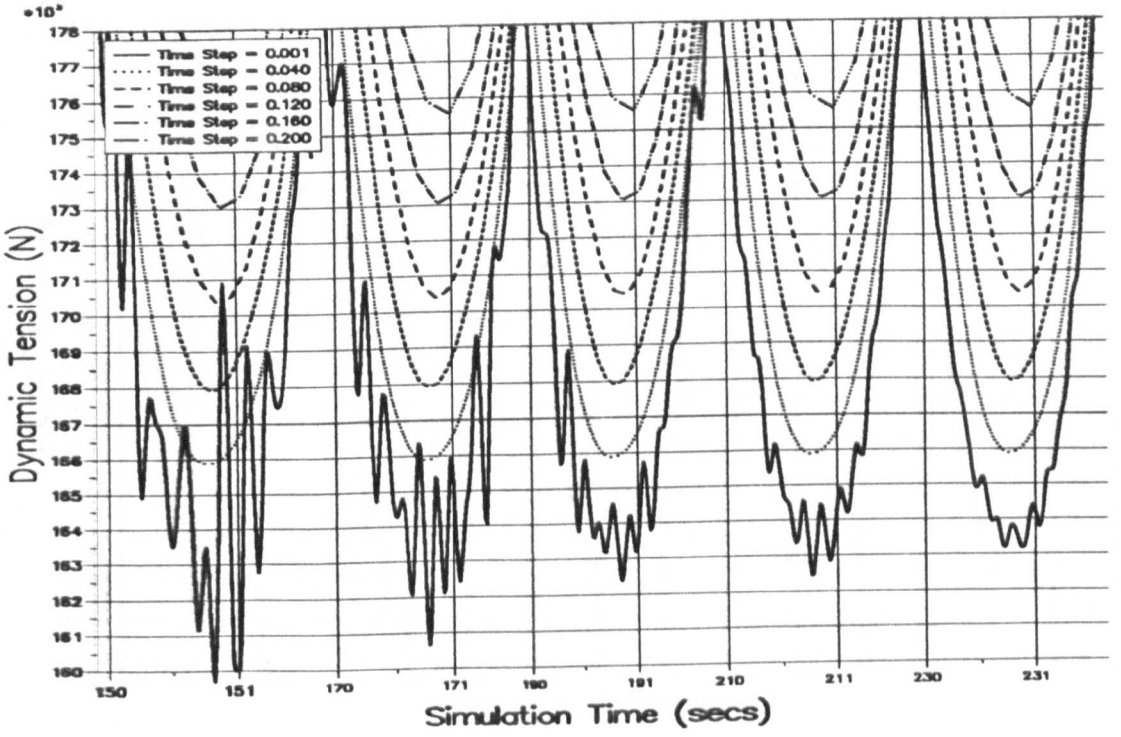

Figure 6.18 — Houbolt Scheme Tension Troughs For $h = 15$.

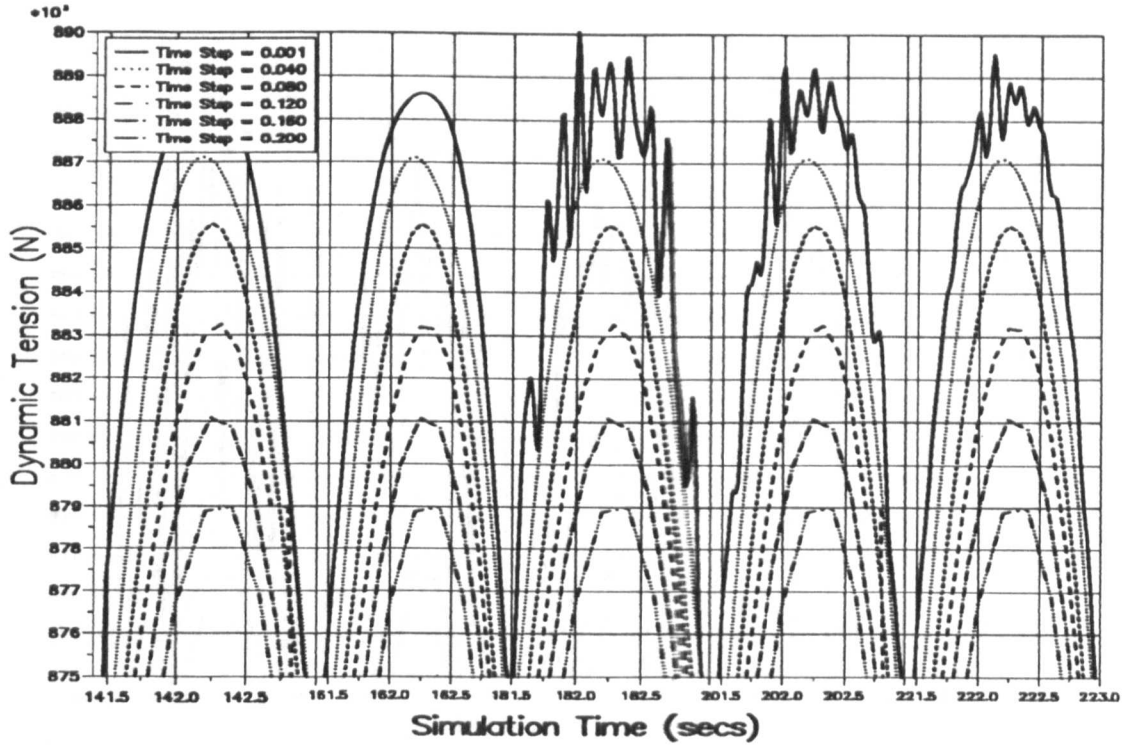

Figure 6.19 — Houbolt Scheme Tension Peaks For $h = 20$.

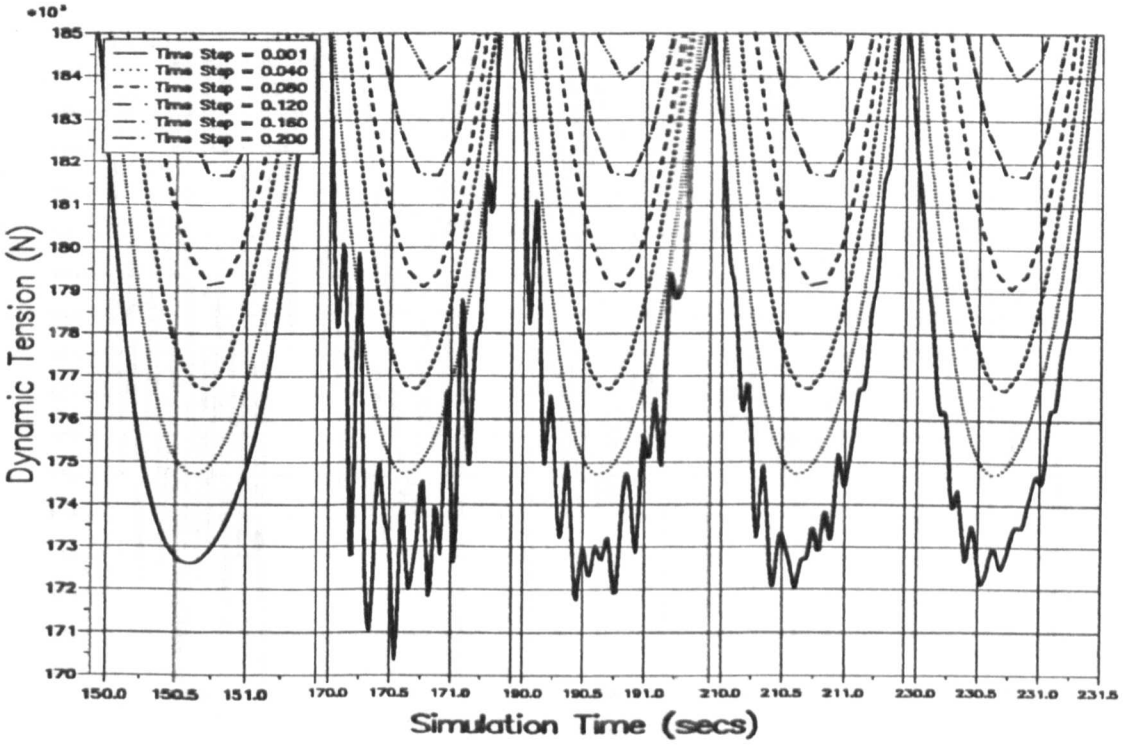

Figure 6.20 — Houbolt Scheme Tension Troughs For $h = 20$.

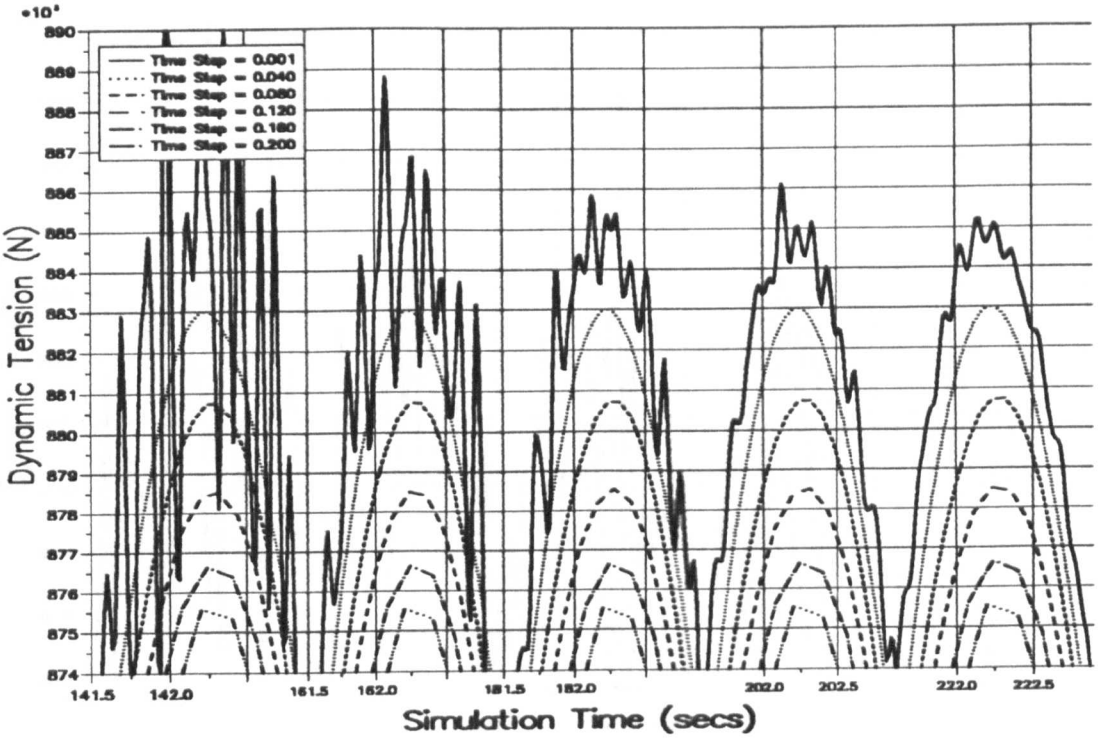

Figure 6.21 — Houbolt Scheme Tension Peaks For $h = 25$.

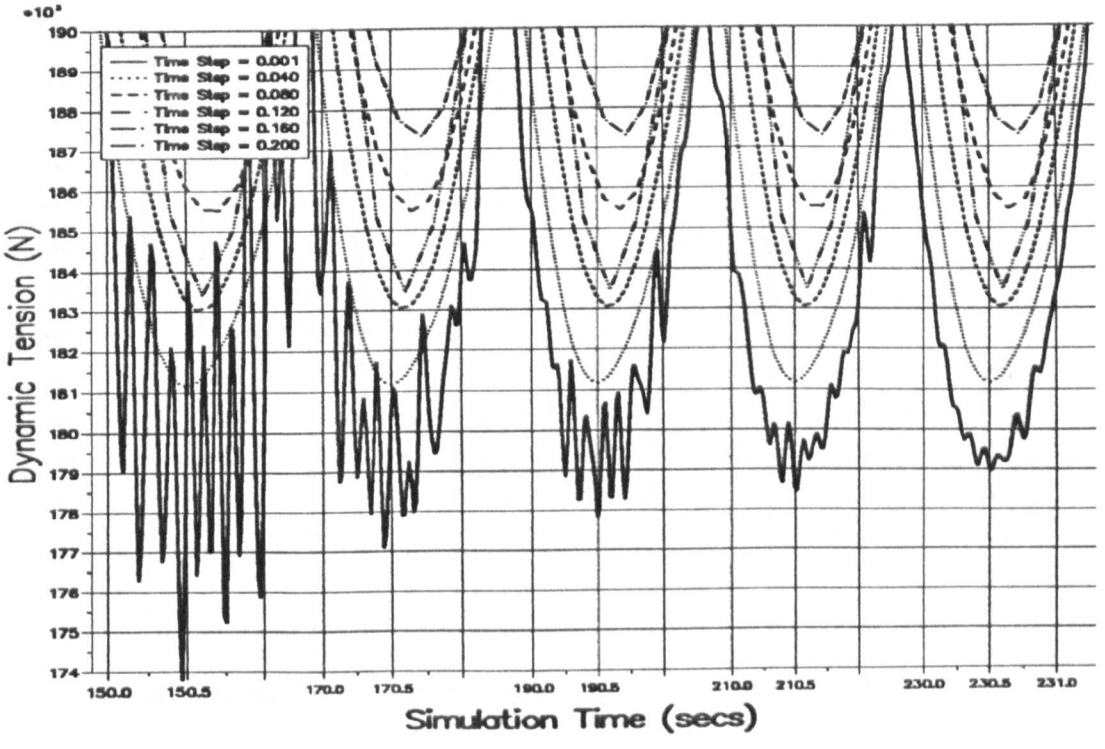

Figure 6.22 — Houbolt Scheme Tension Troughs For $h = 25$.

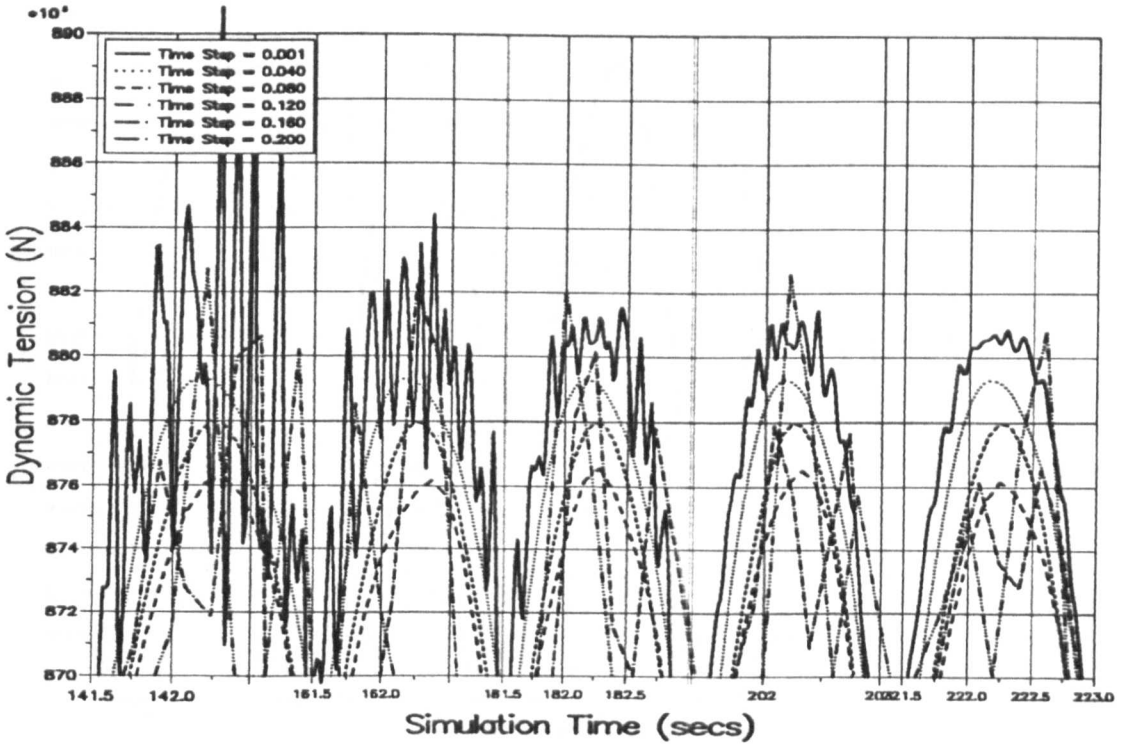

Figure 6.23 — Houbolt Scheme Tension Peaks For $h = 30$.

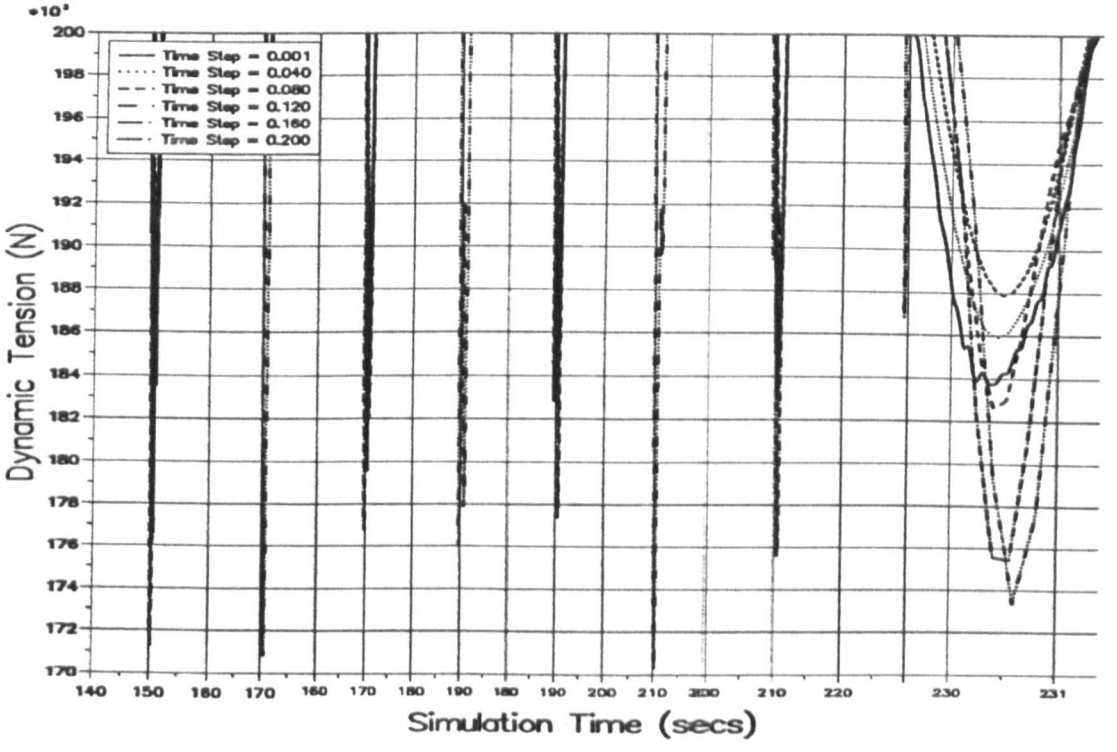

Figure 6.24 — Houbolt Scheme Tension Troughs For $h = 30$.

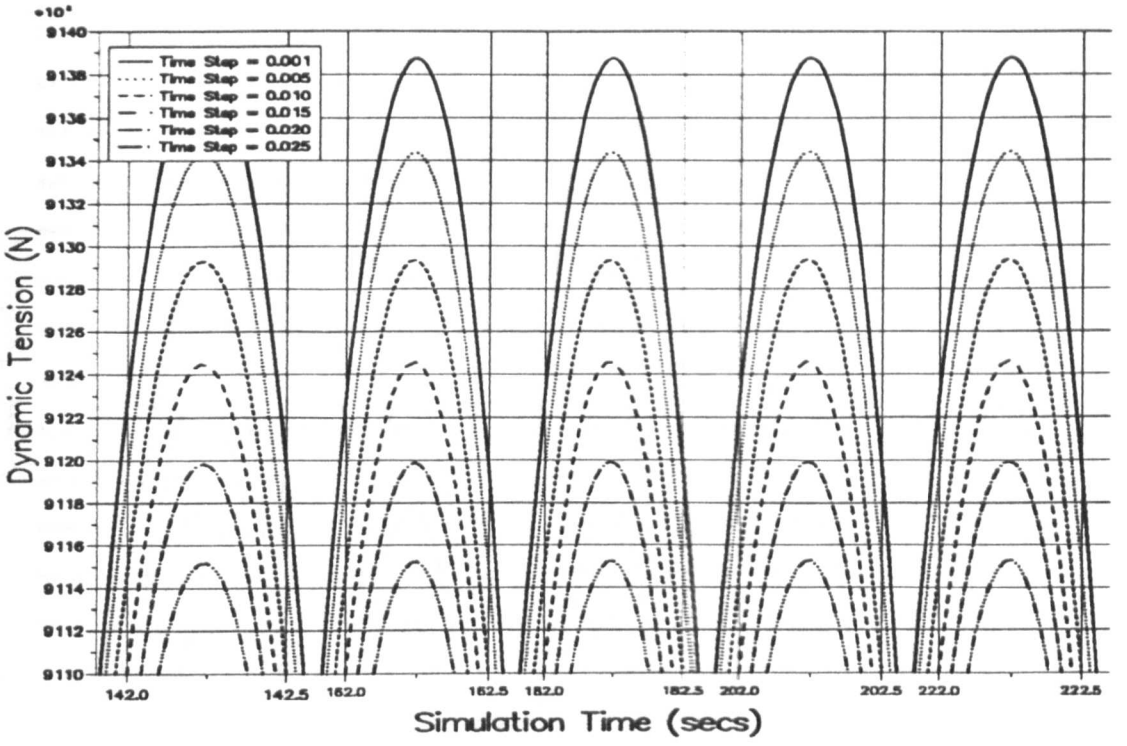

Figure 6.25 — Central Difference Scheme Tension Peaks **For** $h = 10$.

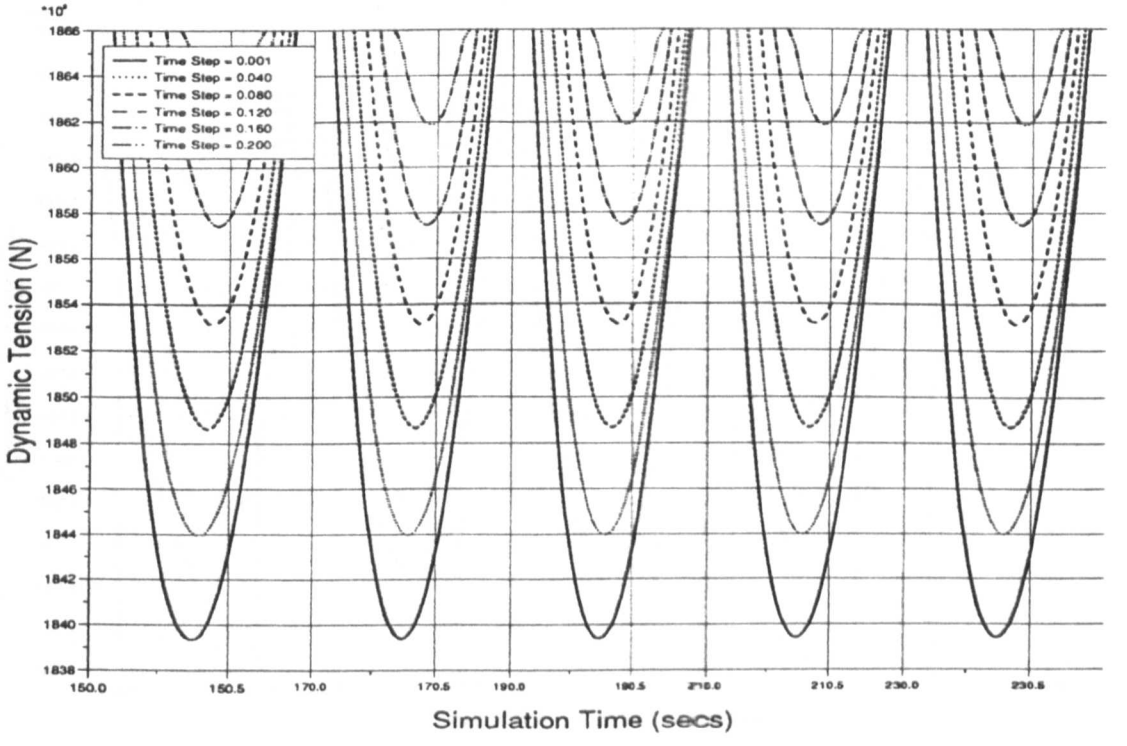

Figure 6.26 — Central Difference Scheme Tension Troughs **For** $h = 10$.

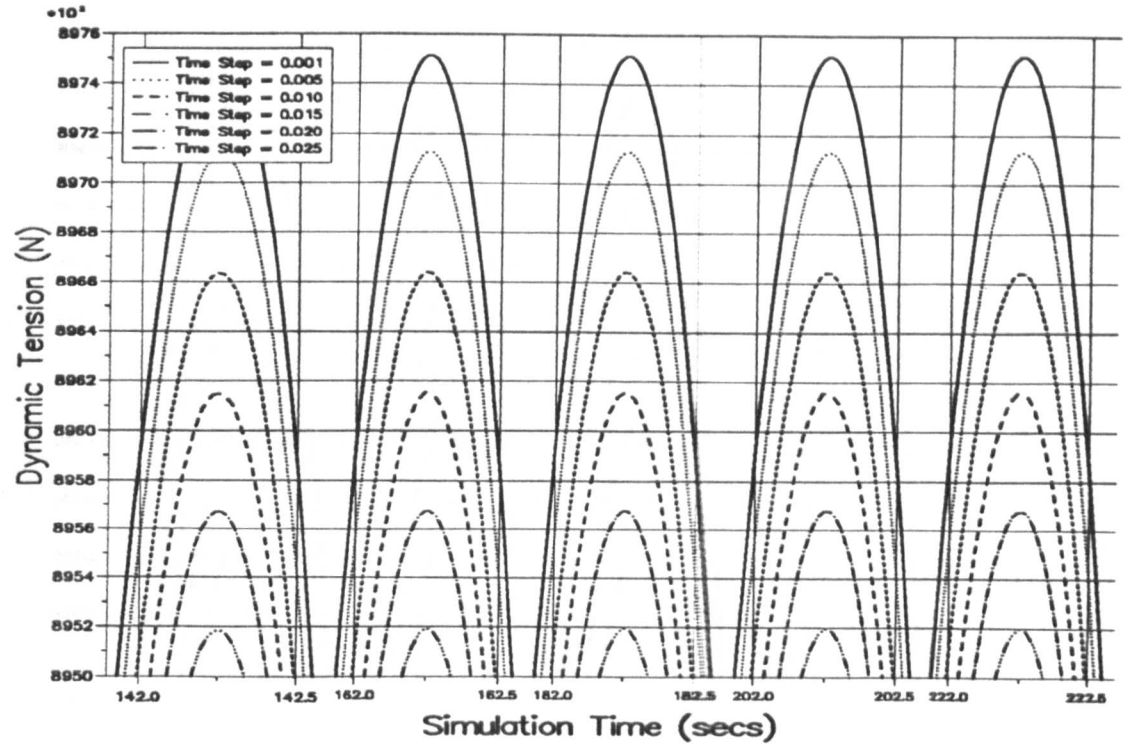

Figure 6.27 — Central Difference Scheme Tension Peaks For $h = 15$.

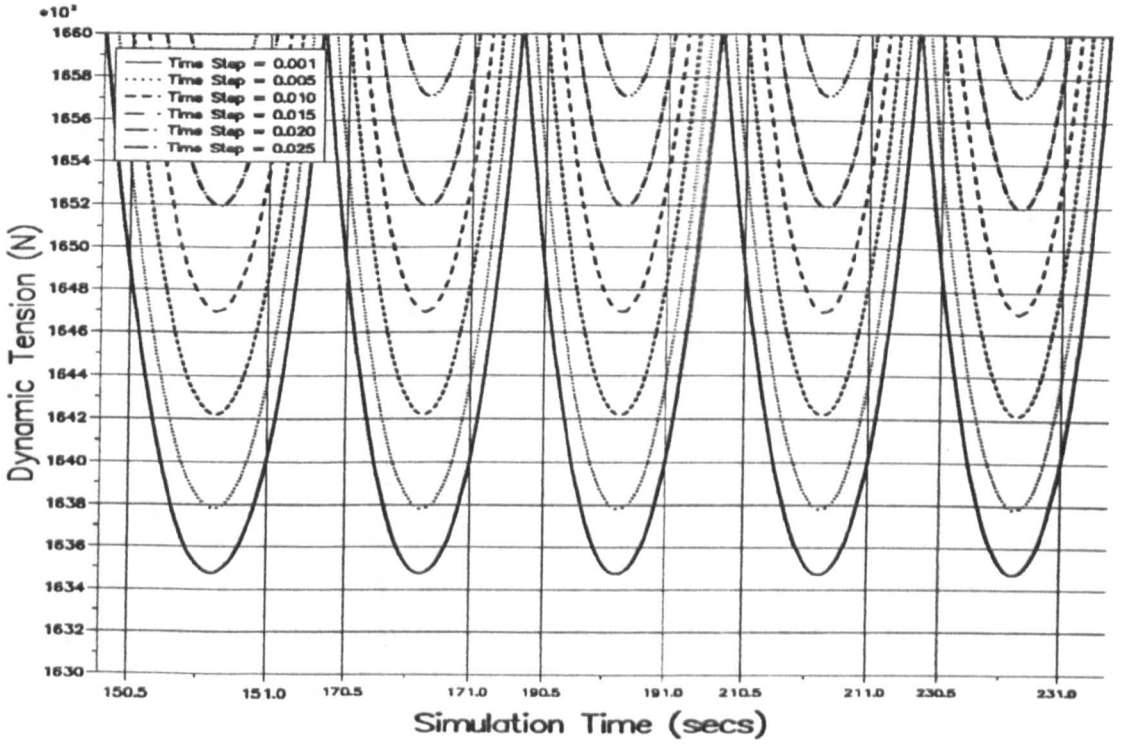

Figure 6.28 — Central Difference Scheme Tension Troughs For $h = 15$.

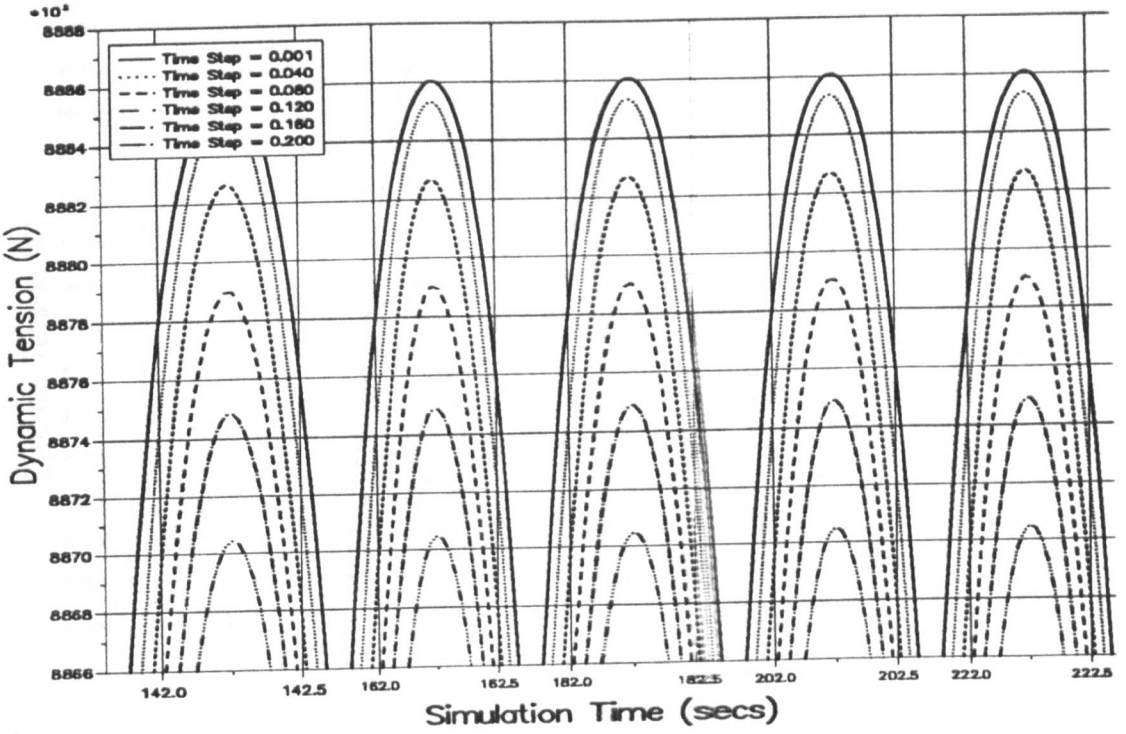

Figure 6.29 — Central Difference Scheme Tension Peaks For $h = 20$.

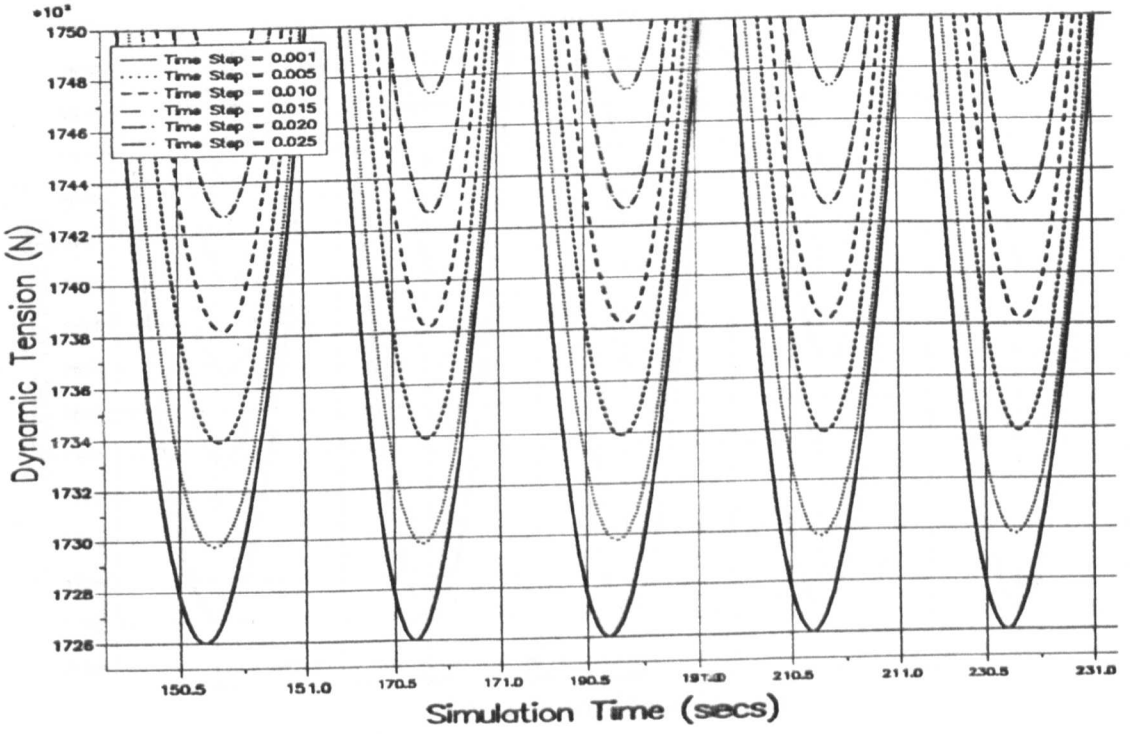

Figure 6.30 — Central Difference Scheme Tension Troughs For $h = 20$.

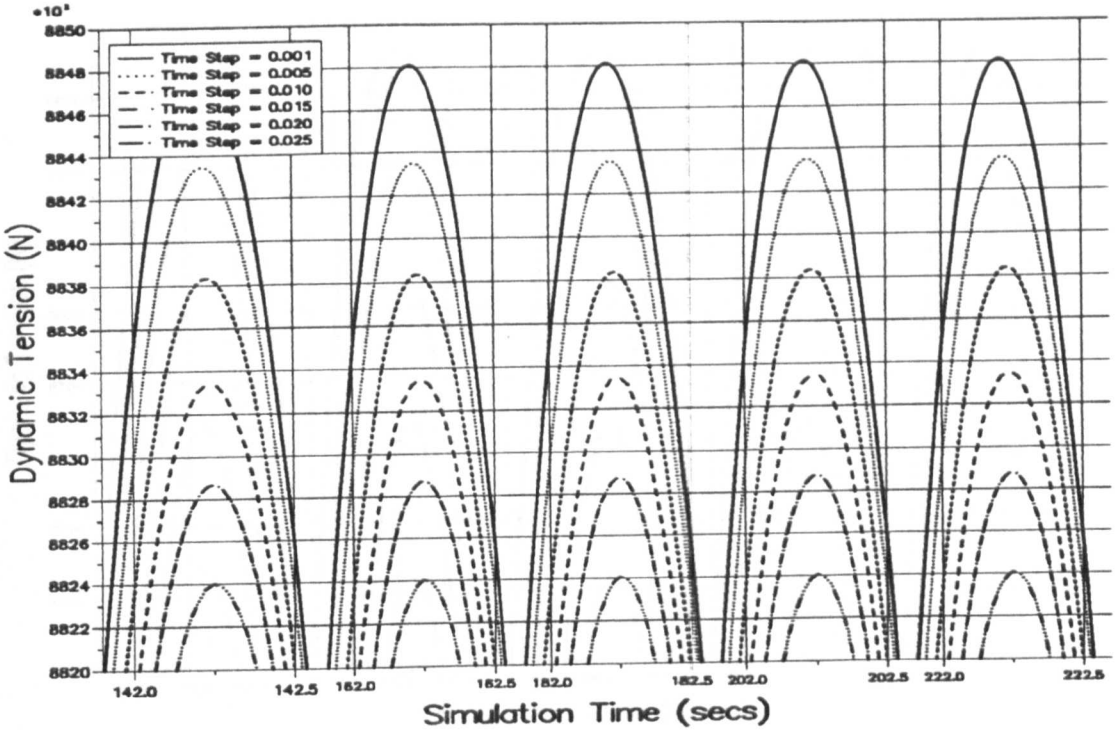

Figure 6.31 — Central Difference Scheme Tension Peaks For $h = 25$.

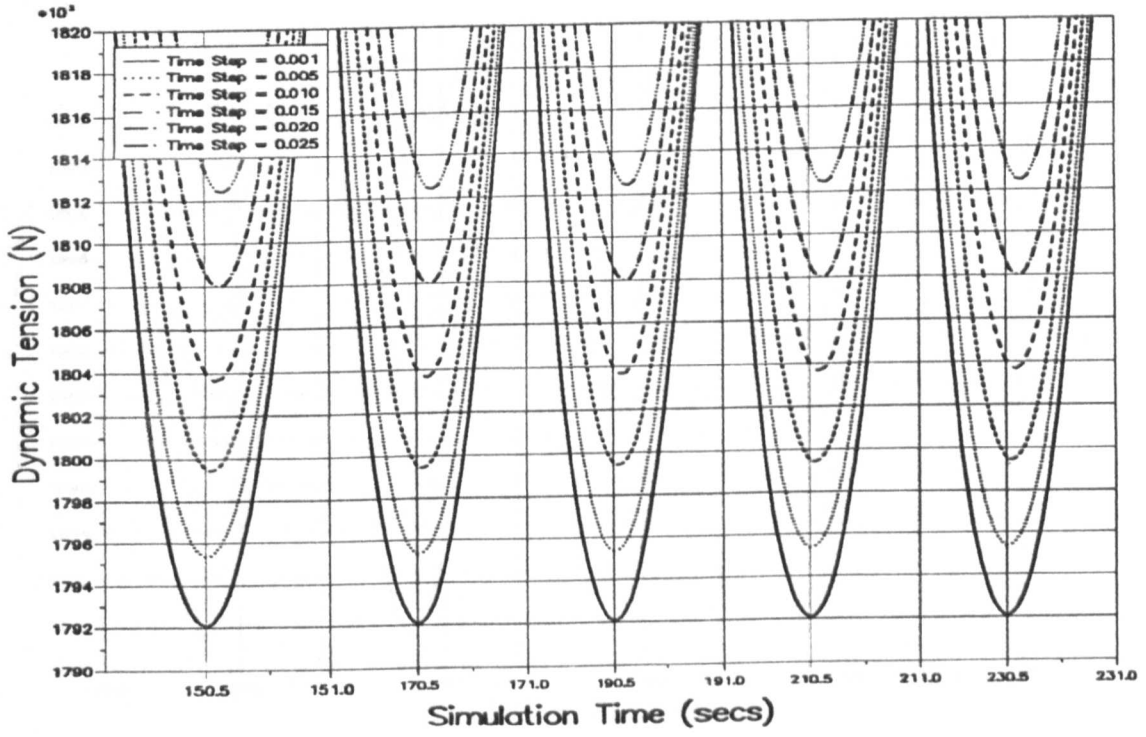

Figure 6.32 — Central Difference Scheme Tension Troughs For $h = 25$.

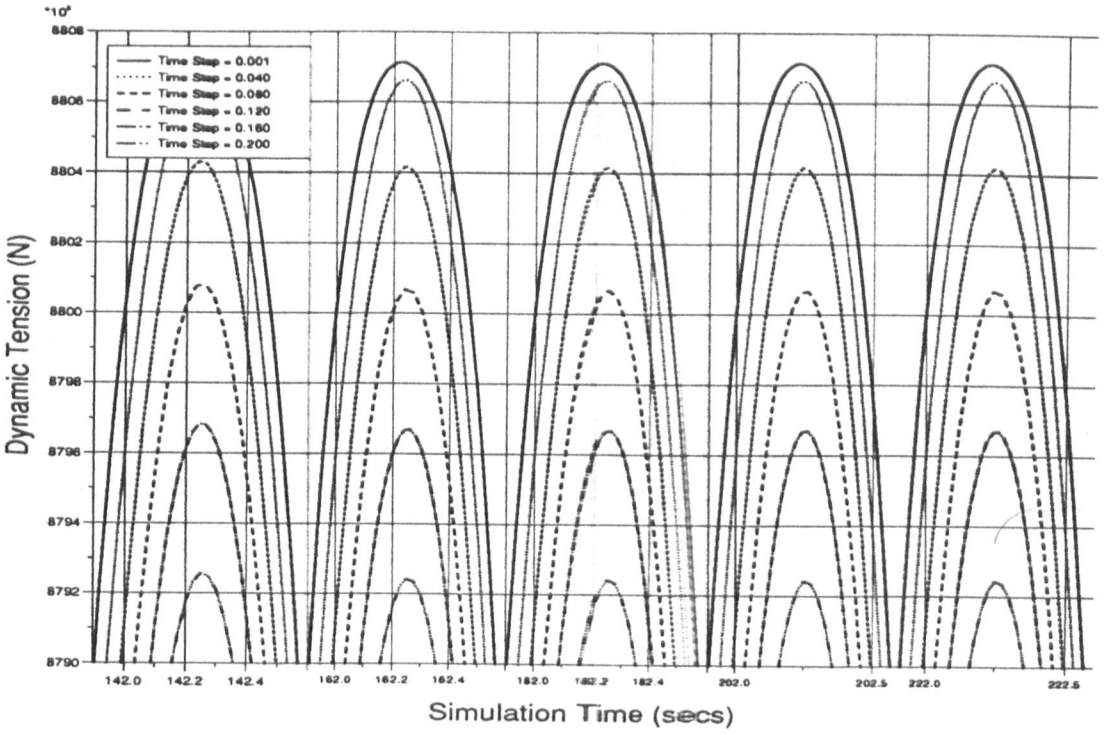

Figure 6.33 — Central Difference Scheme Tension Peaks For $h = 30$.

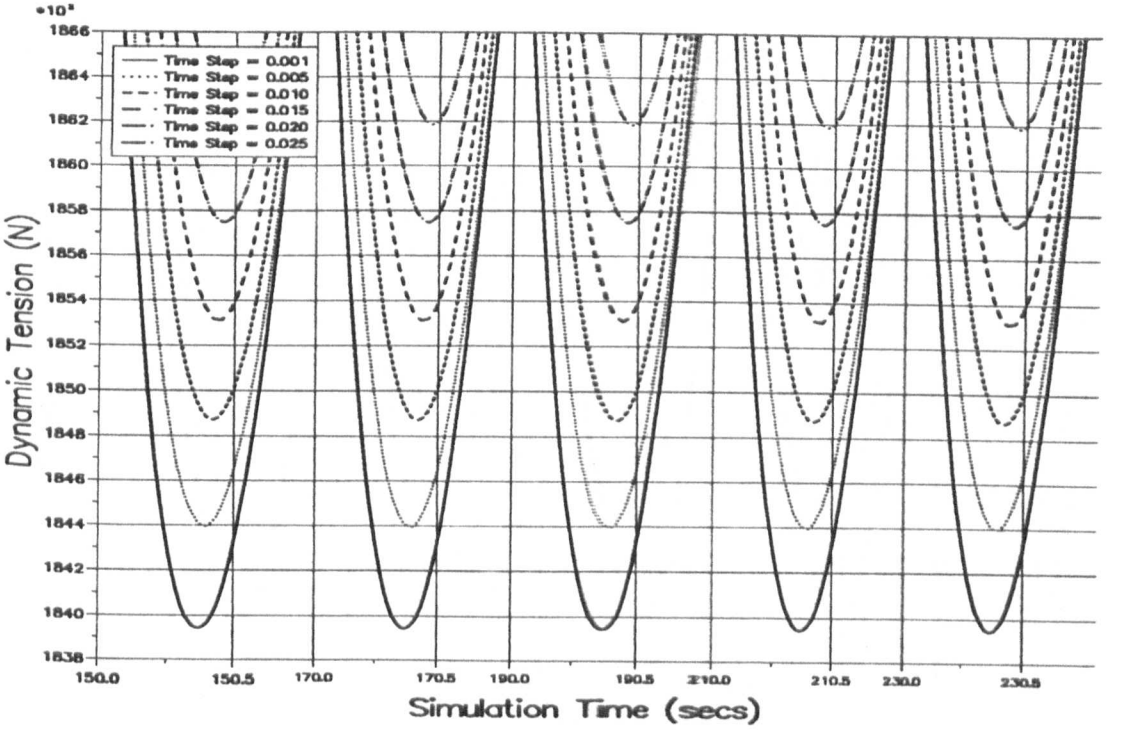

Figure 6.34 — Central Difference Scheme Tension Troughs For $h = 30$.

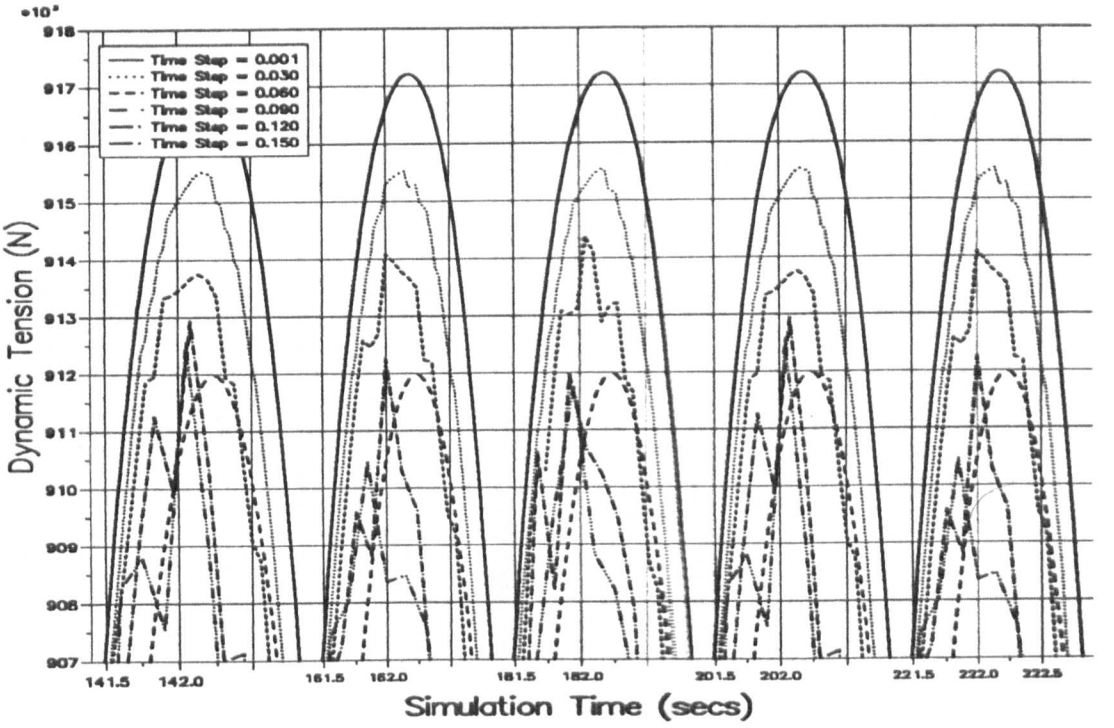

Figure 6.35 — Wilson Scheme Tension Peaks For $h = 10$.

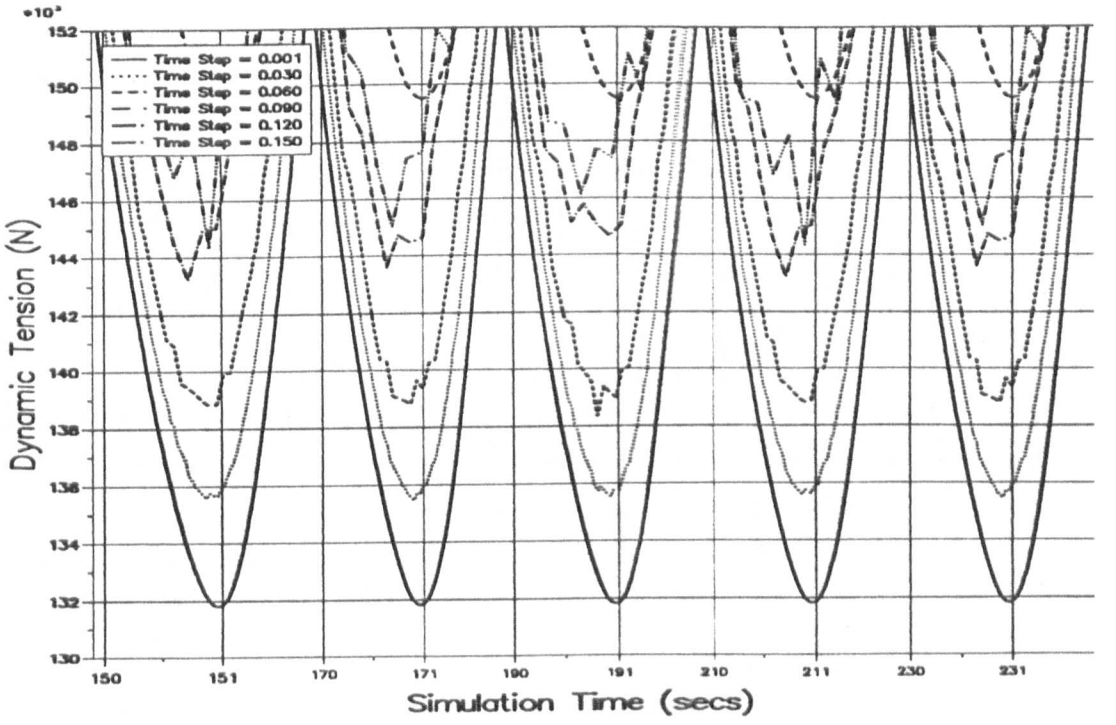

Figure 6.36 — Wilson Scheme Tension Troughs For $h = 10$.

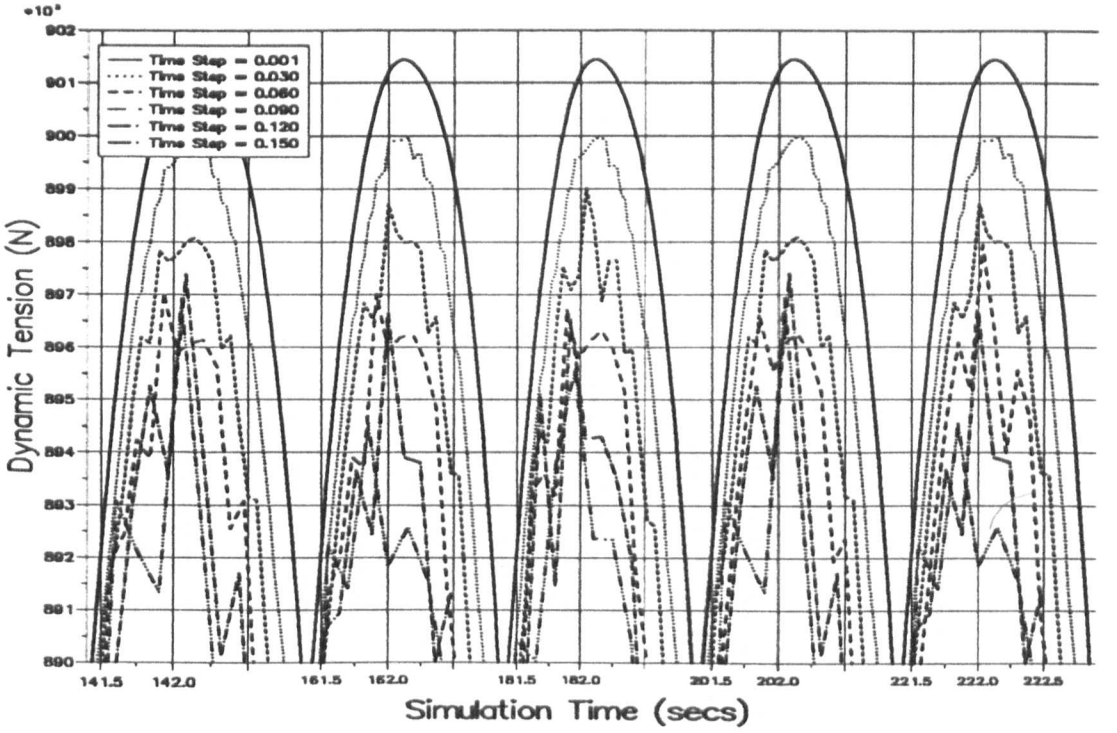

Figure 6.37 — Wilson Scheme Tension Peaks For $h = 15$.

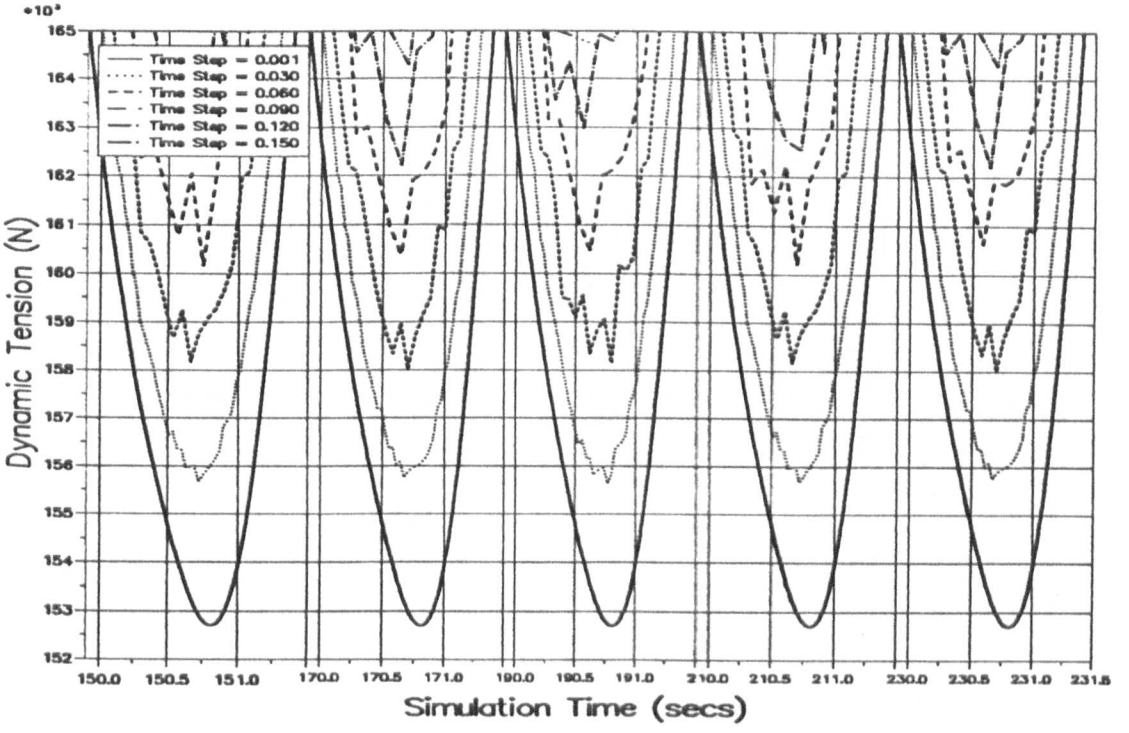

Figure 6.38 — Wilson Scheme Tension Troughs For $h = 15$.

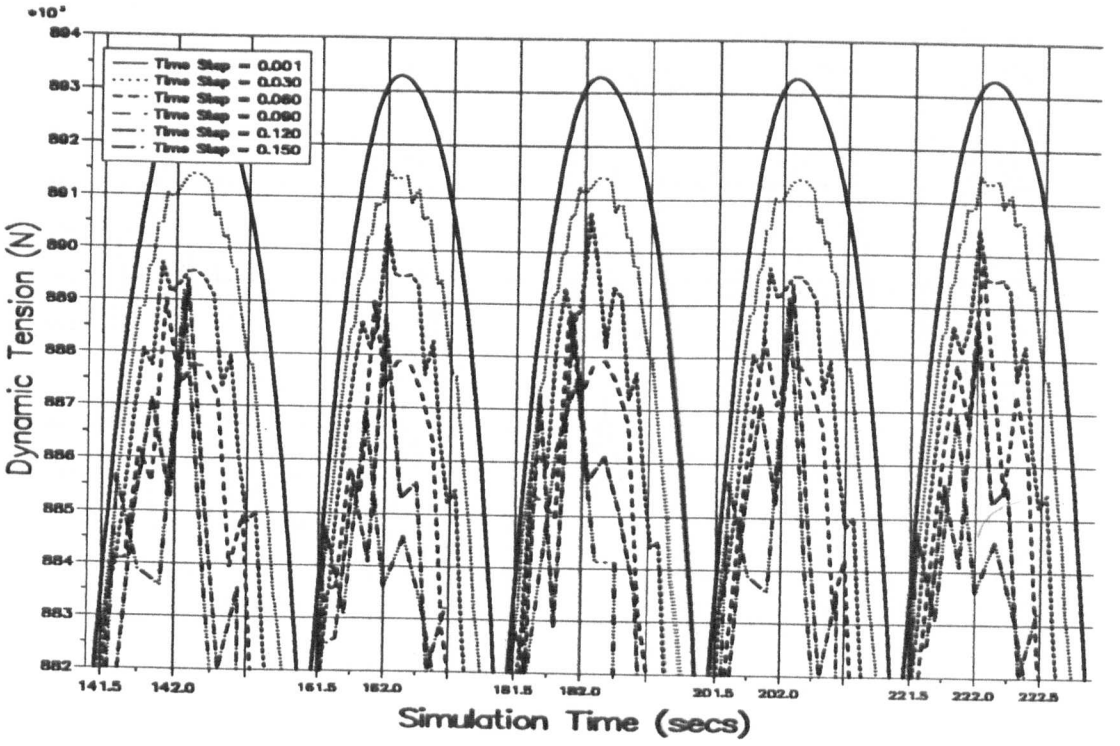

Figure 6.39 — Wilson Scheme Tension Peaks For $h = 20$.

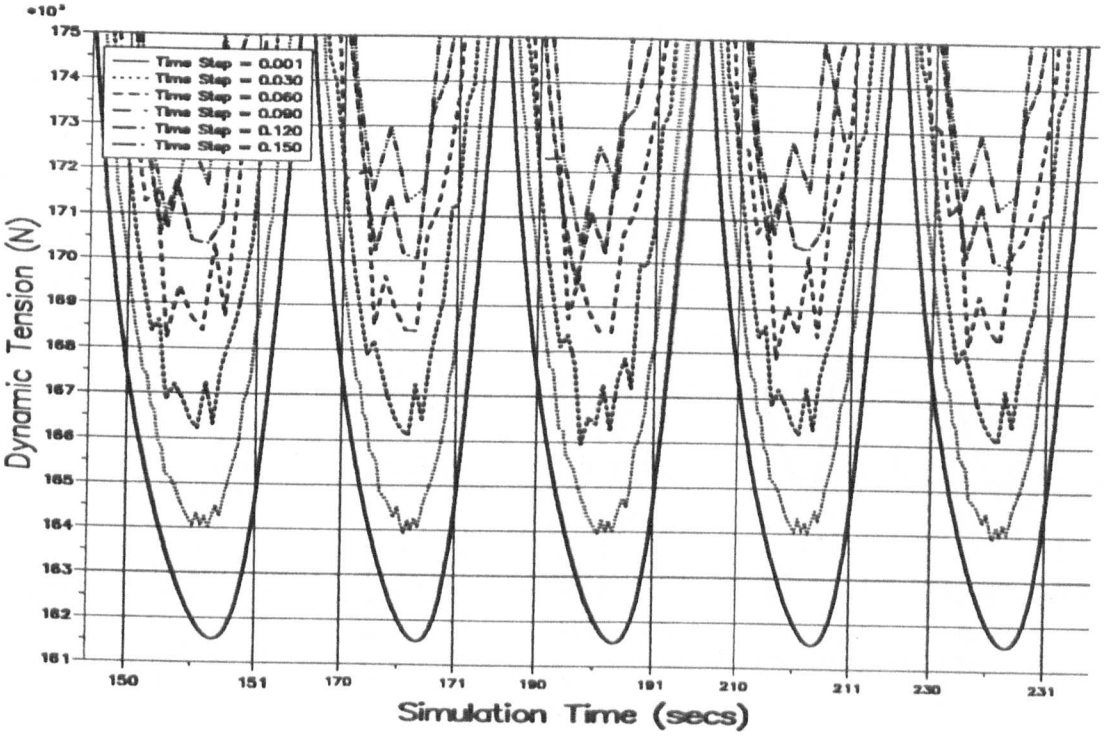

Figure 6.40 — Wilson Scheme Tension Troughs For $h = 20$.

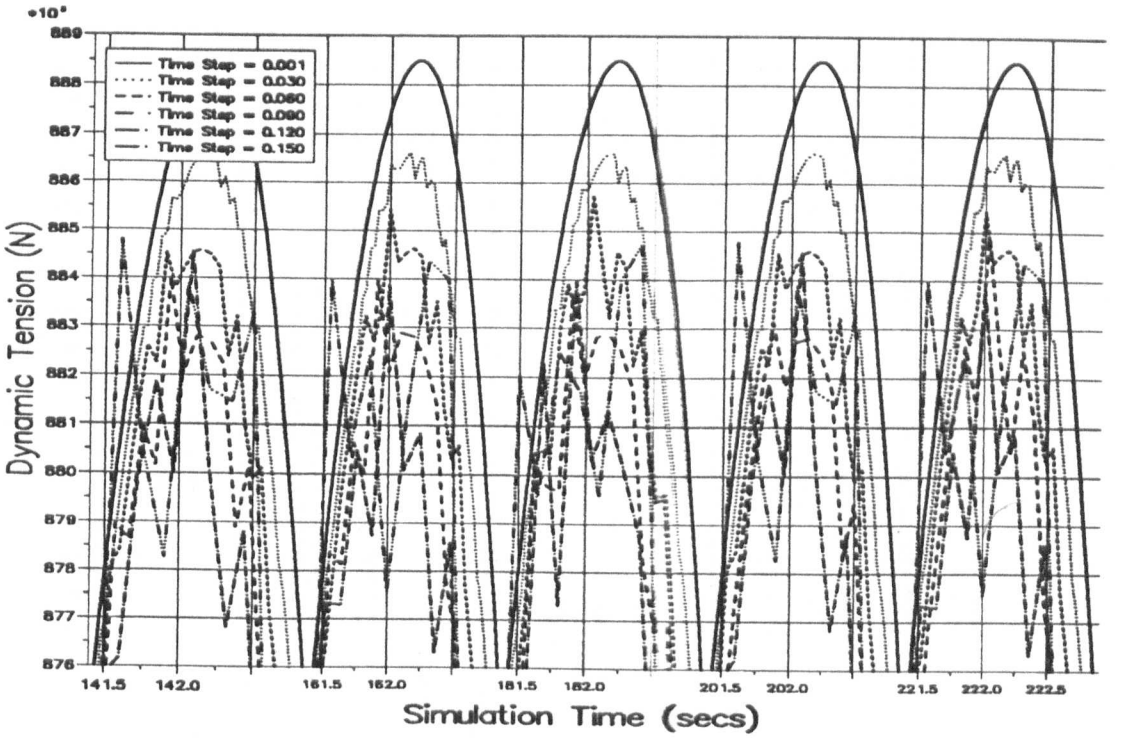

Figure 6.41 — Wilson Scheme Tension Peaks For $h = 25$.

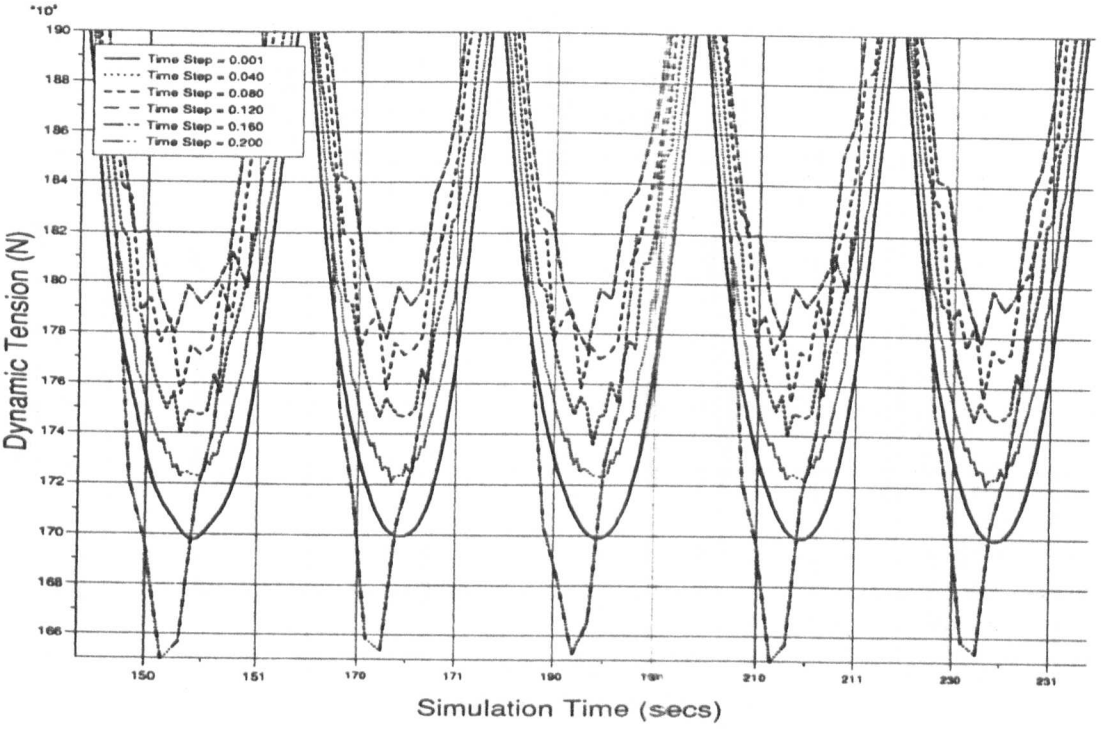

Figure 6.42 — Wilson Scheme Tension Troughs For $h = 25$.

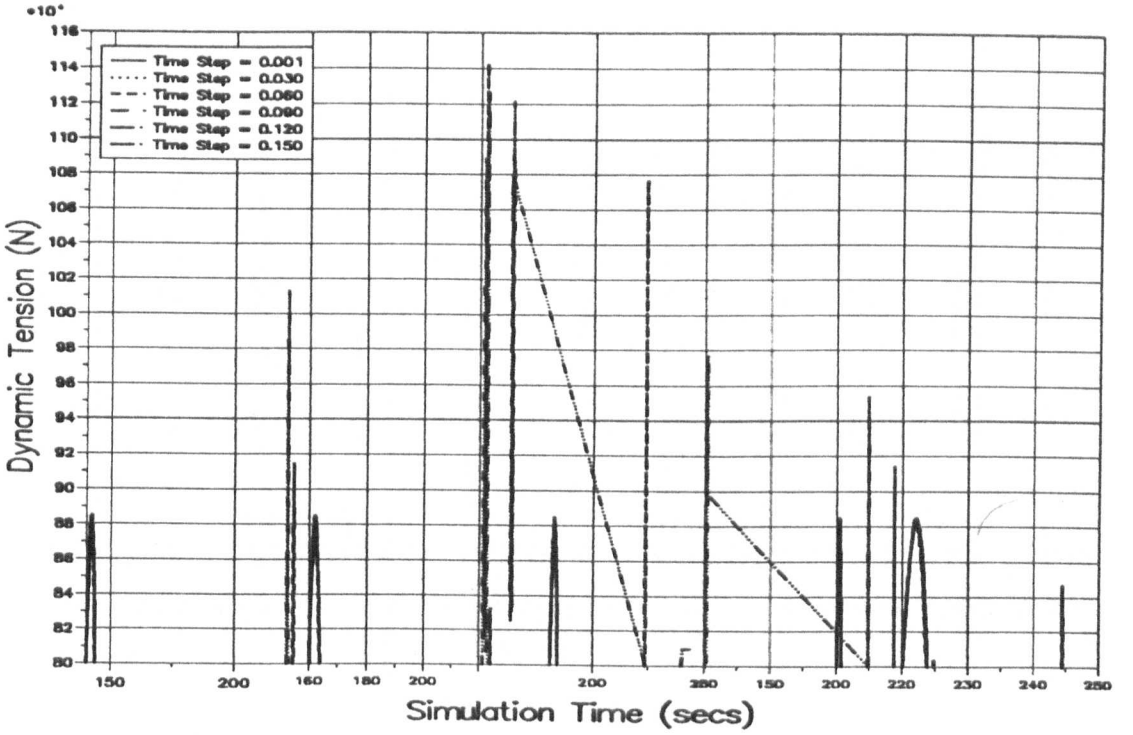

Figure 6.43 — Wilson Scheme Tension Peaks For $h = 30$.

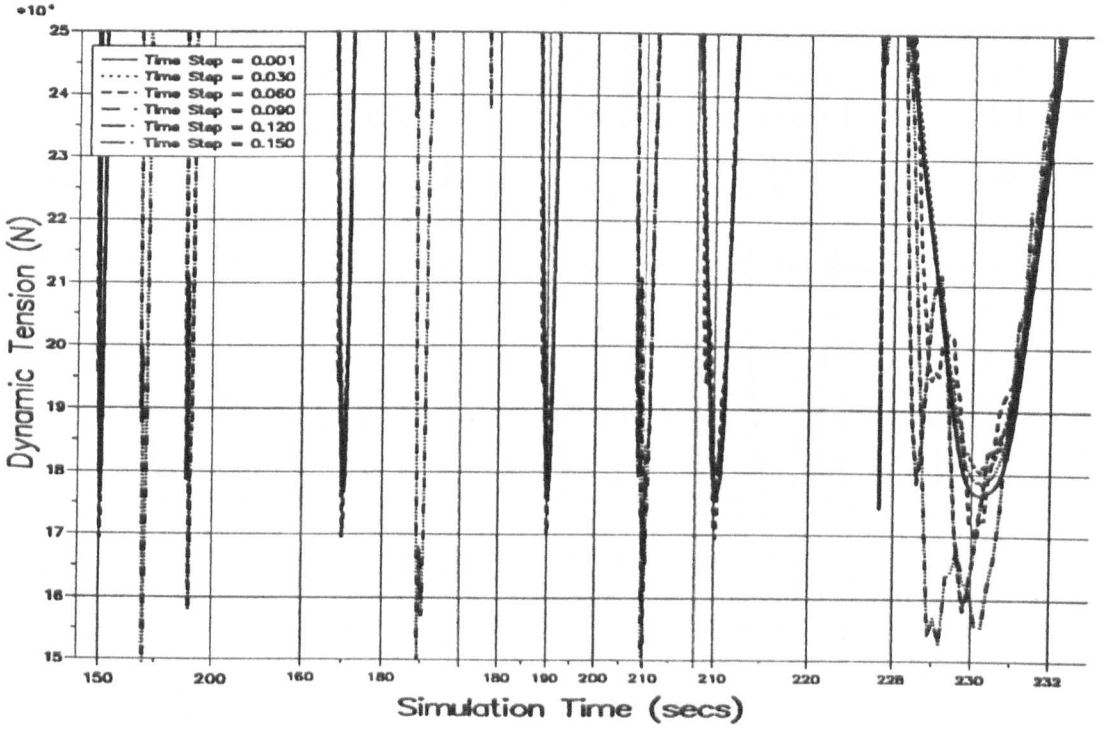

Figure 6.44 — Wilson Scheme Tension Troughs For $h = 30$.

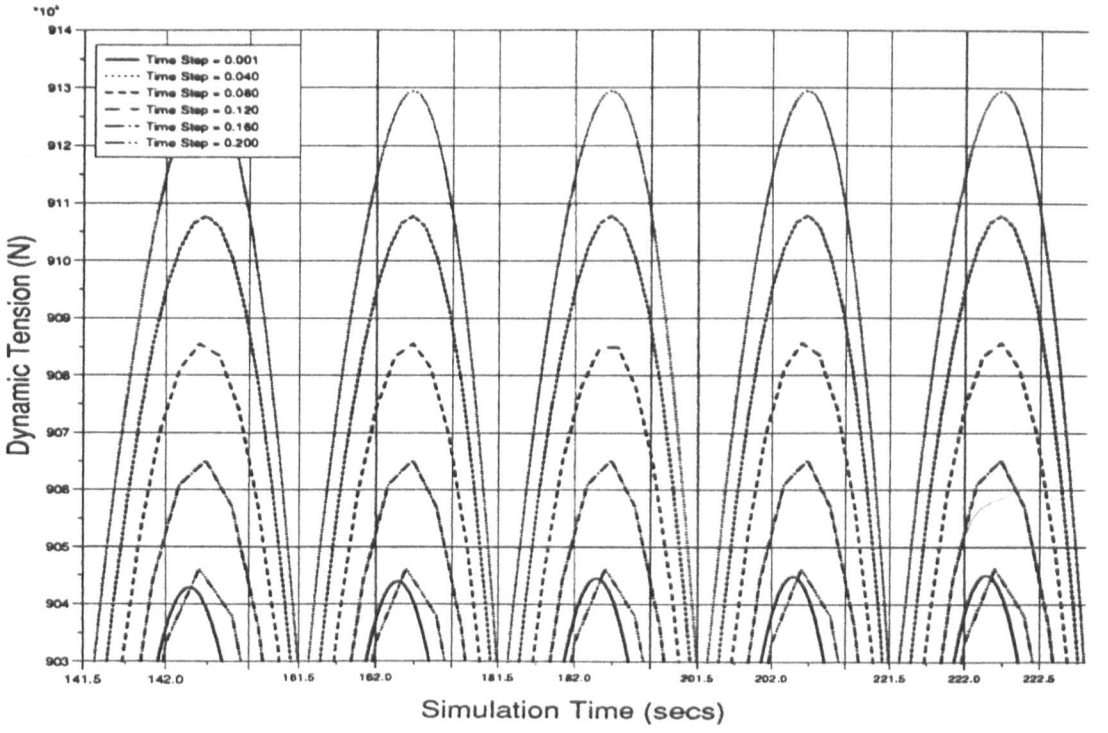

Figure 6.45 — Newmark Scheme Tension Peaks For $h = 10$.

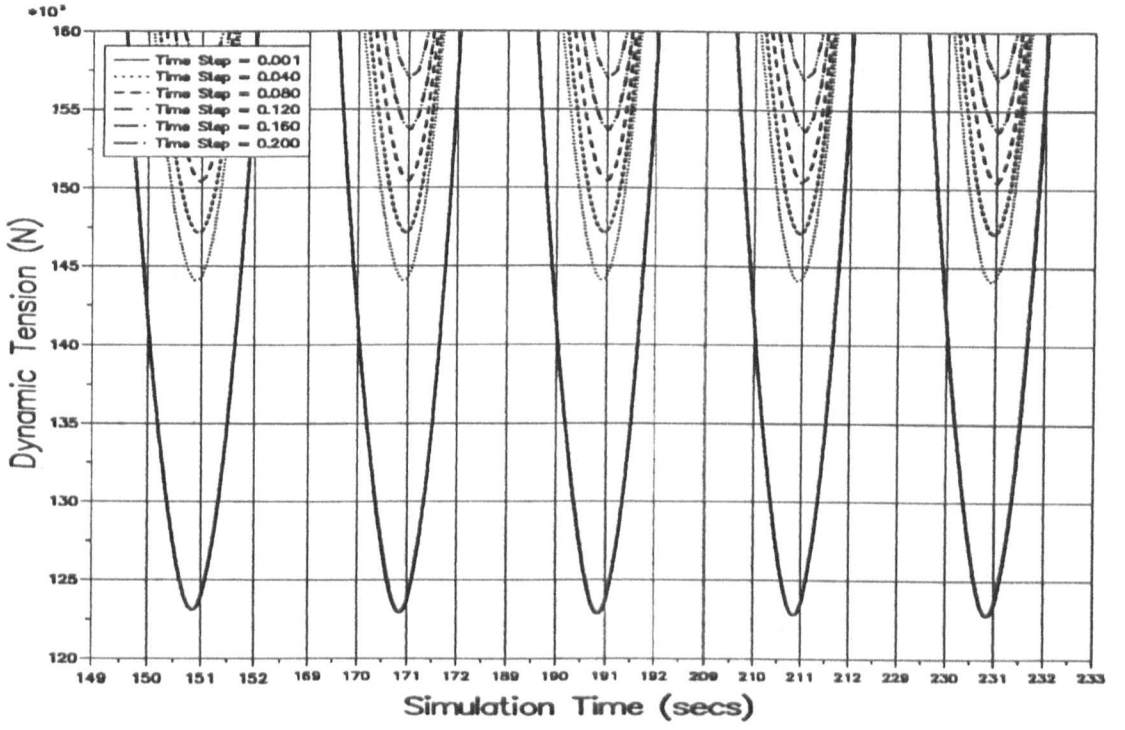

Figure 6.46 — Newmark Scheme Tension Troughs For $h = 10$.

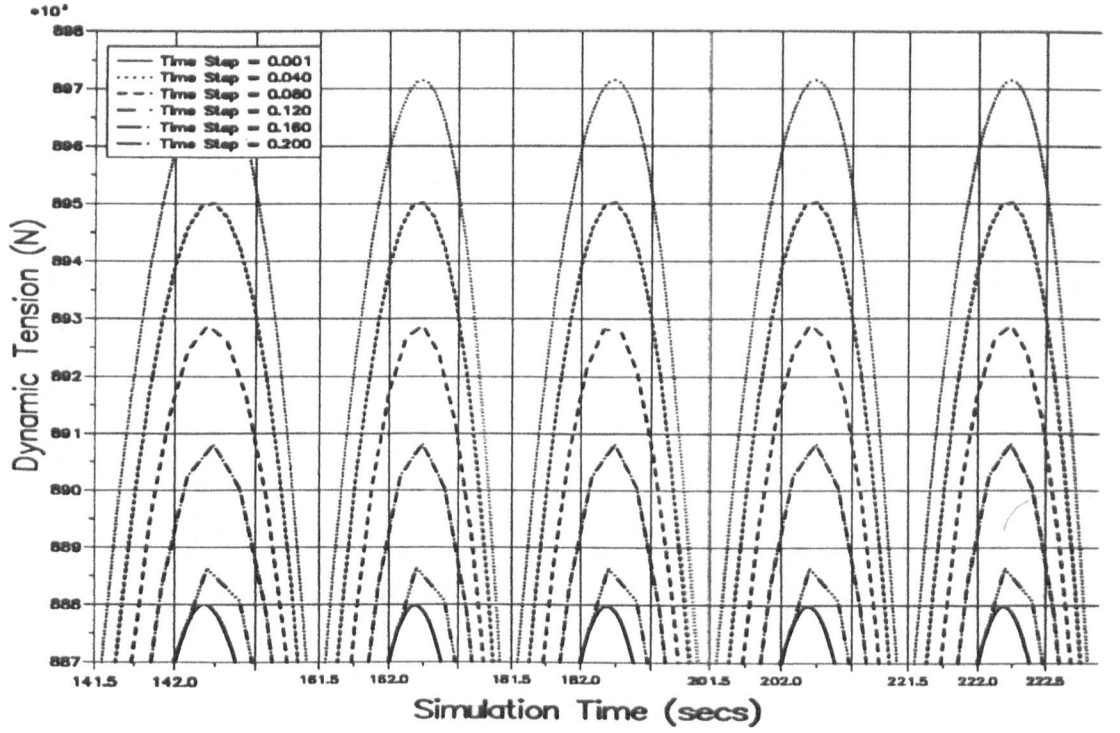

Figure 6.47 — Newmark Scheme Tension Peaks For $h = 15$.

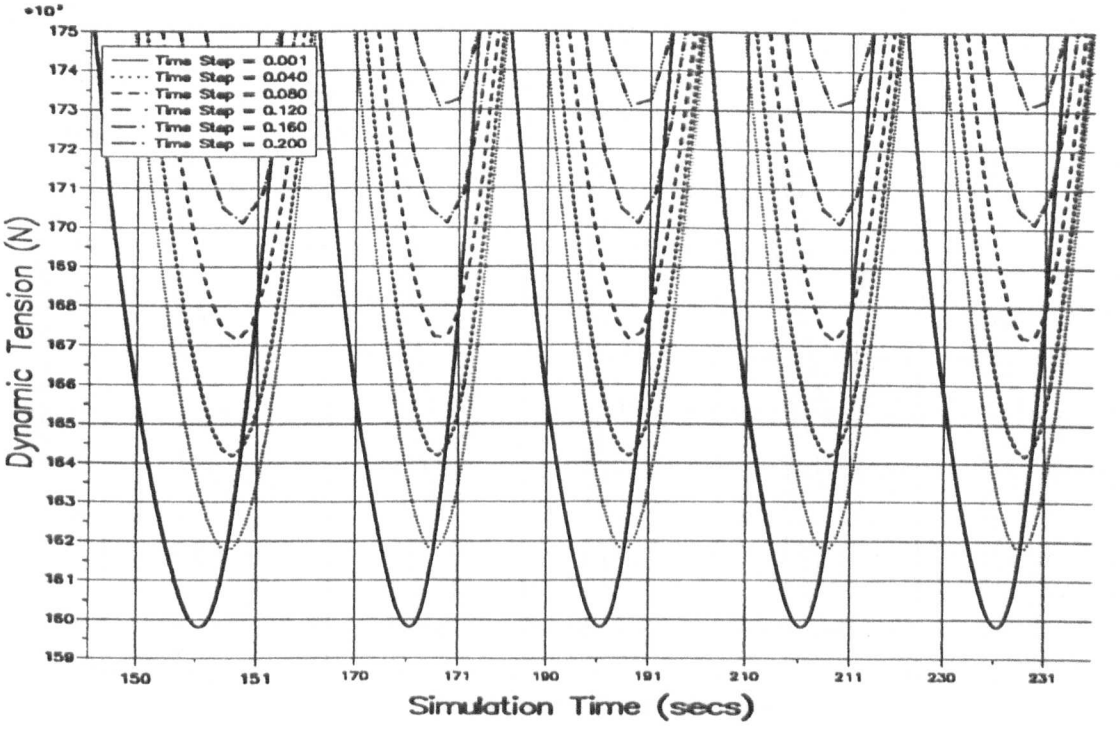

Figure 6.48 — Newmark Scheme Tension Troughs For $h = 15$.

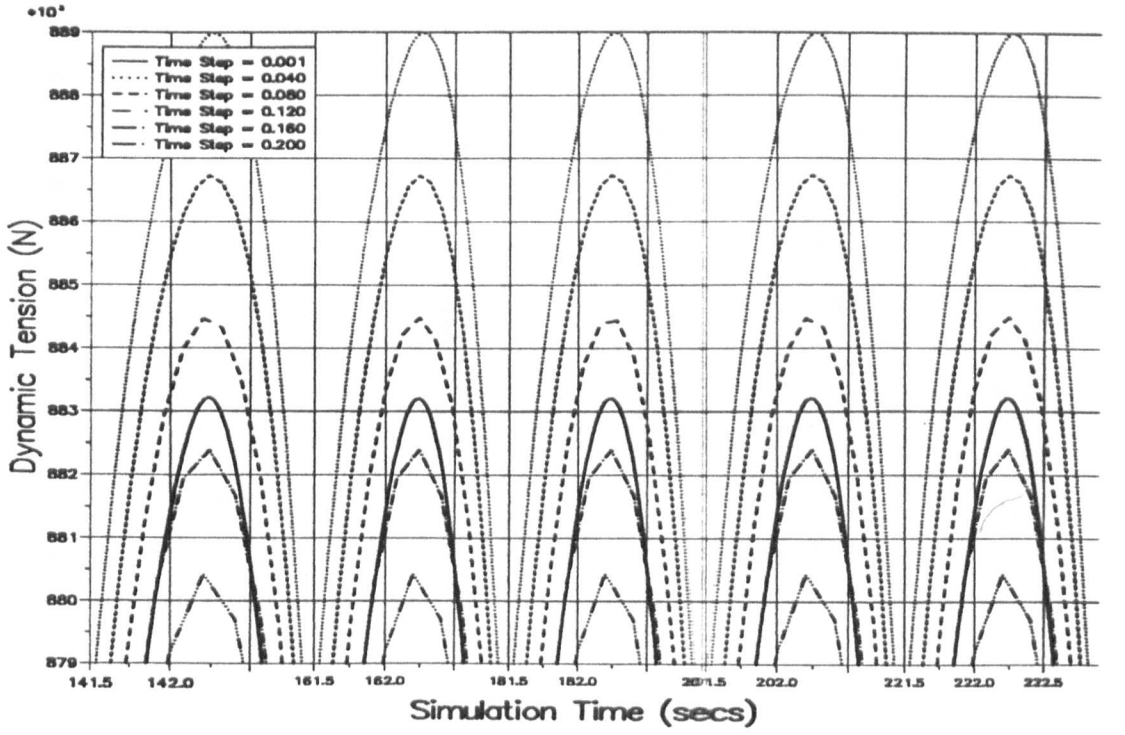

Figure 6.49 — Newmark Scheme Tension Peaks For $h = 20$.

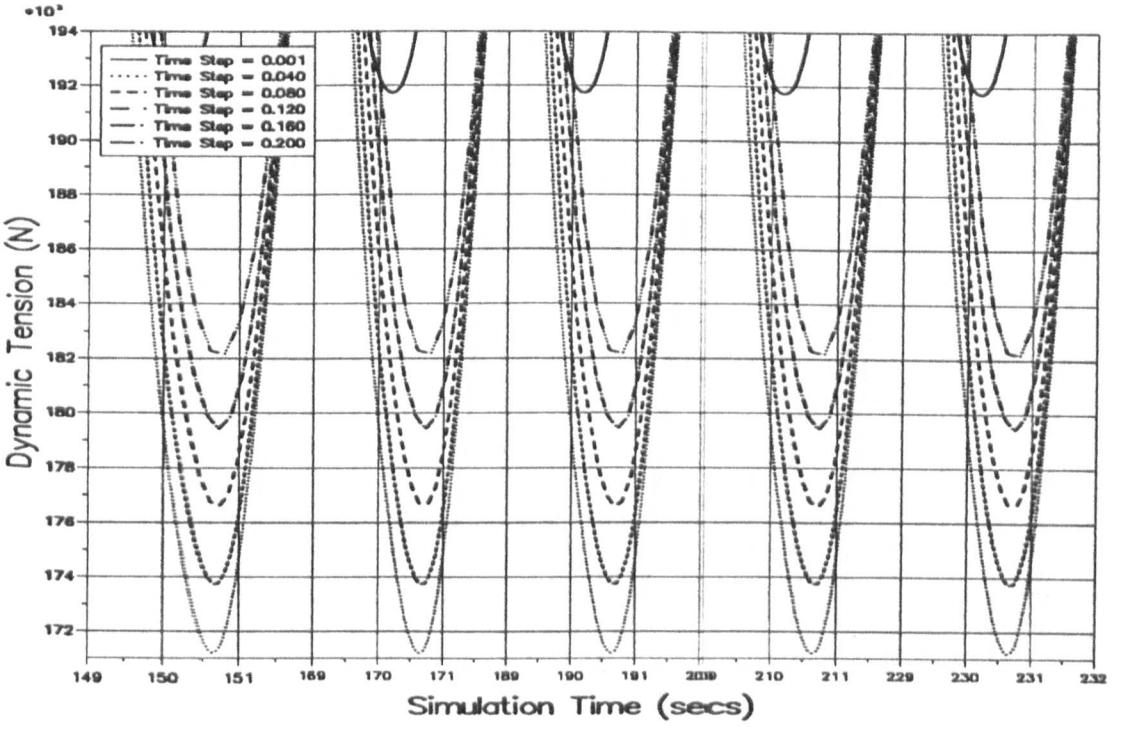

Figure 6.50 — Newmark Scheme Tension Troughs For $h = 20$.

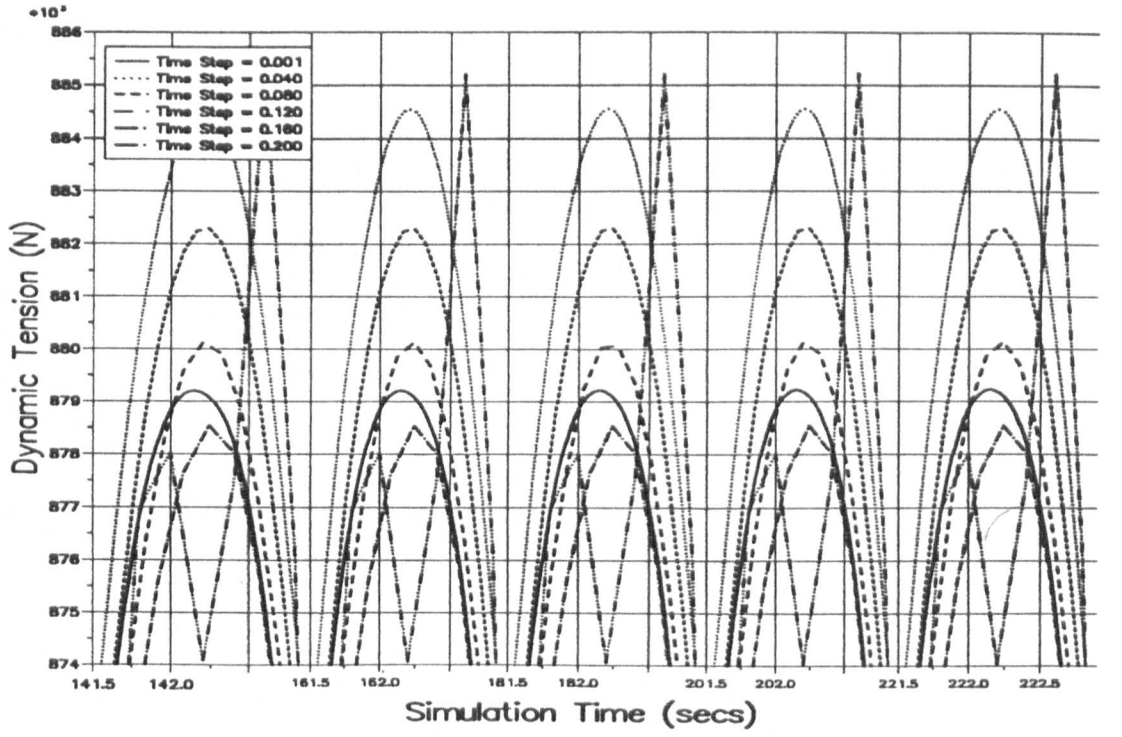

Figure 6.51 — Newmark Scheme Tension Peaks For $h = 25$.

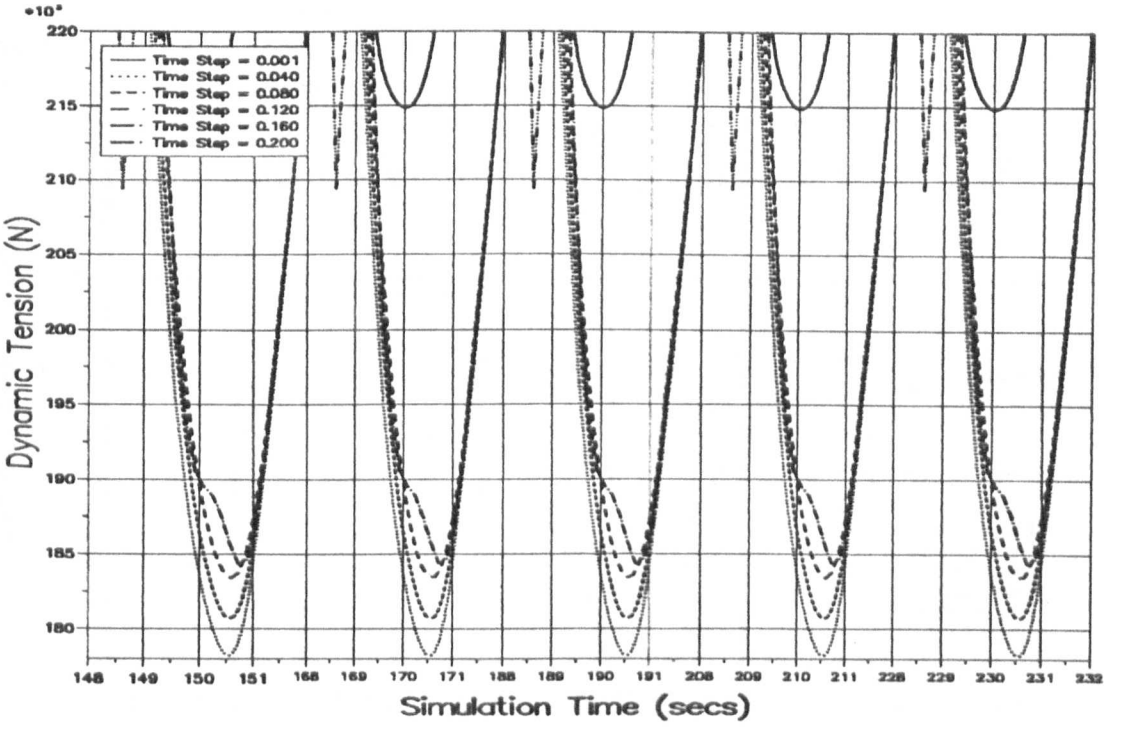

Figure 6.52 — Newmark Scheme Tension Troughs For $h = 25$.

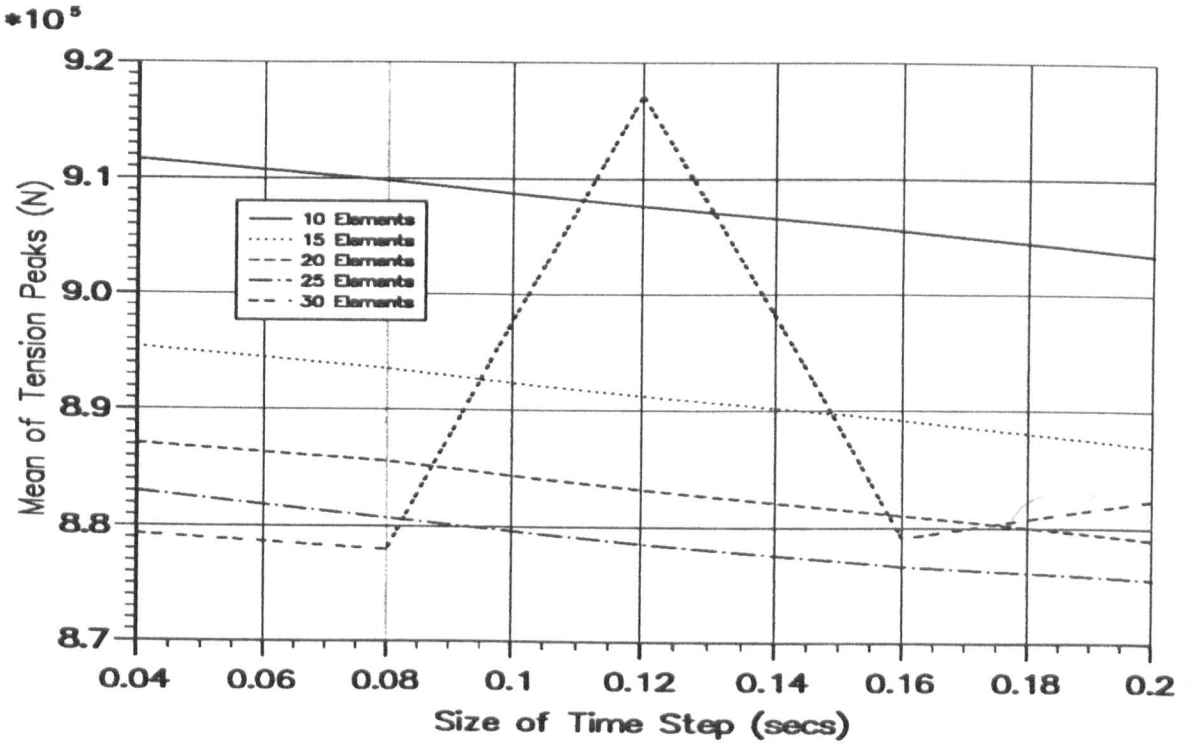

Figure 6.53 — Mean of Tension Peaks Vs. Δt for Houbolt Scheme.

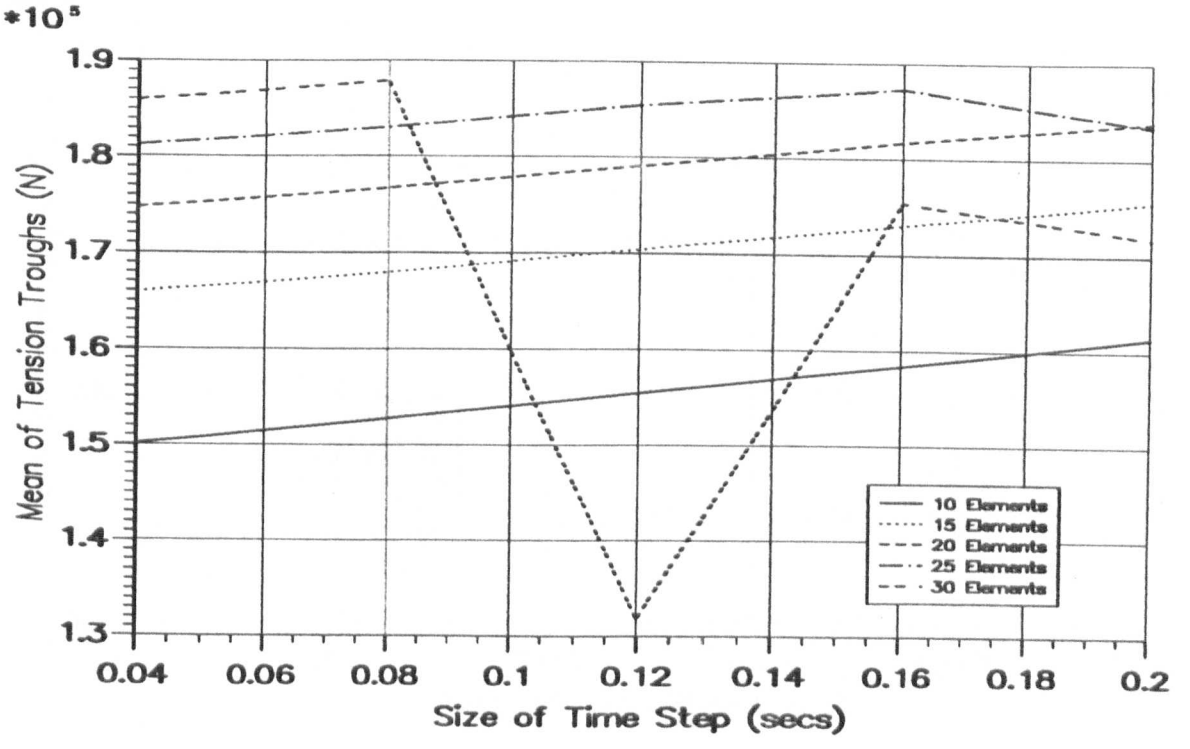

Figure 6.54 — Mean of Tension Troughs Vs. Δt for Houbolt Scheme.

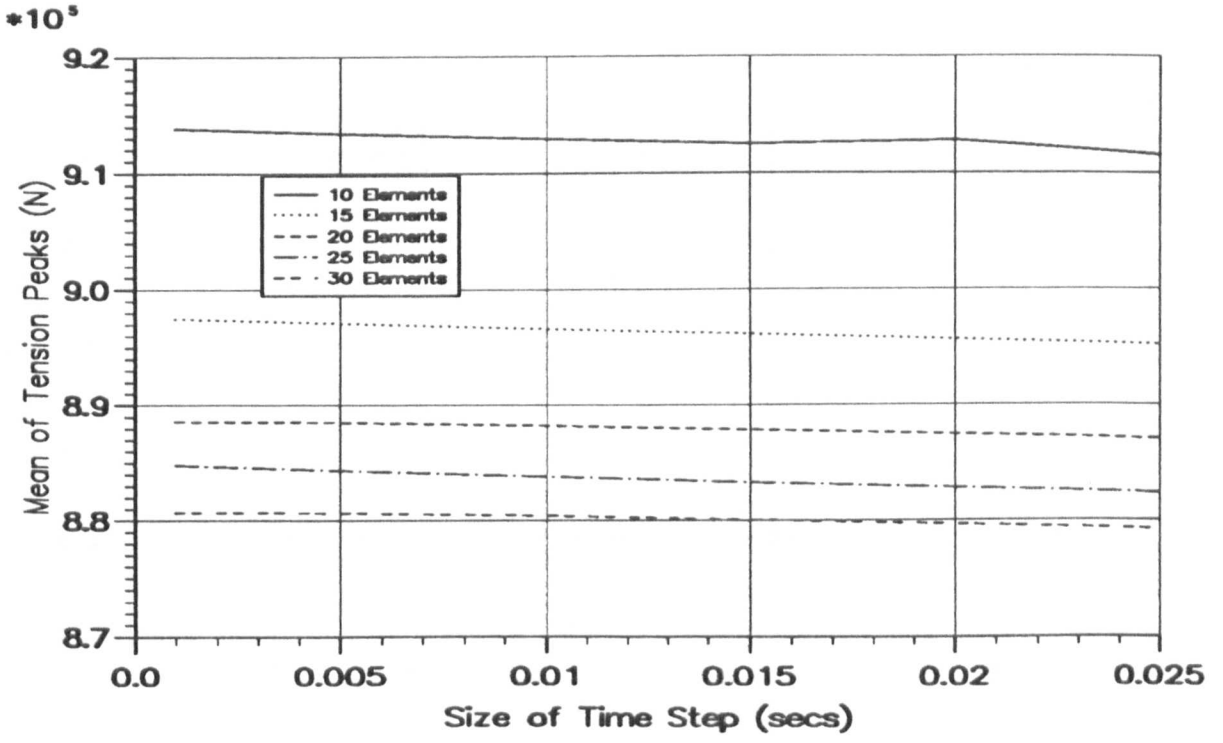

Figure 6.55 — Mean of Tension Peaks Vs. Δt for CD Scheme.

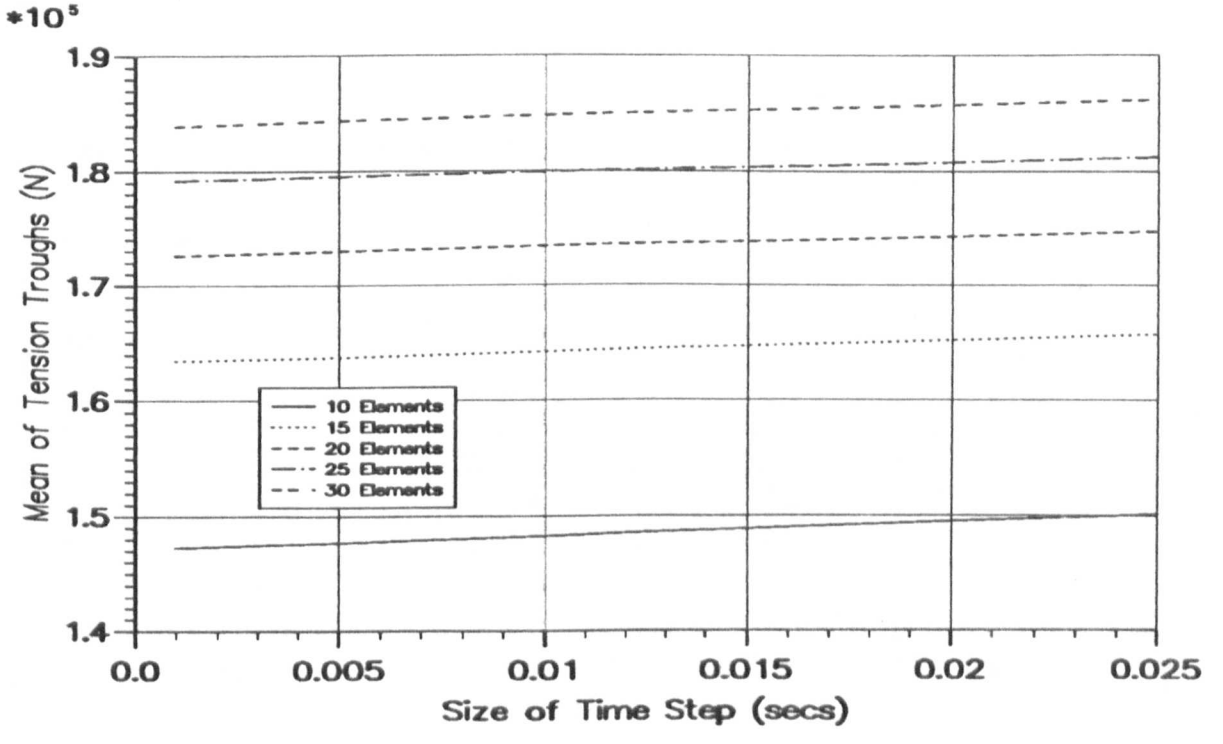

Figure 6.56 — Mean of Tension Troughs Vs. Δt for CD Scheme.

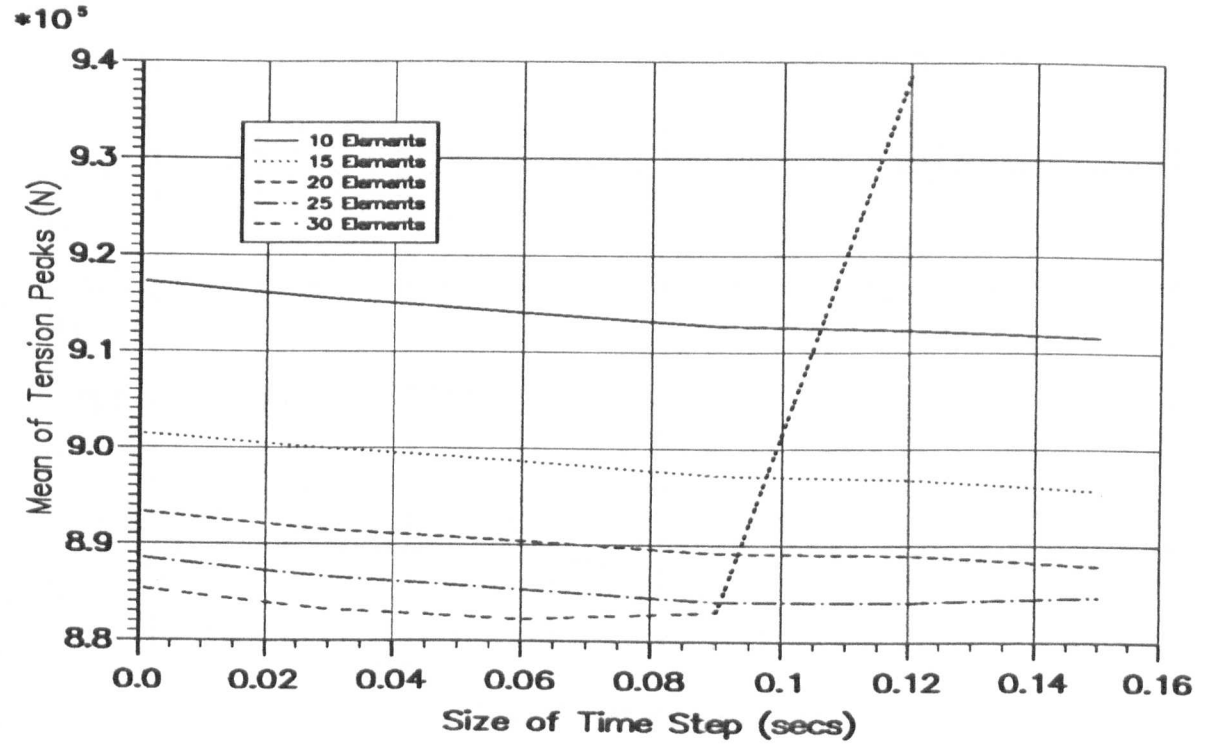

Figure 6.57 — Mean of Tension Peaks Vs. Δt for Wilson Scheme.

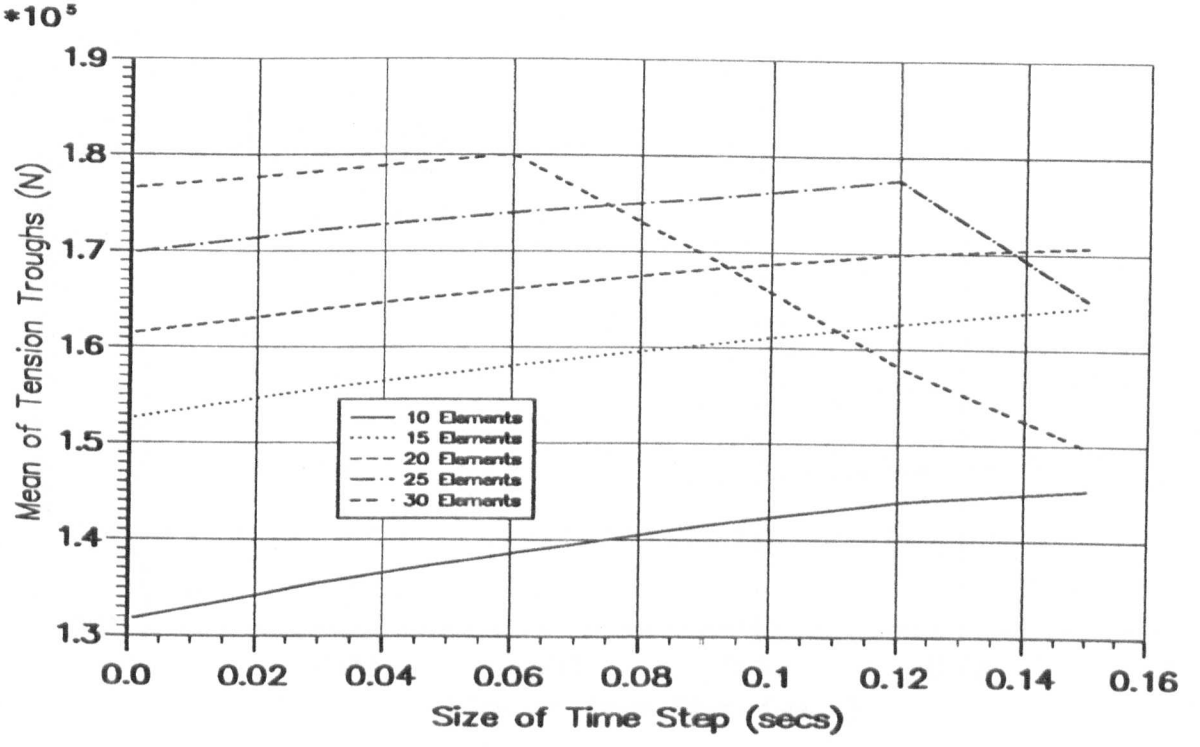

Figure 6.58 — Mean of Tension Troughs Vs. Δt for Wilson Scheme.

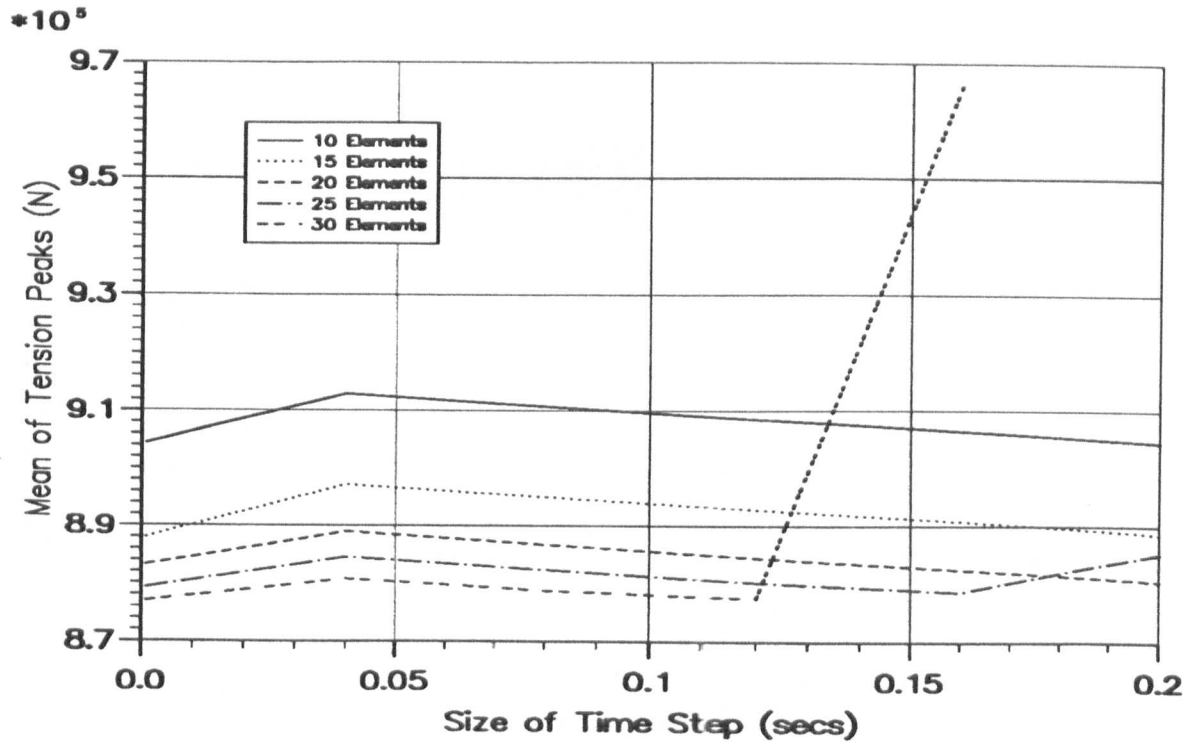

Figure 6.59 — Mean of Tension Peaks Vs. Δt for Newmark Scheme.

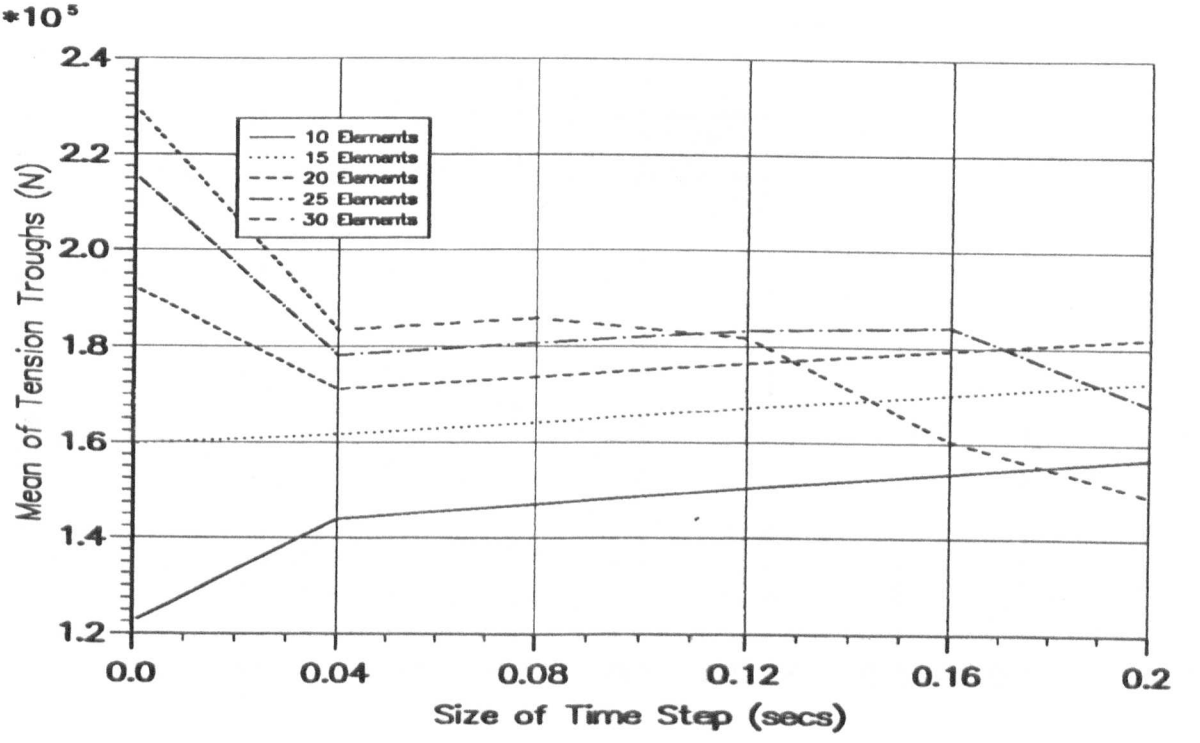

Figure 6.60 — Mean of Tension Troughs Vs. Δt for Newmark Scheme.

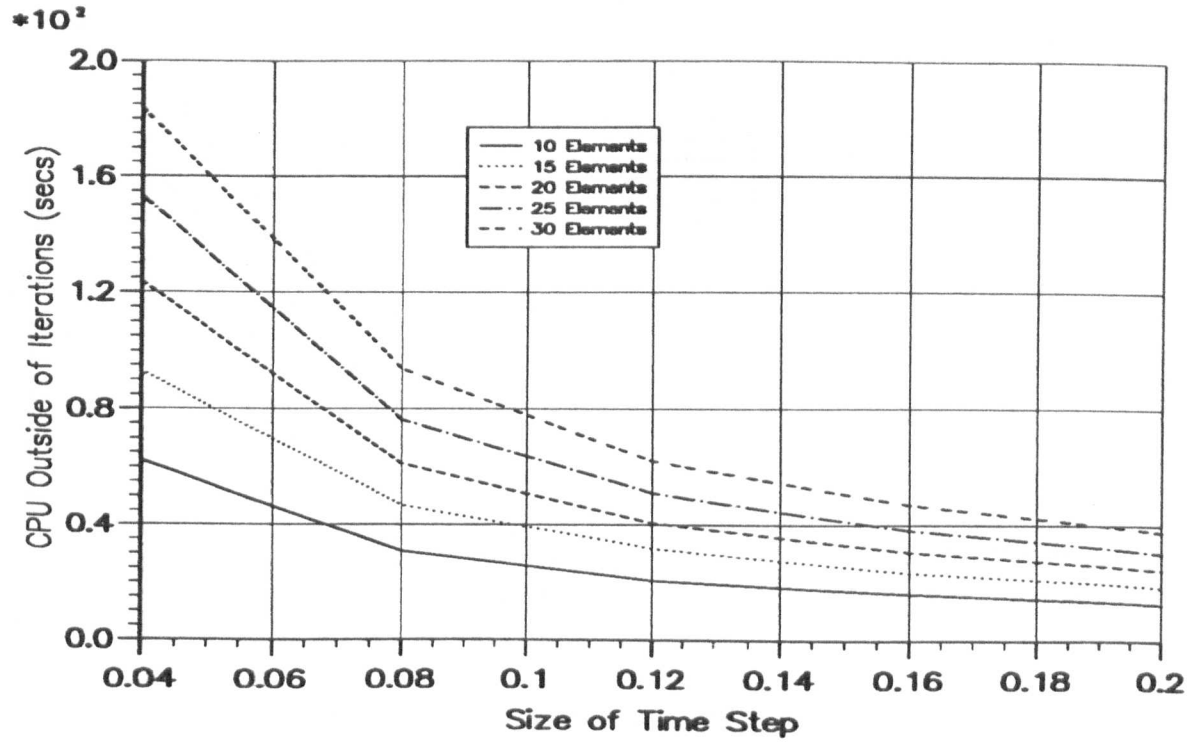

Figure 6.61 — CPU_1 Vs. Δt for Houbolt Scheme.

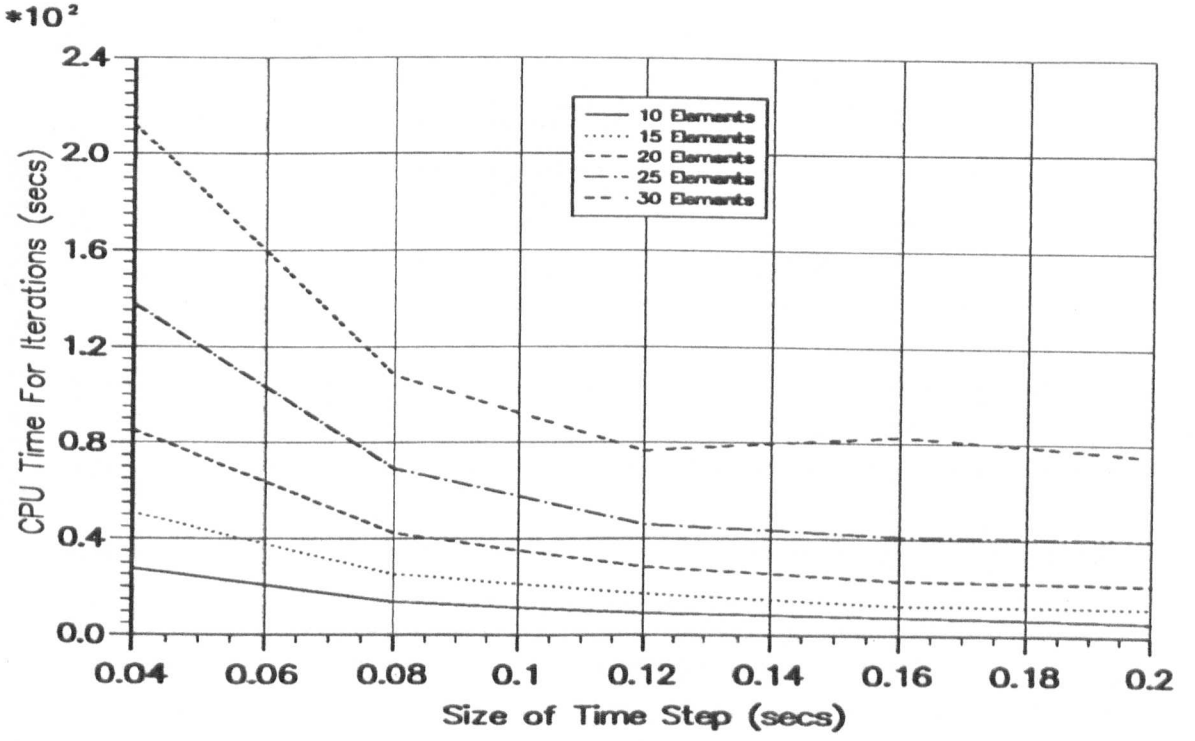

Figure 6.62 — CPU_2 Vs. Δt for Houbolt Scheme.

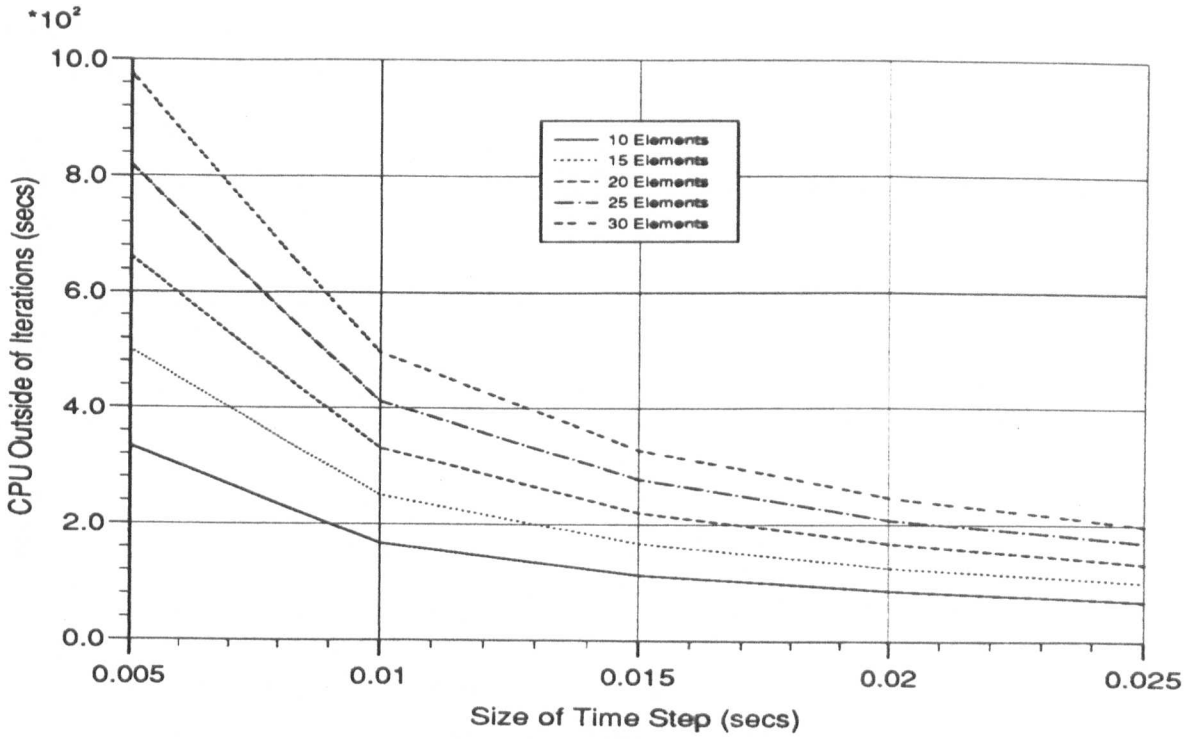

Figure 6.63 — CPU_1 Vs. Δt for CD Scheme.

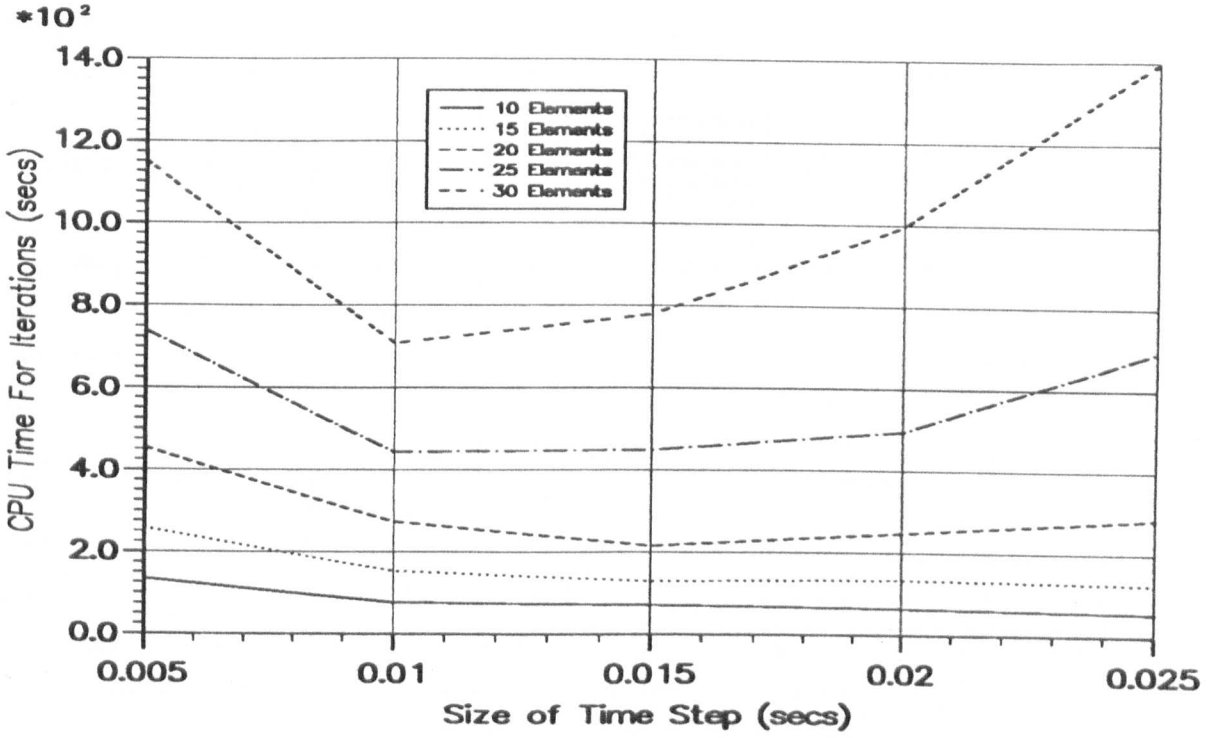

Figure 6.64 — CPU_2 Vs. Δt for CD Scheme.

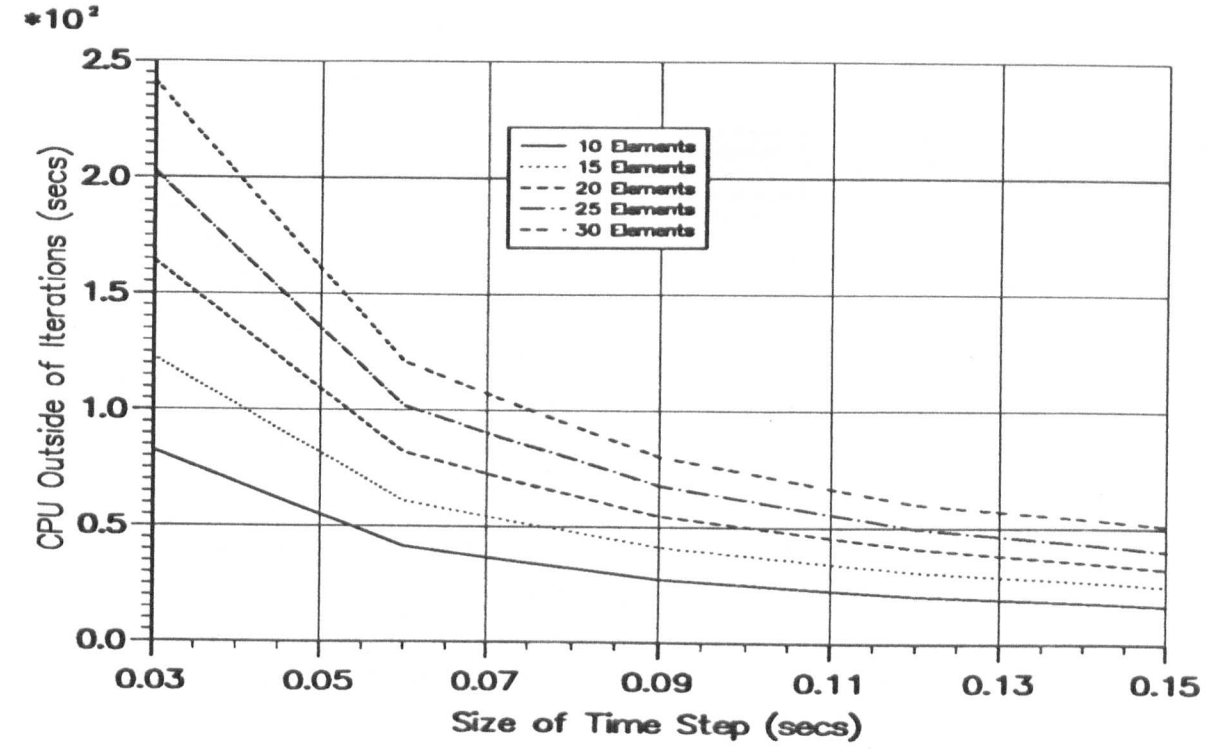

Figure 6.65 — CPU_1 Vs. Δt for Wilson Scheme.

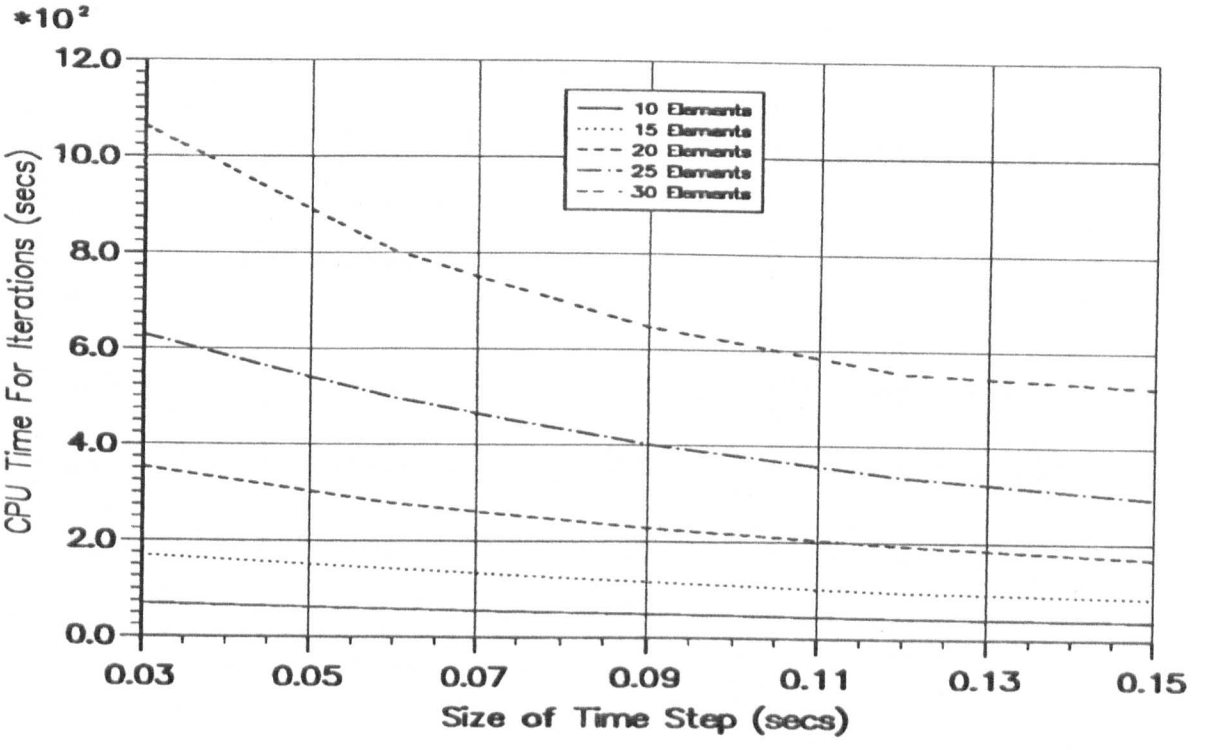

Figure 6.66 — CPU_2 Vs. Δt for Wilson Scheme.

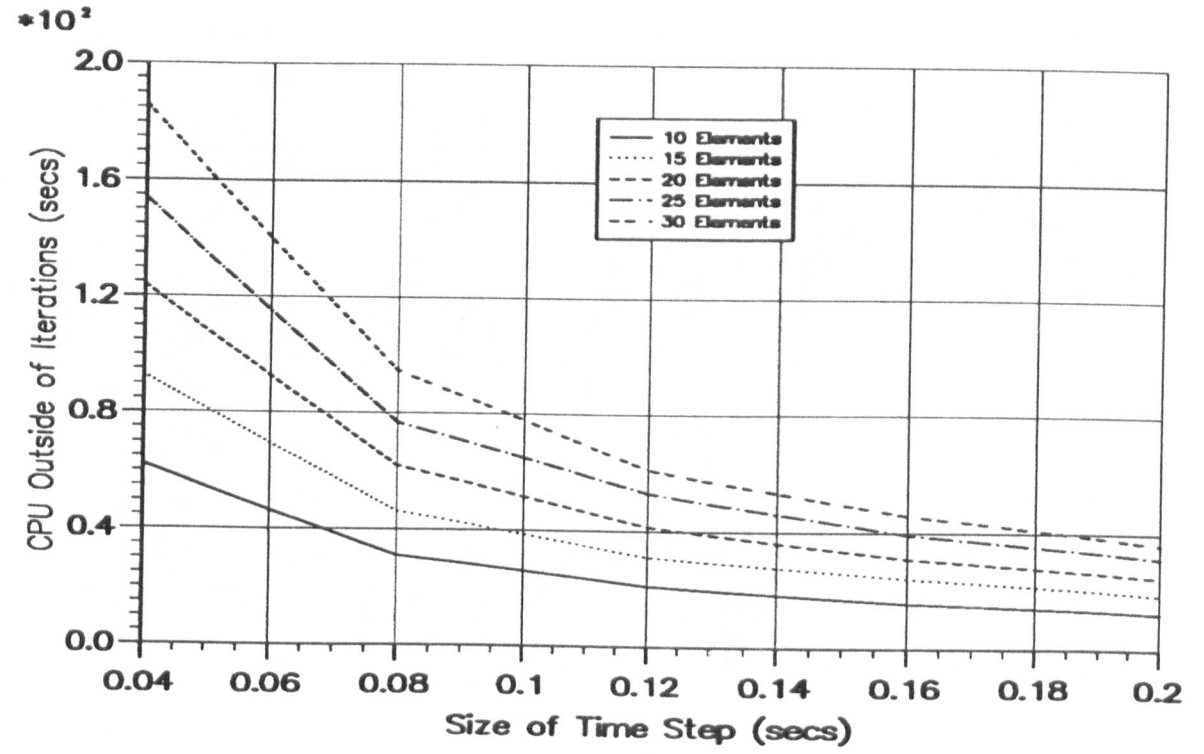

Figure 6.67 — CPU_1 Vs. Δt for Newmark Scheme.

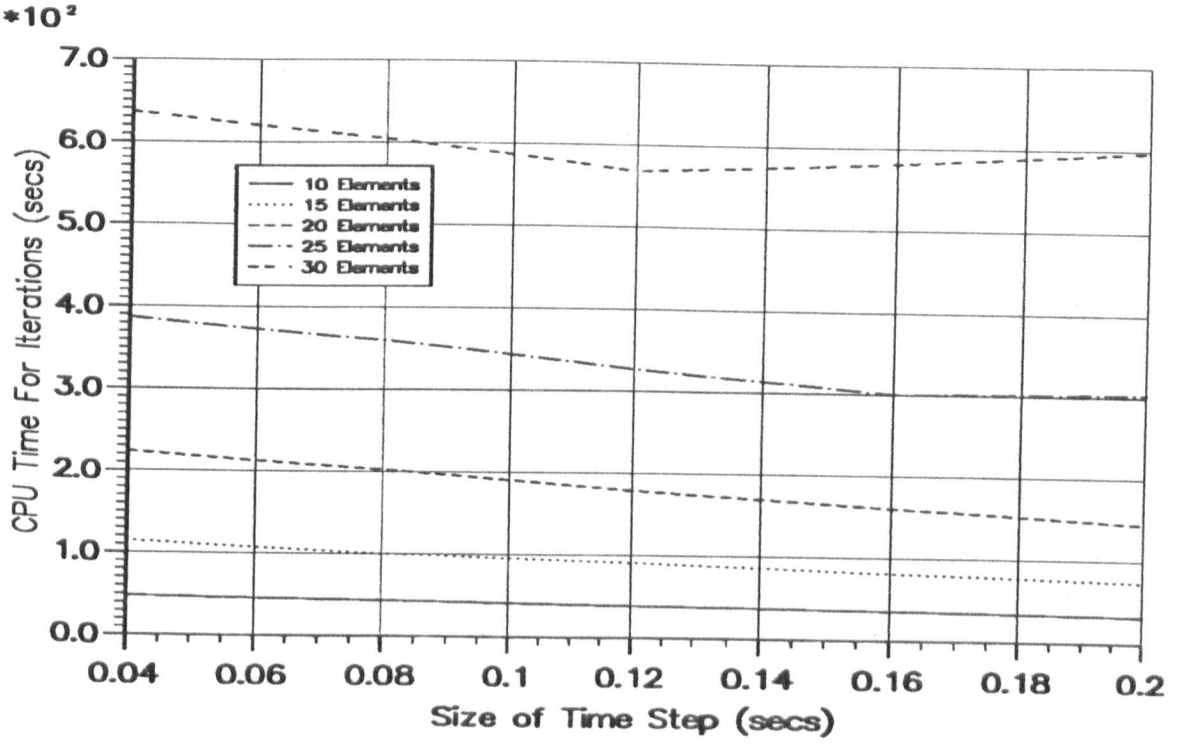

Figure 6.68 — CPU_2 Vs. Δt for Newmark Scheme.

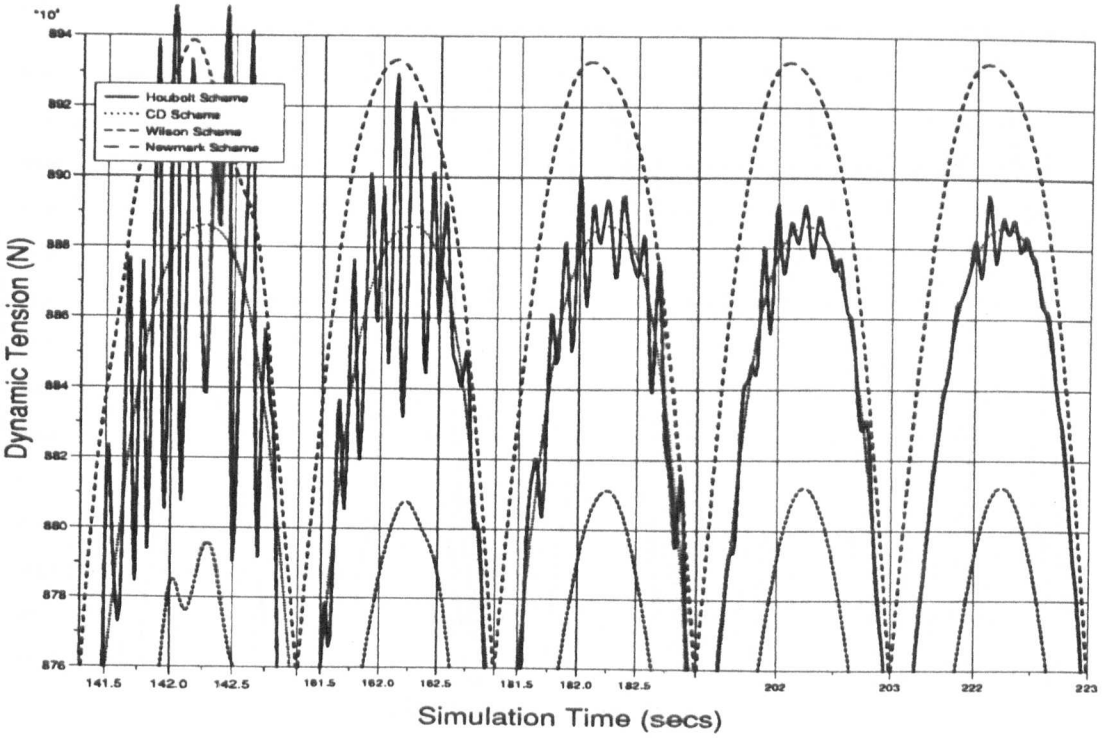

Figure 6.69 — The Four Schemes for $\Delta t = 0.001$.

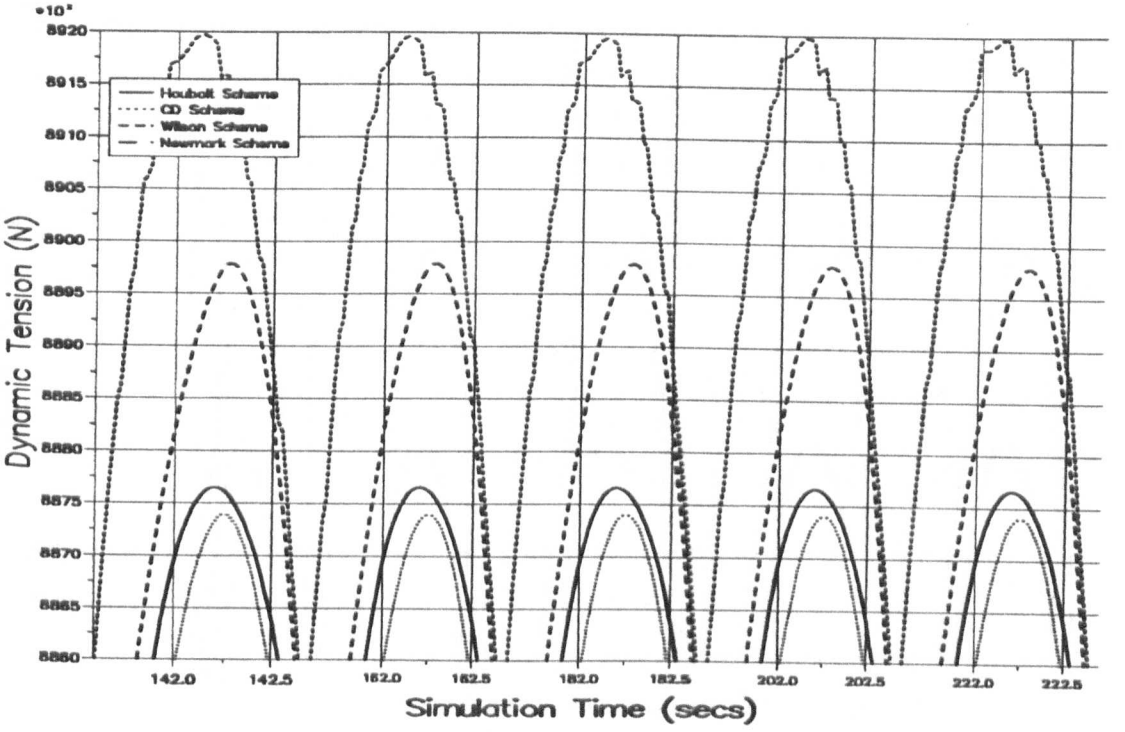

Figure 6.70 — The Four Schemes for $\Delta t = 0.021$.

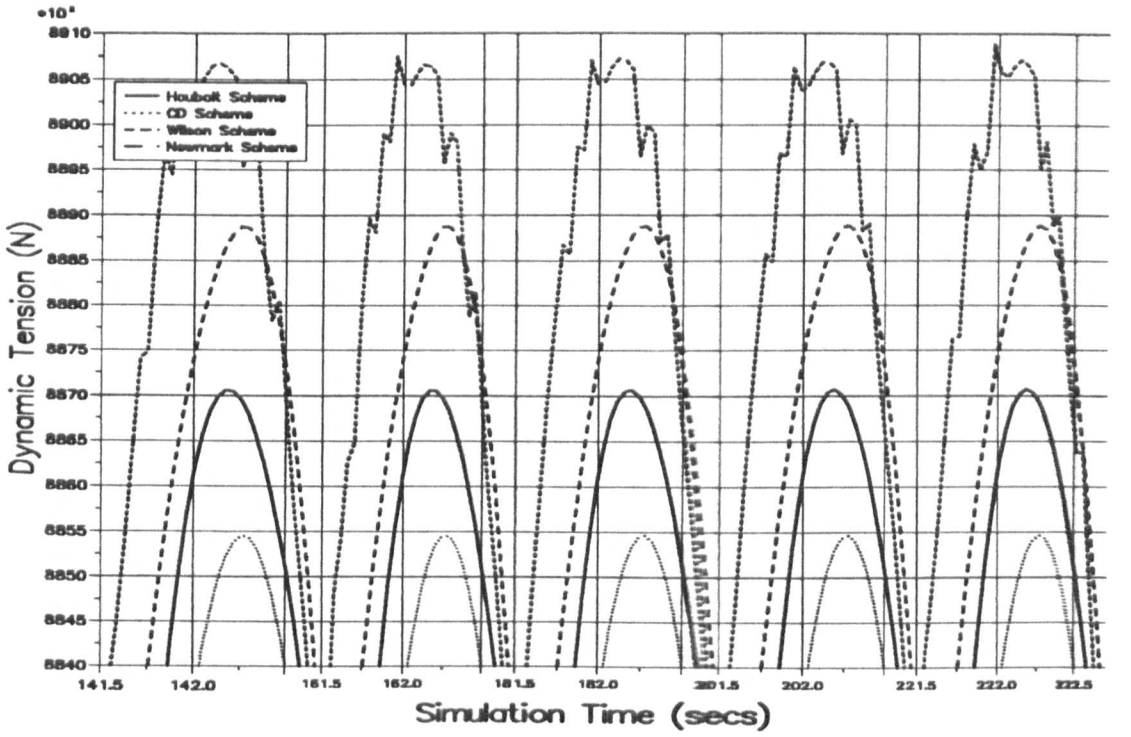

Figure 6.71 — The Four Schemes for $\Delta t = 0.042$.

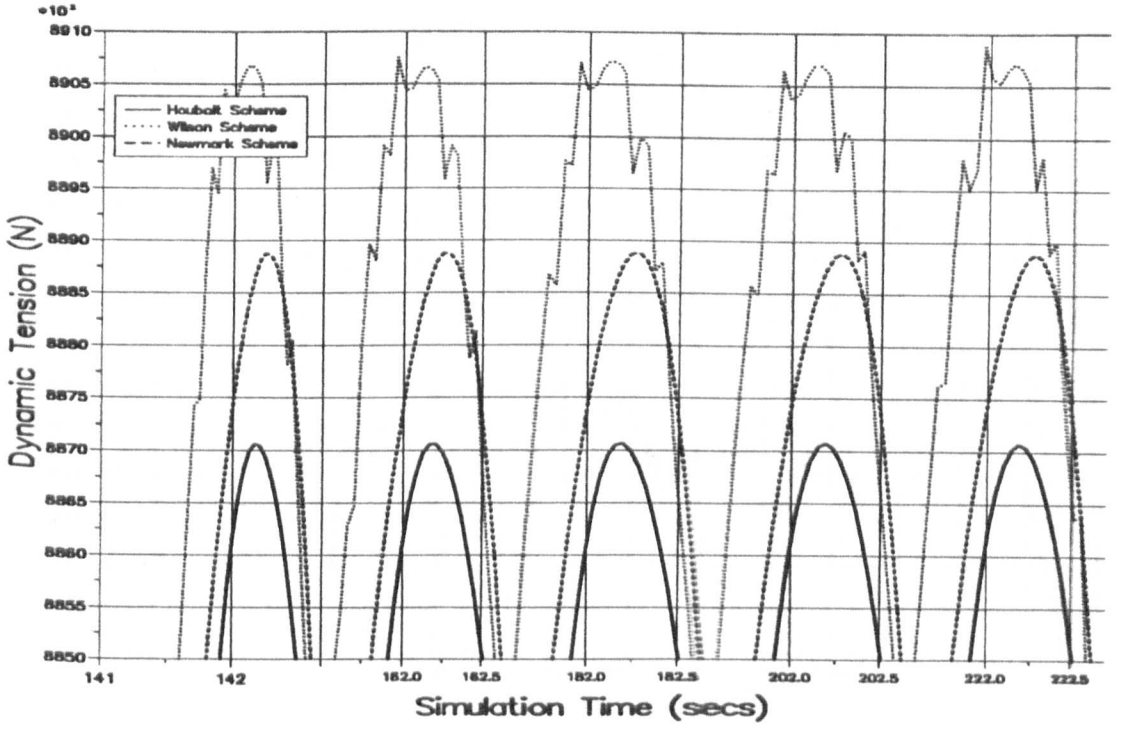

Figure 6.72 — The Three Implicit Schemes for $\Delta t = 0.042$.

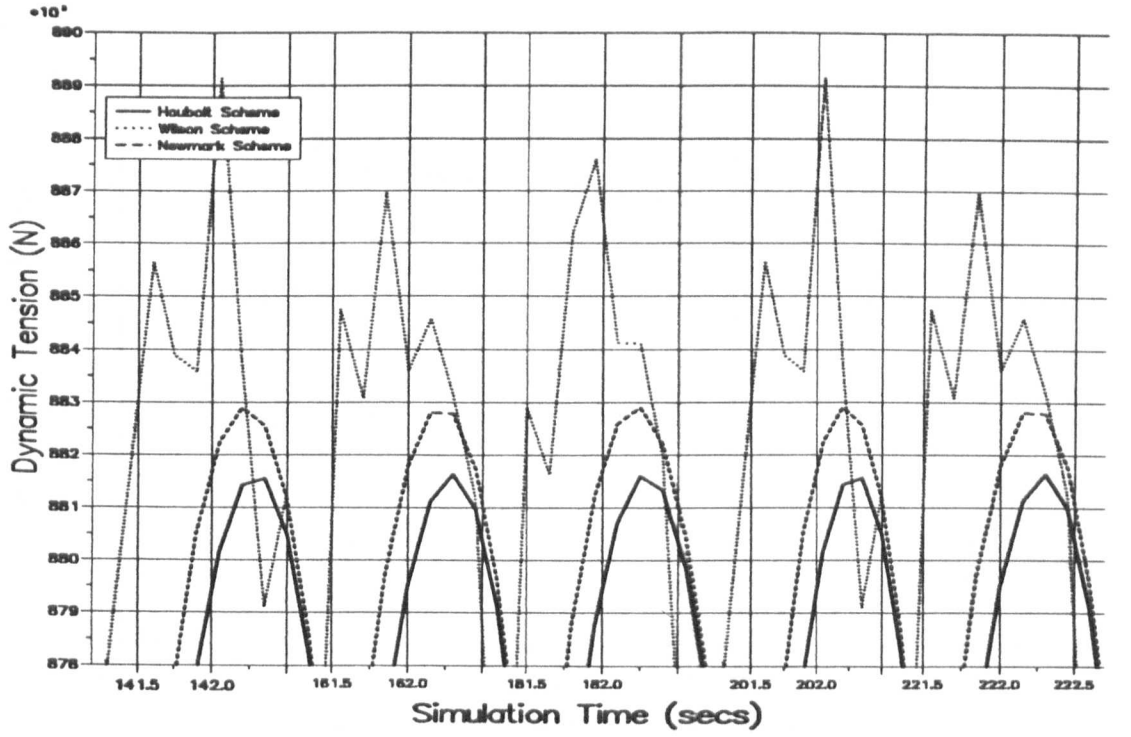

Figure 6.73 — The Three Implicit Schemes for $\Delta t = 0.15$.

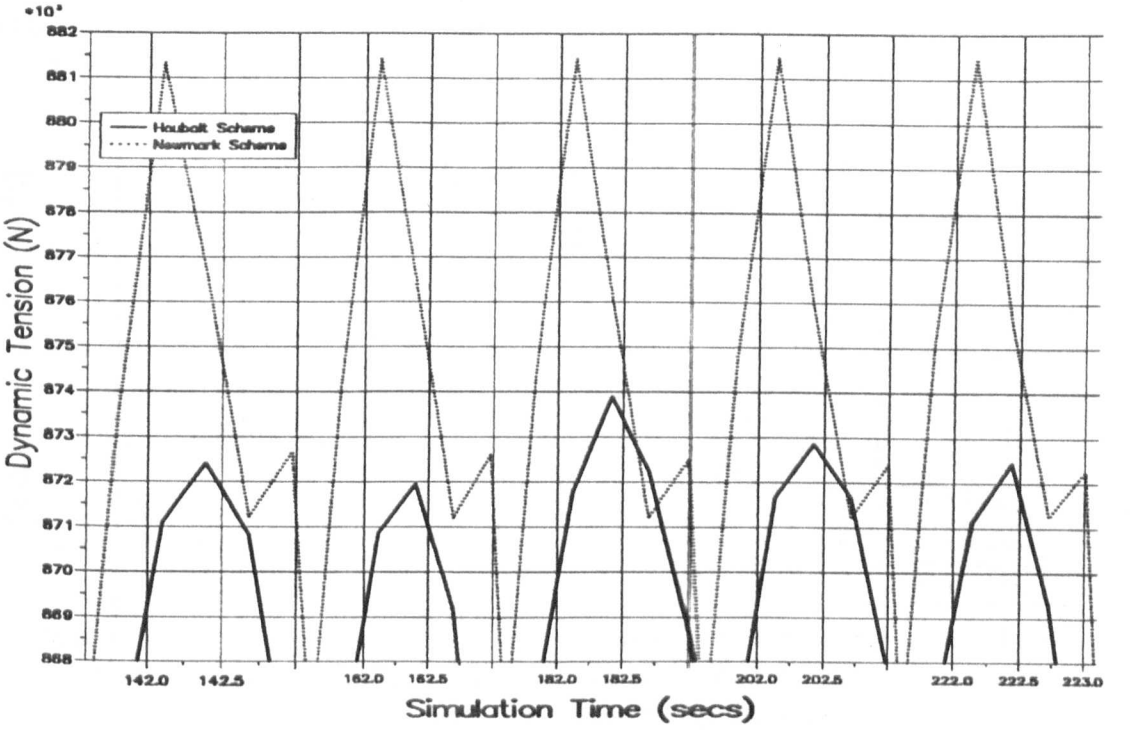

Figure 6.74 — The Three Implicit Schemes for $\Delta t = 0.29$.

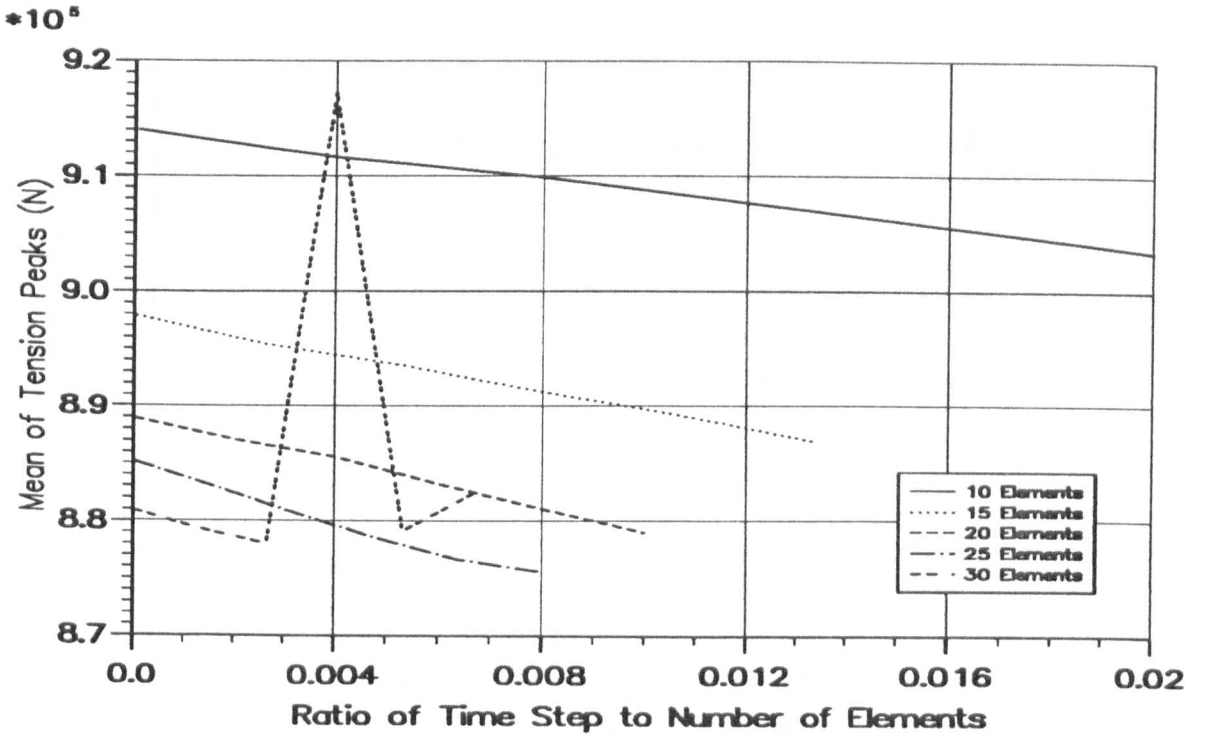

Figure 6.75 — $\frac{\Delta t}{h}$ Vs. Mean of Tension Peaks for Houbolt Scheme.

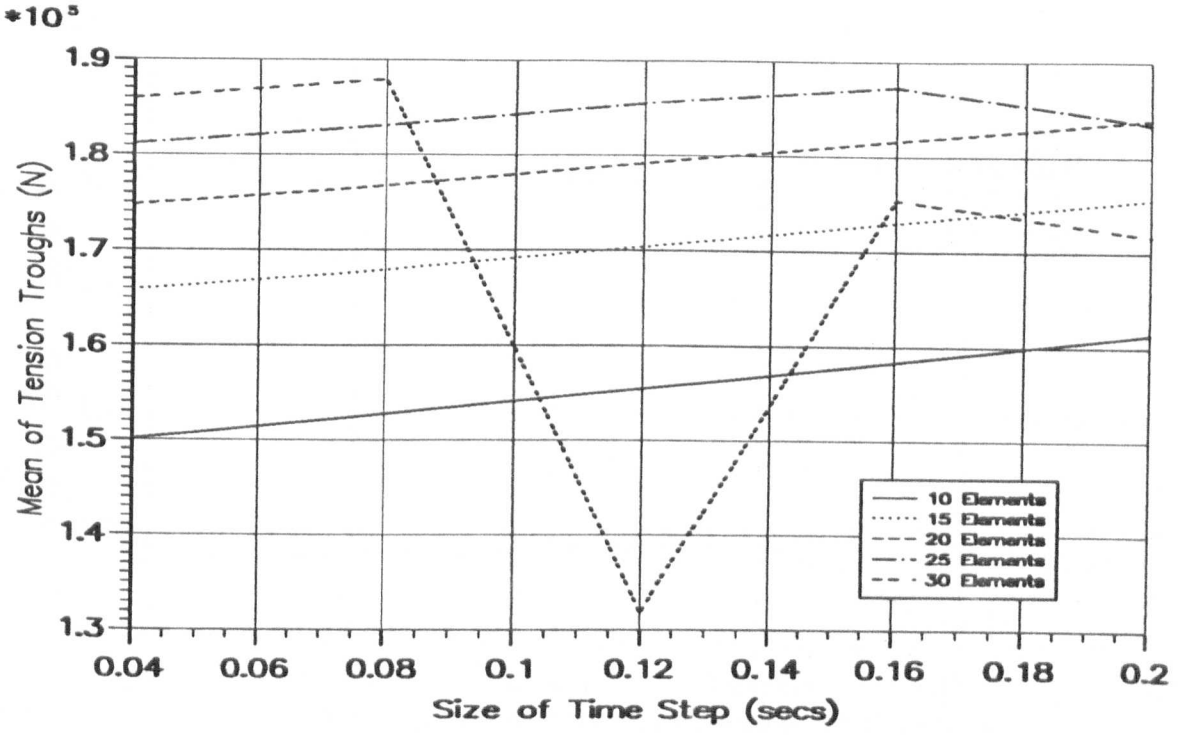

Figure 6.76 — $\frac{\Delta t}{h}$ Vs. Mean of Tension Troughs for Houbolt Scheme.

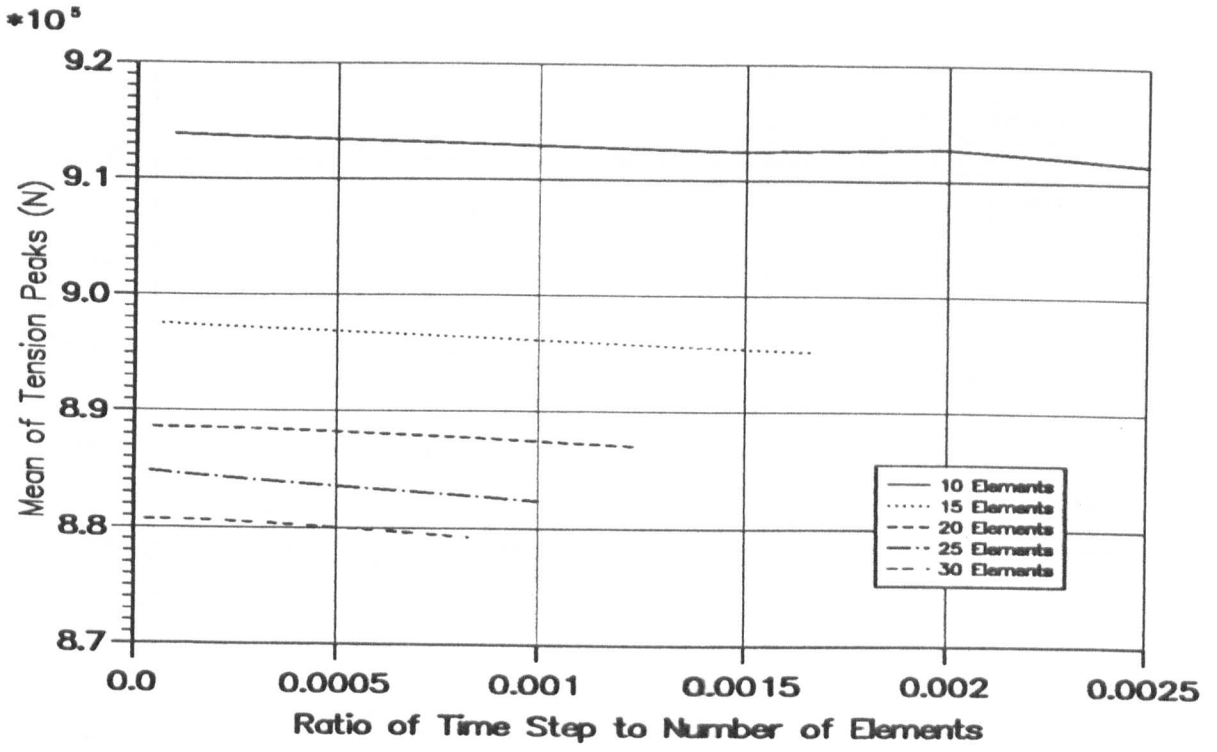

Figure 6.77 — $\frac{\Delta t}{h}$ Vs. Mean of Tension Peaks for CD Scheme.

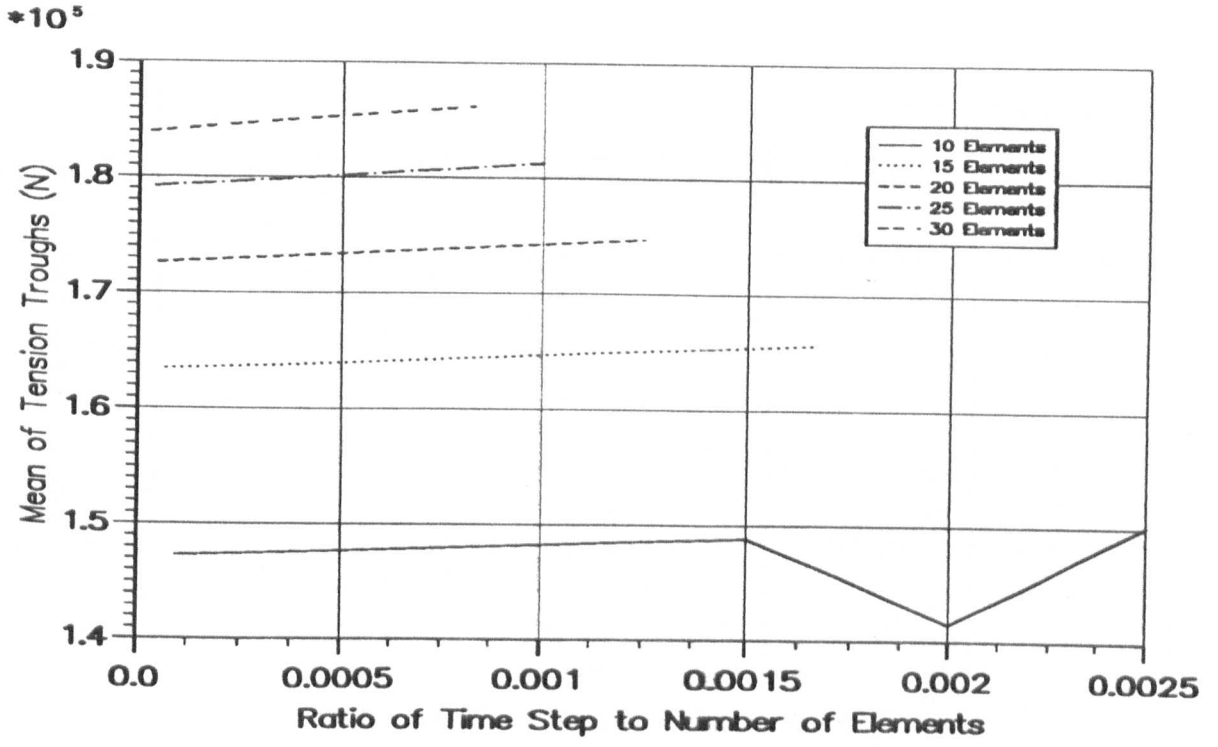

Figure 6.78 — $\frac{\Delta t}{h}$ Vs. Mean of Tension Troughs for CD Scheme.

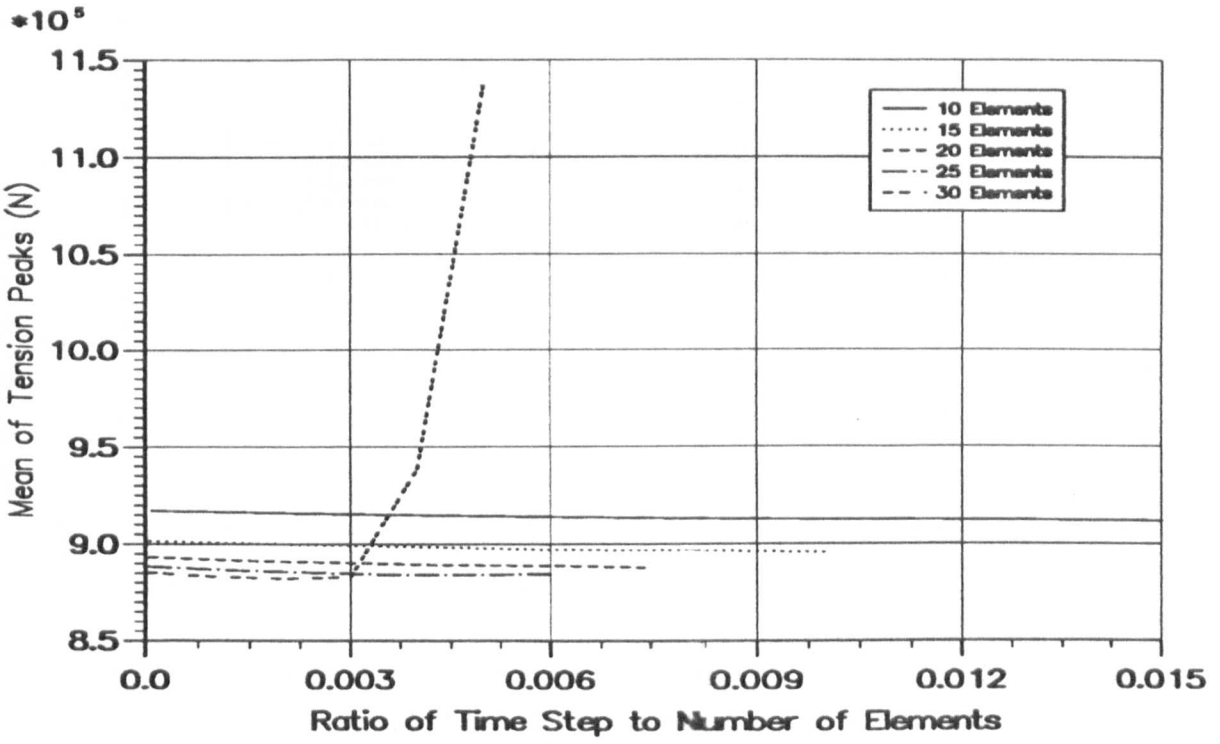

Figure 6.79 — $\frac{\Delta t}{h}$ Vs. Mean of Tension Peaks for Wilson Scheme.

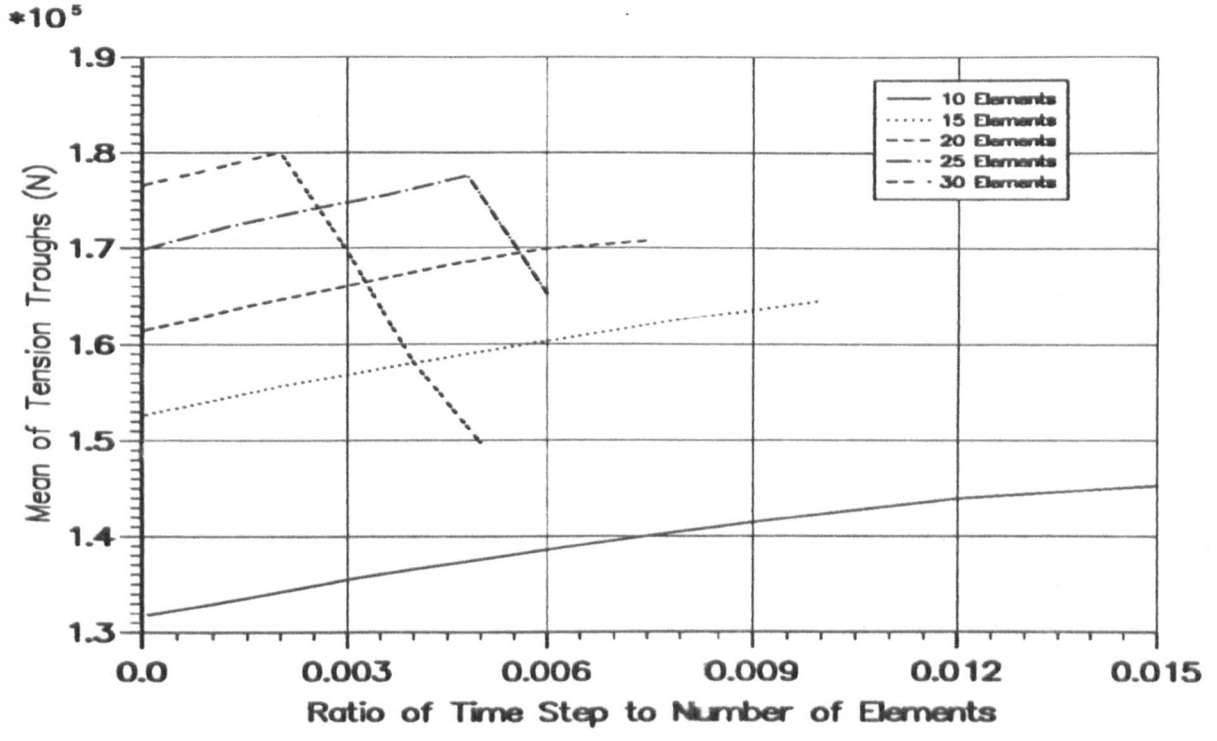

Figure 6.80 — $\frac{\Delta t}{h}$ Vs. Mean of Tension Troughs for Wilson Scheme.

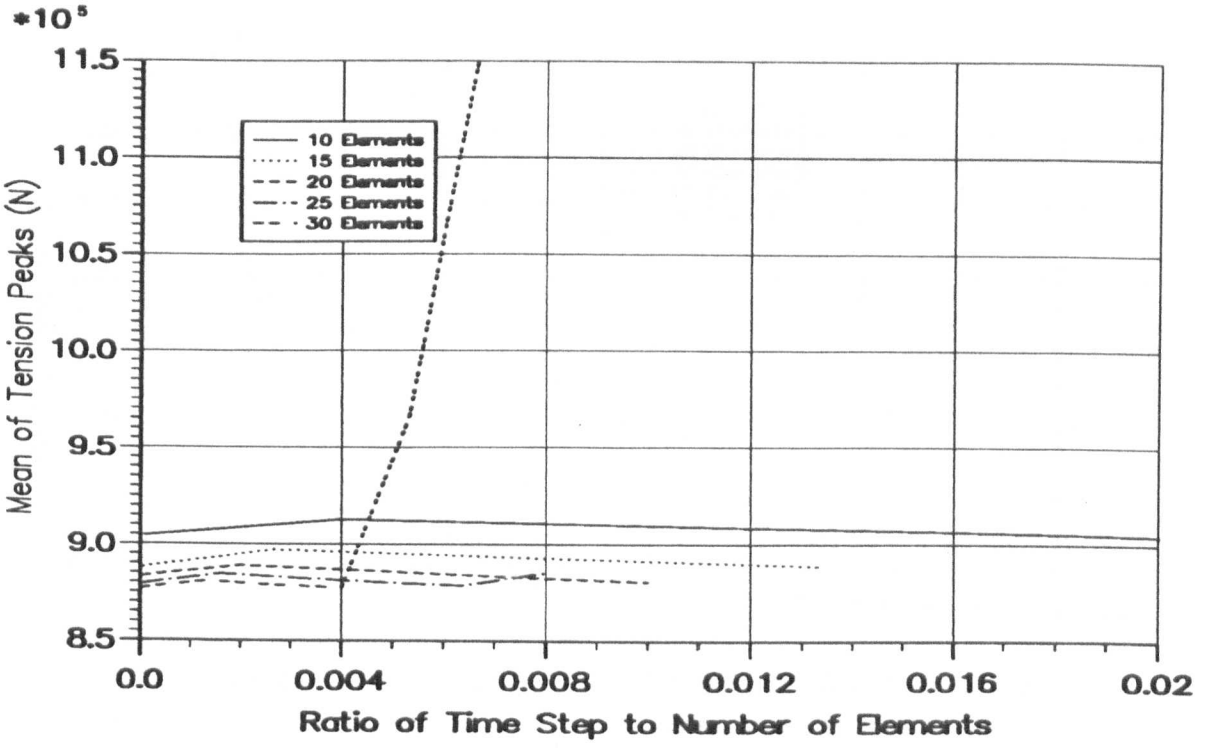

Figure 6.81 — $\frac{\Delta t}{h}$ Vs. Mean of Tension Peaks for Newmark Scheme.

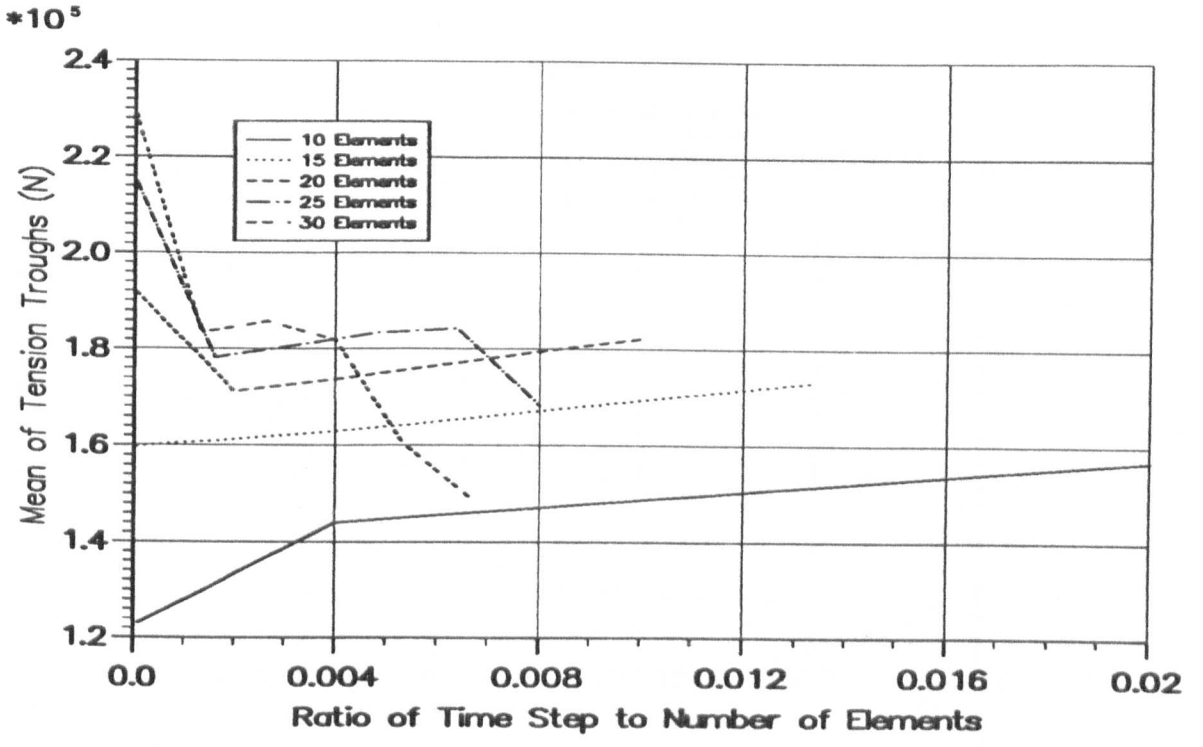

Figure 6.82 — $\frac{\Delta t}{h}$ Vs. Mean of Tension Troughs for Newmark Scheme.

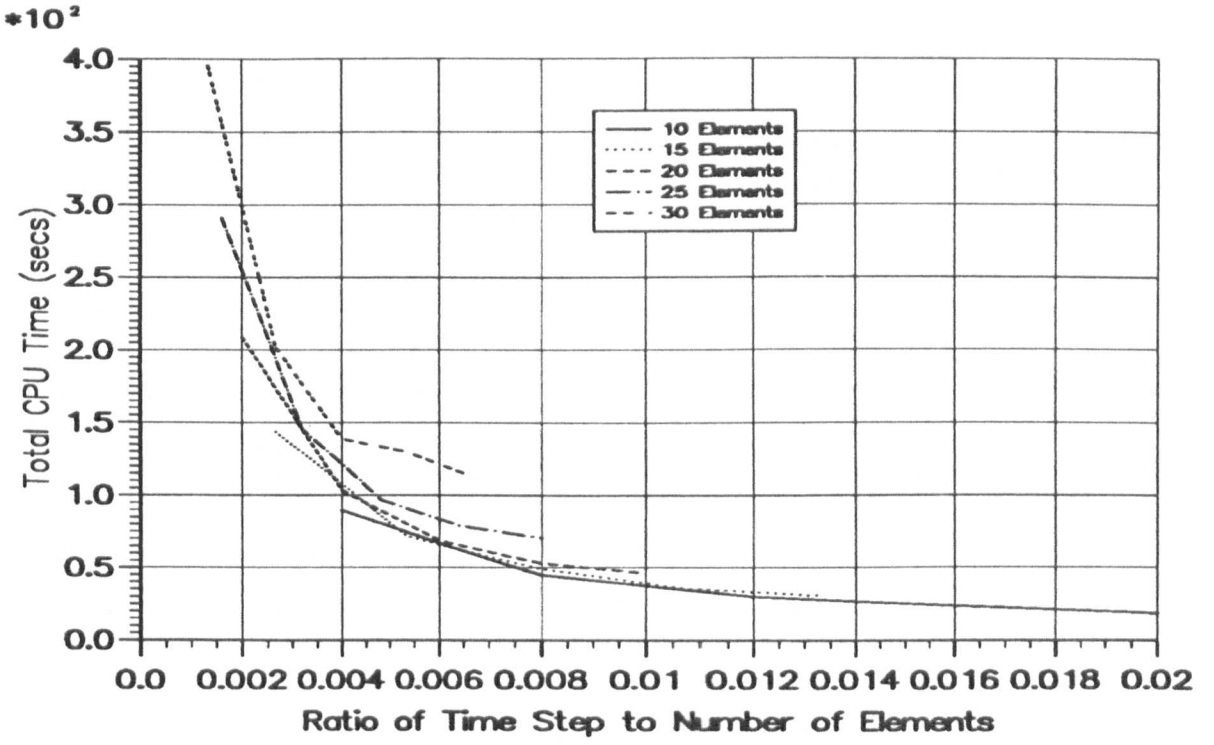

Figure 6.83 — $\frac{\Delta t}{h}$ Vs. CPU Time for Houbolt Scheme.

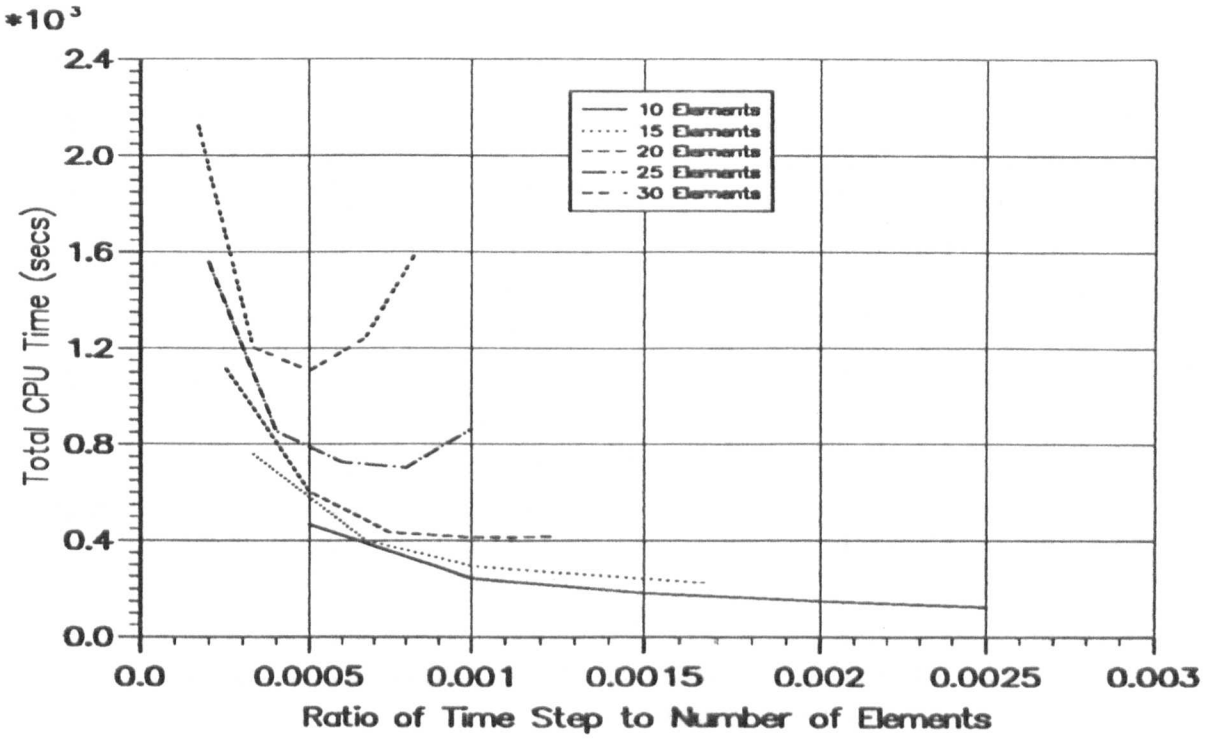

Figure 6.84 — $\frac{\Delta t}{h}$ Vs. CPU Time for CD Scheme.

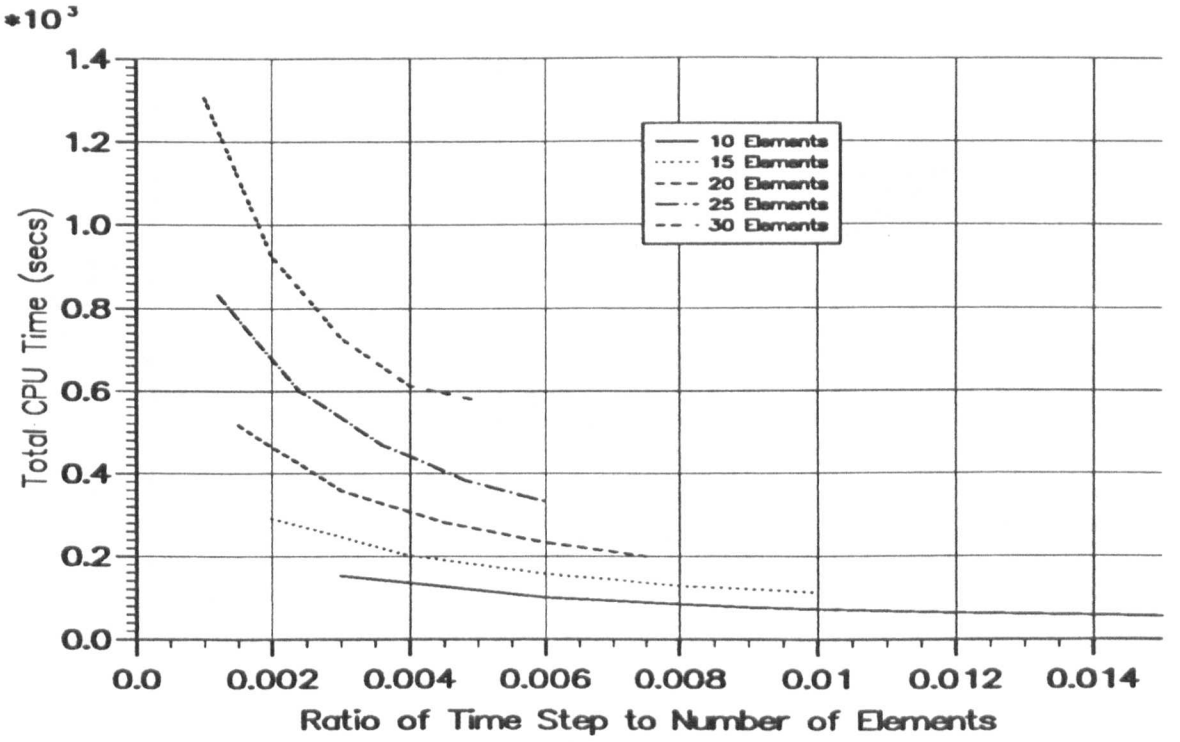

Figure 6.85 — $\frac{\Delta t}{h}$ Vs. CPU Time for Wilson Scheme.

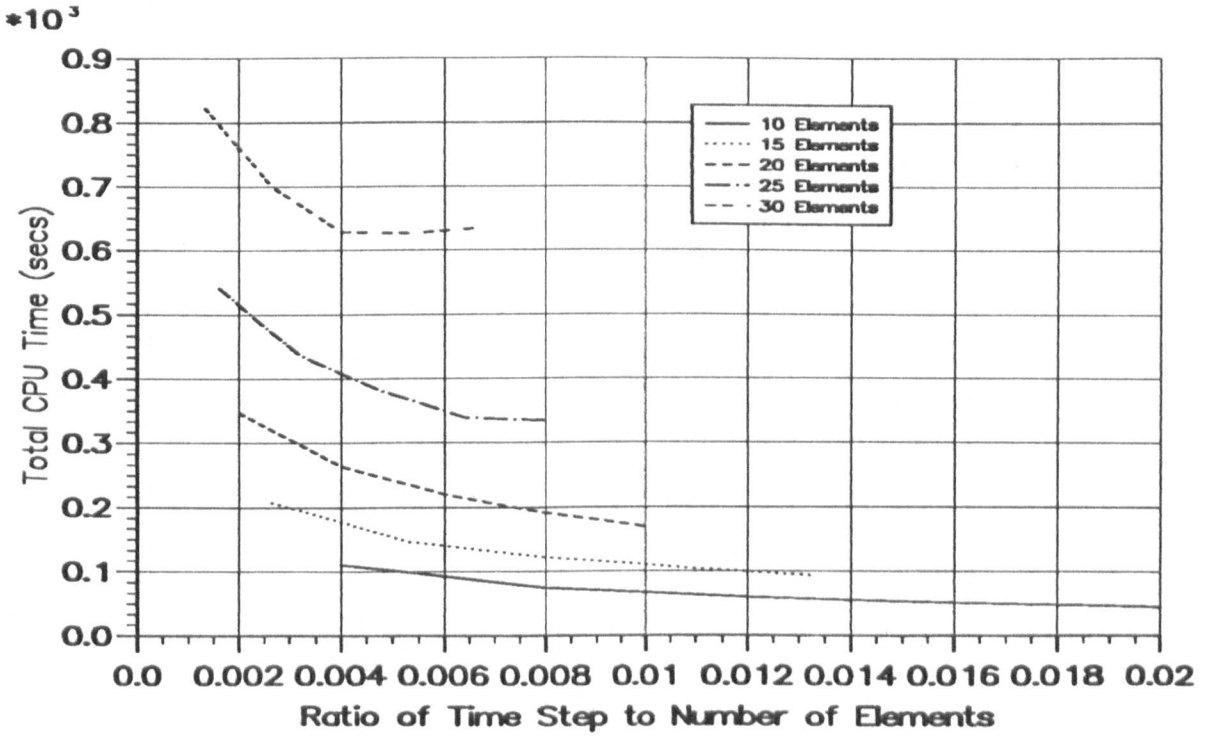

Figure 6.86 — $\frac{\Delta t}{h}$ Vs. CPU Time for Newmark Scheme.

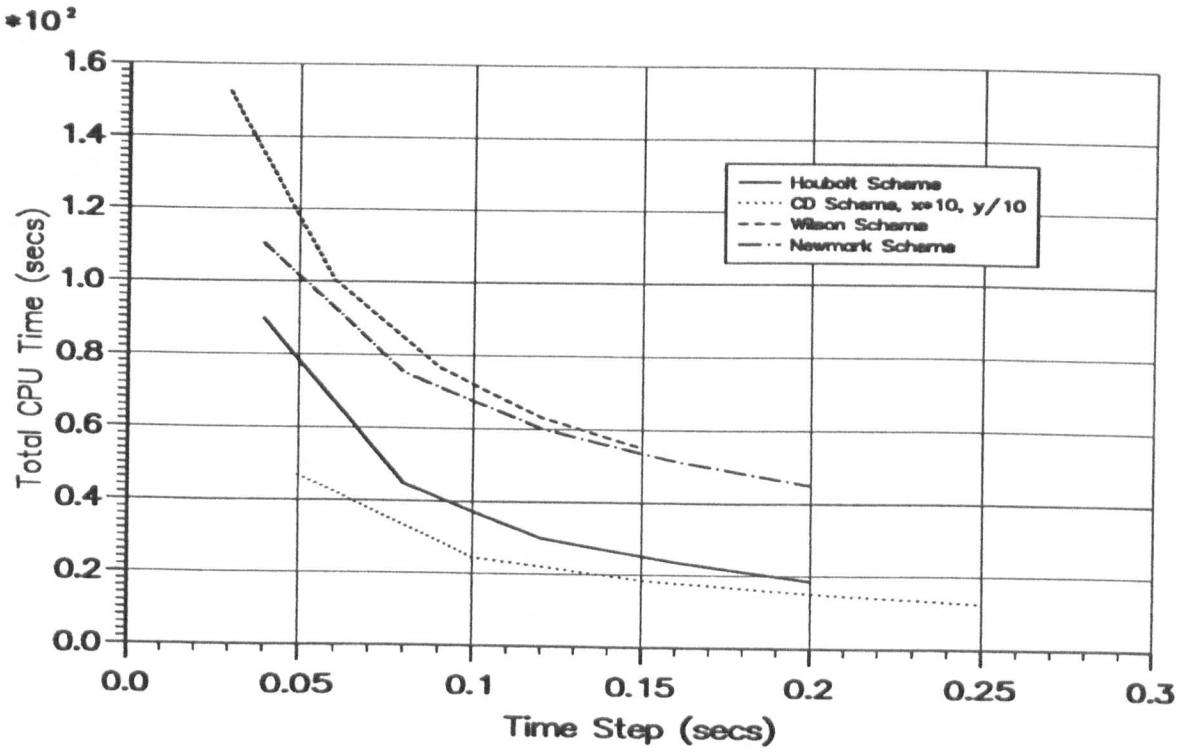

Figure 6.87 — CPU Time for 10 Elements.

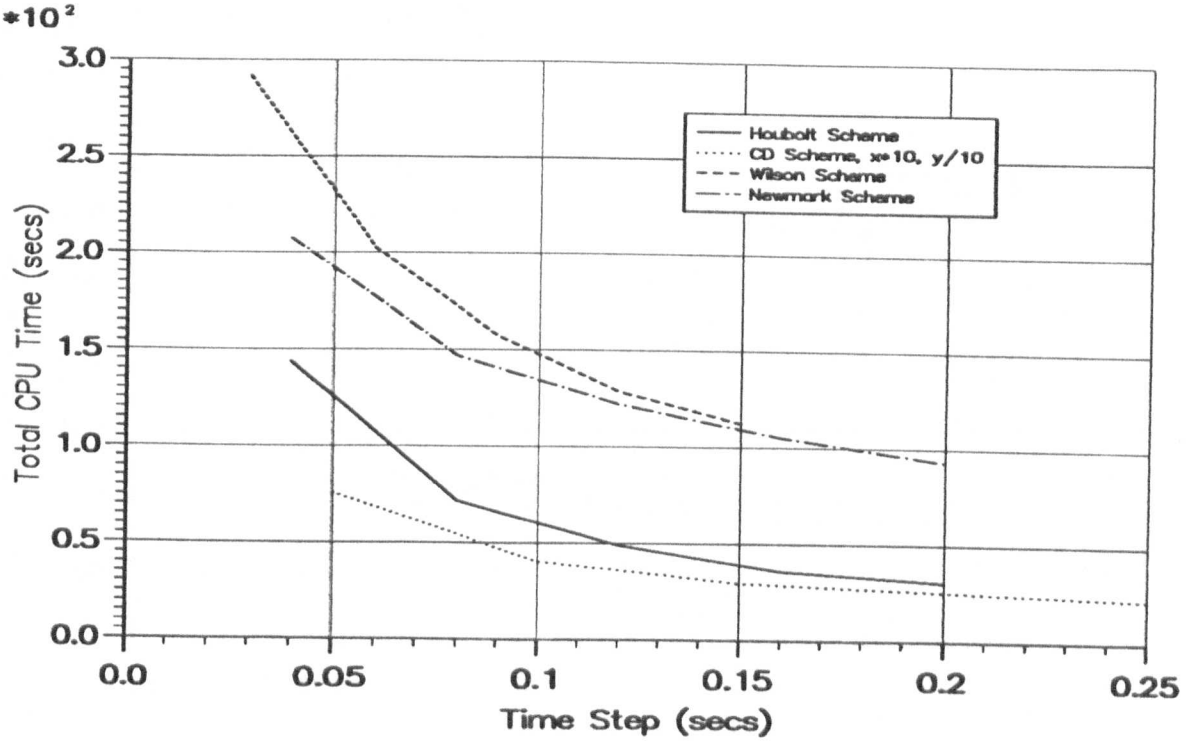

Figure 6.88 — CPU Time for 15 Elements.

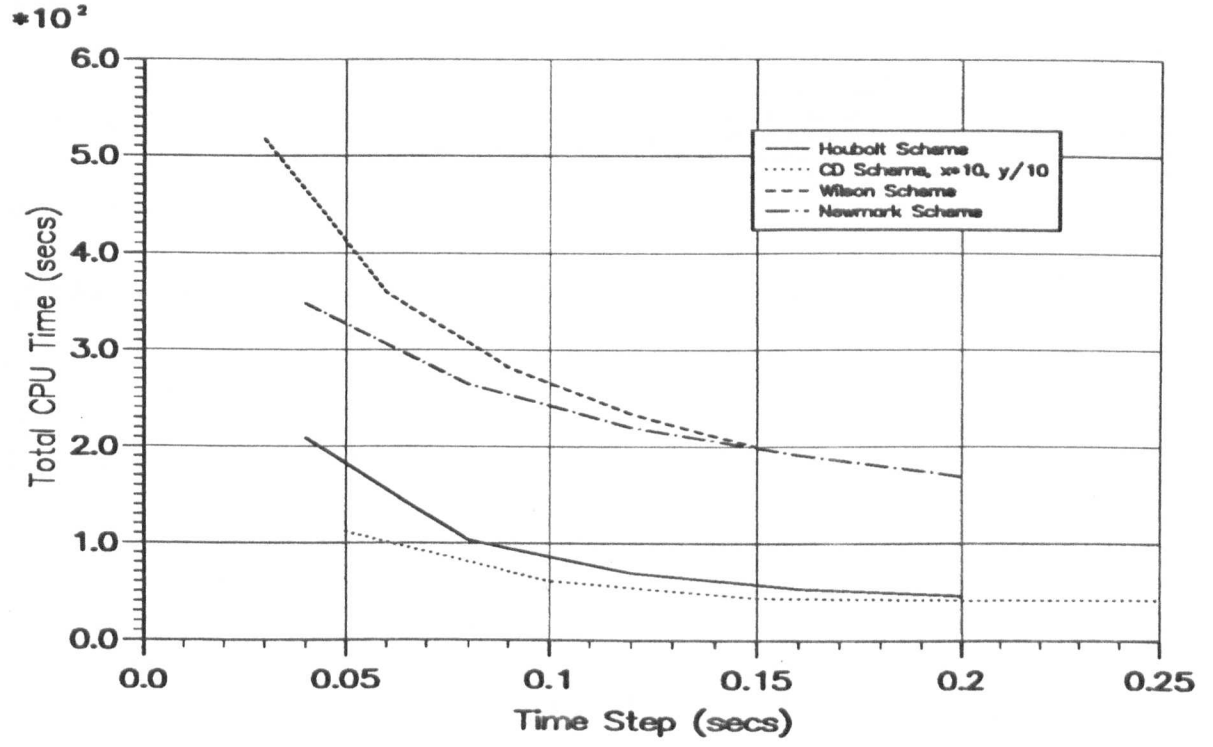

Figure 6.89 — CPU Time for 20 Elements.

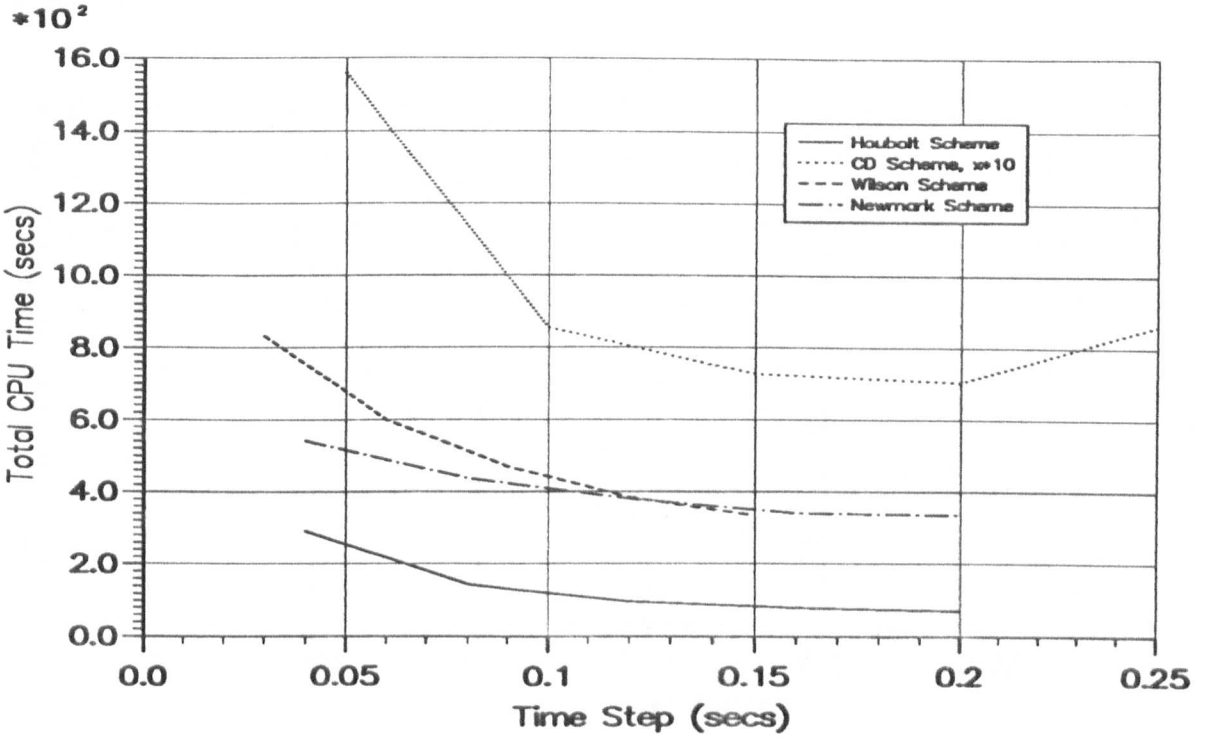

Figure 6.90 — CPU Time for 25 Elements.

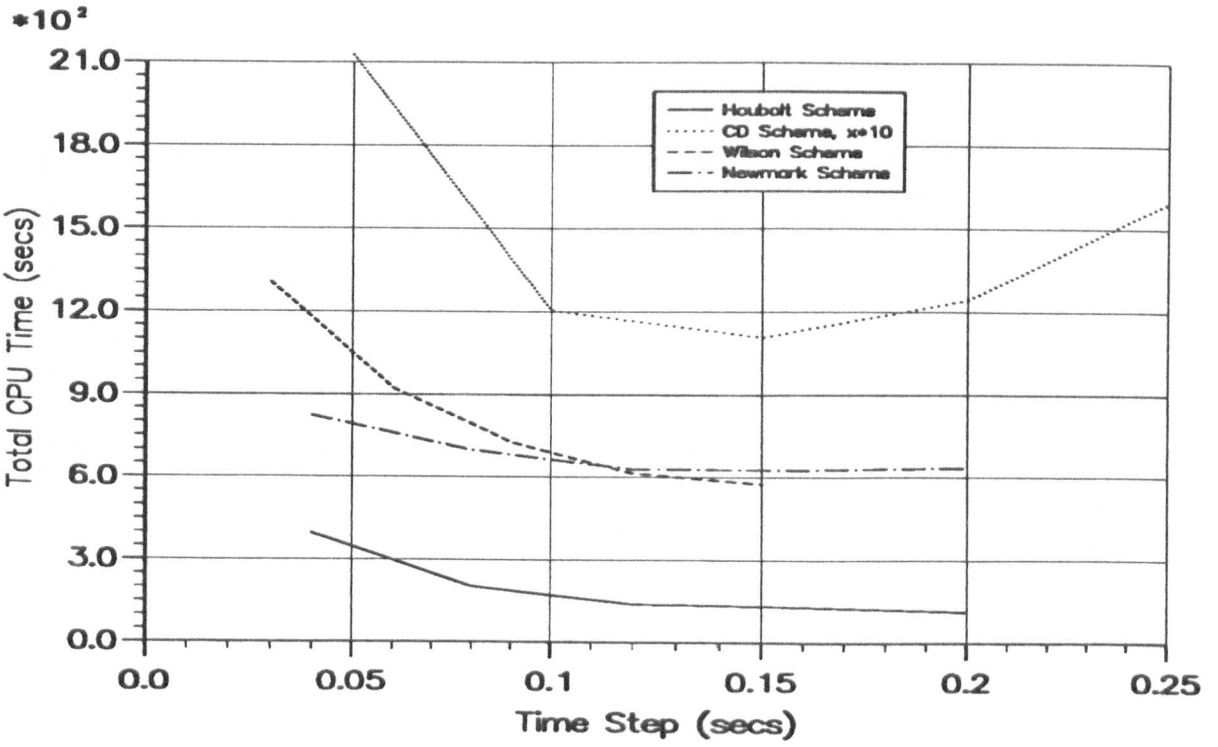

Figure 6.91 — CPU Time for 30 Elements.

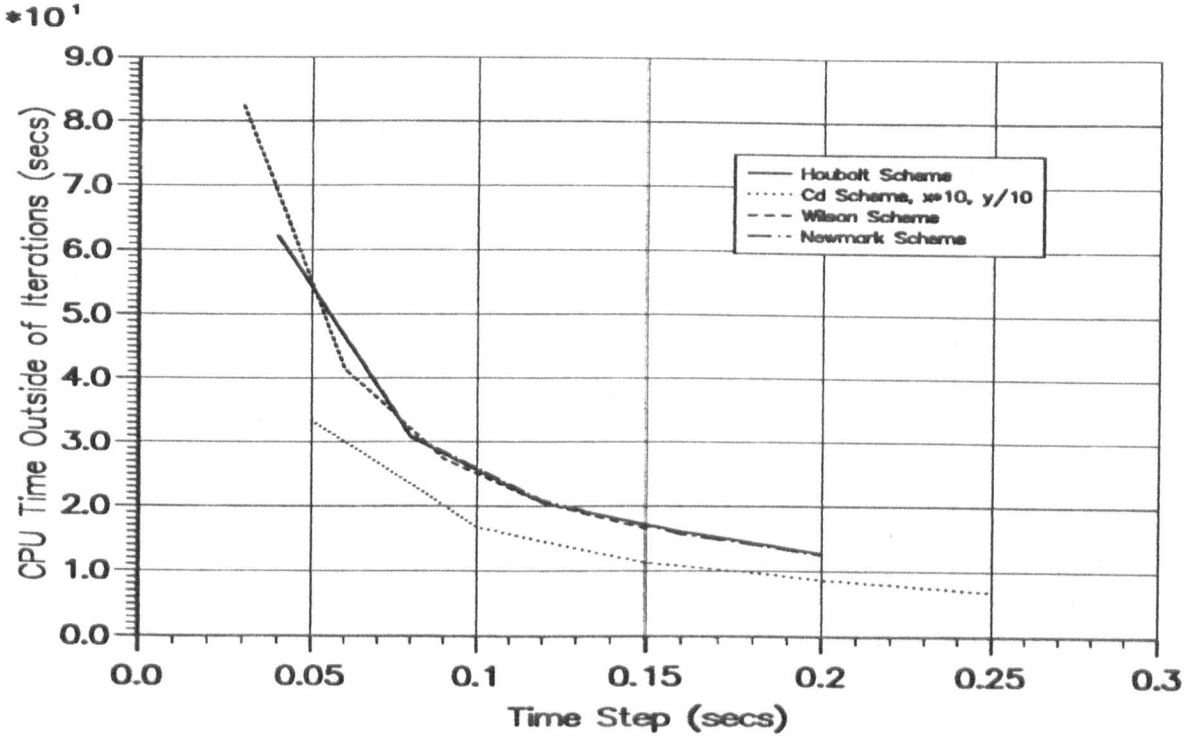

Figure 6.92 — CPU_1 for 10 Elements.

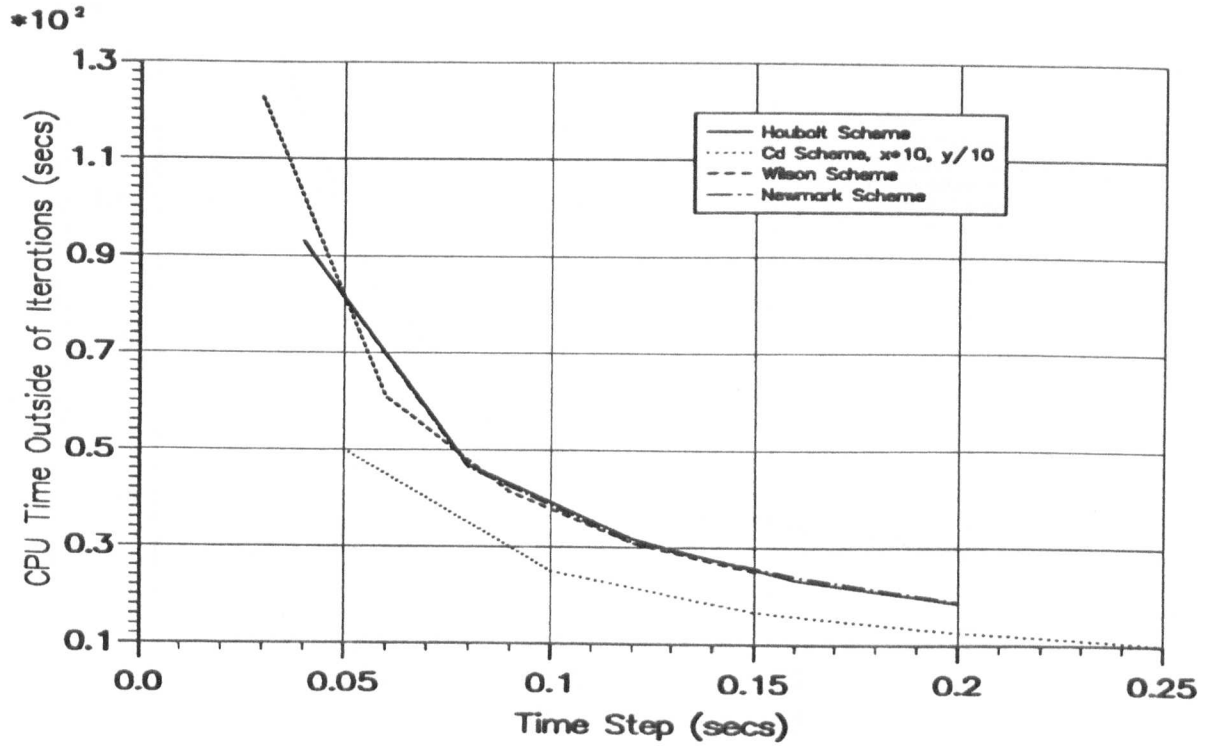

Figure 6.93 — CPU_1 for 15 Elements.

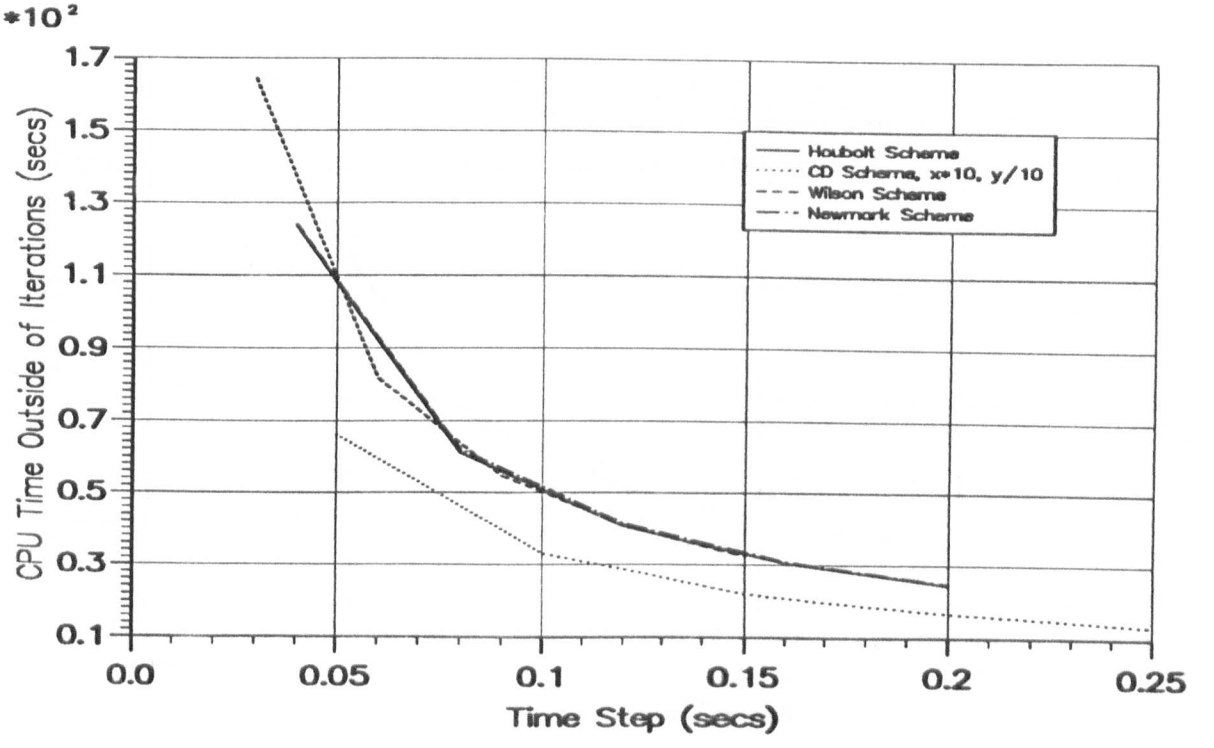

Figure 6.94 — CPU_1 for 20 Elements.

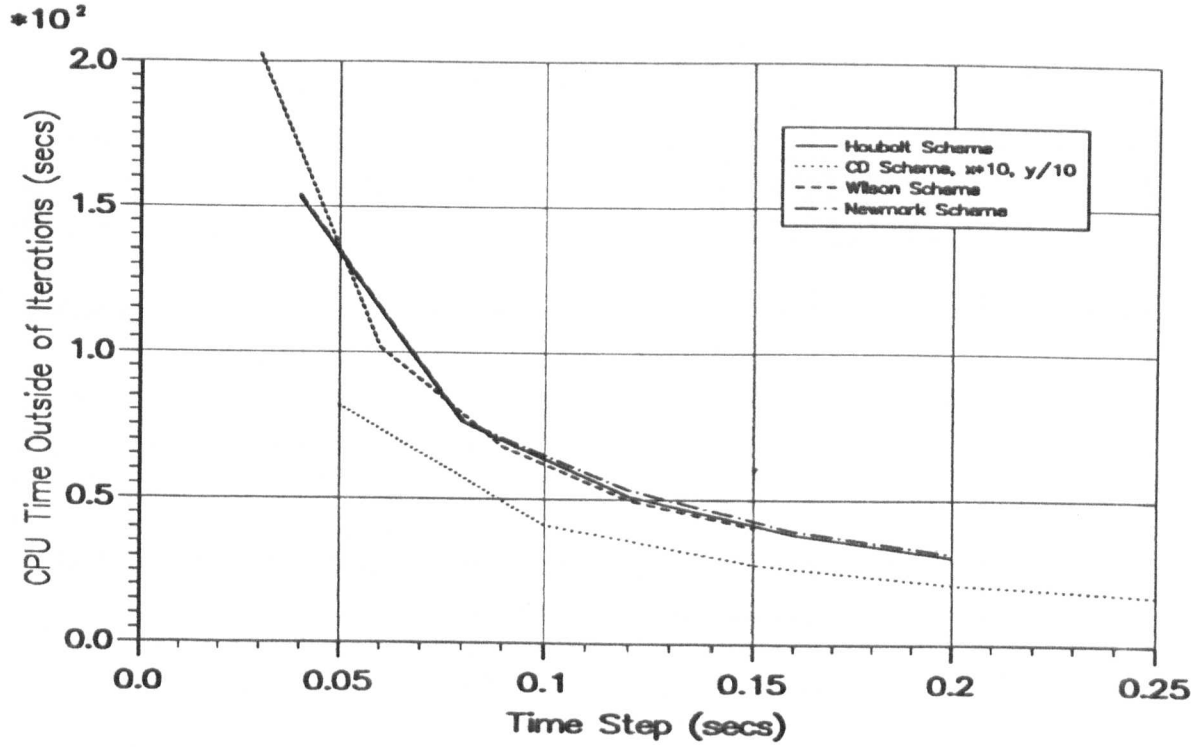

Figure 6.95 — CPU_1 for 25 Elements.

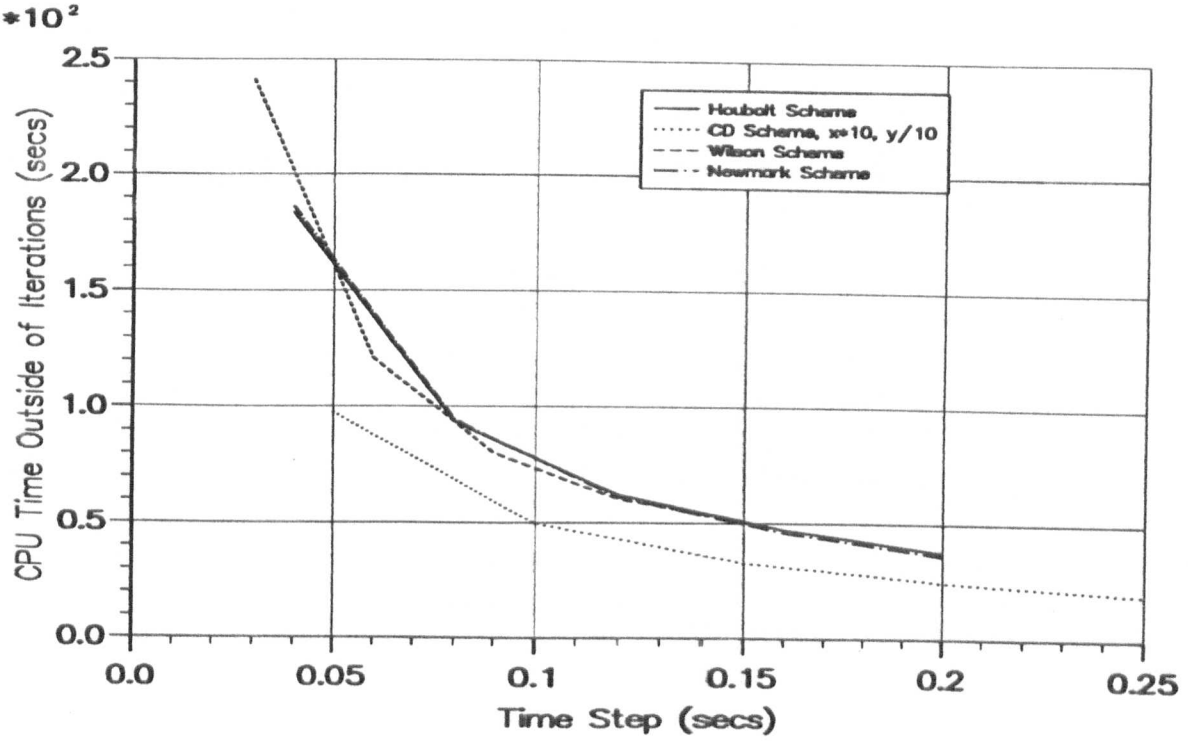

Figure 6.96 — CPU_1 for 30 Elements.

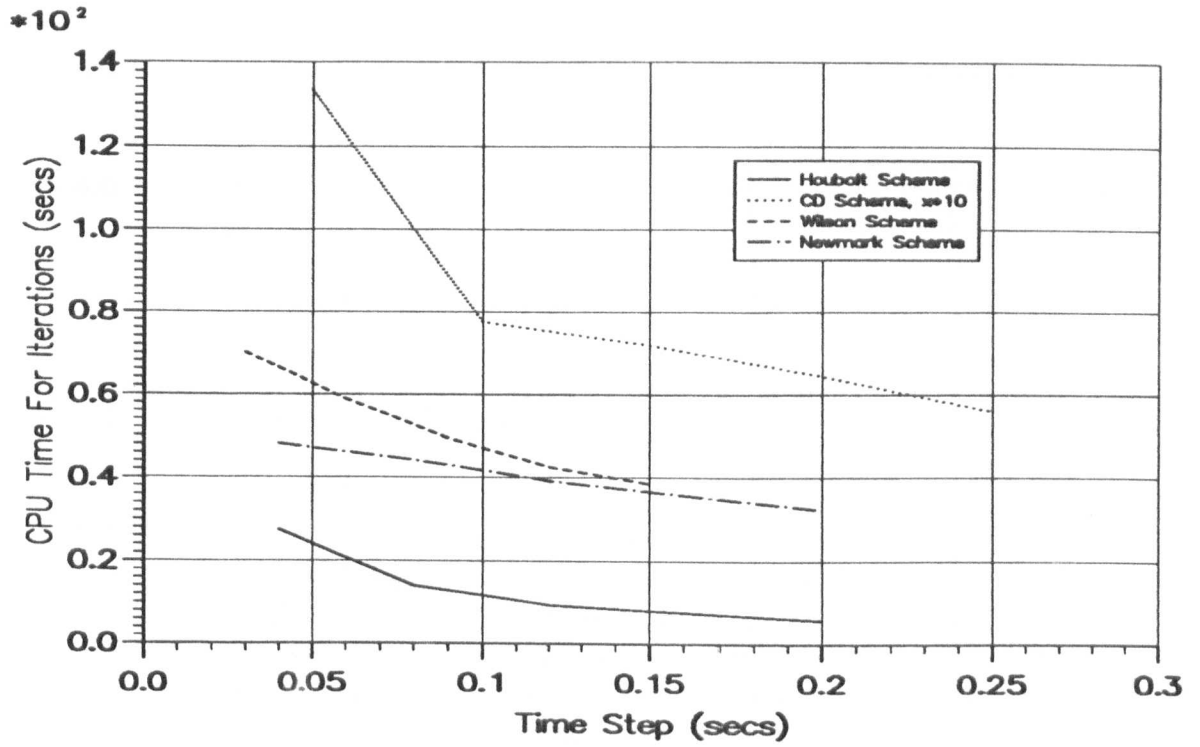

Figure 6.97 — CPU_2 for 10 Elements.

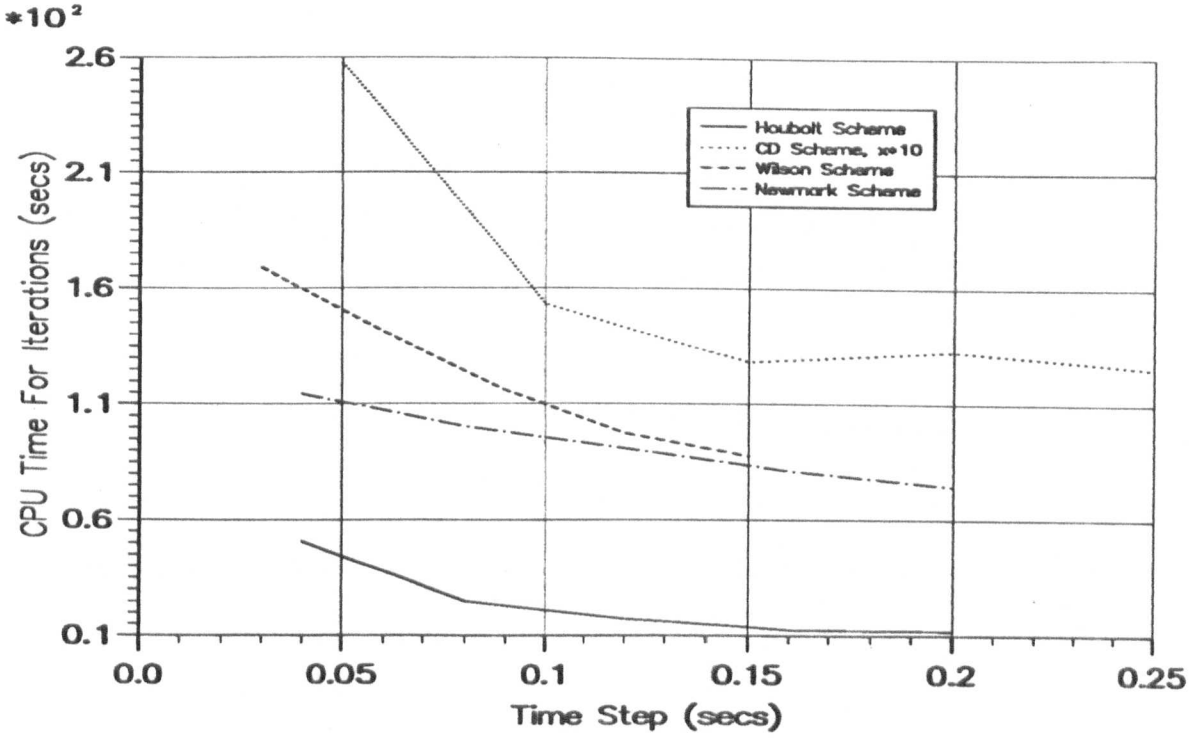

Figure 6.98 — CPU_2 for 15 Elements.

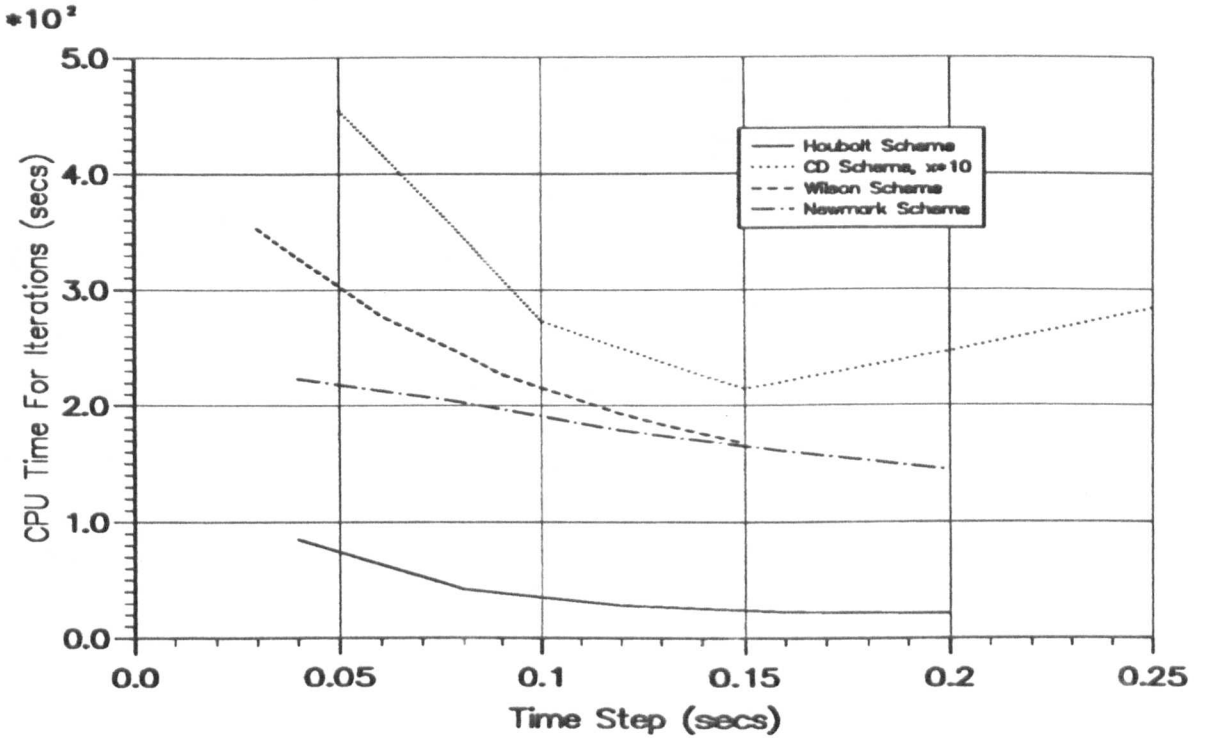

Figure 6.99 — CPU_2 for 20 Elements.

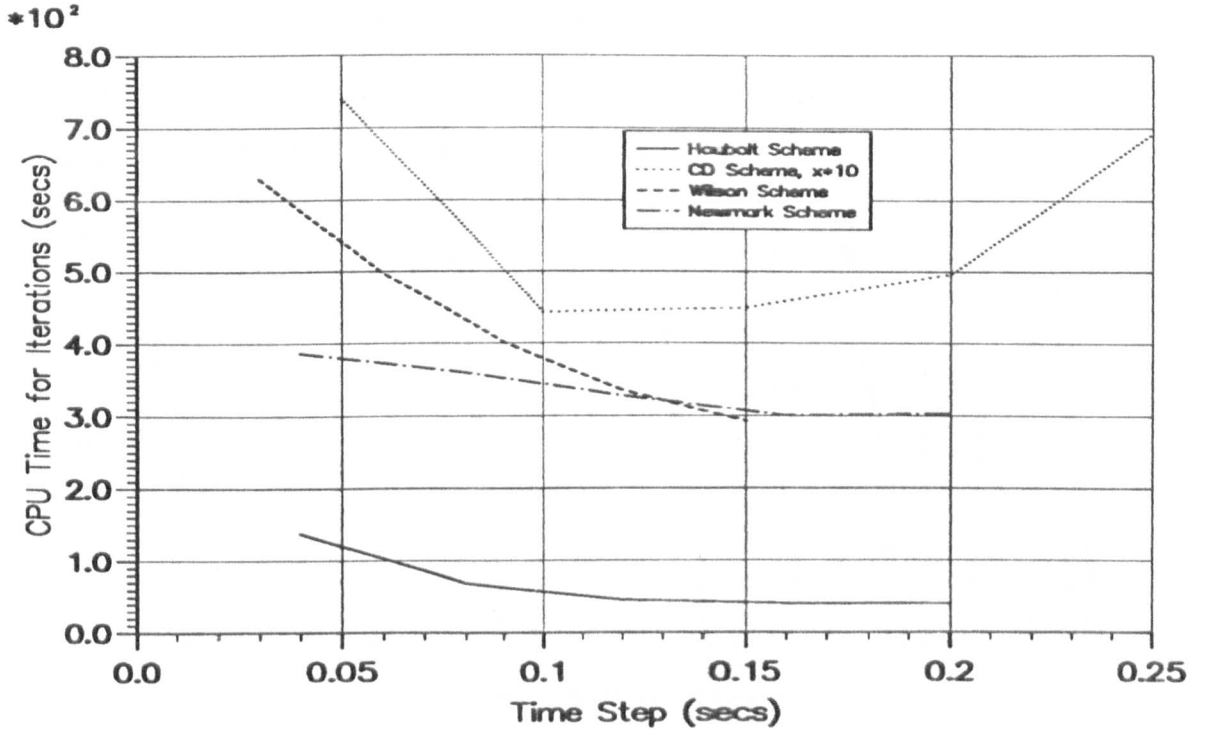

Figure 6.100 — CPU_2 for 25 Elements.

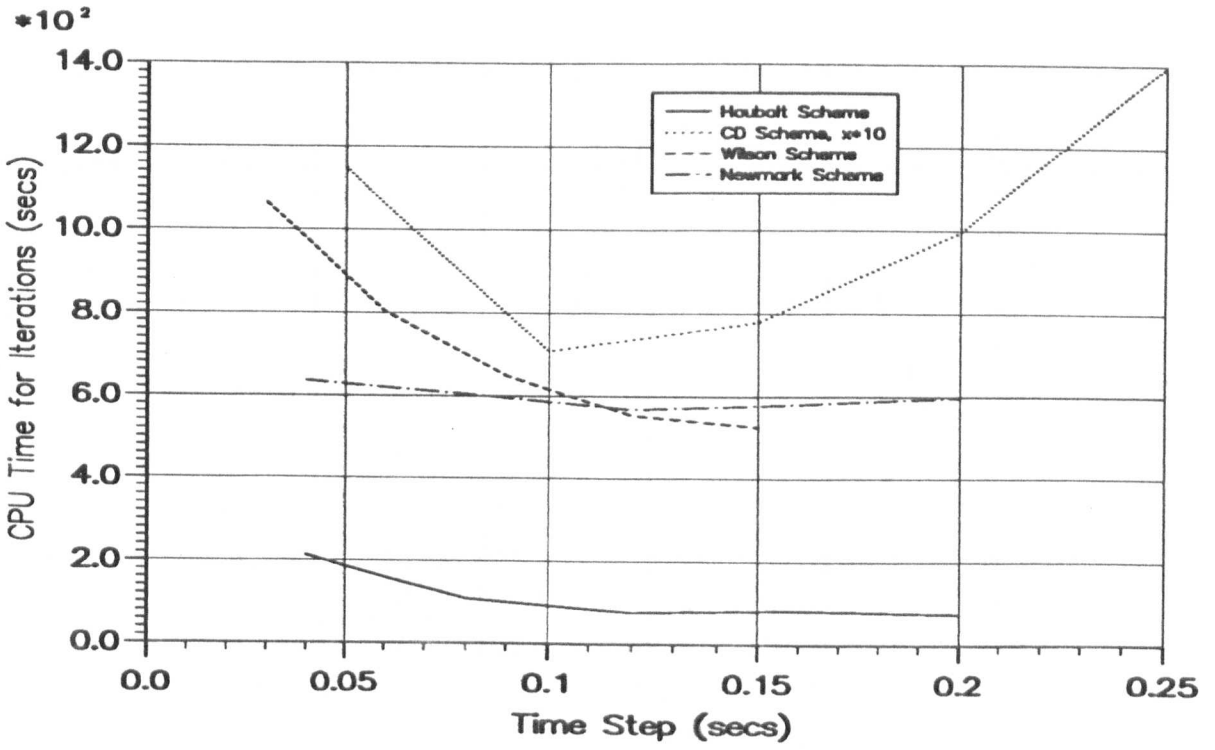

Figure 6.101 — CPU_2 for 30 Elements.

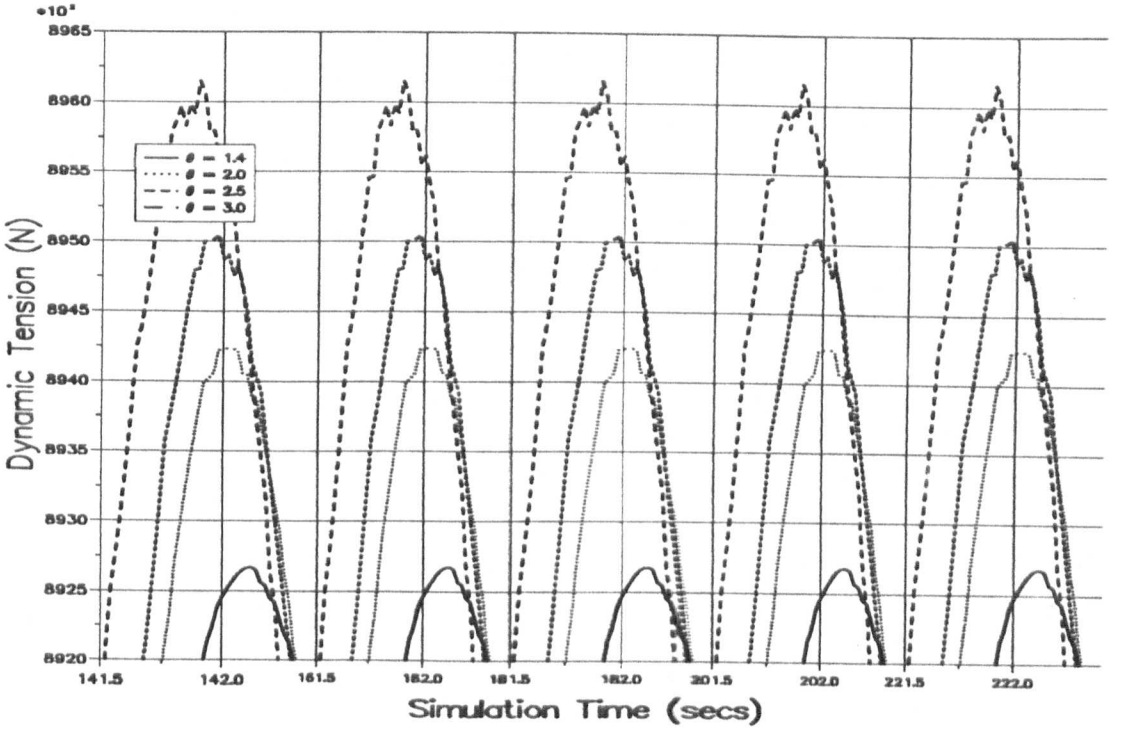

Figure 6.102 — Tension Peaks for Wilson Scheme with Different θ.

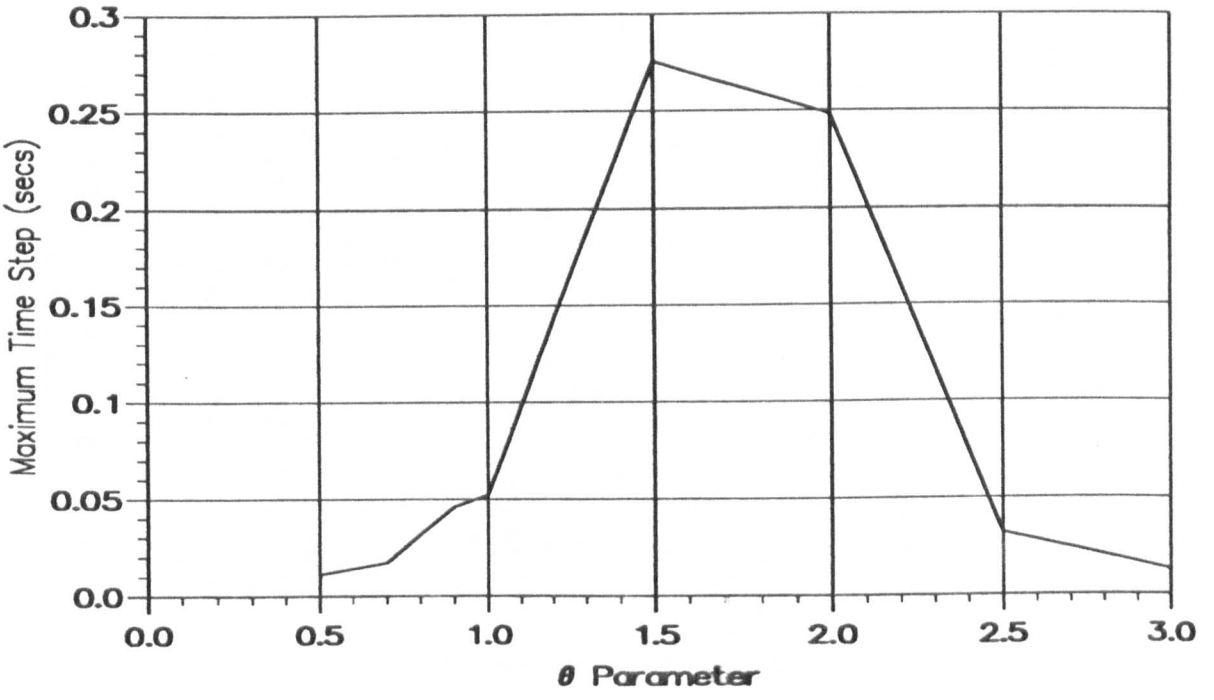

Figure 6.103 — Max. Time Step Vs. θ for Wilson Scheme.

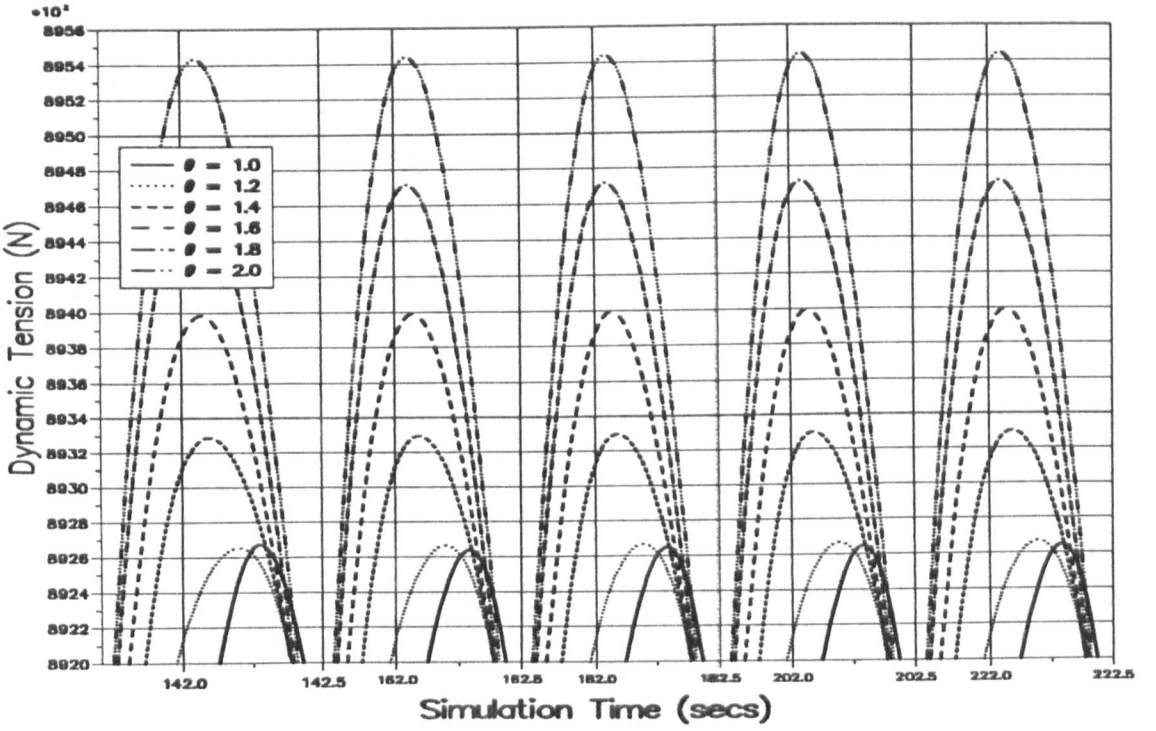

Figure 6.104 — Wilson Scheme Tension Peaks For $\Delta t = 0.001$.

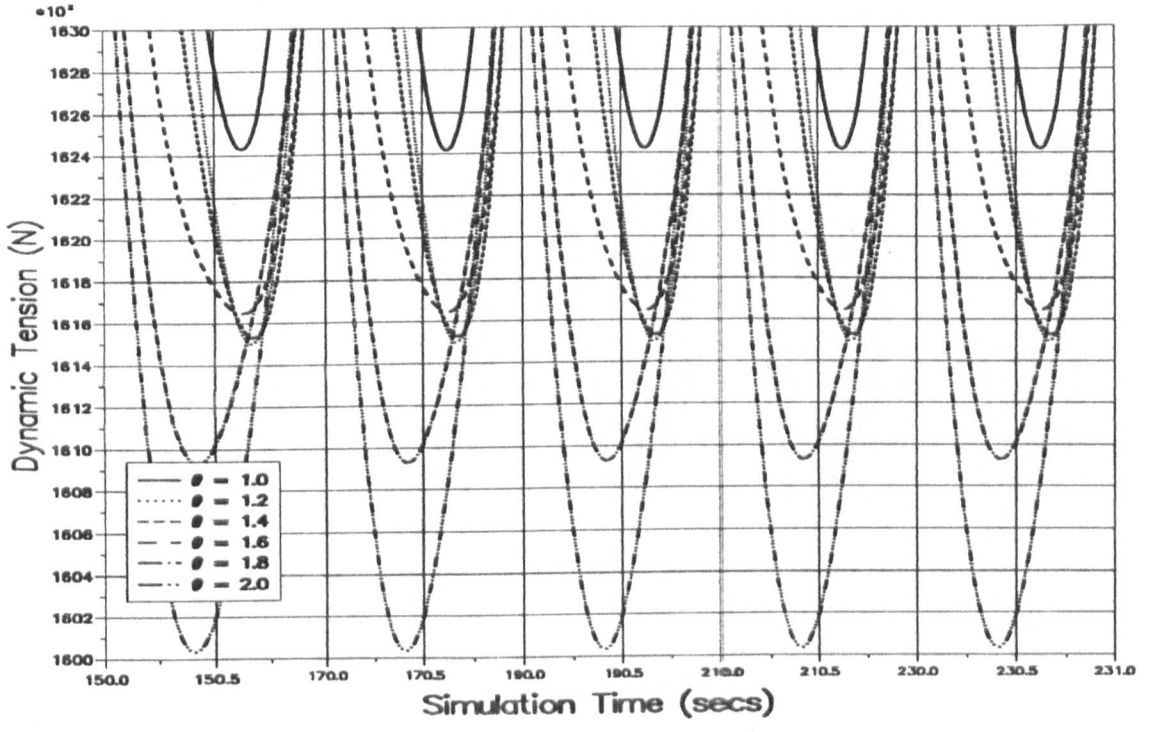

Figure 6.105 — Wilson Scheme Tension Troughs For $\Delta t = 0.001$.

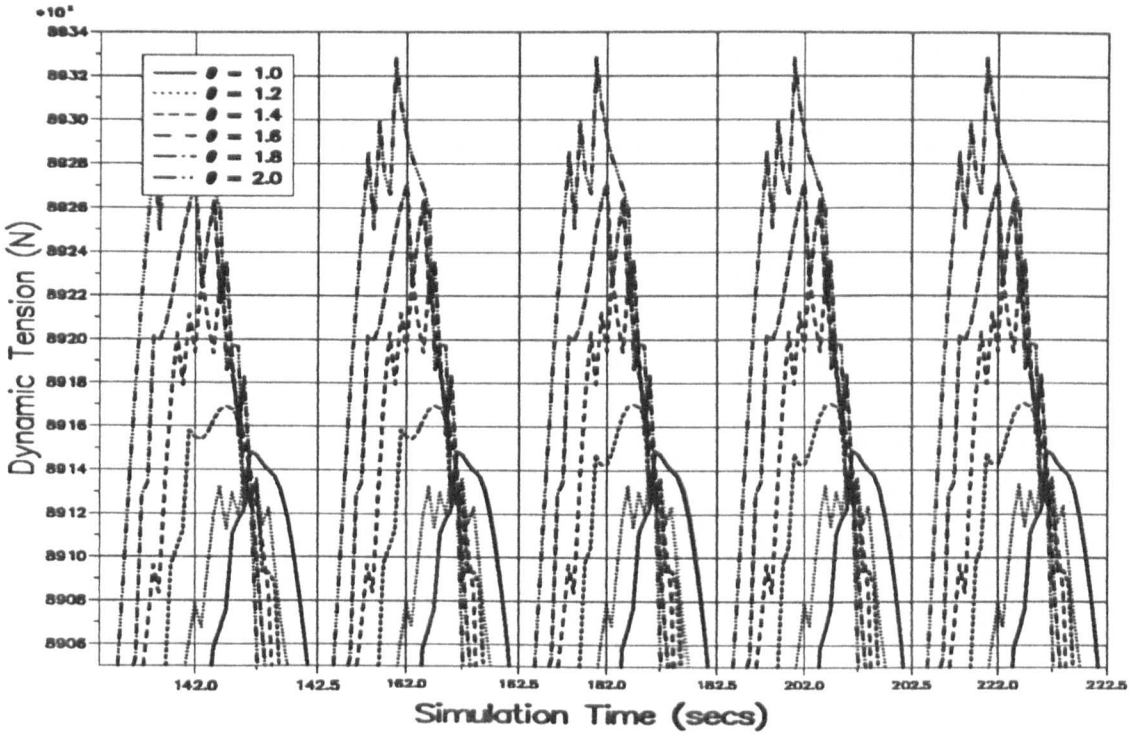

Figure 6.106 — Wilson Scheme Tension Peaks For $\Delta t = 0.025$.

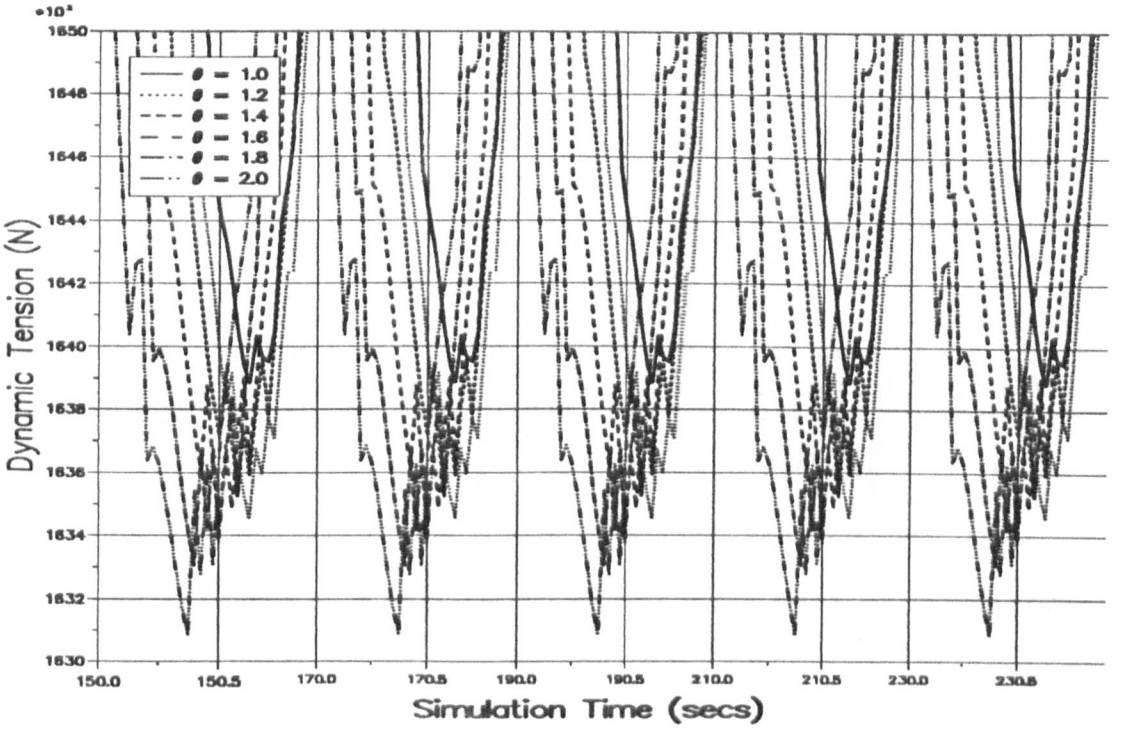

Figure 6.107 — Wilson Scheme Tension Troughs For $\Delta t = 0.025$.

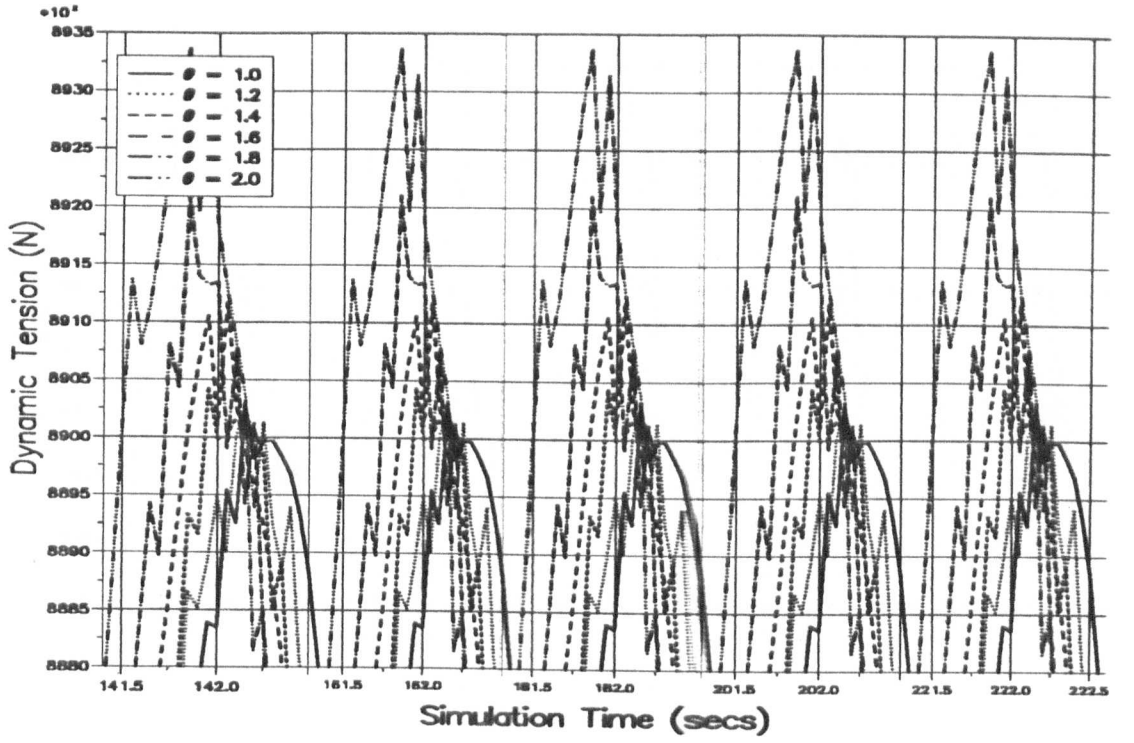

Figure 6.108 — Wilson Scheme Tension Peaks For $\Delta t = 0.05$.

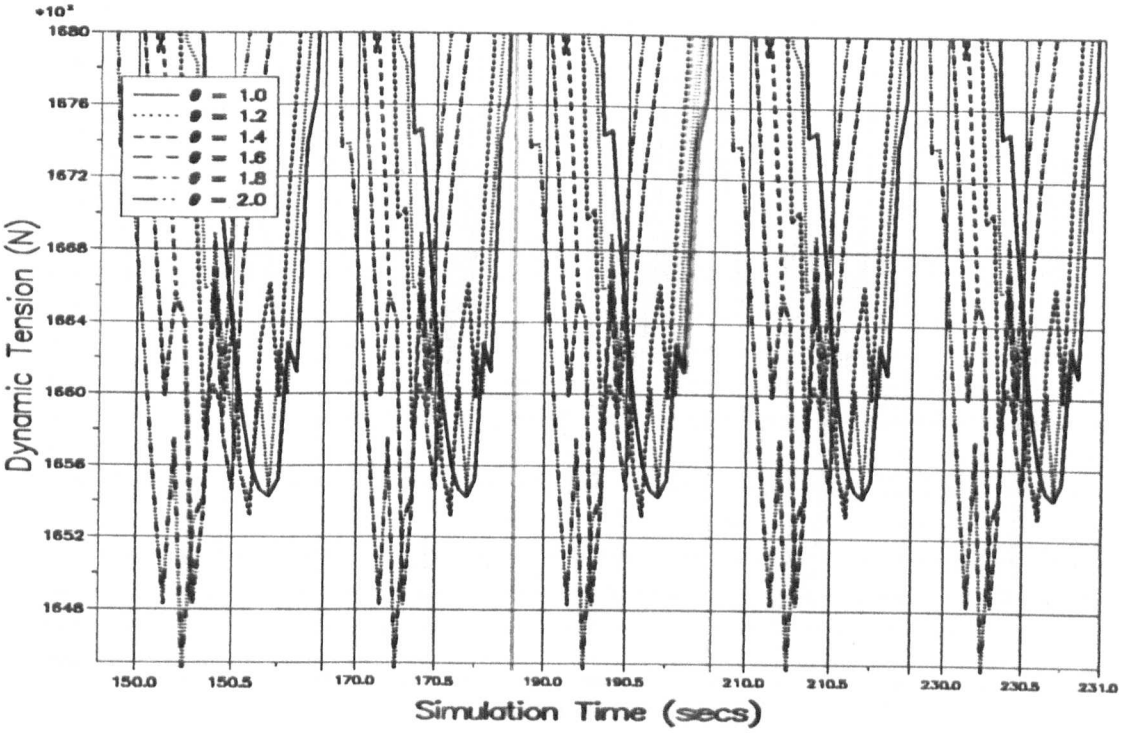

Figure 6.109 — Wilson Scheme Tension Troughs For $\Delta t = 0.05$.

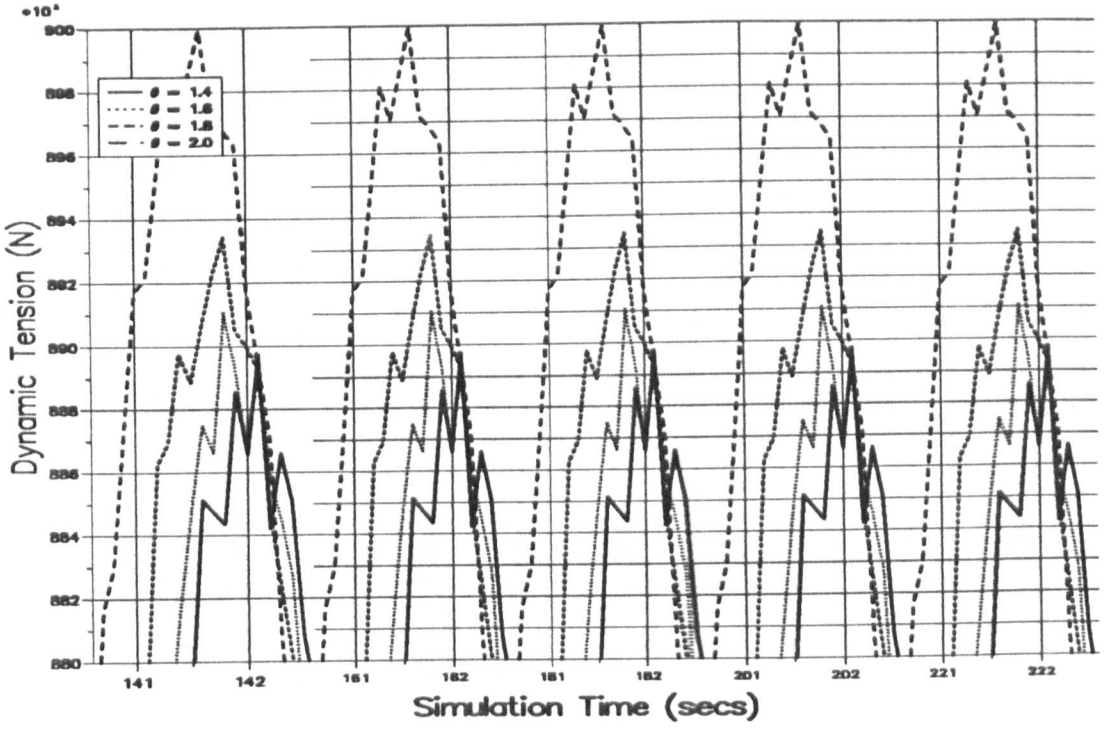

Figure 6.110 — Wilson Scheme Tension Peaks For $\Delta t = 0.1$.

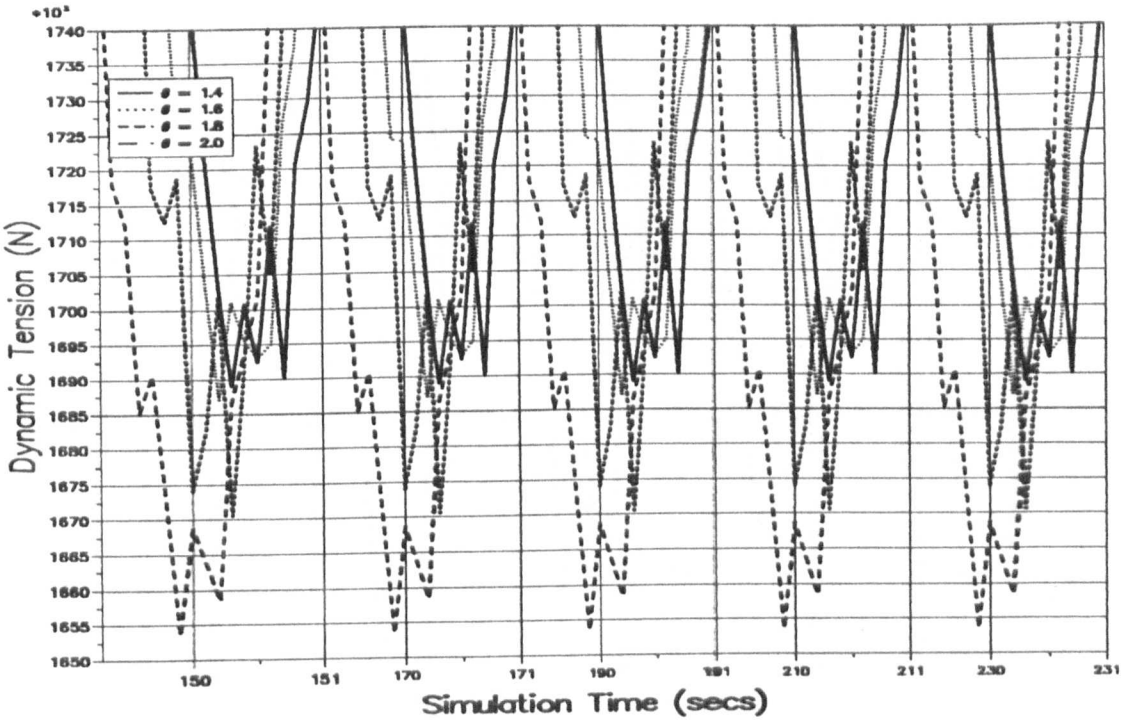

Figure 6.111 — Wilson Scheme Tension Troughs For $\Delta t = 0.1$.

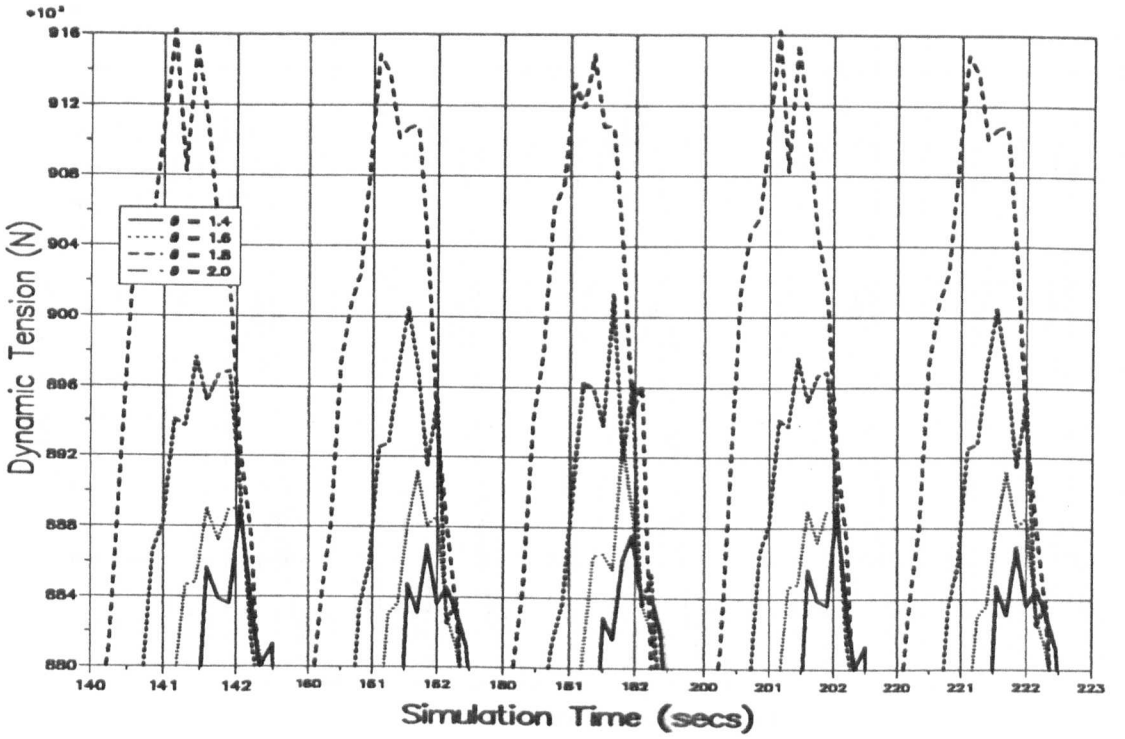

Figure 6.112 — Wilson Scheme Tension Peaks For $\Delta t = 0.15$.

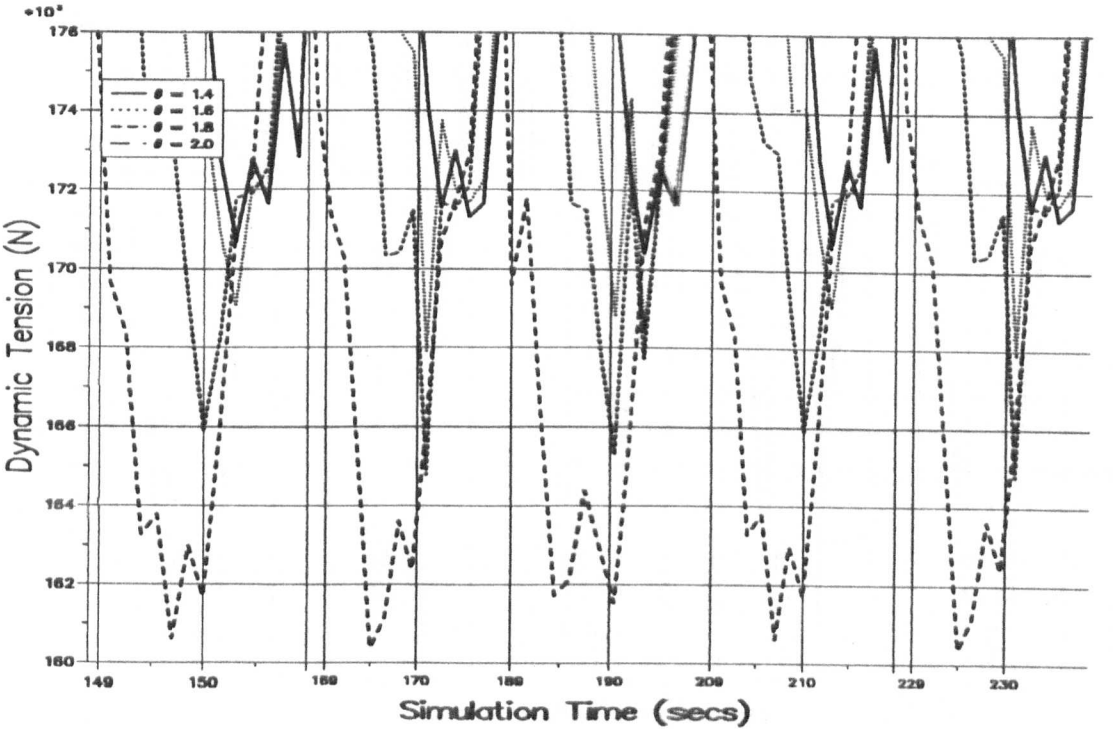

Figure 6.113 — Wilson Scheme Tension Troughs For $\Delta t = 0.15$.

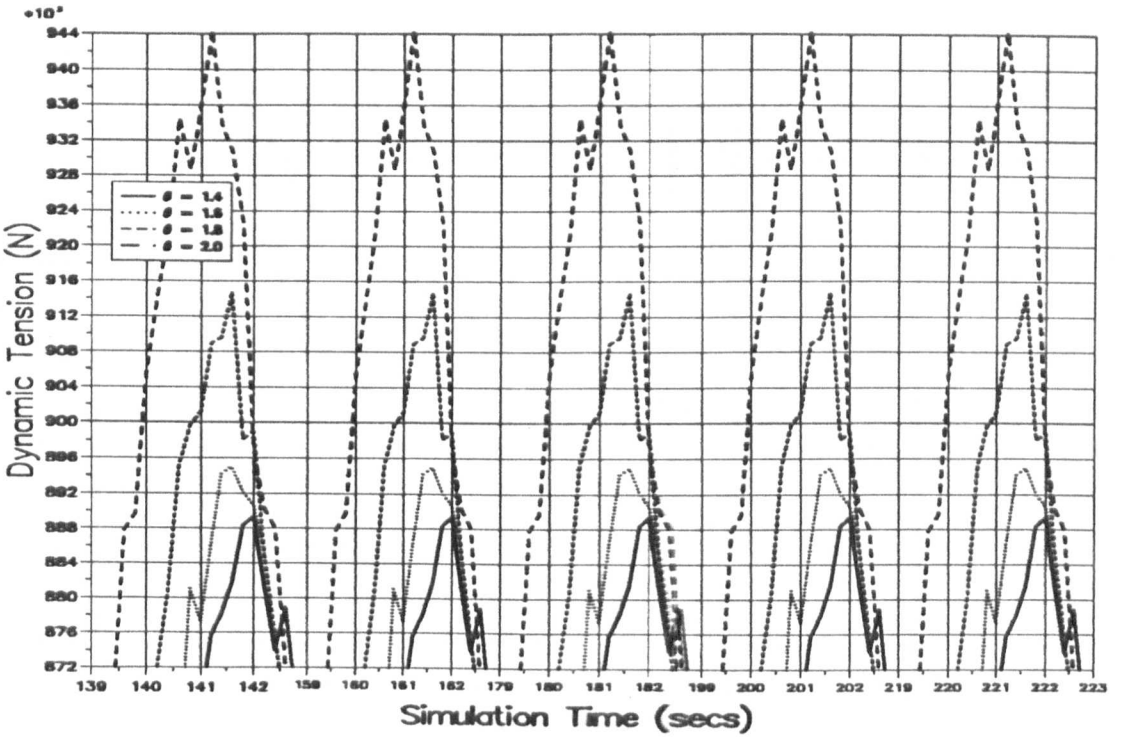

Figure 6.114 — Wilson Scheme Tension Peaks For $\Delta t = 0.2$.

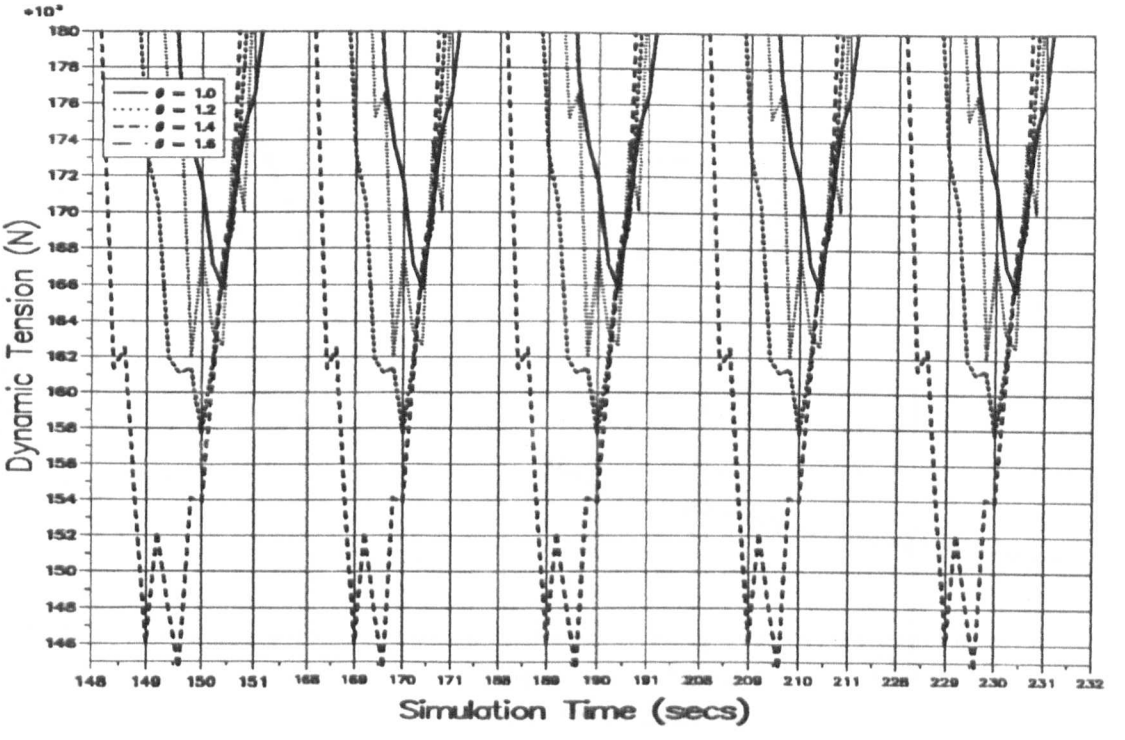

Figure 6.115 — Wilson Scheme Tension Troughs For $\Delta t = 0.2$.

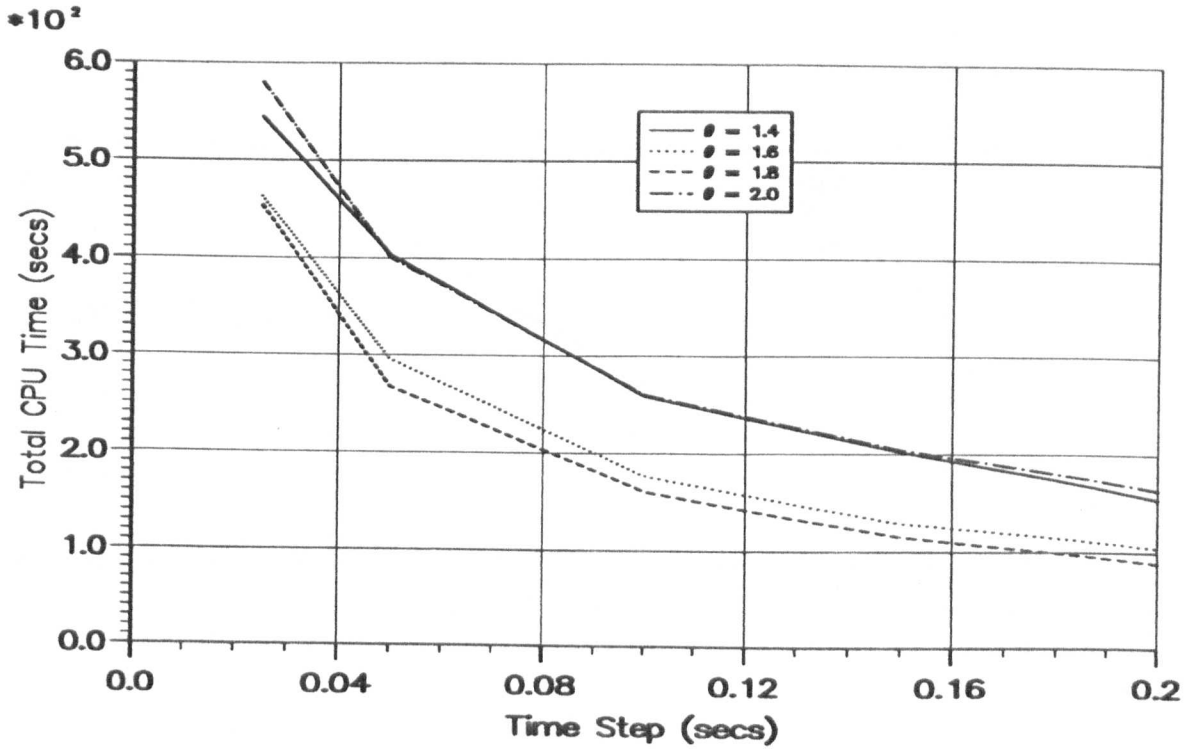

Figure 6.116 — Total CPU Time For Wilson Scheme With Different θ.

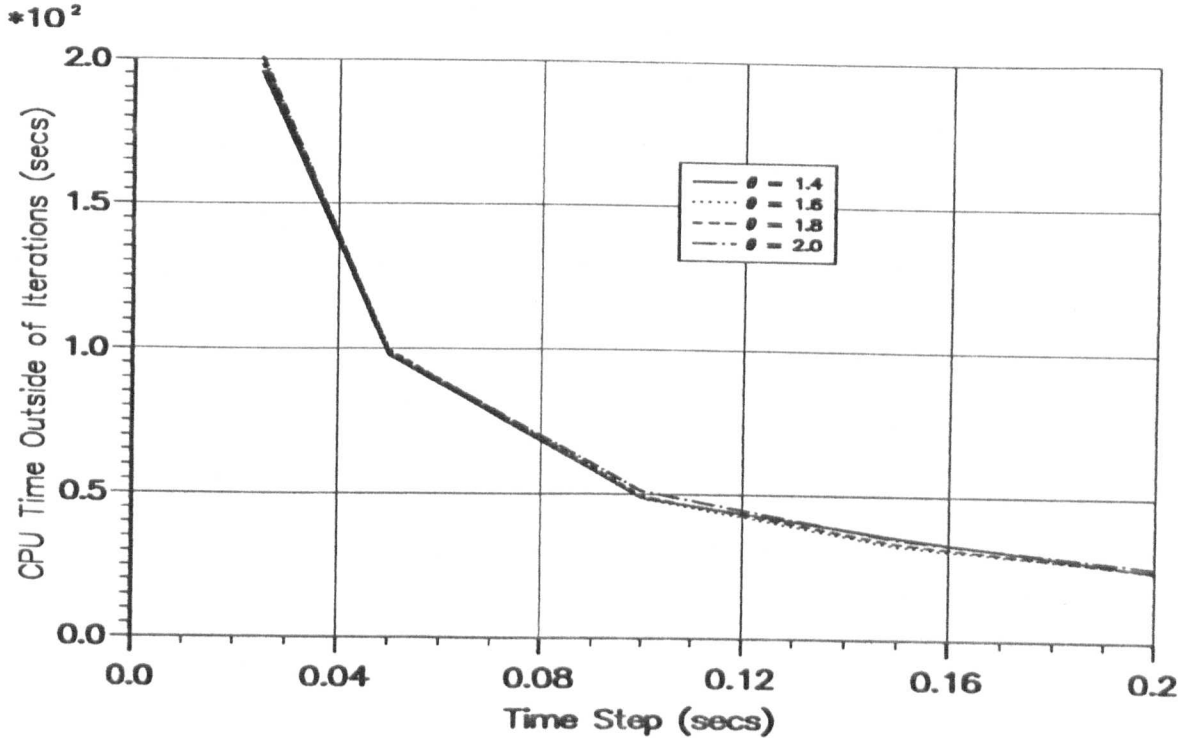

Figure 6.117 — CPU_1 For Different θ.

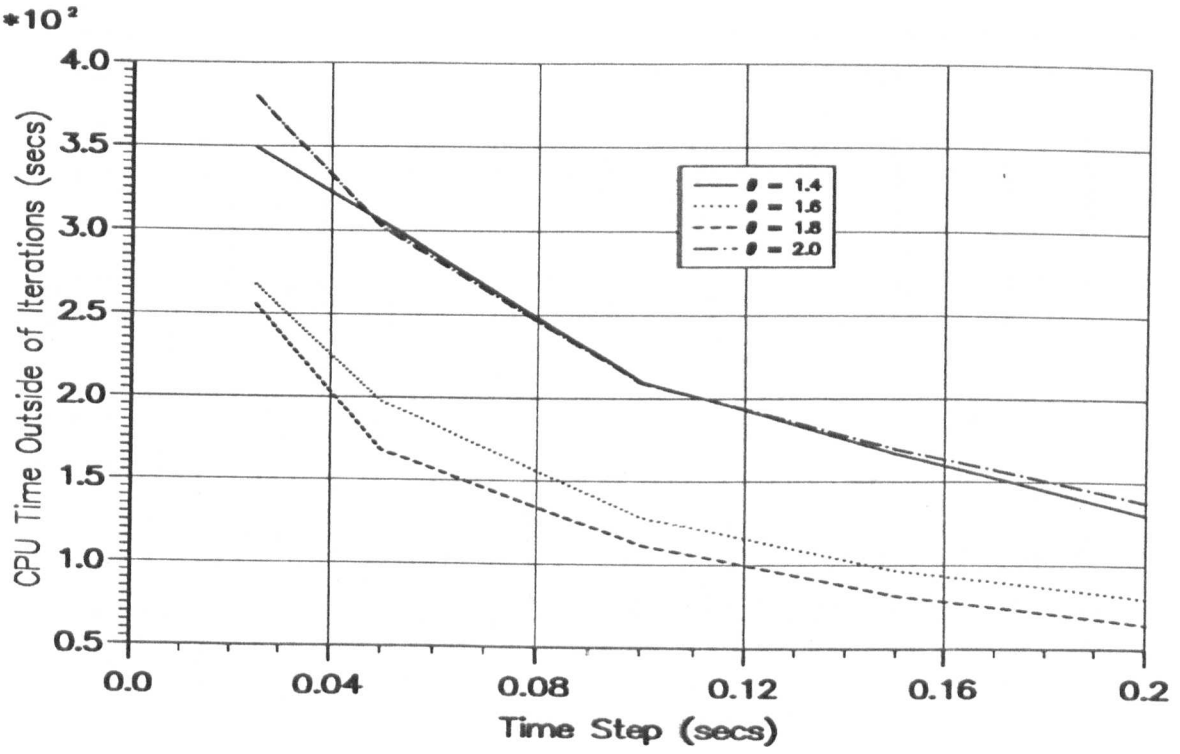

Figure 6.118 — CPU_2 For Different θ.

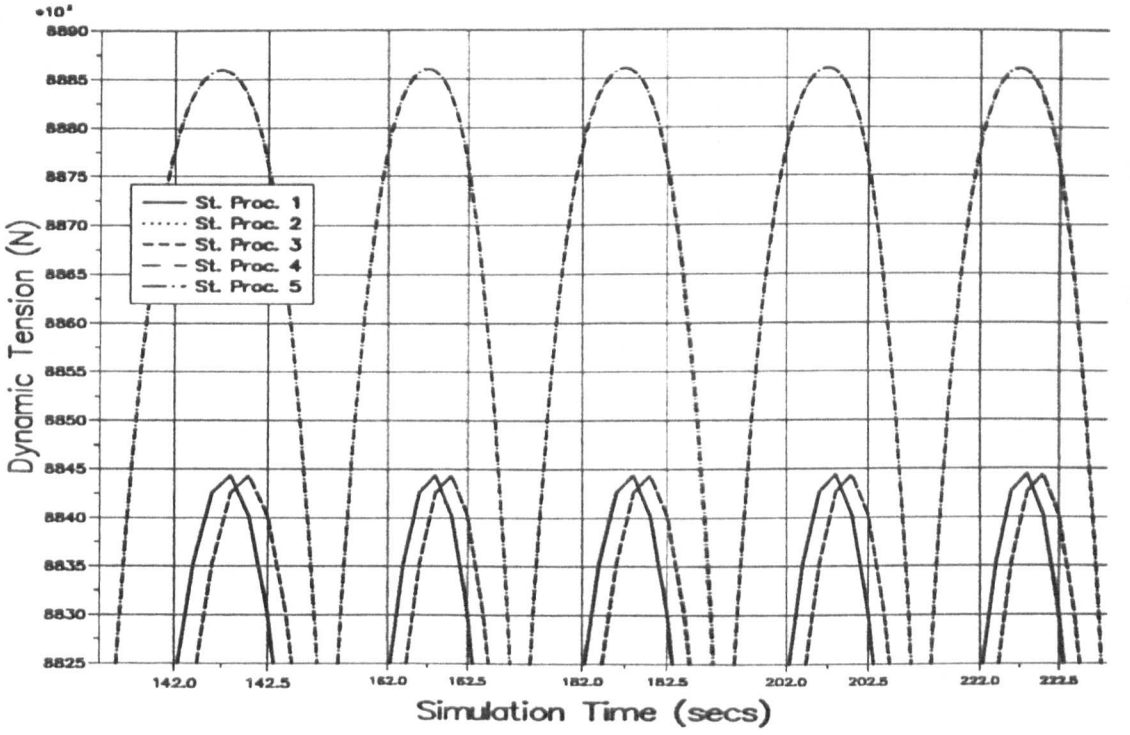

Figure 6.119 — Houbolt Peaks With Different Starting Procedures.

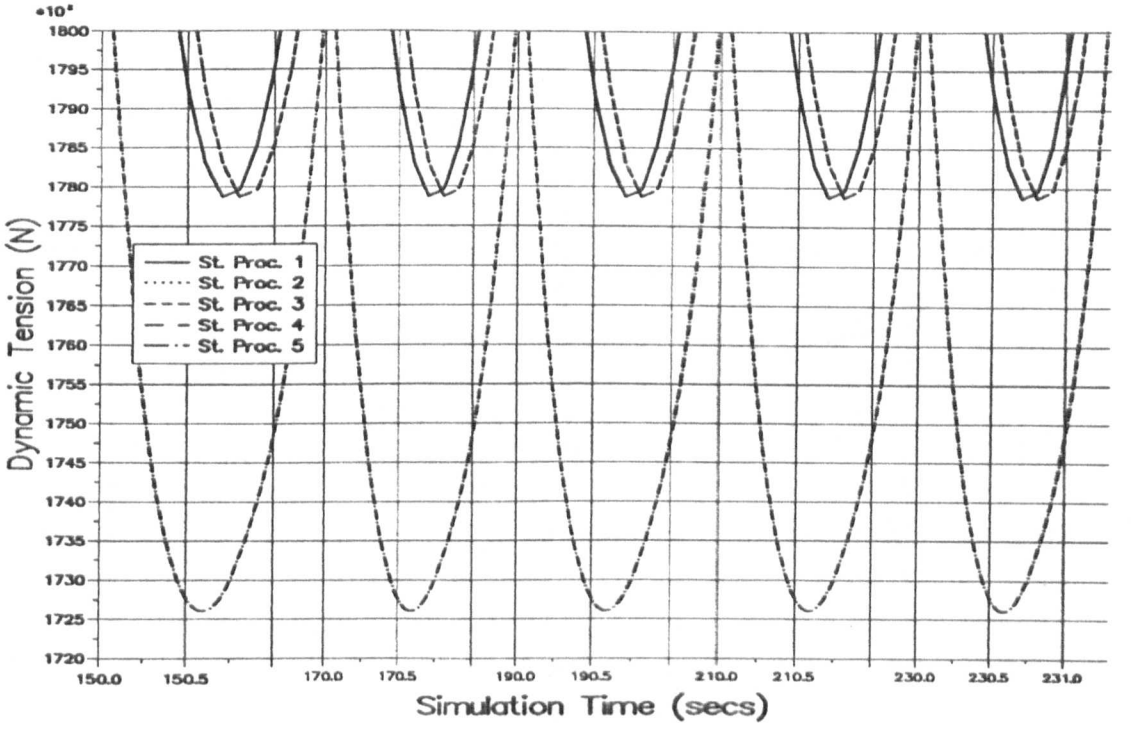

Figure 6.120 — Houbolt Troughs With Different Starting Procedures.

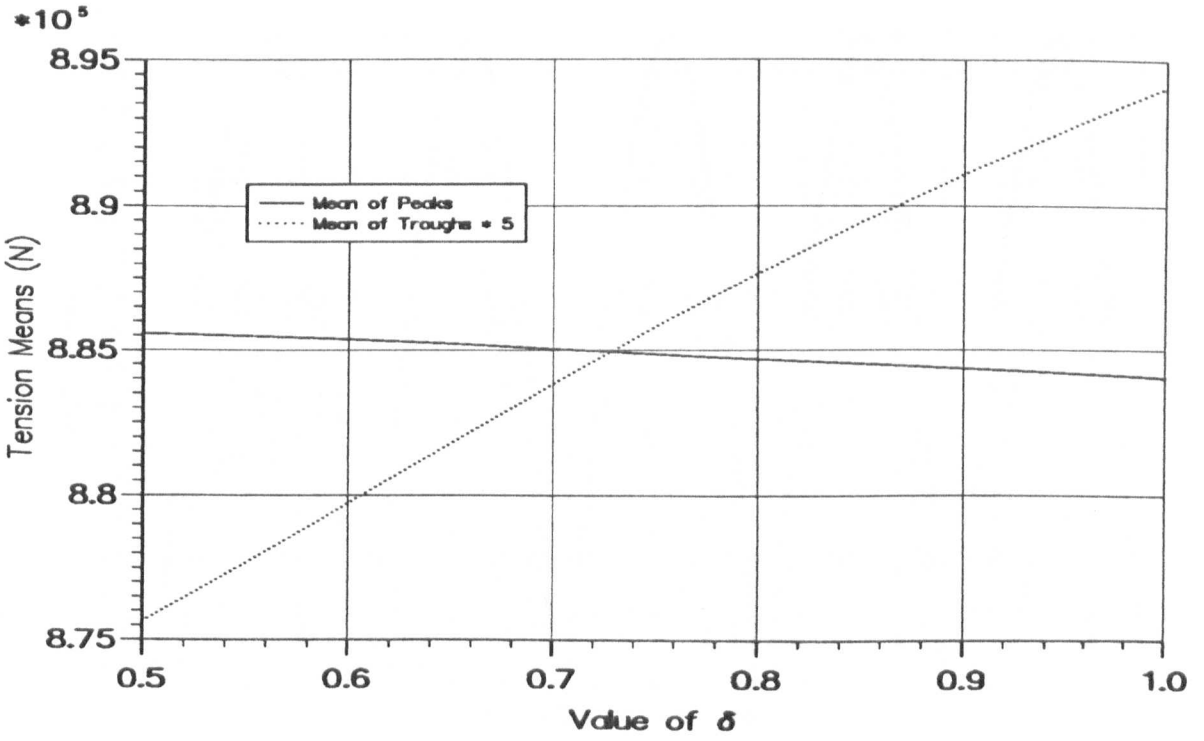

Figure 6.121 — Variation of Newmark Peaks and Troughs With δ.

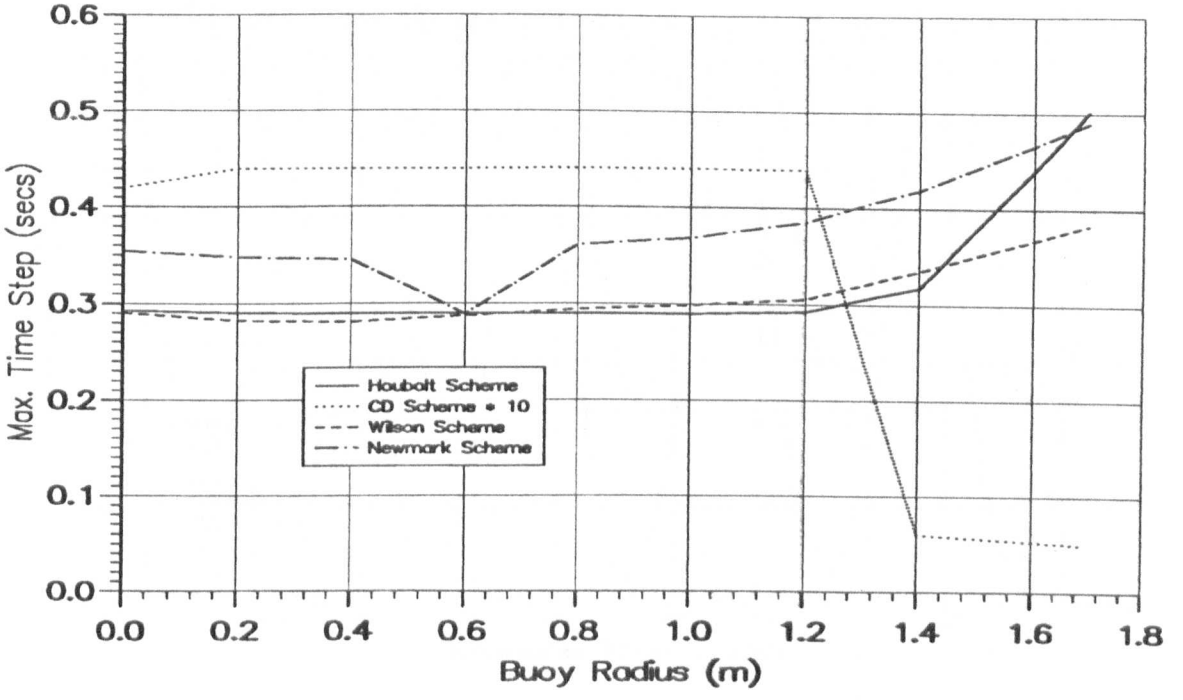

Figure 6.122 — Influence of SSB on the Max. Value of Δt.

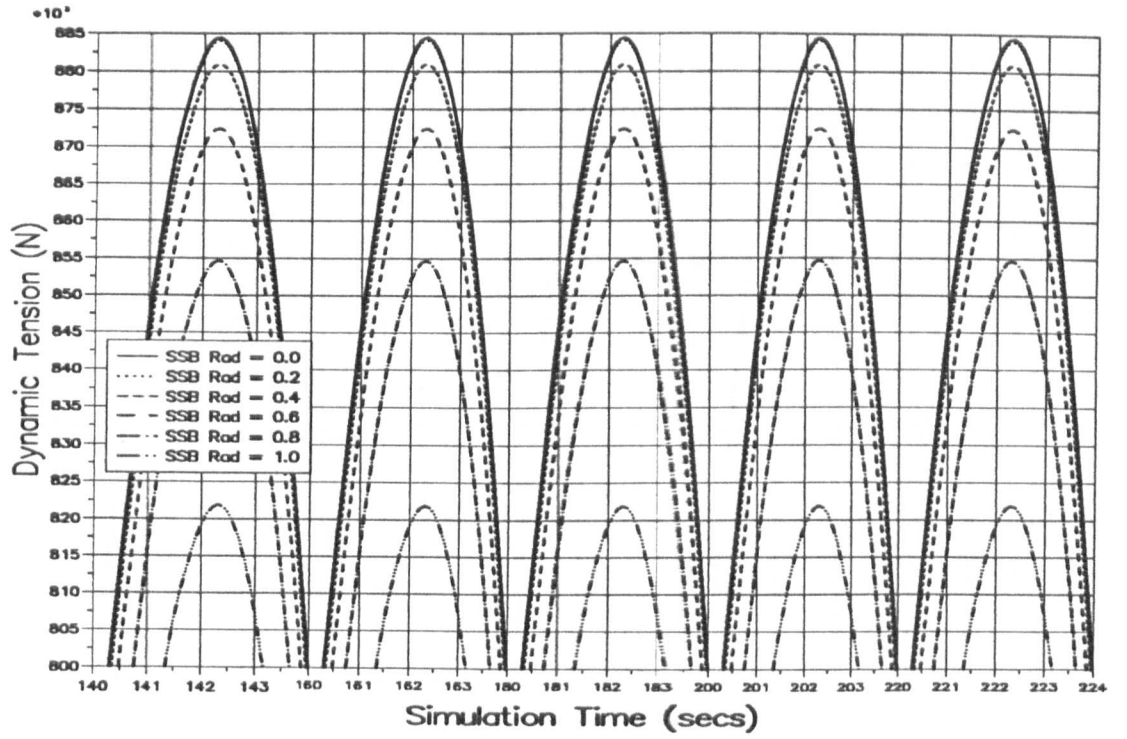

Figure 6.123 — Houbolt Peaks for Different SSB Radii.

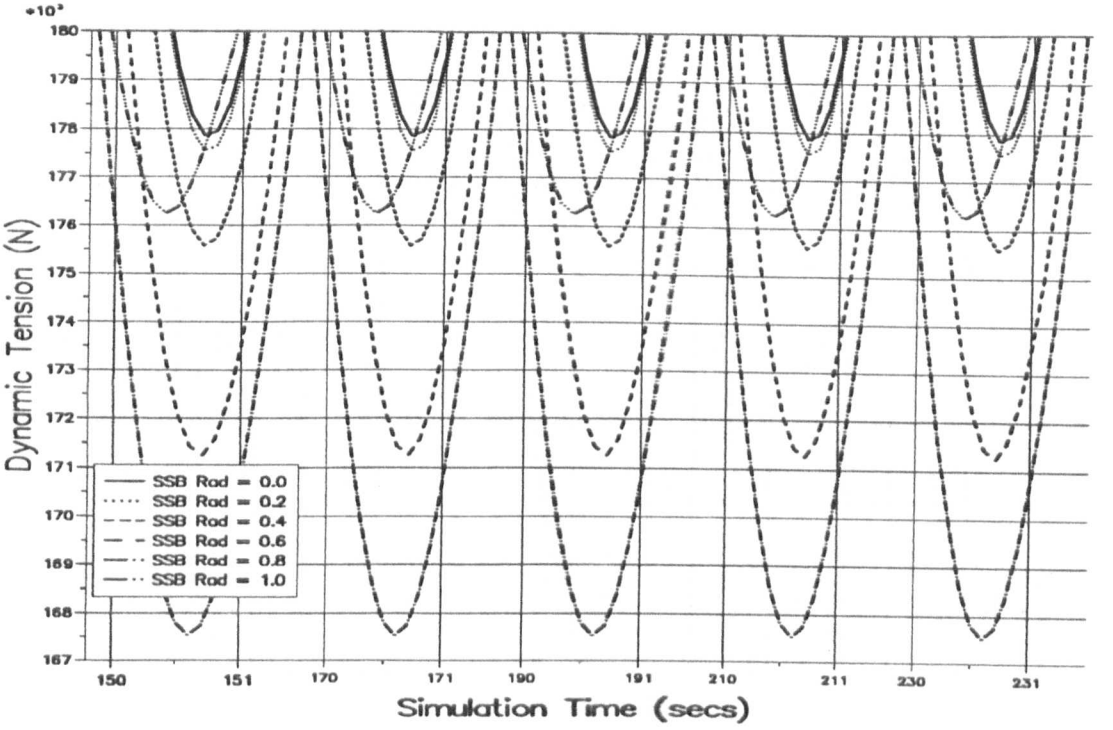

Figure 6.124 — Houbolt Troughs for Different SSB Radii.

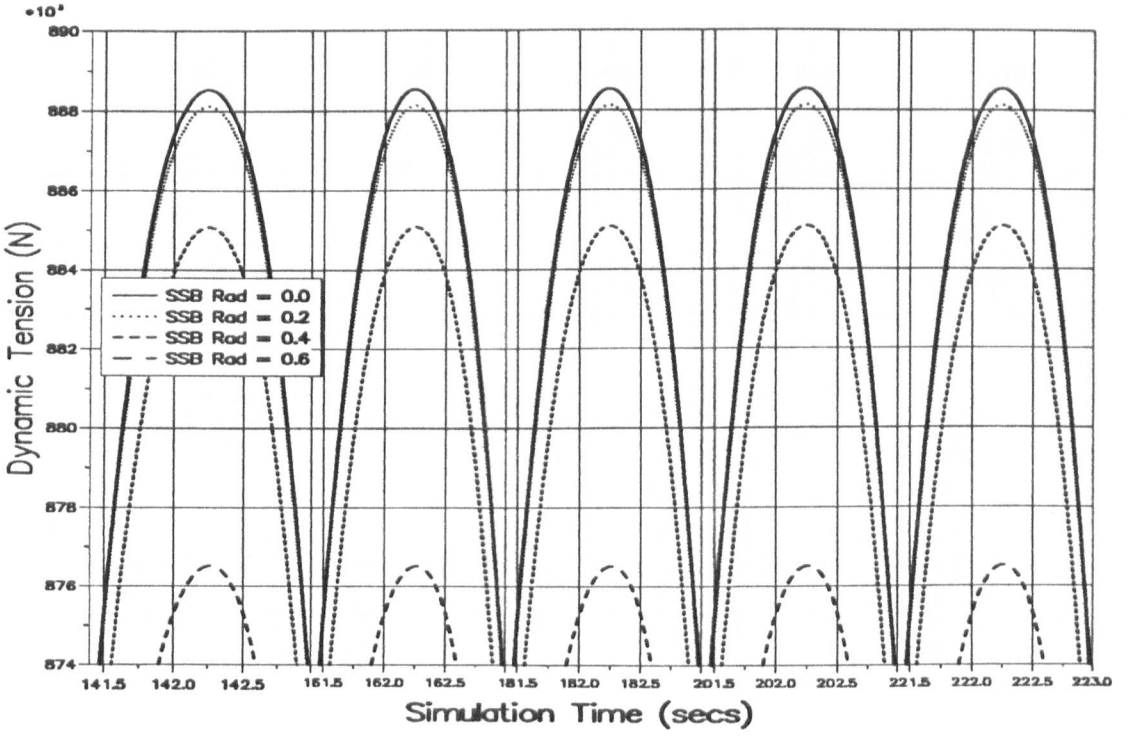

Figure 6.125 — CD Peaks for Different SSB Radii.

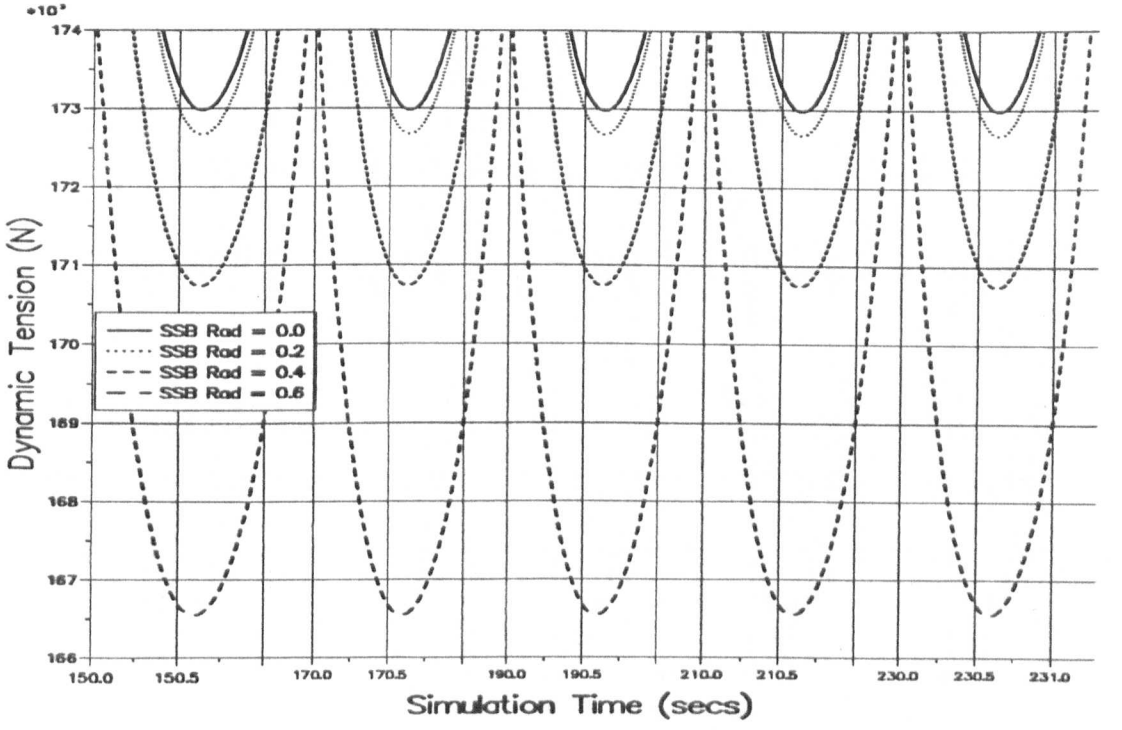

Figure 6.126 — CD Troughs for Different SSB Radii.

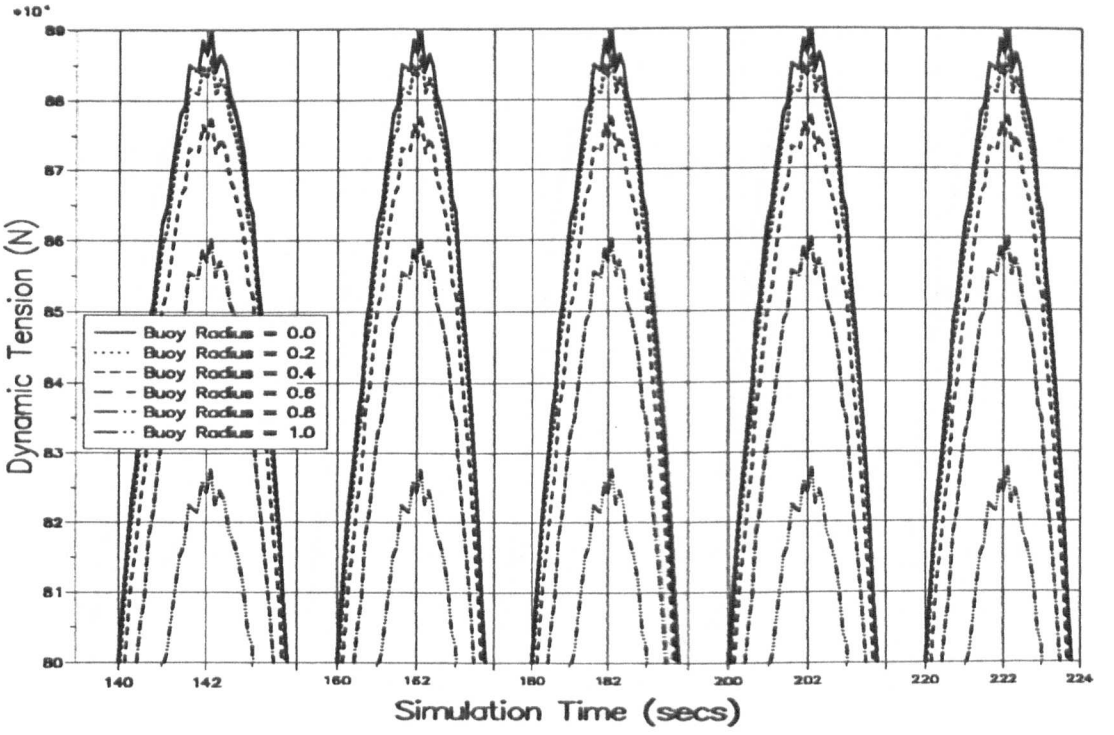

Figure 6.127 — Wilson Peaks for Different SSB Radii.

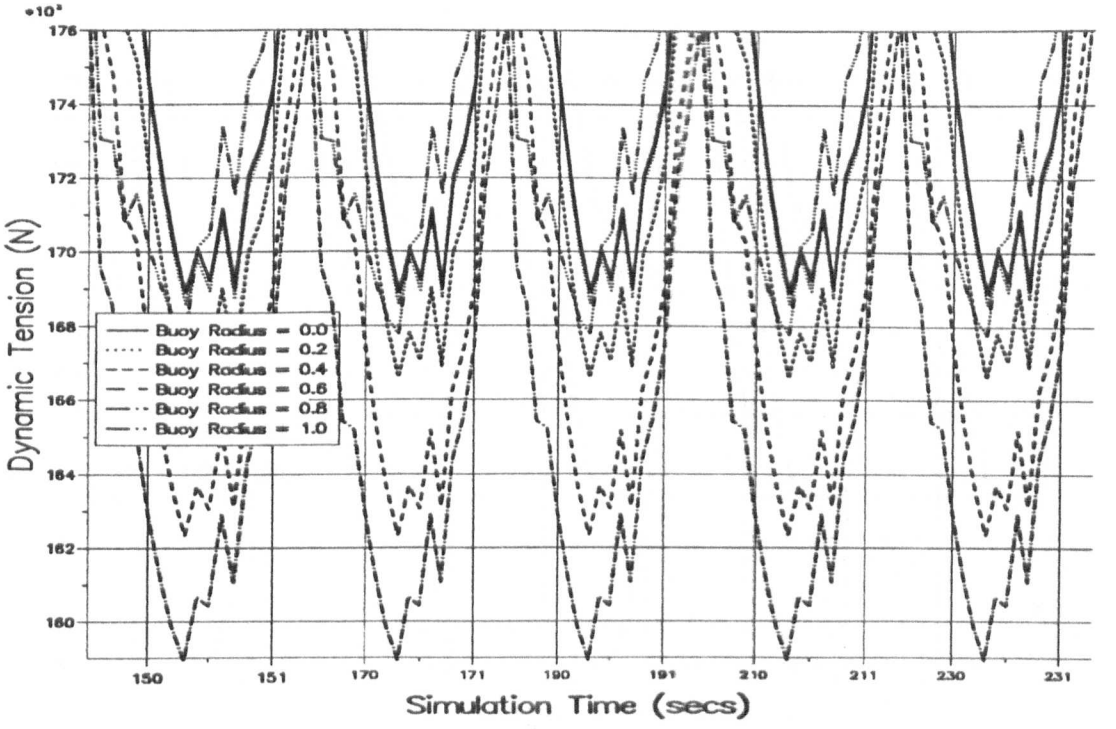

Figure 6.128 — Wilson Troughs for Different SSB Radii.

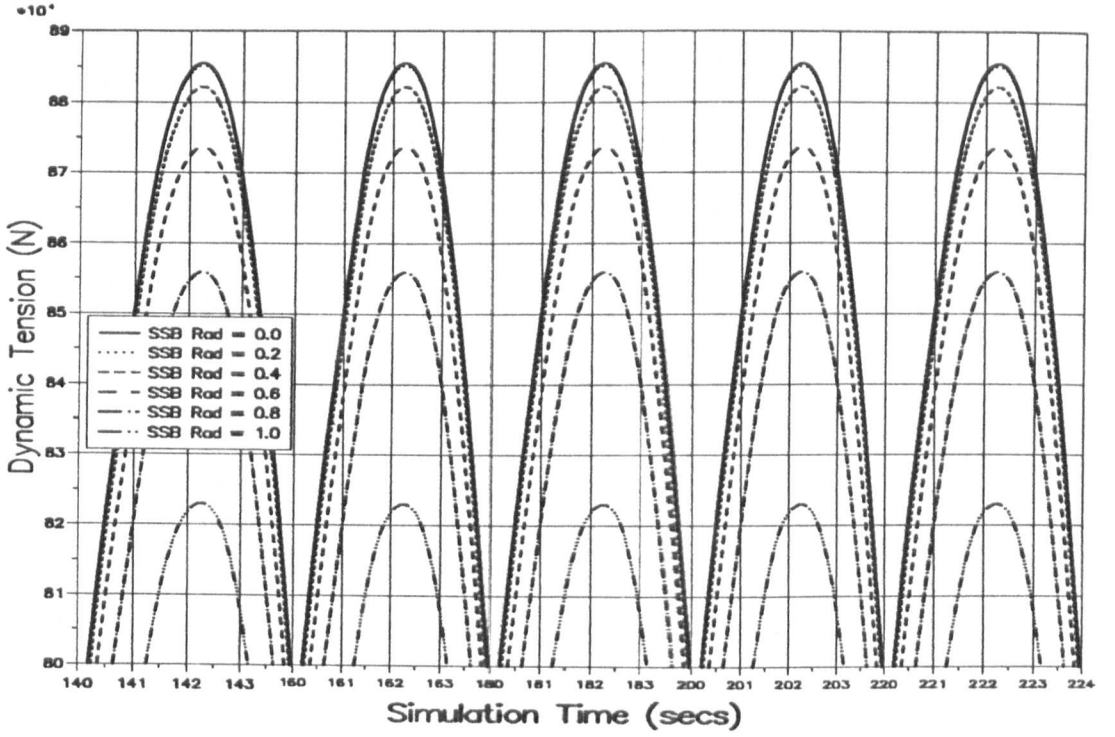

Figure 6.129 — Newmark Peaks for Different SSB Radii.

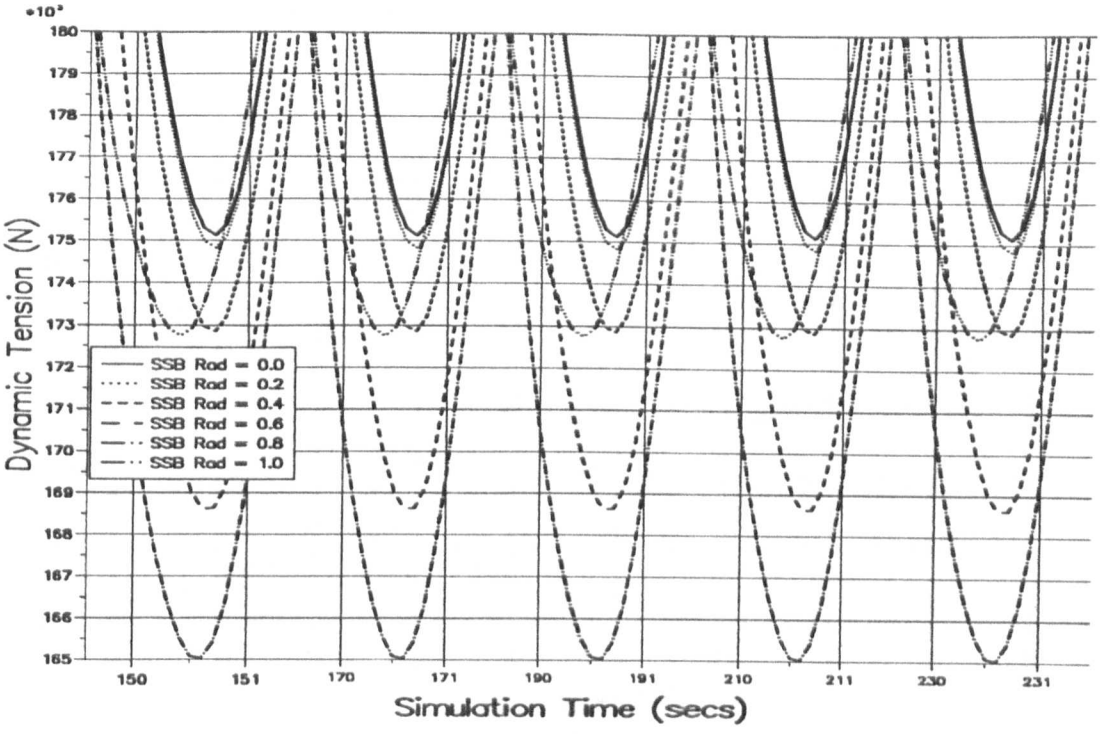

Figure 6.130 — Newmark Troughs for Different SSB Radii.

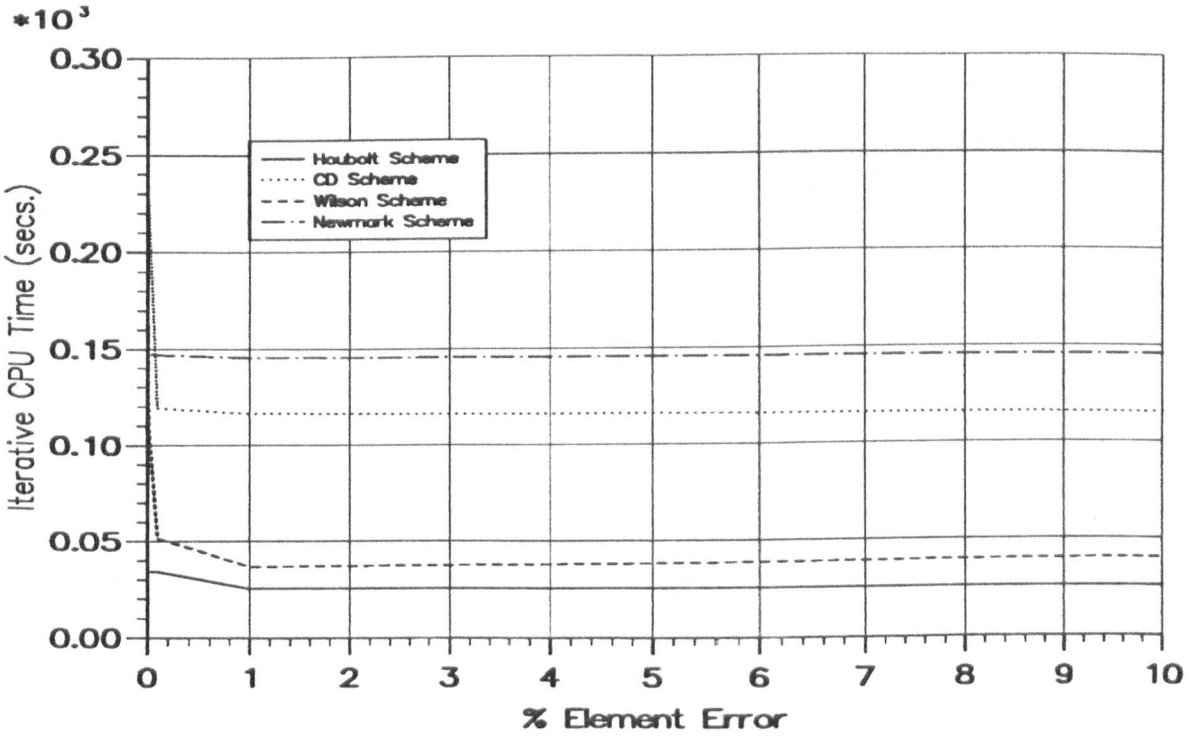

Figure 6.131 — CPU_2 vs. % Convergence Limit For Elements.

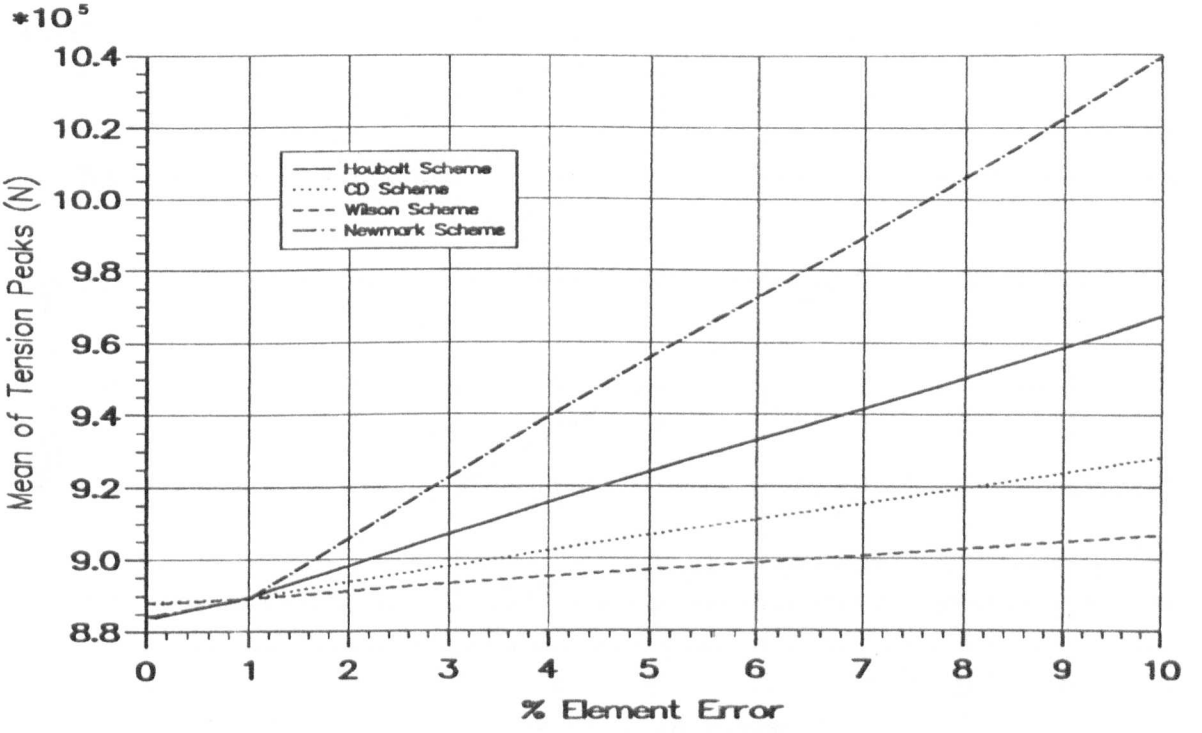

Figure 6.132 — $\bar{T}_p$ vs. % Convergence Limit For Elements.

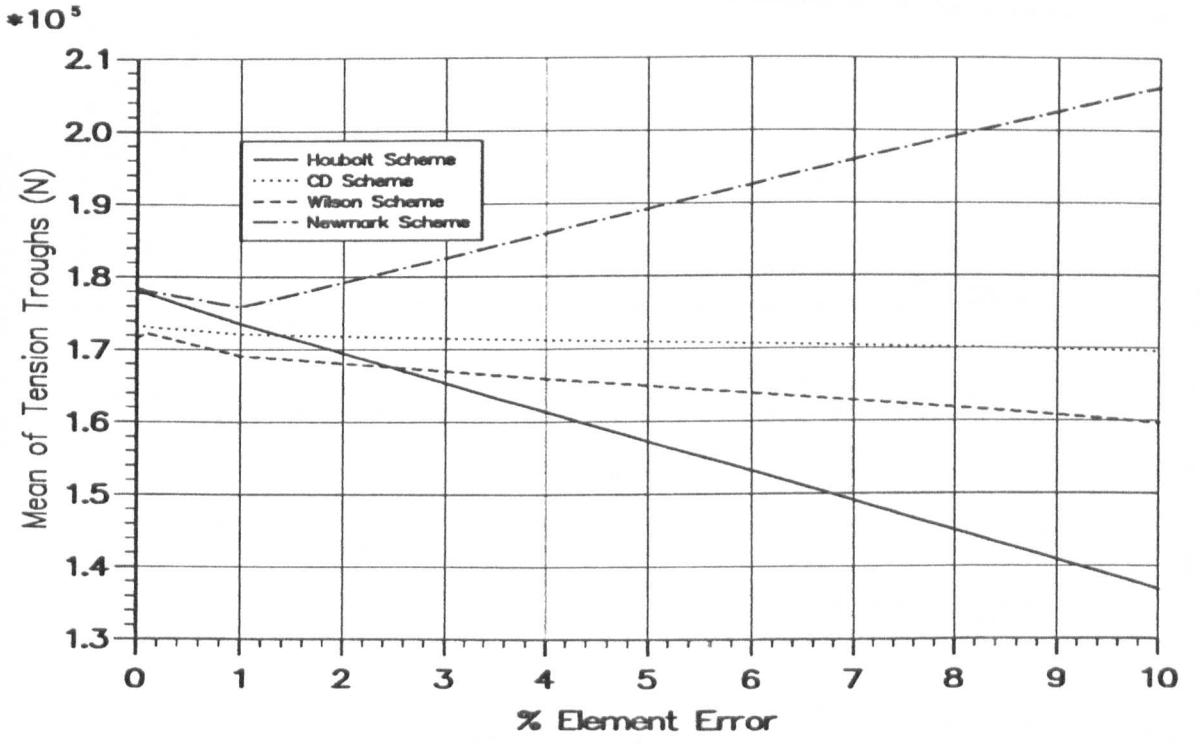

Figure 6.133 — $\bar{T}_t$ vs. % Convergence Limit For Elements.

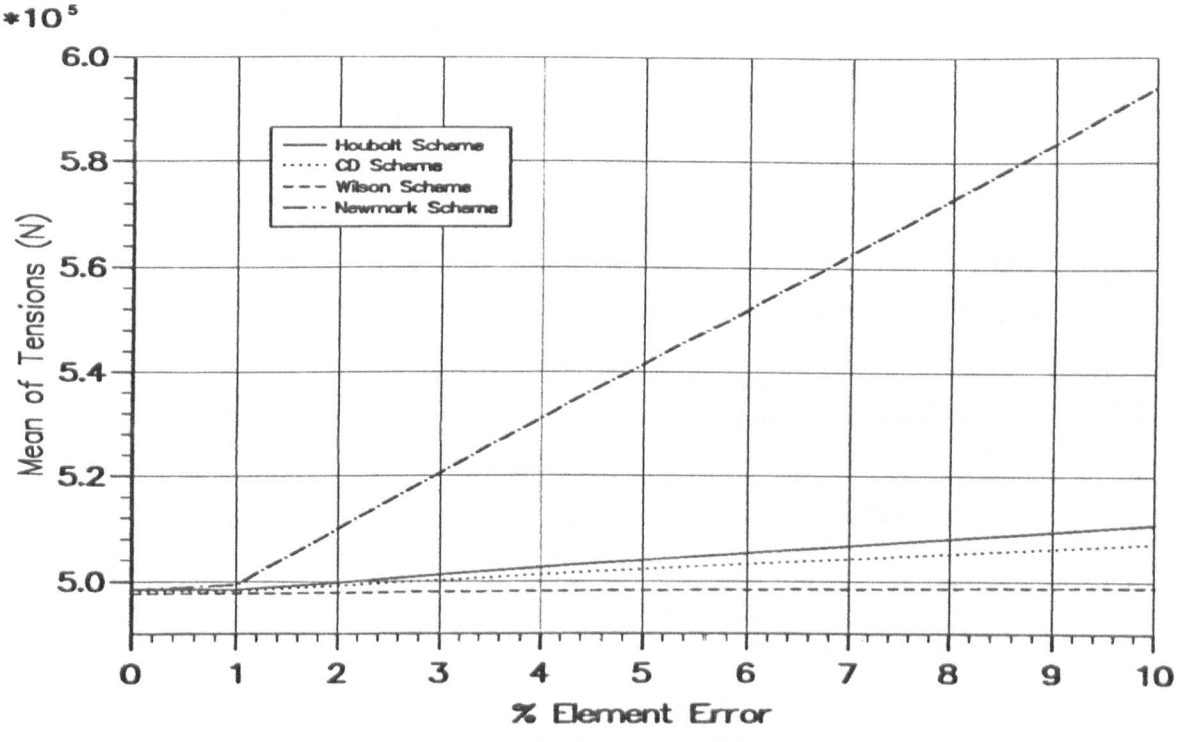

Figure 6.134 — $\bar{T}_m$ vs. % Convergence Limit For Elements.

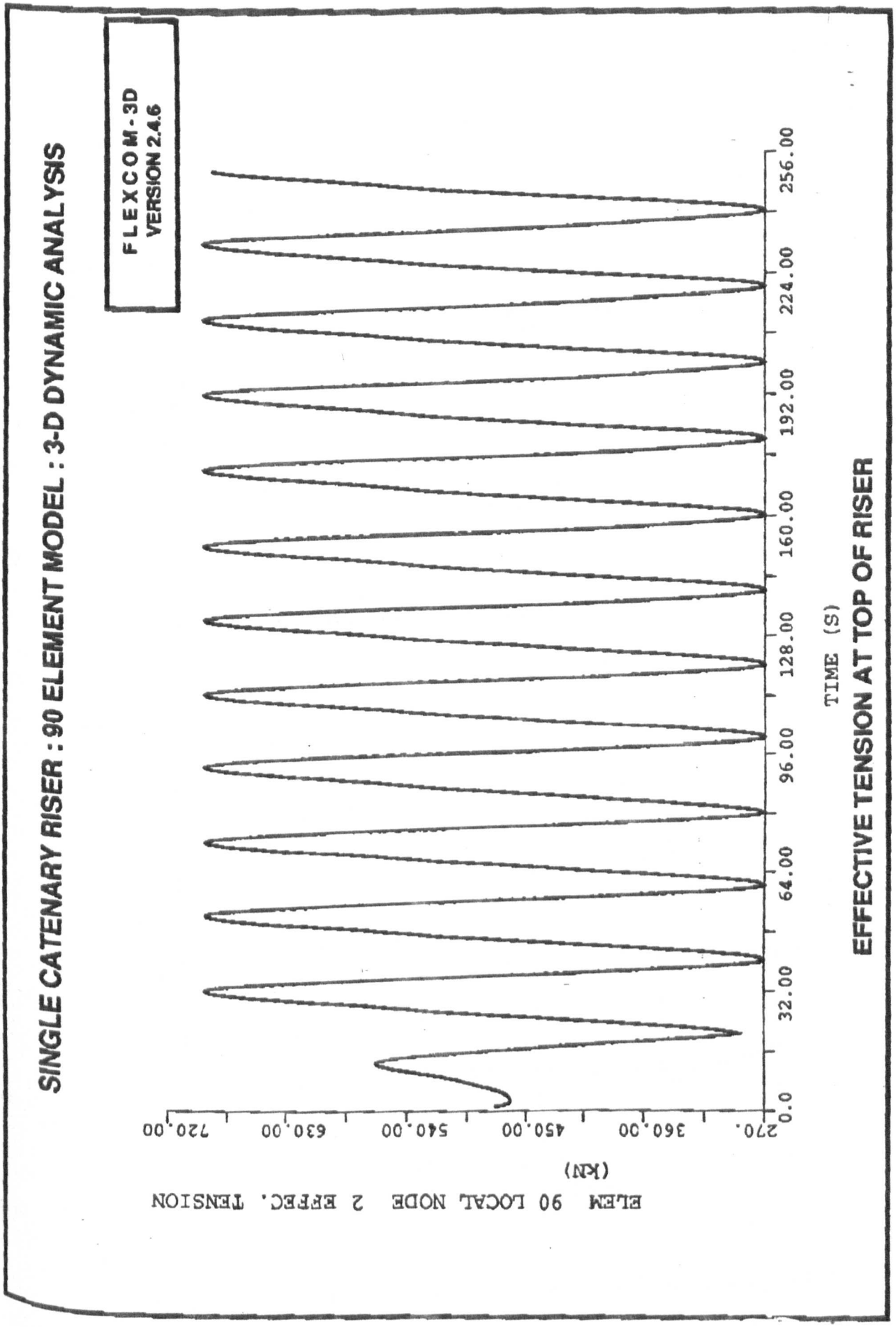

Figure 7.0 - FLEXCOM-3D (90E), McNamara(1993)

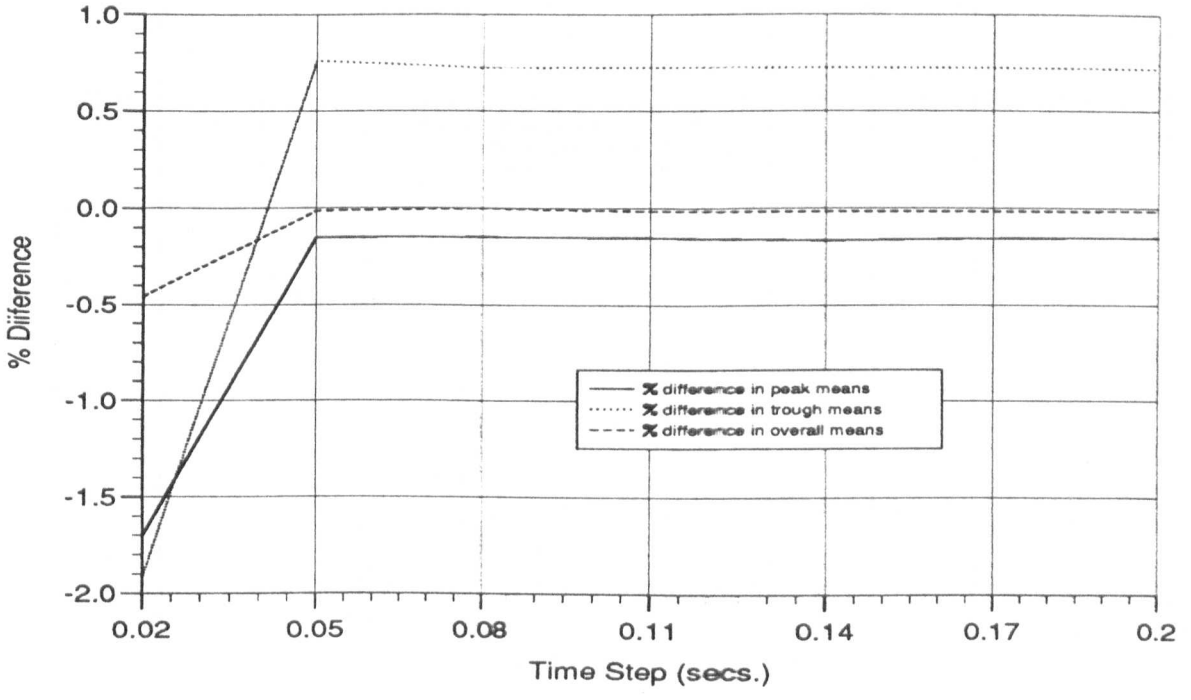

Figure 7.1 — % Differences in $\bar{T}_p$, $\bar{T}_t$ and $\bar{T}_m$ for 2D and 3D vs. Δt.

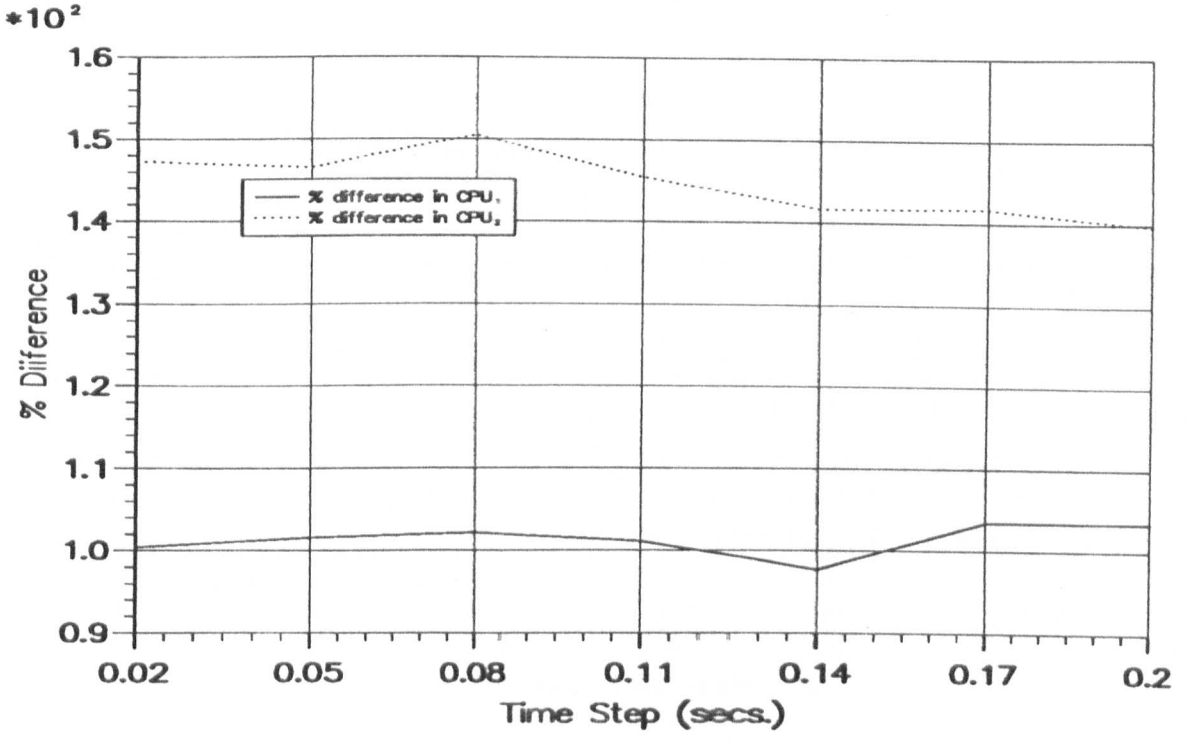

Figure 7.2 — % Differences in CPU_1 and CPU_2 for 2D and 3D vs. Δt.

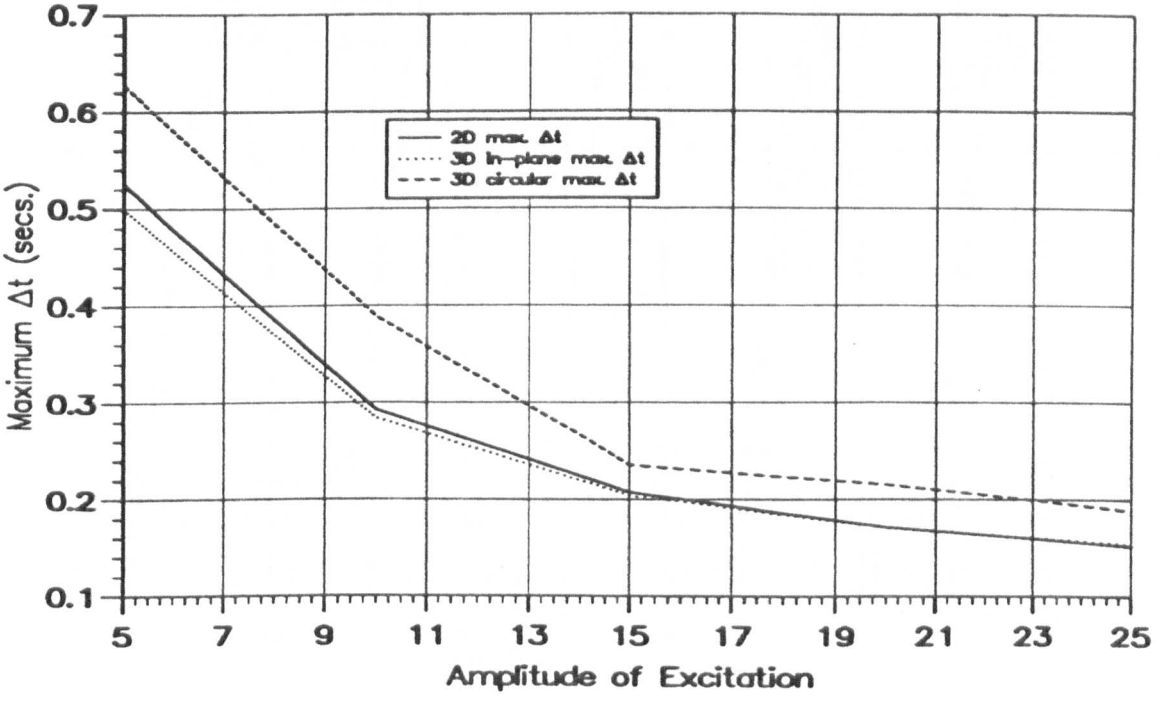

Figure 7.3 — Max. Δt vs. Excitation Amplitude for 3D Model.

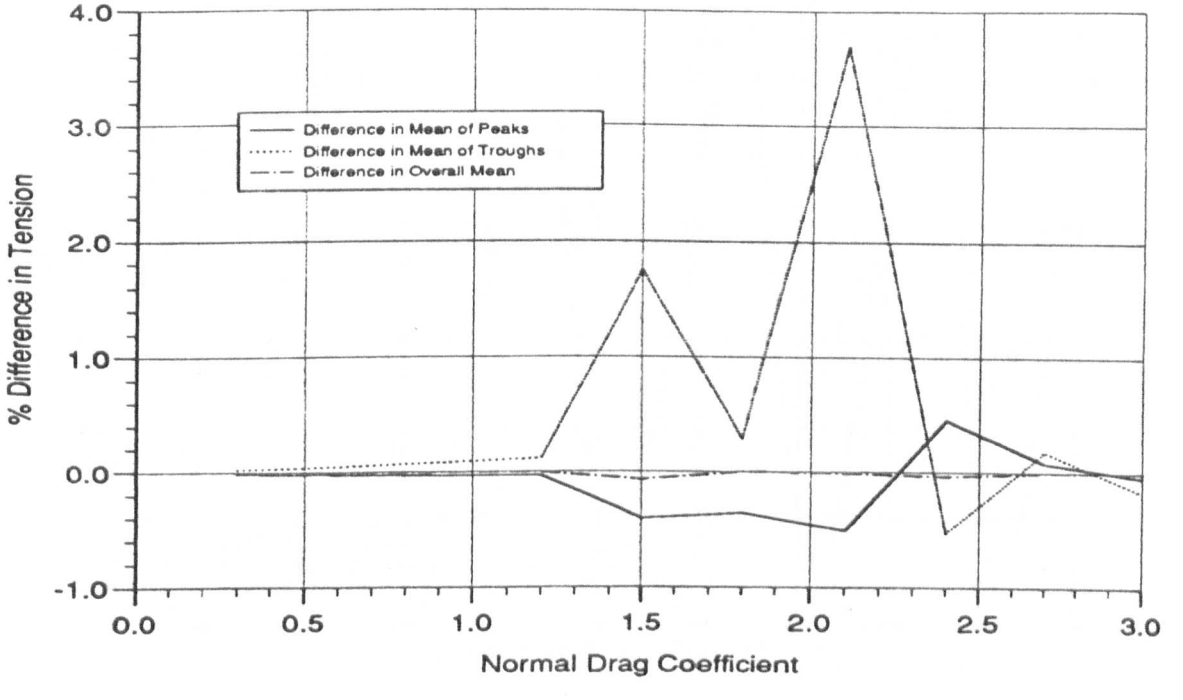

Figure 7.4 — $\bar{T}_p$, $\bar{T}_t$ and $\bar{T}_m$ with and Without Tang. Drag vs. Cd_n.

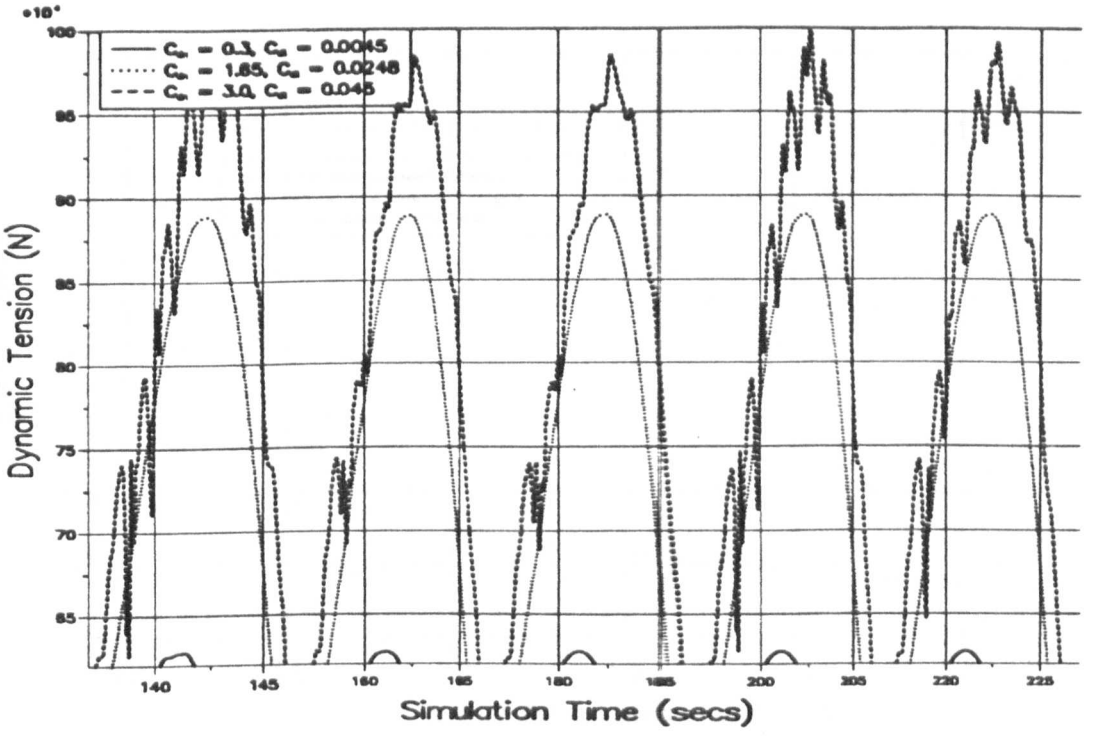

Figure 7.5 — Tension Peaks With Different Drag Coefficients.

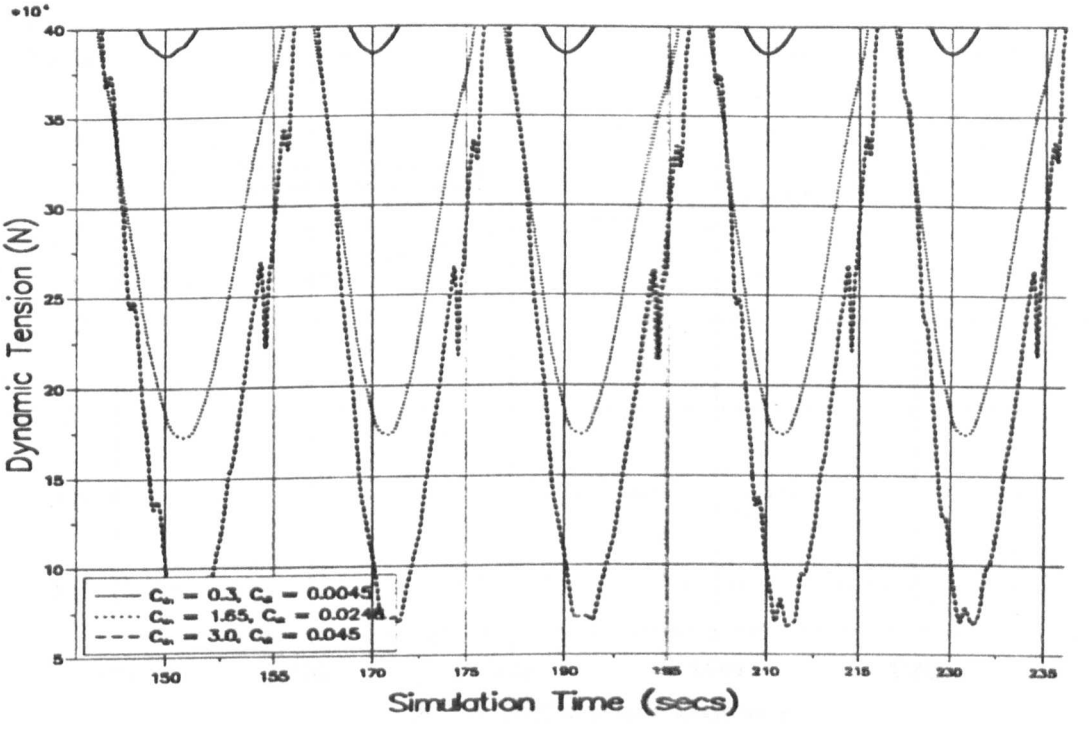

Figure 7.6 — Tension Troughs With Different Drag Coefficients.

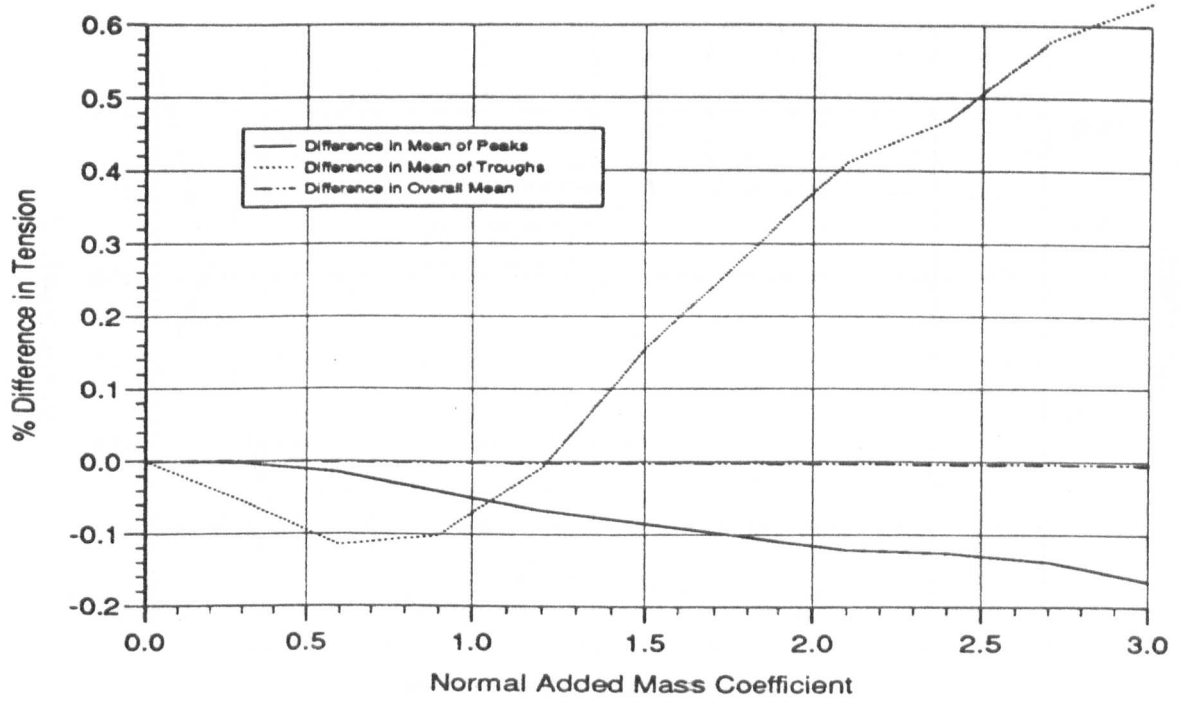

Figure 7.7 — $\bar{T}_p$, $\bar{T}_m$ and $\bar{T}_t$ with and Without Ca_t vs. Ca_n

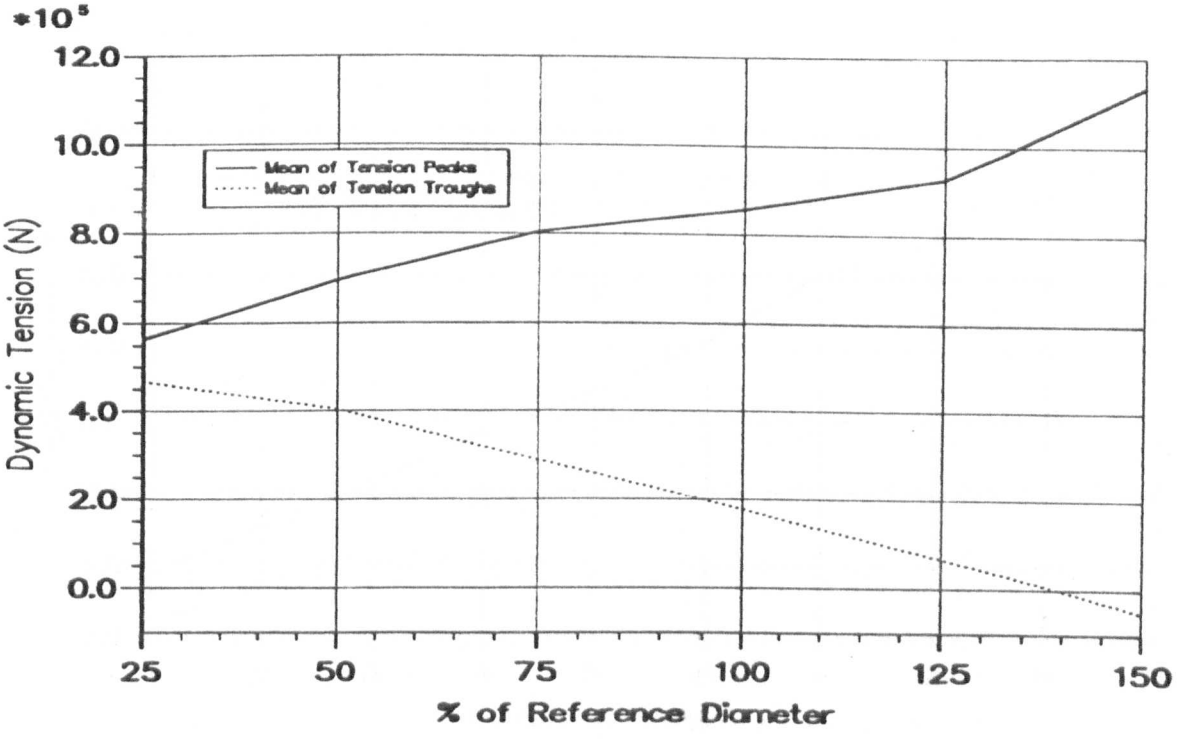

Figure 7.8 — $\bar{T}_p$ and $\bar{T}_t$ vs. % of Reference Diameter.

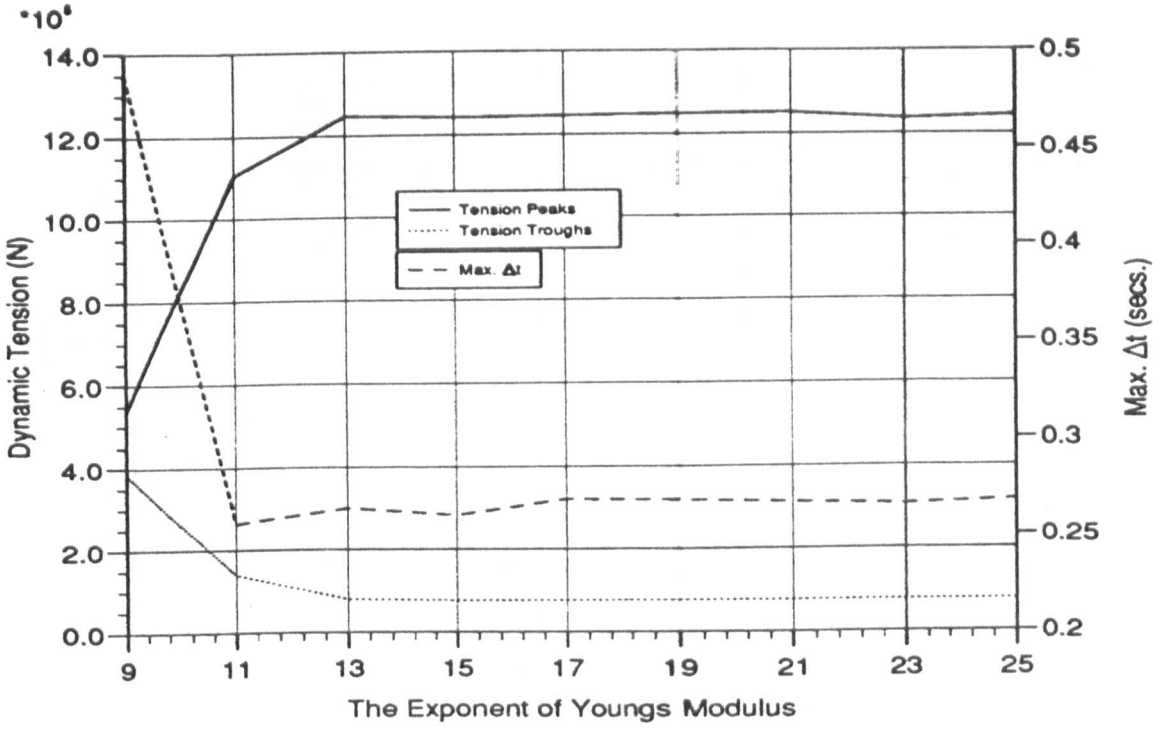

Figure 7.9 — $\bar{T}_p$, $\bar{T}_t$ and Max. Δt vs. the Exponent of E.

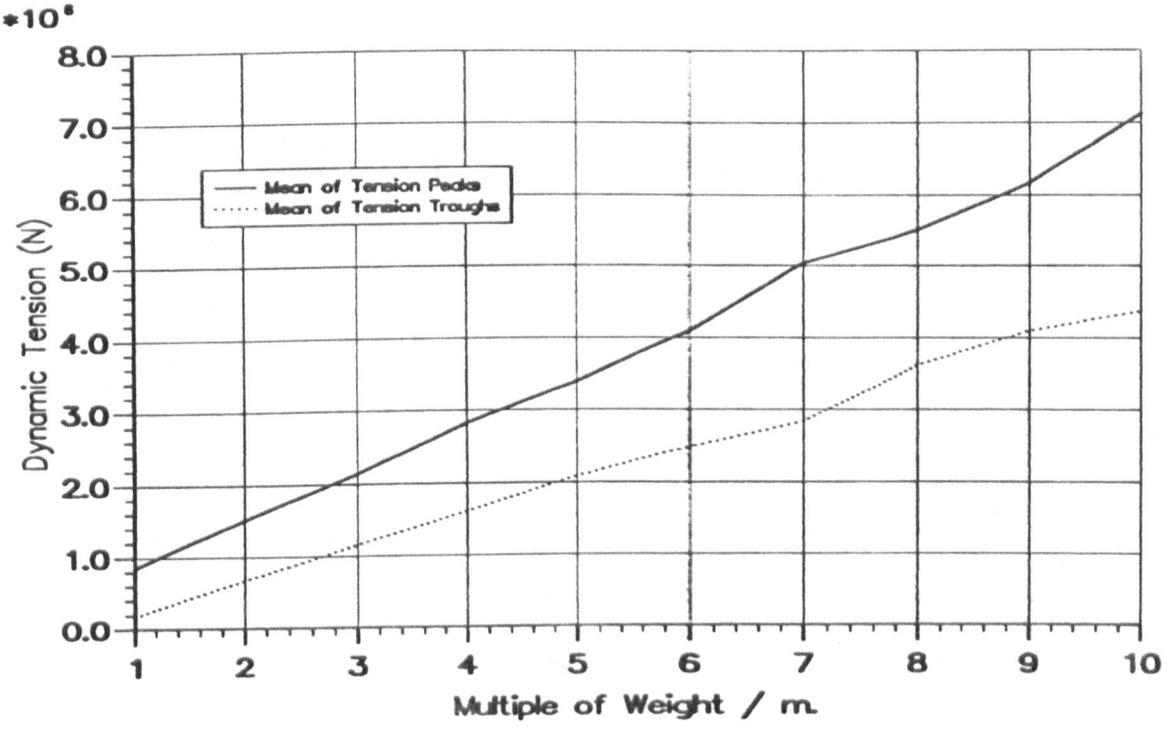

Figure 7.10 — $\bar{T}_p$ and $\bar{T}_t$ vs. the Multiple of Weight/m.

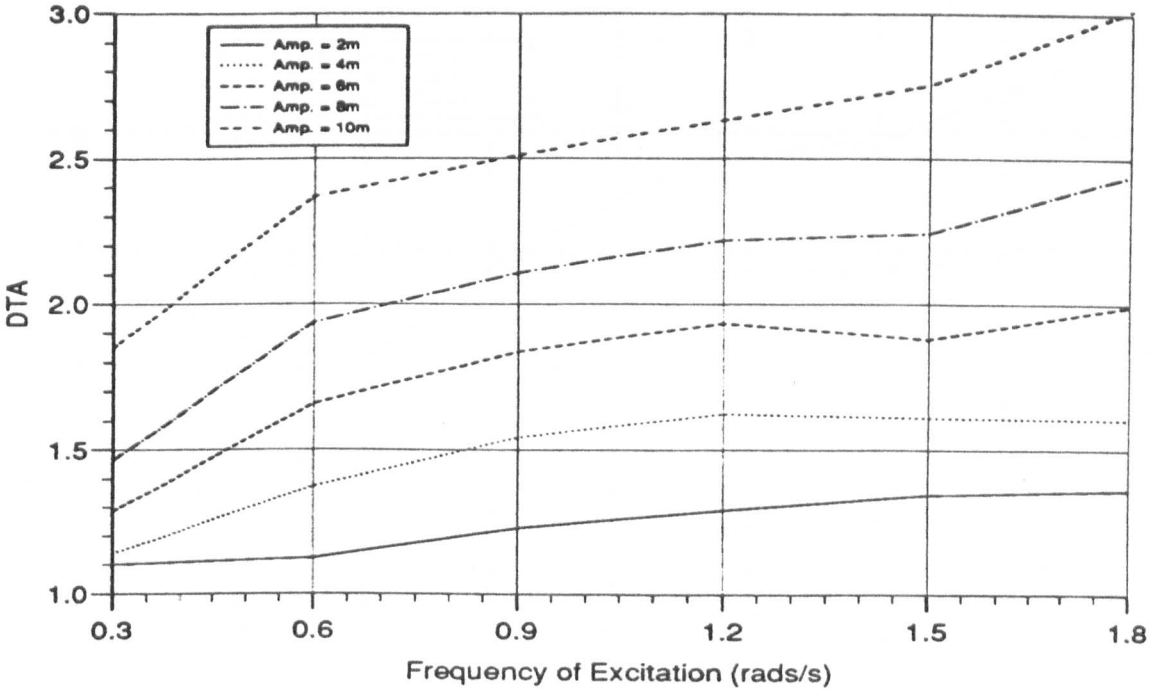

Figure 7.11 — Peak DTAs vs. Frequency of Endpoint Excitation.

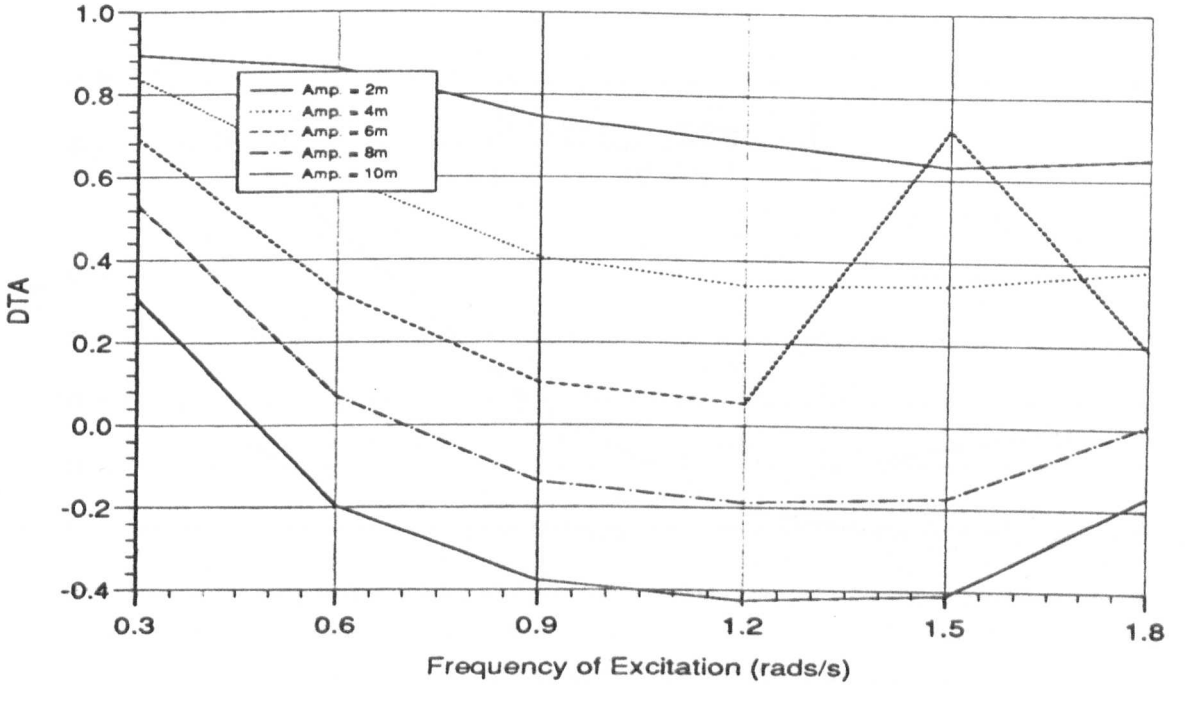

Figure 7.12 — Trough DTAs vs. Frequency of Endpoint Excitation.

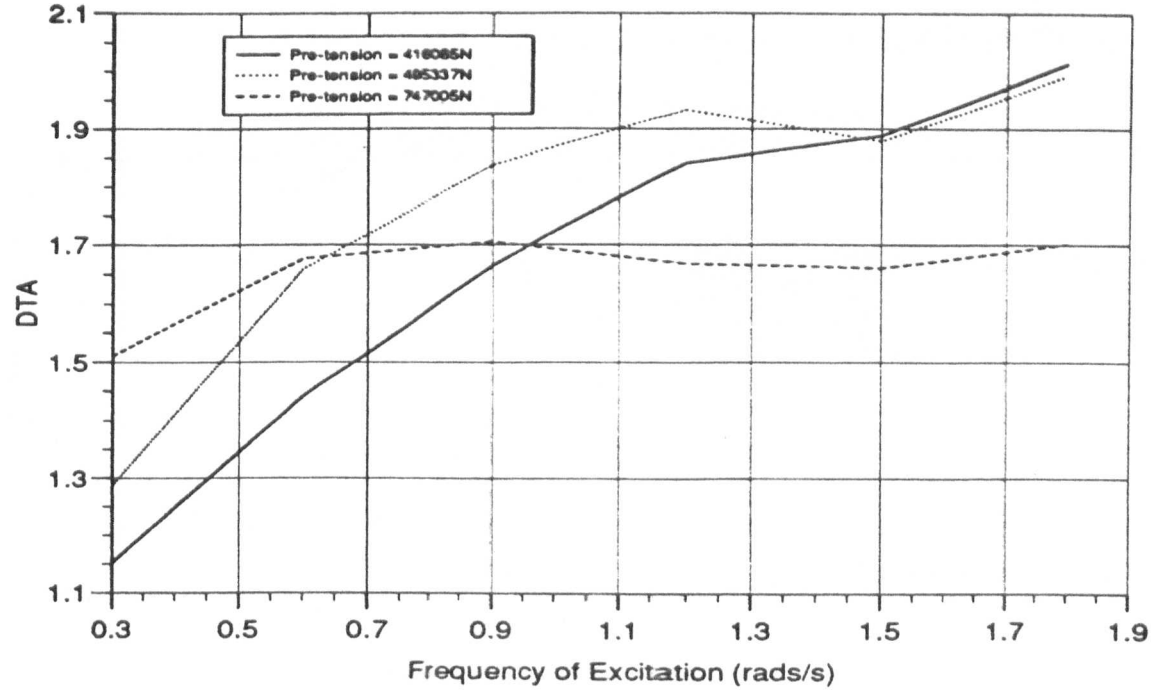

Figure 7.13 — Peak DTAs for Different T_o vs. ω.

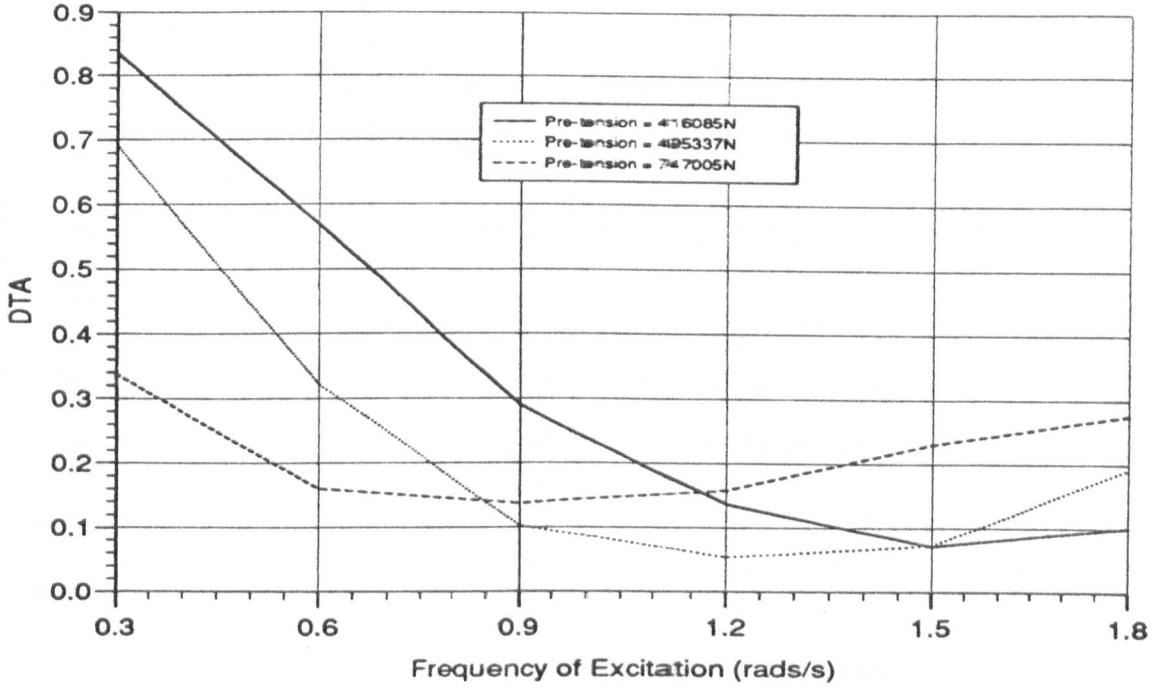

Figure 7.14 — Trough DTAs for Different T_o vs. ω.

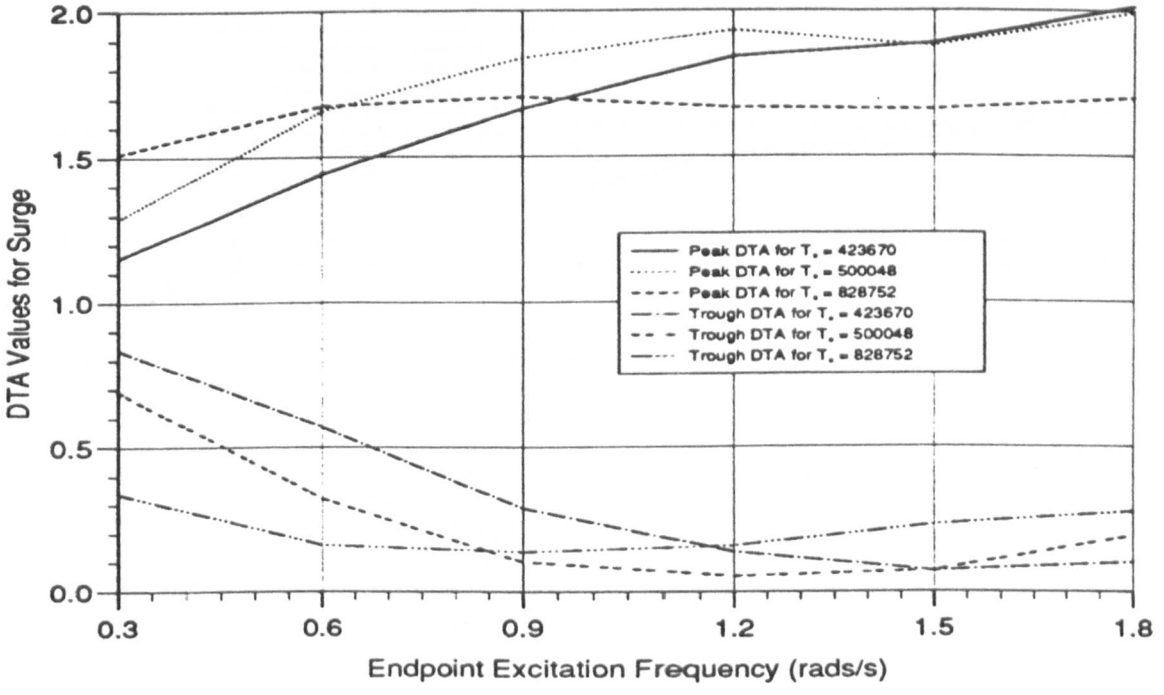

Figure 7.15 — Peak and Trough DTAs for Surge vs. ω.

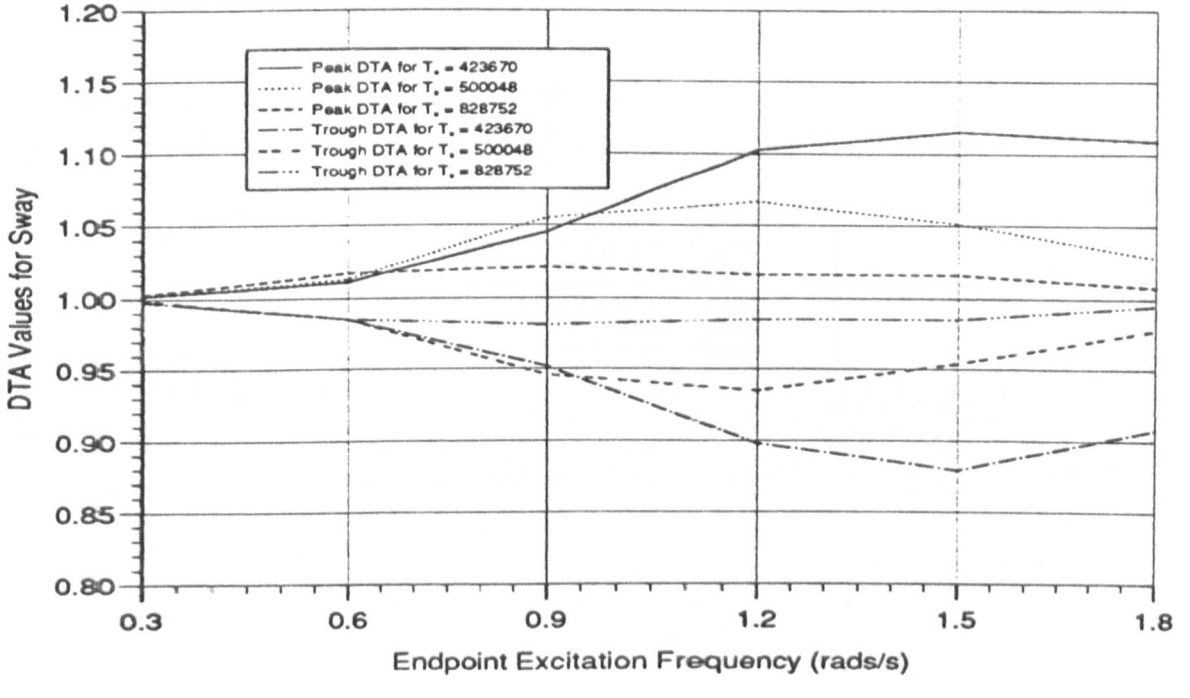

Figure 7.16 — Peak and Trough DTAs for Sway vs. ω.

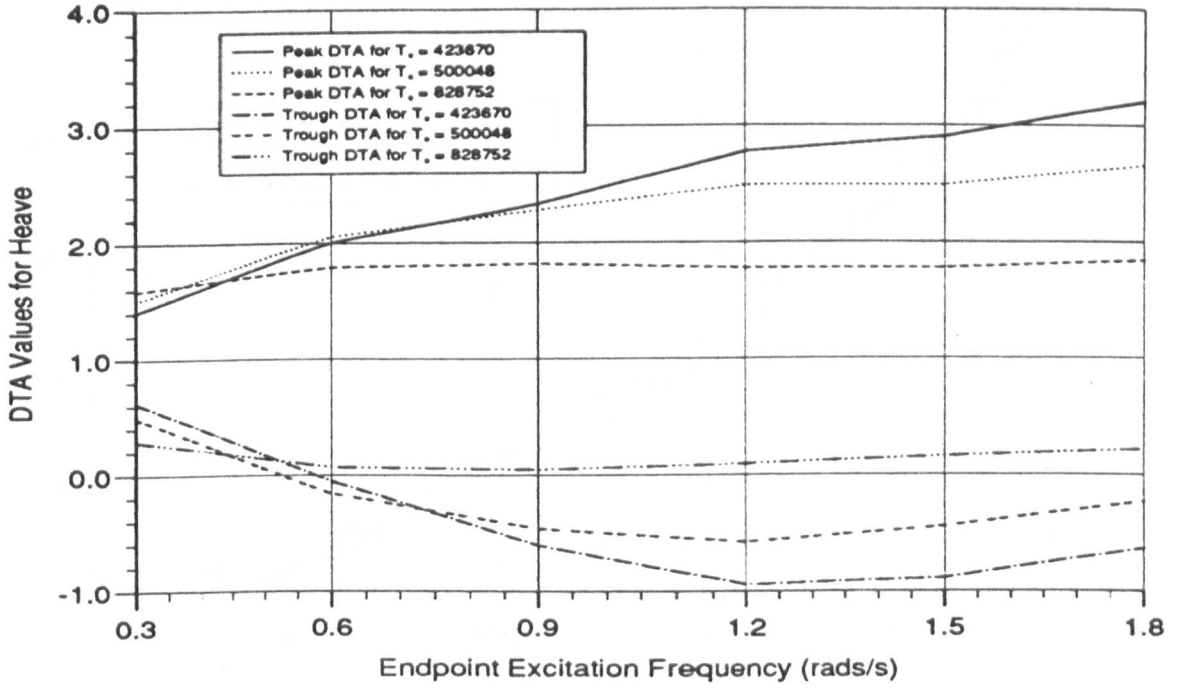

Figure 7.17 — Peak and Trough DTAs for Heave vs. ω.

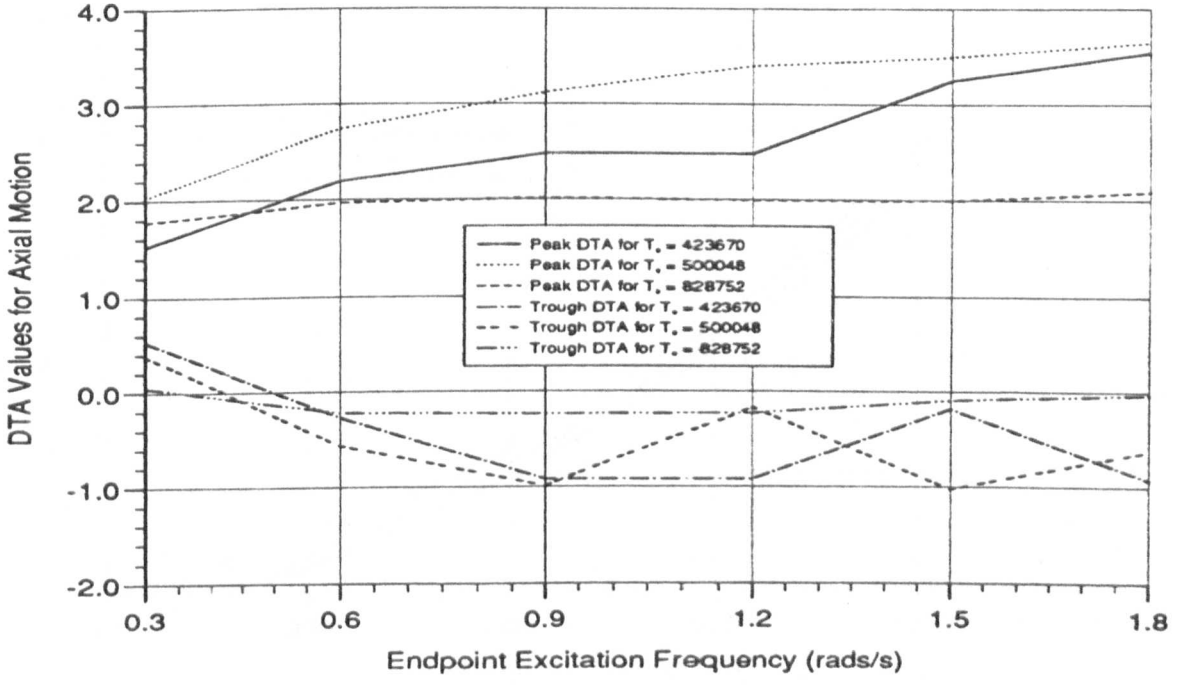

Figure 7.18 — Peak and Trough DTAs for Axial Motion vs. ω.

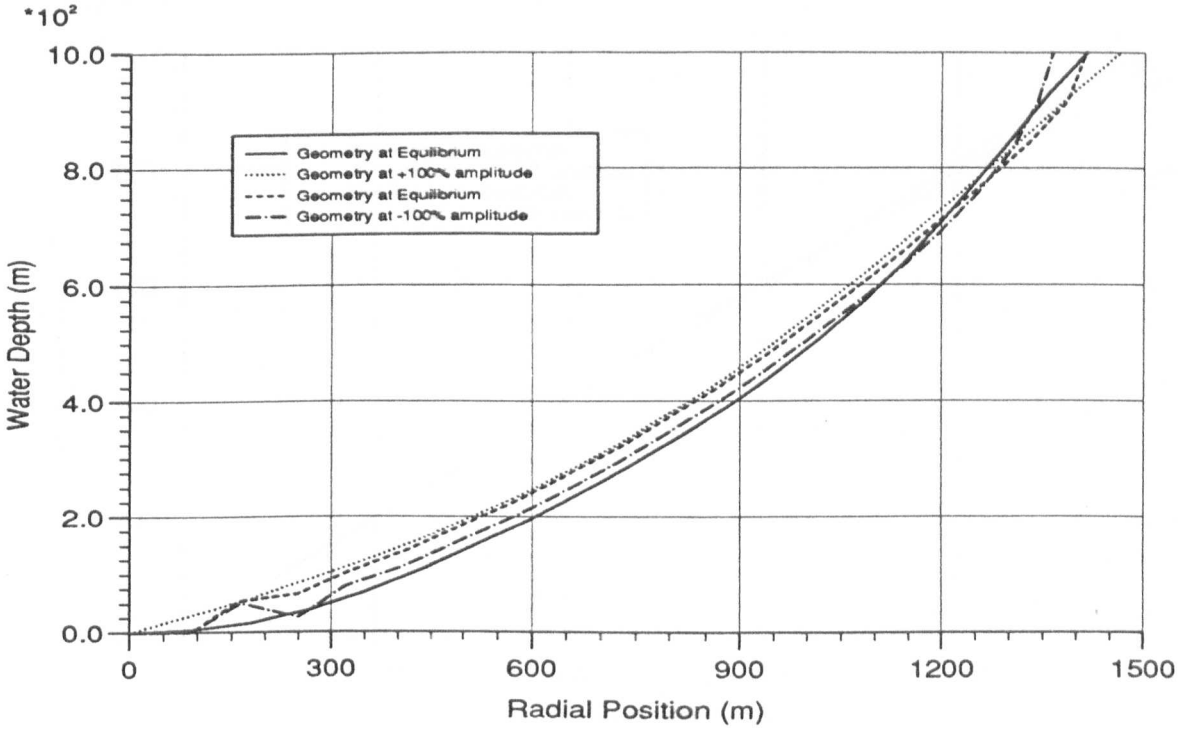

Figure 7.19 — Cable Geometry for One Surge Cycle.

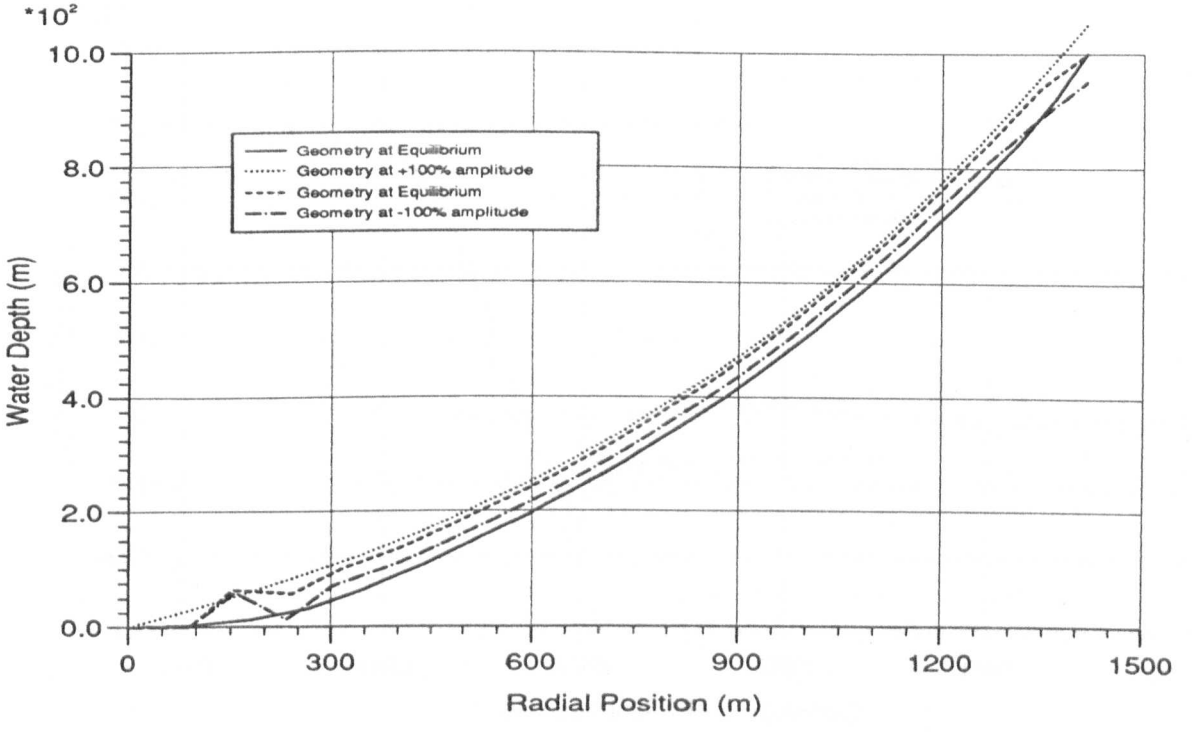

Figure 7.20 — Cable Geometry for One Heave Cycle.

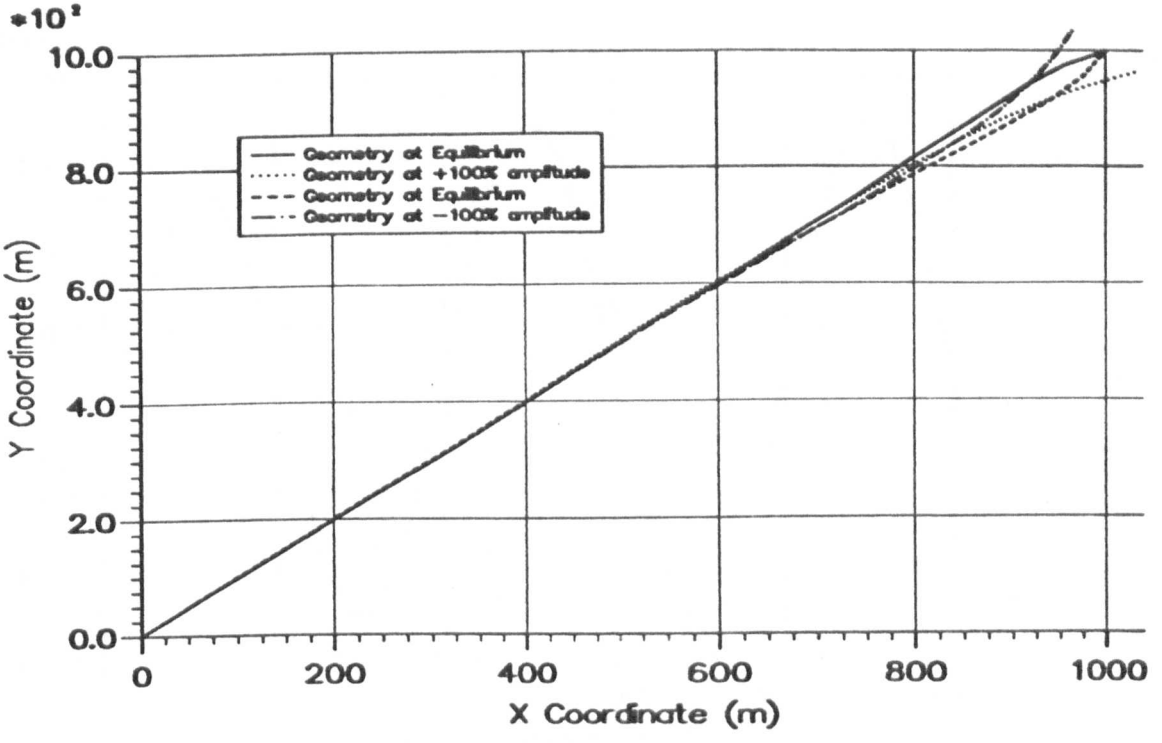

Figure 7.21 — Cable Geometry for One Sway Cycle.

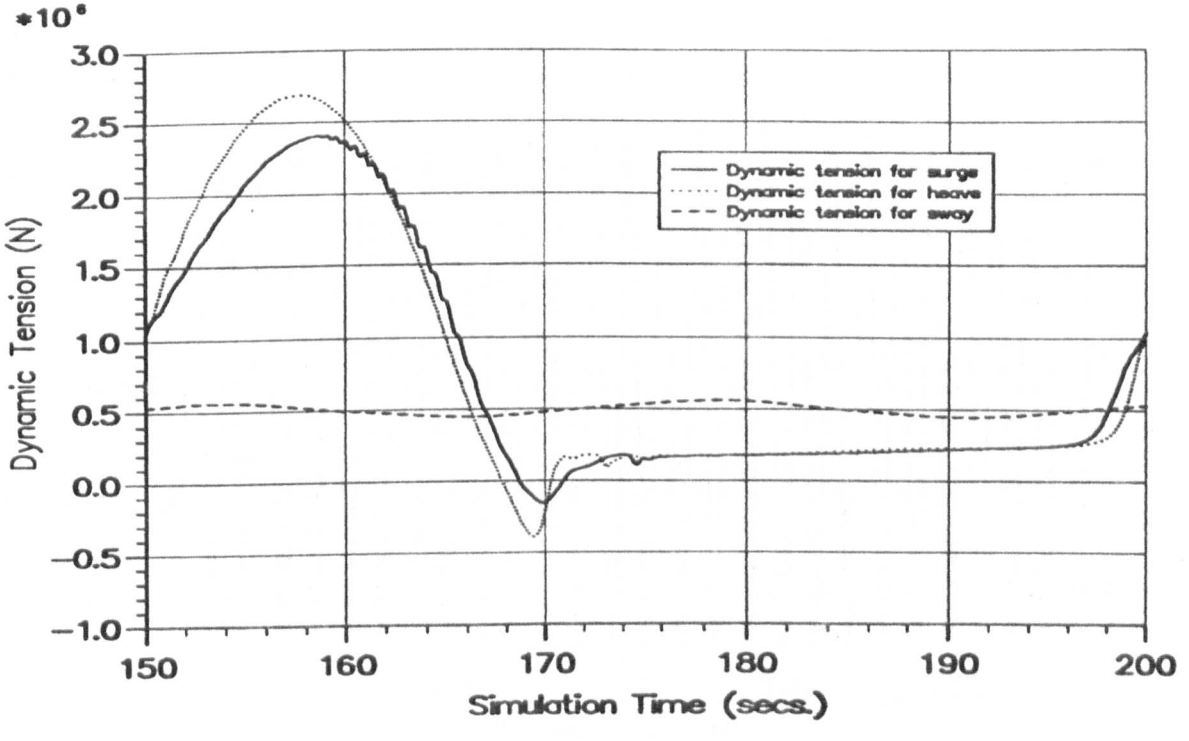

Figure 7.22 — Tensions for Surge, Sway and Heave for One Cycle.

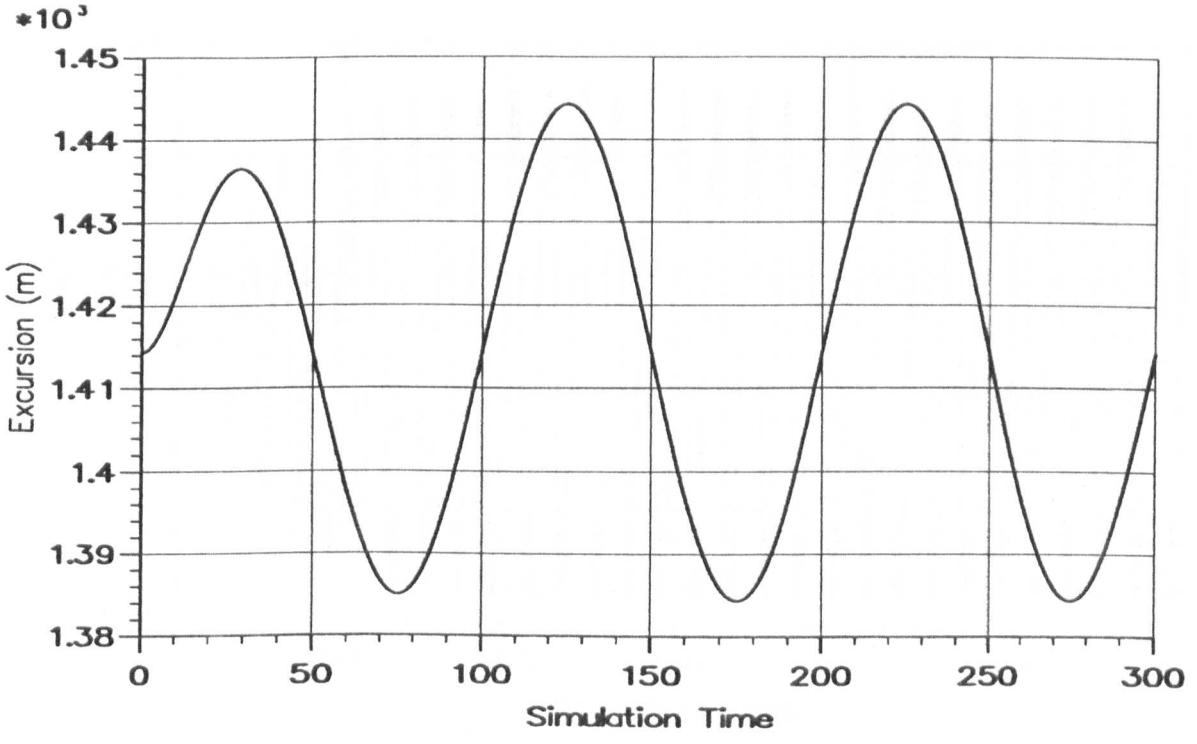

Figure 7.23 — Low Frequency (LF) Surge Only.

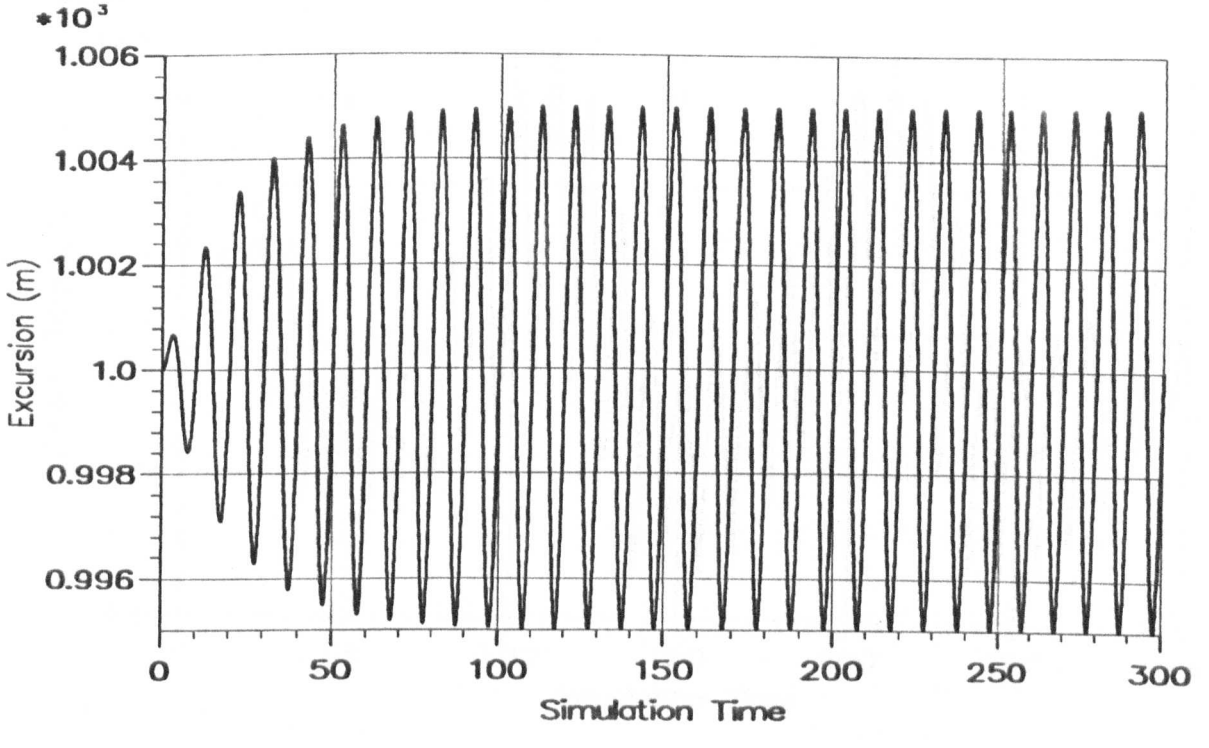

Figure 7.24 — High Frequency (HF) Heave Only.

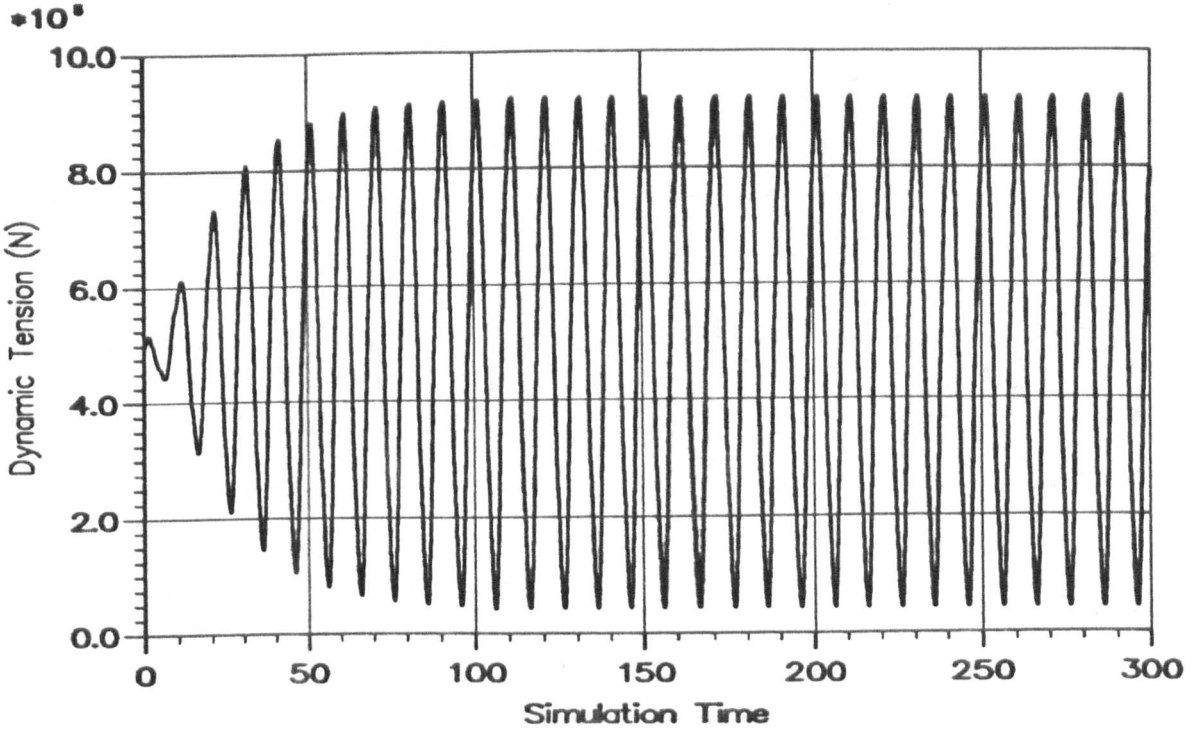

Figure 7.25 — Tension History For HF Heave Only.

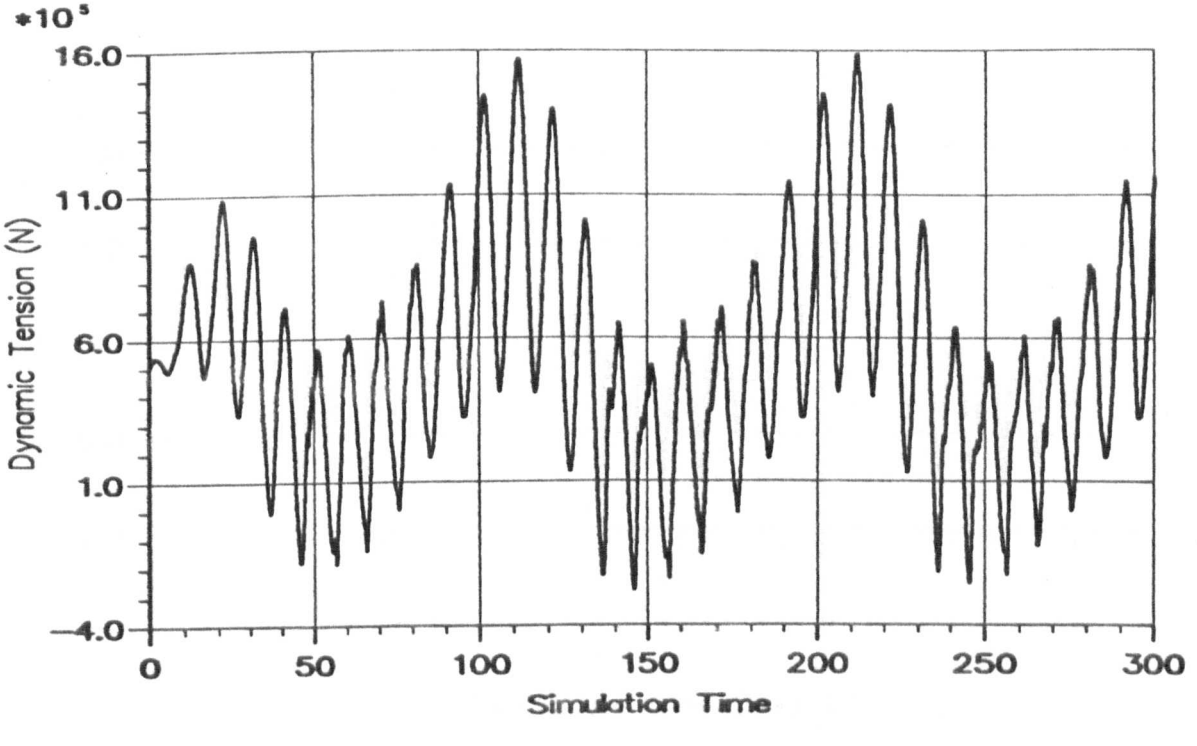

Figure 7.26 — Tension History For LF Surge and HF Heave.

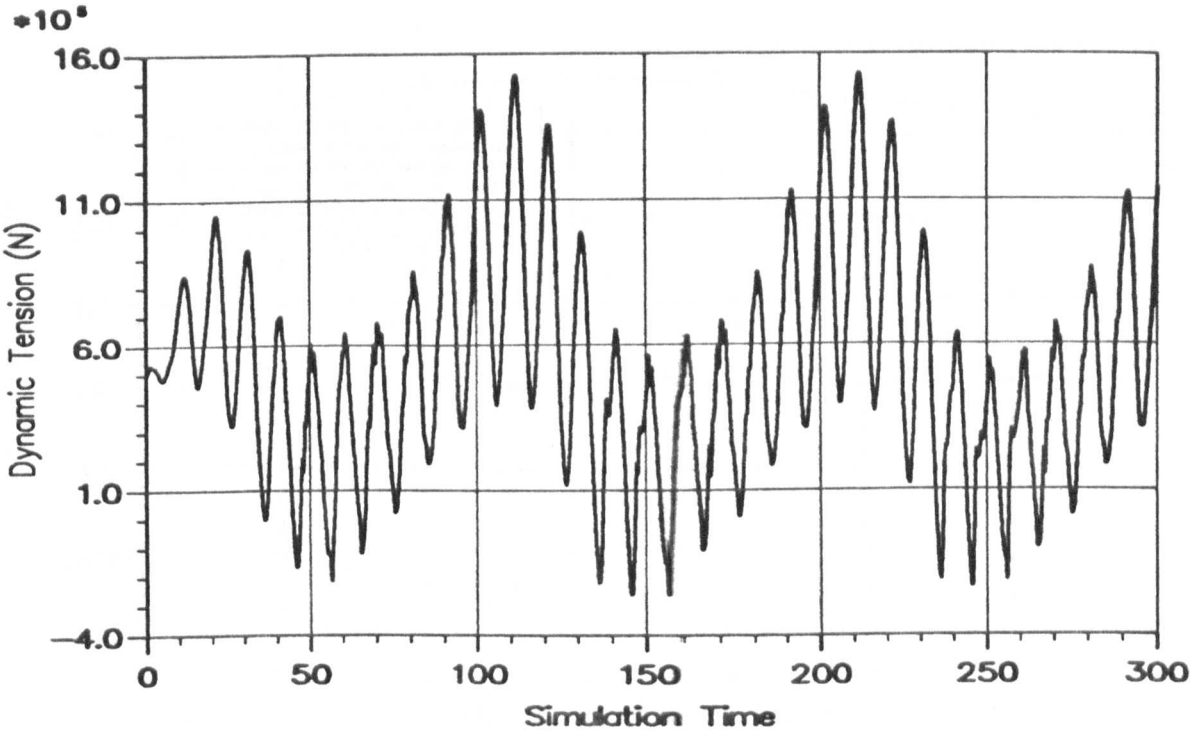

Figure 7.27 — Tension History For LF Sway and HF Heave.

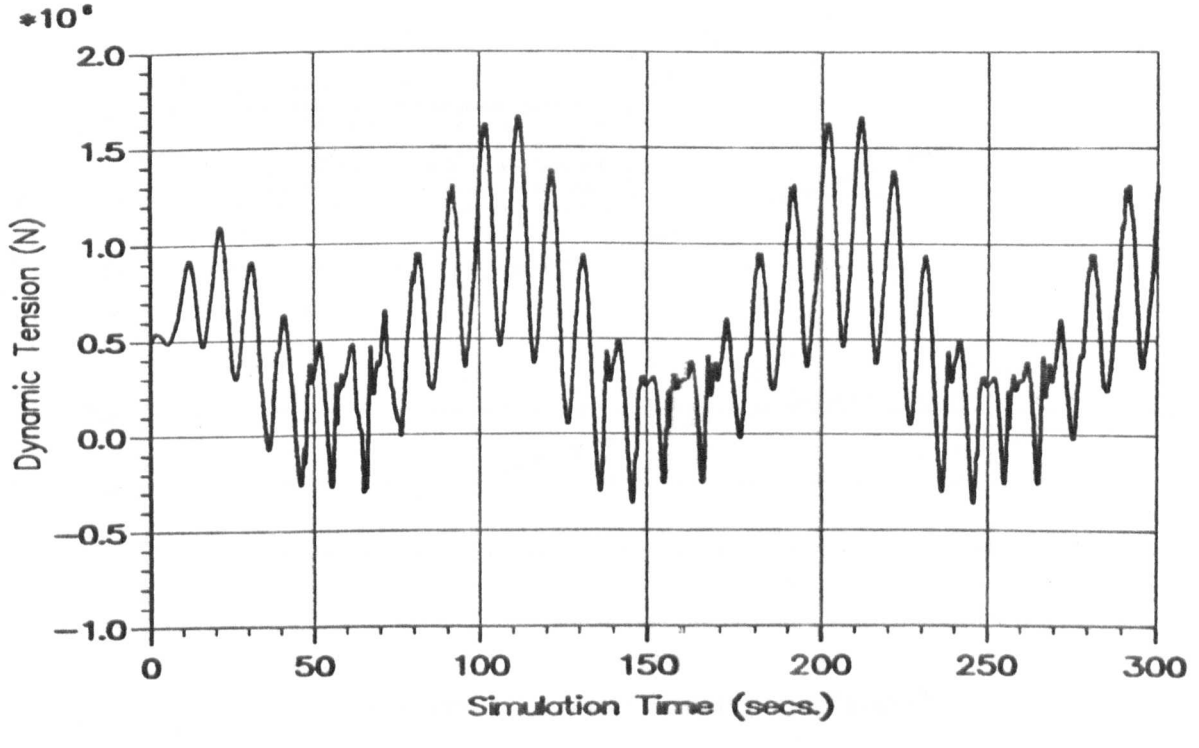

Figure 7.28 — Tension History For LF and HF Heave.

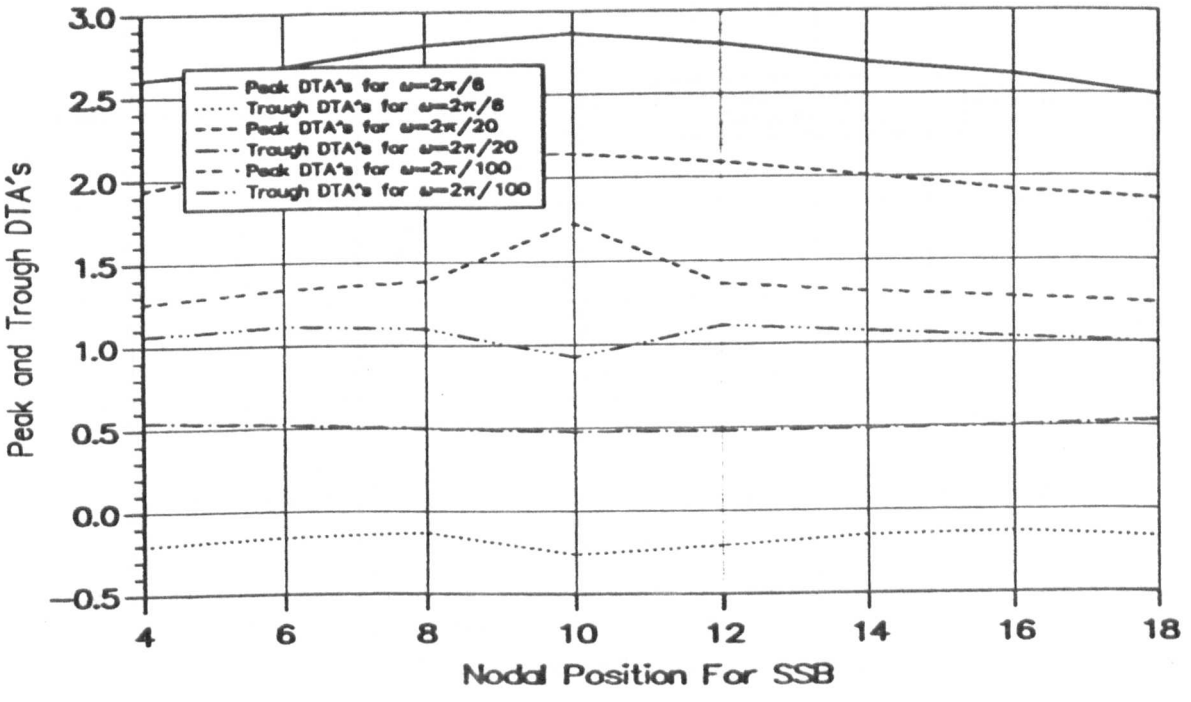

Figure 7.29 — DTAs vs. ω With a SSB at New Positions.

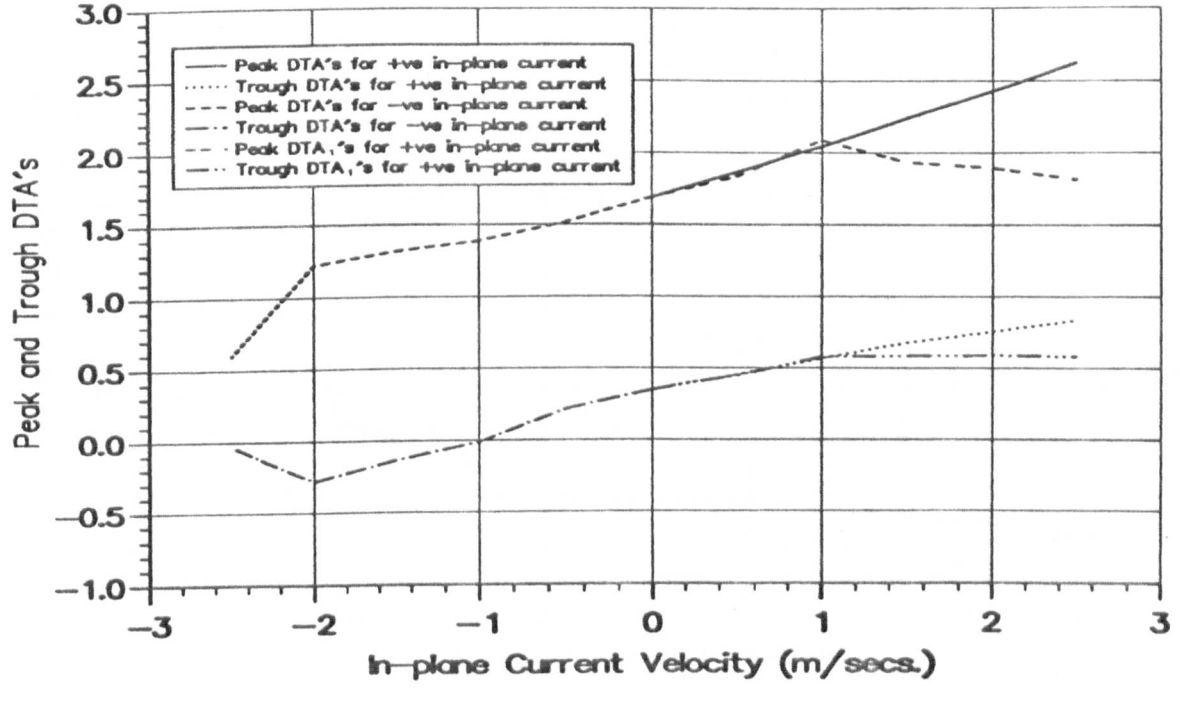

Figure 7.30 — DTAs vs. Different In-plane Current Velocities.

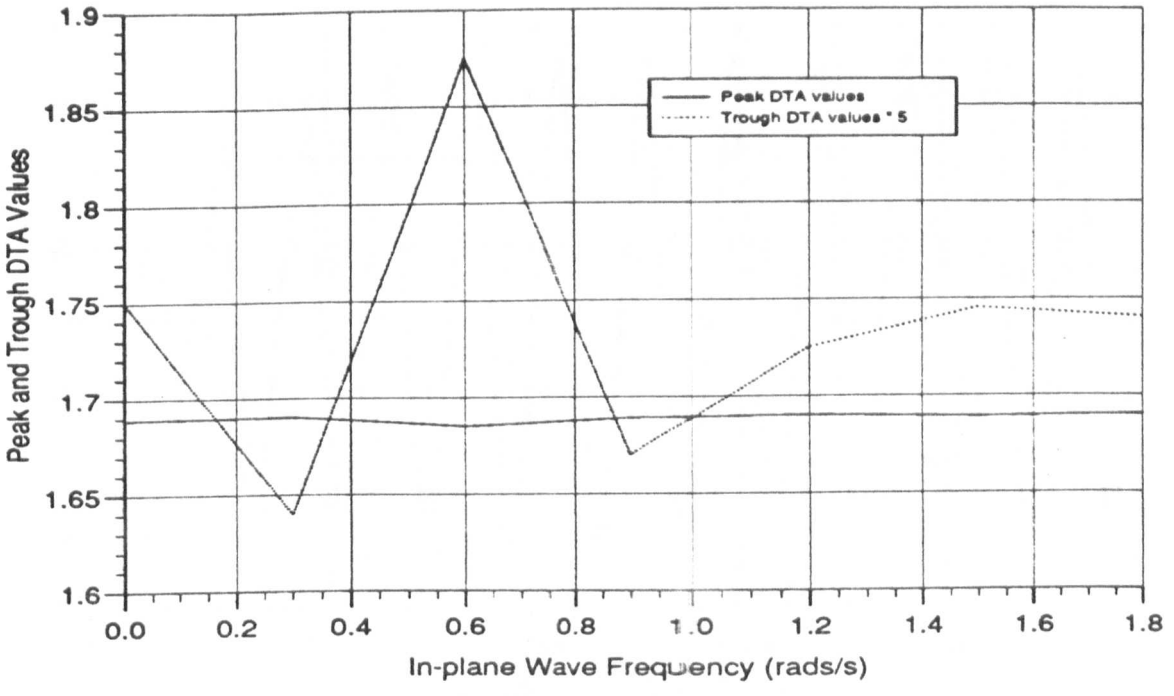

Figure 7.31 — DTAs vs. Wave Frequency.

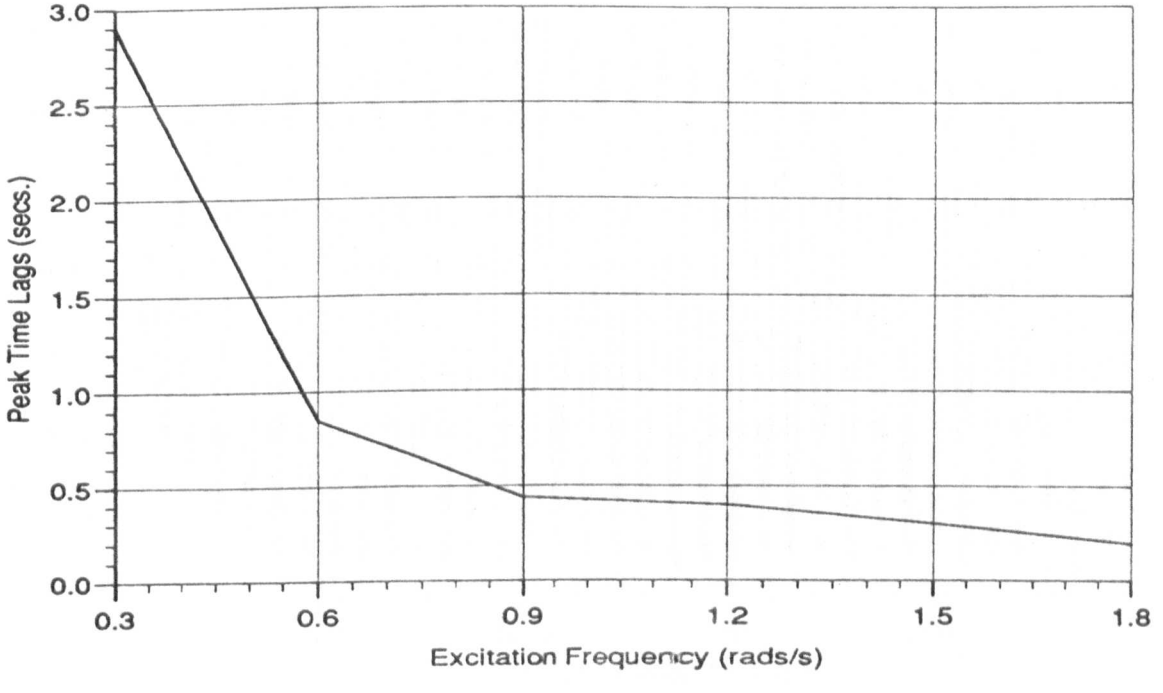

Figure 7.32 — Peak Time Lags vs. ω.

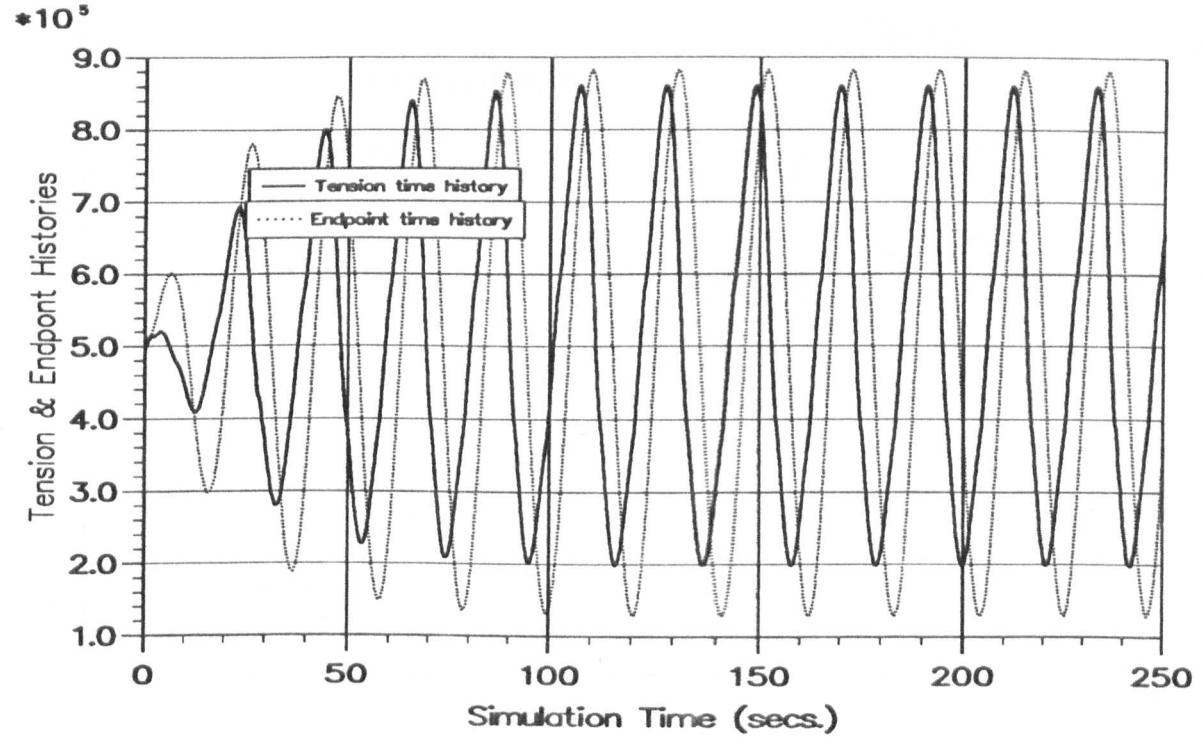

Figure 7.33 — Tension and Endpoint Time Histories for $\omega = 0.3$.

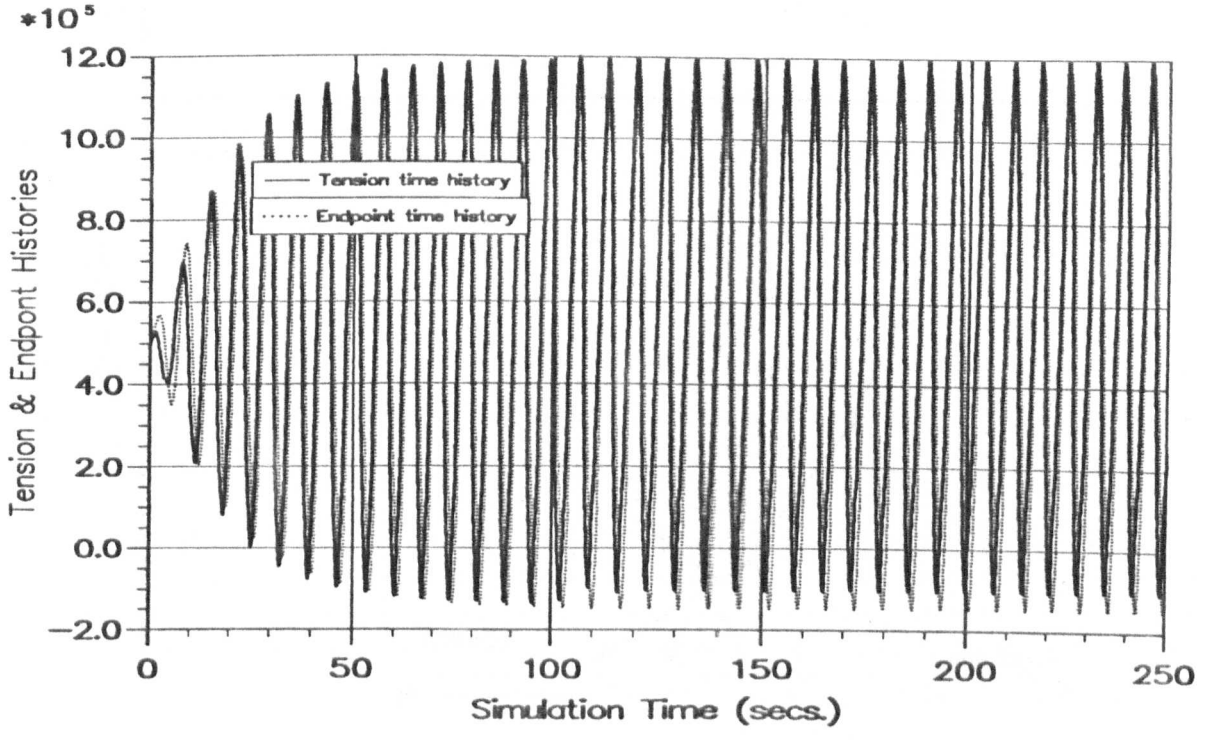

Figure 7.34 — Tension and Endpoint Time Histories for $\omega = 0.9$.

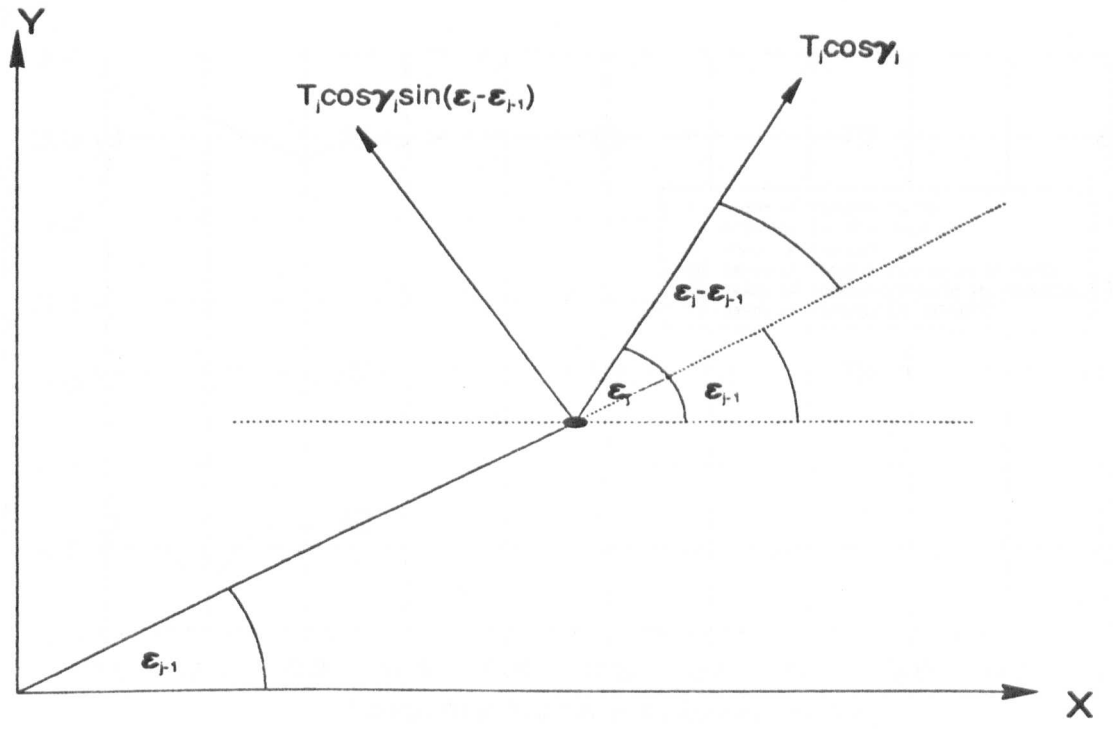

Figure 8.1 — Plan View of Touchdown Area

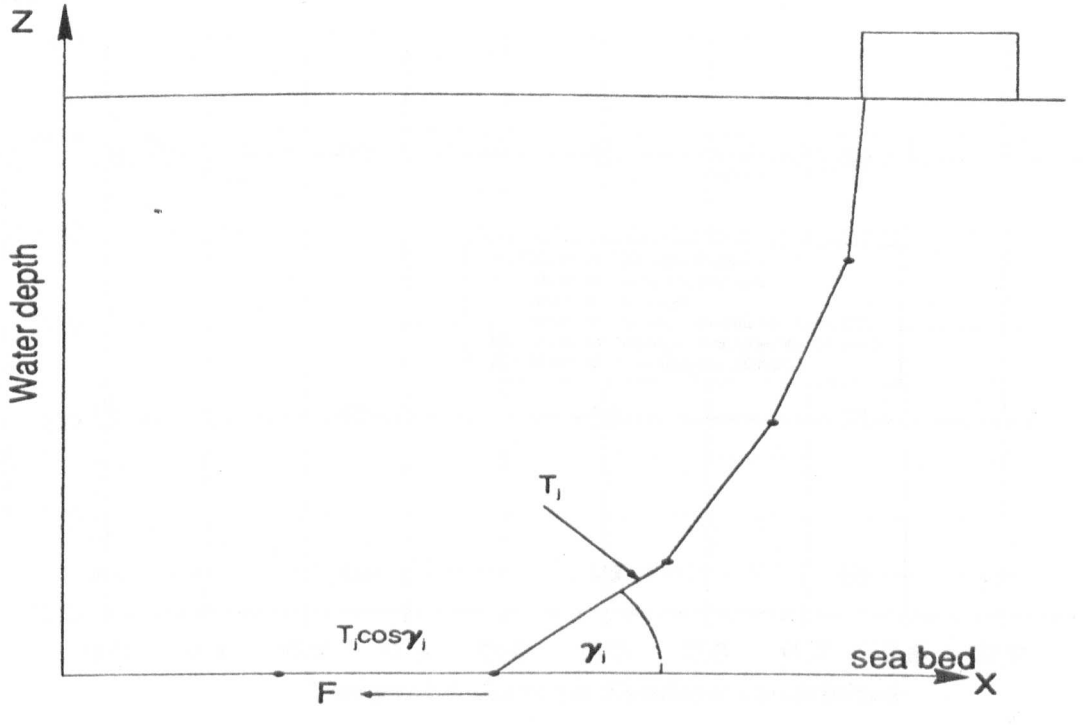

Figure 8.2 — Side View of Cable Discretisation and Forces

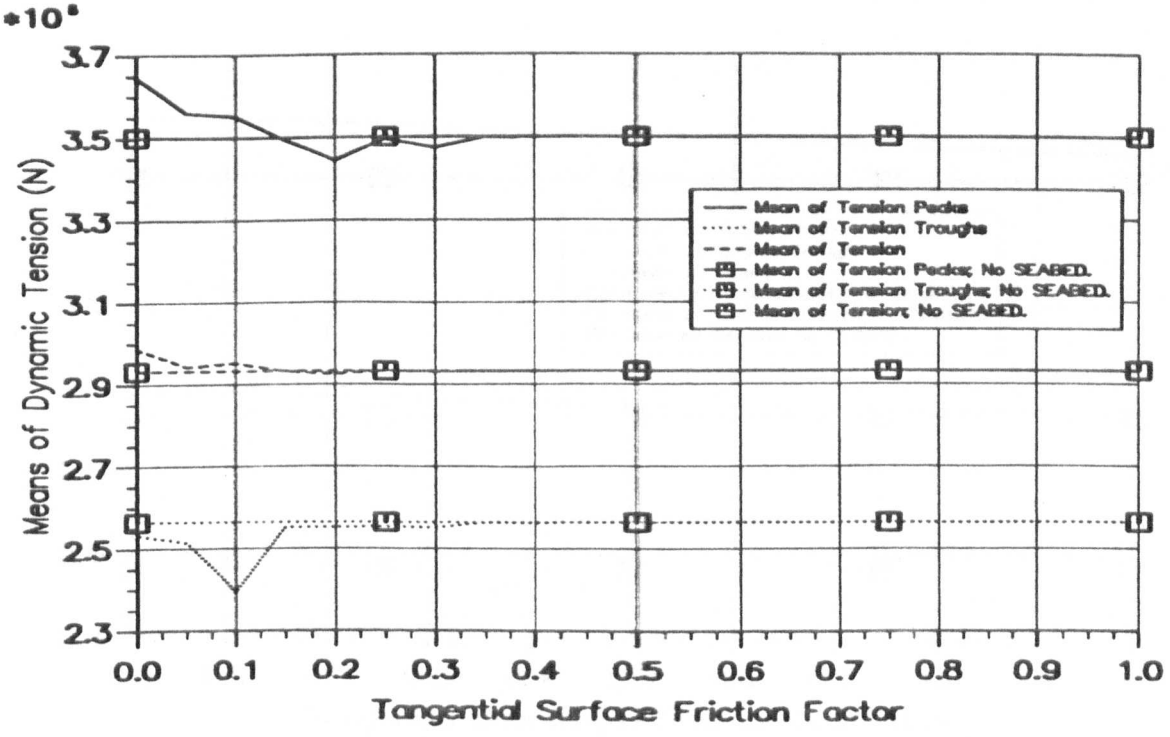

Figure 8.3 — Tangential Motion, $a_x = a_y = 10\text{m}$

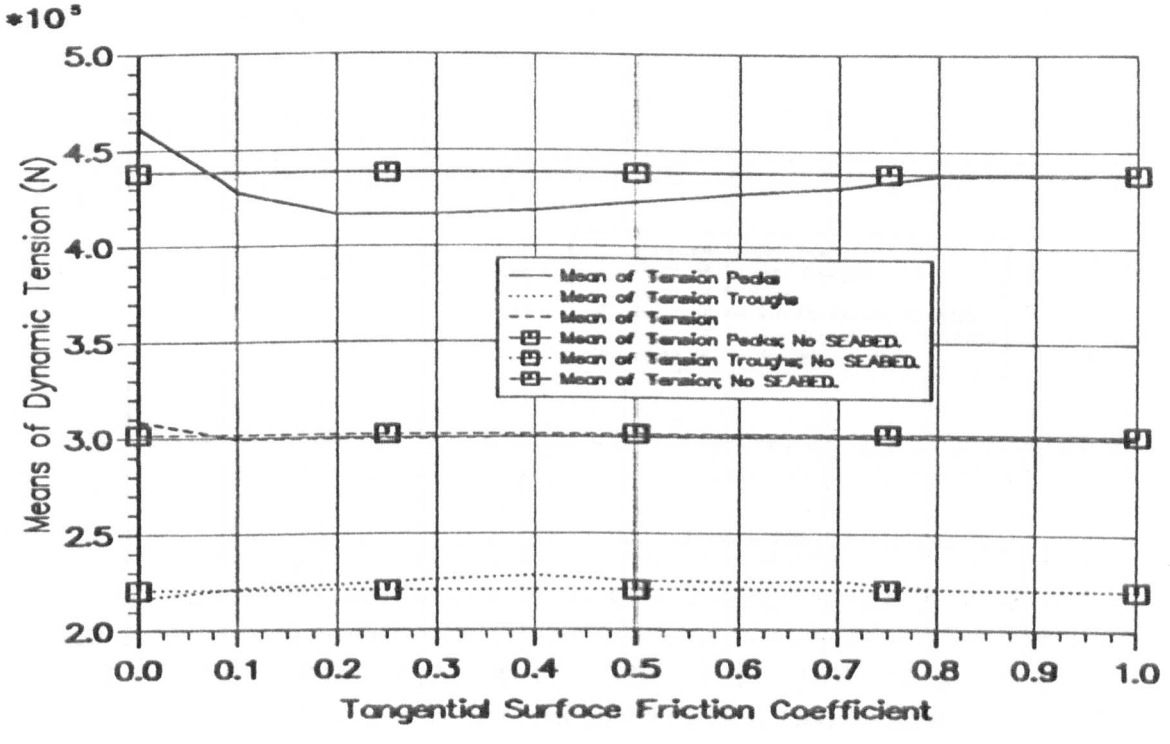

Figure 8.4 — Tangential Motion, $a_x = a_y = 15\text{m}$

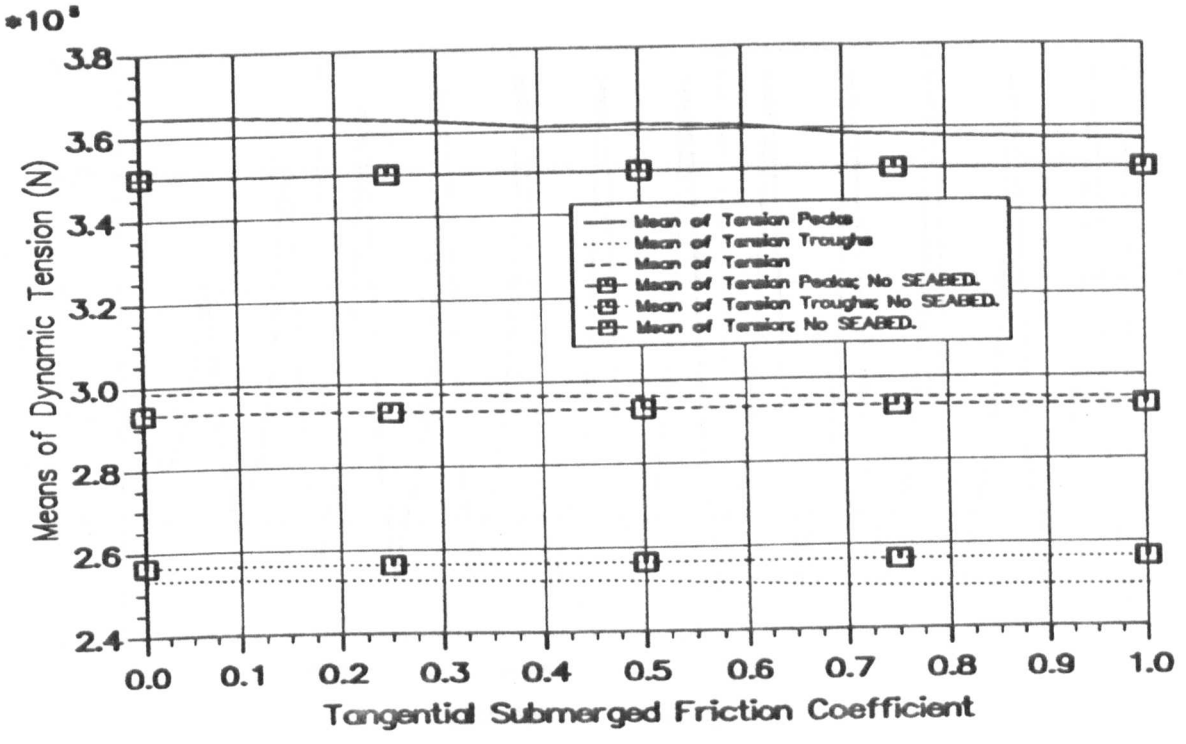

Figure 8.5 — Tangential Motion, Line Submerged $a_x = a_y = 10\text{m}$

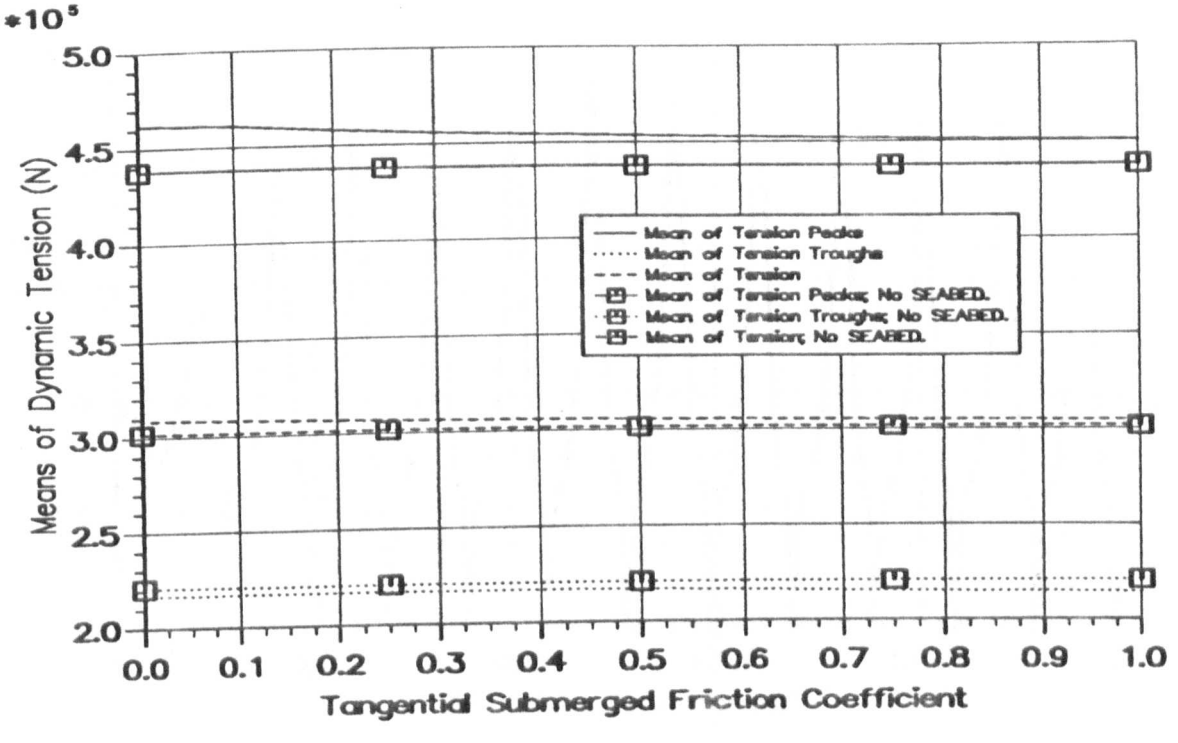

Figure 8.6 — Tangential Motion, Line Submerged $a_x = a_y = 15\text{m}$

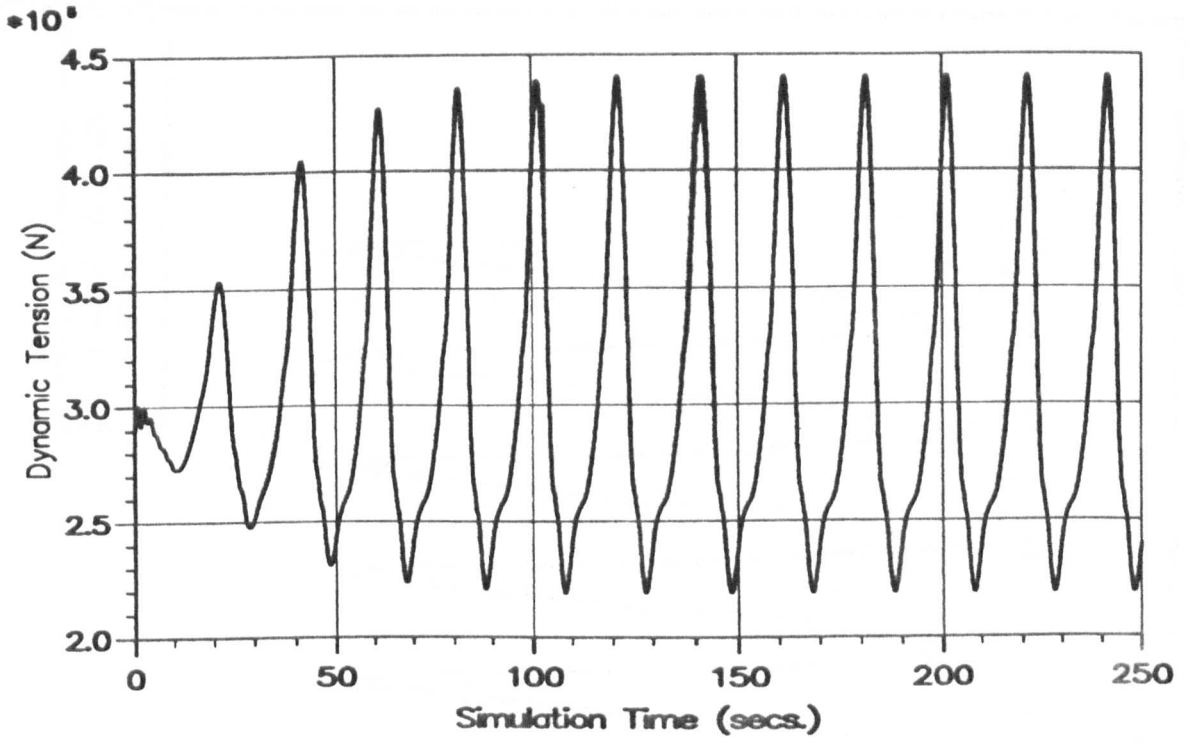

Figure 8.7 — No Nodal Lifting/Grounding

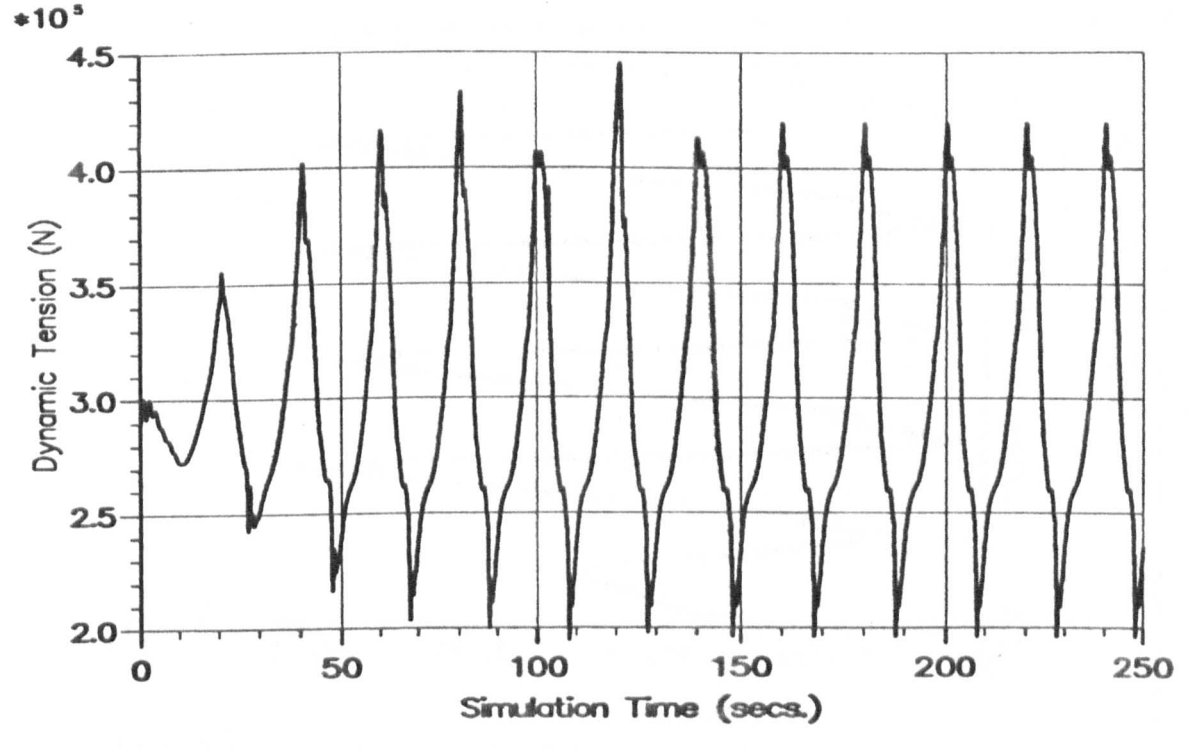

Figure 8.8 — Effect of Nodal Lifting/Grounding : No Friction

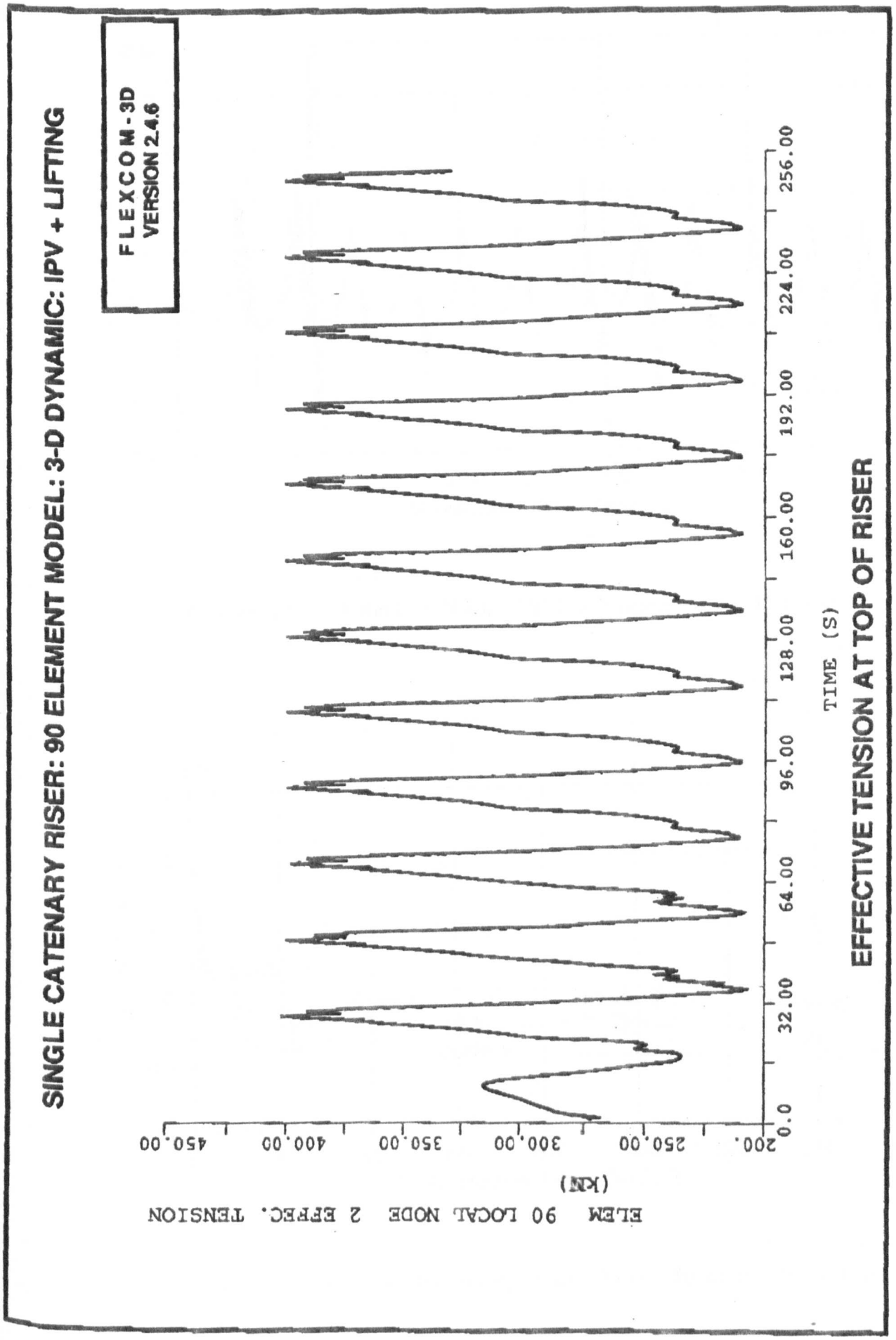

Figure 8.8A - FLEXCOM-3D (90E), McNamara(1993)

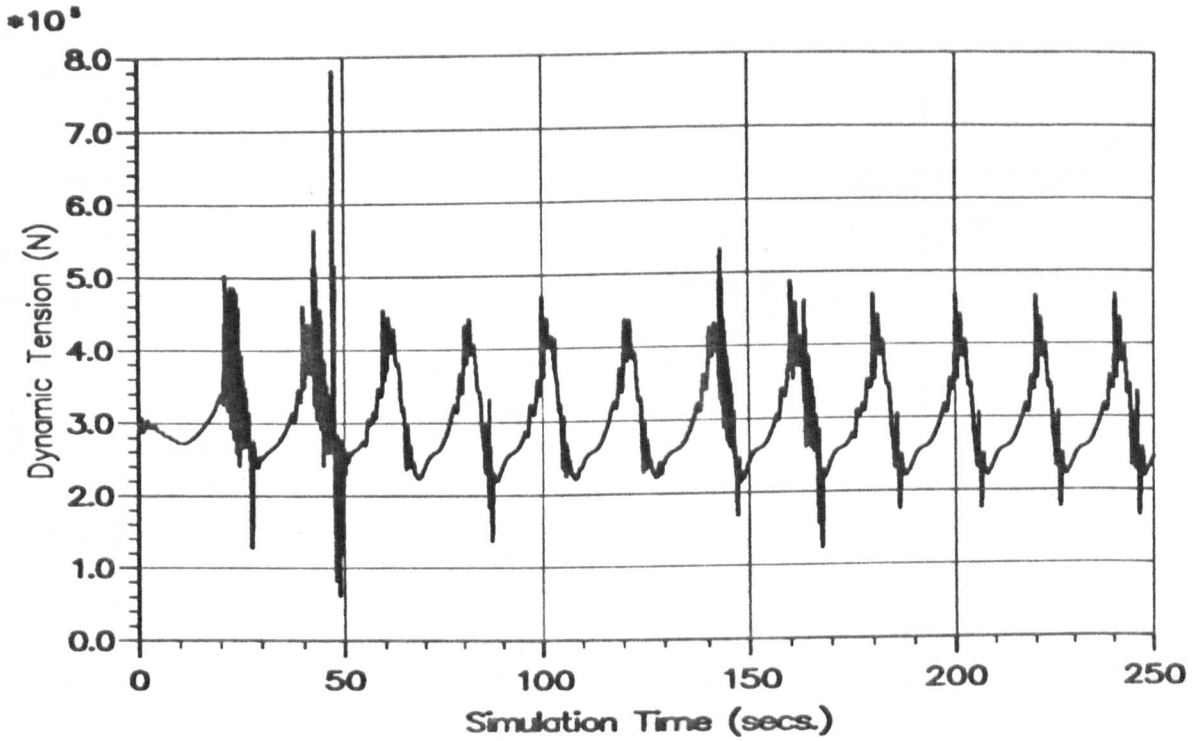

Figure 8.9 — Effect of Nodal Lifting/Grounding : Friction

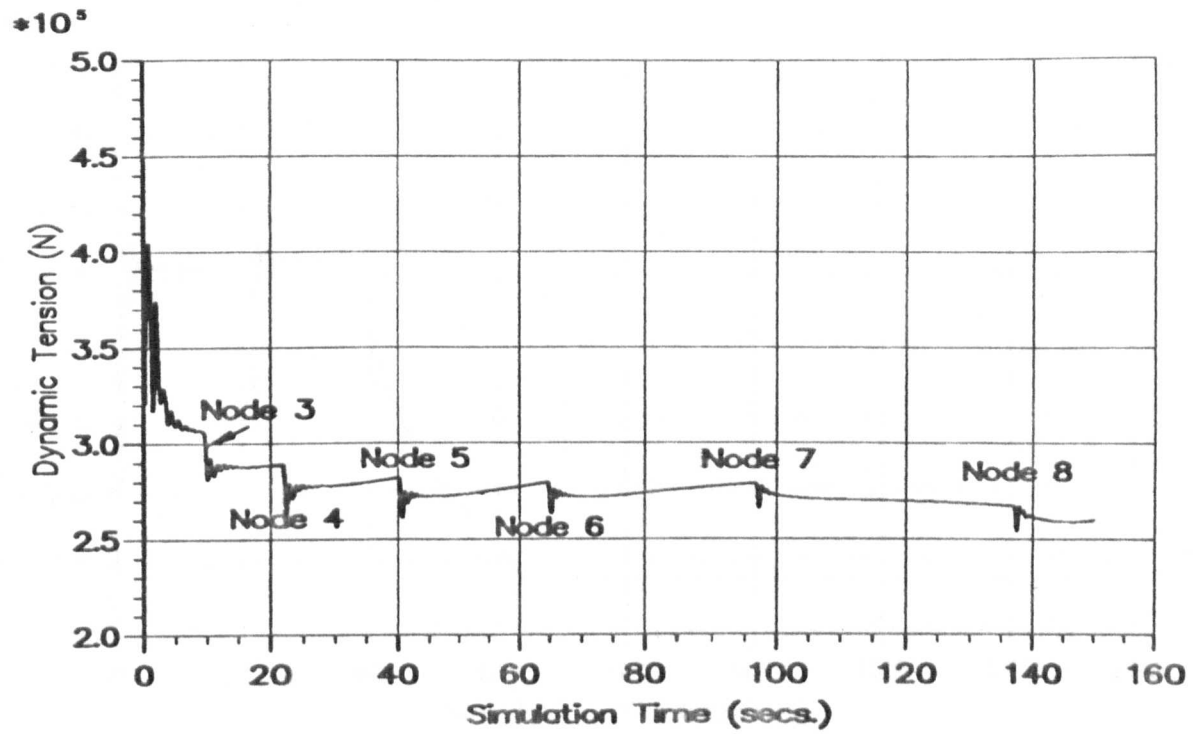

Figure 8.10 — Node Grounding From Max. To Min. Excursion

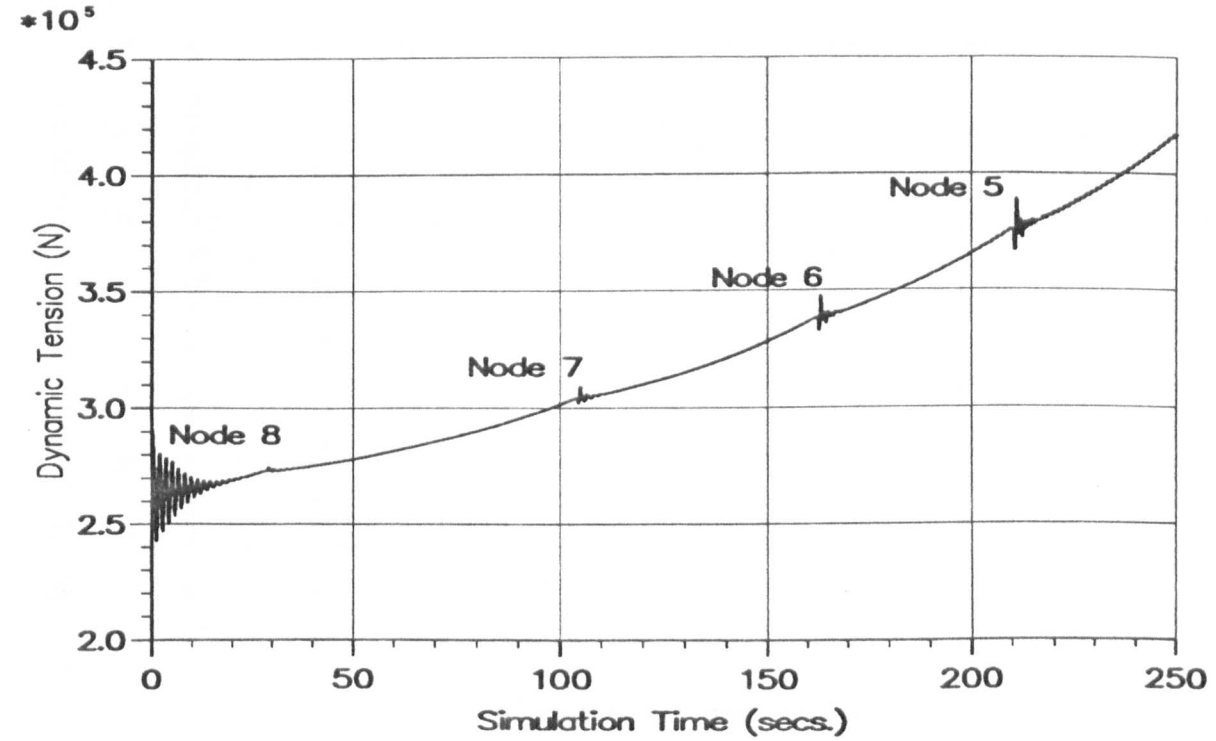

Figure 8.11 — Node Lifting From Min. To Max. Excursion

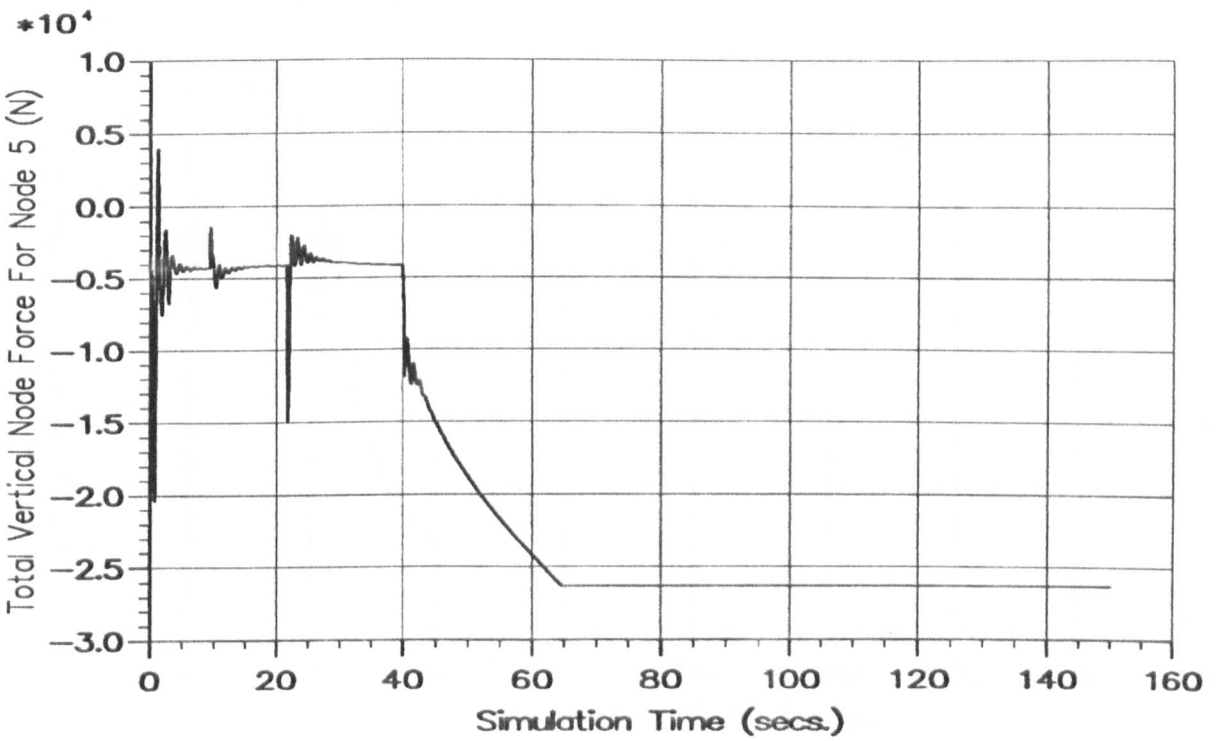

Figure 8.12 — Total Vertical Force for Node 5

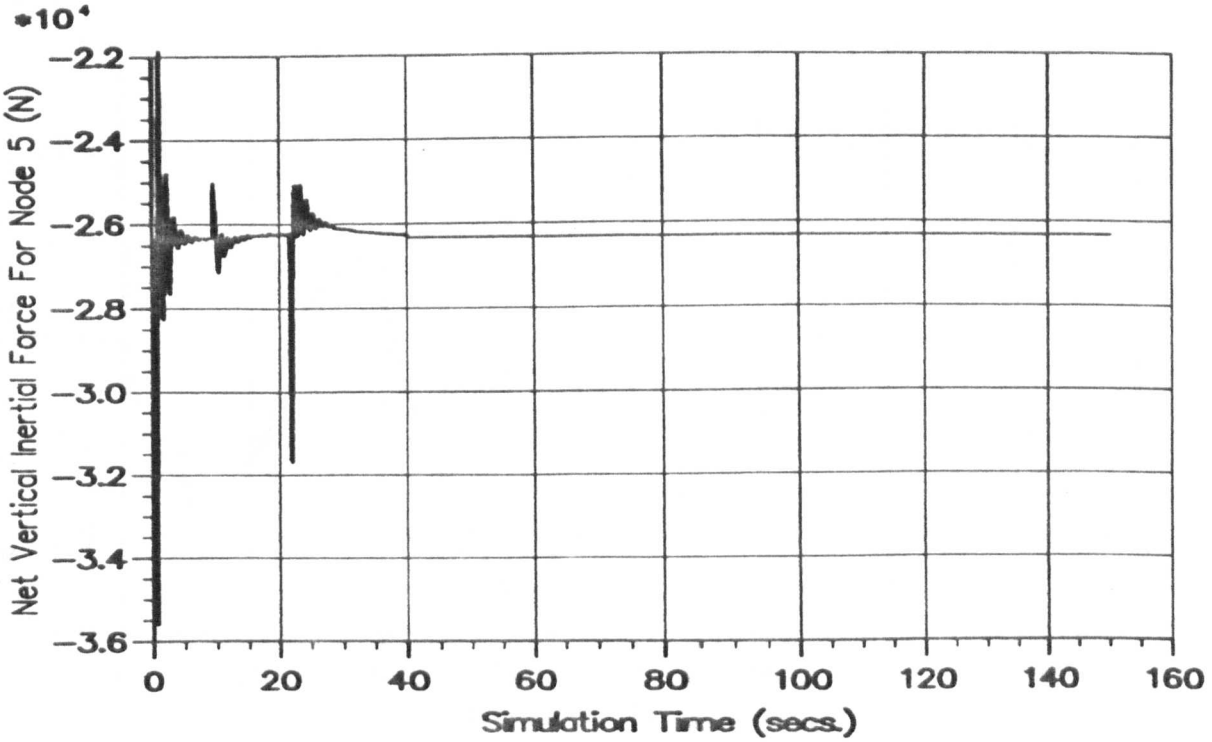

Figure 8.13 — Inertial Force for Node 5

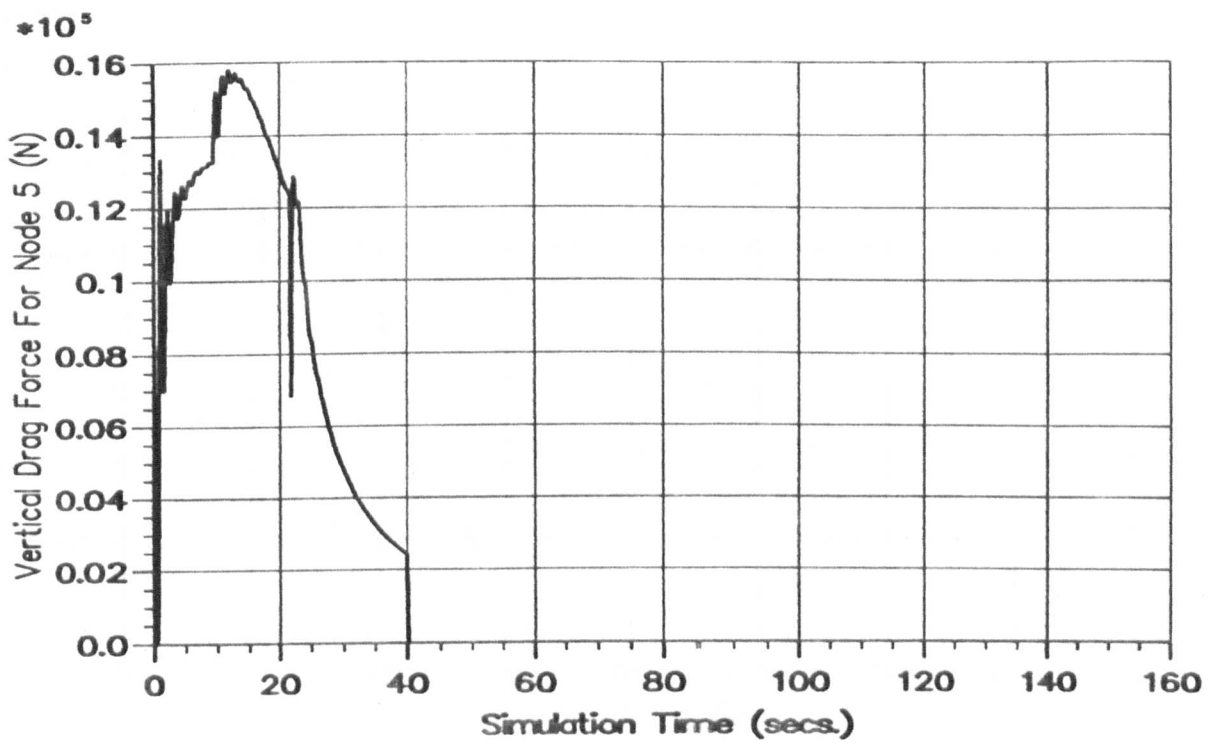

Figure 8.14 — Vertical Drag Force for Node 5

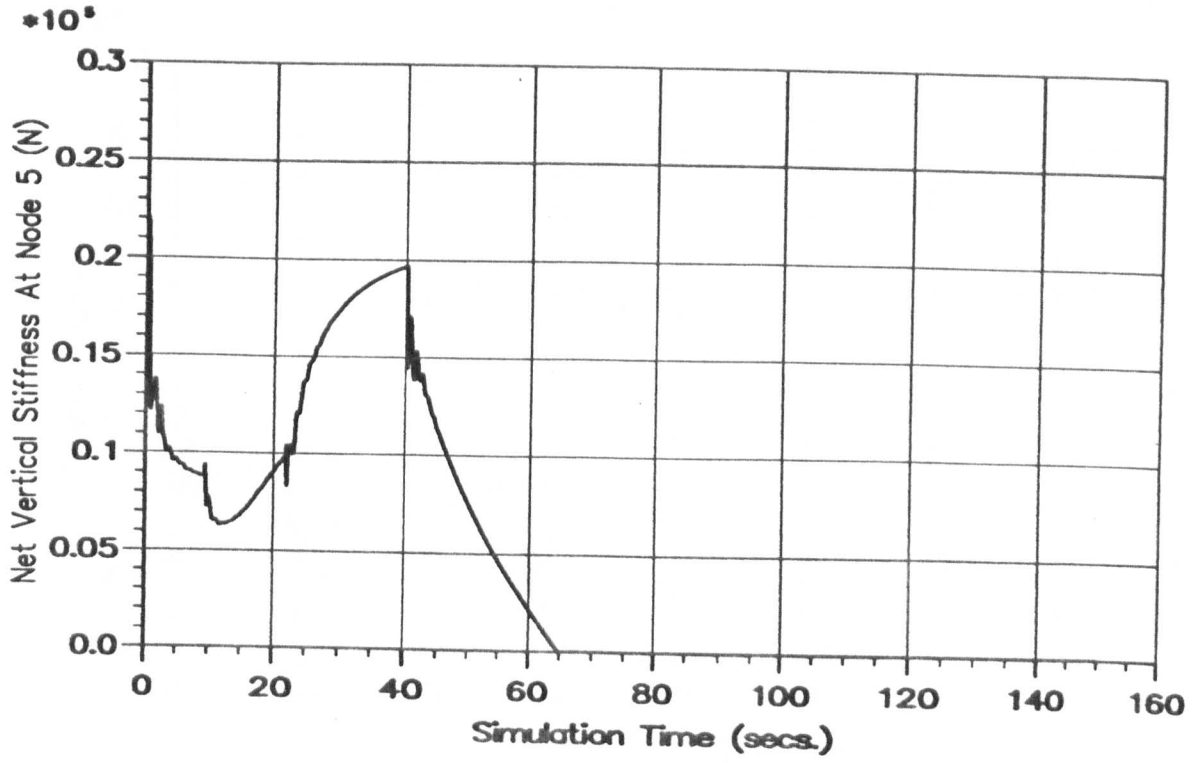

Figure 8.15 — Vertical Stiffness for Node 5

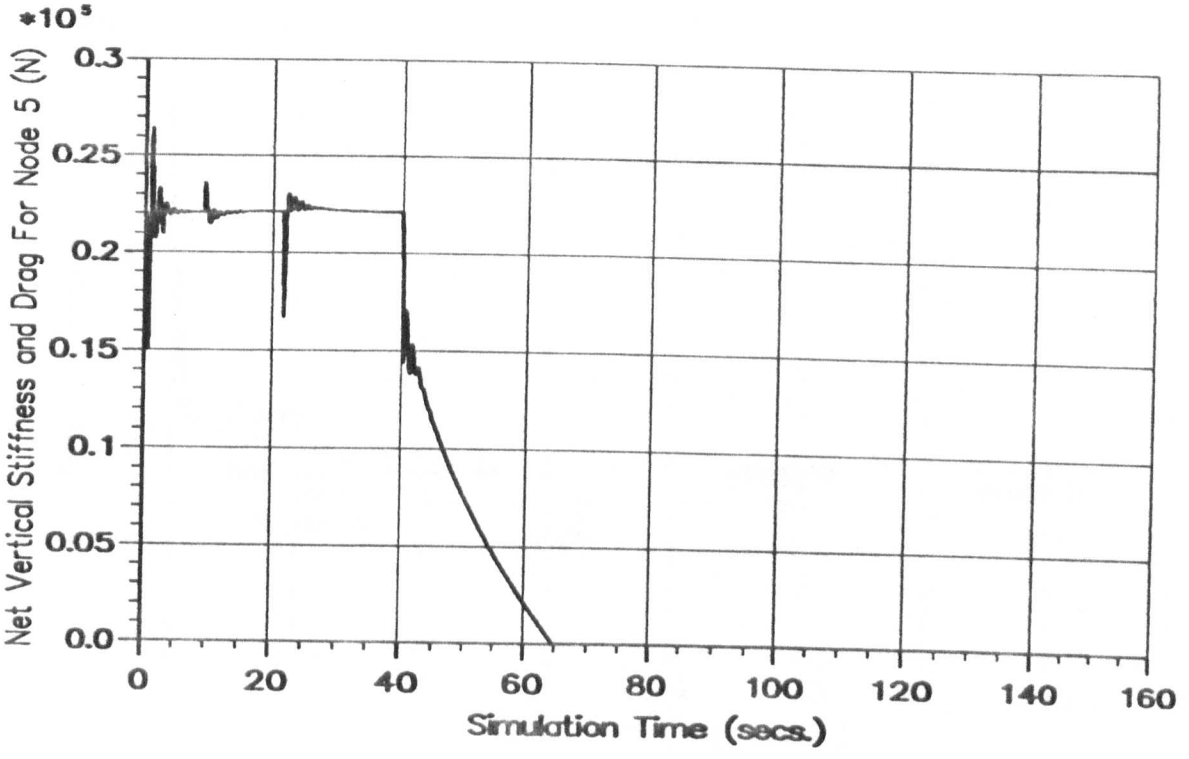

Figure 8.16 — Vertical Stiffness and Drag Force for Node 5

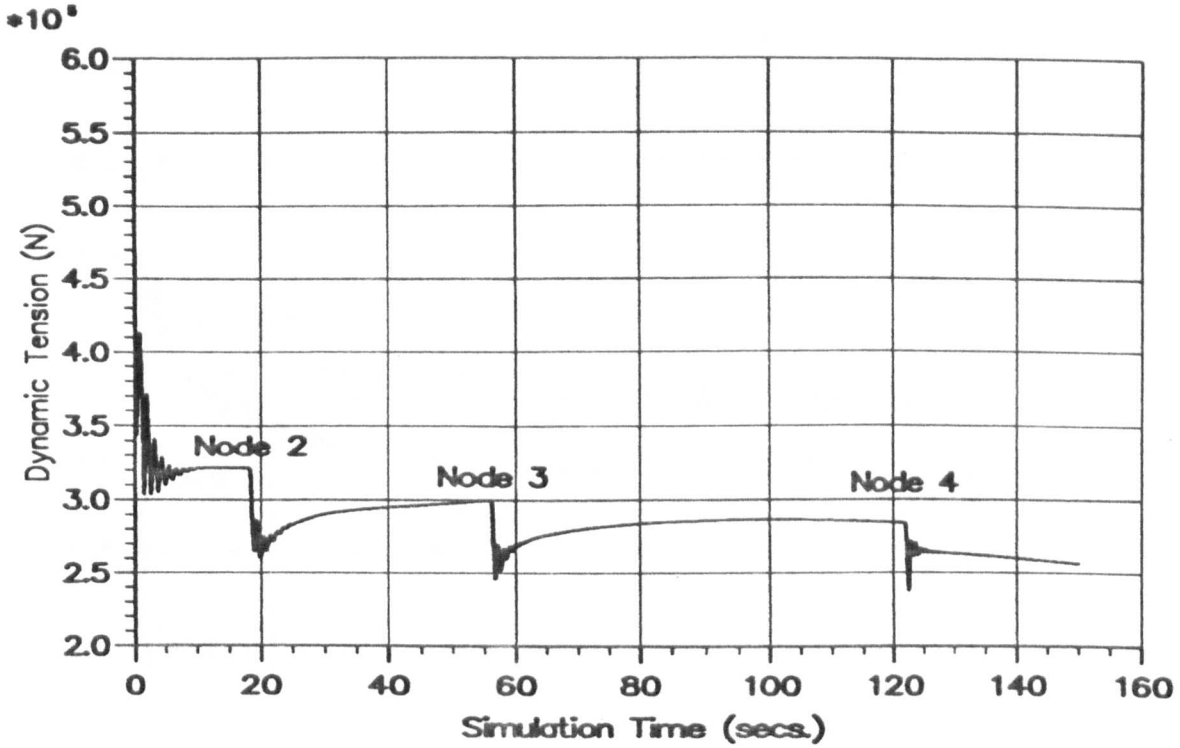

Figure 8.17 — Nodal Grounding With 10 Elements

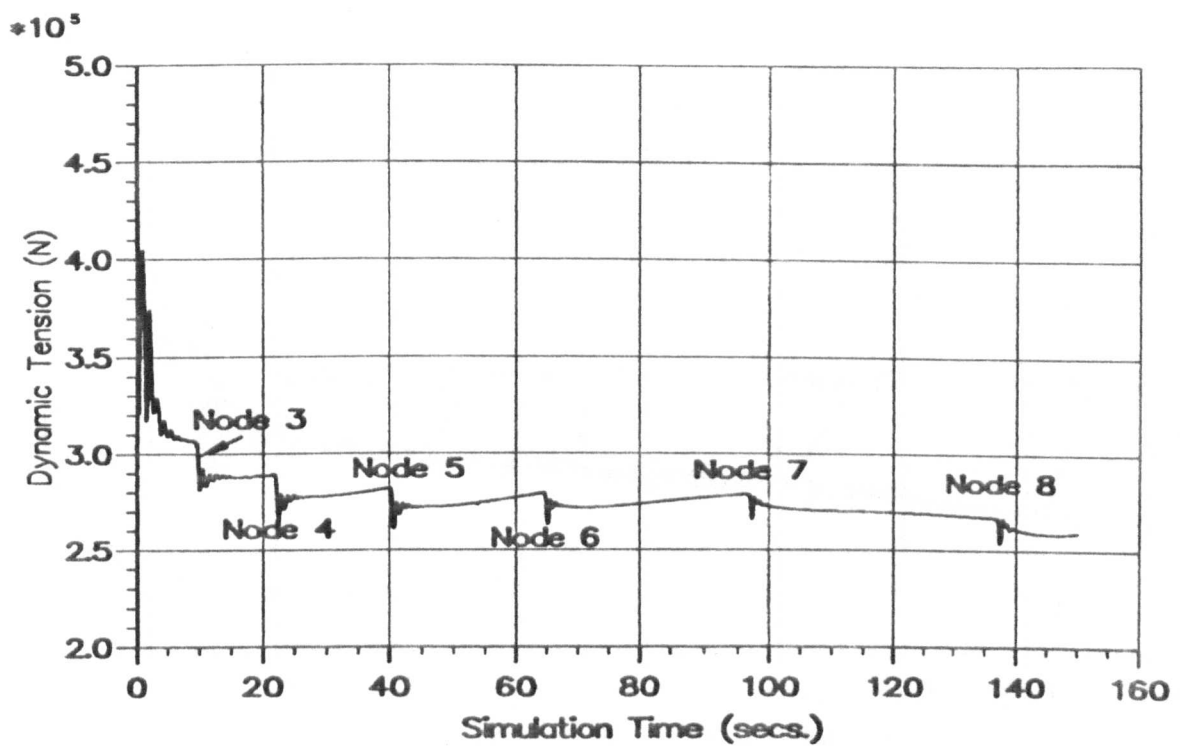

Figure 8.18 — Nodal Grounding With 20 Elements

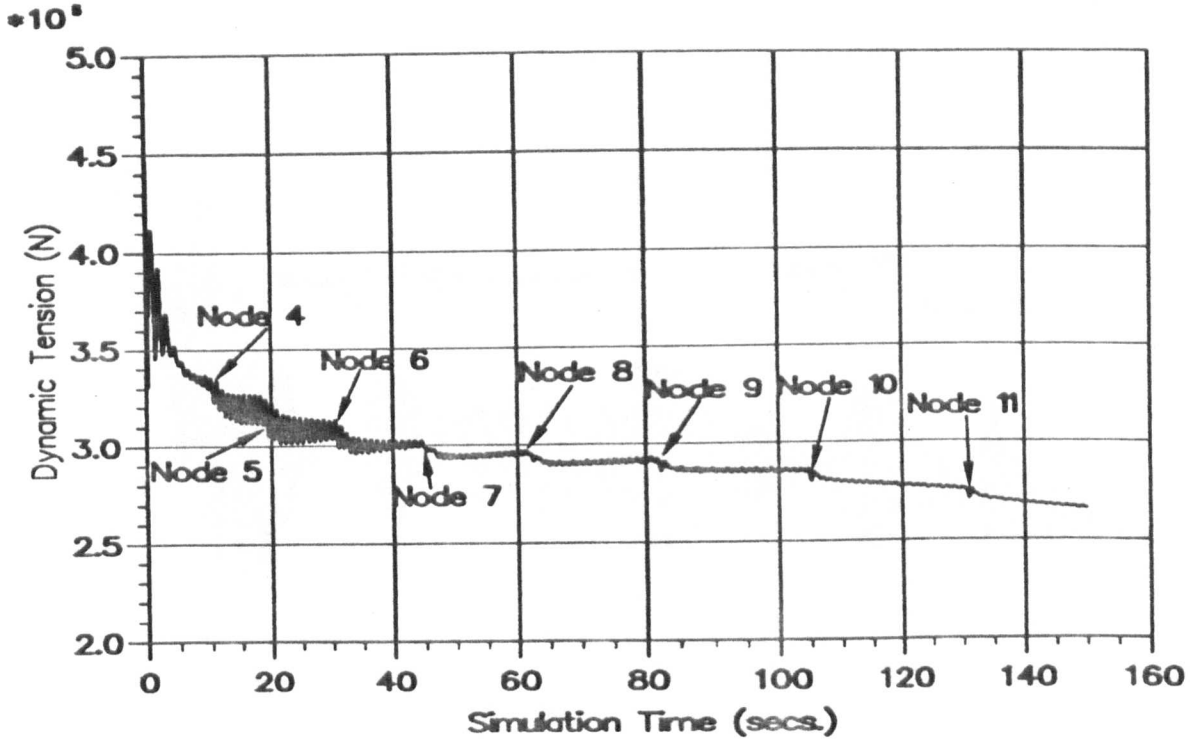

Figure 8.19 — Nodal Grounding With 30 Elements

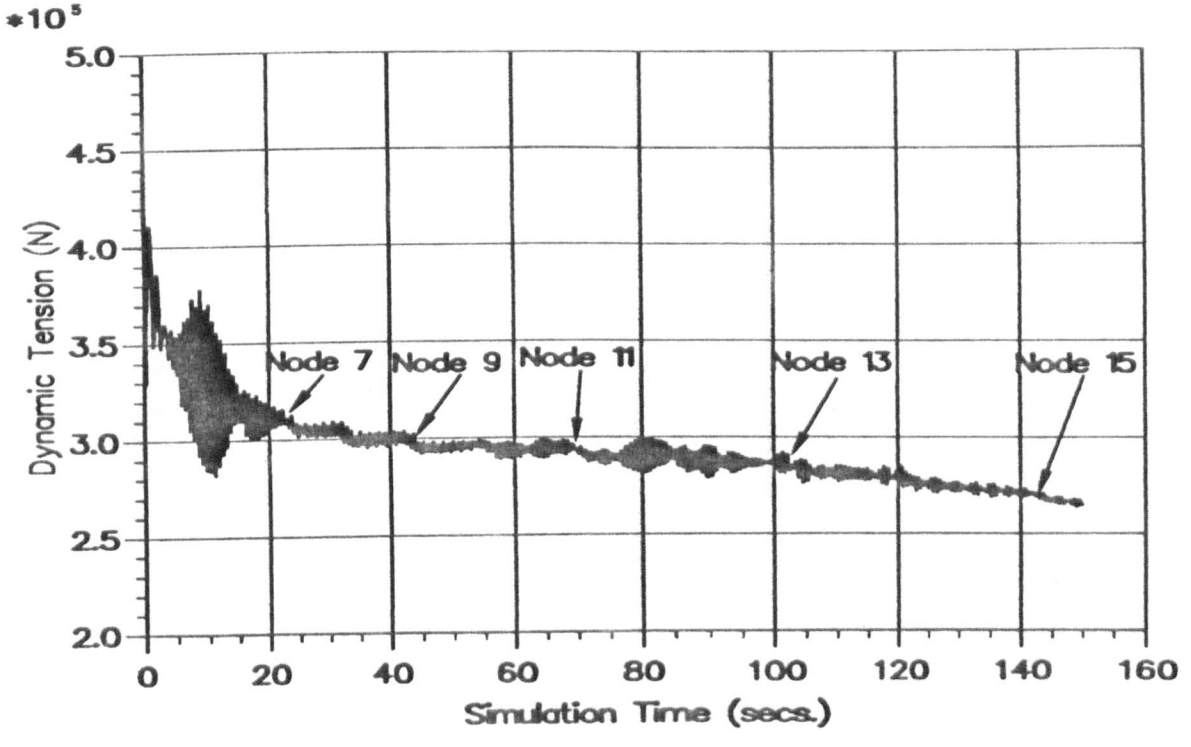

Figure 8.20 — Nodal Grounding With 40 Elements

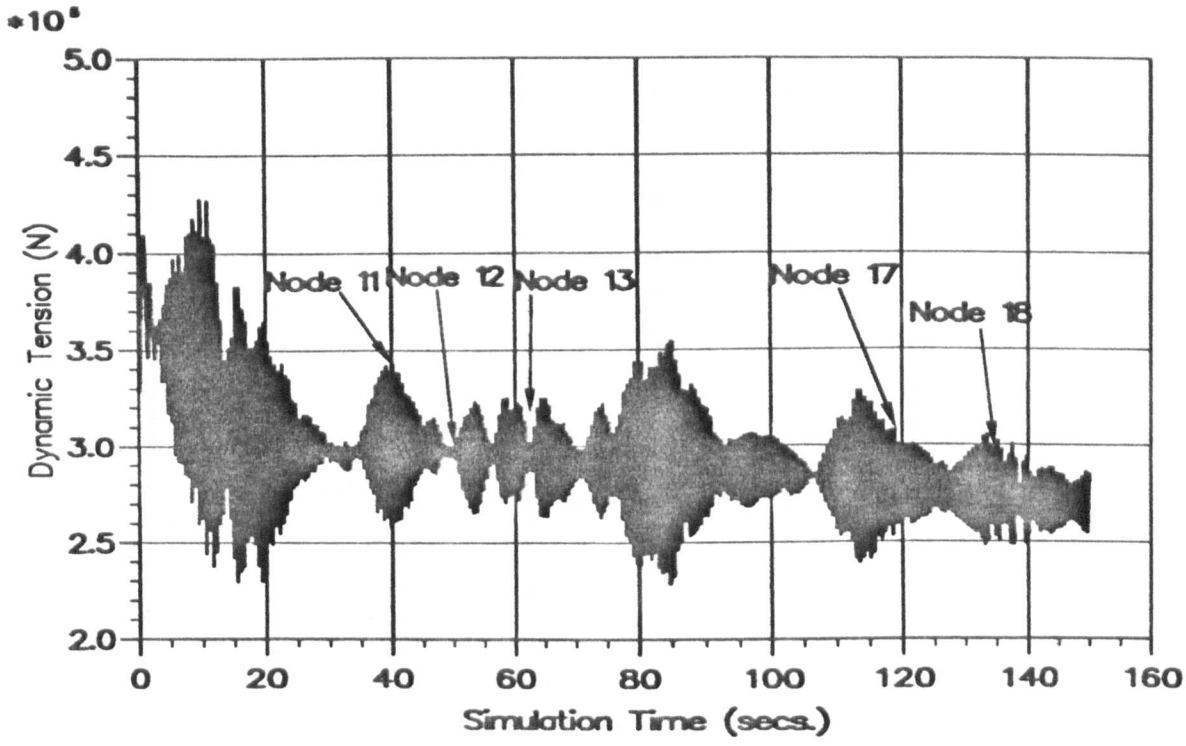

Figure 8.21 — Nodal Grounding With 50 Elements

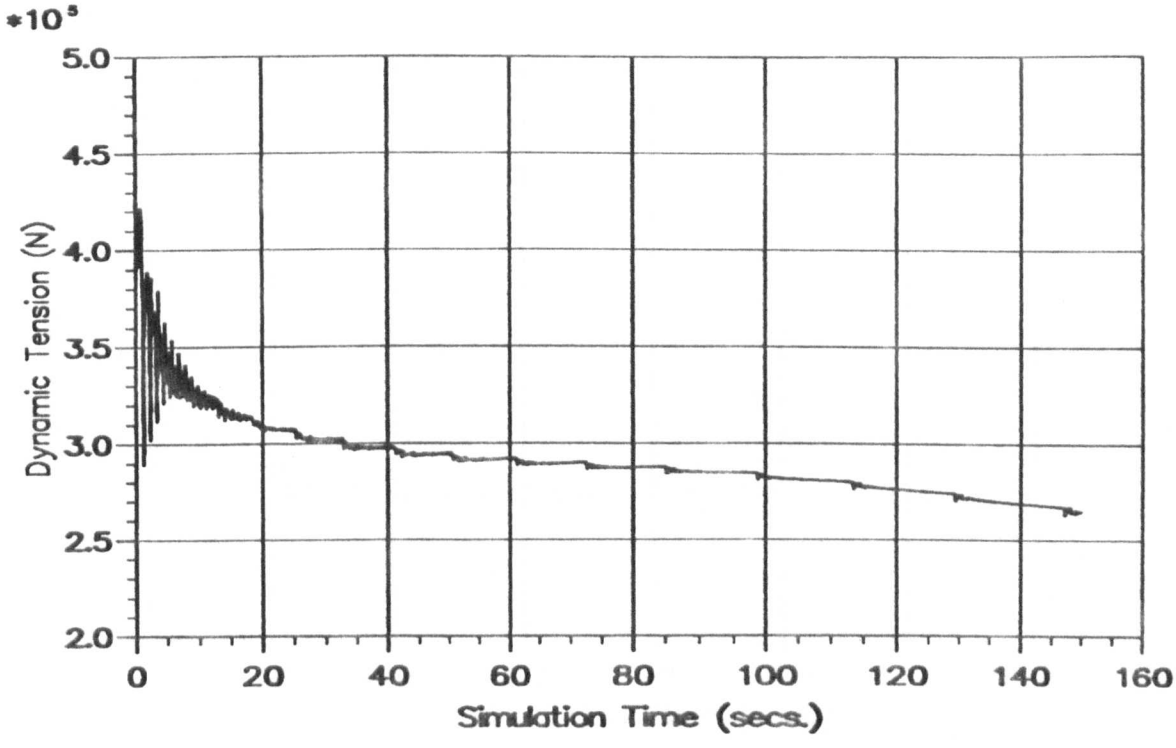

Figure 8.22 — Nodal Grounding With 50 Elements, $\Delta t = 0.02$

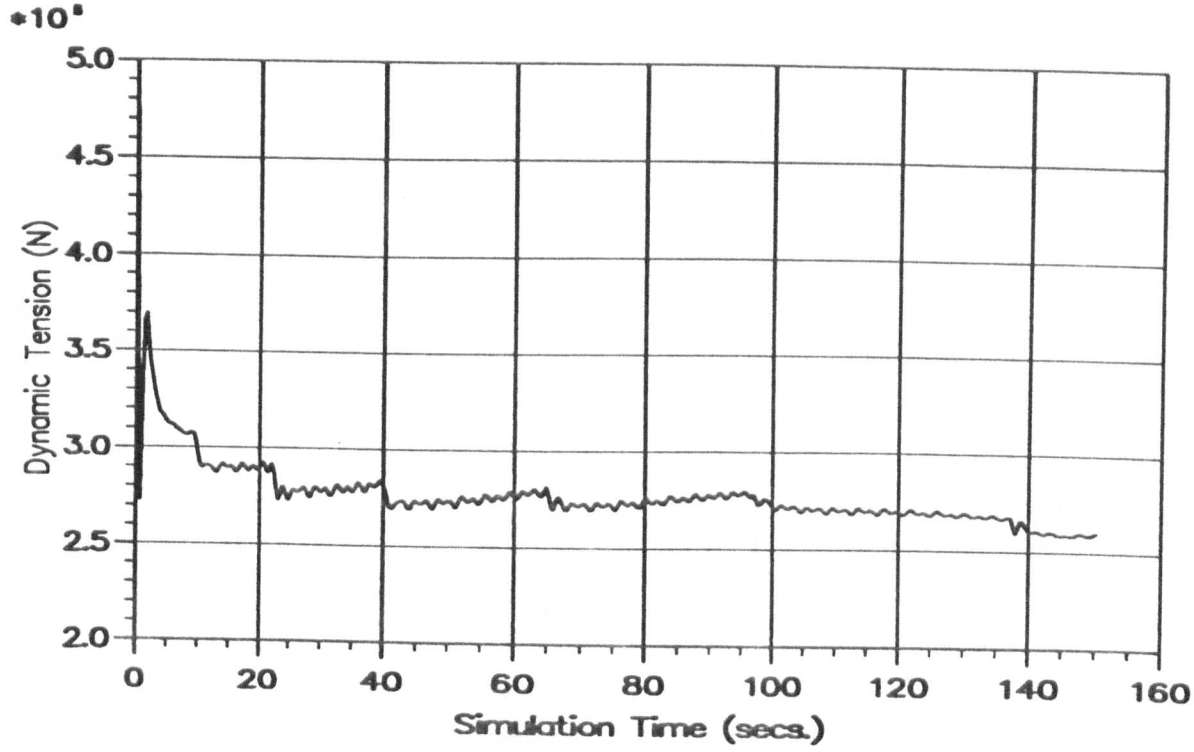

Figure 8.23 — Time Step = 0.35 secs.

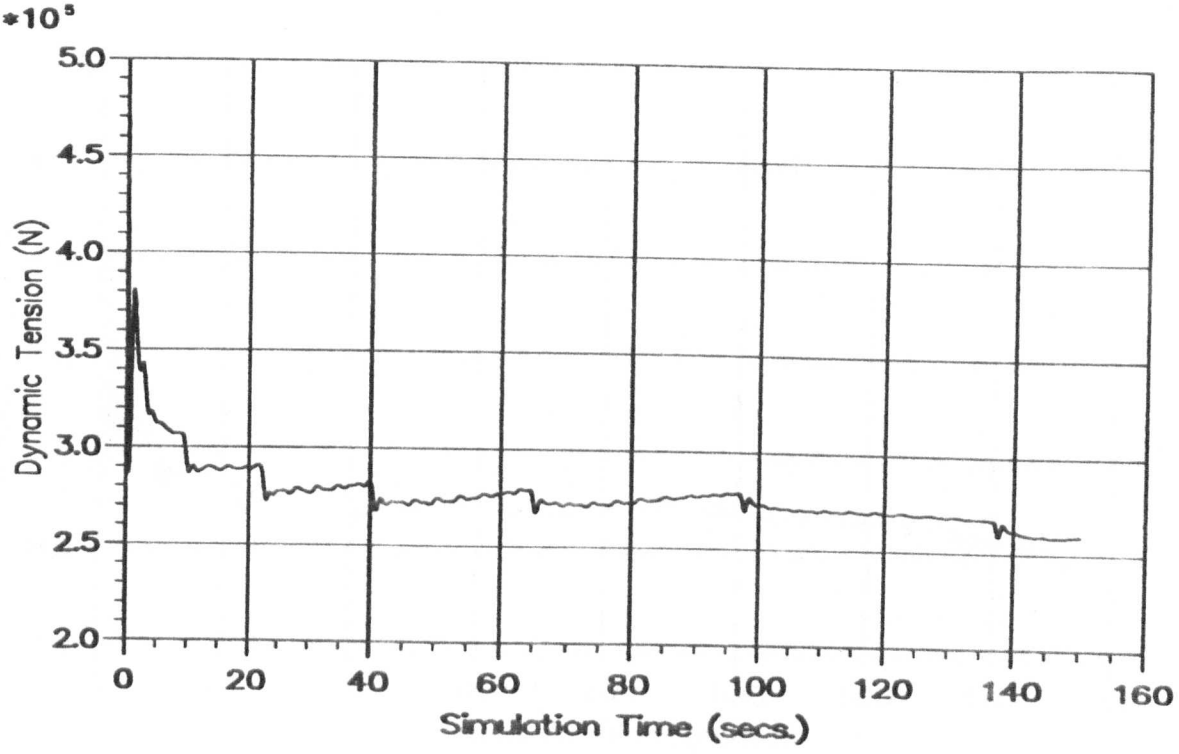

Figure 8.24 — Time Step = 0.25 secs.

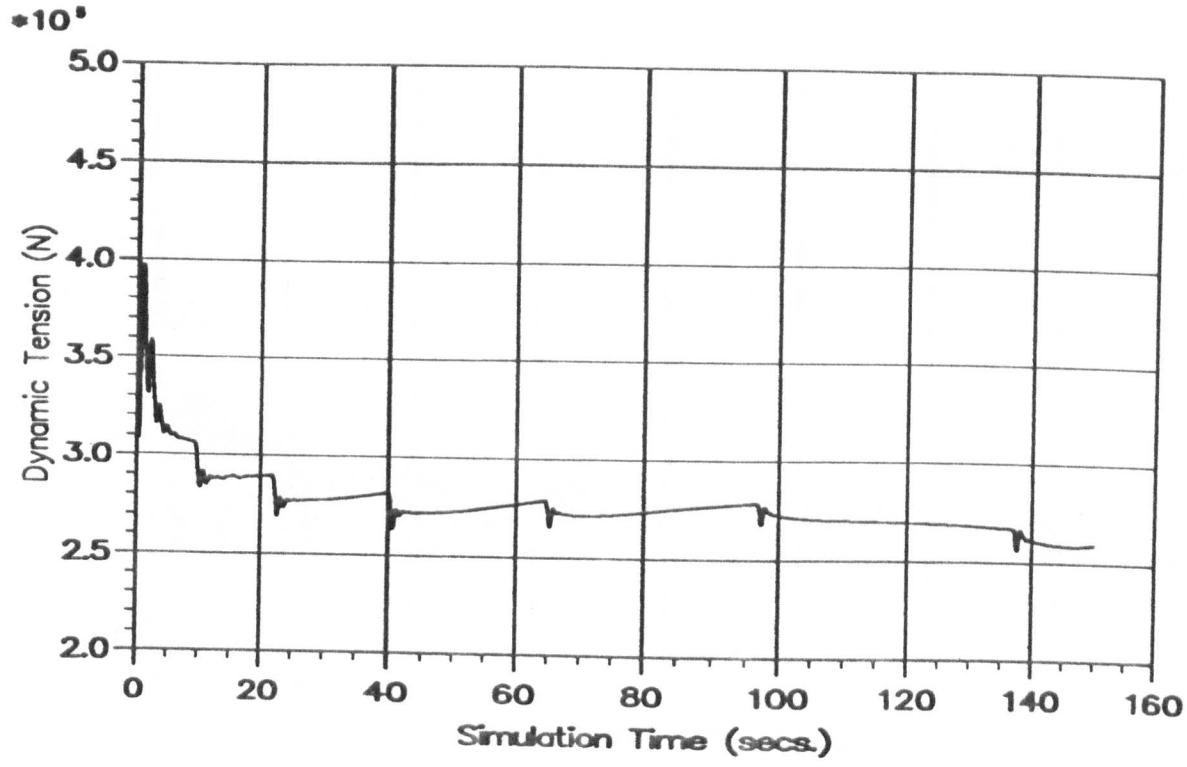

Figure 8.25 — Time Step = 0.15 secs.

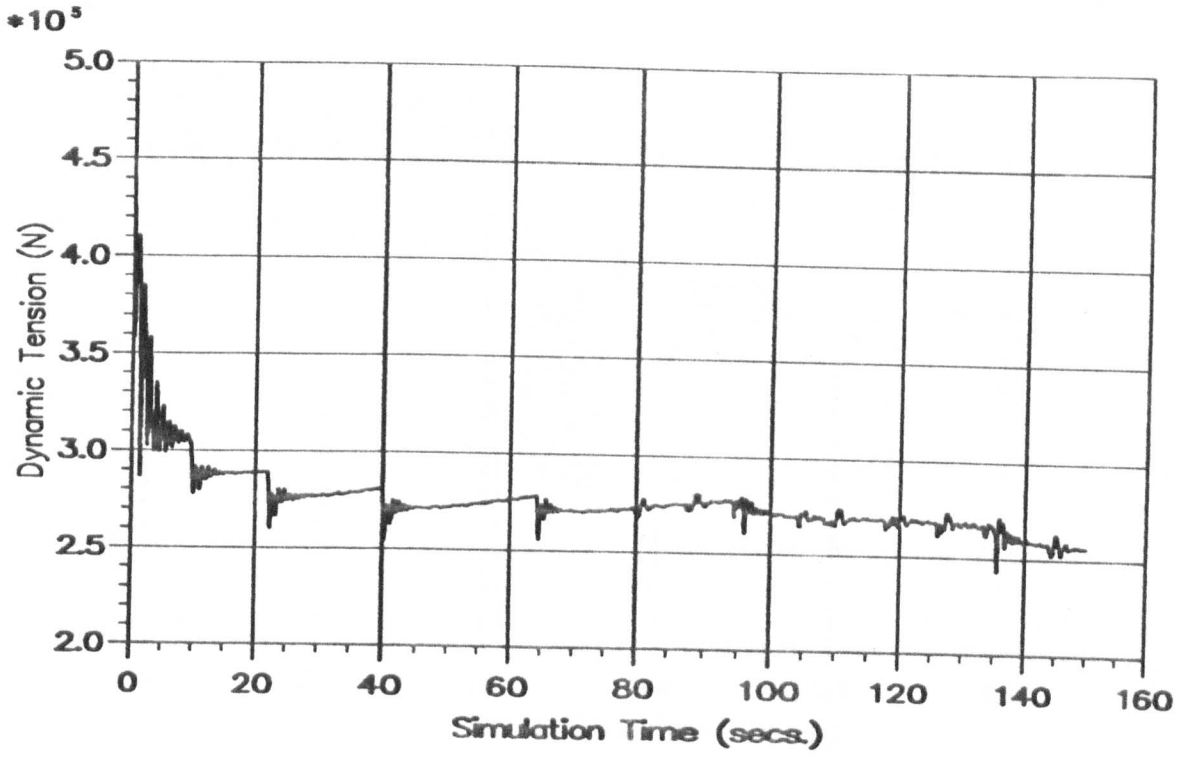

Figure 8.26 — Time Step = 0.05 secs.

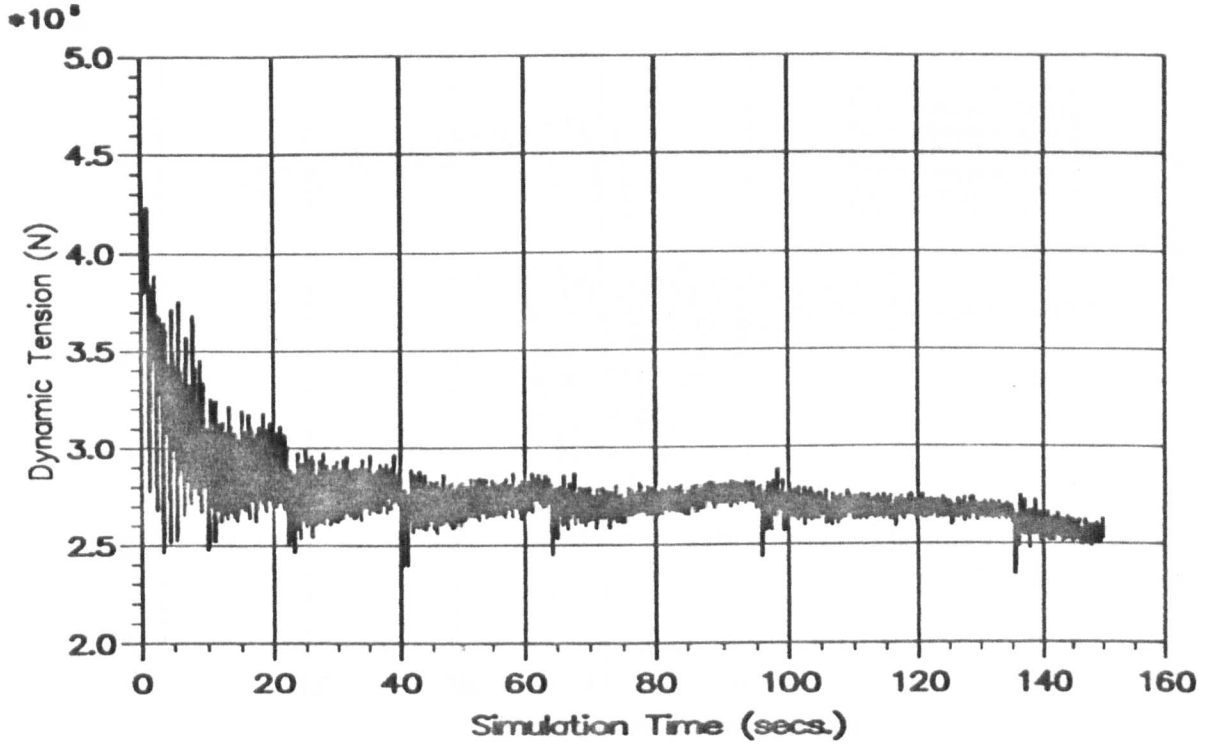

Figure 8.27 — Time Step = 0.001 secs.

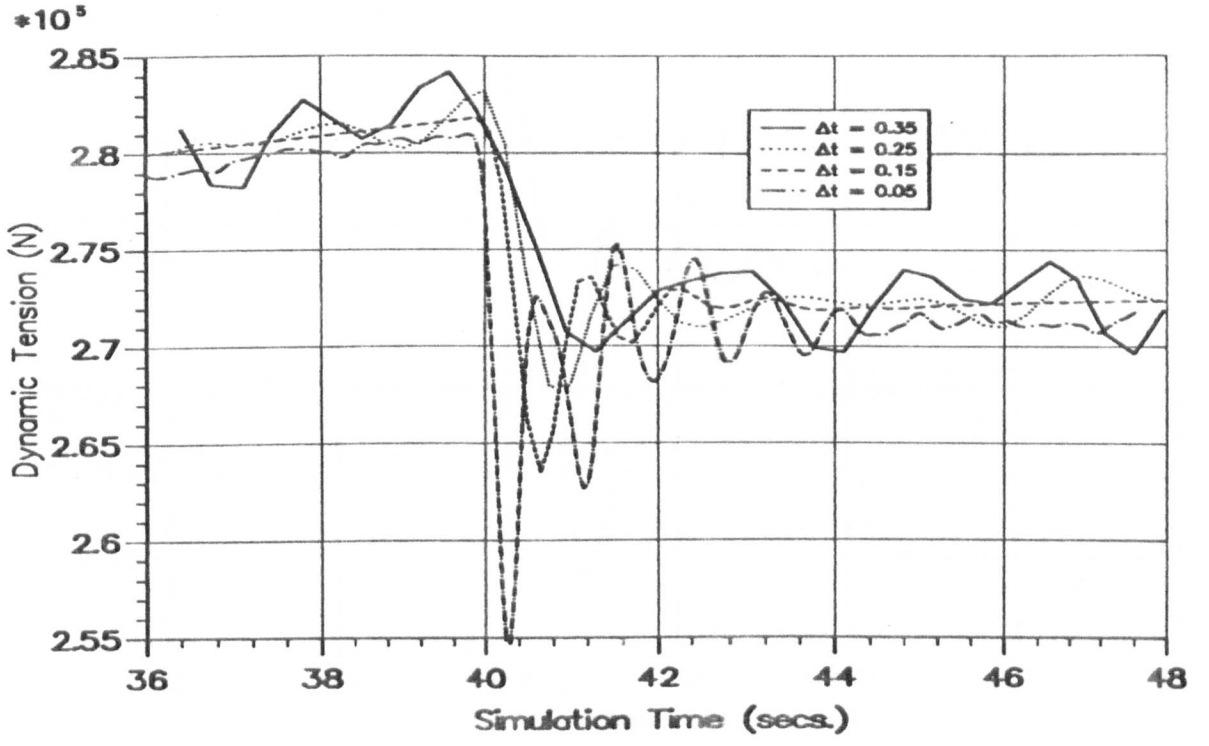

Figure 8.28 — Grounding of Node 5 in Detail

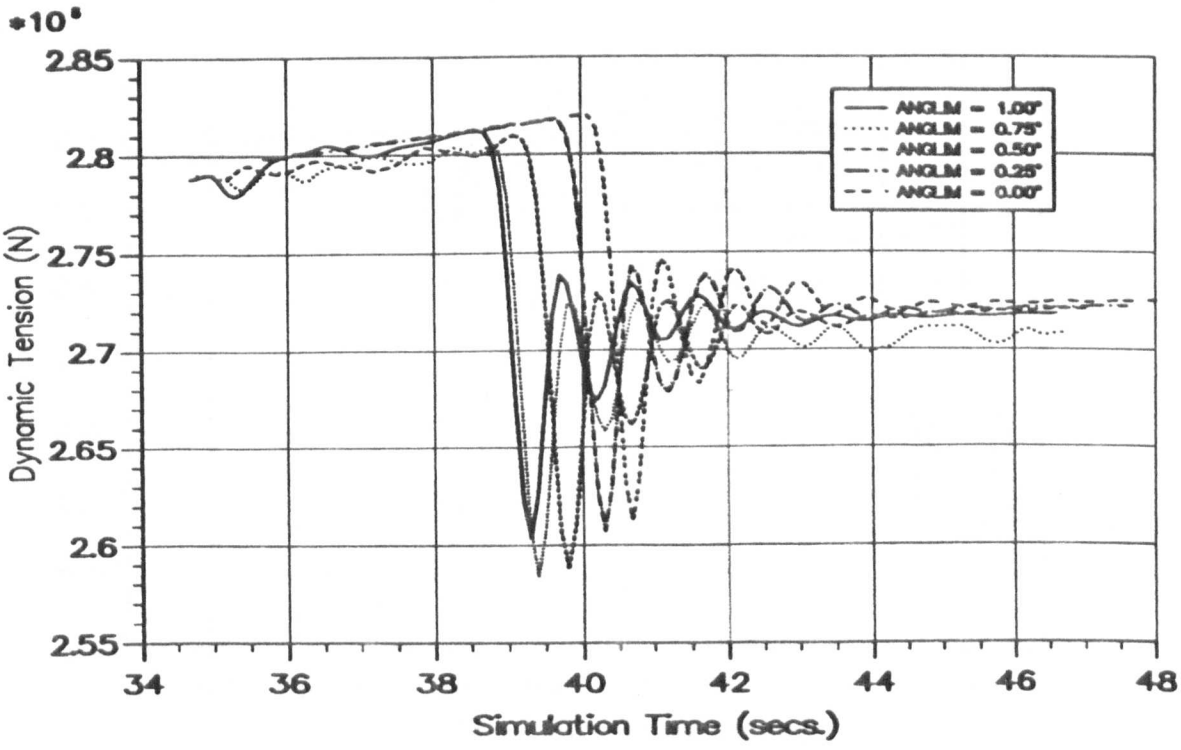

Figure 8.29 — Influence of Grounding Angle on Node 5

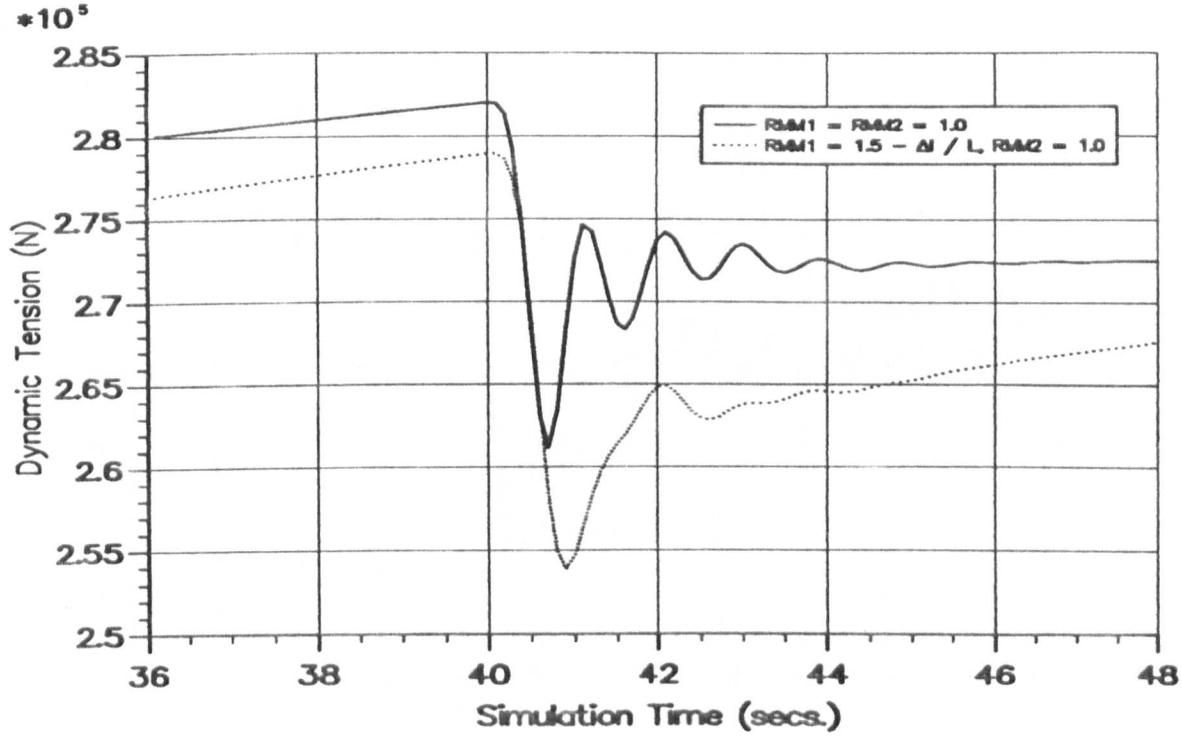

Figure 8.30 — Node 5 Grounding for RMM1 = 1 and $(1.5 - \frac{\Delta l}{L})$

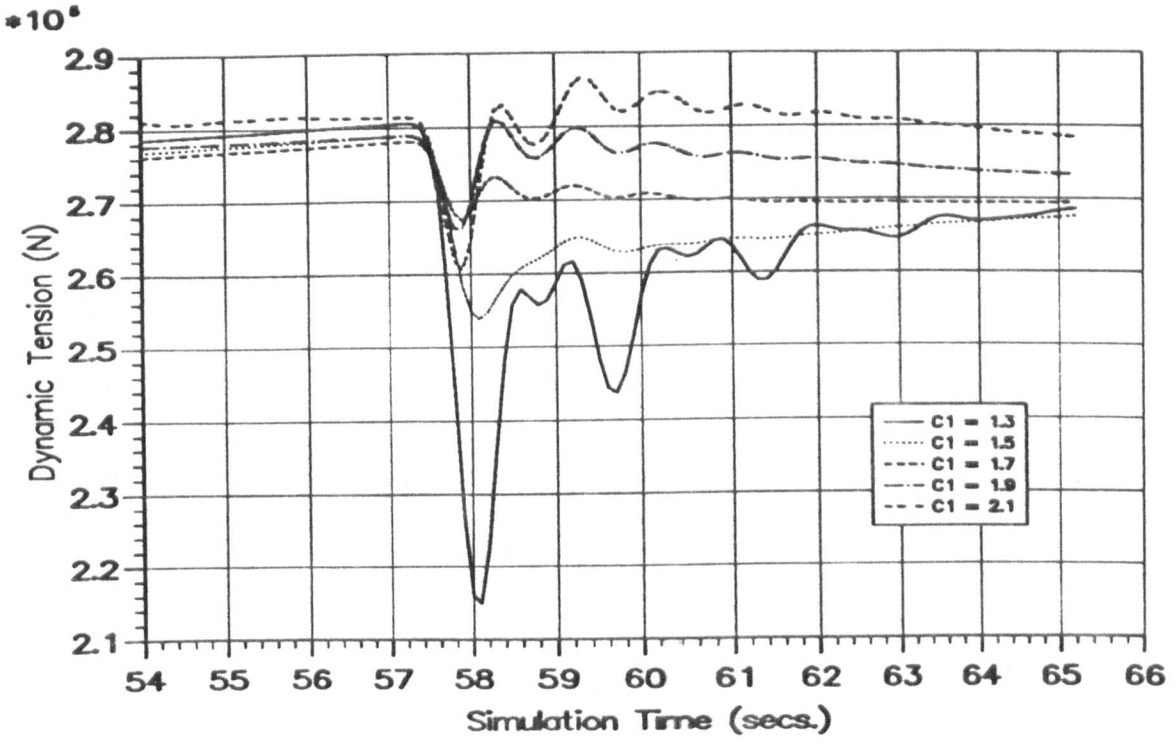

Figure 8.31 — Influence of $C1$ Upon the Solution

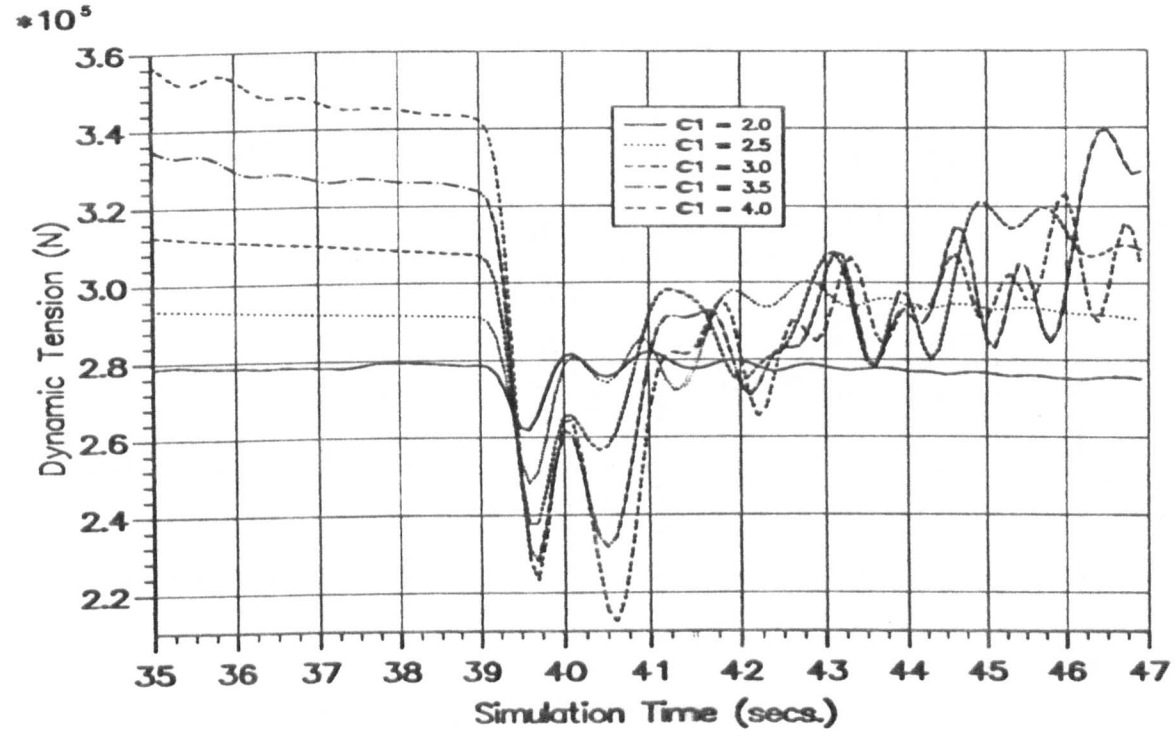

Figure 8.32 — Influence of Larger Values of $C1$ Upon the Solution

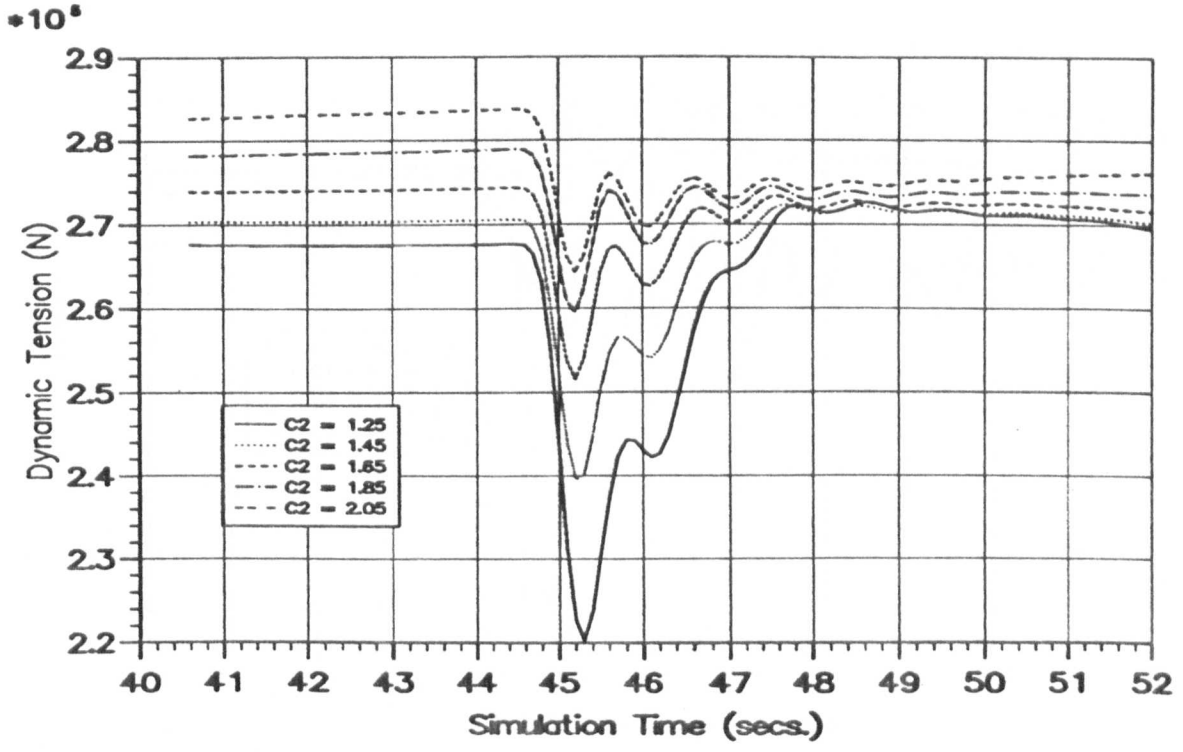

Figure 8.33 — Influence of $C2$ Upon the Solution

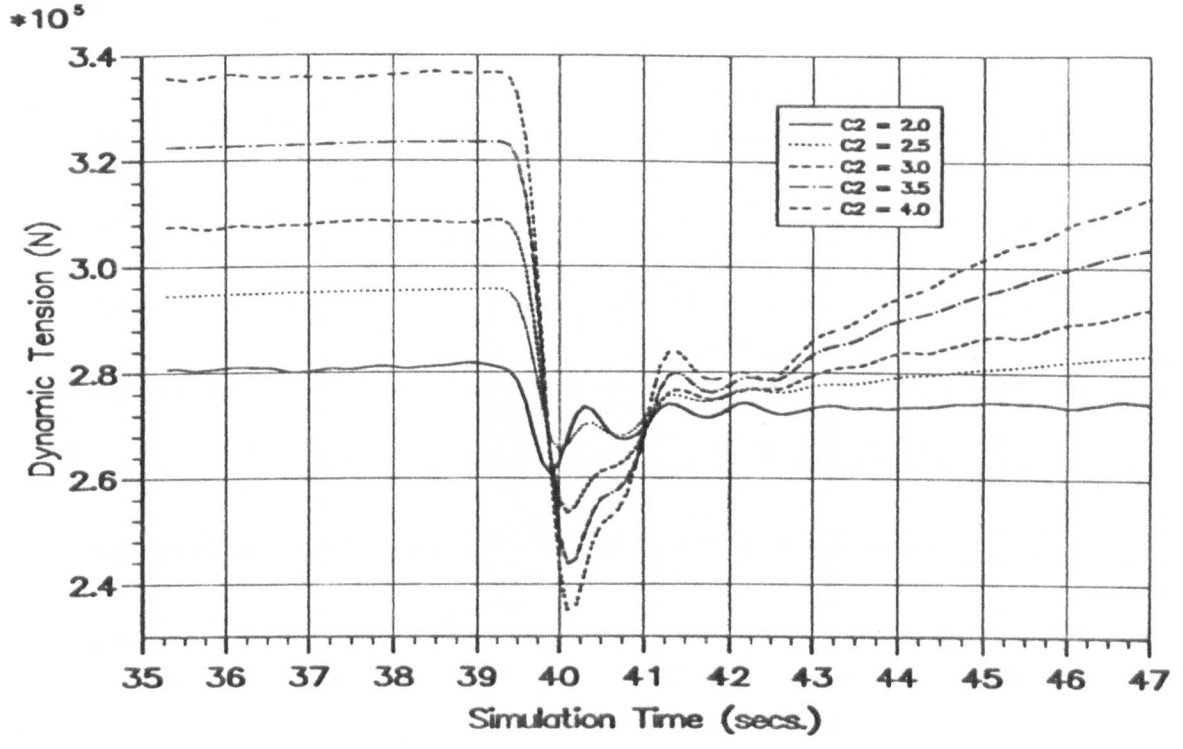

Figure 8.34 — Influence of Larger Values of $C2$ Upon the Solution

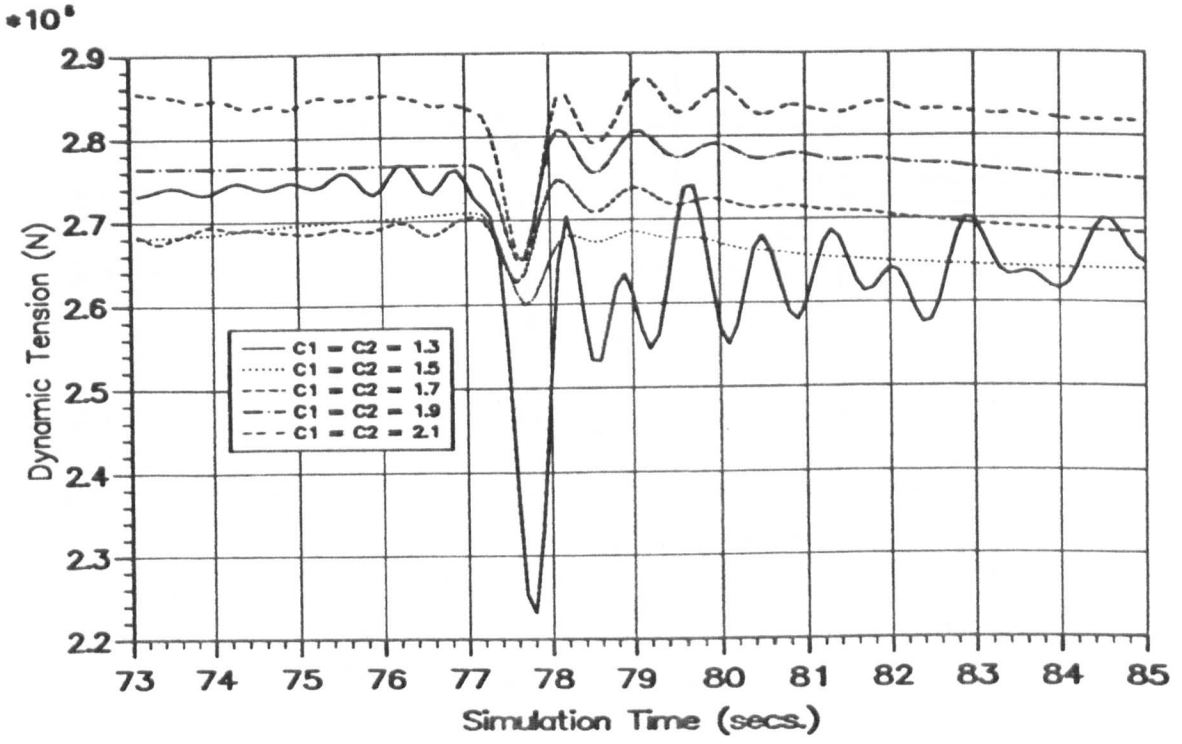

Figure 8.35 — Influence of $C1 = C2$ Upon the Solution

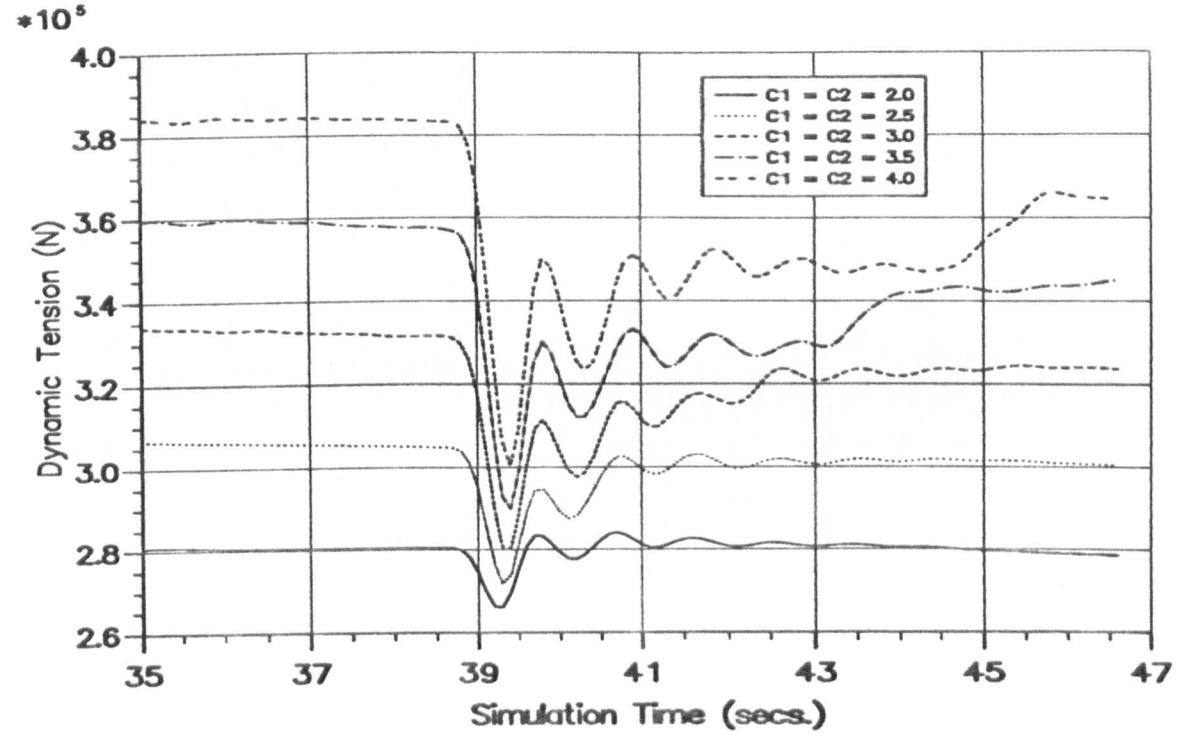

Figure 8.36 — Influence of Larger Values of $C1 = C2$ Upon the Solution

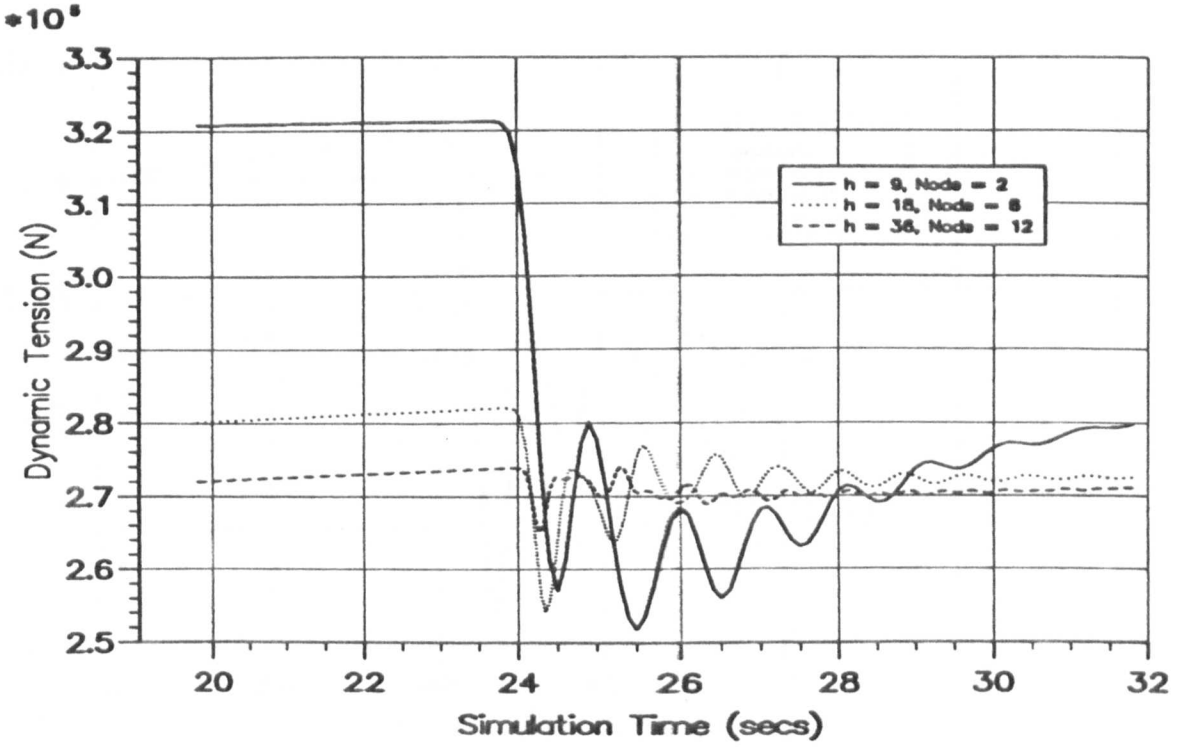

Figure 8.37 — Effect of Reducing Nodal Mass Maintaining a $\frac{\Delta t}{l}$ Ratio

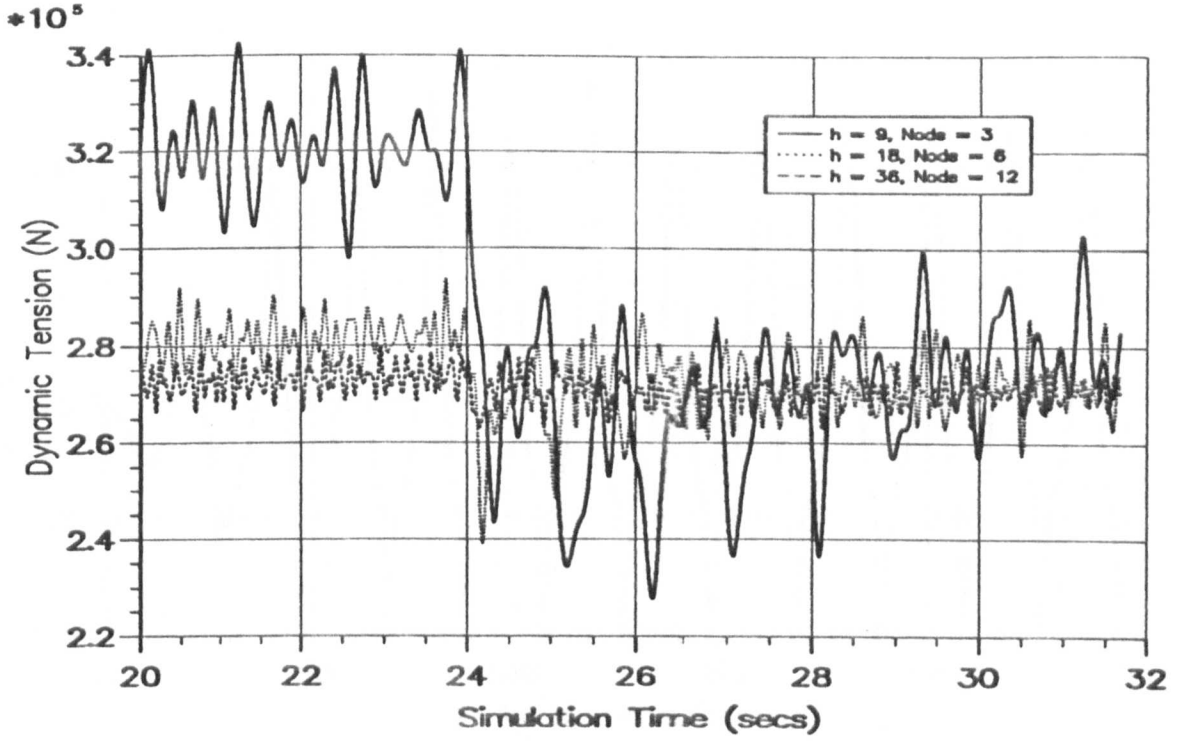

Figure 8.38 — Effect of Reducing Nodal Mass With $\Delta t = 0.001$ secs.

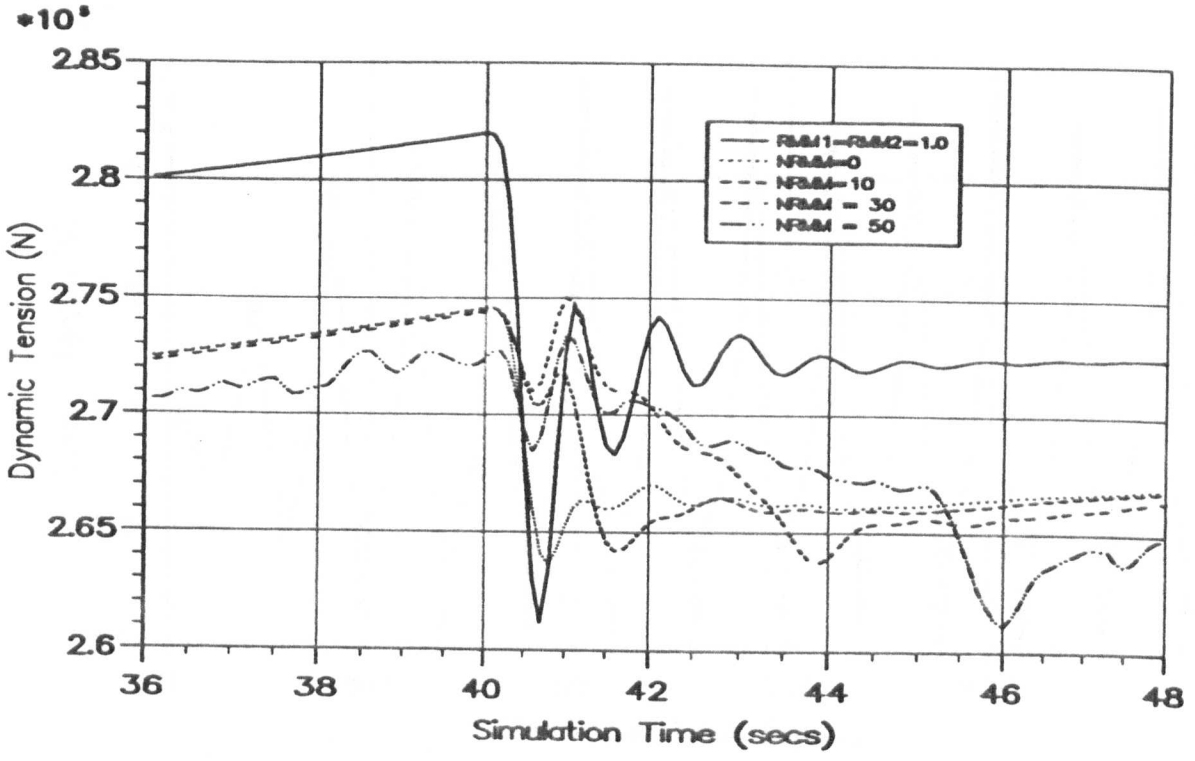

Figure 8.39 — Effect of Ramping Changes in Mass Multipliers

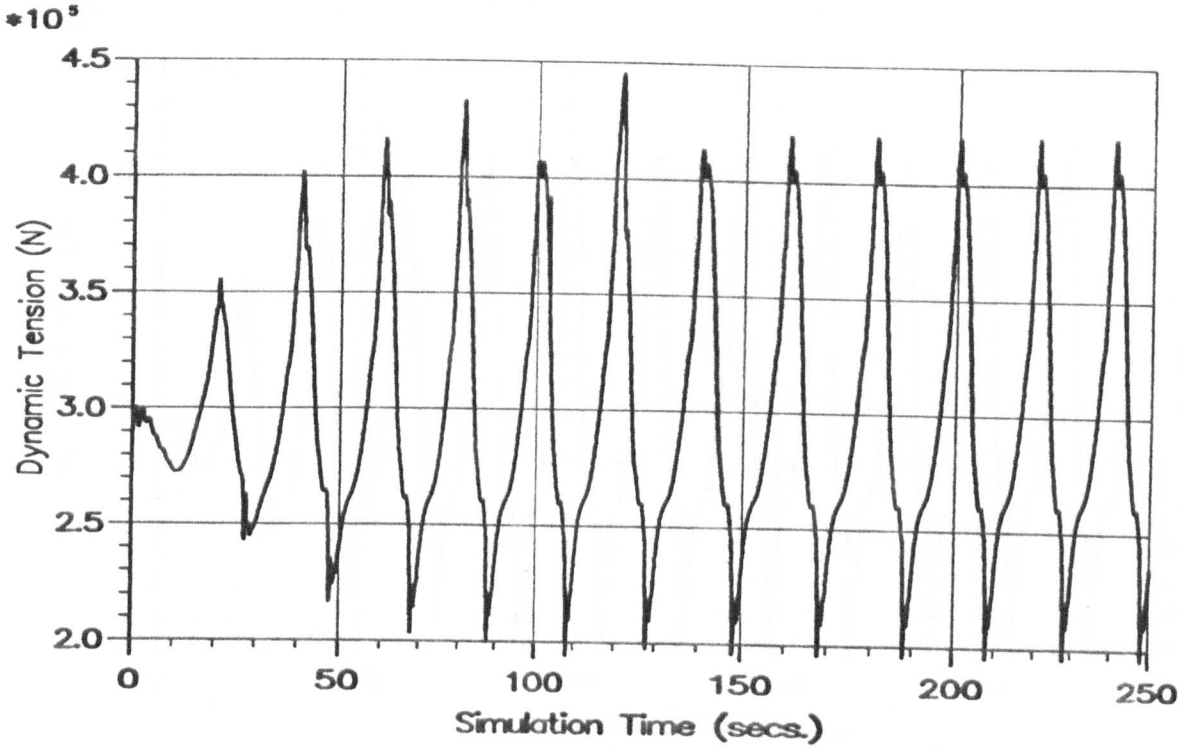

Figure 8.40 — 'Original' Mass Multiplier Changes

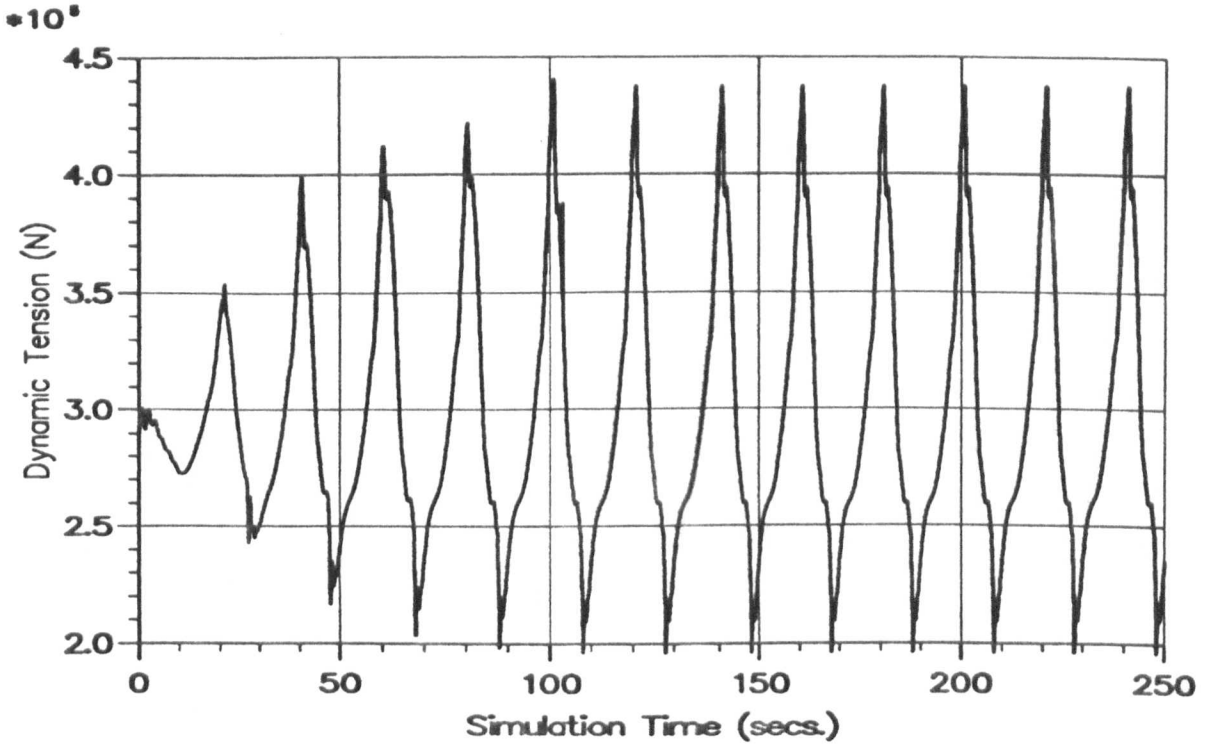

Figure 8.41 — Marginally Increasing Weight of Grounded Node

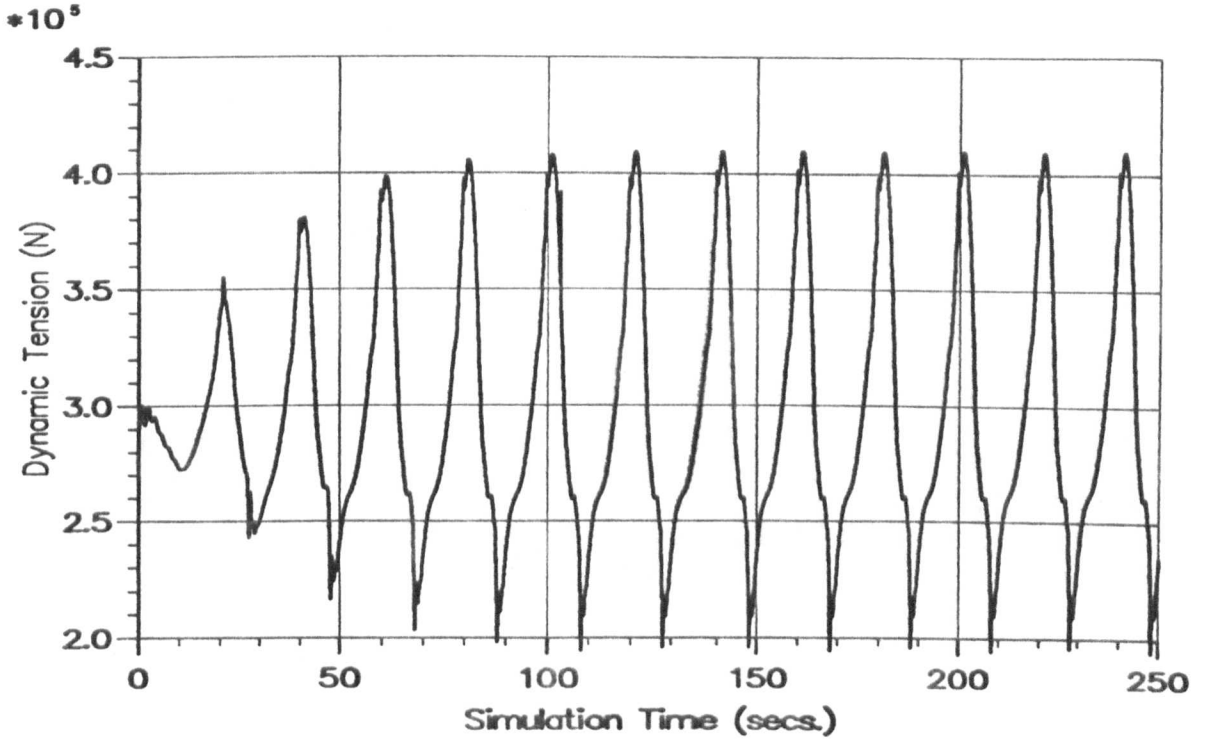

Figure 8.42 — Effect of 'Fixing' the Lifted or Grounded Node

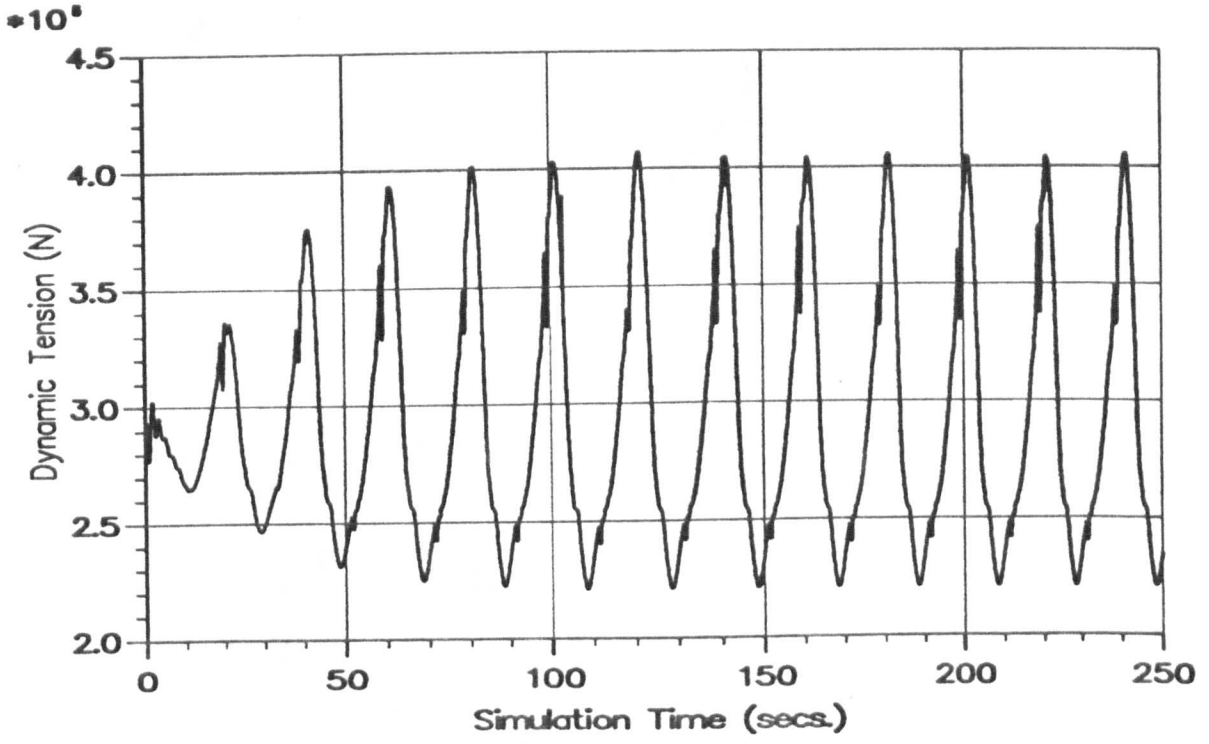

Figure 8.43 — Different Values of C1 and C2

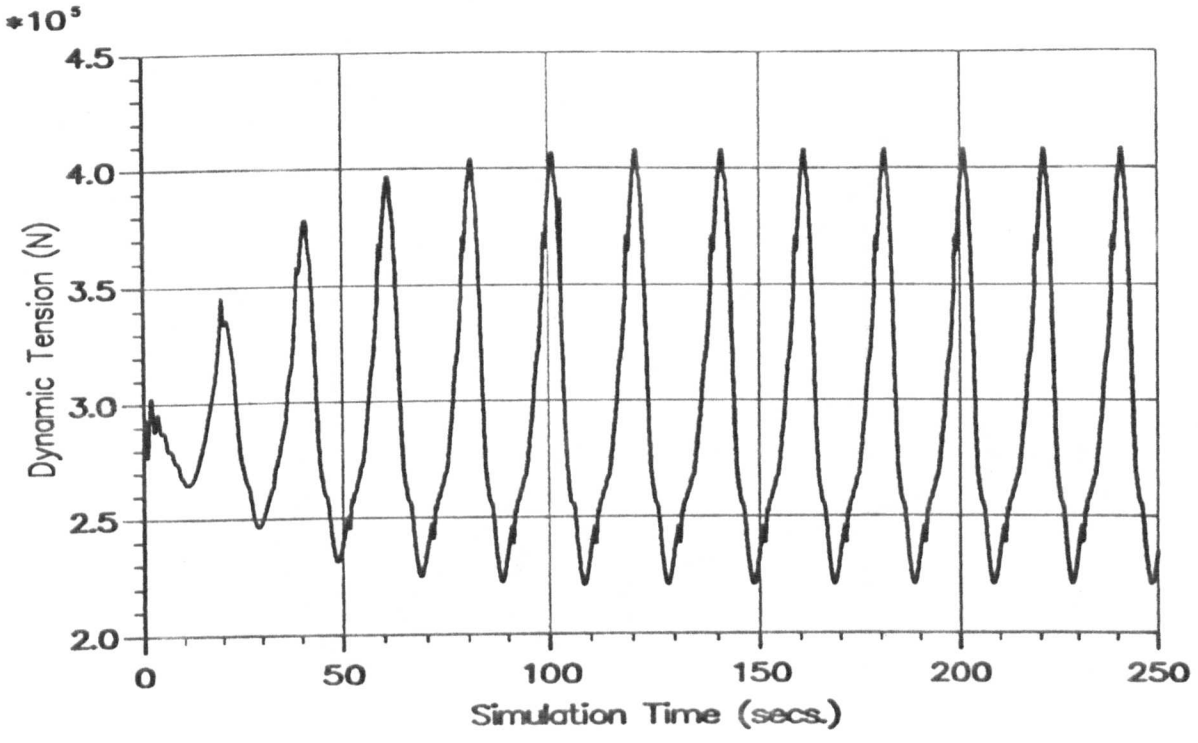

Figure 8.44 — Ramping and 'Fixing' The Mass Multipliers

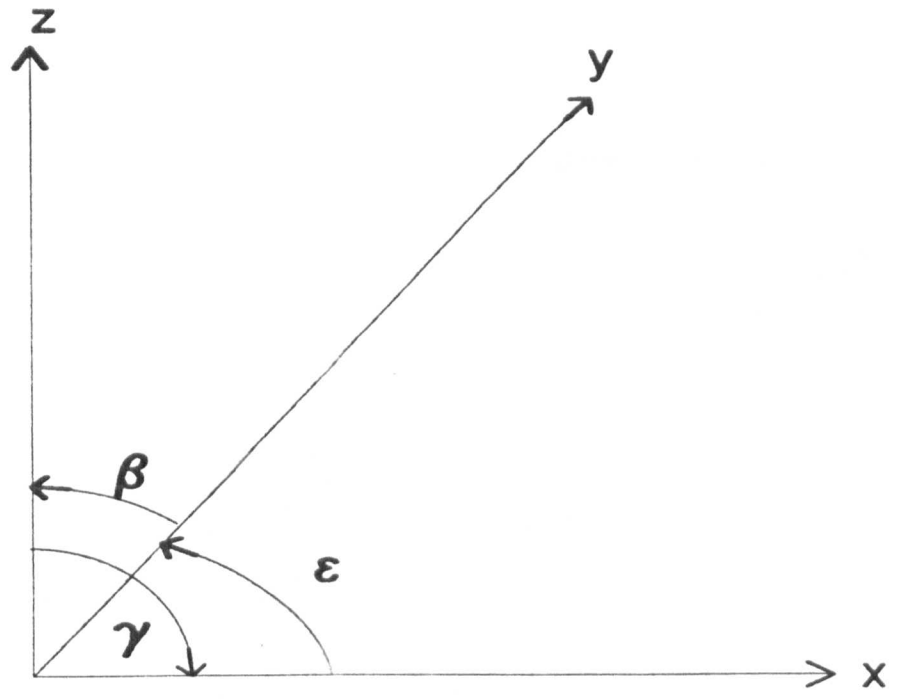

Figure A1 - Euler Rotations in A Right Handed Coordinate System

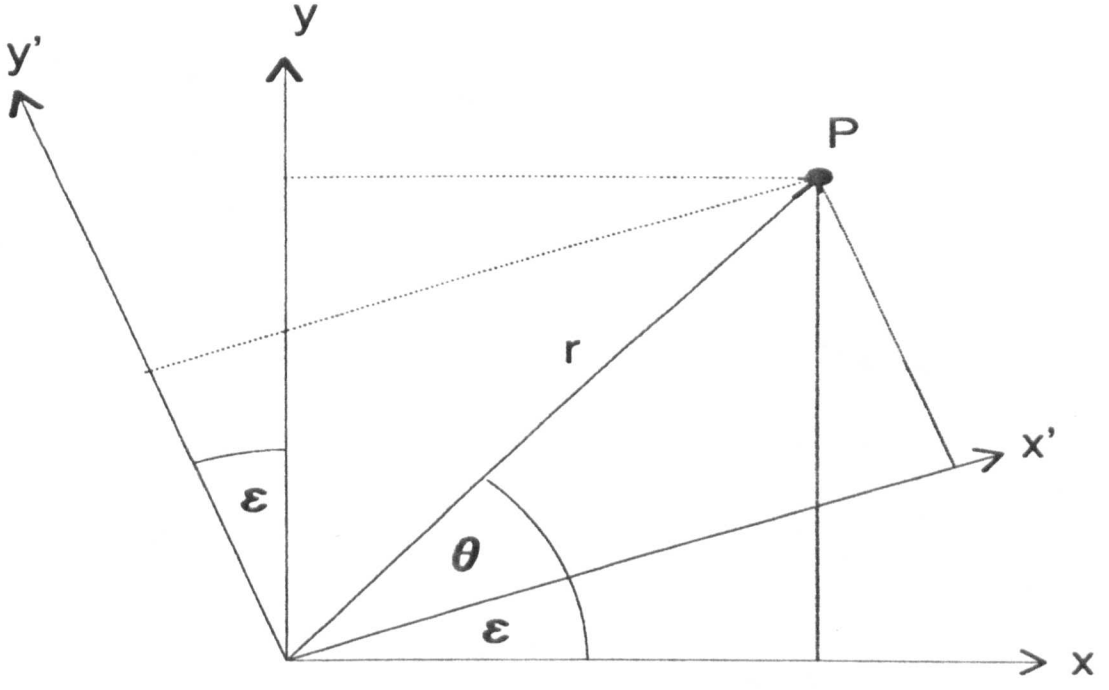

Figure A2 - Euler Rotations About The z Axis

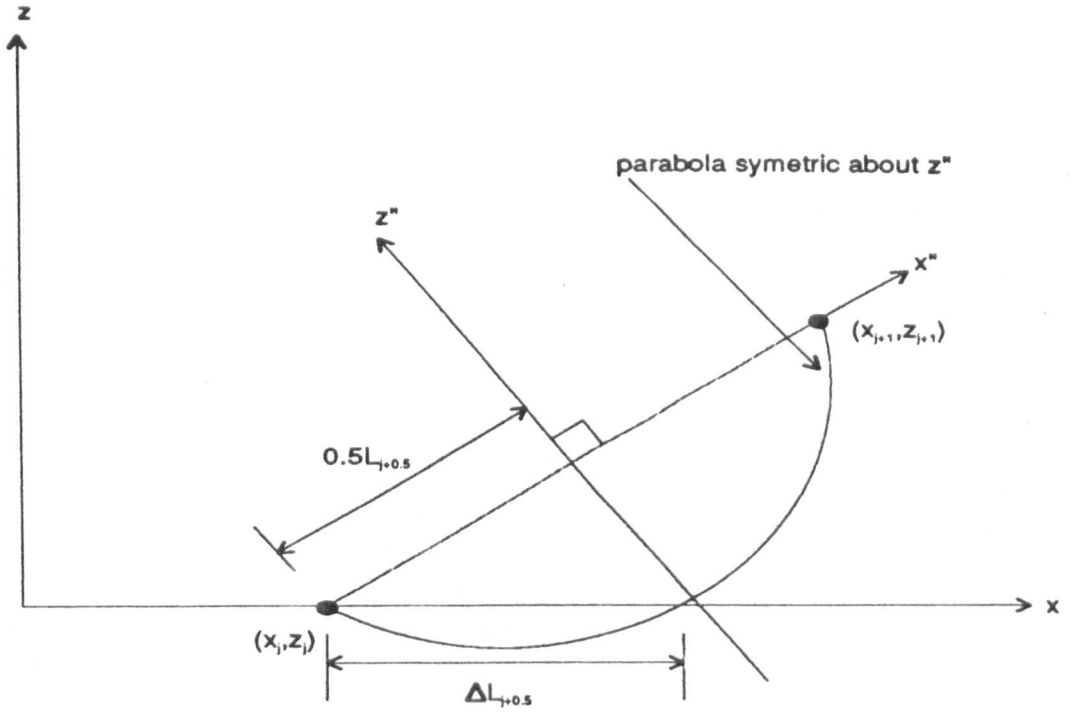

Figure F1 - Parabola Used For Mass Modification

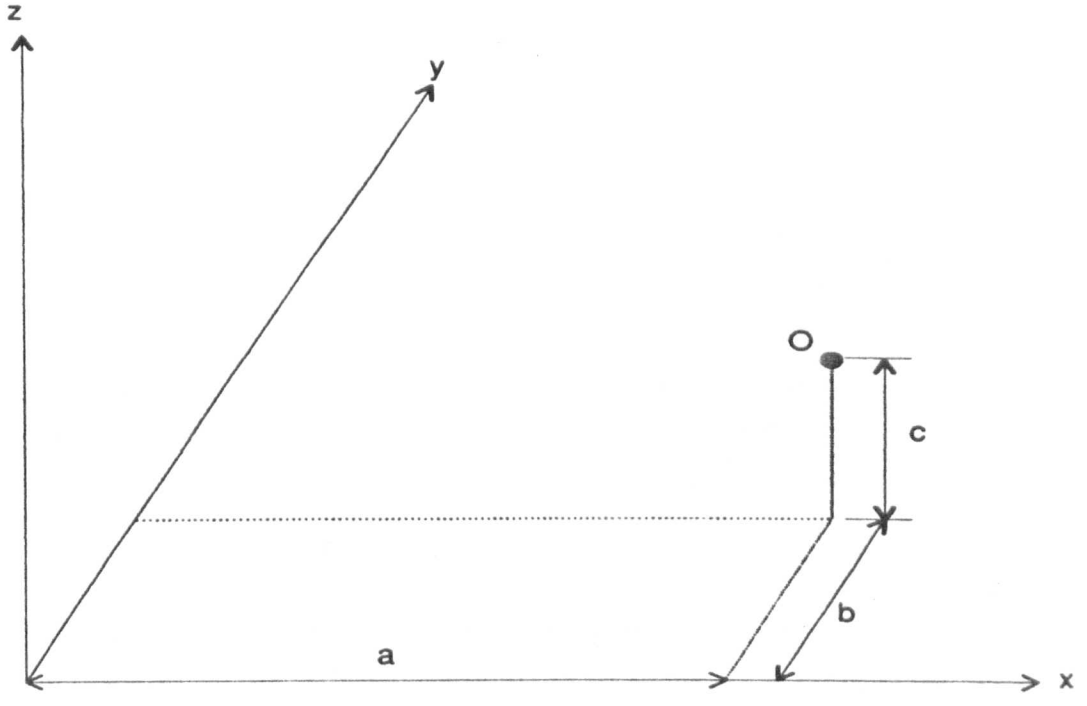

Figure F2 - Coordinates of Translation

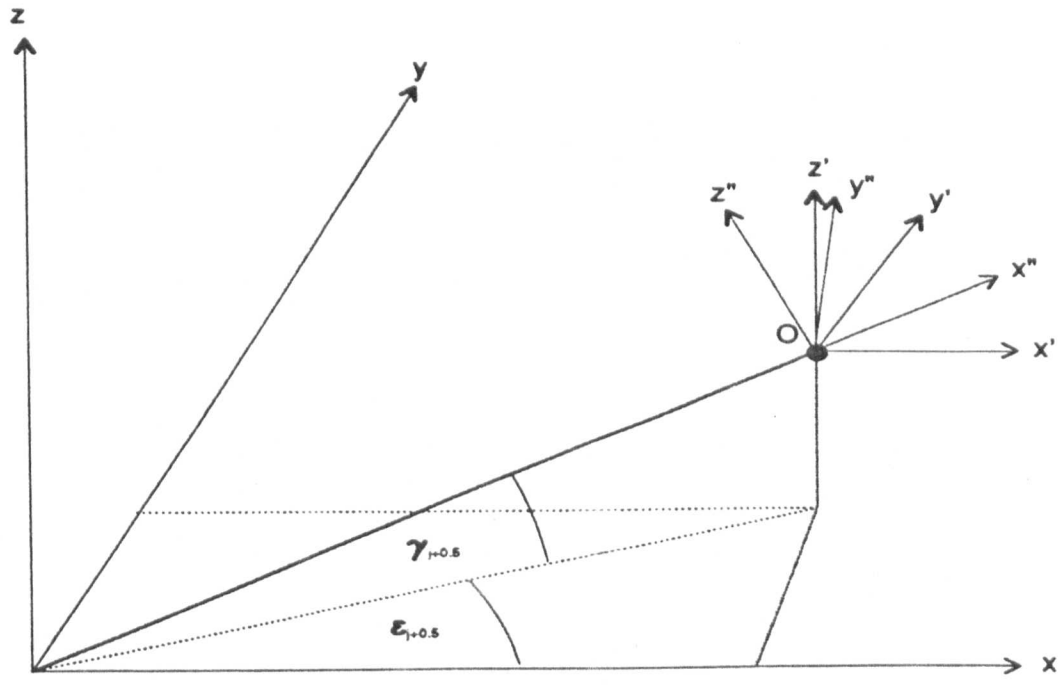

Figure F3 - Rotational Transformations

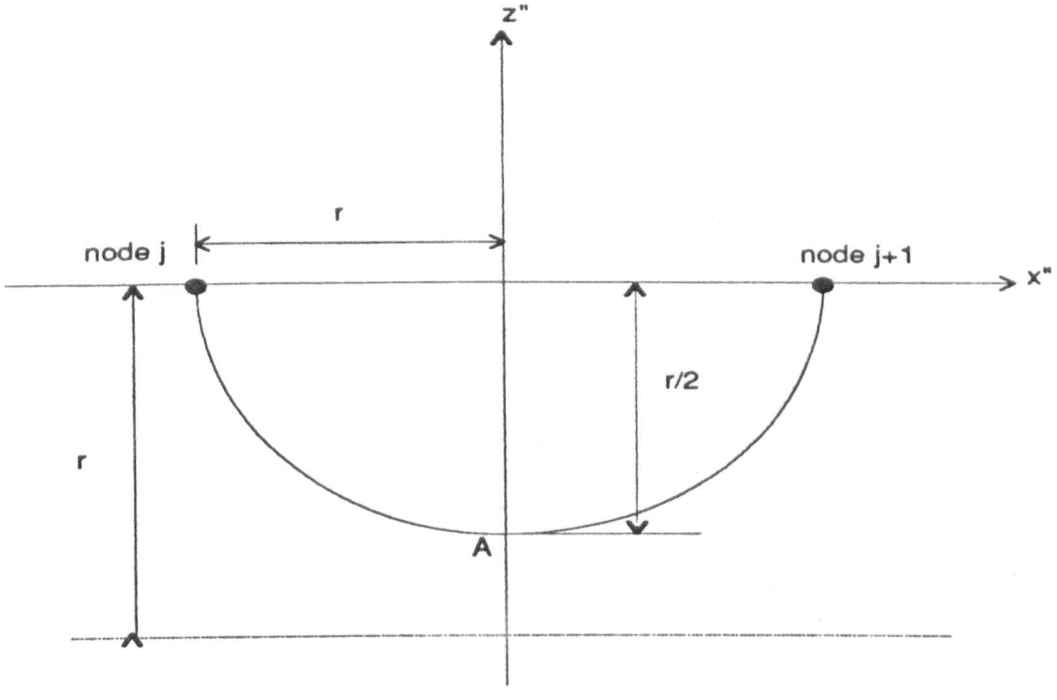

Figure F4 - Parabola Definition in the Local Axes